Mathematical Problems in Engineering

Nanofluids and Entropy Analysis with Electroosmotic Phenomenon

Lead Guest Editor: Arshad Riaz
Guest Editors: Ahmad Zeeshan, Mohsan Hassan, and Mohammad Reza Safaei

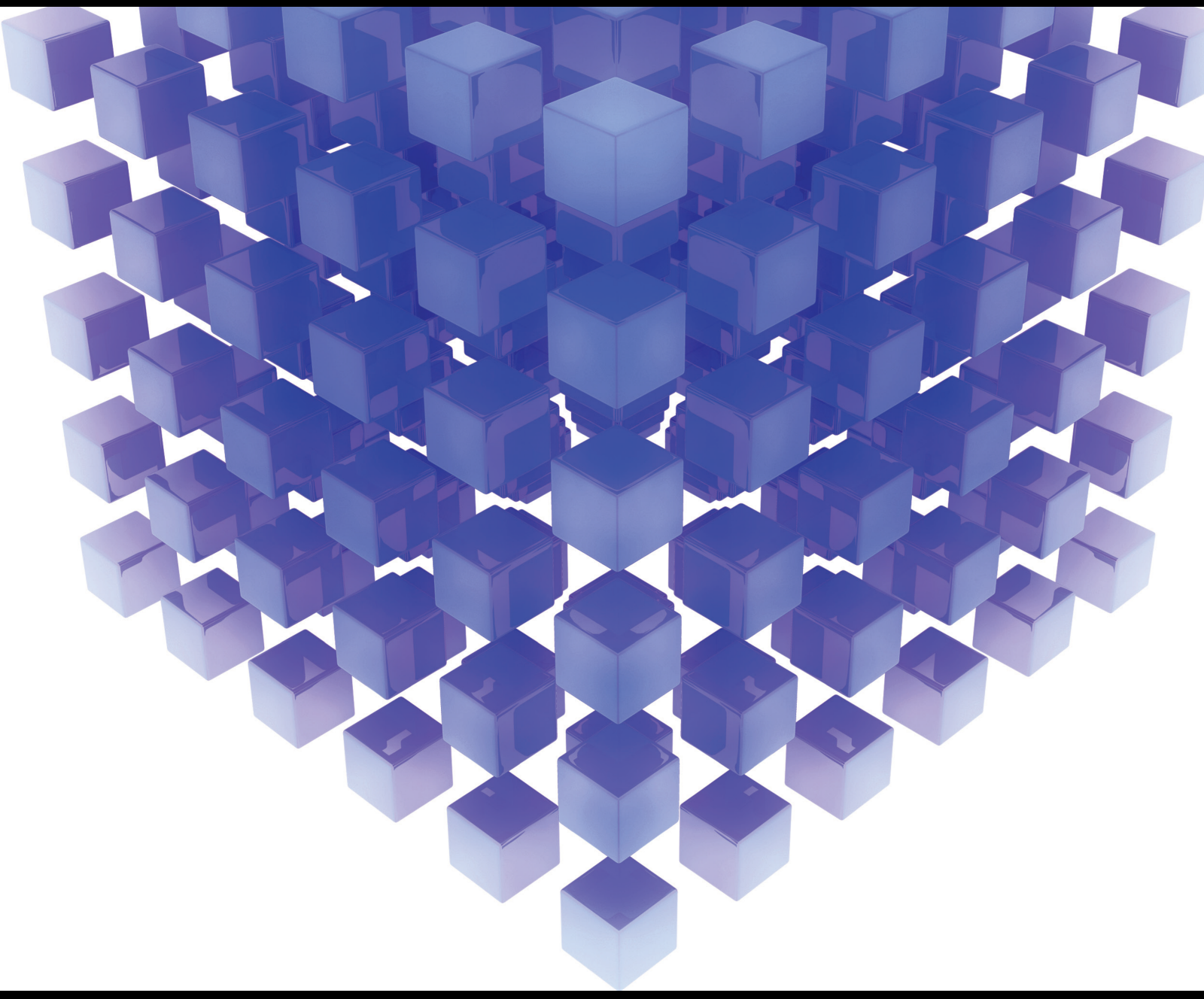

Nanofluids and Entropy Analysis with Electroosmotic Phenomenon

Mathematical Problems in Engineering

Nanofluids and Entropy Analysis with Electroosmotic Phenomenon

Lead Guest Editor: Arshad Riaz
Guest Editors: Ahmad Zeeshan, Mohsan Hassan, and Mohammad Reza Safaei

Chief Editor

Academic Editors

Contents

Hindawi
Mathematical Problems in Engineering
Volume 2022, Article ID 8600591, 14 pages
https://doi.org/10.1155/2022/8600591

Research Article

Analysis of Fractional Bioconvection with Hybrid Nanoparticles in Channel Flow

Muhammad Imran Asjad,[1] **Muhammad Danish Ikram**,[1] **Noman Sarwar**,[1] **Taseer Muhammad**,[2] **Sivanandam Sivasankaran**,[3] **and Sami Ahmed Abdu Subaihi**[3]

[1]*Department of Mathematics, University of Management and Technology, Lahore 54770, Pakistan*
[2]*Department of Mathematics, College of Sciences, King Khalid University, Abha 61413, Saudi Arabia*
[3]*Mathematical Modelling and Applied Computation (MMAC) Research Group, Department of Mathematics, Faculty of Science, King Abdulaziz University, P.O. Box 80203, Jeddah 21589, Saudi Arabia*

Correspondence should be addressed to Taseer Muhammad; taseer_qau@yahoo.com

Received 3 March 2022; Revised 9 May 2022; Accepted 18 June 2022; Published 23 August 2022

Academic Editor: Ardashir Mohammadzadeh

In this paper, MHD Brinkman-type fluid flow containing titanium dioxide and silver nanoparticle hybrid nanoparticles with generalized Mittag–Leffler kernel-based fractional derivative is investigated in the presence of bioconvection. The governing equations with dimensional analysis and fractional approach are obtained by using the fractional Fourier's law for heat flux and Fick's law for diffusion. As a result, the bioconvection Rayleigh number, which is responsible for the declining in the fluid velocity and fractional parameters used to control the thermal and momentum boundary layers thickness of fluid properties. The obtained solutions can be beneficial for proper analysis of real data and provide a tool for testing possible approximate solutions where needed.

1. Introduction

The concepts of fractional Brinkman form models with hybrid nanoparticles through an oscillating vertical plate and a magnetic field having variable direction are not detailed, however. To fill this void, a fractional Brinkman sorting fluid show is used to blend a flow of hybrid nanofluids over a swaying vertical plate. Brinkman's sort of fluid show was created by Brinkman in his pioneering work while investigating fluid flow due to thick constraint on the surface of a thick swarm particle [1, 2]. Saqib et al. [3] discussed the shape impact on the MHD flow of time-fractional, Ferro-Brinkman-sorted nanofluid having slope warming. Asjad et al. [4] introduced non-Newtonian fractional derivatives in a convective channel containing hybrid nanoparticles by Prabhakar. Khan et al. [5] investigated the chemical response and heat era impact of nonofluids of the Brinkman-type H_2O-Cu, Ag, TiO_2, and Al_2O_3 in a porous medium with an MHD flow. Nanjundappa et al. [6] explored the impact of dust particles on Darcy–Brinkman gravity-driven ferro-thermal-convection in a ferrofluid soaked porous layer with an inside heat source: the impact of boundaries. Sarwar et al. [7] explained a comparative ponder on a non-Newtonian fractional-order Brinkman sorted fluid with two different parts. Shafie et al. [8] blended the convection flow of Brinkman sorted hybrid nanofluid based on Atangana–Baleanu fractional demonstration. Ali et al. [9] presented the Caputo–Fabrizio fractional derivative modelling of transitory MHD Brinkman nanofluid. Saqib et al. [10] examined the attractive resistive flow of a generalized Brinkman sort of nanofluid containing carbon nanotubes with inclined warming.

In many circumstances, mathematical models of integer order derivatives, including nonlinear models, do not operate satisfactorily. Fractional calculus has numerous applications in the domains of electromagnetics, visco-elasticity, fluid mechanics, signal processing, and optics. It has been used to demonstrate the physical and design shapes

that can be found in a model to be best described by fractional differential conditions. The fractional derivative models are utilized for exact modelling of those frameworks that require exact modelling of damping. Boutiara et al. [11] debated a lesson of Langevin conditions within the outline of Caputo function-dependent kernel fractional derivatives through antiperiodic edge situations. Ali et al. [12] introduced controlled regulation retention of the common convection flow of hybrid nanofluids with a consistent relative Caputo-fractional derivative due to weight angle. Imran et al. [13] studied the mass and heat transport of a differentially sorted fluid with a noninteger time-fractional Caputo derivative. Ahmad et al. [14] announced the numerical modelling of (Cu-Al_2O_3) water-based Maxwell hybrid nanofluids with Caputo–Fabrizio fractional derivative. Mirza and Vieru [15] considered fundamental arrangements for an advection-diffusion condition with a time-fractional Caputo–Fabrizio derivative. Gul et al. [16] explored subjective investigations of certain Dirichlet boundary value problems aimed at Caputo–Fabrizio fractional differential conditions. Abdo et al. [17] offered a definite Atangana–Baleanu–Caputo derivative with nonlinear pantograph fractional differential conditions. Sweilam et al. [18] mathematically demonstrated that the Atangana–Baleanu–Caputo fractional derivative is an ideal control for cancer treatment. Sarwar et al. [19] investigated the Prabhakar derivative for convection flow Casson fluid over fluctuating plate based on the generalized Fourier law. Shah et al. [20] studied the common convection flow of Prabhakar fractional Maxwell fluid by generalized heat transportation. Elnaqeeb et al. [21] analyzed the normal convection flow of carbon nanotube Prabhakar-like fractional second-grade nanofluids over an infinite plate with Newtonian heating. Garrappa and Kaslik [22] considered the steadiness of fractional-order frameworks with Prabhakar derivatives.

Choi was one of the first to show nanofluids containing nanoparticles in 1995. Nanofluids can provide various benefits, including thermal conductivity. For the most part, these are intended for biomedical engineering, mechanical design, and fluid mechanics by Choi and Eastman [23]. Ali et al. [24] presented an investigation of a scientific fragmentary demonstration of hybrid viscous nanofluids and their application in heat and mass transfer. Ahmad et al. [25] verified expository arrangements for a complimentary convection flow of Casson nanofluid over an infinite vertical plate. Gul et al. [26] studied the hybrid nanofluid flow inside the cone-shaped hole between the cone and the surface of a spinning disk. Rafique et al. [27] defined the Casson nanofluid flow over a slanted permeable inclined surface with energy and mass transport. Khan et al. [28] discussed the effects of interfacial electro kinetic MHD radiative nanofluids flow on porous microchannels by thermophoresis and Brownian movement impacts. Ali Lund et al. [29] conferred hybrid nanofluid on the nonlinear contracting sheet with double branches of an MHD three-dimensional pivoting stream. Shah et al. [30] debated the recreation of entropy optimization and the warm behavior of nanofluids through the permeable media. Kumar et al. [31] deliberated a novel approach for the examination of warm exchange development through ferromagnetic hybrid nanofluid via considering sun-oriented radiation. Dadheech et al. [32] discussed natural convection and an angled magnetic field being used to compare the heat transfer of MoS2/C2H6O2 and SiO2-MoS2/C2H6O2 nanofluids. Dhif et al. [33] conducted a deliberate thermal study of a hybrid nanofluids solar collector and storage system. Khan et al. [34] examined the squeezing flow of nanofluids using mixed convection. Bu et al. [35] conducted a squeezing flow of nanofluids in a rotating channel with mixed convection and thermal radiation. By considering diverse physical flow conditions, thermal transport in aluminum alloy nanomaterials based on radiative nanofluids was investigated by Ullah Khan et al. [36]. In a triangular enclosure with zigzags and an elliptic obstacle, MHD flow of a hybrid nanofluid was introduced by Chabani et al. [37]. According to Rajashekhar et al. [38], the peristaltic flow of a Ree–Eyring liquid is affected by the different qualities of hemodynamic flow, mass, and heat transport. In a porous lid-driven hollow with a magnetic field, the entropy formation and heat transmission of Cu–water nanofluid were described by Marzougui et al. [39].

Bioconvection is defined as the wonder of macroscopic convection motion of fluid caused by the thickness angle established by the directional collective swimming of microorganisms. Plat proposed the concept of bioconvection in 1961. Bioconvection applications include biological polymer manufacture, biotechnology, and bio-sensors, as well as the testing and laboratory industries, among others [40, 41]. Ge-Jile et al. [42] analyzed nanofluid with motile microorganisms through the three-dimensional radiative bioconvective stream of a Sisko. Ramzan et al. [43] present bioconvection as a component in a three-dimensional digression hyperbolic partially ionized magnetized nanofluid stream with Cattaneo–Christov heat flux and activation vitality. Alhussain et al. [44] analyzed the warm conductivity and magneto-bioconvective augmentation in a nanofluid stream holding gyrotactic microorganisms. Farooq et al. [45] adjusted exponential space-based heat sources and Cattaneo–Christov expressions with a thermally radioactive bioconvection flow of Carreau nanofluid. Yousuf et al. [46] discussed the magneto-bioconvection flow of Williamson nanofluids through an inclined plate by entropy generation and gyrotactic microorganisms. Saqib et al. [47] inspected a Brinkman-type fluid (BTF) fractional model with hybrid nanoparticles. Danish Ikram et al. [48] calculated the heat transfer of viscous fluid with clay nanoparticles over an exponentially moving upright plate. Asjad Imran et al. [49] analyzed the thermophysical properties of clay nanofluids using a hybrid fractional operator. Ikram et al. [50] discussed the fractional model of Brinkman-type fluid (BTF) holding hybrid nanoparticles in a bounded microchannel via a constant proportional Caputo fractional operator.

Channel flow is used in a wide range of industrial applications, including heat exchangers in power plants and chemical reactors in the pharmaceutical industry. Although many actual processes with Newtonian behavior in both phases can be termed two-phase flows, there are a huge number of related applications where the continuous liquid phase exhibits non-Newtonian flow properties. There are

several instances in the biochemical and biomedical industries, as well as in the food processing industry [51]. The impact of a vortex generator shape on liquids and the heat transition of hybrid nanofluids in a channel were examined by Zheng et al. [52]. On the scientific scale, D'Ippolito et al. [53] investigated the resistance of open channel flow due to vegetation. Haq et al. [54] demonstrated the fractional viscous liquid influence of MHD channel flow across a porous medium using the Caputo–Fabrizio time-fractional derivative.

In the absence of fractional bioconvection, the analyses above were conducted with or without fractional derivatives. The main objective, on the other hand, is to merge these two interesting subjects, fractional derivatives, and bioconvection. Recently, Asjad et al. [55] presented fractional bioconvection properties for sticky fluid over an infinite perpendicular plate with Caputo fractional derivative. In the above-mentioned literature, there is not a single study on the subject of fractional bioconvection between two parallel plates with a Prabhakar fractional derivative. As a result, our motivation is to use the Laplace transform approach to solve the fluid flow and heat transfer problems of bioconvection. Graphics are used to offer a graphical explanation of flow parameters.

2. Mathematical Formulation

Consider an MHD convection flow happening within a microchannel of a generalized, electrically conductive, $(Ag - TiO_2 - H_2O)$ hybrid nanoparticles situated in xy-plane as shown in Figure 1.

The assumptions are as follows:

(i) Microchannel is measured of length infinite by width L

(ii) At $t \le 0$, the temperature of system is T_0

(iii) The channel is along $x-$ axis and normal to $y-$ axis

(iv) Fluid flow occurs in the x-direction

(v) After $t = 0^+$, the temperature and concentration level of microorganism raised from T_0 to T_w and N_∞ to N_w, respectively

(vi) Magnetics field of strength B_0 is applied normal to the plate

The stream of electrically conductive $(Ag - TiO_2 - H_2O)$ hybrid nanofluids endures electromotive drive, which yields current. The initiated attractive fields are disregarded since there is speculation about really small Reynolds numbers. The electromagnetic force activates the electric flux concentration [56]. The relation of thermophysical properties of nano and hybrid nanofluids is defined in Tables 1 and 2, respectively.

The governing equations of momentum and enegry are as follows [47]:

$$\left(\frac{\partial u(y,t)}{\partial t} + \beta_{b^*} u(y,t)\right)\rho_{hnf} = \mu_{hnf}\frac{\partial^2 u(y,t)}{\partial y^2} - \sigma_{hnf}B_0^2 u(y,t) + g\left[(\rho\beta_T)_{hnf}(T - T_0) - \gamma(\rho_m - \rho)(N - N_0)\right]. \tag{1}$$

The energy equation is as follows:

$$\left(\rho C_p\right)_{hnf}\frac{\partial T(y,t)}{\partial t} = -\frac{\partial q(y,t)}{\partial y}. \tag{2}$$

The generalized Fourier's law for thermal flux is as follows:

$$q(y,t) = -k_{hnf}^C D_{\alpha,\beta,a}^{\gamma}\frac{\partial T(y,t)}{\partial y}. \tag{3}$$

The diffusion balance equation is as follows:

$$\frac{\partial N(y,t)}{\partial t} = -\frac{\partial L(y,t)}{\partial y}. \tag{4}$$

The generalized Fick's law for diffusion equation is as follows:

$$L = -D_{hnf}^C D_{\alpha,\beta,a}^{\gamma}\frac{\partial N(y,t)}{\partial y}, \tag{5}$$

where $cD_{\alpha,\beta,a}^{\gamma}$ denotes the Prabhakar fractional derivative and is defined as [57, 58].

For (1)–(5), we consider the following initial and boundary conditions:

$$\begin{aligned} u(y,0) &= 0,\\ T(y,0) &= T_0,\\ N(y,0) &= N_0,\\ 0 \le y &\le L, \end{aligned} \tag{6}$$

$$\begin{aligned} u(y,t) &= 0,\\ T(0,t) &= T_0,\\ N(0,t) &= N_0,\\ t &> 0, \end{aligned} \tag{7}$$

$$\begin{aligned} u(L,t) &= 0,\\ T(L,t) &= T_w,\\ N(L,t) &= N_w,\\ t &> 0. \end{aligned} \tag{8}$$

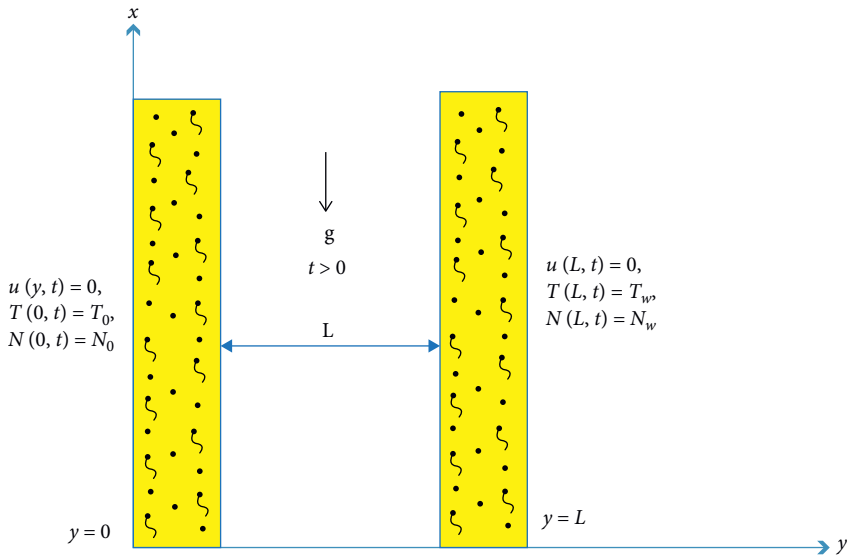

Figure 1: Geometry of the problem.

Table 1: The thermophysical properties of hybrid nanofluid and nanofluid under consideration are given in [50].

Nanofluid	Hybrid nanofluid
$\rho_{nf} = (1-\phi)\rho_f + \phi\rho_s$	$\rho_{hnf} = (1-\phi_{hnf})\rho_f + \phi_{TiO_2}\rho_{TiO_2} + \phi_{Ag}\rho_{Ag}$
$\mu_{nf} = \mu_f/(1-\phi)^{5/2}$	$\mu_{hnf} = \mu_f/[1-(\phi_{Ag}+\phi_{TiO_2})]^{5/2}$
$(\rho C_p)_{nf} = (1-\phi)(\rho C_p)_f + \phi(\rho C_p)_s$	$(\rho C_p)_{hnf} = (1-\phi_{hnf})(\rho C_p)_f + \phi_{Ag}(\rho c_p)_{Ag} + \phi_{TiO_2}(\rho C_p)_{TiO_2}$
$(\rho B_T)_{nf} = (1-\phi)(\rho B_T)_f + \phi(\rho B_T)_s$	$(\rho B_T)_{hnf} = (1-\phi_{hnf})(\rho B_T)_f + \phi_{Ag}(\rho B_T)_{Ag} + \phi_{TiO_2}(\rho B_T)_{TiO_2}$
$\sigma_{nf}/\sigma_f = 1 + 3(\sigma_s/\sigma_f - 1)\phi/(\sigma_s/\sigma_f + 2) - (\sigma_s/\sigma_f - 1)\phi$	$\sigma_{hnf}/\sigma_f = 1 + 3(\phi_{Ag}\sigma_{Ag} + \phi_{TiO_2}\sigma_{TiO_2}/\sigma_f - \phi_{hnf})/(\phi_{Ag}\sigma_{Ag} + \phi_{TiO_2}\sigma_{TiO_2}/\phi_{hnf}\sigma_f + 2) - (\phi_{Ag}\sigma_{Ag} + \phi_{TiO_2}\sigma_{TiO_2}/\sigma_f - \phi_{hnf})$
$K_{nf}/K_f = k_s + 2k_f - 2\phi(k_s - k_f)/k_s + 2k_f + \phi(k_s - k_f)$	$K_{hnf}/K_f = \phi_{Ag}k_{Ag} + \phi_{TiO_2}k_{TiO_2}/\phi_{hnf} + 2k_f + 2(\phi_{Ag}k_{Ag} + \phi_{TiO_2}k_{TiO_2}) - 2\phi_{hnf}K_f/\phi_{Ag}k_{Ag} + \phi_{TiO_2}k_{TiO_2}/\phi_{hnf} + 2k_f + (\phi_{Ag}k_{Ag} + \phi_{TiO_2}k_{TiO_2}) - \phi_{hnf}K_f$

Table 2: Thermophysical possessions of nanoparticles and base fluid [50].

Material	Base fluid water (H_2O)	Nanoparticles silver (Ag)	Nanoparticles titanium dioxide (TiO_2)
ρ	997.1	10500	425
C_p	4179	235	6862
k	0.613	429	8.9538
$\beta_T \times 10^{-5}$	21	1.89	0.9
σ	0.05	3.6×10^7	1×10^{-12}
Pr	6.2	—	—

By introducing dimensionless variables,

$$\begin{aligned}
\tau &= \frac{\nu}{L^2}t,\\
Y &= \frac{y}{L},\\
\theta &= \frac{T-T_0}{T_w-T_0},\\
N^* &= \frac{N-N_0}{N_w-N_0},\\
q^* &= \frac{q}{q_o},\\
L^* &= \frac{L}{L_0},\\
q_0 &= \frac{k_{hnf}(T_w-T_0)u_0}{\nu_{hnf}},\\
L_0 &= \frac{D_{hnf}(N_w-N_0)u_0}{\nu_{hnf}}.
\end{aligned} \tag{9}$$

The dimensionless fundamental equations are obtained by substituting from (9) into (1)–(8) and ignoring the star documentation.

Momentum and bioconvection equations in dimensionless form are as follows:

$$A_o^\bullet\frac{\partial V(Y,\tau)}{\partial\tau}+\beta_b^\bullet V(Y,\tau)=A_1^\bullet\frac{\partial^2 V(Y,\tau)}{\partial Y^2}-A_2^\bullet MV(Y,\tau)+Gr\left[A_3^\bullet\theta(Y,\tau)-RaN(Y,\tau)\right]. \tag{10}$$

Dimensionless form of energy equation is as follows:

$$B_0\frac{\partial\theta(Y,\tau)}{\partial\tau}=-\frac{\partial q(Y,\tau)}{\partial Y}. \tag{11}$$

In dimensionless form, the generalized Fourier's law for thermal flux [57, 58] is as follows:

$$q(Y,\tau)=-{}^{C}D^{\gamma}_{\alpha,\beta,a}\frac{\partial\theta(y,\tau)}{\partial Y}. \tag{12}$$

Dimensionless diffusion balance equation is as follows:

$$Lb\frac{\partial N(Y,\tau)}{\partial\tau}=-\frac{\partial L(Y,\tau)}{\partial Y}. \tag{13}$$

Dimensionless form of Fick's law [57, 58] is as follows:

$$L(Y,\tau)=-{}^{C}D^{\gamma}_{\alpha,\beta,a}\frac{\partial N(Y,\tau)}{\partial y}. \tag{14}$$

Constraints are associated with

$$V(Y,0)=0,\quad \theta(Y,0)=0,\ N(Y,0)=0,\ Y\geq 0, \tag{15}$$

$$V(0,\tau)=0,\quad \theta(0,\tau)=0,\ N(0,\tau)=0,\ \tau>0, \tag{16}$$

$$V(1,\tau)=0,\quad \theta(1,\tau)=1,\ N(1,\tau)=1,\ \tau>0. \tag{17}$$

Variables are as follows:

$$\begin{aligned}
\beta_b^\bullet &= \frac{L^2\beta_{b^*}\rho_f}{\mu_f},\\
M &= \frac{L^2\sigma_f B_0^2}{\mu_f},\\
Gr &= \frac{L^3 g(B_T)_f(T_w-T_0)}{\nu_f^2},\\
\Pr &= \frac{(\mu C_p)_f}{k_f},\\
Lb &= \frac{\nu_f}{D_{hnf}},\\
Ra &= \frac{\gamma(\rho_m-\rho)(N_w-N_0)}{\rho_f(B_T)_f(T_w-T_0)},\\
\lambda_{hnf} &= \frac{k_{hnf}}{k_f},\\
A_0^\bullet &= 1-\phi_{hnf}+\frac{\phi_{Ag}\rho_{Ag}+\phi_{Tio_2}\rho_{Tio_2}}{\rho_f},\\
A_2^\bullet &= \frac{\sigma_{hnf}}{\sigma_f},\\
A_1^\bullet &= \frac{1}{\left[1-\left(\phi_{Ag}+\phi_{Tio_2}\right)\right]^{2.5}},\\
A_3^\bullet &= 1-\phi_{hnf}+\frac{\phi_{Ag}(\rho B_T)_{Ag}+\phi_{Tio_2}(\rho B_T)_{Tio_2}}{(\rho B_T)_f},\\
B_0 &= \frac{\Pr A_4^*}{\lambda_{hnf}},\\
A_4^\bullet &= 1-\phi_{hnf}+\frac{\phi_{Ag}(\rho C_p)_{Ag}+\phi_{Tio_2}(\rho C_p)_{Tio_2}}{(\rho C_p)_f},\\
B_1 &= \frac{A_0^*}{A_1^*},\\
B_5 &= \frac{B_3}{B_2},\\
B_2 &= \frac{A_2^*M+A_o^*\beta_b}{A_1^*},\\
B_3 &= \frac{A_3^*Gr}{A_1^*},\\
B_4 &= \frac{GrRa}{A_1^*},\\
B_6 &= \frac{B_4}{B_2}.
\end{aligned} \tag{18}$$

In the above equations, β_b^* is the Brinkman parameter, M is the dimensionless magnetic field parameter, Pr is dimensionless Prandtl number, Gr is dimensionless Grashof number, and Ra is dimensionless bioconvection Rayleigh number, respectively.

3. Solution of the Problem

3.1. Solution of Temperature Field. We deliberate $\beta \in [0, 1)$ along these lines, and in the above formularies, the boundary m remains equivalent near zero. By utilizing the Laplace change strategy and applying it to equations (11) and (12) through requirements (16) and (17), and using the fractional derivative of Prabhakar, we acquire changed issue for temperature field:

$$sB_0\ \overline{\theta}(Y,s) = -\frac{\partial \overline{q}(Y,s)}{\partial Y}, \tag{19}$$

$$\overline{q}(Y,\ s) = -\,s^{\beta}\left(1 - as^{-\alpha}\right)^{\gamma}\frac{\partial \overline{\theta}(Y,\ s)}{\partial Y}. \tag{20}$$

Using (19) and (20), we have

$$\frac{\partial^2 \overline{\theta}(Y,s)}{\partial Y^2} - \frac{B_0 s\,\overline{\theta}(Y,s)}{s^{\beta}\left(1 - as^{-\alpha}\right)^{\gamma}} = 0. \tag{21}$$

Subject to the constraints,

$$\overline{\theta}(1,s) = \frac{1}{s}, \quad \overline{\theta}(0,s) = 0, \tau > 0. \tag{22}$$

The general solution of equation (21) with equation (22) is as follows:

$$\overline{\theta}(Y,s) = \frac{1}{s}\left(\frac{1}{\left(e^{-\sqrt{B_0 s/s^{\beta}(1-as^{-\alpha})^{\gamma}}} - e^{\sqrt{B_0 s/s^{\beta}(1-as^{-\alpha})^{\gamma}}}\right)/2}\right) \cdot \left(\frac{e^{-Y\sqrt{B_0 s/s^{\beta}(1-as^{-\alpha})^{\gamma}}} - e^{Y\sqrt{B_0 s/s^{\beta}(1-as^{-\alpha})^{\gamma}}}}{2}\right). \tag{23}$$

Or,

$$\overline{\theta}(Y,s) = \frac{1}{s}\left[\frac{\sinh\ Y\sqrt{B_0 s/s^{\beta}\left(1 - as^{-\alpha}\right)^{\gamma}}}{\sinh\sqrt{B_0 s/s^{\beta}\left(1 - as^{-\alpha}\right)^{\gamma}}}\right]. \tag{24}$$

It is important that equation (24) can be written in the equivalent form

$$\overline{\theta}(Y,s) = \frac{1}{s}\sum_{n=0}^{\infty}\left[e^{-(2n+1-Y)\sqrt{B_0 s/s^{\beta}(1-as^{-\alpha})^{\gamma}}} - e^{-(2n+1+Y)\sqrt{B_0 s/s^{\beta}(1-as^{-\alpha})^{\gamma}}}\right]. \tag{25}$$

Moreover, equation (25) can also be expressed as a series approach, allowing us to rationally determine the inverse Laplace transform.

$$\overline{\theta}(Y,s) = \frac{1}{s} + \left[\sum_{n=0}^{\infty}\sum_{m=1}^{\infty}\sum_{k=0}^{\infty}\frac{(Y-2n-1)^m (a)^k \left(B_0\right)^{m/2}\Gamma(\gamma m/2+k)}{m!k!\Gamma(\gamma m/2)}\frac{1}{s^{\alpha k - m/2+\beta m/2+1}}\right] - \left[\sum_{p=0}^{\infty}\sum_{n=0}^{\infty}\sum_{l=0}^{\infty}\frac{(-2n-1-Y)^l (a)^p \left(B_0\right)^{l/2}\Gamma(\gamma l/2+p)}{l!p!\Gamma(\gamma l/2)}\frac{1}{s^{\alpha p+\beta l/2-l/2+1}}\right]. \tag{26}$$

Taking inverse Laplace transform on equation (26), we get

$$\theta(Y,\tau) = 1 + \sum_{n=0}^{\infty}\sum_{m=1}^{\infty}\sum_{k=0}^{\infty}\frac{(Y-2n-1)^m (a)^k \left(B_0\right)^{m/2}\Gamma(\gamma m/2+k)}{m!k!\Gamma(\gamma m/2)}\frac{\tau^{\alpha k+\beta m/2-m/2}}{\Gamma(\alpha k+\beta m/2-m/2+1)} - \sum_{n=0}^{\infty}\sum_{l=0}^{\infty}\sum_{p=0}^{\infty}\frac{(-2n-1-Y)^l \left(B_0\right)^{l/2}(a)^p\Gamma(\gamma l/2+p)}{l!p!\Gamma(\gamma l/2)}\frac{\tau^{\alpha p-l/2+\beta l/2}}{\Gamma(\alpha p+\beta l/2-l/2+1)}. \tag{27}$$

3.2. Solution of Bioconvection Field. By utilizing the Laplace change approach and applying it to equations (13) and (14) with requirements (16) and (17) and utilizing the Prabhakar derivative, we acquire the changed issue for the bioconvection field.

$$Lbs\,\overline{N}(Y,s) = -\frac{\partial \overline{L}(Y,s)}{\partial Y}, \tag{28}$$

$$\overline{L}(Y,s) = -s^{\beta}\left(1 - as^{-\alpha}\right)^{\gamma}\frac{\partial \overline{N}(Y,s)}{\partial Y}. \tag{29}$$

Using equations (28) and (29), we have

$$\frac{\partial^2 \overline{N}(Y,s)}{\partial Y^2} - \frac{sLb}{s^{\beta}\left(1-as^{-\alpha}\right)^{\gamma}}\overline{N}(Y,s) = 0. \tag{30}$$

Subject to the constraints,

$$\overline{N}(1,s) = \frac{1}{s},\ \overline{N}(0,s) = 0. \tag{31}$$

The general solution of equation (30) with equation (31) is as follows:

$$\overline{N}(Y,s) = \frac{1}{s}\left(\frac{1}{\left(e^{-\sqrt{sLb/s^{\beta}(1-as^{-\alpha})^{\gamma}}} - e^{\sqrt{sLb/s^{\beta}(1-as^{-\alpha})^{\gamma}}}\right)/2}\right) \cdot \left(\frac{e^{-Y\sqrt{sLb/s^{\beta}(1-as^{-\alpha})^{\gamma}}} - e^{Y\sqrt{sLb/s^{\beta}(1-as^{-\alpha})^{\gamma}}}}{2}\right). \tag{32}$$

Or,

$$\overline{N}(Y,s) = \frac{1}{s}\left[\frac{\sinh Y\sqrt{sLb/s^{\beta}\left(1-as^{-\alpha}\right)^{\gamma}}}{\sinh\sqrt{sLb/s^{\beta}\left(1-as^{-\alpha}\right)^{\gamma}}}\right]. \tag{33}$$

It is important that equation (33) can be composed within the comparable form

$$\overline{N}(Y,s) = \frac{1}{s}\sum_{d=0}^{\infty}\left[e^{-(2d+1-Y)\sqrt{sLb/s^{\beta}(1-as^{-\alpha})^{\gamma}}} - e^{-(2d+1+Y)\sqrt{sLb/s^{\beta}(1-as^{-\alpha})^{\gamma}}}\right]. \tag{34}$$

Moreover, equation (34) can be communicated in an arrangement shape so that we are able to discover the Laplace inverse transform logically.

$$\overline{N}(Y,s) = \frac{1}{s} + \left[\sum_{d=0}^{\infty}\sum_{s_1=1}^{\infty}\sum_{s_2=0}^{\infty}\frac{(-2d-1+Y)^{s_1}\,(a)^{s_2}\,(Lb)^{s_1/2}\,\Gamma\left(\gamma s_1/2+s_2\right)}{s_1!s_2!\Gamma\left(\gamma s_1/2\right)}\frac{1}{s^{\alpha s_2+\beta s_1/2-s_1/2+1}}\right] - \left[\sum_{d=0}^{\infty}\sum_{p_1=0}^{\infty}\sum_{p_2=0}^{\infty}\frac{(-2d-1-Y)^{p_1}\,(a)^{p_2}\,(Lb)^{p_1/2}\,\Gamma\left(\gamma p_1/2+p_2\right)}{p_1!p_2!\Gamma\left(\gamma p_1/2\right)}\frac{1}{s^{\alpha p_2+\beta p_1/2-p_1/2+1}}\right]. \tag{35}$$

Taking inverse Laplace transform on equation (35), we get

$$N(Y,\tau) = 1 + \sum_{d=0}^{\infty}\sum_{s_1=1}^{\infty}\sum_{s_2=0}^{\infty}\frac{(-2d-1+Y)^{s_1}\,(a)^{s_2}\,(Lb)^{s_1/2}\,\Gamma\left(\gamma s_1/2+s_2\right)}{s_1!s_2!\Gamma\left(\gamma s_1/2\right)}\frac{\tau^{\alpha s_2+\beta s_1/2-s_1/2}}{\Gamma\left(\alpha s_2+\beta s_1/2-s_1/2+1\right)} - \sum_{d=0}^{\infty}\sum_{p_1=0}^{\infty}\sum_{p_2=0}^{\infty}\frac{(-2d-1-Y)^{p_1}\,(a)^{p_2}\,(Lb)^{p_1/2}\,\Gamma\left(\gamma p_1/2+p_2\right)}{p_1!p_2!\Gamma\left(\gamma p_1/2\right)}\frac{\tau^{\alpha p_2+\beta p_1/2-p_1/2}}{\Gamma\left(\alpha p_2+\beta p_1/2-p_1/2+1\right)}. \tag{36}$$

3.3. Solution of Velocity Field. The Laplace transform is used in equation (10) using expressions from (15)–(17), and we attain

$$\left[\frac{\partial^2}{\partial Y^2} - B_1 s - B_2\right]\overline{V}(Y,s) = -B_3\overline{\theta}(Y,s) + B_4\overline{N}(Y,s), \tag{37}$$

which satisfies the following constraints:

$$\overline{V}(1,\ s) = 0,\ \overline{V}(0,\ s) = 0. \tag{38}$$

The solution of equation (37) subject to constraints (38), we have

$$\begin{aligned}\overline{V}(Y,s) = &-\frac{B_5}{s}\sum_{n=0}^{\infty}\left[\frac{e^{-(2n)\sqrt{B_0 s/s^{\beta}(1-as^{-\alpha})^{\gamma}}}-e^{-(2n+2)\sqrt{B_0 s/s^{\beta}(1-as^{-\alpha})^{\gamma}}}}{\left[1+\left(B_1 s/B_2-B_0 s/B_2 s^{\beta}\left(1-as^{-\alpha}\right)^{\gamma}\right)\right]}\right]\times\left[\sum_{m=0}^{\infty}e^{-(2m+1-Y)\sqrt{B_2+B_1 s}}-\sum_{m=0}^{\infty}e^{-(2m+1+Y)\sqrt{B_2+B_1 s}}\right]\\ &+\frac{B_6}{s}\sum_{d=0}^{\infty}\left[\frac{e^{-(2d)\sqrt{sLb/s^{\beta}(1-as^{-\alpha})^{\gamma}}}-e^{-(2d+2)\sqrt{sLb/s^{\beta}(1-as^{-\alpha})^{\gamma}}}}{\left[1+\left(B_1 s/B_2-sLb/B_2 s^{\beta}\left(1-as^{-\alpha}\right)^{\gamma}\right)\right]}\right]\times\left[\sum_{m=0}^{\infty}e^{-(2m+1-Y)\sqrt{B_2+B_1 s}}-\sum_{m=0}^{\infty}e^{-(2m+1+Y)\sqrt{B_2+B_1 s}}\right]\\ &+\frac{B_5}{s}\sum_{n=0}^{\infty}\left[\frac{e^{-(2n+1-Y)\sqrt{B_0 s/s^{\beta}(1-as^{-\alpha})^{\gamma}}}-e^{-(2n+1+Y)\sqrt{B_0 s/s^{\beta}(1-as^{-\alpha})^{\gamma}}}}{\left[1+\left(B_1 s/B_2-B_0 s/B_2 s^{\beta}\left(1-as^{-\alpha}\right)^{\gamma}\right)\right]}\right]\\ &-\frac{B_6}{s}\sum_{d=0}^{\infty}\left[\frac{e^{-(2d+1-Y)\sqrt{sLb/s^{\beta}(1-as^{-\alpha})^{\gamma}}}-e^{-(2d+1+Y)\sqrt{sLb/s^{\beta}(1-as^{-\alpha})^{\gamma}}}}{\left[1+\left(B_1 s/B_2-sLb/B_2 s^{\beta}\left(1-as^{-\alpha}\right)^{\gamma}\right)\right]}\right].\end{aligned} \tag{39}$$

Equation (39) can be written in component form as follows:

$$\begin{aligned}\overline{V}(Y,\ s) = &\overline{V}_1(Y,\ s)+\overline{V}_2(Y,\ s)+\overline{V}_3(Y,\ s)+\overline{V}_4(Y,\ s)+\overline{V}_5(Y,\ s)+\overline{V}_6(Y,\ s)+\overline{V}_7(Y,\ s)+\overline{V}_8(Y,\ s)+\overline{V}_9(Y,\ s)\\ &+\overline{V}_{10}(Y,\ s)+\overline{V}_{11}(Y,\ s)+\overline{V}_{12}(Y,\ s).\end{aligned} \tag{40}$$

It is challenging to find the inverse Laplace transform of equation (40), so we can rewrite it in a suitable series.

$$\begin{aligned}V(Y,\tau) = &V_1(Y,\tau)+V_2(Y,\tau)+V_3(Y,\tau)+V_4(Y,\tau)+V_5(Y,\tau)+V_6(Y,\tau)+V_7(Y,\tau)+V_8(Y,\tau)+V_9(Y,\tau)\\ &+V_{10}(Y,\tau)+V_{11}(Y,\tau)+V_{12}(Y,\tau).\end{aligned} \tag{41}$$

Next, taking the inverse Laplace of equation (41), component wise, we have

$$\begin{aligned}V_1(Y,\tau) = &-B_5\sum_{n=0}^{\infty}\sum_{m=0}^{\infty}\sum_{\delta_2=0}^{\infty}\sum_{\delta_1=0}^{\infty}\sum_{w_2=0}^{\infty}\sum_{w_1=0}^{\infty}\sum_{z_1=0}^{\infty}\sum_{z_2=0}^{\infty}\sum_{z_3=0}^{\infty}\frac{(Y-2m-1)^{w_1}\left(-B_1\right)^{z_1}\left(B_0\right)^{\delta_1/2}}{\delta_1!\delta_2!w_1!w_2!z_2!z_3!\left(B_1\right)^{z_2-w_2}\left(B_2\right)^{w_2+z_1-w_1/2}}\\ &\times\frac{(-2n)^{\delta_1}\left(-B_0\right)^{z_2}(a)^{\delta_2+z_3}\tau^{\alpha\delta_2+\beta\delta_1/2-\delta_1/2-w_2+\alpha z_3+\beta z_2-z_1}}{\Gamma\left(\alpha\delta_2+\beta\delta_1/2-\delta_1/2-w_2+\alpha z_3+\beta z_2-z_1+1\right)}\frac{\Gamma\left(\gamma\delta_1/2+\delta_2\right)\Gamma\left(w_1/2+1\right)\Gamma\left(z_1+1\right)\Gamma\left(\gamma z_2+z_3\right)}{\Gamma\left(\gamma\delta_1/2\right)\Gamma\left(w_1/2+1-w_2\right)\Gamma\left(z_1+1-z_2\right)\Gamma\left(\gamma z_2\right)},\end{aligned}$$

$$\begin{aligned}V_2(Y,\tau) = &B_5\sum_{n=0}^{\infty}\sum_{m=0}^{\infty}\sum_{\delta_1=0}^{\infty}\sum_{\delta_2=0}^{\infty}\sum_{q_1=0}^{\infty}\sum_{q_2=0}^{\infty}\sum_{z_1=0}^{\infty}\sum_{z_2=0}^{\infty}\sum_{z_3=0}^{\infty}\frac{(-(Y+2m+1))^{q_1}\left(-B_1\right)^{z_1}\left(B_0\right)^{\delta_1/2}}{\delta_1!\delta_2!q_1!q_2!z_2!z_3!\left(B_1\right)^{z_2-q_2}\left(B_2\right)^{q_2+z_1-q_1/2}}\\ &\times\frac{(-2n)^{\delta_1}\left(-B_0\right)^{z_2}(a)^{\delta_2+z_3}\tau^{\alpha\delta_2+\beta\delta_1/2-\delta_1/2-q_2+\alpha z_3+\beta z_2-z_1}}{\Gamma\left(\alpha\delta_2+\beta\delta_1/2-\delta_1/2-q_2+\alpha z_3+\beta z_2-z_1+1\right)}\frac{\Gamma\left(\gamma\delta_1/2+\delta_2\right)\Gamma\left(q_1/2+1\right)\Gamma\left(z_1+1\right)\Gamma\left(\gamma z_2+z_3\right)}{\Gamma\left(\gamma\delta_1/2\right)\Gamma\left(q_1/2+1-q_2\right)\Gamma\left(z_1+1-z_2\right)\Gamma\left(\gamma z_2\right)},\end{aligned}$$

$$\begin{aligned}V_3(Y,\tau) = &B_5\sum_{n=0}^{\infty}\sum_{m=0}^{\infty}\sum_{j_1=0}^{\infty}\sum_{j_2=0}^{\infty}\sum_{w_1=0}^{\infty}\sum_{w_2=0}^{\infty}\sum_{z_1=0}^{\infty}\sum_{z_2=0}^{\infty}\sum_{z_3=0}^{\infty}\frac{(Y-2m-1)^{w_1}\left(-B_1\right)^{z_1}(\mathrm{Pr})^{j_1/2}}{j_1!j_2!w_1!w_2!z_2!z_3!\left(B_1\right)^{z_2-w_2}\left(B_2\right)^{w_2+z_1-w_1/2}}\\ &\times\frac{(-2n-2)^{j_1}\left(-B_0\right)^{z_2}(a)^{j_2+z_3}\tau^{\alpha j_2+\beta j_1/2-j_1/2-w_2+\alpha z_3+\beta z_2-z_1}}{\Gamma\left(\alpha j_2+\beta j_1/2-j_1/2-w_2+\alpha z_3+\beta z_2-z_1+1\right)}\frac{\Gamma\left(\gamma j_1/2+j_2\right)\Gamma\left(w_1/2+1\right)\Gamma\left(z_1+1\right)\Gamma\left(\gamma z_2+z_3\right)}{\Gamma\left(\gamma j_1/2\right)\Gamma\left(w_1/2+1-w_2\right)\Gamma\left(z_1+1-z_2\right)\Gamma\left(\gamma z_2\right)},\end{aligned}$$

$$V_4(Y,\tau) = -B_5 \sum_{n=0}^{\infty}\sum_{m=0}^{\infty}\sum_{j_1=0}^{\infty}\sum_{j_2=0}^{\infty}\sum_{q_1=0}^{\infty}\sum_{q_2=0}^{\infty}\sum_{z_1=0}^{\infty}\sum_{z_2=0}^{\infty}\sum_{z_3=0}^{\infty} \frac{(-(Y+2m+1))^{q_1}\left(-B_1\right)^{z_1}\left(B_0\right)^{j_1/2}}{j_1!j_2!q_1!q_2!z_2!z_3!\left(B_1\right)^{z_2-q_2}\left(B_2\right)^{q_2+z_1-q_1/2}}$$
$$\times \frac{(-2n-2)^{j_1}\left(-B_0\right)^{z_2}(a)^{j_2+z_3}\tau^{\alpha j_2+\beta j_1/2-\, j_1/2-\, q_2+\alpha z_3+\beta z_2-\, z_1}}{\Gamma\left(\alpha j_2+\beta j_1/2-j_1/2-q_2+\alpha z_3+\beta z_2-z_1+1\right)} \frac{\Gamma\left(\gamma j_1/2+j_2\right)\Gamma\left(q_1/2+1\right)\Gamma\left(z_1+1\right)\Gamma\left(\gamma z_2+z_3\right)}{\Gamma\left(\gamma j_1/2\right)\Gamma\left(q_1/2+1-q_2\right)\Gamma\left(z_1+1-z_2\right)\Gamma\left(\gamma z_2\right)},$$

$$V_5(Y,\tau) = B_6 \sum_{d=0}^{\infty}\sum_{m=0}^{\infty}\sum_{n_1=0}^{\infty}\sum_{n_2=0}^{\infty}\sum_{w_1=0}^{\infty}\sum_{w_2=0}^{\infty}\sum_{h_1=0}^{\infty}\sum_{h_2=0}^{\infty}\sum_{h_3=0}^{\infty} \frac{(Y-2m-1)^{w_1}\left(-B_1\right)^{h_1}(Lb)^{n_1/2}}{n_1!n_2!w_1!w_2!h_2!h_3!\left(B_1\right)^{h_2-w_2}\left(B_2\right)^{w_2+h_1-w_1/2}}$$
$$\times \frac{(-2d)^{n_1}(-Lb)^{h_2}(a)^{n_2+h_3}\tau^{\alpha n_2+\beta n_1/2-\, n_1/2-\, w_2+\alpha h_3+\beta h_2-\, h_1}}{\Gamma\left(\alpha n_2+\beta n_1/2-n_1/2-w_2+\alpha h_3+\beta h_2-h_1+1\right)} \frac{\Gamma\left(\gamma n_1/2+n_2\right)\Gamma\left(w_1/2+1\right)\Gamma\left(h_1+1\right)\Gamma\left(\gamma h_2+h_3\right)}{\Gamma\left(\gamma n_1/2\right)\Gamma\left(w_1/2+1-w_2\right)\Gamma\left(h_1+1-h_2\right)\Gamma\left(\gamma h_2\right)},$$

$$V_6(Y,\tau) = -B_6 \sum_{d=0}^{\infty}\sum_{m=0}^{\infty}\sum_{n_1=0}^{\infty}\sum_{n_2=0}^{\infty}\sum_{q_1=0}^{\infty}\sum_{q_2=0}^{\infty}\sum_{h_1=0}^{\infty}\sum_{h_2=0}^{\infty}\sum_{h_3=0}^{\infty} \frac{(-(Y+2m+1))^{q_1}\left(-B_1\right)^{h_1}(Lb)^{n_1/2}}{n_1!n_2!q_1!q_2!h_2!h_3!\left(B_1\right)^{h_2-q_2}\left(B_2\right)^{q_2+h_1-q_1/2}}$$
$$\times \frac{(-2d)^{n_1}(-Lb)^{h_2}(a)^{n_2+h_3}\tau^{\alpha n_2+\beta n_1/2-\, n_1/2-\, q_2+\alpha h_3+\beta h_2-\, h}}{\Gamma\left(\alpha n_2+\beta n_1/2-n_1/2-q_2+\alpha h_3+\beta h_2-h_1+1\right)} \frac{\Gamma\left(\gamma n_1/2+n_2\right)\Gamma\left(q_1/2+1\right)\Gamma\left(z_1+1\right)\Gamma\left(\gamma h_2+h_3\right)}{\Gamma\left(\gamma n_1/2\right)\Gamma\left(q_1/2+1-q_2\right)\Gamma\left(h_1+1-h_2\right)\Gamma\left(\gamma z_2\right)},$$

$$V_7(Y,\tau) = -B_6 \sum_{d=0}^{\infty}\sum_{m=0}^{\infty}\sum_{m_1=0}^{\infty}\sum_{m_2=0}^{\infty}\sum_{w_1=0}^{\infty}\sum_{w_2=0}^{\infty}\sum_{h_1=0}^{\infty}\sum_{h_2=0}^{\infty}\sum_{h_3=0}^{\infty} \frac{(Y-2m-1)^{w_1}\left(-B_1\right)^{h_1}(Lb)^{m_1/2}}{m_1!m_2!w_1!w_2!h_2!h_3!\left(B_1\right)^{h_2-w_2}\left(B_2\right)^{w_2+h_1-w_1/2}}$$
$$\times \frac{(-2d-2)^{m_1}\left(-B_0\right)^{h_2}(a)^{m_2+h_3}\tau^{\alpha m_2+\beta m_1/2-\, m_1/2-\, w_2+\alpha h_3+\beta h_2-\, h_1}}{\left(\alpha m_2+\beta m_1/2-m_1/2-w_2+\alpha h_3+\beta h_2-h_1+1\right)} \frac{\Gamma\left(\gamma m_1/2+m_2\right)\Gamma\left(w_1/2+1\right)\Gamma\left(h_1+1\right)\Gamma\left(\gamma h_2+h_3\right)}{\Gamma\left(\gamma m_1/2\right)\Gamma\left(w_1/2+1-w_2\right)\Gamma\left(h_1+1-h_2\right)\Gamma\left(\gamma h_2\right)},$$

$$V_8(Y,\tau) = B_6 \sum_{d=0}^{\infty}\sum_{m=0}^{\infty}\sum_{m_1=0}^{\infty}\sum_{m_2=0}^{\infty}\sum_{q_1=0}^{\infty}\sum_{q_2=0}^{\infty}\sum_{h_1=0}^{\infty}\sum_{h_2=0}^{\infty}\sum_{h_3=0}^{\infty} \frac{(-(Y+2m+1))^{q_1}\left(-B_1\right)^{h_1}(Lb)^{m_1/2}}{m_1!m_2!q_1!q_2!h_2!h_3!\left(B_1\right)^{h_2-q_2}\left(B_2\right)^{q_2+h_1-q_1/2}}$$
$$\times \frac{(-2d-2)^{m_1}(-Lb)^{h_2}(a)^{m_2+h_3}\tau^{\alpha m_2+\beta m_1/2-\, m_1/2-\, q_2+\alpha h_3+\beta h_2-\, h_1}}{\Gamma\left(\alpha m_2+\beta m_1/2-m_1/2-q_2+\alpha h_3+\beta h_2-h_1+1\right)} \frac{\Gamma\left(\gamma m_1/2+m_2\right)\Gamma\left(q_1/2+1\right)\Gamma\left(h_1+1\right)\Gamma\left(\gamma h_2+h_3\right)}{\Gamma\left(\gamma m_1/2\right)\Gamma\left(q_1/2+1-q_2\right)\Gamma\left(h_1+1-h_2\right)\Gamma\left(\gamma h_2\right)},$$

$$V_9(Y,\tau) = B_5 \sum_{n=0}^{\infty}\sum_{t_1=0}^{\infty}\sum_{t_2=0}^{\infty}\sum_{z_1=0}^{\infty}\sum_{z_2=0}^{\infty}\sum_{z_3=0}^{\infty} \frac{(Y-2n-1)^{t_1}\left(-B_1\right)^{z_1}\left(B_0\right)^{t_1/2}}{t_1!t_2!z_2!z_3!\left(B_1\right)^{z_2}\left(B_2\right)^{z_1}}$$
$$\times \frac{\left(-B_0\right)^{z_2}(a)^{t_2+z_3}\tau^{\alpha t_2+\beta t_1/2-\, t_1/2+\alpha z_3+\beta z_2-\, z_1}}{\Gamma\left(\alpha t_2+\beta t_1/2-t_1/2+\alpha z_3+\beta z_2-z_1+1\right)} \frac{\Gamma\left(\gamma t_1/2+t_2\right)\Gamma\left(z_1+1\right)\Gamma\left(\gamma z_2+z_3\right)}{\Gamma\left(\gamma t_1/2\right)\Gamma\left(z_1+1-z_2\right)\Gamma\left(\gamma z_2\right)},$$

$$V_{10}(Y,\tau) = -B_5 \sum_{n=0}^{\infty}\sum_{\nu_1=0}^{\infty}\sum_{\nu_2=0}^{\infty}\sum_{z_1=0}^{\infty}\sum_{z_2=0}^{\infty}\sum_{z_3=0}^{\infty} \frac{(-(Y+2n+1))^{\nu_1}\left(-B_1\right)^{z_1}\left(B_0\right)^{\nu_1/2}}{\nu_1!\nu_2!z_2!z_3!\left(B_1\right)^{z_2}\left(B_2\right)^{z_1}}$$
$$\times \frac{\left(-B_0\right)^{z_2}(a)^{\nu_2+z_3}\tau^{\alpha\nu_2+\beta\nu_1/2-\, \nu_1/2+\alpha z_3+\beta z_2-\, z_1}}{\Gamma\left(\alpha\nu_2+\beta\nu_1/2-\nu_1/2+\alpha z_3+\beta z_2-z_1+1\right)} \frac{\Gamma\left(\gamma\nu_1/2+\nu_2\right)\Gamma\left(z_1+1\right)\Gamma\left(\gamma z_2+z_3\right)}{\Gamma\left(\gamma\nu_1/2\right)\Gamma\left(z_1+1-z_2\right)\Gamma\left(\gamma z_2\right)},$$

$$V_{11}(Y,\tau) = -B_6 \sum_{d=0}^{\infty}\sum_{l_1=0}^{\infty}\sum_{l_2=0}^{\infty}\sum_{h_1=0}^{\infty}\sum_{h_2=0}^{\infty}\sum_{h_3=0}^{\infty} \frac{(Y-2d-1)^{l_1}\left(-B_1\right)^{h_1}(Lb)^{l_1/2}}{l_1!l_2!h_2!h_3!\left(B_1\right)^{h_2}\left(B_2\right)^{h_1}}$$
$$\times \frac{(-Lb)^{h_2}(a)^{l_2+h_3}\tau^{\alpha l_2+\beta l_1/2-\, l_1/2+\alpha h_3+\beta h_2-\, h_1}}{\Gamma\left(\alpha l_2+\beta l_1/2-l_1/2+\alpha h_3+\beta h_2-h_1+1\right)} \frac{\Gamma\left(\gamma l_1/2+l_2\right)\Gamma\left(h_1+1\right)\Gamma\left(\gamma h_2+h_3\right)}{\Gamma\left(\gamma l_1/2\right)\Gamma\left(h_1+1-h_2\right)\Gamma\left(\gamma h_2\right)},$$

$$V_{12}(Y,\tau) = B_6 \sum_{d=0}^{\infty}\sum_{k_1=0}^{\infty}\sum_{k_2=0}^{\infty}\sum_{h_1=0}^{\infty}\sum_{h_2=0}^{\infty}\sum_{h_3=0}^{\infty} \frac{(-(Y+2d+1))^{k_1}\left(-B_1\right)^{h_1}(Lb)^{k_1/2}}{k_1!k_2!h_2!h_3!\left(B_1\right)^{h_2}\left(B_2\right)^{h_1}}$$
$$\times \frac{(-Lb)^{h_2}(a)^{k_2+h_3}\tau^{\alpha k_2+\beta k_1/2-\, k_1/2+\alpha h_3+\beta h_2-\, h_1}}{\Gamma\left(\alpha k_2+\beta k_1/2-k_1/2+\alpha h_3+\beta h_2-h_1+1\right)} \frac{\Gamma\left(\gamma k_1/2+k_2\right)\Gamma\left(h_1+1\right)\Gamma\left(\gamma h_2+h_3\right)}{\Gamma\left(\gamma k_1/2\right)\Gamma\left(h_1+1-h_2\right)\Gamma\left(\gamma h_2\right)}.$$

(42)

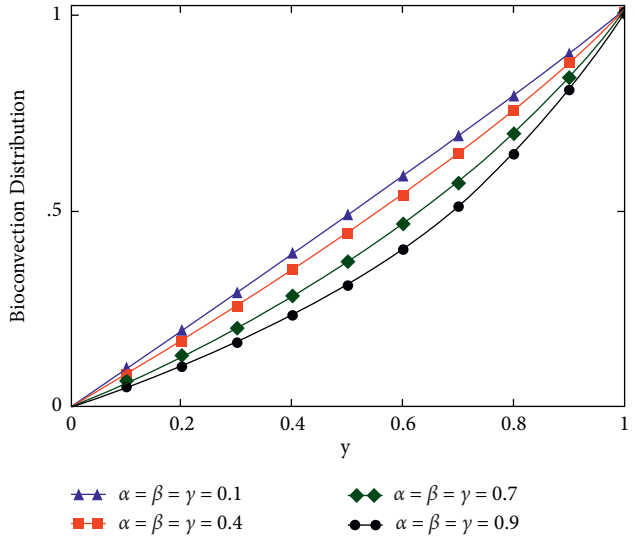

Figure 2: The effects of fractional parameters on bioconvection field, when $t = 3, Lb = 3$, and $a = 0.2$.

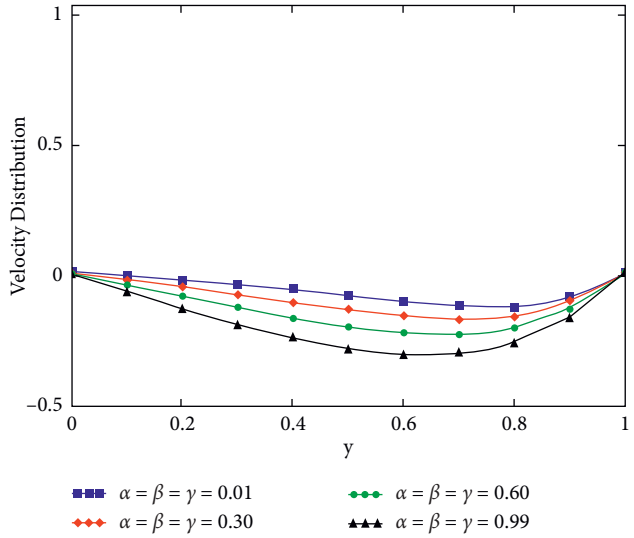

Figure 4: The effects of fractional parameters on velocity field for large time, when. $t = 2, \Pr = 6.2, Gr = 12, a = 0.2, Lb = 30, M = 0.01, \beta^* = 0.006, \phi_{hnf} = 0.04$, and $Ra = 4$.

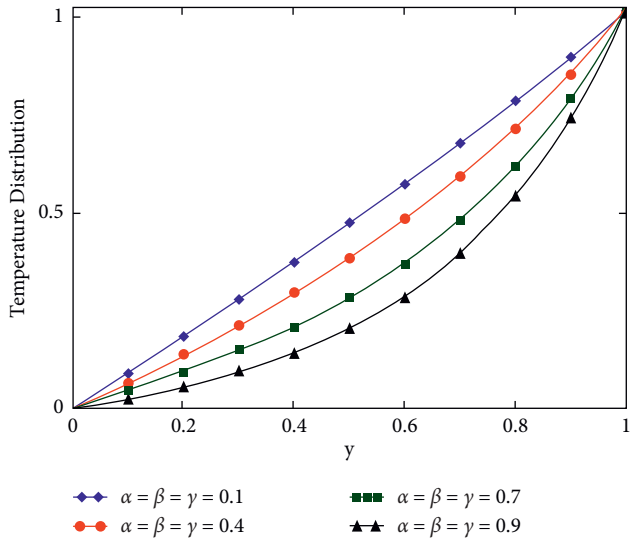

Figure 3: The effects of fractional parameters on temperature field for large time, when $t = 3, \Pr = 6.2$, and $a = 0.2$.

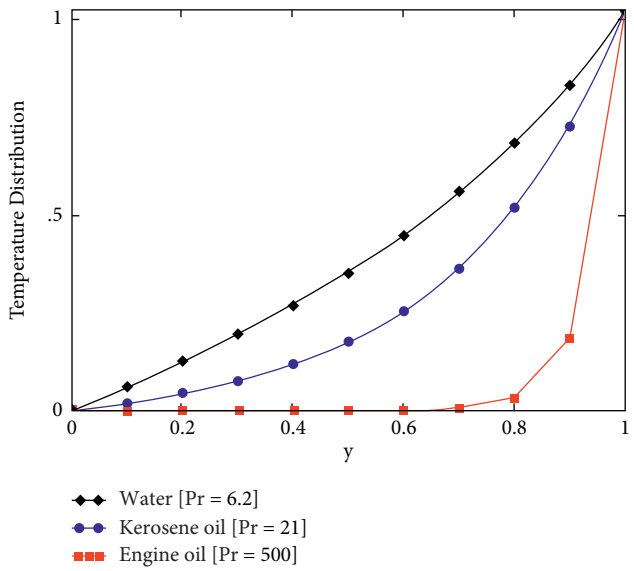

Figure 5: The comparison between different base fluids (water, kerosene oil, and engine oil) on temperature field for small time, when $t = 3, \alpha = \beta = \gamma = 0.5$, and $a = 0.2$.

4. Graphical Results and Discussion

Bioconvection has been studied using an MHD effect and thermal transfer model with a Prabhakar fractional approach. Laplace transform procedures are used to provide exact solutions for dimensionless governing equations. Graphical illustrations have been used to explain some of the physical effects of flow parameters.

Figures 2–4 are projected to show the impact of the fractional parameters α, β, γ on bioconvection, temperature, and velocity fields. For a large time, bioconvection, temperature, and velocity decreased by increasing values of α, β, γ. This is due to the boundary layer becoming wider; therefore, bioconvection, temperature, and velocity decrease. Usually, we can say that in fluid dynamics, a fractional approach is better for controlling the boundary layer thickness of the fluid properties.

Figure 5 shows the comparison between several base fluids (water, engine oil, and kerosene oil) on the temperature field. It is clearly noticed that the temperature of water is higher than all other Newtonian liquids, such as kerosene and engine oil. Meanwhile, viscosity and Prandtl numbers are very low for water compared to the other two, so water heats up faster than them physically.

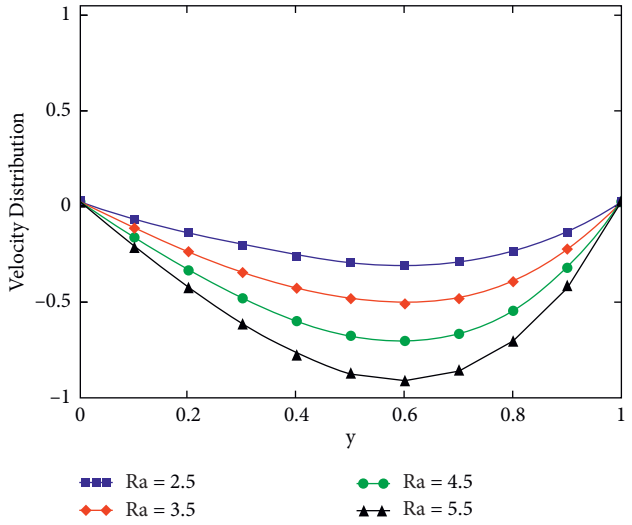

FIGURE 6: The effects of Rayleigh number on velocity field, when. Pr = 6.2, t = 5, α = 0.5, β = 0.5, γ = 0.5, Lb = 5,Gr = 5, β^* = 0.006, ϕ_{hnf} = 0.04, a = 0.2, and M = 0.2.

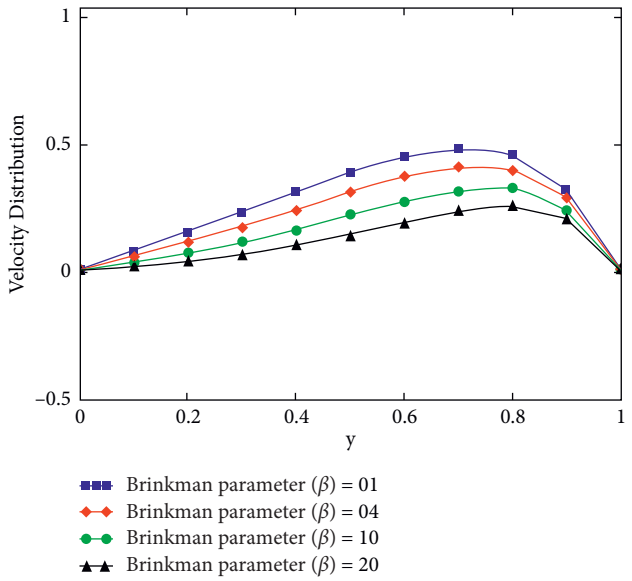

FIGURE 7: The effects of Brinkman parameter on velocity field, when Pr = 6.2, t = 5, α = β = γ = 0.5, Lb = 30, Gr = 12, a = 0.2, Ra = 4, ϕ_{hnf} = 0.08, and M = 0.01.

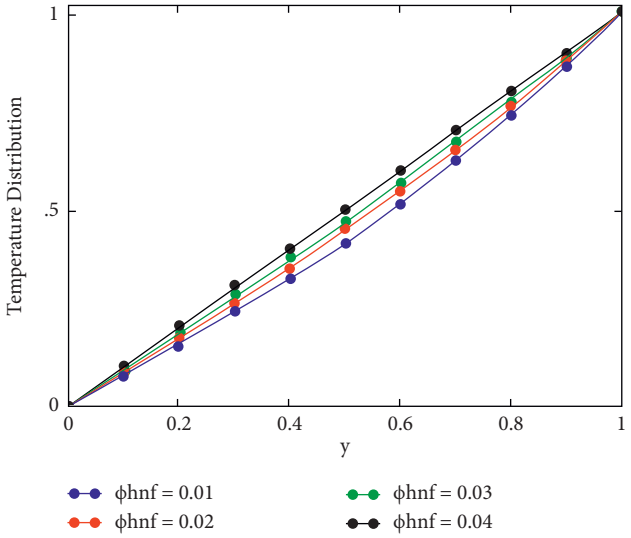

FIGURE 8: The effects of ϕ_{hnf} on temperature field, when Pr = 6.2, t = 3, α = β = γ = 0.5, and a = 0.2.

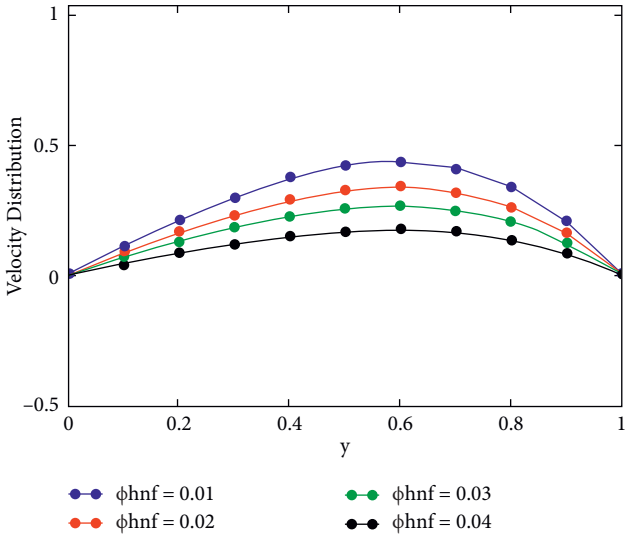

FIGURE 9: The effects of ϕ_{hnf} on velocity field, when. Pr = 6.2, t = 4, α = β = γ = 0.5, Lb = 30, a = 0.2, Gr = 15, Ra = 4, and M = 2.0.

To see the impact of bioconvection Rayleigh number Ra on velocity, Figure 6 is plotted. It is proved that velocity near the plate decreases for greater values of Ra. Ra decreases the fluid velocity since the buoyancy influenced by the transference of microorganisms is decreased by Ra. The consequences of the Brinkman parameter on the velocity field will be shown in Figure 7. Velocity decreased as the Brinkman parameter's value increased. This is because, by increasing the values of the Brinkman parameter, the drag forces become stronger, so velocity reduces.

Figures 8 and 9 show the effects of the ϕ_{hnf} volume fraction on hybrid nanoparticles. It is discovered that for higher values of ϕ_{hnf} and velocity indicated drops, the temperature can be increased. The nanofluid density has important significance in the velocity field. By mixing nanoparticles through base fluid, the consequent hybrid nanofluids improve considerably thicker which decreases velocity and increases temperature.

In the end, we have presented a comparison between our results and those of Saqib et al. [47]. It is clearly evident that the solution obtained with generalized Mittage–Leffler kernel in the presence of bioconvection shows stronger memory rather than exponential kernel that appeared in Caputo-Fabrizio fractional derivative as presented in Figure 10. It is concluded with the remark that our results can be enhanced in terms of memory.

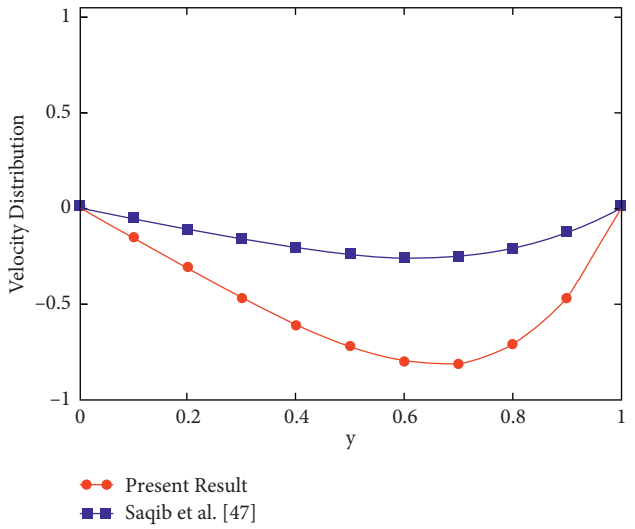

FIGURE 10: The comparison among our results and Saqib et al. [47] for velocity field, when $\Pr = 6.2, t = 2, \beta = \gamma = 0.5, Lb = 10, \beta^* = 0.006, Ra = 5, Gr = 10, \phi_{hnf} = 0.04$, and $M = 0.02$.

5. Conclusions

The current study investigated bioconvection using a heat transfer and MHD effects model, as well as a Prabhakar fractional approach. Laplace transform techniques are used to provide exact solutions for dimensionless governing equations. Graphical illustrations have been used to explain some of the physical effects of flow parameters. The followings are the significant outcomes:

(i) Obtained solutions are predicted for different values of fractional parameters based on generalized Fourier's law are responsible to attain better memory instead of artificial replacement

(ii) For a large time, fluid properties such as temperature, bioconvection, and velocity depict history/memory.

(iii) The temperature of water base nanoparticles is comparatively higher than kerosene and engine oil.

(iv) Bioconvection Rayleigh is responsible for the rapid decline in the momentum equation.

(v) The obtained solutions can be beneficial for proper analysis of real data and provide a tool for testing possible approximate solutions where needed.

For the future direction of readers, this work can be extended to include a large class of fluids of non-Newtonian nature and different thermal and mechanical boundary conditions. Also, you can extend this work with the fuzzy boundary conditions.

Data Availability

The data used to support the findings of this study are included within the article.

Conflicts of Interest

The authors declare that they have no conflicts of interest.

Authors' Contributions

All of the authors contributed substantially to the study.

Acknowledgments

The Deanship of Scientific Research (DSR) at King Abdulaziz University (KAU), Jeddah, Saudi Arabia has funded this project, under grant no. (KEP-MSc: 111-130-1443).

References

[1] H. C. Brinkman, "A calculation of the viscous force exerted by a flowing fluid on a dense swarm of particles," *Flow, Turbulence and Combustion*, vol. 1, no. 1, p. 27, 1949.

[2] H. C. Brinkman, "On the permeability of media consisting of closely packed porous particles," *Flow, Turbulence and Combustion*, vol. 1, no. 1, p. 81, 1949.

[3] M. Saqib, I. Khan, S. Shafie, and A. Q. Mohamad, "Shape effect on MHD flow of time fractional Ferro-Brinkman type nanofluid with ramped heating," *Scientific Reports*, vol. 11, no. 1, p. 3725, 2021.

[4] M. I. Asjad, N. Sarwar, M. B. Hafeez, W. Sumelka, and T. Muhammad, "Advancement of non-Newtonian fluid with hybrid nanoparticles in a convective channel and prabhakar's fractional derivative—analytical solution," *Fractal and Fractional*, vol. 5, no. 3, p. 99, 2021.

[5] A. Khan, D. Khan, I. Khan, F. Ali, F. u. Karim, and K. S. Nisar, "MHD flow of brinkman type H_2O-Cu, Ag, TiO_2 and Al_2O_3 nanofluids with chemical reaction and heat generation effects in a porous medium," *Journal of Magnetics*, vol. 24, no. 2, pp. 262–270, 2019.

[6] C. E. Nanjundappa, A. Pavithra, and I. S. Shivakuamara, "Effect of dusty particles on Darcy-brinkman gravity-driven ferro-thermal-convection in a ferrofluid saturated porous layer with internal heat source: influence of boundaries," *International Journal of Algorithms, Computing and Mathematics*, vol. 7, no. 1, p. 21, 2021.

[7] S. Sarwar, M. Aleem, M. A. Imran, and A. Akgül, "A comparative study on non-Newtonian fractional order Brinkman type fluid with two different kernels," *Numerical Methods for Partial Differential Equations*, vol. 4, 2020.

[8] S. Shafie, M. Saqib, I. Khan, and A. Qushairi, "Mixed convection flow of brinkman type hybrid nanofluid based on atangana-baleanu fractional model," *Journal of Physics: Conference Series*, vol. 1366, no. 1, 2019.

[9] F. Ali, F. Ali, N. A. Sheikh, I. Khan, and K. S. Nisar, "Caputo–Fabrizio fractional derivatives modeling of transient MHD Brinkman nanoliquid: applications in food technology," *Chaos, Solitons & Fractals*, vol. 131, 2020.

[10] M. Saqib, I. Khan, S. Shafie, A. Qushairi Mohamad, and E. S. M Sherif, "Analysis of magnetic resistive flow of generalized brinkman type nanofluid containing carbon nanotubes with ramped heating," *Computers, Materials & Continua*, vol. 67, no. 1, pp. 1069–1084, 2021.

[11] A. Boutiara, M. S. Abdo, M. A. Alqudah, and T. Abdeljawad, "On a class of Langevin equations in the frame of Caputo function-dependent-kernel fractional derivatives with

antiperiodic boundary conditions," *AIMS Mathematics*, vol. 6, pp. 5518–5534, 2021.

[12] R. Ali, A. Akgül, and M. I. Asjad, "Power law memory of natural convection flow of hybrid nanofluids with constant proportional Caputo fractional derivative due to pressure gradient," *Pramana*, vol. 94, no. 1, p. 131, 2020.

[13] M. A. Imran, I. Khan, M. Ahmad, N. A. Shah, and M. Nazar, "Heat and mass transport of differential type fluid with non-integer order time-fractional Caputo derivatives," *Journal of Molecular Liquids*, vol. 229, pp. 67–75, 2017.

[14] M. Ahmad, M. A. Imran, and M. Nazar, "Mathematical modeling of (Cu– A l 2 O 3) water-based Maxwell hybrid nanofluids with Caputo-Fabrizio fractional derivative," *Advances in Mechanical Engineering*, vol. 12, no. 9, 2020.

[15] I. A. Mirza and D. Vieru, "Fundamental solutions to advection–diffusion equation with time-fractional Caputo–Fabrizio derivative," *Computers & Mathematics with Applications*, vol. 73, no. 1, pp. 1–10, 2017.

[16] R. Gul, M. Sarwar, K. Shah, T. Abdeljawad, and F. Jarad, "Qualitative analysis of implicit dirichlet boundary value problem for caputo-fabrizio fractional differential equations," *Journal of Function Spaces*, vol. 22, pp. 1–9, 2020.

[17] M. S. Abdo, T. Abdeljawad, K. D. Kucche, M. A. Alqudah, S. M. Ali, and M. B. Jeelani, "On nonlinear pantograph fractional differential equations with Atangana–Baleanu–Caputo derivative," *Advances in Difference Equations*, vol. 65, no. 1, 2021.

[18] N. H. Sweilam, S. M. Al-Mekhlafi, T. Assiri, and A. Atangana, "Optimal control for cancer treatment mathematical model using Atangana–Baleanu–Caputo fractional derivative," *Advances in Difference Equations*, vol. 34, no. 1, p. 334, 2020.

[19] N. Sarwar, M. I. Asjad, T. Sitthiwirattham, N. Patanarapeelert, and T. Muhammad, "A prabhakar fractional approach for the convection flow of Casson fluid across an oscillating surface based on the generalized fourier law," *Symmetry*, vol. 13, no. 11, p. 2039, 2021.

[20] N. A. Shah, C. Fetecau, and D. Vieru, "Natural convection flows of Prabhakar-like fractional Maxwell fluids with generalized thermal transport," *Journal of Thermal Analysis and Calorimetry*, vol. 143, no. 3, pp. 2245–2258, 2021.

[21] T. Elnaqeeb, N. A. Shah, and A. Rauf, "Natural convection flows of carbon nanotube Prabhakar-like fractional second-grade nanofluids over an infinite plate with Newtonian heating," *Mathematical Methods in the Applied Sciences*, vol. 27, 2020.

[22] R. Garrappa and E. Kaslik, "Stability of fractional-order systems with Prabhakar derivatives," *Nonlinear Dynamics*, vol. 102, no. 1, pp. 567–578, 2020.

[23] S. U. Choi and J. A. Eastman, "Enhancing thermal conductivity of fluids with nanoparticles," *ASME International Mechanical Engineering Congress and Exposition*, vol. 66, pp. 99–105, 1995.

[24] R. Ali, M. I. Asjad, and A. Akgül, "An analysis of a mathematical fractional model of hybrid viscous nanofluids and its application in heat and mass transfer," *Journal of Computational and Applied Mathematics*, vol. 383, 2021.

[25] M. Ahmad, M. I. Asjad, A. Akgül, and D. Baleanu, "Analytical solutions for free convection flow of Casson nanofluid over an infinite vertical plate," *AIMS Mathematics*, vol. 6, no. 3, pp. 2344–2358, 2020.

[26] T. Gul, M. Bilal, M. Bilal, W. Alghamdi, M. I. Asjad, and T. Abdeljawad, "Hybrid nanofluid flow within the conical gap between the cone and the surface of a rotating disk," *Scientific Reports*, vol. 11, no. 1, p. 1180, 2021.

[27] K. Rafique, M. A. Imran, M. I. Anwar, M. Misiran, and A. Ahmadian, "Energy and mass transport of Casson nanofluid flow over a slanted permeable inclined surface," *Journal of Thermal Analysis and Calorimetry*, vol. 144, no. 6, pp. 2031–2042, 2021.

[28] A. S. Khan, Y. Nie, Z. Shah et al., "Influence of interfacial electrokinetic on MHD radiative nanofluid flow in a permeable microchannel with Brownian motion and thermophoresis effects," *Open Physics*, vol. 18, no. 1, pp. 726–737, 2020.

[29] L. Ali Lund, Z. Omar, I. Khan, and E. M Sherif, "Dual branches of MHD three-dimensional rotating flow of hybrid nanofluid on nonlinear shrinking sheet," *Computers, Materials & Continua*, vol. 66, no. 1, pp. 127–139, 2020.

[30] Z. Shah, M. Sheikholeslami, P. Kumam, and P. Kumam, "Simulation of entropy optimization and thermal behavior of nanofluid through the porous media," *International Communications in Heat and Mass Transfer*, vol. 120, 2021.

[31] K. G. Kumar, E. H. B. Hani, M. E. H. Assad, M. Rahimi-Gorji, and S. Nadeem, "A novel approach for investigation of heat transfer enhancement with ferromagnetic hybrid nanofluid by considering solar radiation," *Microsystem Technologies*, vol. 27, no. 1, pp. 97–104, 2021.

[32] P. K. Dadheech, P. Agrawal, F. Mebarek-Oudina, N. H. Abu-Hamdeh, and A. Sharma, "Comparative heat transfer analysis of MoS2/C2H6O2 and SiO2-MoS2/C2H6O2 nanofluids with natural convection and inclined magnetic field," *Journal of Nanofluids*, vol. 9, no. 3, pp. 161–167, 2020.

[33] K. Dhif, F. Mebarek-Oudina, S. Chouf, H. Vaidya, and A. J. Chamkha, "Thermal analysis of the solar collector cum storage system using a hybrid-nanofluids," *Journal of Nanofluids*, vol. 10, no. 4, pp. 616–626, 2021.

[34] S. I. U. Khan, E. Alzahrani, U. Khan, N. Zeb, and A. Zeb, "On mixed convection squeezing flow of nanofluids," *Energies*, vol. 13, no. 12, p. 3138, 2020.

[35] W. Bu, H. Xu, I. Khan, S. I. Ullah Khan, and A. Zeb, "Mixed convection squeezing flow of nanofluids in a rotating channel with thermal radiation," *Journal of Mathematics*, vol. 15, p. 1, 2022.

[36] S. I. Ullah Khan, U. Khan, N. Ahmed, S. T. Mohyud-Din, I. Khan, and K. S. Nisar, "Thermal transport investigation in AA7072 and AA7075 aluminum alloys nanomaterials based radiative nanofluids by considering the multiple physical flow conditions," *Scientific Reports*, vol. 11, no. 1, pp. 1–11, 2021.

[37] I. Chabani, F. Mebarek-Oudina, and A. A. I. Ismail, "MHD flow of a hybrid nano-fluid in a triangular enclosure with zigzags and an elliptic obstacle," *Micromachines*, vol. 13, no. 2, p. 224, 2022.

[38] C. Rajashekhar, F. Mebarek-Oudina, H. Vaidya, K. V. Prasad, G. Manjunatha, and H. Balachandra, "Mass and heat transport impact on the peristaltic flow of a Ree–Eyring liquid through variable properties for hemodynamic flow," *Heat Transfer*, vol. 50, no. 5, pp. 5106–5122, 2021.

[39] S. Marzougui, F. Mebarek-Oudina, M. Magherbi, and A. Mchirgui, "Entropy generation and heat transport of Cu–water nanoliquid in porous lid-driven cavity through magnetic field," *International Journal of Numerical Methods for Heat and Fluid Flow*, vol. 32, no. 6, pp. 2047–2069, 2021.

[40] M. I. Asjad, N. Sarwar, B. Ali, S. Hussain, T. Sitthiwirattham, and J. Reunsumrit, "Impact of bioconvection and chemical reaction on MHD nanofluid flow due to exponential stretching sheet," *Symmetry*, vol. 13, no. 12, p. 2334, 2021.

[41] J. R. Platt, "Bioconvection patterns" in cultures of free-swimming organisms," *Science*, vol. 133, no. 3466, pp. 1766-1767, 1961.

[42] H. Ge-Jile, H. Waqas, S. U. Khan, M. I. Khan, S. Farooq, and S. Hussain, "Three-dimensional radiative bioconvective flow of a sisko nanofluid with motile microorganisms," *Coatings*, vol. 11, no. 3, p. 335, 2021.

[43] M. Ramzan, H. Gul, S. Kadry, and Y. M. Chu, "Role of bioconvection in a three dimensional tangent hyperbolic partially ionized magnetized nanofluid flow with Cattaneo-Christov heat flux and activation energy," *International Communications in Heat and Mass Transfer*, vol. 120, 2021.

[44] Z. A. Alhussain, A. Renuka, and M. Muthtamilselvan, "A magneto-bioconvective and thermal conductivity enhancement in nanofluid flow containing gyrotactic microorganism," *Case Studies in Thermal Engineering*, vol. 23, 2021.

[45] U. Farooq, H. Waqas, M. I. Khan, S. U. Khan, Y. M. Chu, and S. Kadry, "Thermally radioactive bioconvection flow of Carreau nanofluid with modified Cattaneo-Christov expressions and exponential space-based heat source," *Alexandria Engineering Journal*, vol. 60, no. 3, pp. 3073–3086, 2021.

[46] T. A. Yusuf, F. Mabood, B. C. Prasannakumara, and I. E. Sarris, "Magneto-bioconvection flow of Williamson nanofluid over an inclined plate with gyrotactic microorganisms and entropy generation," *Fluid*, vol. 6, no. 3, p. 109, 2021.

[47] M. Saqib, S. Shafie, I. Khan, Y. M. Chu, and K. S. Nisar, "Symmetric MHD channel flow of nonlocal fractional model of BTF containing hybrid nanoparticles," *Symmetry*, vol. 12, no. 4, p. 663, 2020.

[48] M. Danish Ikram, M. Imran Asjad, A. Ahmadian, and M. Ferrara, "A new fractional mathematical model of extraction nanofluids using clay nanoparticles for different based fluids," *Mathematical Methods in the Applied Sciences*, vol. 66, 2020.

[49] M. I. Asjad, M. D. Ikram, R. Ali, D. Baleanu, and A. S. Alshomrani, "New analytical solutions of heat transfer flow of clay-water base nanoparticles with the application of novel hybrid fractional derivative," *Thermal Science*, vol. 24, no. Suppl. 1, pp. 343–350, 2020.

[50] M. D. Ikram, M. I. Asjad, A. Akgül, and D. Baleanu, "Effects of hybrid nanofluid on novel fractional model of heat transfer flow between two parallel plates," *Alexandria Engineering Journal*, vol. 60, no. 4, pp. 3593–3604, 2021.

[51] F. Bräuer, E. Trautner, J. Hasslberger, P. Cifani, and M. Klein, "Turbulent bubble-laden channel flow of power-law fluids: a direct numerical simulation study," *Fluid*, vol. 6, no. 1, p. 40, 2021.

[52] Y. Zheng, H. Yang, H. Mazaheri, A. Aghaei, N. Mokhtari, and M. Afrand, "An investigation on the influence of the shape of the vortex generator on fluid flow and turbulent heat transfer of hybrid nanofluid in a channel," *Journal of Thermal Analysis and Calorimetry*, vol. 143, no. 2, pp. 1425–1438, 2021.

[53] A. D'Ippolito, F. Calomino, G. Alfonsi, and A. Lauria, "Flow resistance in open channel due to vegetation at reach scale: a review," *Water*, vol. 13, no. 2, p. 116, 2021.

[54] S. U. Haq, M. A. Khan, Z. A. Khan, and F. Ali, "MHD effects on the channel flow of a fractional viscous fluid through a porous medium: an application of the Caputo-Fabrizio time-fractional derivative," *Chinese Journal of Physics*, vol. 65, pp. 14–23, 2020.

[55] M. I. Asjad, S. U. Ur Rehman, A. Ahmadian, S. Salahshour, and M. Salimi, "First solution of fractional bioconvection with power law kernel for a vertical surface," *Mathematics*, vol. 9, no. 12, p. 1366, 2021.

[56] B. Tashtoush and A. Magableh, "Magnetic field effect on heat transfer and fluid flow characteristics of blood flow in multi-stenosis arteries," *Heat and Mass Transfer*, vol. 44, no. 3, pp. 297–304, 2007.

[57] F. Polito and Z. Tomovski, "Some properties of Prabhakar-type fractional calculus operators," *Fractional Differential Calculus*, vol. 6, no. 1, pp. 73–94, 2015.

[58] A. Giusti and I. Colombaro, "Prabhakar-like fractional viscoelasticity," *Communications in Nonlinear Science and Numerical Simulation*, vol. 56, pp. 138–143, 2018.

Hindawi
Mathematical Problems in Engineering
Volume 2022, Article ID 9451091, 11 pages
https://doi.org/10.1155/2022/9451091

Research Article

Intelligent Computing of Levenberg-Marquard Technique Backpropagation Neural Networks for Numerical Treatment of Squeezing Nanofluid Flow between Two Circular Plates

Hakeem Ullah,[1] **Mehreen Fiza**,[1] **Muhammad Asif Zahoor Raja**,[2] **Imran Khan**,[1] **Muhammad Shoaib**,[3] **and Seham M. Al-Mekhlafi**[4]

[1]*Department of Mathematics, Abdul Wali Khan University, Mardan 23200, KP, Pakistan*
[2]*Future Technology Research Center, National Yunlin University of Science and Technology, 123 University Road, Section 3, Douliou, Yunlin 64002, Taiwan*
[3]*Department of Mathematics, COMSATS University Islamabad, Attock Campus, Attock 43600, Pakistan*
[4]*Department of Mathematics, Sana'a University, Sana'a, Yemen*

Correspondence should be addressed to Mehreen Fiza; drmehreenfiza@gmail.com and Seham M. Al-Mekhlafi; smdk100@gmail.com

Received 7 March 2022; Revised 25 June 2022; Accepted 6 July 2022; Published 19 August 2022

Academic Editor: Arshad Riaz

This study presents new techniques based on the artificial intelligence neural network with Levenberg-Marquardt Scheme with backpropagation (ANN-LMS). The boundary value problem BVP is obtained from the governing equations of the flow model. Along with ANN-LMS, the semianalytical method namely the optimal homotopy analysis method (OHAM) is used for validating the results. ANN-LMS optimized the absolute error and increased the accuracy of the solution. The effect of physical parameters is discussed with the help of plots and tables.

1. Introduction

The squeezing flow has many important applications in engineering, material science, and physics. The squeezing flow has captured the imagination of many scientists and engineers in recent years due to its frequent applications in industrial and engineering such as stirring pistons, squeezed film and polymer manufacturing, sweet fillers, hydraulic lift, electric motors, flow within the nozzle and nasogastric tube, power transmission, modeling of chewing and eating, heart values and blood vessels [1–6]. Stefan [7] initiated pioneering works in this direction. Verma [8] examined the numerical solution of squeezing flow between the two plates. Sheikholeslami et al. [9] used the Adomian decomposition method (ADM) to explore the unsteady squeezing flow of nanofluids. Gupta and Ray [10] investigated the unsteady squeezing flow of nanofluid between two parallel plates numerically. The squeezing flow of a second-grade fluid was investigated by Rajagopal and Gupta [11]. Hayat et al. [12] investigated the squeezing flow of second-grade material by two disks. Hayat et al. [13] presented a three-dimensional squeezing flow between two parallel plates with mixed convection. The squeezing flow of electrically conducting fluids between parallel plates under the influence of a magnetic field has been studied extensively in recent years. Siddiqui et al. [14] adopted the homotopy perturbation method and investigated the magnetic effect of squeezing viscous magnetohydrodynamics (MHD) fluid flow. Ahmed et al. [15] investigated MHD squeezing flow of Casson fluid between parallel disks. For the solutions of the system of ODEs/PDEs, both the analytical and numerical methods are in practice. The numerical methods required linearization and discretization techniques which distress the accuracy. The AI-based numerical technique was frequently used in different applications to solve differential equations [16–18], but there is a need to explore and exploit the stochastic

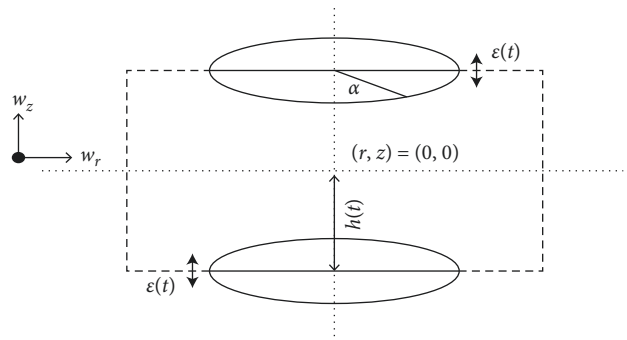

Figure 1: Flow diagram.

numerical technique based on intelligent computing paradigms to solve and analyze the problems given in Equations (14)–(16). A few recently published studies of paramount importance contain mathematical model solution in nonlinear optics [19], atomic physics [20], and financial models [21, 22], eye model [23], COVID-19 virus spread models [24, 25], entropy generation system [26, 27], and flow problems [28–40]. According to our literature research, to examine the SFNM between two circular plates, we apply the AI technique through the ANN-LMS to realize nonlinear backpropagation of neural network to Equations (14)–(16). This outlines the creative features of the emerging computing model as follows:

(1) A unique two-layer feed-forward backpropagation of ANN-LMS is proposed for the analysis of squeezed flow between two circular plates

(2) The MSE-based merit function is planned for the realization of ANN-LMS for estimated modeling of squeezed flow between two circular plates by means of the PF, TT, FT, and VL reference dataset

(3) The accurate, consistent, and convergent PR of the constructed proposal ANN-LMS is authenticated for the problem while the solver values are further authorized by the error analysis and EH and RG studies.

2. Flow Analysis

Let us assume an incompressible squeezing flow between two circular disks with separation $2s(t)$. The plane for the mentioned flow is suggested as $(\tilde{z}, \tilde{r})$ plane, and the plate movements are about the central axis $\tilde{z} = 0$, and the axisymmetric is about $\tilde{r} = 0$. The plate movement is about the z axis which is symmetric and nonrotating as shown in Figure 1.

The velocity field is given as $V = (u(r, z, t), 0, w(r, z, t))$. The governing equations are given as follows:

$$\frac{1}{r}\partial_r(ru) + \partial_z w = 0,$$

$$\left(\partial_t u + u\partial_r u + w\partial_z u\right) = -\frac{\partial_r p}{\rho} + \nu\left(\nabla^2 u - \frac{u}{r^2}\right), \tag{1}$$

$$\left(\partial_t w + u\partial_r w + w\partial_z w\right) = -\frac{\partial_z p}{\rho} + \nu\left(\nabla^2 w\right).$$

With BCs,

$$\begin{aligned} u = 0, w = v_c \quad z = h, \\ \partial_z u = 0, w = 0 \quad z = 0, \end{aligned} \tag{2}$$

where v_c is the velocity of circular plates and $\overline{\nabla}^2$ as dell operator also using the nondimensional variable $\eta = z/h$ and $u = -rv_c/2h(t)f'(\eta), \quad w = v_c f(\eta)$. The governing equations becomes

$$\begin{aligned} f''''' + R(\eta - f)f''' + 2f'' - Qf'' = 0, \\ R = \frac{h\varepsilon}{\nu}, Q = \frac{h^2}{\nu c}\frac{d\varepsilon}{dt}, \\ f(1) = 1, f'(1) = 0, \\ f(0) = 0, f''(0) = 0. \end{aligned} \tag{3}$$

3. Numerical Results and Explanation

This section provides a concise explanation of the approach used, and the results of the numerical simulations received through the backpropagated supervised network ANN-LMS designed for the fluid flow system represented via 14–15 based on SFNM. The six steps of the proposed methodology's step-by-step process flow are shown in Figure 2. The 201 input grid between the closed intervals of 0 and 1 is used to produce the proposal dataset for ANN-LMS for the problem. Presently, 10% of the data are used for TT, 10% for VL, and 80% of the data are used at random for TR. Neural network-based supervised learning is constructed after constructing the data through Equations (14)–(15). TR data are utilized to formulate the estimated solution based on an MSE-based merit function. This article presents numerical experimentation for the ANN-LMM for SFNM between two plates that are circular. For one scenario, in the g, the design of the ANN-LMM is used as shown in Tables 1 and 2. The "nts" method of Matlab's neural network toolbox is used to create ANN-LMS, which has a two-layer feed-forward network structure with backpropagation. Figure 3 depicts the structural layout for the designed network, which uses the concept of the hidden layer through activation function and appropriated adjustments of weights.

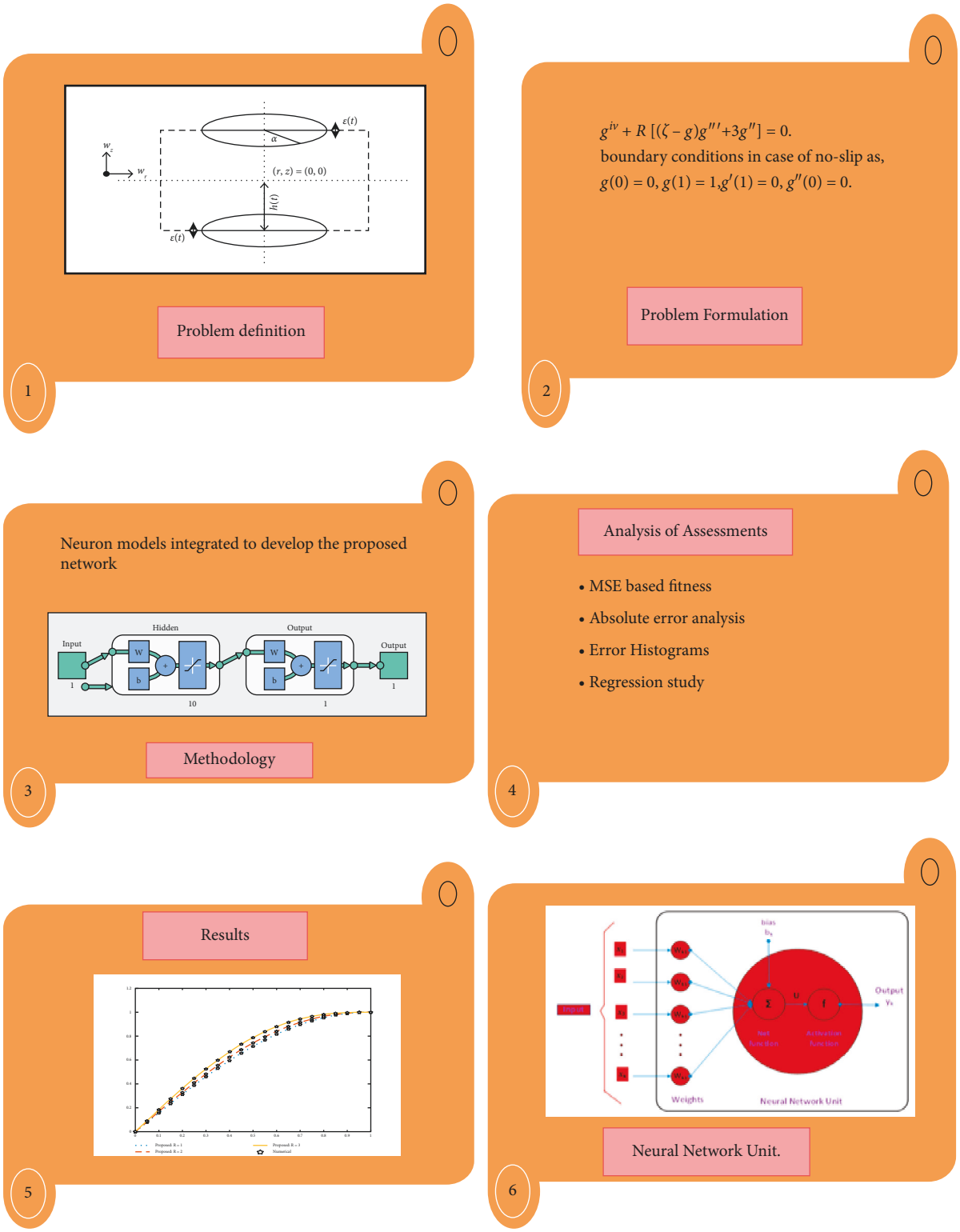

Figure 2: (1–6): Operational flow between two circular plates for the proposed ANN-LMS for SFNM.

In Figures 4–7, for the scenario one case one of f and f' results of ANN-LMS, error histogram, and FT are shown, respectively. In Figure 8, the RG analysis of SFNM between two plates that are circular is shown. For case one scenario one, there is a convergence of MSE for TR, VL, and TT progression in Figures 4(a) and 4(b). This scenario involves one SFNM between two circular plates. In Tables 3 and 4, for the scenario one case, one different numerical values are

Table 1: Values of physical quantities affecting f for the fluid flow problem under consideration.

Physical quantities R	Scenarios	Cases
1		1
3	1	2
5		3

Table 2: Values of physical quantities effecting f' for the fluid flow problem under consideration.

Physical quantities R	Scenarios	Cases
1		1
3	1	2
5		3

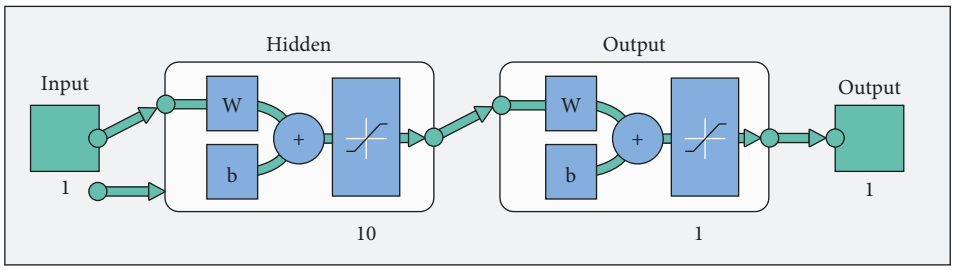

Figure 3: Networks flow diagram.

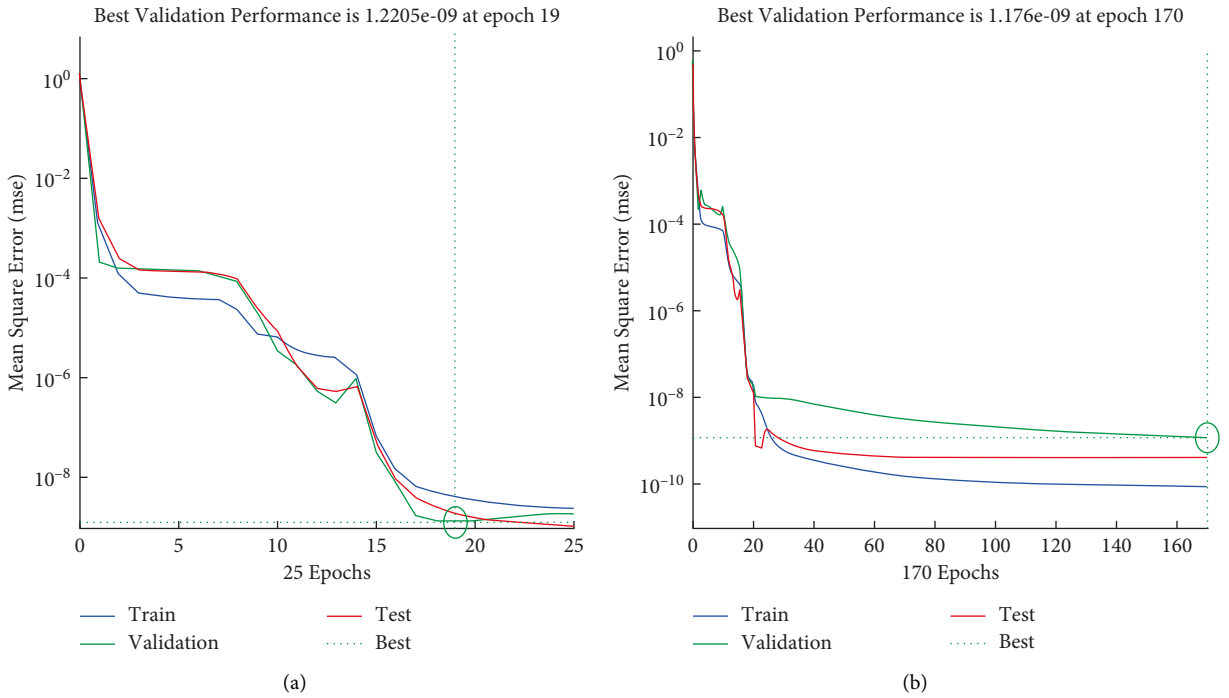

Figure 4: Case one of scenario one SFNM between two circular plates, PF result of MSE for proposed ANN-LMS.

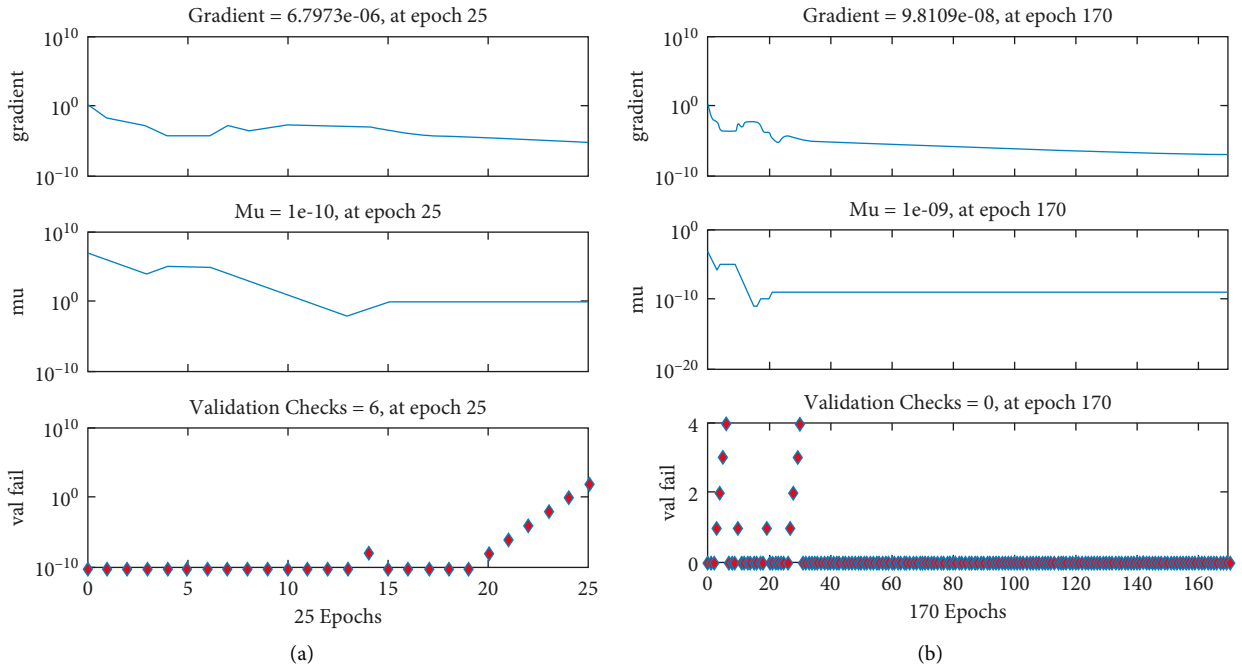

Figure 5: The outcome of the intended ANN-state LMS's transition dynamic for the first scenario (case1).

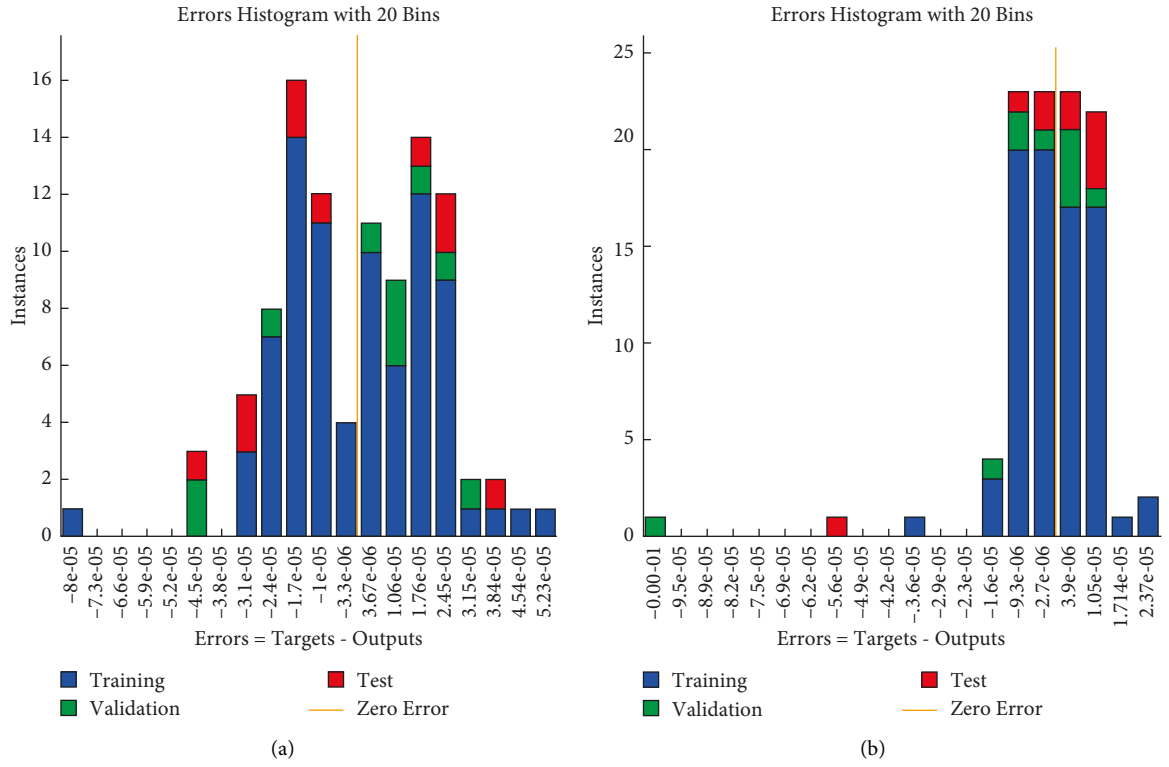

Figure 6: EH representation against first scenario (case1).

presented. We noticed that at epochs 170, the greatest network PF are $1.176e^{-9}$, and at epoch 19 $1.2e^{-9}$, respectively. In Figures 5(a) and 5(b), the back-gradient propagation's and step size Mu are approximately (at the epochs 25 and at the epochs 170) and $(10^{-10}, 10^{-9})$, respectively. The ANN-LMS′ PF-generated results are

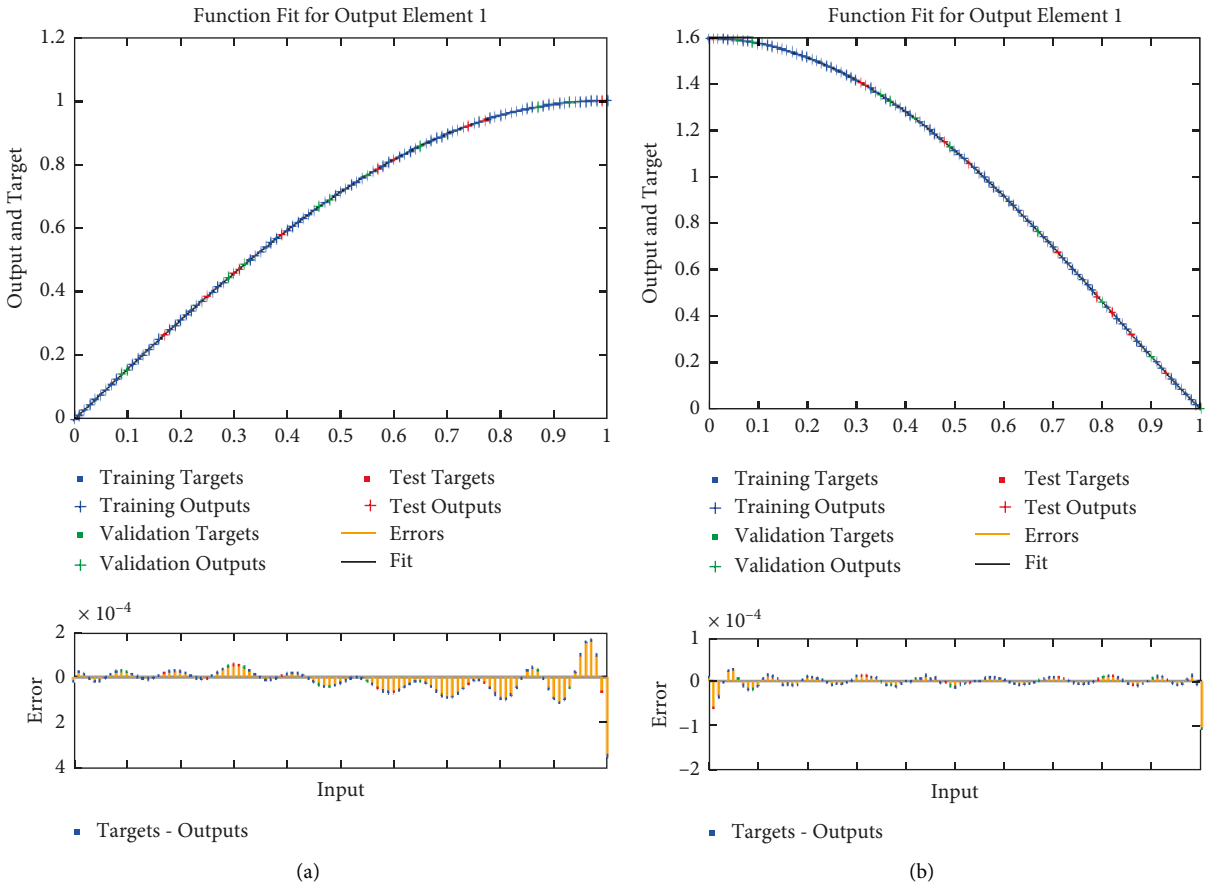

Figure 7: FTs representation against first scenario (case1).

Table 3: Results for scenario 1 of the flow problem for f.

Case	MSE			Performance	Gradient (E)	Mu (E)	Epoch	Time
	Training	Validation	Testing					
1	$3.85913E-10$	$8.05434E-10$	$4.08718E-10$	$8.61E-11$	9.81–8	1–9	270	0
2	$1.744E-9$	$6.13895E-9$	$3.05430E-8$	$1.74E-9$	9.99–8	1–8	245	0
3	$4.408E-10$	$6.56798E-10$	$7.06632E-10$	$4.41E-10$	9.98–8	1–9	241	0

Table 4: Results for scenario 1 of the flow problem f'.

Case	MSE			Performance	Gradient (E)	Mu	Epoch	Time
	Training	Validation	Testing					
1	$8.60809E-11$	$1.17599E-9$	$4.08718E-10$	$8.61E-11$	9.88–8	$1E-9$	278	0
2	$8.3733E-9$	$5.74998E-9$	$1.34309E-8$	$5.81E-12$	1.00–8	$1E-11$	220	0
3	$7.891E-11$	$5.34501E-11$	$9.06819E-11$	$4.789E-11$	1.43–8	$1E-9$	1000	3

examined along with a numerical recommendation from the OHAM technique against Scenario 1 (first case). Figures 7(a) and 7(b) show the outcomes in terms of solution and errors. Step size is 0.01 for the domain values lies between 0 and 1. Figure 8 reflects the outcomes of Regression for the scenario 1 of the flow problem. Figures 6(a) and 6(b) corresponding to scenario 1 (first case) represent the error analysis through EH. The maximum error that the intended ANN-LMS can accomplish for TT, TR, and VL data is less than 1 e^4 and 4 e^4 for case one scenario one of the system model. R values for correlations are always close to one. Tables 3 and 4 show the results of the fluid flow system ANN-LMS approach for

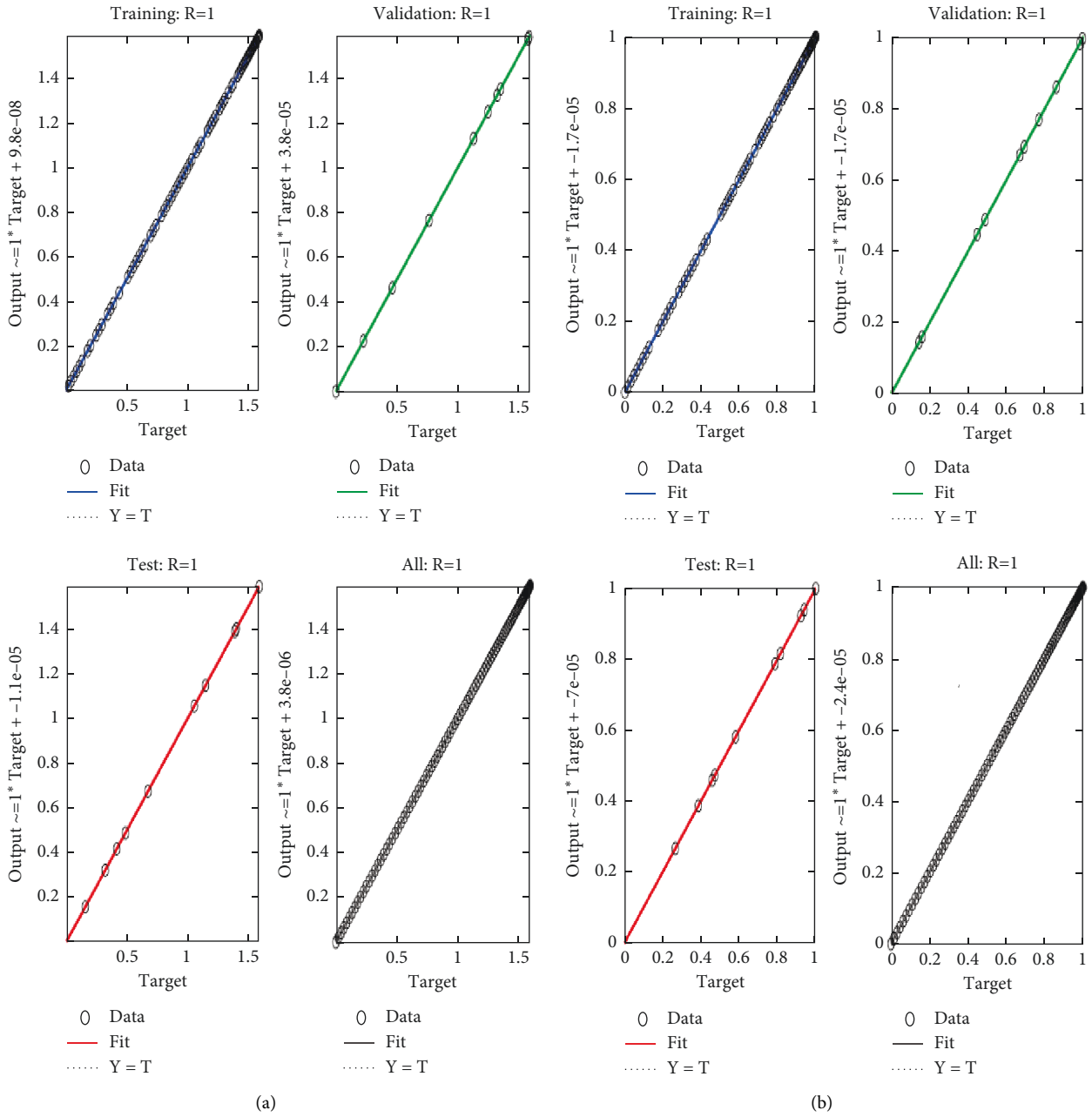

Figure 8: FTs representation against first scenario (case1).

resolving Case 1 and scenario one of the SFNM. For scenarios one and case one of SFNM between two circular plates, the PF of ANN-LMS is approximately 10^{-11}, 10^{-12}, and 10^{-9} to 10^{-10}. These results show that ANN-LMS can solve SFNM between two circular plates with a reliable PF. In light of this, scenario one's velocity profiles and ANN-LMS results are calculated. Figures 9–10 are constructed for the outcomes $f(\zeta)$ and $f(\zeta)$. As a consequence of the ANN-coordination LMMs with standard OHAM solutions in Case 1 and Scenario 1, the absolute error from orientation solutions has been determined, and the results are displayed in Figures 9(b) and 10(b) for scenario one case one. Absolute errors for the $f(\zeta)$ and $f(\zeta)$ are 10^{-4} to 10^{-7}, 10^{-3} to 10^{-05}, 10^{-5} to 10^{-6}, and 10^{-3} to 10^{-6}, 10^{-4} to 10^{-6}, 10^{-4} to 10^{-5}, respectively. The absoulte errors ofscenario 1 for f and f' are 10-3 to 10-6, 10-4 to 10-6, 10-4 to 10-5, and 10-4 to 10-7, 10 -3 to 10-05 , 10-5 to 10-6, respectively. As the plates come together, the pressure between them is greater than the pressure in the center, and vice versa. The pressure differential for various values of R is shown in Figure.

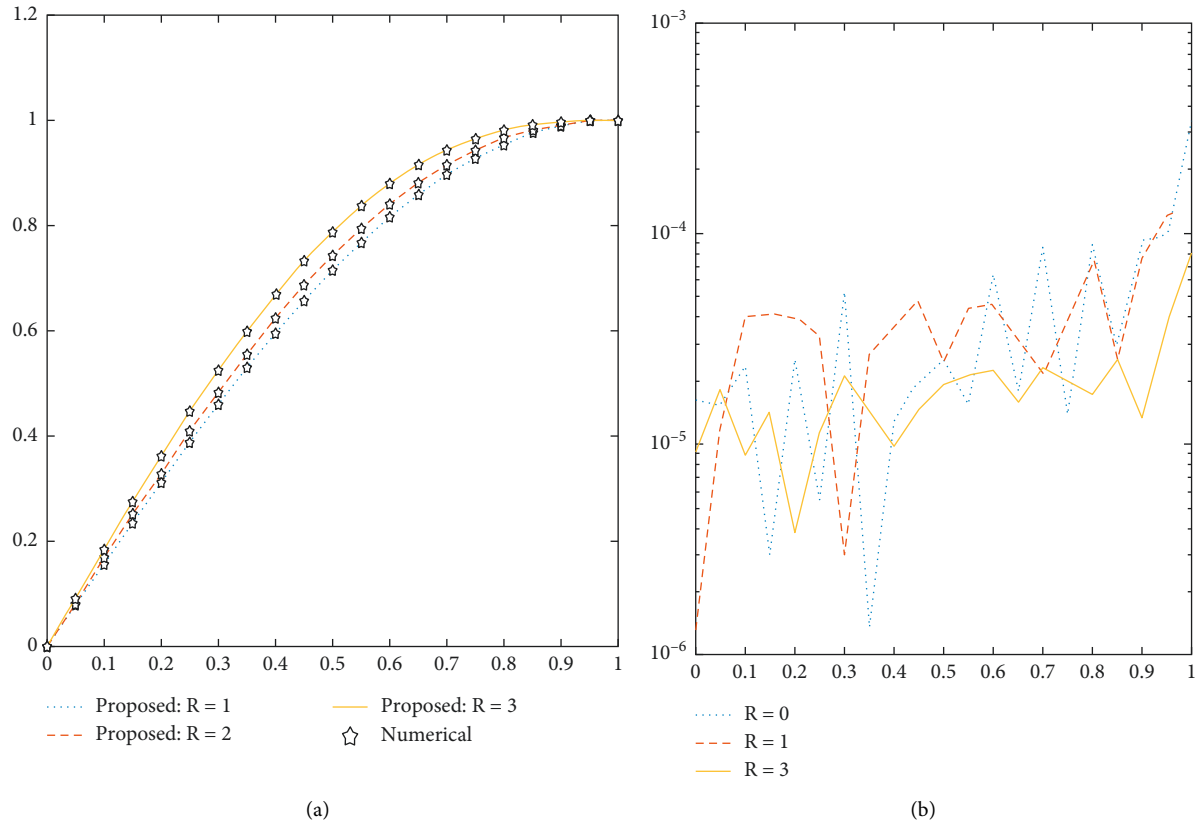

Figure 9: A comparison of OHAM and ANN-LMS is presented along with a suggested numerical result corresponding to the first scenario for g.

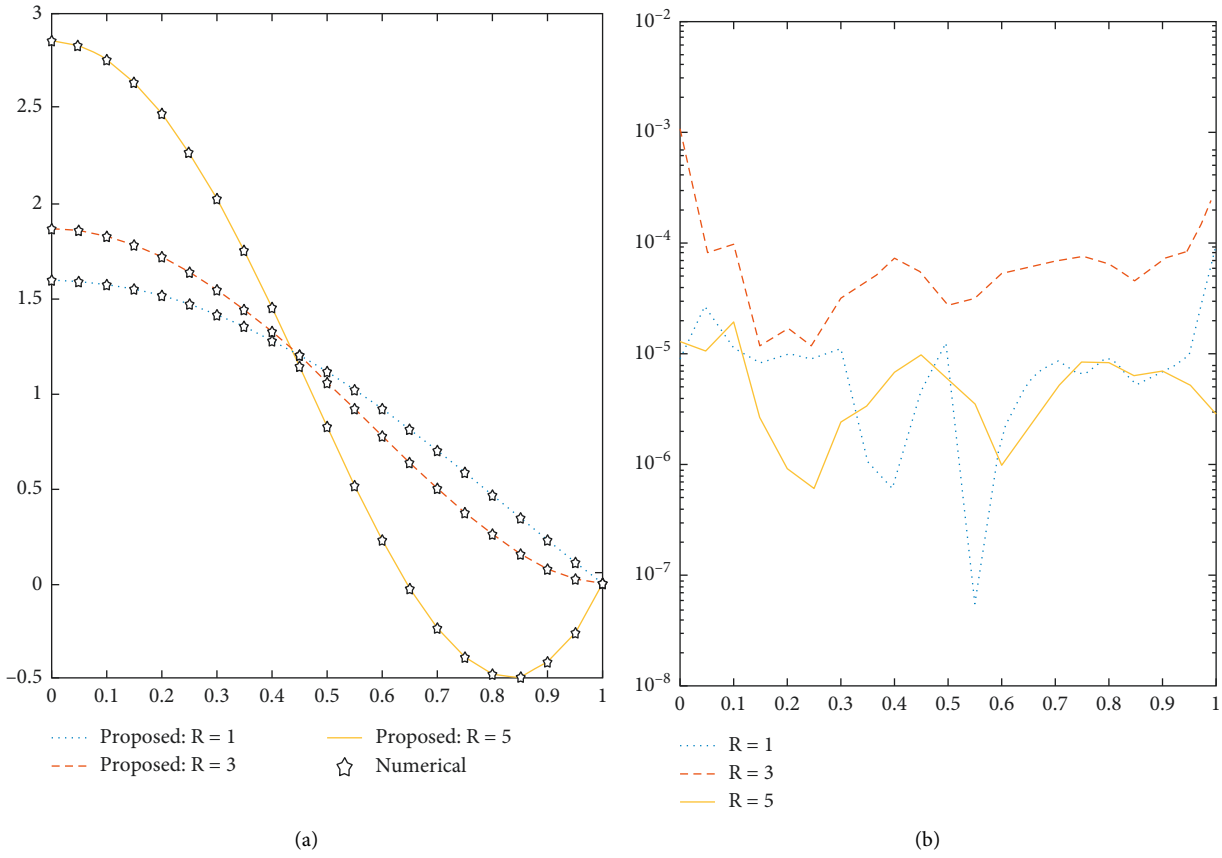

Figure 10: OHAM and ANN-LMS solutions comparison with suggested numerical results for scenario 1.

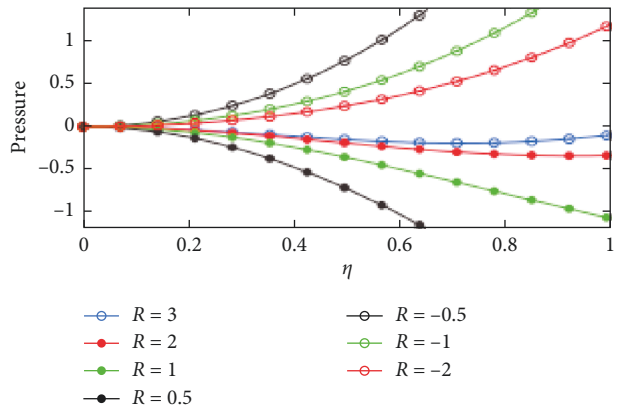

Figure 11: Variation of pressure for different values of R.

4. Concluding Remarks

Intelligence-based intellectual computing backpropagation provides an alternative environment for the solution of fluid flow problem under consideration in terms of performance plots, regression metrics, gradient analysis, and error dynamics through histograms consisting of a variety of bins. The followings are the main results of the study:

(1) As the plates become closer to one another, the pressure between them rises more than the pressure in the centre and vice versa

(2) Velocity profile depicts the opposite trends corresponding to positive and negative values of Reynolds number

(3) The selction of dataset such as 80% fortraining, 10% for validation and 10% for testing proves that our method is stable, relaiable, and fast convergent than the other methods

(4) Pressure rises in the direction towards the middle region between two plates when both plates get closer to each other.

(5) By contrasting the results with a numerical method, the method's validity is established (Runge–Kutta method having order 4)

(6) The initial guess and linearization methods are not necessary for ANN-LMS

(7) Due to its ability to reduce accuracy and absolute error, ANN-LMS performs better than other approaches

Future direction: the authors are motivated to work on new unsupervised learning algorithms after successful completion of work representing supervised learning [34–36].

Nomenclature

ANNs: Artificial neural network
SF: Squeezing flow
v: Kinematic viscosity
NN: Neural network
BL: Boundary layer
k: Thermal conductive
BVP: Boundary value problem
Pr: Prandtl number
Eh: Epoch MSE mean square error
ρ: Fluid density
μ: Dynamic viscosity
PF: Performance
TT: Testing
TR: Training
VD: Validation
EB: Error bin
EH: Histogram
GD: Gradient
RG: Regression
AE: Absolute error
Ep: Epoch
MSE: Mean square error.

Data Availability

All the relevant data are presented in the paper.

Conflicts of Interest

The authors declare that they have no conflicts of interest.

References

[1] P. S. Gupta and A. S. Gupta, "Squeezing flow between parallel plates," *Wear*, vol. 45, no. 2, pp. 177–185, 1977.

[2] R. T¨ornqvist, P. Sunderland, and J. A. E. Manson, "Nonisothermal process rheology of thermoplastic composites for compression flow moulding," *Composites Part A: Applied Science and Manufacturing*, vol. 31, no. 9, pp. 917–927, 2000.

[3] P. Shirodkar, A. Bravo, and S Middleman, "Lubrication flows in viscoelastic liquids: 2. Effect of slip on squeezing flow between approaching parallel rigid planes," *Chemical Engineering Communications*, vol. 14, no. 3–6, pp. 151–175, 1982.

[4] Y. Tian, S Wen, and Y Meng, "Compressions of electrorheological fluids under different initial gap distances," *Physical Review A*, vol. 67, no. 5, Article ID 051501, 2003.

[5] R. B. Bird, R. C. Armstrong, and O. Hassager, "Dynamics of polymeric liquids," *Fluid Mechanics*, vol. 1, 1987.

[6] J. L. Kokini, J. B. Kadane, and E. L. Cussler, "Liquid texture perceived in the mouth," *Journal of Texture Studies*, vol. 8, no. 2, pp. 195–218, 1977.

[7] M. J. Stefan, "Versuchs Uber die scheinbare adhesion, Sitzungsberichte der Akademie der Wissenschaften in Wien," *Mathematik-Naturwissen*, vol. 69, pp. 713–721, 1874.

[8] R. L. Verma, "A numerical solution for squeezing flow between parallel channels," *Wear*, vol. 72, no. 1, pp. 89–95, 1981.

[9] M. Sheikholeslami, D. D. Ganji, and H. R. Ashorynejad, "Investigation of squeezing unsteady nanofluid flow using ADM," *Powder Technology*, vol. 239, pp. 259–265, 2013.

[10] A. K. Gupta and S. S. Ray, "Numerical treatment for investigation of squeezing unsteady nanofluid flow between two parallel plates," *Powder Technology*, vol. 279, pp. 282–289, 2015.

[11] K. R. Rajagopal and A. S. Gupta, "Remarks on "a class of exact solutions to the equations of motion of a second grade fluid"," *International Journal of Engineering Science*, vol. 21, no. 1, pp. 61–63, 1983.

[12] T. Hayat, A. Yousaf, M. Mustafa, and S. Obaidat, "MHD squeezing flow of second-grade fluid between two parallel disks," *International Journal for Numerical Methods in Fluids*, vol. 69, no. 2, pp. 399–410, 2012.

[13] T. Hayat, A. Qayyum, and A. Alsaedi, "Three-dimensional mixed convection squeezing flow," *Applied Mathematics and Mechanics*, vol. 36, no. 1, pp. 47–60, 2015.

[14] A. M. Siddiqui, S. Irum, and A. R. Ansari, "Unsteady squeezing flow of viscous MHD fluid between parallel plates," *Mathematical Modelling and Analysis*, vol. 13, no. 4, pp. 565–576, 2008.

[15] N. Ahmed, U. Khan, X. J. Yang, S. I. U. Khan, Z. A. Zaidi, and S. T. Mohyud-Din, "Magneto hydrodynamic (MHD) squeezing flow of a Casson fluid between parallel disks," *International Journal of the Physical Sciences*, vol. 8, no. 36, pp. 1788–1799, 2013.

[16] M. A. Z. Raja, I. Ahmad, I. Khan, M. I. Syam, and A. M. Wazwaz, "Neuro-heuristic computational intelligence for solving nonlinear pantograph systems," *Frontiers of Information Technology & Electronic Engineering*, vol. 18, no. 4, pp. 464–484, 2017.

[17] Z. Sabir, M. A. Z. Raja, M. Umar, and M. Shoaib, "Neuro-swarm intelligent computing to solve the second-order singular functional differential model," *The European Physical Journal Plus*, vol. 135, no. 6, p. 474, 2020.

[18] Y. Wang, Y. Cao, Z. Guo, and S. Wen, "Passivity and passification of memristive recurrent neural networks with multi-proportional delays and impulse," *Applied Mathematics and Computation*, vol. 369, Article ID 124838, 2020.

[19] I. Ahmad, S. Ahmad, M. Awais, S. Ul Islam Ahmad, and M. Asif Zahoor Raja, "Neuro-evolutionary computing paradigm for Painlevé equation-II in nonlinear optics," *The European Physical Journal Plus*, vol. 133, no. 5, p. 184, 2018.

[20] S. u. I. Ahmad, F. Faisal, M. Shoaib, and M. A. Z. Raja, "A new heuristic computational solver for nonlinear singular Thomas–Fermi system using evolutionary optimized cubic splines," *European Physical Journal A: Hadrons and Nuclei*, vol. 135, no. 1, p. 55, 2020, https://doi.org/10.1140/epjp/s13360-019-00066-3.

[21] A. H. Bukhari, M. A. Z. Raja, M. Sulaiman, S. Islam, M. Shoaib, and P. Kumam, "Fractional neuro-sequential ARFIMA-LSTM for financial market forecasting," *IEEE Access*, vol. 8, pp. 71326–71338, 2020.

[22] A. Ara, N. A. Khan, O. A. Razzaq, T. Hameed, and M. A. Z. Raja, "Wavelets optimization method for evaluation of fractional partial differential equations: an application to financial modelling," *Advances in Difference Equations*, vol. 2018, no. 1, p. 8, 2018.

[23] I. Ahmad, "Integrated neuro-evolution-based computing solver for dynamics of nonlinear corneal shape model numerically," *Neural Computing & Applications*, vol. 33, 2020.

[24] M. Shoaib, M. A. Z. Raja, M. T. Sabir et al., "A stochastic numerical analysis based on hybrid NAR-RBFs networks nonlinear SITR model for novel COVID-19 dynamics," *Computer Methods and Programs in Biomedicine*, vol. 202, Article ID 105973, 2021.

[25] T. N. Cheema, M. A. Z. Raja, I. Ahmad, S. Naz, H. Ilyas, and M. Shoaib, "Intelligent computing with Levenberg–Marquardt artificial neural networks for nonlinear system of COVID-19 epidemic model for future generation disease control," *The European Physical Journal Plus*, vol. 135, no. 11, pp. 932–935, 2020.

[26] M. Shoaib, M. A. Z. Raja, M. A. R. Khan, I. Farhat, and S. E. Awan, "Neuro-computing networks for entropy generation under the influence of MHD and thermal radiation," *Surfaces and Interfaces*, vol. 25, Article ID 101243, 2021.

[27] M. Shoaib, M. A. Z. Raja, W. Jamshed, K. S. Nisar, I. Khan, and I. Farhat, "Intelligent computing Levenberg Marquardt approach for entropy optimized single-phase comparative study of second grade nanofluidic system," *International Communications in Heat and Mass Transfer*, vol. 127, Article ID 105544, 2021.

[28] RA. Khan, H. Ullah, M. A. Z. Raja, M. A. R. Khan, S. Islam, and M. Shoaib, "Heat transfer between two porous parallel plates of steady nanofludis with Brownian and Thermophoretic effects: a new stochastic numerical approach," *International Communications in Heat and Mass Transfer*, vol. 126, Article ID 105436, 2021.

[29] I. Khan, H. Ullah, H. AlSalman et al., "Fractional analysis of MHD boundary layer flow over a stretching sheet in porous medium: a new stochastic method," *Journal of Function Spaces*, vol. 2021, Article ID 5844741, 1 page, 2021.

[30] I. Khan, H. Ullah, H. AlSalman et al., "Falkner–skan equation with heat transfer: a new stochastic numerical approach," *Mathematical Problems in Engineering*, vol. 2021, Article ID 3921481, 1 page, 2021.

[31] H. Bilal, H. Ullah, M. Fiza et al., "A Levenberg-Marquardt backpropagation method for unsteady squeezing flow of heat and mass transfer behaviour between parallel plates," *Advances in Mechanical Engineering Advances in Mechanical Engineering*, vol. 13, no. 10, pp. 168781402110408–168781402110415, 2021.

[32] H. Ullah, I. Khan, M. Fiza et al., "MHD boundary layer flow over a stretching sheet: a new stochastic method," *Mathematical Problems in Engineering*, vol. 2021, Article ID 9924593, 1 page, 2021.

[33] H. Ullah, I. Khan, H. AlSalman et al., "Levenberg–marquardt backpropagation for numerical treatment of micropolar flow in a porous channel with mass injection," *Complexity*, vol. 2021, Article ID 5337589, 1 page, 2021.

[34] M. Shoaib, M. Kausar, M. I. Khan et al., "Intelligent backpropagated neural networks application on Darcy-Forchheimer ferrofluid slip flow system," *International Communications in Heat and Mass Transfer*, vol. 129, Article ID 105730, 2021.

[35] M. Shoaib, M. Kausar, K. S. Nisar, M. A. Z. Raja, M. Zeb, and A. Morsy, "The design of intelligent networks for entropy

generation in Ree-Eyring dissipative fluid flow system along quartic autocatalysis chemical reactions," *International Communications in Heat and Mass Transfer*, vol. 133, Article ID 105971, 2022.

[36] M. Shoaib, G. Zubair, K. S. Nisar et al., "Ohmic heating effects and entropy generation for nanofluidic system of Ree-Eyring fluid: intelligent computing paradigm," *International Communications in Heat and Mass Transfer*, vol. 129, Article ID 105683, 2021.

[37] R. Ellahi and A Riaz, "Analytical solutions for MHD flow in a third-grade fluid with variable viscosity," *Mathematical and Computer Modelling*, vol. 52, no. 9-10, pp. 1783–1793, 2010.

[38] A. Riaz, A. Zeeshan, and M. M. Bhati, "Entropy analysis of a three dimensional wavy flowof erying powell nanofluid," *Math.Prob.Eng*, vol. 2021, Article ID 6672158, 2021.

[39] A. Riaz, A. Razaq, and A. U. Awan, "Magnetic field and permeability effects on Jeffrey fluid in eccentric tubes having flexible porous boundaries," *Journal of Magnetics*, vol. 22, no. 4, pp. 642–648, 2017.

[40] A. Zeeshan, N Ijaz, A Riaz, A. B. Mann, and A. Hobiny, "Flow of nonspherical nanoparticles in electro-magnetohydrodynamics of nanofluids through a porous medium between eccentric cylinders," *Journal of Porous Media*, vol. 23, no. 12, pp. 1201–1212, 2020.

Hindawi
Mathematical Problems in Engineering
Volume 2022, Article ID 8452862, 10 pages
https://doi.org/10.1155/2022/8452862

Research Article

Comparative Analysis of the Effect of Joule Heating and Slip Velocity on Unsteady Squeezing Nanofluid Flow

Hakeem Ullah,[1] **Hina Khan**,[1] **Mehreen Fiza**,[1] **Kashif Ullah**,[1] **Saeed Islam**,[1] **and Seham M. Al-Mekhlafi**[2]

[1]*Department of Mathematics, Abdul Wali Khan University, Mardan, Khyber Pakhtunkhwa, Pakistan*
[2]*Department of Mathematics, Sana'a University, Sanna, Yemen*

Correspondence should be addressed to Mehreen Fiza; drmehreenfiza@gmail.com and Seham M. Al-Mekhlafi; smdk100@gmail.com

Received 14 March 2022; Revised 25 May 2022; Accepted 6 July 2022; Published 16 August 2022

Academic Editor: Arshad Riaz

In this paper, we studied unsteady MHD nanofluid squeezing flow between two parallel plates considering the effect of Joule heating and thermal radiation. The governing equations in the form of partial differential equations (PDEs) are transformed into a system of ordinary differential equations (ODEs) with the help of similarity transformation. The obtained boundary value problem is solved analytically by optimal auxiliary function method (OAFM) and numerically by Runge–Kutta method of order 4 (RKMO4). The OAFM results are validated and compared to the results of RKMO4. The effects of physical parameters such as stretching parameter S, Prandtl number Pr, Eckert number Ec, magnetic number M, volume friction φ electric parameter E_1, and porous parameter γ on the velocity, temperature, and concentration profiles are discussed with the help of plots. Also, the skin friction and Nusselt numbers effects are discussed with the help of tabular data. As the plates move apart, the Nusselt number and the skin friction coefficient decline and the Prandtl number decreases the temperature profile, whereas the stretching and Eckert number increases causing to increase the temperature field.

1. Introduction

A nanofluid is a fluid made up of nanoparticles, which are nanometer-sized particles having diameter less than 100 nm. The concept of nanofluid was given by Choi and Eastman [1]. These fluids are colloidal nanoparticle deferments in a base fluid such as metals, oxides, carbides, and carbon nanotubes are often used as nanoparticles in nanofluids and the base fluids contain water, ethylene glycol, oil, toluene, biofluids, and polymer solution. The nanoparticles are up to 5% of volume fraction in nanofluids. In recent years, many researchers have studied and reported nanofluid technology experimentally or numerically in the presence of heat transfer. The nanofluid have industrial and engineering applications such as electronic cooling devices, chemical factors, heat pumps, and heat exchangers [2–13]. Nanofluid have a variety of features that could make them beneficial in a variety of heat transfer applications. As the heating/cooling fluids have an important role in the energy efficient heat transfer materials. The heat and mass transfer is an important phenomenon in the nanofluid because of its industrial applications such as polymer formation, compression, power transmitting, lubricant system, and food processing. Stephen [14] introduced the idea of squeezing flow under lubrication. Domairry and Hatami studied the flow of squeezed nanofluid between two plates [15]. The unsteady flow of squeezing flow between two parallel plates is studied by Pourmehran et al. [16]. The unsteady squeezed flow is studied by Gupta and Ray [17]. This study has extended by Khan et al. [18] by considering the viscous dissipation properties. Magnetohydrodynamics (MHD) is the effect of magnetic field on the electrical conducting fluid, such as water and [19], which have been presented for the first time. This field have many applications in industry and engineering such as MHD sensors, MHD cooling reactors, and casting. The MHD and heat transfer

analysis with thermal radiation of nanofluid is studied by Ibrahim and Shankar [20]. Malvandi and Ganji [21] studied the MHD and heat transfer of nanofluid. The impact of thermal radiation and slip on MHD nanofluid was studied by Haq et al. [22]. Govindaraju et al. [23] studied the entropy analysis of MHD nanofluid. Uddin et al. [24] studied the porous medium of MHD nanofluid flow on the horizontal plate. The stagnation point flow of MHD nanofluid is investigated by Hsaio [25]. The dissipation and chemical reaction analysis for MHD nanofluid is study by Kameswaran et al. [26]. Matin et al. [27] and Pal et al. [28] studied the dissipation analysis and heat transfer analysis over the stretching sheet. The analysis of porous medium on MHD nanofluid flow was studied by Zhang et al. [29]. Elshehbey and Ahmed [30] studied the Buongiorno nanofluid model. The thermal radiation and Ohmic dissipation effects on the MHD flow with heat transfer is studied by Olanreaju [31]. Ullah et al. studied the MHD nanofluid with thermal radiation [32], whereas Rashidi et al. [33] examined the MHD flow caused by heat generation. From the literature, it is shown that the MHD flow over stretching sheets with heat transfer, the effect of electric field, Ohmic dissipation joule, and thermal radiation have not been considered and very little consideration is devoted towards it in the viscous fluids. Having this view, the unsteady MHD nanofluid squeezing flow between two parallel plates considering the effect of Joule heating and thermal radiation is considered. The effect of electric and magnetic fields are considered in the momentum and energy equations, and thermal radiation and Ohmic dissipation are taken into description. The skin friction Nusselt number and Sherwood number are elaborated with the help of tables. The analytical and numerical techniques are used for the treatment of BVP. Normally the numerical techniques require the process of linearization and discretization, which may turn to divergent solutions in some cases. Recently Herisanu [34, 35] presented a new optimal technique OAFM that do not need the linearization/discretization and small parameters issues such as perturbation method. OAFM has a large convergence region, which control the convergence with the help of optimal constant. OAFM provides us the accurate solution at just the first iteration without using the complex mathematical algorithms, and even a low specified computer can run the algorithm easily, and also the procedure of OAFM is very easy in implementation and quick convergent as compared to the other semianalytical methods such as HAM and OHAM. Some recent development in this area can be seen in [37–41].

The objective of this study is to find the analytical (OAFM) and numerical (RKMO4) solutions of unsteady MHD nanofluid squeezing flow considering the effect of Joule heating and thermal radiation. The OAFM results are validated and compared to numerical method results.

2. Basic Ideas of Optimal Auxiliary Functions Method [38, 39]

Assume that the nonlinear differential equation

$$L[\Theta(\eta)] + s(\eta) + \mathrm{N}[\Theta((\eta))] = 0, \tag{1}$$

with the BCs

$$\mathrm{B}\left(\Theta(\eta), \frac{d\Theta(\eta)}{d\eta}\right) = 0. \tag{2}$$

We write the solutions as follows:

$$\Theta(\eta) = \Theta_0(\eta) + \Theta_1(\eta, E_i), \quad i = 1, 2, 3, \ldots\ldots s. \tag{3}$$

The initial approximate solutions is of the following form:

$$L[\Theta_0(\eta)] + s(\eta) = 0, B\left(\Theta_0(\eta), \frac{d\Theta_0(\eta)}{d\eta}\right) = 0. \tag{4}$$

And the first approximation solutions is as follows:

$$\begin{aligned} &[\Theta_1(\eta, E_i)] + N[\Theta_0(\eta) + \Theta_1(\eta, E_i)] = 0, \\ &B\left(\Theta_1(\eta, E_i), \frac{d\Theta_1(\eta, E_i)}{d\eta}\right) = 0. \end{aligned} \tag{5}$$

Also,

$$\begin{aligned} &N[\Theta_0(\eta) + \Theta_1(\eta, E_i)] \\ &\quad = N[\Theta_0(\eta)] + \sum \frac{d\Theta_1^k(\eta, E_i)}{k} N^k[\Theta_0(\eta)]. \end{aligned} \tag{6}$$

The approximated solution is obtained by using equation(3).

The auxiliary functions *Eis* can be obtained by using the method of least square,

$$J(E_i, E_j) = \int_a^b R^2(m, \lambda, \alpha, \varepsilon) d\varepsilon, \tag{7}$$

where

$$\begin{aligned} R(m, \lambda, \alpha, \varepsilon) = L\left[\Theta\left(E_i, E_j\right)\right] + g(\varepsilon) + N\left[\Theta\left(E_i, E_j\right)\right], \\ i = 1, 2, \ldots P, j = p + 1, p + 2 \ldots s. \end{aligned} \tag{8}$$

And

$$\frac{\partial J}{\partial E_1} = \frac{\partial J}{\partial E_2} = \frac{\partial J}{\partial E_3} = \ldots \frac{\partial J}{\partial C_P} = \frac{\partial J}{\partial E_{P+1}} = \ldots \frac{\partial J}{\partial E_s} = 0. \tag{9}$$

3. Problem Formulation and Solution

We consider the unsteady two-dimensional flow of squeezed nanofluid between two parallel plates with heat and mass transfer with water as base fluid and nanoparticles as copper (Cu), silver (Ag), alumina (Al_2O_3), and titanium oxide (TiO_2). A uniform magnetic field is applied vertically to the direction of flow and the plates. The separation of the plates is given as $z = \pm l(1 - \alpha t)^{(1/2)} = \pm h(t)$, where l is the initial position (at time $t = 0$). The flow is considered incompressible with no chemical reaction. The fluid is electrically conducting in the presence of applied magnetic field $\overline{B} = (0, B_0, 0)$ and electric field $\overline{E} = (0, 0, -E_0)$. The flow is due to

squeezing. The electric and magnetic fields obeys the Ohms law "$\overline{J} = \sigma(\overline{E} + \overline{V} \times \overline{B})$," where $\overline{J}$ is the Joule current, σ is the electrical conduction, and $\overline{E}$ and $\overline{V}$ are electric and velocity fields. The induced magnetic field and Hall current are ignored and the electric and magnetic field contribute in the momentum and thermal heat equation. The flow description can be seen in Figure 1.

The fundamental equations are as follows:

$$\begin{aligned}
&\partial_x u + \partial_y v = 0,\\
&\rho_{nf}\left(\partial_t u + u\partial_x u + v\partial_y u\right)\\
&= -\frac{\partial p}{\partial x} + \mu_{nf}\left(\partial_{xx} u + \partial_{yy} u\right) - \sigma_{nf}\left(E_0 B_0 - B_0^2 u\right),\\
&\rho_{nf}\left(\partial_t v + u\partial_x v + v\partial_y v\right)\\
&= -\frac{\partial p}{\partial y} + \mu_{nf}\left(\partial_{xx} v + \partial_{yy} v\right),\\
&\left(\partial_t T + u\partial_x T + v\partial_y T\right)\\
&= \frac{k_{nf}}{\left(\rho C_p\right)_{nf}}\left(\partial_{xx} T + \partial_{yy} T\right)\\
&+ \frac{\mu_{nf}}{\left(\rho C_p\right)_{nf}}\left(4\left(\partial_{xx} u\right)^2 + \left(\partial_y u + \partial_x v\right)^2\right)\\
&+ \frac{\sigma_{nf}}{\rho}\left(uB_0 - E_0\right)^2, \text{ and}\\
&\partial_t C + u\partial_x C + v\partial_y C = D\left(\partial_{xx} C + \partial_{yy} C\right).
\end{aligned} \tag{10}$$

With BCs,

$$\begin{aligned}
v &= \frac{dh}{dt},\\
u &= -L\partial_y u,\\
C &= C_h,\\
T &= T_h,\\
y &= h(t),\\
v &= \partial_y u\\
&= \partial_y T\\
&= 0,\\
C &= C_0,\\
T &= T_0,\\
y &= 0,
\end{aligned} \tag{11}$$

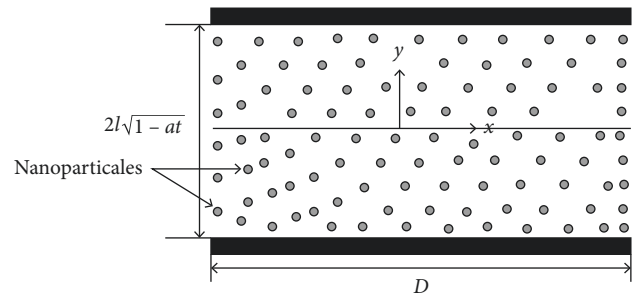

Figure 1: Schematic representation of the problem.

and

$$\begin{aligned}
&\mu_{nf} = \frac{\mu_f}{(1-\phi)^{2.5}} \text{ (Brinkman)},\\
&\frac{K_{nf}}{K_f} = \frac{2K_f + K_s - 2\phi\left(K_f - K_s\right)}{2K_f + K_s + 2\phi\left(K_f - K_s\right)} \text{ (Garnetts Maxwell), } \textit{and}\\
&\sigma_{nf} = (1-\phi)\sigma_f + \phi\sigma_s.
\end{aligned} \tag{12}$$

Using the following similarity variable as [40].

$$\begin{aligned}
u &= \frac{\alpha x}{2(1-\alpha t)} f'(\eta),\\
\theta &= \frac{T - T_0}{T_h - T_0},\\
\phi &= \frac{C - C_0}{C_h - C_0},\\
\eta &= \frac{y}{l(1-\alpha t)^{1/2}}.
\end{aligned} \tag{13}$$

With the help of similarity variable obtain in the above codes,

$$\begin{aligned}
&f'''' - \mathrm{SA}_1(1-\varphi)^{2.5}\left(f' f'' + 3f'' + \eta f''' - f f'''\right) -\\
&- M^2\left(E_1 - f'\right) = 0, -M^2\left(E_1 - f'\right),
\end{aligned} \tag{14}$$

and

$$\begin{aligned}
A_1 &= (1-\varphi) + \varphi\frac{\rho_S}{\rho_f},\\
A_2 &= (1-\varphi) + \varphi\frac{\left(\rho C_p\right)_s}{\left(\rho C_p\right)_f}, \text{ and}\\
A_3 &= \frac{k_{nf}}{k_f}.
\end{aligned} \tag{15}$$

Here, A1, A2, and A3 are dimensionless constants, $S = ((al2)/(2vf))$ is the squeeze number, $\mathrm{Pr} = \mu f(((pCp)f)/(pfkf))$ is the Prandtl number, $Sc = ((vf)/(Dn\ f))$ is Schmidt number, and

$\delta = ((L)/l(1-\alpha t)^{(1/2)})$ is the velocity slip parameter, $Ec = (pf/((pCp)f))((\alpha\eta)/2(1-\alpha t))^2$ is the Eckert number, $M^2 = ((\sigma B_0^2)/(\rho\alpha))$ is magnetic number, and $E_1 = ((2E_0(1-\alpha t))/(B_0))$ is the electrical number.

The BCs are as follows:

$$\begin{aligned} \theta'(0) &= 0, \\ f''(0) &= 0, \\ f(0) &= 0, \\ \phi(0) &= 0, \\ f(1) &= 1, \\ f'(1) &= -\delta f''(1), \\ \theta(1) &= 1, \text{ and} \\ \phi(1) &= 1. \end{aligned} \tag{16}$$

The physical quantities of interest are the skin-friction coefficient Cf, the Nusselt number Nu_x, and the Sherwood number Sh_x, defined as follows:

$$\begin{aligned} Nu_x &= \frac{Iq_w}{k_f(T_h - T_0)}, \\ C_{\mathrm{f}} &= \frac{T_w}{\rho_{nf}\nu^2 w}, \\ Sh_x &= \frac{lm_w}{D(C_h - C_0)}, \\ \text{where } m_w &= -D_{nf}\left(\partial_y C\right)_{y=h(t)}, \text{ and} \\ T_w &= \mu_{nf}\left(\partial_y u\right)_{y=h(t)}. \end{aligned} \tag{17}$$

Using the dimensionless form as follows:

$$\begin{aligned} -A_3\theta'(1) &= Nu_x, \\ Sh &= -\phi(1), \text{ and} \\ C_f &= \frac{f''(1)}{A_1(1-\varphi)^{2.5}}, \end{aligned} \tag{18}$$

we obtained

$$\begin{aligned} &f^{iv} - \mathrm{SA}_1(1-\varphi)^{2.5}\left(f'f'' + 3f'' + \eta f^{'''}ff^{'''}\right) \\ &\quad - M^2(E_1 - f') = 0, \\ &\theta'' + \mathrm{PrS}\left(\frac{A_2}{A_3}\right)(\theta' f - \eta\theta') + \frac{EcPr}{A_3(1-\varphi)^{2.5}}\left(f''^2 4\phi^2 + f'^2\right) \\ &\quad + M^2\mathrm{Pr}(f' - E_1)^2 = 0, \textit{ and} \\ &\phi'' + (ScSf\phi' - ScS\eta\phi') = 0. \end{aligned} \tag{19}$$

Boundary conditions are as follows:

$$\begin{aligned} \theta'(0) &= 0, \\ f(0) &= 0, \\ f'(0) &= 0, \\ \phi(0) &= 0, \\ f(1) &= 1, \\ f'(1) &= -\delta f''(1), \\ \theta(1) &= 1, \text{ and} \\ \phi(1) &= 1. \end{aligned} \tag{20}$$

The linear and nonlinear operators are given as follows:

$$\begin{aligned} L(f(\eta)) &= f^{iv}(\eta), \\ L(\theta(\eta)) &= \theta''(\eta), \\ \phi L(\theta(\eta)) &= \phi''(\eta), \\ N(f(\eta)) &= \mathrm{SA}_1(1-\varphi)^{2.5}(f'f'' + 3f^{'''} + \eta f^{'''} - ff^{'''}) \\ &\quad - M^2(E_1 - f') \\ &= 0, \\ N(\theta(\eta)) &= \mathrm{PrS}\left(\frac{A_2}{A_3}\right)(\theta' f - \eta\theta') \\ &\quad + \frac{EcPr}{A_3(1-\varphi)^{2.5}}\left(4\phi^2 f'^2 + f''^2\right) + M^2\mathrm{Pr}(f' - E_1)^2 \\ &= 0, \text{ and} \\ N(\phi(\eta)) &= (ScSf\phi' - ScS\eta\phi') = 0. \end{aligned} \tag{21}$$

We have,

$$\begin{aligned} \theta'(0) &= 0, \\ f''(0) &= 0, \\ f(0) &= 0, \\ \phi(0) &= 0, \\ &\text{when } x = 0, \\ f(1) &= 1, \\ f'(1) &= -\delta f'(1), \\ \theta(1) &= 1, \\ \phi(1) &= 1, \\ &\text{when } x = 1, \\ \phi''(\eta) &= 0, \text{ and} \\ \phi(1) &= 1. \end{aligned} \tag{22}$$

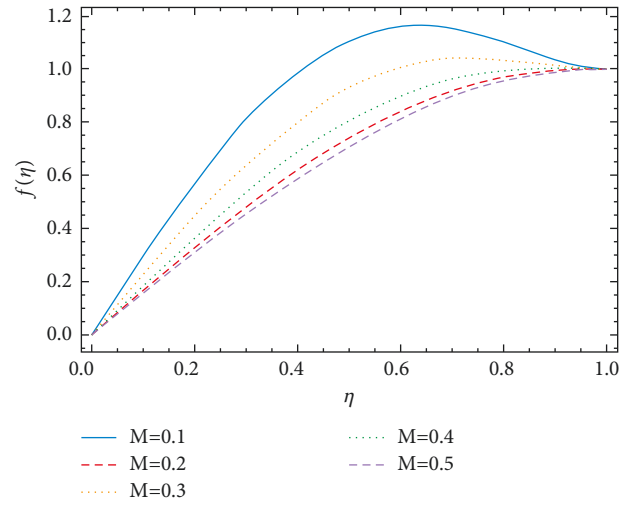

Figure 2: M versus $f(\eta)$.

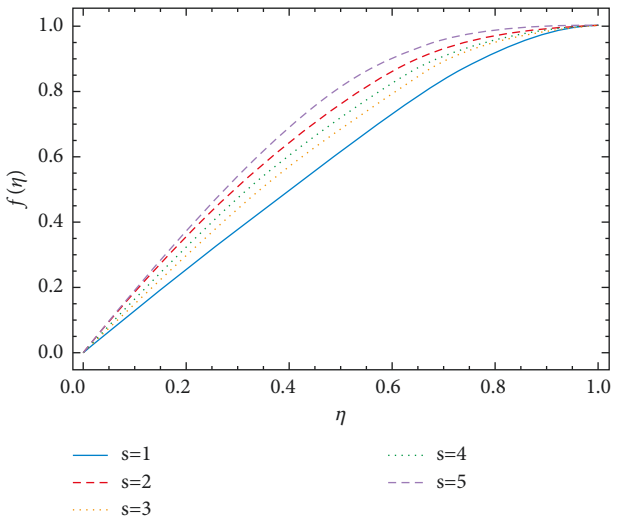

Figure 3: S versus $f(\eta)$.

The initial solutions are as follows:

$$f(\eta) = \frac{1}{2}\left(3\eta - \eta^3\right),$$
$$\theta(\eta) = \eta^2, \text{ and} \tag{23}$$
$$\phi(\eta) = \eta.$$

Also,

$$N(f(\eta)) = -SA_1(1-\phi)^{2.5}\left[-3\eta - 9 - 3x\left(\frac{3-x^2}{2}\right) + 3\left(\frac{3x-x^3}{2}\right)\right],$$
$$N(\theta(\eta)) = \Pr S\left(\frac{A_2}{A_3}\right)\left[3x^2 - x^4\right] - 2\eta x + \frac{\Pr Ec}{A_3(1-\varphi)^{2.5}} - 5x^2\left\{\frac{9}{2}\left(1 - x^2 + \frac{1}{2}x^4\right)\right\}, \text{ and} \tag{24}$$
$$N(\phi(\eta)) = ScS\left\{\left(\frac{3x-x^3}{2}\right)\right\} - \eta = 0.$$

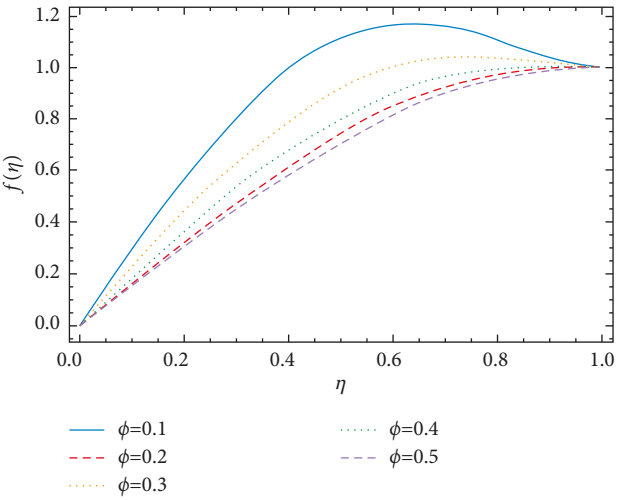

Figure 4: φ versus $f(\eta)$.

The first approximation, we have the following equation:

$$\begin{cases} f^{iv}(\eta) + D_1\left(\eta, \eta^2, E_i\right)\left\{\left(-SA_1(1-\phi)^{2.5}\right)\right\}\left[-3\eta - 9x + \left(\frac{3-3x^2}{2}\right)(-3xM) - \left(\frac{3x-x^3}{2}\right)(-3)\right] + 3E_1 x = 0, \\ \theta''(\eta) + D_3\left(\eta, \eta^2, E_p\right)\Pr S\left(\frac{A_2}{A_3}\right)\left[3x^2 - x^4\right] - 2\eta x + \frac{\Pr Ec}{A_3(1-\phi)^{2.5}} - 5x^2\left\{\frac{9}{2}\left(1 - x^2 + \frac{1}{2}x^4\right)\right\} + D_4\left(\eta, \eta^2, Em\right) = 0, \\ \phi''(\eta) + D_5\left(\eta, \eta^2, E_r\right)ScS\left(\frac{3x-x^3}{2}\right) - \eta + D_6\left(\eta, \eta^2, En\right) = 0. \end{cases} \tag{25}$$

The OAF can be chosen freely as follows:

$$\begin{cases} D_1(f_0(\eta), E_i) = -(E_1 + E_2\eta), \\ D_2(f_0(\eta), E_j) = -(E_3 + E_4\eta)e^{-\eta} - (E_5 + E_6\eta + E_7\eta^2)e^{-2\eta}, \\ D_3(f_0(\eta), E_P) = 0, \\ D_4(f_0(\eta), E_m) = -(E_8 + E_9\eta)e^{-\eta} - (E_{10} + E_{11}\eta + E_{12}\eta^2)e^{-2\eta}, \\ D_5(f_0(\eta), Er) = -(E_{13} + E_{14}\eta)e^{-\eta} - (E_{15} + E_{16}\eta + E_{17}\eta^2)e^{-2\eta} \\ D_6(f_0(\eta), E_n) = -(E_{18} + E_{19}\eta)e^{-\eta} - (E_{20} + E_{21}\eta + E_{22}\eta^2)e^{-2\eta}. \end{cases} \tag{26}$$

We get,

$$\begin{aligned} & f^{iv}(\eta) + D_1(\eta, \eta^2, E_i)\{(-SA_1(1-\phi)^{2.5})\} \\ & \left[-3\eta - 9x + \left(\frac{3-3x^2}{2}\right)(-3x) - \left(\frac{3x-x^3}{2}\right)(-3)\right] \\ & + 3ME_1 x = 0, \\ & \theta''(\eta) + D_3(\eta, \eta^2, E_p)\Pr S\left(\frac{A_2}{A_3}\right)\left[3x^2 - x^4\right] - 2\eta x \\ & + \frac{\Pr Ec}{A_3(1-\phi)^{2.5}} - 5x^2\left\{\frac{9}{2}\left(1 - x^2 + \frac{1}{2}x^4\right)\right\} \\ & + D_4(\eta, \eta^2, Em) = 0, \text{ and} \\ & \phi''(\eta) + D_5(\eta, \eta^2, E_r)ScS\left(\frac{3x-x^3}{2}\right) - \eta \\ & + D_6(\eta, \eta^2, En) = 0. \end{aligned} \tag{27}$$

The final results is furnished by using the convergence control constants Es.

4. Results and Discussion

4.1. Graphical Discussion. In this section, the results are discussed in detail with the help of graphs. Figure 2 shows the effect of the magnetic and electric fields on the velocity profile. As the magnetic and electric fields increases, the velocity profile decreases. Since the magnetic and electric field oppose the electrically conducting fluid and as a result the velocity of the fluid reduces. Figure 3 shows the effect of stretching parameter s on the velocity field. Growth in the stretching parameter causes the velocity profile to rise. Since the stretching parameter is increased, it assists the flow, and hence the velocity of the fluid is increased. The effect of the volume friction on the velocity profile can be seen in Figure 4. The volume friction reduces the velocity profile and act as opposing force to the flow. The effect of the Prandtl number and volume friction numbers on the temperature profile are observed in Figures 5 and 6. The temperature profile is reduced when increasing the Prandtl and volume friction numbers. Since the Prandtl/volume friction number increase kinetic energy of the particle and the elastic collision of the particles reduces the temperature profile. The effect of stretching parameter and Eckert number are depicted in Figures 7 and 8. The same behavior

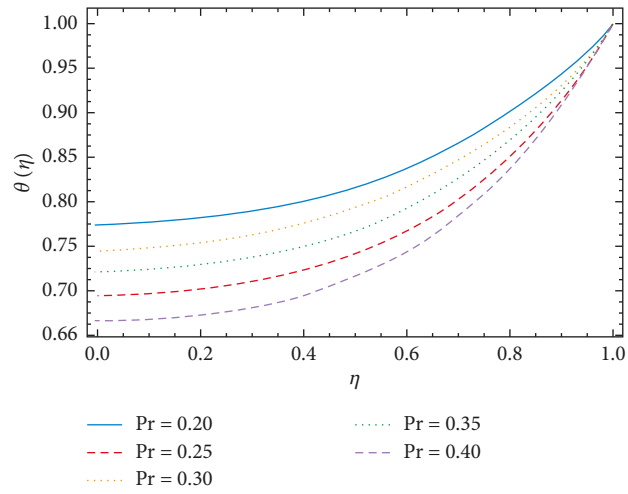

Figure 5: Pr versus $\theta(\eta)$.

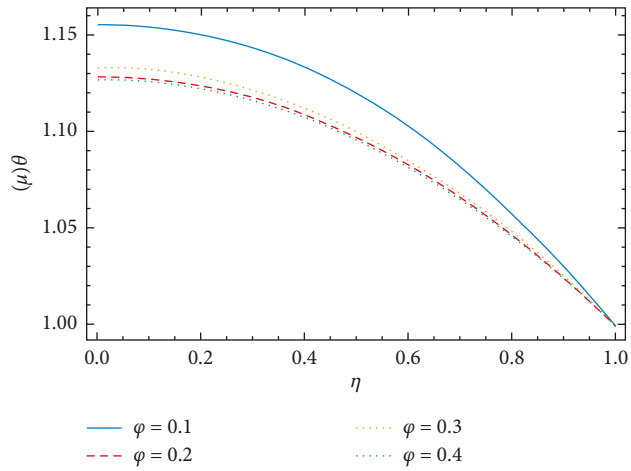

Figure 6: φ versus $\theta(\eta)$.

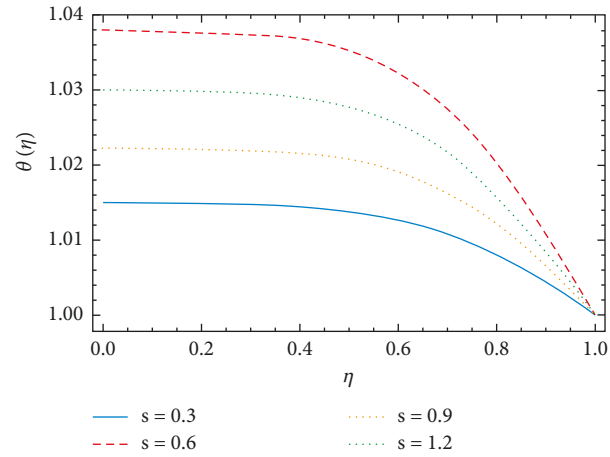

Figure 7: s versus $\theta(\eta)$.

of both the parameter is observed for the temperature profile as it increases the temperature profile. Also the effect of the stretching parameter and Schmidt number on the concentration profile can be seen in Figures 9–11. By increasing the stretching and Schmidt numbers the

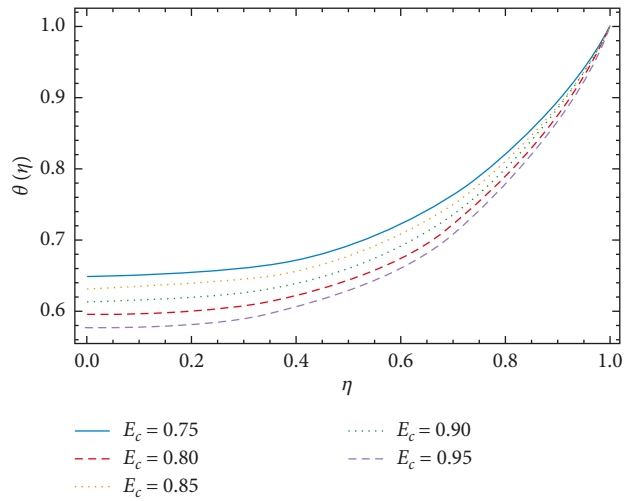

Figure 8: Ec versus $\theta(\eta)$.

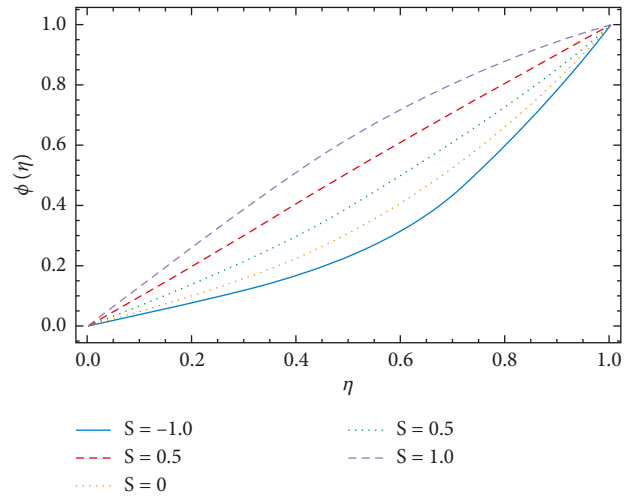

Figure 9: S versus $\theta(\eta)$.

concentration profile increases. Also, the effects of magnetic and electric fields on the temperature profiles are given in Figures 12 and 13. The temperature profile decreases by increasing the magnetic field. It is due to the fact that increasing the magnetic field increases the elastic collision of the nanoparticles, which reduces the temperature profile. We obtain the opposite effect of the electric field on the temperature profile as compared to the magnetic effect on the temperature profile.

4.2. Tables Discussion. The influence of S on the skin-friction coefficient Cf, Nusselt number Nux, and the Sherwood number Sh are tabulated in Table 1. By increasing S, the Cf and Nux decreases while Sh increases. The influence of Ec on Cf, Nux, and Sh are shown in Table 2. By increasing Sc, the Cf, Nux, and Sh decreases. Also the influence of M is tabulated for various values of M on Cf, Nux, and Sh in Table 3. From this table it is clear that by increasing M, Cf reduces while Nux and Sh

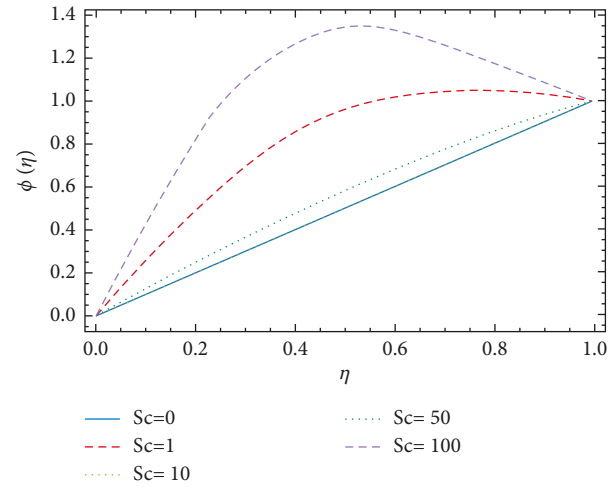

Figure 10: Sc versus $\theta(\eta)$.

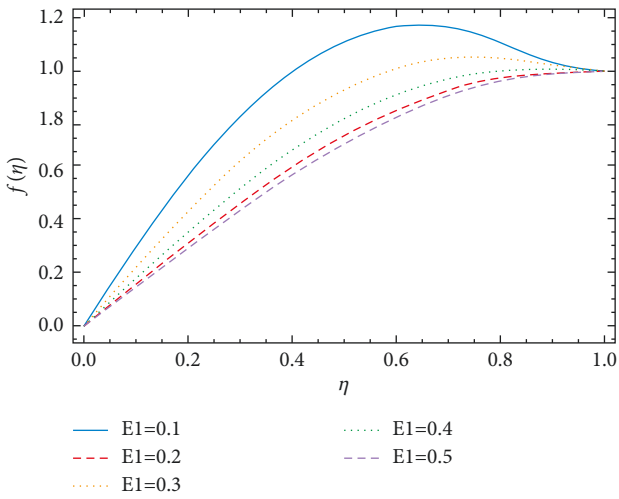

Figure 11: E1 versus $f(\eta)$.

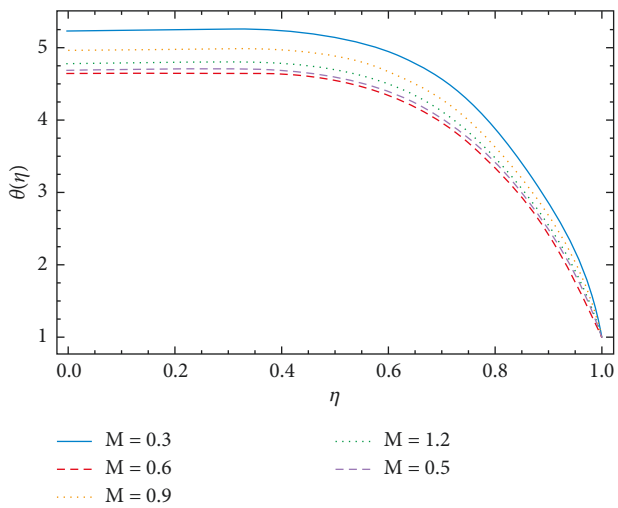

Figure 12: M versus $\theta(\eta)$.

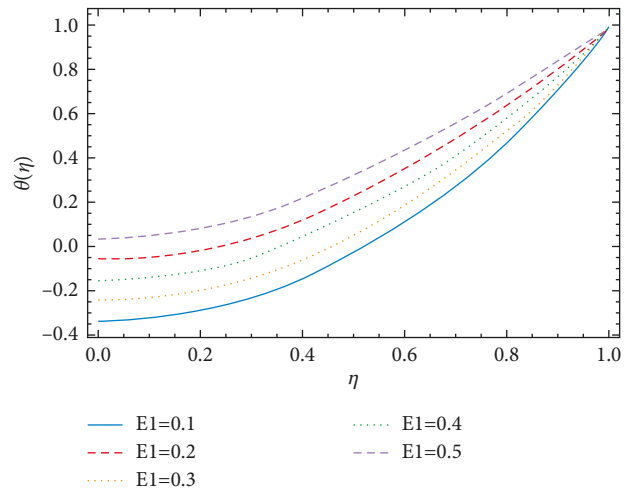

Figure 13: E1 versus $\theta(\eta)$.

Table 1: Impact of S on Cf, Nux, and Sh.

s	C_f	Nu_x	Sh_x
0.1	−2.54526	0.25486	−2.065879
0.2	−1.34295	0.187977	−1.0694254
0.3	−2.09419	0.104693	−1.0000000
0.4	−3.054689	0.054896	−0.987563
0.5	−4.021458	0.0012458	−0.568963

Table 2: Impact of Ec on Cf, Nux, and Sh.

Ec	C_f	Nu_x	Sh_x
0.1	−2.54862	0.025486	−0.56896
0.2	−2.52145	0.087562	−0.56875
0.3	−2.47856	0.082542	−0.58952
0.4	−2.36548	0.081546	−0.487563

Table 3: Impact of M on Cf, Nux, and Sh.

M	C_f	Nu_x	Sh_x
1	−2.854785	0.035689	−0.487596
2	−2.88546	0.087546	−0.487593
3	−2.98563	0.087562	−0.488236
4	−2.845263	0.045785	−0.489596

Table 4: Impact of φ on Cf, Nux, and Sh.

φ	C_f	Nu_x	Sh_x
0.10	−1.02154	0.054256	−0.63256
0.20	−1.021485	0.054120	−0.658523
0.30	−1.021496	0.051243	−0.658745
0.40	−1.21458	0.050852	−0.532110

increases. The effect of nanoparticle volume fraction φ on Cf, Nux, and Sh is presented in Table 4. By increasing φ, Cf increases while Nux and Sh decreases. Again the present method is validated by comparing the results as given in Table 5.

Table 5: Comparison of OAFM and RKMO4 results.

η	$f(\eta)$	$\theta(\eta)$	$f(\eta)$	$\theta(\eta)$
0	0.000000000	0.000000000	0.000000000	0.000000000
0.1	0.14135879	1.14135878	0.14135863	0.14135878
0.2	0.28066639	0.28066638	0.28066669	0.28066638
0.3	0.41578137	0.41578131	0.41578136	0.41578136
0.4	0.54437979	0.54437975	0.54437989	0.54437978
0.5	0.66385837	0.66385835	0.66385852	0.66385836
0.6	0.77123132	0.77123131	0.77123131	0.77123131
0.7	0.86301853	0.86301853	0.86301851	0.86301852
0.8	0.93512364	0.93512365	0.93512362	0.93512362
0.9	0.98270044	0.98270045	0.98270041	0.98270042
1.0	1.00000000	1.00000000	1.00000000	1.00000000

5. Conclusion

The OAFM results are identical to the results obtain from RKMO4 results. OAFM provide us a convenient way to control the convergence in the large flexible region with the help of optimal constants. OAFM contain less computational work and can be easily handle by a low specification computer. The OAFM provides us the first iteration results, which in comparison is proving that the method is simply applicable and provide us the accurate solution even at first iteration.

From the above discussion the following points is of importance.

(i) By increasing S, the Cf and Nux decreases while Sh increases

(ii) By increasing Sc, the Cf, Nux, and Sh decreases.

(iii) By increasing M, Cf reduces while Nux and Sh increases

(iv) By increasing φ, Cf increases while Nux and Sh decreases

(v) Schmidt number increases the concentration profile

(vi) The electrical current resists the flow whereas the stretching parameter assists the flow velocity

(vii) The Prandtl number decreases the temperature profile whereas the stretching and Eckert number increases causes to increase the temperature field

(viii) The stretching and Schmidt numbers increase causes to decrease the concentration profile

(ix) The mention techniques can be applied in future for more complex physical models

Data Availability

All data are available in the paper.

Conflicts of Interest

The authors declare that they have no conflicts of interest.

References

[1] S. U. S. Choi and J. A. Eastman, "Enhancing thermal conductivity of fluids with nanoparticle," in *Proceedings of the International Mechanical Engineering Congress and Exhibition*, pp. 99–105, San Francisco, Calif, USA, November 1995.

[2] M. Azimi and R. Riazi, "Heat transfer analysis of GO-water nanofluid flow between two parallel disks," *Propulsion and Power Research*, vol. 4, no. 1, pp. 23–30, 2015.

[3] M. Fakour, D. D. Ganji, and M. Abbasi, "Scrutiny of underdeveloped nanofluid MHD flow and heat conduction in a channel with porous walls," *Case Studies in Thermal Engineering*, vol. 4, pp. 202–214, 2014.

[4] T. Groşan, C. Revnic, I. Pop, and D. B. Ingham, "Free convection heat transfer in a square cavity filled with a porous medium saturated by a nanofluid," *International Journal of Heat and Mass Transfer*, vol. 87, pp. 36–41, 2015.

[5] A. V. Kuznetsov and D. A. Nield, "The Cheng-Minkowycz problem for natural convective boundary layer flow in a porous medium saturated by a nanofluid: a revised model," *International Journal of Heat and Mass Transfer*, vol. 65, pp. 682–685, 2013.

[6] P. Rana, R. Bhargava, and O. A. Bég, "Numerical solution for mixed convection boundary layer flow of a nanofluid along an inclined plate embedded in a porous medium," *Computers & Mathematics with Applications*, vol. 64, no. 9, pp. 2816–2832, 2012.

[7] A. M. Rashad, A. J. Chamkha, and M. Modather, "Mixed convection boundary-layer flow past a horizontal circular cylinder embedded in a porous medium filled with a nanofluid under convective boundary condition," *Computers & Fluids*, vol. 86, pp. 380–388, 2013.

[8] N. Vishnu Ganesh, B. Ganga, and A. K. Abdul Hakeem, "Lie symmetry group analysis of magnetic field effects on free convective flow of a nanofluid over a semi-infinite stretching sheet," *Journal of the Egyptian Mathematical Society*, vol. 22, no. 2, pp. 304–310, 2014.

[9] Y. Lin, L. Zheng, and G. Chen, "Unsteady flow and heat transfer of pseudo-plastic nanoliquid in a finite thin film on a stretching surface with variable thermal conductivity and viscous dissipation," *Powder Technology*, vol. 274, pp. 324–332, 2015.

[10] M. Sheikholeslami, M. M. Rashidi, and D. D. Ganji, "Numerical investigation of magnetic nanofluid forced convective heat transfer in existence of variable magnetic field using two phase model," *Journal of Molecular Liquids*, vol. 212, pp. 117–126, 2015.

[11] T. Hayat, M. Waqas, S. A. Shehzad, and A. Alsaedi, "Mixed convection flow of a Burgers nanofluid in the presence of stratifications and heat generation/absorption," *The European Physical Journal Plus*, vol. 131, no. 8, p. 253, 2016.

[12] F. M. Abbasi, T. Hayat, S. A. Shehzad, F. Alsaadi, and N. Altoaibi, "Hydromagnetic peristaltic transport of copper-water nanofluid with temperature-dependent effective viscosity," *Particuology*, vol. 27, pp. 133–140, 2016.

[13] M. Sheikholeslami, D. D. Ganji, and M. M. Rashidi, "Magnetic field effect on unsteady nanofluid flow and heat transfer using Buongiorno model," *Journal of Magnetism and Magnetic Materials*, vol. 416, pp. 164–173, 2016.

[14] M. J. Stefan, "Versuchs Uber die scheinbare adhesion, Sitzungs berichte der Akademie der Wissenschaften in Wien," *MathematikNaturwissen*, vol. 69, pp. 713–721, 1874.

[15] G. Domairry and M. Hatami, "Squeezing Cu-water nanofluid flow analysis between parallel plates by DTM-Padé Method," *Journal of Molecular Liquids*, vol. 193, pp. 37–44, 2014.

[16] O. Pourmehran, M. Rahimi-Gorji, M. Gorji-Bandpy, and D. D. Ganji, "RETRACTED: analytical investigation of squeezing unsteady nanofluid flow between parallel plates by LSM and CM," *Alexandria Engineering Journal*, vol. 54, no. 1, pp. 17–26, 2015.

[17] A. K. Gupta and S. Saha Ray, "Numerical treatment for investigation of squeezing unsteady nanofluid flow between two parallel plates," *Powder Technology*, vol. 279, pp. 282–289, 2015.

[18] U. Khan, N. Ahmed, M. Asadullah, and S. Tauseef Mohyuddin, "Effects of viscous dissipation and slip velocity on two-dimensional and axisymmetric squeezing flow of Cu-water and Cu-kerosene nanofluids," *Propulsion and Power Research*, vol. 4, no. 1, pp. 40–49, 2015.

[19] H. Alfvén, "Existence of electromagnetic-hydrodynamic waves," *Nature*, vol. 150, no. 3805, pp. 405-406, 1942.

[20] W. Ibrahim and B. Shankar, "MHD boundary layer flow and heat transfer of a nanofluid past a permeable stretching sheet with velocity, thermal and solutal slip boundary conditions," *Computers & Fluids*, vol. 75, pp. 1–10, 2013.

[21] A. Malvandi and D. D. Ganji, "Brownian motion and thermophoresis effects on slip flow of alumina/water nanofluid inside a circular microchannel in the presence of a magnetic field," *International Journal of Thermal Sciences*, vol. 84, pp. 196–206, 2014.

[22] R. Ul Haq, S. Nadeem, Z. Hayat Khan, and N. Sher Akbar, "Thermal radiation and slip effects on MHD stagnation point flow of nanofluid over a stretching sheet," *Physica E: Low-Dimensional Systems and Nanostructures*, vol. 65, pp. 17–23, 2015.

[23] M. Govindaraju, S. Saranya, A. A. Hakeem, R. Jayaprakash, and B. Ganga, "Analysis of slip MHD nanofluid flow on entropy generation in a stretching sheet," *Procedia Engineering*, vol. 127, pp. 501–507, 2015.

[24] M. J. Uddin, M. N. Kabir, and O. A. Bég, "Computational investigation of Stefan blowing and multiple-slip effects on buoyancy-driven bioconvection nanofluid flow with microorganisms," *International Journal of Heat and Mass Transfer*, vol. 95, pp. 116–130, 2016.

[25] K.-L. Hsiao, "Stagnation electrical MHD nanofluid mixed convection with slip boundary on a stretching sheet," *Applied Thermal Engineering*, vol. 98, pp. 850–861, 2016.

[26] P. K. Kameswaran, M. Narayana, P. Sibanda, and P. V. S. N. Murthy, "Hydromagnetic nanofluid flow due to a stretching or shrinking sheet with viscous dissipation and chemical reaction effects," *International Journal of Heat and Mass Transfer*, vol. 55, no. 25-26, pp. 7587–7595, 2012.

[27] M. H. Matin and I. Pop, "Forced convection heat and mass transfer flow of a nanofluid through a porous channel with a first order chemical reaction on the wall," *International Communications in Heat and Mass Transfer*, vol. 46, pp. 134–141, 2013.

[28] D. Pal and G. Mandal, "Influence of thermal radiation on mixed convection heat and mass transfer stagnation-point flow in nanofluids over stretching/shrinking sheet in a porous medium with chemical reaction," *Nuclear Engineering and Design*, vol. 273, pp. 644–652, 2014.

[29] C. Zhang, L. Zheng, X. Zhang, and G. Chen, "MHD flow and radiation heat transfer of nanofluids in porous media with variable surface heat flux and chemical reaction," *Applied Mathematical Modelling*, vol. 39, no. 1, pp. 165–181, 2015.

[30] H. M. Elshehabey and S. E. Ahmed, "MHD mixed convection in a lid-driven cavity filled by a nanofluid with sinusoidal temperature distribution on the both vertical walls using Buongiorno's nanofluid model," *International Journal of Heat and Mass Transfer*, vol. 88, pp. 181–202, 2015.

[31] P. O. Olanrewaju, "Effects of internal heat generation on hydromagnetic non-Darcy flow and heat transfer over a stretching sheet in the presence of thermal radiation and ohmic dissipation," *World Applied Sciences Journal*, vol. 16, pp. 37–45, 2012.

[32] H. Ullah, M. A. Khan, M. Fiza, K. Ullah, M. Ayaz, and M Seham, "Analytical and numerical analysis of the squeezed unsteady MHD nanofluid flow in the presence of thermal radiation," *Journal of nanomaterial*, vol. 2022, Article ID 1668206, 14 pages, 2022.

[33] M. M. Rashidi, S. Abelman, and N. F. Freidooni Mehr, "Entropy generation in steady MHD flow due to a rotating porous disk in a nanofluid," *International Journal of Heat and Mass Transfer*, vol. 62, pp. 515–525, 2013.

[34] R. Ellahi and A. Riaz, "Analytical solutions for MHD flow in a third-grade fluid with variable viscosity," *Mathematical and Computer Modelling*, vol. 52, no. 9-10, pp. 1783–1793, 2010.

[35] A. Riaz, A. Zeeshan, and M. M. Bhati, "Entropy analysis of a three dimensional wavy flowof erying powell nanofluid," *Math.Prob.Eng.*vol. 2021, Article ID 6672158, 14 pages, 2022.

[36] A. Riaz, A. Razaq, and A. U. Awan, "Magnetic field and permeability effects on Jeffrey fluid in eccentric tubes having flexible porous boundaries," *Journal of Magnetics*, vol. 22, no. 4, pp. 642–648, 2017.

[37] A. Zeeshan, N. Ijaz, A. Riaz, A. B. Mann, and A. Hobiny, "Flow of nonspherical nanoparticles in electro-magnetohydrodynamics of nanofluids through a porous medium between eccentric cylinders," *Journal of Porous Media*, vol. 23, no. 12, pp. 1201–1212, 2020.

[38] N. Herisanu and V. Marinca, "An efficient analytical approach to investigate the dynamics of a misaligned multirotor system," *Mathematics*, vol. 8, no. 7, p. 1083, 2020.

[39] N. Herisanu, V. Marinca, G. Madescu, and F. Dragan, "Dynamic response of a permanent magnet synchronous generator to a wind gust," *Energies*, vol. 12, no. 5, p. 915, 2019.

[40] K. Singh, S. K. Rawat, and M. Kumar, "Heat and mass transfer on squeezing unsteady MHD nanofluid flow between parallel plates with slip velocity effect," *Journal of Nanoscience*, vol. 2016, Article ID 9708562, 11 pages, 2016.

[41] M. Sheikholeslami and D. D. Ganji, "Nanofluid flow and heat transfer between parallel plates considering Brownian motion using DTM," *Computer Methods in Applied Mechanics and Engineering*, vol. 283, pp. 651–663, 2015.

Hindawi
Mathematical Problems in Engineering
Volume 2022, Article ID 7975101, 16 pages
https://doi.org/10.1155/2022/7975101

Research Article

Comparative Evaluation of the Optimal Auxiliary Function Method and Numerical Method to Explore the Heat Transfer between Two Parallel Porous Plates of Steady Nanofluids with Brownian and Thermophoretic Influences

Hakeem Ullah,[1] **Rafaqat Ali Khan**,[1] **Mehreen Fiza**,[1] **Saeed Islam**,[1] **and Seham M. Al-Mekhlafi**[2]

[1]*Department of Mathematics, Abdul Wali Khan University, Mardan 23200, KP, Pakistan*
[2]*Department of Mathematics, Sanna University, Sana'a, Yemen*

Correspondence should be addressed to Mehreen Fiza; drmehreenfiza@gmail.com and Seham M. Al-Mekhlafi; smdk100@gmail.com

Received 19 February 2022; Revised 20 April 2022; Accepted 17 May 2022; Published 1 July 2022

Academic Editor: Arshad Riaz

In this study, we used the newly established optimal approach, namely, optimal auxilary function method (OAFM) along with the Adams numerical solver technique in order to investigate the heat transfer between two permeable parallel plates of steady nanofluids (HTBTP-SNFs) through Brownian and thermophoretic consequences. The new scheme model (HTBTP-SNFs) in terms of partial differential equations (PDEs) is changed to nonlinear ordinary differential equations (ODEs) by utilizing similarity transformations. The OAFM and Adams numerical methods are used to solve the resulting ODEs with boundary conditions. The OAFM along with convergence and Adams numerical method are studied in detail. The influences of the physical parameters of HTBTP-SNFs model for instance porosity parameter (m), parameter of magnetic (M), parameter of Brownian (Nb), viscosity parameter (R), Schmidt number (Sc), thermophores parameter (Nt), and Prandlt number (Pr) are discussed with the help of tabular data and graphs. The reliability and effectiveness of the technique are achieved by equating the results available in the literature.

1. Introduction

Energy is incredibly essential in today's world. Nanofluids show a significant title part in the industrial sector by enhancing heat transfer processes. Despite their wide variety of applications, heat transfers of nanofluids have become more essential in engineering and industrial innovations. Nanofluids are made up of nanoparticle-sized specks in fluid-termed nanoparticles. Nanofluids are particularly beneficial in managing cooling difficulties in many thermal structures. Maximum thermal conductivity can be beneficial in coolants, lubricants, automatic fluid diffusion, and engine oils. On the other hand, solid nanoparticles with minimal thermal conductivity, can improve the thermal conductivity of fluids [1]. Choi et al. [2, 3], the pioneers of nanofluid research, computed thermal conductivity and demonstrated thermal conductivity enhancement. In a base fluid, Choi and Eastman scrutinized the suspension of nanoparticles for the first time [4]. Shehzad et al. [5] studied the influence of heat transfer of nanofluid within a wavy channel by applying the Buongiorno paradigm. Xuan and Li [6] detected the proficiency of the heat transfer flow in the nanofluid. A great deal of study has on several fluid models [7–12]. Carbides, metals, carbon nanotubes, and oxides are commonly used as nanoparticles. The significance of nanofluids for convective heat transfer usages in determining their appropriateness has been discovered to be highly essential [13, 14]. Nanofluids are colloidal deferments of base fluid nanoparticles

that have been manufactured [15, 16]. Oil, ethylene glycol, and water are the most common base fluids. In most research, nanofluid has assumed a normal pure fluid. In renewable energy system and in industrial thermal management, they discovered that utilizing a revolving magnetic disk improves the rate of heat transfer. The investigators looked at several models and physical effects for heat transfer and nanofluid flow improvement [17–27]. Nanofluids also have valuable audial characteristics, in ultrasonic environments demonstrating more shear wave reconversion of an occurrence compression wave; the impact gets further dramatic as concentration rises [28]. Nanofluids have a potential function in the manufacture of airplanes, micromachineries, microdevices, vehicles, and other items, according to the current technology.

In a variety of heat transfer applications, nanofluids have numerous properties that make them potentially useful, such as machining, pharmaceutical procedures, fuel cells, vehicle cooling/thermal control, domestic refrigerators, hybrid-powered engines, chillers, microelectronics, lowering boiler flue gas temperature, and heat exchangers [29]. Zubaidi et al. [30–31] has a great contribution regarding heat transfer applications of nanofluids. Jou and Tzeng [32] quantitatively investigated the vital convection enhancement of a two-dimensional nanofluid. The rise in the average coefficient of heat transmission is evident when the parameter of buoyancy and the nanofluid volume percentage are increased. Rashidi and Pour [33] simulate the fluid moving above the permeable rotating disc when using the second thermodynamic law to an electrically behaving incompressible nanofluid.

There are numerous applications of the steady nanofluids and many researchers perform their great work in this regard. Rashidi et al. [34] discussed the entropy generation in steady magneto hydro dynamics flow owing to a rotating permeable disk in a nanofluid. Veera Krishna [35] inspected the application of steady nanofluid on steady magneto hydrodynamics flow of copper and alumina nanofluids as heat transport past a stretching permeable surface; similarly, Lin and Ghaffari [36] discussed the heat and mass transfer above the surface of a stretching wedge in a steady flow of sutter by nanofluid. The literature study reveals that a great deal of significance has pursued in the case of flows in permeable channel. In fluid-saturated permeable channels, the importance of convective flow has been largely motivated by its function in numerous natural and developed challenges in latest studies of concern. Fetecau et al. [37] examined analytical solutions through a porous plate channel relating to unsteady motions of Maxwell fluids for two mixed initial boundary value problems. Zeeshan et al. [38] scrutinized nanofluid of electroosmotic-modulated bioflow induced by complex traveling wave with zeta potential and heat source via a rectangular peristaltic pump. Abel et al. [39] may see the 2nd grade fluid heat transfer with a nonuniform heat sink/source study through a permeable channel from a penetrable stretched sheet in conjunction with the current research. For the analytic approximated solution, Rashidi et al. [40] employed the HAM in a permeable channel for the issue of steady flow on a spinning disk, including two auxiliary parameters. Khalili et al. [41] investigated mass- and time-dependent convective heat transmission in pseudoplastic nanofluids, calculating the nonlinear mechanism beyond a stretched wall using a fourth-order R-K methodology paired with a conventional shooting technique. By making use of two auxiliary parameters, Abolbashari et al. [42] used an analytic approximated solution of the magneto hydrodynamics flow problem of boundary coating continuously flowing through an extending surface, which has been solved using HAM to evaluate the improvement of the solution convergence rate. Similarly, in a 2nd grade fluid to solve the problem of heat transmission, Rashidi et al. [43] used a permeable medium and a modified differential transform method (DTM). Furthermore, to these deterministic techniques, nanosubstances are utilized for the problems of fluid dynamics managed by non-Newtonian fluidics systems [44–47].

Concern with the related investigation many researchers did a tremendous job in the computational analysis of nanofluids. Beside a vertical wavy surface, Iqbal et al. [48] discussed a computational investigation of dissipation influences on the flow of hydro magnetic convective of hybrid nanofluids. Similarly, Ghaffari et al. [49] analyzed entropy generation above a stretchable rotatory permeable disk in a flow of power-law nanofluid. The analytical and numerical approaches investigated have both merits and disadvantages. Numerical techniques necessitated linearization and discretization, which may have an impact on accuracy. Many researchers use analytical methods to solve nonlinear equations, such as the DTM (differential transform method) [50], HPM (homotopy perturbation method) [51, 52], ADM (Adomian decomposition method) [53], VIM (variational iteration method) [54], radial basis function [55], HAM (homotopy analysis method) [56] and artificial parameters method [57, 58]. All of these methods required the assumption of a tiny parameter, such as HPM, or a first guess. Again, poor selection has an impact on accuracy. Currently, Herisanu et al. [59, 60] have proposed an optimum method (OAFM). The small parameter and initial guess assumptions are not necessary in OAFM. We propose the OAFM for the HTBTP-SNF model in this work. The methodology of the Adams numerical technique and OAFM have been formulated in Section 2. The problem formulation and the results assessments have been discussed in Sections 3 and 4, respectively. While the comparison tables of OAFM and Adams numerical method are given in Section 5 (Tables1–3), the conclusion is provided in Section 6.

Table 1: Comparison of the OAFM and Adams numerical method for $f(x)$.

x	OAFM	Numerical solution	Absolute error (AE)
0	0	0	0
0.1	0.0805954451	0.080595445138914	8.9141×10^{-12}
0.2	0.1268821951	0.126882195101887	1.8873×10^{-12}
0.3	0.1453119717	0.145311971751876	1.8761×10^{-12}
0.4	0.1420660044	0.142066004420172	4.2017×10^{-10}
0.5	0.1231630169	0.123163016993000	9.3213×10^{-11}
0.6	0.0945265113	0.094526511335266	3.5266×10^{-11}
0.7	0.0620287942	0.062028794245478	4.5478×10^{-11}
0.8	0.0315236584	0.031523658481825	8.1825×10^{-11}
0.9	0.0088766024	0.008876602424646	2.4646×10^{-11}
1.0	-3.049910×10^{-9}	$-3.0499100129 \times 10^{-9}$	-6.9106×10^{-15}

Table 2: Comparison of the OAFM and Adams numerical method for $g(x)$.

x	OAFM	Numerical solution	Absolute error (AE)
0	1	1	0
0.1	0.890979091	0.89097909180232	8.0232×10^{-10}
0.2	0.783826564	0.78382656476964	7.6964×10^{-11}
0.3	0.678936228	0.67893622838875	3.8875×10^{-11}
0.4	0.5764164678	0.576416467884122	8.4122×10^{-11}
0.5	0.4761733918	0.476173391863718	6.3718×10^{-11}
0.6	0.3779836568	0.377983656802516	2.5161×10^{-11}
0.7	0.2815564324	0.281556432496159	9.6159×10^{-11}
0.8	0.1865863193	0.1865863193618622	1.8622×10^{-11}
0.9	0.0928000588	0.0928000588063435	6.3435×10^{-11}
1.0	-1.025373×10^{-9}	$-1.025373530 \times 10^{-9}$	-7.353×10^{-14}

Table 3: Comparison of the OAFM and Adams numerical method for $h(x)$.

x	OAFM	Numerical solution	Absolute error (AE)
0	1	1	0
0.1	0.9048468313	0.904846831361751	6.1751×10^{-11}
0.2	0.8084909694	0.808490969412694	1.2694×10^{-11}
0.3	0.7109459674	0.710945967436434	3.6434×10^{-11}
0.4	0.6122751974	0.612275197451976	5.1976×10^{-11}
0.5	0.5125576533	0.512557653304655	4.6550×10^{-12}
0.6	0.4118639265	0.411863926563999	6.3999×10^{-11}
0.7	0.3102436548	0.310243654829592	2.9592×10^{-11}
0.8	0.20772288512	0.2077228851230552	3.0552×10^{-12}
0.9	0.10430886568	0.1043088656840427	4.0427×10^{-12}
1.0	$9.4218732 \times 10^{-10}$	$9.4218732684 \times 10^{-10}$	4.4476×10^{-16}

The innovative contributions of computing procedure are as follows:

(i) The numerical and analytical computation have been designed through the technique of Adams numerical solver and optimal auxilary function method (OAFM) for the comparative study to investigate the heat transfer between two permeable parallel plates of steady nanofluids (HTBTP-SNFs) through Brownian and thermophoretic influences.

(ii) The PDEs representing HTBTP-SNFs are converted into a system of ODEs by utilizing appropriate transformation.

(iii) The Mathematica software command "NDSolve" is used to compute the dataset for HTBTP-SNFs for the alternative of parameter of porosity (m), magnetic parameter (M), Brownian parameter (Nb), viscosity parameter (R), Schmidt quantity (Sc), thermophores parameter (Nt), and Prandlt number (Pr).

(iv) The MATLAB software has been used to interpret the solution and the AE analysis plots of HTBTP-SNFs.

(v) The correctness and the validation of the HTBTP-SNFs are examined by both analytical and numerical techniques.

2. Methodology

The methodology in this section includes two parts. Firstly, the formation of data set by the Adams numerical method and secondly, the explanation of fundamental idea of OAFM is illuminated.

2.1. Adams Numerical Method. For the first-order system, the Adams numerical approach is written as

$$\frac{d\zeta}{dx} = f(x,\zeta),$$
$$\chi_{l+1} = \zeta_l + \int_{t_l}^{t_{l+1}} \frac{d\zeta}{dx} dt = \zeta_l + \int_{t_l}^{t_{l+1}} f(\zeta,t)dt, \tag{1}$$

where ζ specifies the first-order output of linear ordinary differential equations (ODEs), x indicates the input value, χ_{l+1}represent the 1st order interpolation iterative structure, and t represents the time interval.

Within the interval (t_l, t_{l+1}), Adams techniques are grounded on the basis of estimating the integral with a polynomial. Adams approaches are of two kinds, the explicit and the implicit classes. The explicit sort techniques are known as Adams–Bashforth techniques (ABT) while the implicit kinds are called the Adams–Moulton techniques (AMT). The ABT and AMT techniques of the 1st order are the approaches of forward and backward Euler. By applying a linear interpolant, the second-order procedures of these approaches are attained which are very informal. The second-order Adams–Bashforth technique (ABT2) is specified as follows:

$$\chi_{l+1} = \zeta_l + \frac{h}{2}(3f(\zeta_l, t_l - f(\zeta_{l-1}, t_{l-1}))), \tag{2}$$

where the step interval signify by h. The Adams–Moulton technique of second order (AMT2) is an implicit technique, also inspected to as the principle of trapezoidal specified under

$$\chi_{l+1} = \zeta_l + \frac{h}{2}(f(\zeta_{l+1}, t_{l+1} + f(\zeta_l, t_l))). \tag{3}$$

2.2. Fundamental Idea of OAFM. For the nonlinear ordinary differential equation of the OAFM,

$$L(g(\xi)) + S(\xi) + N(g(\xi)) = 0, \tag{4}$$

where the operators of linear and nonlinear equations are L and N, S is a source function, and at this phase, the unknown function is $g(\xi)$.

The initial and boundary conditions are

$$B\left(g(\xi), \frac{dg(\xi)}{d\xi}\right) = 0. \tag{5}$$

It is extremely hard to locate out the exact solution of strongly nonlinear equations. The suggested estimated solution is as follows:

$$\widehat{g}(\xi, F_i) = g_0(\xi) + g_1(\xi, F_i), i = 1, 2, \ldots, s. \tag{6}$$

Utilizing equation (6) into equation (4), we obtain

$$L(g_0(\xi)) + L(g_1(\xi, F_i)) + S(\xi) + N(g_0(\xi) + g_1(\xi, F_i)) = 0, \tag{7}$$

where $F_i, i = 1, 2, \ldots, s$ are parameters of control convergence, which are to be concluded.

The initial guess is found out as

$$L(g_0(\xi)) + S(\xi) = 0,$$
$$B\left(g_0(\xi), \frac{g_0(\xi)}{d\xi}\right) = 0. \tag{8}$$

The first approximation is attained as

$$L(g_1(\xi, F_i)) + N(g_0(\xi) + g_1(\xi, F_i)) = 0,$$
$$B\left(g_1(\xi), \frac{g_1(\xi)}{d\xi}\right) = 0. \tag{9}$$

The nonlinear term is given as

$$N(g_0(\xi) + g_1(\xi, F_i)) = N(g_0(\xi)) + \sum_{l=1}^{\infty} u_1^l(t, F_i) N^l(g_0(\xi)). \tag{10}$$

In equation (10), the last term looks tough to solve, thus to depart of this complexity and to the convergence of the solution rapidly, equation (10) can be composed as

$$L(g_1(\xi, F_i)) + D_1((g_0(\xi), F_n)E(N(g_0(\xi)))) + D_2(g_0(\xi), F_m) = 0,$$
$$B\left(g_1(\xi, F_i), \frac{dg_1(\xi, F_i)}{d\xi}\right) = 0, m = 1, 2, \ldots, q, n = q+1, q+2, \ldots s, \tag{11}$$

where the optimal auxiliary functions that depend on $g_0(\xi)$ are D_1 and D_2. While F_m, F_n and $E(N(g_0(\xi)))$ are the functions which depend on the expression emerging inside in the nonlinear term of $N(g_0(\xi))$. If $g_0(\xi)$ is polynomial, trigonometric, and exponential, then the optimal auxiliary functions D_1 and D_2 would be the sum of polynomial, trigonometric, and exponential correspondingly. Also, if $N(g_0(\xi)) = 0$, then $g_0(\xi)$ would be the accurate solution of the innovative problem. From the "Galerkin method," "method of least square," "Ritz method," and "collocation method," the optimal auxiliary function method (OAFM) can be achieved.

2.3. Convergence of the Technique. In order to get the convergent solution, we evaluated the optimum constants, which are also recognized as control convergence constants by the "least square method." So, to obtain the series solution, these optimal constants are resubmitted into the original equation:

$$J(F_1, F_2, ..F_s) = \int_I R^2(\xi, F_1, F_2, .., F_s)\mathrm{d}\xi, \tag{12}$$

where I denotes the domain of the equation.

The constants which are unknown can be obtained as

$$\partial_{F_1} J = 0, \partial_{F_2} J = 0, \ldots \partial_{F_s} J = 0. \tag{13}$$

3. Problem Formulation

An incompressible laminar steady nanofluid flow has been considered between two horizontal equivalent plates. A coordinate structure in which the both axes x and y are preferred along and normal to the plate. Both fluid and plate are revolving with angular velocity along the y-axis, whereas the bottom plate has stretched by two equal and contrary forces along the x-axis, leaving the location (0, 0) unaltered. As displayed in Figure 1, a uniform and constant magnetic pitch (field) B_0 has provided to the flow in a normal manner. The medium is maintained to be permeable.

The lower plate is permeable and the system is rotating, whereas the flow is subjected to homogeneous magnetic field of density B_0. The governing equations for the suggested fluidic systems are specified as

$$\begin{aligned}
&\frac{\partial u}{\partial x} + \frac{\partial v}{\partial y} = 0\\
&\left(\frac{\partial u}{\partial x}u + \frac{\partial u}{\partial y}v\right)\rho = \left(\frac{\partial^2 u}{\partial x^2} + \frac{\partial^2 u}{\partial y^2}\right)\mu - \frac{\partial p^*}{\partial x} - \sigma B_0^2 u - \frac{\mu}{\eta}u\\
&\rho\left(v\frac{\partial v}{\partial y}\right) = \mu\left(\frac{\partial^2 v}{\partial x^2} + \frac{\partial^2 v}{\partial y^2}\right) - \frac{\partial p^*}{\partial y}\\
&\frac{\partial T}{\partial x}u + \frac{\partial T}{\partial y}v = \alpha\left(\frac{\partial^2 T}{\partial x^2} + \frac{\partial^2 T}{\partial y^2}\right) + \frac{(\rho c_i)_v}{(\rho c_i)_f}\left[\begin{array}{l} D\left(\frac{\partial C}{\partial x} * \frac{\partial T}{\partial x} + \frac{\partial C}{\partial y} * \frac{\partial T}{\partial y}\right) + \\ \left\{\left(\frac{\partial T}{\partial x}\right)^2 + \left(\frac{D}{T}\right)\left(\frac{\partial T}{\partial y}\right)^2\right\}\end{array}\right]\\
&\frac{\partial C}{\partial y}v + \frac{\partial C}{\partial x}u = \left(\frac{\partial^2 C}{\partial x^2} + \frac{\partial^2 C}{\partial y^2}\right)D_B + \left(\frac{D_T}{T_0}\right)\left\{\frac{\partial^2 T}{\partial x^2} + \frac{\partial^2 T}{\partial y^2}\right\},
\end{aligned} \tag{14}$$

where the velocities of the fluid along axes are u and v, correspondingly. Also, ρ indicates the base fluid density, modified pressure is expressed by p^*, σ denotes the electrical conductivity, μ symbolizes dynamic viscosity, temperature is denoted by T, (μ/η) is porosity parameter, C is concentration, the specific heat of nanofluid is denoted by c_i, and D_B represents the diffusing coefficient of diffusing classes.

$$\begin{aligned}
&u = ax, v = 0, T = T_h, C = C_h, \text{at } y = 0,\\
&u = 0, v = 0, C = C_0, T = T_0, \text{at } y = h.
\end{aligned} \tag{15}$$

Applying the correspondence transformation,

$$\begin{aligned}
&\eta = \frac{y}{h}, u = axf'(\eta), v = -ahf'(\eta),\\
&\phi(\eta) = \frac{C - C_h}{C_0 - C_h}, \theta(\eta) = \frac{T - T_h}{T_0 - T_h}.
\end{aligned} \tag{16}$$

For the dimensionless scheme, together with boundary conditions, the governing equations are stated as

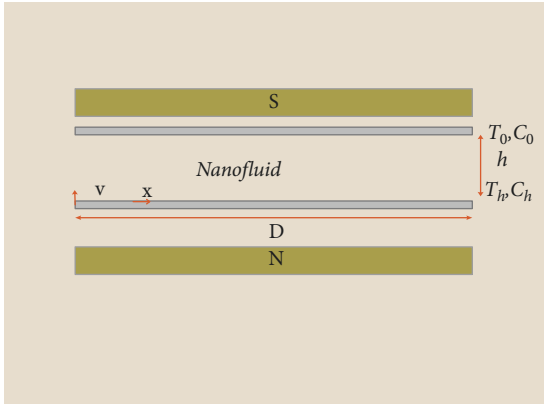

Figure 1: Flow problem geometry.

$$f^{iv} - R\left(f'f'' - ff''\right) - (M+m)f'' = 0, \tag{17}$$

$$\phi'' + R\bullet Scf\phi' + \frac{Nt}{Nb}\theta'' = 0, \tag{18}$$

$$R\,\mathrm{Pr}\,f\theta' + \theta'' + Nt\theta'^2 + \phi'\theta' Nb = 0. \tag{19}$$

$$\begin{aligned} f(0) = 0, f'(0) = 1, \theta(0) = 1, \varphi(0) = 1, \\ f'(1) = 0, f(1) = 0, \theta(1) = 0, \varphi(1) = 0. \end{aligned} \tag{20}$$

The dimensionless quantities are explained as

$$\begin{aligned} R &= \frac{ah^2}{\nu}, \\ M &= \frac{\sigma B_0^2 h^2}{\rho\nu}, \\ \mathrm{Pr} &= \frac{\mu}{\rho\alpha}, \\ Sc &= \frac{\mu}{\rho D}, \\ m &= \frac{\mu h^2}{\rho\eta k}, \\ N_b &= \frac{D_B C_h (\rho c)_p}{(\rho c)_f \alpha}, \\ N_t &= \frac{D_T T_h (\rho c)_p}{(\rho c)_f \alpha T_c}, \end{aligned} \tag{21}$$

where the viscosity parameter is R, the magnetic parameter is M, the Prandlt quantity is denoted by Pr, the Schmidt quantity is specified by Sc, m is the porosity parameter, and the Brownian and thermophoretic parameters are specified by Nb and Nt, respectively. Nu represents the Nusselt number and C_f indicates the coefficient of skin friction beside the stretching wall and are specified by

$$\begin{aligned} C_f &= \left(\frac{Rx}{h}\right), \\ C_f &= f''(0), \\ \mathrm{Nu} &= -\theta. \end{aligned} \tag{22}$$

4. Results Assessment

The Adams numerical solver technique has been used for the variants of HTBTP-SNFs model. Numerical and analytical investigation showed the HTBTP-SNFs model has accompanied steady nanofluids between two permeable parallel plates with heat impact, displayed in equations (17)–(20).

Figure 2 shows the mathematical model together with relevant geometry, methodology, and results.

The variation of $M, m, R,$ Pr , Sc, Nb, and Nt individually, apiece with three cases of the HTBTP-SNFs model, is tabulated in Table 4.

For velocity profile $f'(\eta)$, temperature distribution $\theta(\eta)$, and concentration distribution $\varphi(\eta)$, the comparative variation of physical parameters of the HTBTP-SNFs model such as magnetic parameter M, parameters of porosity, Brownian motion, viscosity, and thermophoretic are m, Nb, Nt, R, Schmidt number Sc, and Prandlt number Pr through OAFM and Adams numerical method are shown in Figures 3–12, respectively, along with error plots. The consequences of velocity distribution $f'(\eta)$ are given in subfigures 3(a), 4(a), and 5(a) for the deviation of magnetic parameter (M), viscosity parameter (R), and porosity parameter (m) of the HTBTP-SNFs model whereas the corresponding values of AE are plotted in subfigures 3(b), 4(b), and 5(b) in order to obtain the execution of the HTBTP-SNFs approach. The reliable overlapping of analytic and numerical solutions can be detected. The impact of magnetic turf (M) on $f'(\eta)$ is presented in subfigure 3(a), which shows that when the magnetic field increase the velocity decreases. This is due to the reality that the increasing M develops the friction force of the movement and is identified as the Lorentz force. In the boundary sheet, Lorentz force has the correspondence to reduce the flow velocity. The influence of porosity parameter m on $f'(\eta)$ has been exposed in subfigure 4(a). The graph shows that when the porosity increases and the magnetic field is kept constant, the velocity profile increase in interval 0 to 0.5 and decrease in interval 0.5 to 1. Similarly, the impact of viscosity parameter R on $f'(\eta)$ has displayed in subfigure 5(a). It is obvious that when viscosity parameter (R) escalates with constant porous medium and magnetic field, the velocity of the fluid escalates in interval 0 to 0.5 and decrease in interval 0.5 to 1.

Accordingly, the outcomes of temperature profile $\theta(\eta)$ are given in subfigures 6(a), 7(a), 8(a), and 9(a) of the HTBTP-SNFs model. The relevant values of AE are plotted in subfigures 6(b), 7(b), 8(b), and 9(b) for the HTBTP-SNFs model. It is observed from subfigure 6(a) that escalating Nb reduces the temperature field. Actually, escalating Nb kinetic

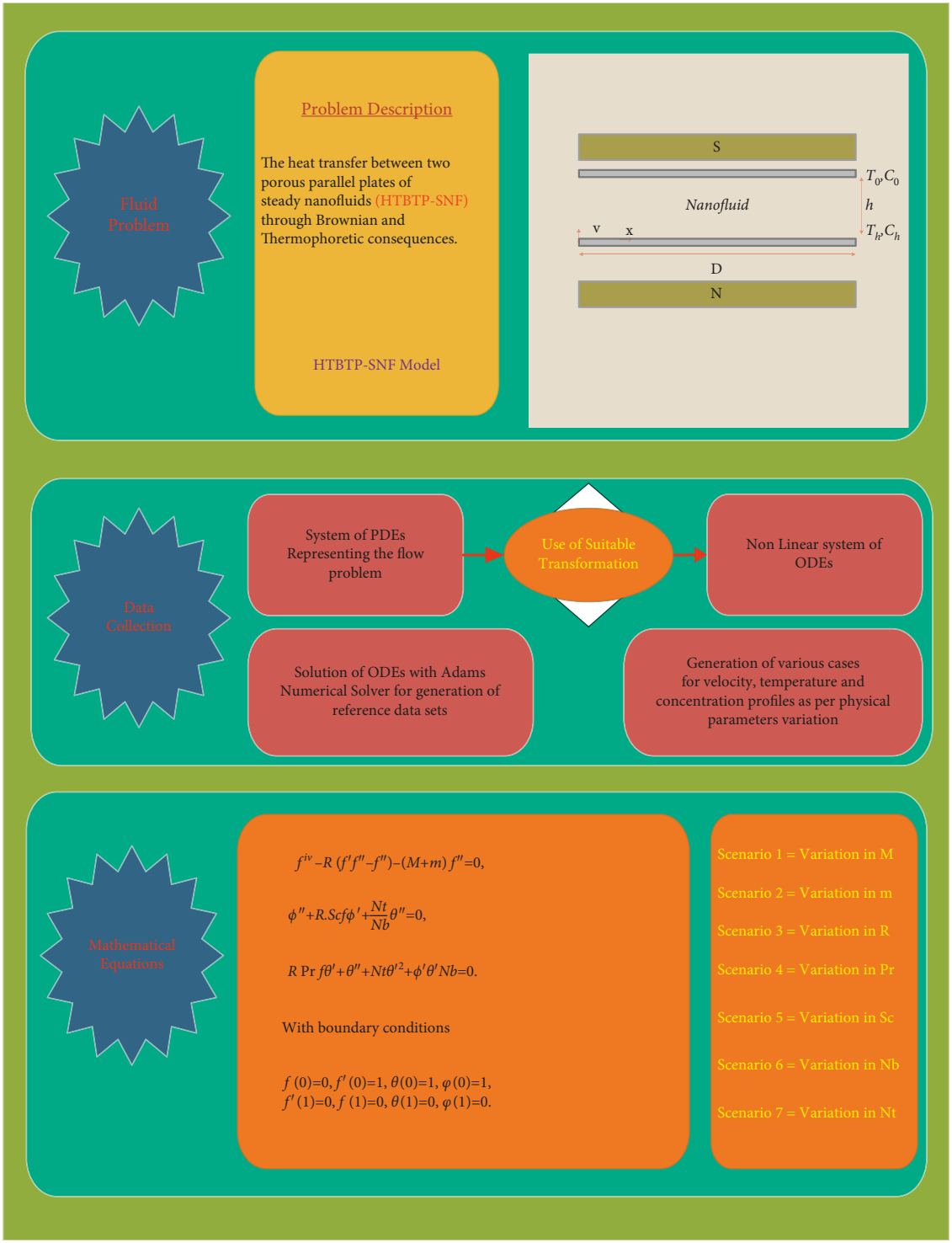

Figure 2: Overall working flowchart.

energy increases due to which the nanoparticles within the fluid raise the heat transfer rate and boundary thickness coating, which decrease the temperature field. Subfigure 7(a) shows the effect of the thermophoretic parameter on $\theta(\eta)$. It is clear from subfigure 7(a) that when value of Nt escalates, the temperature field is decreased. This is because of the reality that the thermophoresis parameter (Nt) depend on the gradient of temperature in the nearby nanofluid molecules. Escalating Nt decreases the kinetic energy of the nanofluid molecule, which results in the decrement in the temperature distribution. The influence of Pr on temperature distributions is presented in subfigure 8(a), temperature profile vary directly with Pr. The greater value of Pr causes decrement in the temperature profile. Subfigure 9(a) displays

Table 4: Scenarios interpretation beside with cases for the HTBTP-SNFs model.

Scenarios	Cases	Physical measures of concern						
		M	m	R	Pr	Sc	Nb	Nt
1	1	1	1	1	1	0.7	0.1	0.1
	2	2	1	1	1	0.7	0.1	0.1
	3	3	1	1	1	0.7	0.1	0.1
2	1	1	1	1	1	0.7	0.1	0.1
	2	1	3	1	1	0.7	0.1	0.1
	3	1	5	1	1	0.7	0.1	0.1
3	1	1	1	1	1	0.7	0.1	0.1
	2	1	1	3	1	0.7	0.1	0.1
	3	1	1	5	1	0.7	0.1	0.1
4	1	1	1	1	1	0.7	0.1	0.1
	2	1	1	1	2	0.7	0.1	0.1
	3	1	1	1	3	0.7	0.1	0.1
5	1	1	1	1	1	1	0.1	0.1
	2	1	1	1	1	2	0.1	0.1
	3	1	1	1	1	3	0.1	0.1
6	1	1	1	1	1	0.7	0.1	0.1
	2	1	1	1	1	0.7	0.2	0.1
	3	1	1	1	1	0.7	0.3	0.1
7	1	1	1	1	1	0.7	0.1	0.1
	2	1	1	1	1	0.7	0.1	0.2
	3	1	1	1	1	0.7	0.1	0.3

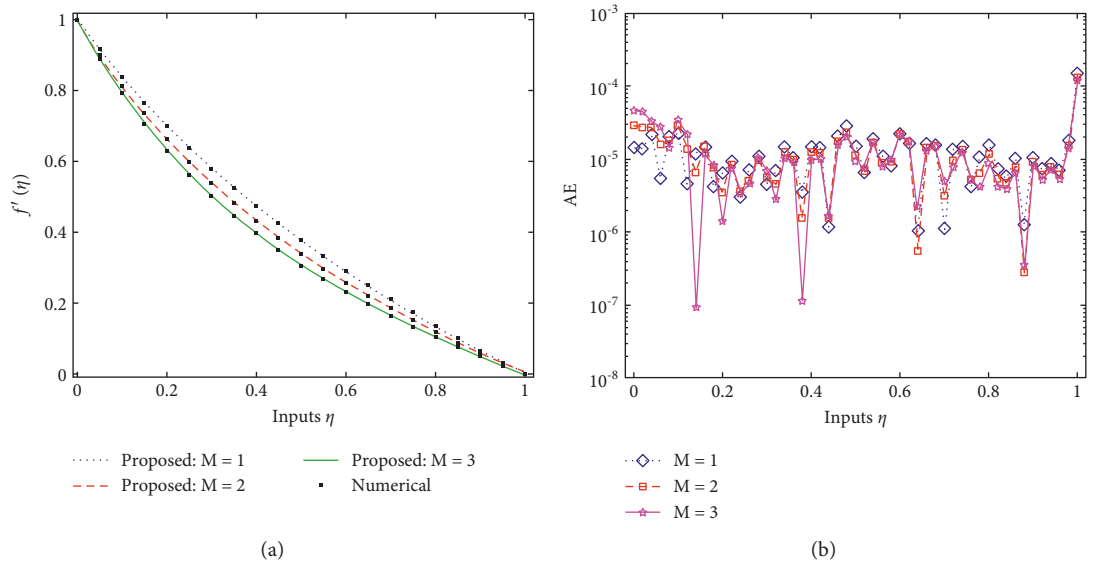

Figure 3: (a) Influence of M. (b) Analysis on AE.

the impact of viscosity parameter (R) on temperature distribution, which shows the direct relation when R increases and the temperature distribution is deaccelerated. This decrement caused by the increase of inertial force, which increase with incensement in R. Because when the values of viscosity parameter (R) increase, the inertial forces get strong and the temperature field has a tendency to decrease. Furthermore, between numerical and analytical effects, these results also show the uniform overlapping.

Similarly, the outcomes of concentration distribution $\varphi(\eta)$ are given in subfigures 10(a), 11(a), and 12(a) of the HTBTP-SNFs model. The appropriate values of AE are mapped in subfigures 10(b), 11(b), and 12(b). Subfigure 10(a) indicates the effect of Schmidt quantity (Sc) on concentration profile $\varphi(\eta)$, where Sc represent momentum and mass diffusivity ratio. Subfigure 11(a) explains the influence of thermophoresis parameter (Nt) on $\varphi(\eta)$. It is clear from subfigure 11(a) that when value of Nt increase the concentration field decreases. Escalating Nt decreases the kinetic energy of the nanofluid molecule, which causes the decrement in the concentration profile. It is observed from subfigure 12(a) that increasing Nb reduces the concentration

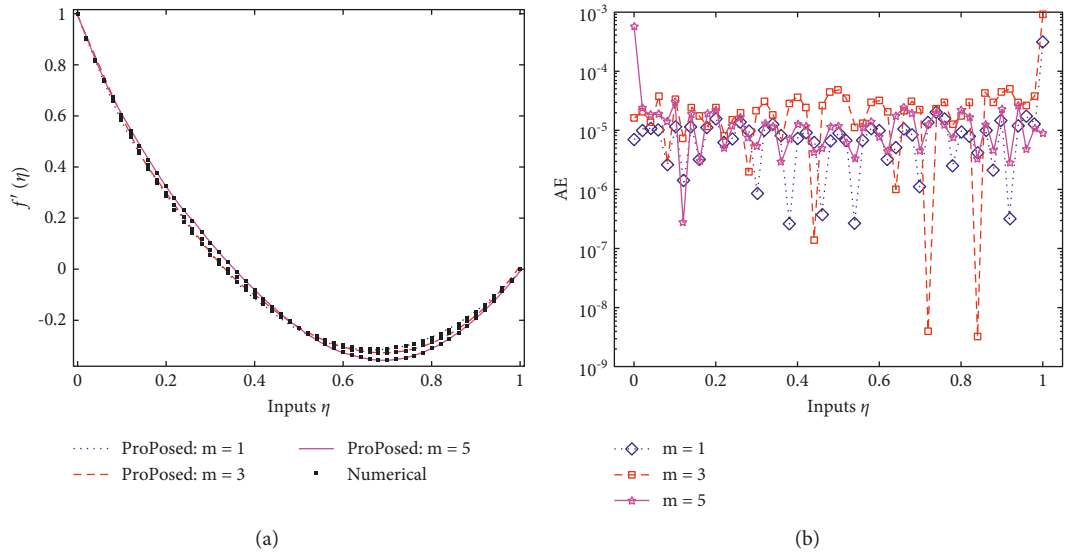

Figure 4: (a) Influence of m. (b) Analysis on AE.

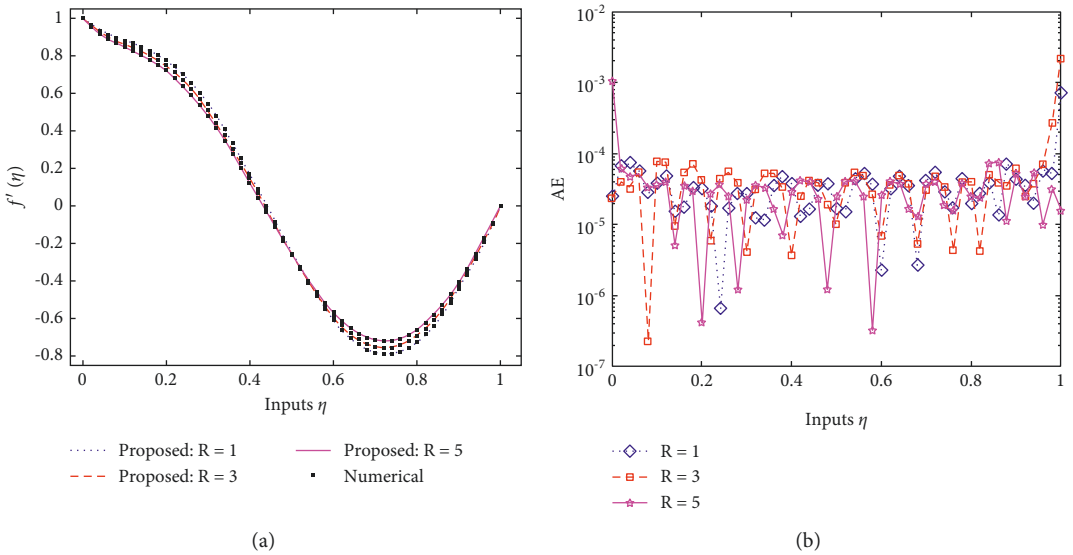

Figure 5: (a) Influence of R. (b) Analysis on AE.

field. The concentration profile reduces by increasing the Brownian motion parameter (Nb). The boundary coating thicknesses decreases because of rise of Brownian motion, which cause to reduce concentrations. These results also show the consistent overlapping between analytical and numerical solution.

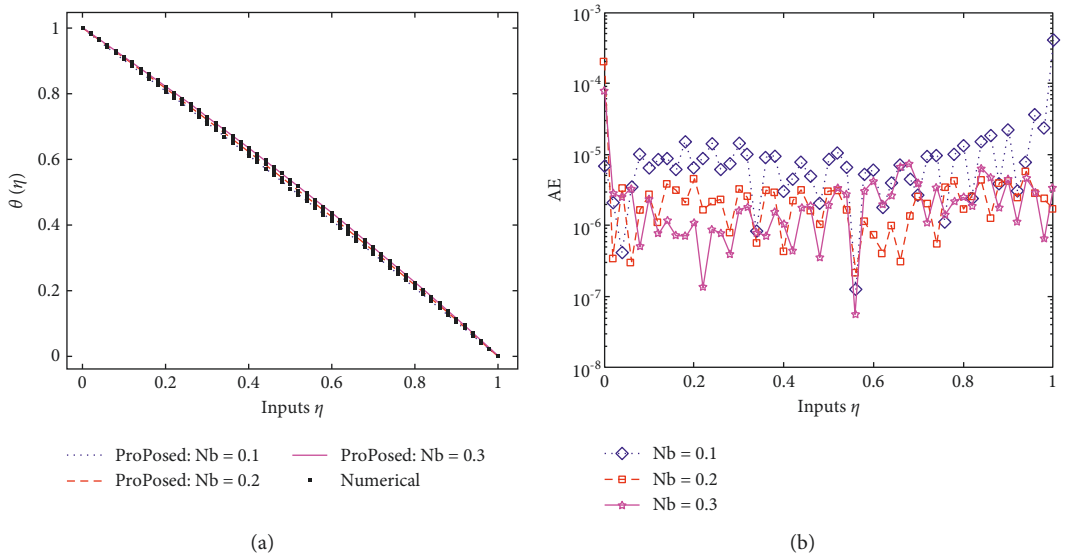

(a) (b)

Figure 6: (a) Influence of Nb. (b) Analysis on AE.

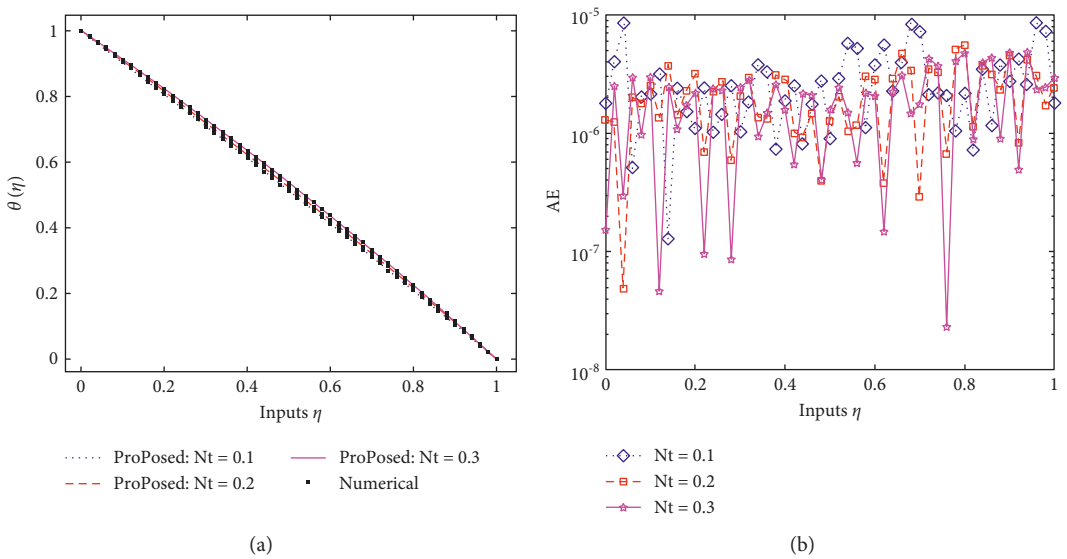

(a) (b)

Figure 7: (a) Influence of Nt. (b) Analysis on AE.

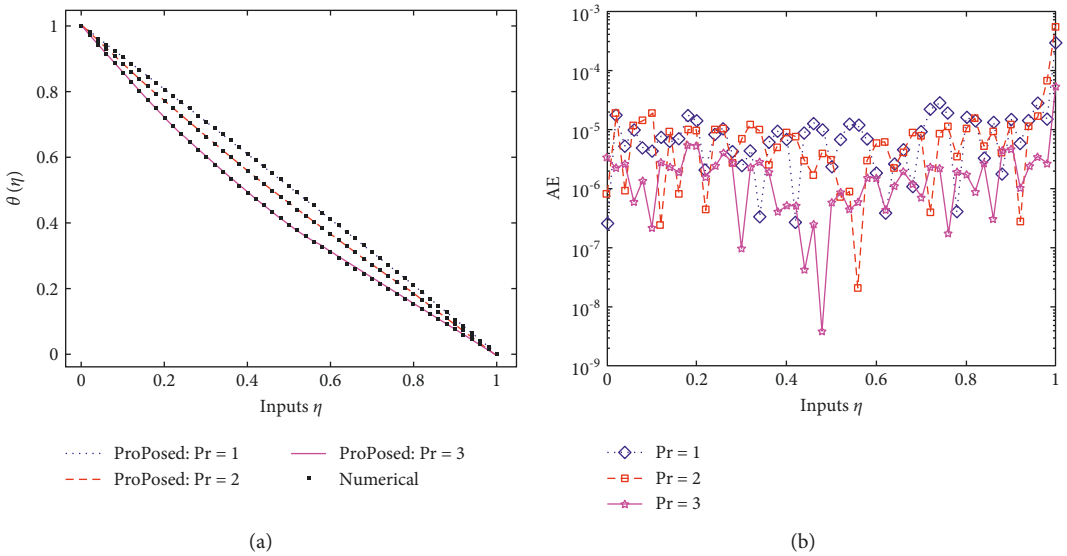

(a) (b)

Figure 8: (a) Influence of Pr. (b) Analysis on AE.

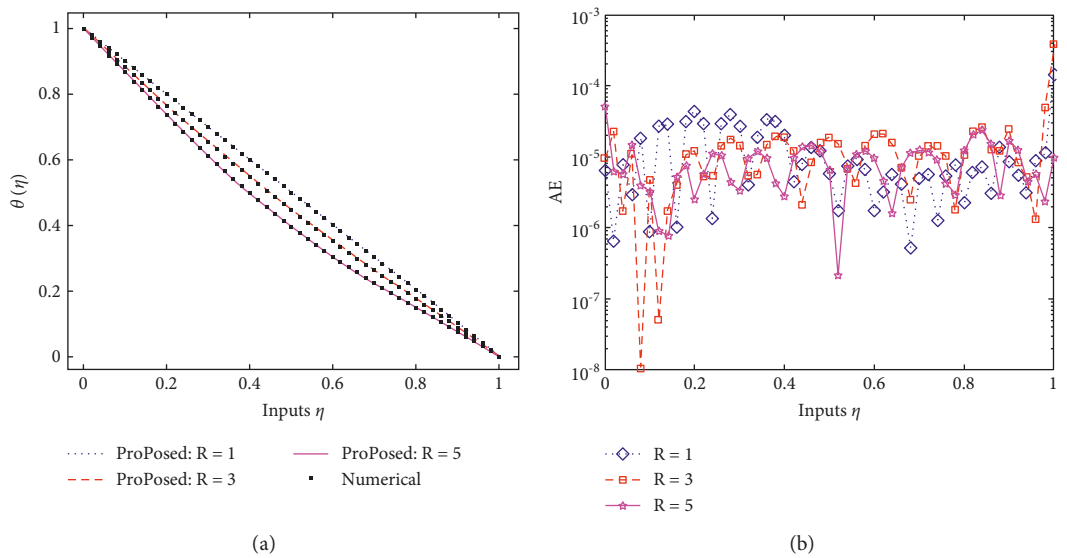

(a) (b)

Figure 9: (a) Influence of R. (b) Analysis on AE.

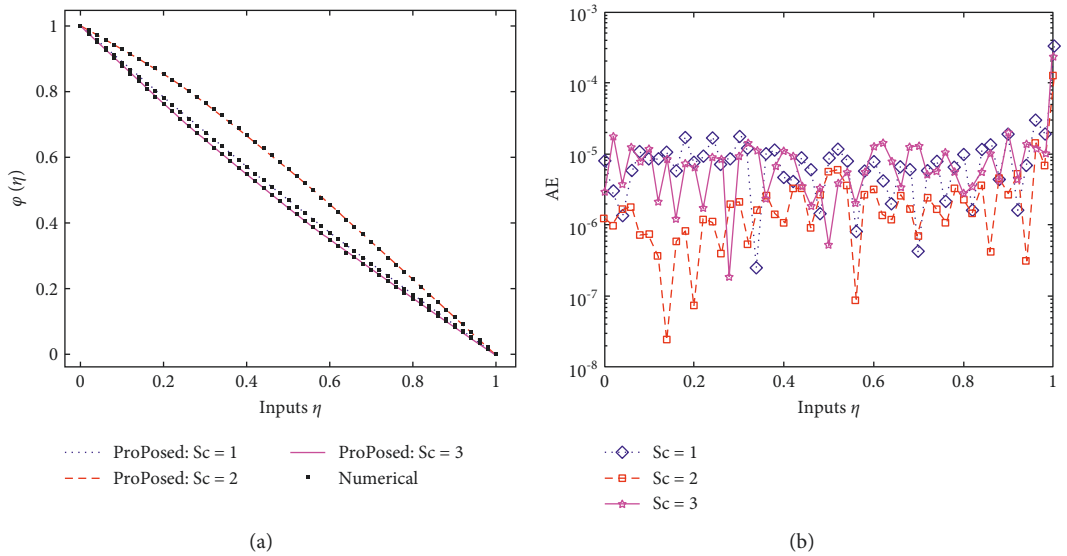

(a) (b)

Figure 10: (a) Influence of Sc. (b) Analysis on AE.

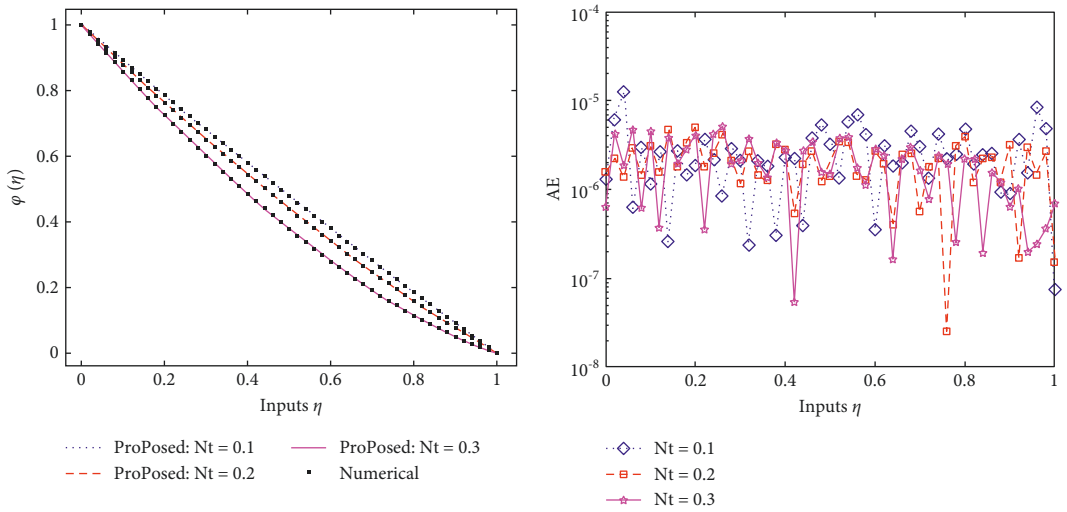

(a) (b)

Figure 11: (a) Influence of Nt. (b) Analysis on AE.

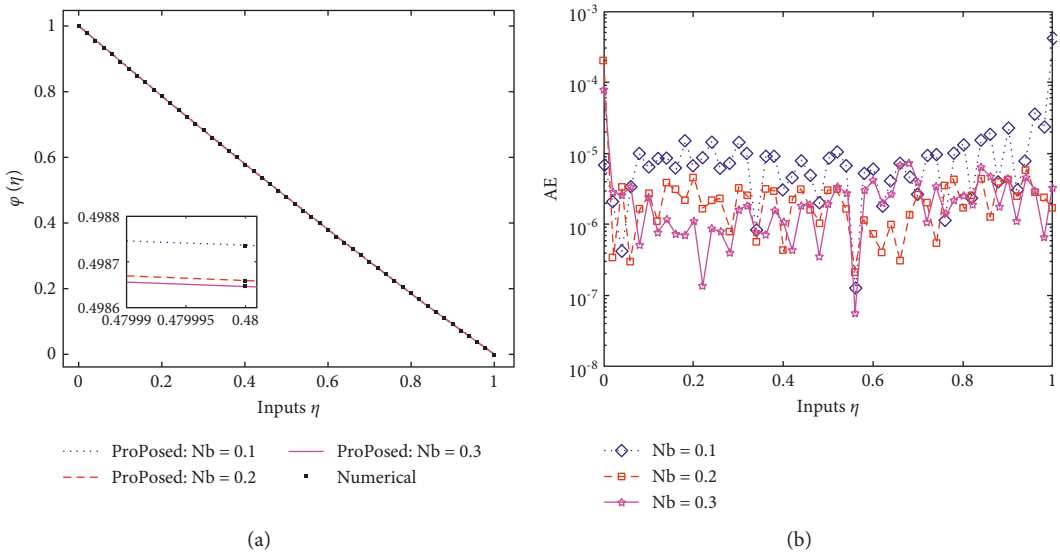

Figure 12: (a) Influence of Nb. (b) Analysis on AE.

5. Comparison Tables of the OAFM and Adams Numerical Method

6. Conclusion

In this analysis, a novel analytical technique for solving the boundary layer flow model was proposed (HTBTP-SNFs). The governing equations of the HTBTP-SNFs model are explained in first-order series, and the first-order solution is reached with excellent accuracy. We associated the OAFM findings with the numerical results produced using the Adams numerical technique to ensure the perfection and strength of our method. The comparison shows that the recommended approach is perfect, and the decent agreement of our consequences with the numerical data demonstrates the method's validity. Though the nonlinear beginning/boundary value issue does not comprise the tiny parameter, OAFM is extremely straightforward to apply to large nonlinear primary and boundary value problems. In compared to other analytical methods, OAFM is relatively simple to use and produces excellent results for more complicated nonlinear initial/boundary value issues. Since the OAFM contains the control convergence constansts, which are also known as optimal constants, we can control the convergence of the method. When compared to other approaches, OAFM requires less computing labor, and even a low-spec machine may readily complete the task. There are currently no limitations to this approach, allowing us to apply this effective and quick convergent method to increasingly complicated models originating from real-world situations in the future. The Adams numerical technique is a reliable numerical method for obtaining precise results. The Adams numerical method is an iterative technique that requires the most space and time, whereas OAFM is a short method that converges quickly. For addressing any nonlinear system of equations, both the Adams numerical technique and OAFM are good approaches.

The aim of the present research work is to present a novel application of comparative analysis of the new scheme paradigm (HTBTP-SNFs) of the heat transfer between two permeable parallel plates of steady nanofluids through Brownian and thermophoretic consequences. This comparative analysis of the HTBTP-SNFs model is based on the newly established optimal approach, namely, optimal auxilary function method (OAFM) and the Adams numerical technique to find the analytical and numerical solutions of the HTBTP-SNFs model. Both results give a close resemblance of their approaches which indicates that both techniques converge quickly and both are strongly accurate and efficient methods.

Nomenclature

u, v:	Components of velocity
x, y:	Coordinates system
p^*:	Modified pressure
μ:	Fluid dynamic viscosity
C:	Nanoparticles concentration
Ci:	Specific heat of nanofluid
Nb:	Parameter of Brownian motion
θ:	Dimensionless temperature
T:	Fluid temperature
R:	Viscosity parameter
^{D}T:	Coefficient of thermophoresis diffusion
Sc:	Schmidt number
OAFM:	Optimal auxilary function method
t:	Time for steady flow
ϕ:	Dimensionless concentration
C_f:	Skin friction coefficient
B0:	Uniform magnetic field
M:	Magnetic parameter
D_B:	Brownian diffusion coefficient
m:	Parameter of porosity
Pr:	Prandlt quantity
Nu:	Nusselt number

ρ: Fluid density
ρ: Efficient heat capacity of nanoparticle
σ: Electrical conductivity heat transfer between two porous parallel plates of steady nanofluids.

Data Availability

All the data are available in the manuscript.

Conflicts of Interest

The authors declare that they have no conflicts of interest.

References

[1] D. M. Forrester, J. Huang, V. J. Pinfield, and F. Luppé, "Experimental verification of nanofluid shear-wave reconversion in ultrasonic fields," *Nanoscale*, vol. 8, no. 10, pp. 5497–5506, 2016.

[2] W. Yu and S. U. S. Choi, "The role of interfacal layers in the enhanced thermal conductivity of nanofluids: a renovated Maxwell model," *Journal of Nanoparticle Research*, vol. 5, no. 1-2, pp. 167–171, 2003.

[3] S. U. S. Choi and J. A. Eastman, "Enhancing thermal conductivity of fluids with nanoparticles," *Materials Science*, vol. 231, pp. 99–105, 1995.

[4] S. U. Choi and J. A. Eastman, *Enhancing thermal Conductivity of Fluids with Nanoparticles (No. ANL/MSD/CP-84938; CONF-951135-29)*, Argonne National Lab (ANL), Argonne, IL, USA, 1995.

[5] N. Shehzad, A. Zeeshan, R. Ellahi, and K. Vafai, "Convective heat transfer of nanofluid in a wavy channel: buongiorno's mathematical model," *Journal of Molecular Liquids*, vol. 222, pp. 446–455, 2016.

[6] Y. Xuan and Q. Li, "Investigation on convective heat transfer and flow features of nanofluids," *Journal of Heat Transfer*, vol. 125, no. 1, pp. 151–155, 2003.

[7] A. A. Mahmoud and E. Shimaa, "MHD flow and heat transfer of a micropolar fluid over a stretching surface with heat generation (absorption) and slip velocity," *Journal of the Egyptian Mathematical Society*, vol. 20, no. 1, pp. 20–27, 2012.

[8] F. Awad, M. S. Ahamed, P. Sibanda, and M. Khumalo, "The effect of thermophoresis on unsteady oldroyd-B nanofluid flow over stretching surface," *PLoS One*, vol. 10, no. 8, Article ID e0135914.

[9] S. Nadeem and S. T. Hussain, "Analysis of MHD williamson nano fluid flow over a heated surface," *Journal of Applied Fluid Mechanics*, vol. 9, no. 2, pp. 729–739, 2016.

[10] B. Mahanthesh, B. J. Gireesha, and R. Subba, "Unsteady three-dimensional MHD flow of a nano Eyring-Powell fluid past a convectively heated stretching sheet in the presence of thermal radiation, viscous dissipation and Joule heating," *Journal of the Association of Arab Universities for Basic and Applied Sciences*, vol. 23, no. 1, pp. 75–84.

[11] M. Khan, R. Mali, A. Munir, and W. A. Khan, "Flow and heat transfer to Sisko nanofluid over a nonlinear stretching sheet," *PLoS One*, vol. 10.

[12] S. Qayyum, T. Hayat, A. Alsaedi, and B. Ahmad, "Magnetohydrodynamic (MHD) nonlinear convective flow of Jeffrey nanofluid over a nonlinear stretching surface with variable thickness and chemical reaction," *International Journal of Mechanical Sciences*, vol. 134, pp. 306–314, 2017.

[13] S. Witharana, H. Chen, and Y. Ding, "Stability of nanofluids in quiescent and shear flow fields," *Nanoscale Research Letters*, vol. 6, no. 1, p. 231, 2011.

[14] S. Zeinali Heris, S. G. Etemad, and M. Nasr Esfahany, "Experimental investigation of oxide nanofluids laminar flow convective heat transfer," *International Communications in Heat and Mass Transfer*, vol. 33, no. 4, pp. 529–535, 2006.

[15] R. Taylor, S. Coulombe, T. Otanicar et al., "Small particles, big impacts: a review of the diverse applications of nanofluids," *Journal of Applied Physics*, vol. 113, no. 1, pp. 1–8, 2013.

[16] J. Buongiorno, "Convective transport in nanofluids," *Journal of Heat Transfer*, vol. 128, no. 3, pp. 240–250, 2006.

[17] R. Y. Jou and S. C. Tzeng, "Numerical research of nature convective heat transfer enhancement filled with nanofluids in rectangular enclosures," *International Communications in Heat and Mass Transfer*, vol. 33, no. 6, pp. 727–736, 2006.

[18] M. M. Rashidi, S. Abelman, S. Abelman, and N. Freidooni Mehr, "Entropy generation in steady MHD flow due to a rotating porous disk in a nanofluid," *International Journal of Heat and Mass Transfer*, vol. 62, pp. 515–525, 2013.

[19] F. Garoosi, G. Bagheri, and M. M. Rashidi, "Two phase simulation of natural convection and mixed convection of the nanofluid in a square cavity," *Powder Technology*, vol. 275, pp. 239–256, 2015.

[20] F. Garoosi, B. Rohani, and M. M. Rashidi, "Two-phase mixture modeling of mixed convection of nanofluids in a square cavity with internal and external heating," *Powder Technology*, vol. 275, pp. 304–321, 2015.

[21] F. Garoosi, L. Jahanshaloo, M. M. Rashidi, A. Badakhsh, and M. E. Ali, "Numerical simulation of natural convection of the nanofluid in a heat exchangers using a Buongiorno model," *Applied Mathematics and Computation*, vol. 254, pp. 183–203, 2015.

[22] H. R. Ashorynejad, M. Sheikholeslami, I. Pop, and D. D. Ganji, "Nanofluid flow and heat transfer due to a stretching cylinder in the presence of magnetic field," *Heat and Mass Transfer*, vol. 49, no. 3, pp. 427–436, 2013.

[23] H. R. Ashorynejad, A. A. Mohamad, M. Sheikholeslami, I. Pop, and D. D. Ganji, "Magnetic field effects on natural convection flow of a nanofluid in a horizontal cylindrical annulus using Lattice Boltzmann method," *International Journal of Thermal Sciences*, vol. 64, pp. 240–250, 2013.

[24] M. Hatami, M. Sheikholeslami, M. Hosseini, and D. D. Ganji, "Analytical investigation of MHD nanofluid flow in non-parallel walls," *Journal of Molecular Liquids*, vol. 194, pp. 251–259, 2014.

[25] M. Hatami, M. Sheikholeslami, and D. D. Ganji, "Nanofluid flow and heat transfer in an asymmetric porous channel with expanding or contracting wall," *Journal of Molecular Liquids*, vol. 195, pp. 230–239, 2014.

[26] M. Hatami, M. Sheikholeslami, D. D. Ganji, and D. D. Ganji, "RETRACTED: laminar flow and heat transfer of nanofluid between contracting and rotating disks by least square method," *Powder Technology*, vol. 253, pp. 769–779, 2014.

[27] D. Domairry, M. Sheikholeslami, H. R. Ashorynejad, R. S. R. Gorla, and M. Khani, "Natural convection flow of a non-Newtonian nanofluid between two vertical flat plates," *Proceedings of the Institution of Mechanical Engineers - Part N: Journal of Nanoengineering and Nanosystems*, vol. 225, no. 3, pp. 115–122, 2012.

[28] H. Chen, S. Witharana, Y. Jin, C. Kim, and Y. Ding, "Predicting thermal conductivity of liquid suspensions of nanoparticles (nanofluids) based on rheology," *Particuology*, vol. 7, no. 2, pp. 151–157, 2009.

[29] S. K. Das, U. C. H. Stephen, Y. Wenhua, and T. Pradeep, *Nanofluids: Science and Technology*, Wiley-Interscience, Hoboken, NJ, USA, 2010.

[30] A. Zubaidi, M. Nazeer, S. Saleem, F. Hussain, and F. Ahmad, "Flow of nanofluid towards a Riga surface with heat and mass transfer under the effects of activation energy and thermal radiation," *International Journal of Modern Physics B*, vol. 35, no. 26, Article ID 2150266, 2021.

[31] H. Chen, S. Saleem, and M. Ghaderi, "Using artificial neural network to optimize the flow and natural heat transfer of a magnetic nanofluid in a square enclosure with a fin on its vertical wall: a Lattice Boltzmann simulation," *Journal of Thermal Analysis and Calorimetry*, vol. 145, 2021.

[32] R.-Y. Jou and S.-C. Tzeng, "Numerical research of nature convective heat transfer enhancement filled with nanofluids in rectangular enclosures," *International Communications in Heat and Mass Transfer*, vol. 33, no. 6, pp. 727–736, 2006.

[33] M. M. Rashidi and S. A. M. Pour, "Analytic approximate solutions for steady flow over a rotating disk in porous medium by homotopy analysis method with two auxiliary parameters," *International Journal of Applied Mathematics & Statistics*, 2010.

[34] M. M. Rashidi, S. Abelman, and N. Freidooni Mehr, "Entropy generation in steady MHD flow due to a rotating porous disk in a nanofluid," *International Journal of Heat and Mass Transfer*, vol. 62, pp. 515–525, 2013.

[35] M. Veera Krishna, "Heat transport on steady MHD flow of copper and alumina nanofluids past a stretching porous surface," *Heat Transfer*, vol. 49, no. 3, pp. 1374–1385, 2020.

[36] P. Lin and A. Ghaffari, "Heat and mass transfer in a steady flow of Sutterby nanofluid over the surface of a stretching wedge," *Physica Scripta*, vol. 96, no. 6, Article ID 065003, 2021.

[37] C. Fetecau, D. Vieru, and A. Zeeshan, "Analytical solutions for two mixed initial-boundary value problems corresponding to unsteady motions of Maxwell fluids through a porous plate channel," *Mathematical Problems in Engineering*, vol. 2021, Article ID 5539007, 13 pages, 2021.

[38] A. Zeeshan, A. Riaz, and F. Alzahrani, "Electroosmosis-modulated bio-flow of nanofluid through a rectangular peristaltic pump induced by complex traveling wave with zeta potential and heat source," *Electrophoresis*, vol. 42, no. 21-22, pp. 2143–2153, 2021.

[39] M. S. Abel, M. M. Nandeppanavar, and S. B. Malipatil, "Heat transfer in a second grade fluid through a porous medium from a permeable stretching sheet with non-uniform heat source/sink," *International Journal of Heat and Mass Transfer*, vol. 53, no. 9-10, pp. 1788–1795, 2010.

[40] M. M. Rashidi, E. Momoniat, and B. Rostami, "Analytic approximate solutions for MHD boundary-layer viscoelastic fluid flow over continuously moving stretching surface by homotopy analysis method with two auxiliary parameters," *Journal of Applied Mathematics*, vol. 2012, Article ID 780415, 19 pages, 2012.

[41] S. Khalili, H. Tamim, A. Khalili, and M. M. Rashidi, "Unsteady convective heat and mass transfer in pseudoplastic nanofluid over a stretching wall," *Advanced Powder Technology*, vol. 26, no. 5, pp. 1319–1326, 2015.

[42] M. H. Abolbashari, N. Freidoonimehr, F. Nazari, and M. M. Rashidi, "Analytical modeling of entropy generation for Casson nano-fluid flow induced by a stretching surface," *Advanced Powder Technology*, vol. 26, no. 2, pp. 542–552, 2015.

[43] M. M. Rashidi, T. Hayat, M. Keimanesh, and H. Yousefian, "A study on heat transfer in a second-Grade fluid through a porous medium with the modified differential transform method," *Heat Transfer - Asian Research*, vol. 42, 2013.

[44] M. Irani, M. Afrand, and B. Mehmandoust, "Curve fitting on experimental data of a new hybrid nano-antifreeze viscosity: presenting new correlations for non- Newtonian nanofluid," *Physica A: Statistical Mechanics and Its Applications*, vol. 531, Article ID 120837, 2019.

[45] P. M. Nafchi, A. Karimipour, and M. Afrand, "The evaluation on a new non-Newtonian hybrid mixture composed of TiO2/ZnO/EG to present a statistical approach of power law for its rheological and thermal properties," *Physica A: Statistical Mechanics and Its Applications*, vol. 516, pp. 1–18, 2019.

[46] C. Amanulla, A. Wakif, Z. Boulahia, S. Fazuruddin, and S. Noor Mohammed, "A study on non-Newtonian transport phenomena in MHD fluid flow from a vertical cone with Navier slip and convective heating," *Nonlinear Engineering*, vol. 8, no. 1, pp. 534–545, 2019.

[47] I. Kazemi, M. Sefid, and M. Afrand, "A novel comparative experimental study on rheological behavior of mono & hybrid nanofluids concerned graphene and silica nano-powders: c," *Powder Technology*, vol. 366, pp. 216–229, 2020.

[48] M. S. Iqbal, I. Mustafa, A. Ghaffari, and Usman, "A computational analysis of dissipation effects on the hydromagnetic convective flow of hybrid nanofluids along a vertical wavy surface," *Heat Transfer*, vol. 50, no. 8, pp. 8035–8051, 2021.

[49] A. Ghaffari, I. Mustafa, T. Muhammad, and Y. Altaf, "Analysis of entropy generation in a power-law nanofluid flow over a stretchable rotatory porous disk," *Case Studies in Thermal Engineering*, vol. 28, Article ID 101370, 2021.

[50] H. Yaghoobi and M. Torabi, "The application of differential transformation method to nonlinear equations arising in heat transfer," *International Communications in Heat and Mass Transfer*, vol. 38, no. 6, pp. 815–820, 2011.

[51] J. H. He, "Homotopy perturbation technique," *Computer Methods in Applied Mechanics and Engineering*, vol. 178, pp. 257–262, 1999.

[52] D. D. Ganji, "The application of He's homotopy perturbation method to nonlinear equations arising in heat transfer," *Physics Letters A*, vol. 355, no. 4-5, pp. 337–341, 2006.

[53] R. Bellman, *Perturbation Techniques in Mathematics, physics, and engineering*, New York, Holt, Rinehart and Winston, New York, NY, USA, 1964.

[54] S. H. Chowdhury, "A comparison between the modified homotopy perturbation method and adomian decomposition method for solving nonlinear heat transfer equations," *Journal of Applied Sciences*, vol. 11, no. 8, pp. 1416–1420, 2011.

[55] D. D. Ganji, G. A. Afrouzi, and R. A. Talarposhti, "Application of variational iteration method and homotopy-perturbation method for nonlinear heat diffusion and heat transfer equations," *Physics Letters A*, vol. 368, no. 6, pp. 450–457, 2007.

[56] H. Yaghoobi and M. Torabi, "The application of differential transformation method to nonlinear equations arising in heat

transfer," *International Communications in Heat and Mass Transfer*, vol. 38, no. 6, pp. 815–820, 2011.

[57] S. J. Liao, *The proposed homotopy analysis technique for the solution of nonlinear problems*, PhD Thesis, Shanghai Jiao Tong University, Shanghai, China, 1992.

[58] G. L. Liu, "New research direction in singular perturbation theory: artificial parameter approach and inverse perturbation technique," in *Proceedings of the 7th Conference on Modern Mathematics and Mechanics*, Shanghai, China, September 1997.

[59] N. Herisanu and V. Marinca, "An efficient analytical approach to investigate the dynamics of a misaligned multirotor system," *Mathematics*, vol. 8, no. 7, p. 1083, 2020.

[60] N. Herisanu, V. Marinca, G. Madescu, and F. Dragan, "Dynamic response of a permanent magnet synchronous generator to a wind gust," *Energies*, vol. 12, no. 5, p. 915, 2019.

Hindawi
Mathematical Problems in Engineering
Volume 2022, Article ID 1736516, 11 pages
https://doi.org/10.1155/2022/1736516

Research Article

Radiative Flow of Copper and Aluminum Nanoparticles with Heat Source Phenomenon: Dual Numerical Simulations and Stability Analysis

Sumera Dero,[1] Liaquat Ali Lund,[2] Al-Khaled Kamel,[3] Asjad Muhammad Imran,[4] Taseer Muhammad,[5] Sami Ullah Khan,[6] and A Abbasi[7]

[1]*Institute of Mathematics and Computer Science, University of Sindh, Jamshoro, Pakistan*
[2]*KCAET Khairpur Mirs, Sindh Agriculture University, Tandojam, Sindh 70060, Pakistan*
[3]*Department of Mathematics & Statistics, Jordan University of Science and Technology, P.O. Box 3030, Irbid 22110, Jordan*
[4]*Department of Mathematics, University of Management and Technology, Lahore, Pakistan*
[5]*Department of Mathematics, College of Science, King Khalid University, Abha 61413, Saudi Arabia*
[6]*Department of Mathematics, COMSATS University Islamabad, Sahiwal 57000, Pakistan*
[7]*Department of Mathematics, University of Azad Jammu and Kashmir, Muzaffarabad 13100, Pakistan*

Correspondence should be addressed to Taseer Muhammad; taseer_qau@yahoo.com

Received 29 August 2021; Revised 7 December 2021; Accepted 19 April 2022; Published 1 July 2022

Academic Editor: Alessandro Formisano

The thermally developed flow of nanoparticles due to bidirectional moving space has been presented numerically. The additional impact of heat source and sink are also incorporated for enhancing the heat transfer rate. The copper and aluminum nanoparticles are selected for enhancing the thermal diffusion system. The thermal stability of nanoparticles is carefully addressed. The moving surface allows the shrinking and stretching phenomenon. The system of resulting equations with nonlinear nature is numerically swapped via shooting technique with help of MATLAB software. The dual numerical simulations for the thermally radiative problem with external heating phenomenon are being performed. It is noted from results that thermal stability of nanoparticles is more stable in the upper branch of shrinking/stretching surface. The presence of heat source provides extra heat and improves the thermal transportation phenomenon which is more progressive in upper branch. The enhancement in temperature profile due to copper nanoparticles is more stable as compared to aluminum nanoparticles. Moreover, the increasing change in the velocity is resulted upon increasing the rotation constant. The obtained results reflect applications in thermal sciences, heating systems, energy production, solar applications, nuclear reactions, biomedical applications, etc.

1. Introduction

Recently, motivations of researchers are noticed towards the nanofluid which reports leading contributions in the thermal engineering and industrial processes. The growing interest in nanomaterials is justified due to highly attractive applications in solar energy, thermal transportation systems, engineering devices, cooling systems, heating objectives, nuclear reactions, medical sciences, emission processes, etc. With nanostructured (1–100 nm), the nanofluids report excellent thermal activities. The interaction between nanoparticles and some base fluids reports results enhanced thermal mechanism of base fluids. Choi [1] focused first time on the thermal aspect of nanofluids via experimental approach. Later on, diverse research is being performed by investigators to highlight the thermal mechanism and applications of nanomaterials. Turkyilmazoglu [2] developed a slip nanofluid model for the annuli flow by utilizing the dual nanofluid and single relations of the nanofluid model. Nayak et al. [3] exploited the viscous dissipation consequences for illustrating the nanofluids flow with Oldroyd-B base material via bidirectional space. Basir et al. [4] performed the novel aspect of slip flow of nanofluid with sensitivity insurance and bioconvection phenomenon. The Maxwell nanofluid thermal determinations subject to the interaction of multiple types of slip consequences have been identified

by Ahmad et al. [5]. The Buongiorno nanofluid model implementation for inspecting the viscoelastic fluid thermal capacity was reported in the work of Nadeem et al. [6]. The analytical simulation for the nanofluid Riga surface problem was investigated by Vaidya et al. [7]. Wang et al. [8] focused on the migration of nanofluid material minichannels having parallel plates. Abdelaziz et al. [9] discussed the characteristics of nanofluid pattern via horizontal tubes. The continuation of Sabu et al. [10] determined the heat transfer improvement for the alumina nanoparticles with slip constraints due to heated rotatory disk. Ojjela et al. [11] addressed the viscoelastic behavior and thermal capability for the nanoparticles with non-Newtonian base fluid. The stability determination of nanofluids with experimental approach was determined by Dong et al. [12]. Sivasankaran and Bhuvaneswari [13]investigated the heat transfer mechanism with constraints of pressure loss and porous space. Acharya [14] numerically focused on the natural convective flow of nanofluid due to heated wall surface in square enclosure. Mondal et al. [15] addressed the optimized thermal mechanism due to the couple stress nanofluid with radiative phenomenon. Acharya [16] discussed the finite element numerical simulations for the spinning flow of nanoparticles with active and passive control approach. Shafiq et al. [17] addressed the bioconvection aspect of nanofluid with zero mass constraints. Haya et al. [18] addressed the Joule heating effects while inspecting the enhanced aspect of heat transfer in third grade nanofluid. Some more recent work on nanofluid flow is presented in [19–24].

The hybrid nanofluid is the modified form of nanofluids with more improved thermal activities. In fact, the hybrid nanofluid model is based on the interaction of more than one different types of nanoparticles along with base material. The preferences of the hybrid nanofluid model over simple nanomaterials are due to extra high activities and more thermal stability. Recently, different investigations are performed on hybrid nanofluid with different nanoparticles. Sowmya et al. [25] reported the inclusion of iron nanoparticles with existence of Lorentz force in cavity with two heated fins. Sundar et al. [26] claimed the hybrid nanofluid thermal properties with collector applications. Akhtar et al. [27] modeled a hybrid nanofluid problem in elliptic duct following the peristaltic mechanism. Eid and Mabood [28] noticed the ethylene glycol base fluid thermal inspection with hybrid nanofluid numerically. Eid and Mabood [28] presented the thermal research on the carbon nanotubes flow with heat generation features. Shahid et al. [29] implemented the Darcy porous law for studying the hybrid nanofluid prospective in parabolic surface. Madhukesh et al. [30] explored the thermal efficiencies of AA7072-AA7075 nanoparticles with Newtonian heating enrollment. Acharya [31] discussed the shape characteristics for the hybrid nanofluid in heated obstacles. Devi and Devi [32] visualized the copper and aluminum oxide nanoparticles thermal prospective accounted via stretching surface. Devi and Devi [33] observed the 3D thermal flow problem with Newtonian heating. Lund et al. [34] intended the rotating flow of hybrid nanofluid. Teh and Ashgar [35] determined the Joule heating for the rotating flow of hybrid nanofluid. Zaimi et al. [36] discussed the multiple solution of rotating viscoelastic fluid with hybrid nanofluid.

This analysis deals with the impact of heat source and thermal radiation effects in flow of hybrid nanofluid due to rotating space. The main motivation for performing this investigation is to highlight the enhanced thermal aspect of heat transfer phenomenon subject to the magnetized copper and aluminum nanoparticles. The moving surface attained the stretching and shrinking phenomenon. The thermal stability of hybrid nanoparticles is focused. The shooting numerical algorithm is followed for the simulations process. The dual simulations are performed in each branch of moving space.

2. Problem Formulation

The stretching and shrinking phenomenon of 3D hybrid nanofluid is taken into account. The heat transfer analysis is considered in presence of external heating source and thermal radiation. The magnetic force impact is directed along the z-axis for 3D flow. The three-dimensional moving space attained the velocity $u_w(x) = \lambda c x^n$. The stretching and shrinking results are attained for $\lambda > 0$ and $\lambda < 0$, respectively. The surface temperature of nanoparticles is notified with T_w while T_∞ is for free stream temperature case as shown in Figure 1. The nanoparticles and surface present rotatory behavior with angular velocity $\widetilde{\Omega} = \Omega_0 x^{(1-n)}$ along z-direction. Let u, v, and $w$be representation of velocities along , y, and z directions, respectively. The assumptions of low magnetic Reynolds number reduce the role of induced magnetic force. The governing relations in view of such considerations are as follows [26–28]:

$$u_x + v_y + w_z = 0, \tag{1}$$

$$uu_x + vu_y + wu_z - 2\widetilde{\Omega}v = -\frac{P_x}{\rho_{hnf}} + \frac{\mu_{hnf}}{\rho_{hnf}}\left[u_{xx} + u_{yy} + u_{zz}\right] - \frac{\sigma_{hnf}}{\rho_{hnf}}B^2 u. \tag{2}$$

$$uv_x + vv_y + wv_z + 2\widetilde{\Omega}u = -\frac{P_y}{\rho_{hnf}} + \frac{\mu_{hnf}}{\rho_{hnf}}\left[v_{xx} + v_{yy} + v_{zz}\right]v - \frac{\sigma_{hnf}}{\rho_{hnf}}B^2 v, \tag{3}$$

$$uw_x + vw_y + ww_z = -\frac{P_z}{\rho_{hnf}} + \frac{\mu_{hnf}}{\rho_{hnf}}\left[w_{xx} + w_{yy} + w_{zz}\right], \tag{4}$$

$$\left(\rho c_p\right)_{hnf}\left[uT_x + vT_y + wT_z\right] = k_{hnf}\left[T_{xx} + T_{yy} + T_{zz}\right]T - q_{r\,z} + Q_0\left(T - T_\infty\right). \tag{5}$$

The related boundary conditions are as follows:

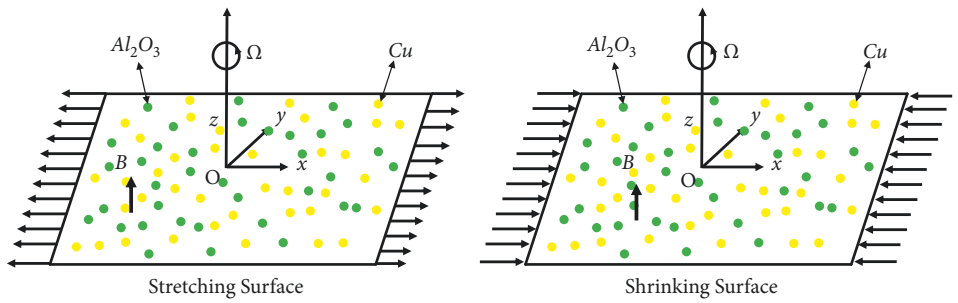

Figure 1: Flow illustration of problem.

$$\begin{cases} w = w_w(x), v = 0, u = u_w(x), T = T_w \text{ at } z = 0 \\ u \longrightarrow 0,\ v \longrightarrow 0,\ T \longrightarrow T_\infty \text{ as } z \longrightarrow \infty \end{cases} \tag{6}$$

The relation for radiative flux q_r is given by $q_r = -(4\sigma^*/3k^*)(\partial T^4/\partial z)$. Table 1 and Table 2 provide the thermophysical properties.

The following similarity variables (7) are used to obtain similarity solutions for equations (1)–(5):

$$\begin{cases} u = cx^n f'(\eta), v = cx^n g(\eta), \eta = z\sqrt{\dfrac{c(n+1)}{2\vartheta_f}}\, x^{(n-1)/2} \\ w = -\sqrt{\dfrac{c\vartheta_f(n+1)}{2}}\, x^{(n-1)/2}\left[f(\eta) + \dfrac{n-1}{n+1}\eta f'(\eta)\right] \\ \theta(\eta) = (T - T_\infty)/(T_w - T_\infty) \end{cases} \tag{7}$$

The dimensionless set of equation is

$$f''' + \xi_1\xi_2\left[ff'' - \frac{2n}{(n+1)}f'^2 + \frac{4\Omega}{(n+1)}g\right] - \frac{2}{(n+1)}\frac{\sigma_{hnf}}{\sigma_f}\xi_2 M f\prime = 0, \tag{8}$$

$$g'' + \xi_1\xi_2\left[fg' - \frac{2n}{(n+1)}f'g - \frac{4\Omega}{(n+1)}f'\right] - \frac{2}{(n+1)}\frac{\sigma_{hnf}}{\sigma_f}\xi_2 M g = 0, \tag{9}$$

$$\frac{\xi_3}{Pr}\left(\frac{k_{hnf}}{k_f} + \frac{4}{3}R\,d\right)\theta'' + \theta' f + \xi_3 Q\theta = 0, \tag{10}$$

subject to BCs,

$$\begin{cases} f(0) = -b\sqrt{\dfrac{2}{n+1}},\ f'(0) = \lambda,\ g(0) = 0, \theta(0) = 1 \\ f'(\eta) \longrightarrow 0, g(\eta) \longrightarrow 0\ \theta(\eta) \longrightarrow 0,\ \ as\,\eta \longrightarrow \infty \end{cases},$$

$$\begin{cases} \xi_1 = \left\{(1-\phi_{Cu})\left[1 - \phi_{Al_2O_3} + \phi_{Al_2O_3}\left(\dfrac{\rho_{Al_2O_3}}{\rho_f}\right)\right] + \phi_{Cu}\left(\dfrac{\rho_{Cu}}{\rho_f}\right)\right\} \\ \xi_2 = (1-\phi_{Cu})^{2.5}\left(1 - \phi_{Al_2O_3}\right)^{2.5} \\ \xi_3 = \dfrac{1}{\left\{(1-\phi_{Cu})\left[1 - \phi_{Al_2O_3} + \phi_{Al_2O_3}\left(\rho c_p\right)_{Al_2O_3}/\left(\rho c_p\right)_f\right] + \phi_{Cu}\left(\rho c_p\right)_{Cu}/\left(\rho c_p\right)_f\right\}} \end{cases}, \tag{11}$$

where prime "ı" denotes the differentiation by η, $M = (\sigma_f B_0^2/c\rho_f)$ is the magnetic number, $Pr = (\vartheta_f/\alpha_f)$ is Prandtl, $\Omega = (\Omega_0/c)$ is rotation parameter, Q shows the heat source/sink parameter, and $R\,d = (4\sigma^* T_\infty^3/k^* k_f)$ denotes the thermal radiation constant and b suction $(b > 0)$/injection $(b > 0)$ constant.

The dynamic of local Nusselt number and skin friction coefficient is

$$C_{fx} = \frac{\mu_{hnf}}{\rho_f u_w^2}\left(\frac{\partial u}{\partial z}\right)|z = 0,\ C_{fy} = \frac{\mu_{hnf}}{\rho_f u_w^2}\left(\frac{\partial v}{\partial z}\right)|z = 0, \tag{12}$$

$$Nu_x = \frac{-k_{hnf}(\partial T/\partial z)_{z=0} + (q_r)_{z=0}}{k_f(T_w - T_\infty)}.$$

Substituting (7) into (12) yields

Table 1: Thermophysical features of hybrid nanofluid [32–34].

Properties	Hybrid nanofluid
Dynamic viscosity	$\mu_{hnf} = \mu_f/(1-\phi_{Cu})^{2.5}(1-\phi_{Al_2O_3})^{2.5}$
Density	$\rho_{hnf} = (1-\phi_{Cu})[(1-\phi_{Al_2O_3})\rho_f + \phi_{Al_2O_3}\rho_{Al_2O_3}] + \phi_{Cu}\rho_{Cu}$
Thermal conductivity	$k_{hnf} = k_{Cu} + 2k_{nf} - 2\phi_{Cu}(k_{nf}-k_{Cu})/k_{Cu} + 2k_{nf} + \phi_{Cu}(k_{nf}-k_{Cu}) \times (k_{nf})$ where $k_{nf} = k_{Al_2O_3} + 2k_f - 2\phi_{Al_2O_3}(k_f - k_{Al_2O_3})/k_{Al_2O_3} + 2k_f + \phi_{Al_2O_3}(k_f - k_{Al_2O_3}) \times (k_f)$
Heat capacity	$(\rho c_p)_{hnf} = (1-\phi_{Cu})[(1-\phi_{Al_2O_3})(\rho c_p)_f + \phi_{Al_2O_3}(\rho c_p)_{Al_2O_3}] + \phi_{Cu}(\rho c_p)_{Cu}$
Electrical conductivity	$\sigma_{hnf} = \sigma_{Cu} + 2\sigma_{nf} - 2\phi_{Cu}(\sigma_{nf}-\sigma_{Cu})/\sigma_{Cu} + 2\sigma_{nf} + \phi_{Cu}(\sigma_{nf}-\sigma_{Cu}) \times (\sigma_{nf})$ where $\sigma_{nf} = \sigma_{Al_2O_3} + 2\sigma_f - 2\phi_{Al_2O_3}(\sigma_f - \sigma_{Al_2O_3})/\sigma_{Al_2O_3} + 2\sigma_f + \phi_{Al_2O_3}(\sigma_f - \sigma_{Al_2O_3}) \times (\sigma_f)$

Table 2: The thermophysical properties [32–34].

Properties	Water (H_2O)	Copper (Cu)	Alumina (Al_2O_3)
$\rho\ (kg/m3)$	997.1	8933	3970
$c_p\ (J/kg\,K)$	4179	385	765
$k\ (W/m\,K)$	0.613	400	40
$\sigma\ (S/m)$	0.05	5.96×10^7	3.69×10^7
Pr	6.2		

$$\sqrt{Re}C_{fx} = \frac{1}{\xi_2}f''(0);\ \sqrt{Re}C_{fy} = \frac{1}{\xi_2}g'(0)\ \sqrt{\frac{Re}{2}}Nu_x = -\left(\frac{k_{hnf}}{k_f} + \frac{4}{3}R\ d\right)\theta'(0), \tag{13}$$

where Re_x is the local Reynolds number.

3. Stability Analysis

Two branches of solution against the involved parameters are observed. In order to inspect the branch of solution with more physical relevance, the stability analysis has been performed for both branches. The governing equations (2)-(5) with unsteady form are

$$u_t + uu_x + vu_y + wu_z - 2\tilde{\Omega}v = -\frac{P_x}{\rho_{hnf}} + \frac{\mu_{hnf}}{\rho_{hnf}}\left[u_{xx} + u_{yy} + u_{zz}\right] - \frac{\sigma_{hnf}}{\rho_{hnf}}B^2u, \tag{14}$$

$$v_t + uv_x + vv_y + wv_z + 2\tilde{\Omega}u = -\frac{P_y}{\rho_{hnf}} + \frac{\mu_{hnf}}{\rho_{hnf}}\left[v_{xx} + v_{yy} + v_{zz}\right]v - \frac{\sigma_{hnf}}{\rho_{hnf}}B^2v, \tag{15}$$

$$w_t + uw_x + vw_y + ww_z = -\frac{P_z}{\rho_{hnf}} + \frac{\mu_{hnf}}{\rho_{hnf}}\left[w_{xx} + w_{yy} + w_{zz}\right], \tag{16}$$

$$\left(\rho c_p\right)_{hnf}\left[T_t + uT_x + vT_y + wT_z\right] = k_{hnf}\left[T_{xx} + T_{yy} + T_{zz}\right]T - q_{r\,z} + Q_0(T - T_\infty). \tag{17}$$

The unsteady similarity solution can be considered as follows [33–35]:

$$\begin{cases} u = cx^n f_\eta(\eta,\tau), v = cx^n g(\eta,\tau), \\ w = -\sqrt{\dfrac{c\vartheta_f(n+1)}{2}}x^{(n-1)/2}\left[f(\eta,\tau) + \dfrac{n-1}{n+1}\eta f_\eta(\eta,\tau) - \dfrac{2\tau}{n+1}\eta f(\eta,\tau)\right], \\ \theta(\eta,\tau) = \left((T-T_\infty)/(T_w-T_\infty)\right). \end{cases} \tag{18}$$

where the η is the same as in equation (7) and the dimensionless time is the $\tau = ctx^{n-1}$, where the subscription represents the derivative of the variable subscripted. Remember that continuity (1) is also satisfied by the values u, v, and w given above. Equation (18) is substituted into equations (14)-(17), and one can get

$$f_{\eta\eta\eta} + \xi_1\xi_2\left[ff_{\eta\eta} - \frac{2n}{(n+1)}\left(f_\eta\right)^2 + \frac{4\Omega}{(n+1)}g + \frac{2(n-1)}{(n+1)}\tau\left(f_\tau f_{\eta\eta} - f_\eta f_{\tau\eta}\right) - \frac{2}{(n+1)}f_{\tau\eta}\right] \tag{19}$$

$$g_{\eta\eta} + \xi_1\xi_2\left[fg_\eta - \frac{2n}{(n+1)}f_\eta g - \frac{4\Omega}{(n+1)}f_\eta + \frac{2(n-1)}{(n+1)}\tau\left(f_\tau g_\eta - g_\tau f_\eta\right) - \frac{2}{(n+1)}g_\tau\right] - \frac{2}{(n+1)}\frac{\sigma_{hnf}}{\sigma_f}\xi_2 Mg = 0, \tag{20}$$

$$\frac{\xi_3}{Pr}\left(\frac{k_{hnf}}{k_f}+\frac{4}{3}R\,d\right)\theta_{\eta\eta}+\theta_\eta f+\xi_3 Q\theta + 2\tau\left(f_\tau\theta_\eta-\theta_\tau f_\eta\right)-\theta_\tau=0, \tag{21}$$

subject to BCs,

$$\begin{cases} f(0,\tau)=-b\sqrt{\dfrac{2}{n+1}},\ f'(0,\tau)=\lambda,\ g(0,\tau)=0,\theta(0,\tau)=1 \\ f'(\eta,\tau)\longrightarrow 0, g(\eta,\tau)\longrightarrow 0\ \theta(\eta,\tau)\longrightarrow 0,\ as\,\eta\longrightarrow\infty \end{cases}. \tag{22}$$

It is assumed that [28]

$$f(\eta,\tau)=f_0(\eta)+e^{-\varepsilon\tau}F(\eta,\tau), g(\eta,\tau). = g_0(\eta)+e^{-\varepsilon\tau}G(\eta,\tau),\ \theta(\eta,\tau)=\theta_0(\eta)+e^{-\varepsilon\tau}H(\eta,\tau). \tag{23}$$

The solution associated to the formulated equations (8)–(10) with boundary conditions (11) is denoted with $f_0(\eta)$, $g_0(\eta)$, and $\theta_0(\eta)$. The decay and growth disturbance rate is defined with ε. It is assumed that (η,τ), $G(\eta,\tau)$, and $H(\eta,\tau)$ and derivatives of these expressions are smaller in contrast to the steady state situation. Such assumptions are followed due to the linear stability of flow pattern. Upon replacing equation (26) into set of expressions (19)–(21) with taking $=0, F(\eta,\tau)$, $G(\eta,\tau)$, and $H(\eta,\tau)$ are associated to $F_0(\eta)$, $G_0(\eta)$, and $H_0(\eta)$. On this end, the linear eigenvalue problem is formulated as

$$F_0'''+\xi_1\xi_2\left\{f_0F_0''+F_0f_0''+\frac{2}{n+1}(\varepsilon-2nf_0')F_0'+\frac{4\Omega}{(n+1)}G_0\right\} -\frac{2}{(n+1)}\frac{\sigma_{hnf}}{\sigma_f}\xi_2MF_0'=0, \tag{24}$$

$$G_0''+\xi_1\xi_2\left[g_0'F_0+G_0'f_0-\frac{2n}{(n+1)}(f_0'G_0+F_0'g_0) -\frac{4\Omega}{(n+1)}F_0'+\frac{2}{(n+1)}\varepsilon G_0\right]-\frac{2}{(n+1)}M\frac{\sigma_{hnf}}{\sigma_f}\xi_2G_0=0, \tag{25}$$

$$\frac{\xi_3}{Pr}\left(\frac{k_{hnf}}{k_f}+\frac{4}{3}R\,d\right)H_0''+\theta_0'F_0+H_0'f_0+\xi_3QH_0+\varepsilon H_0=0, \tag{26}$$

with

$$\begin{cases} F_0(0)=0, F_0'(0)=0, G_0(0)=0, H_0(0)=0 \\ F_0'(\eta)\longrightarrow 0, G_0(\eta)\longrightarrow 0\ H_0(\eta)\longrightarrow 0,\ as\,\eta\longrightarrow\infty \end{cases}. \tag{27}$$

We can solve equations (24)–(26) along with BCs (27) by using the numerical values of $f_0(\eta)$, $g_0(\eta)$, and $\theta_0(\eta)$ which were obtained from the solutions of equations (8)–(10) with BCs (11). It is worth noting that the homogeneous linear equations (24)–(26) subject to constants (27) construct an eigenvalue system with eigenvalue ε. By solving equations (24)–(27), a set of eigenvalues $\varepsilon_1<\varepsilon_2<\varepsilon_3<\ldots$ is obtained.

Table 3: Values of $\sqrt{Re}C_{fx}$ and $\sqrt{Re}C_{fy}$ for several values of Ω when $\lambda=1, \phi_{Al_2O_3}=\phi_{Cu}=0, b=0, n=1$.

	$\sqrt{Re}C_{fx}$		$\sqrt{Re}C_{fy}$	
Ω	[35]	Present results	[28]	Present results
0	−1.0000	−1.0000625	0.0000	0.0000000
0.5	−1.1384	−1.1383806	−0.5128	−0.5127602
1	−1.3250	−1.3250287	−0.8371	−0.8370983
2	−1.6523	−1.6523520	−1.2873	−1.2872588
3	−1.9289	−1.9289315	−1.6248	−1.6247357
4	−2.1716	−2.1715931	−1.9054	−1.9053929
5	−2.3901	−2.3901398	−2.1506	−2.1505265

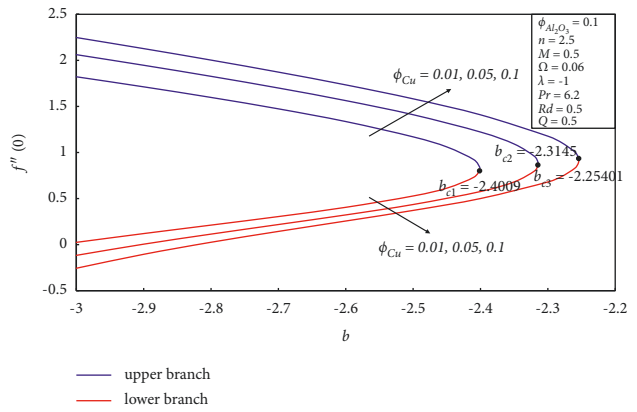

Figure 2: Impact of b on $f''(0)$ for fixed values of ϕ_{Cu}.

4. Results and Discussion

Following to the investigation of Devi and Devi [33, 34] and Lund et al. [35], here water is considered as base material with copper (Cu) and aluminum nanoparticles (Al_2O_3). Moreover, volume fraction of aluminum is kept constant against the variation of copper volume oxide $(0.01\le\phi_{Cu}\le 0.1)$. The comparison validation for ensuring the validity task has been done in Table 3 with work of Zaimi et al. [37] with excellent comparison results.

Figures 2–4 are sketched to observe the physical aspect of ϕ_{Cu} on $f''(0)$, $g'(0)$, and $-\theta\prime(0)$. Results are visualized for suction case. The dual branches of solution are results for various values of suction case. The critical points for $\phi_{Cu}=0.01$ are $b_{c1}=-2.4009$ while $b_{c2}=-2.3145$ and $b_{c3}=-2.25401$ are the critical points against $\phi_{Cu}=0.05$ and $\phi_{Cu}=0.01$, respectively. Two different categories of branches such as dual branch $(b\le b_{ci})$ and no branch $(b>b_{ci})$ for suction parameter b exist. Moreover, larger change in ϕ_{Cu} results increment in b_{ci} which preserve a separation. The dominant values of suction do not allow tension in moving particles, and vorticity is not smothered. In upper branch, with larger suction, the decrement in wall shear force and heat transfer rate is noted. In lower branch, the heat transfer rate is lower but wall shear force

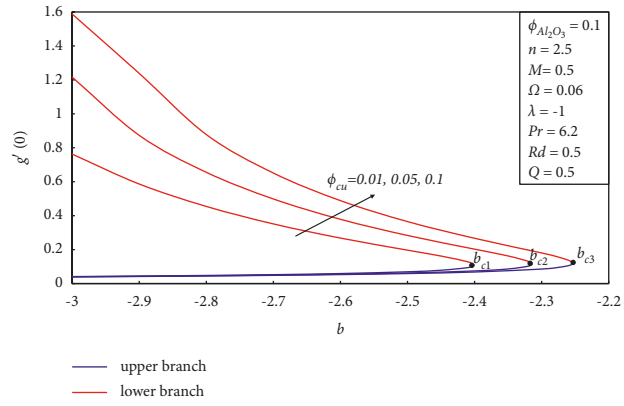

Figure 3: Impact of b on $g'(0)$ for fixed values of ϕ_{Cu}.

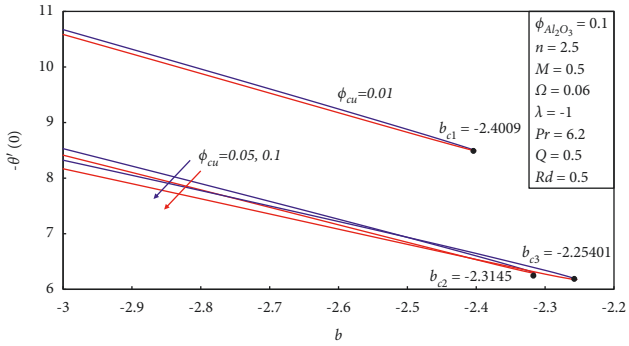

Figure 4: Impact of b on $-\theta'(0)$ for fixed values of ϕ_{Cu}.

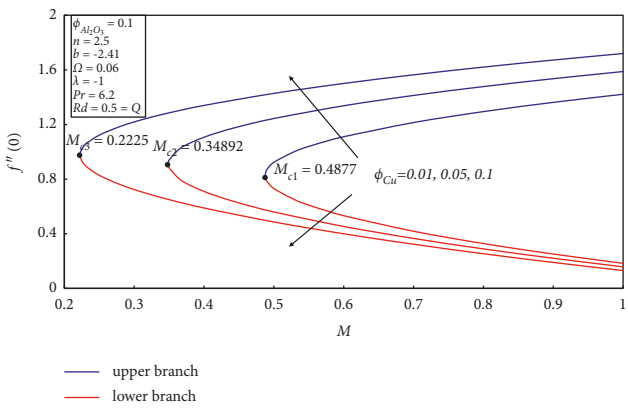

Figure 5: Impact of M on $f''(0)$ for fixed values of ϕ_{Cu}.

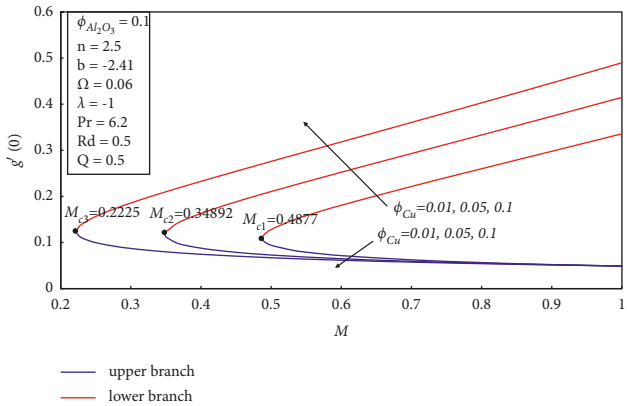

Figure 6: Impact of M on $g'(0)$ for fixed values of ϕ_{Cu}.

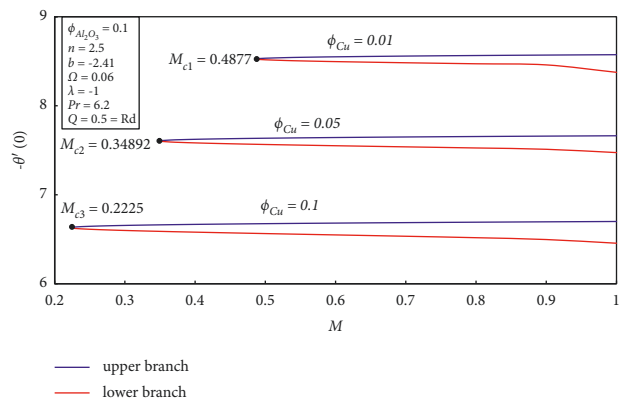

Figure 7: Impact of M on $-\theta'(0)$ for fixed values of ϕ_{Cu}.

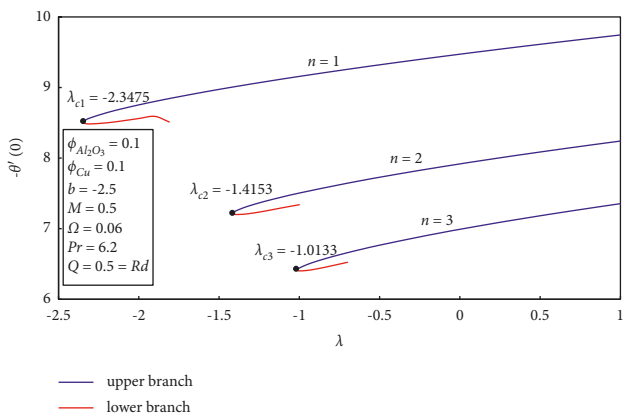

Figure 8: Impact of λ on $-\theta'(0)$ for fixed values of n.

enhanced. In upper branch, no significant change in $g'(0)$ due to suction parameter is inspected while in lower branch, $g'(0)$ declined.

Figures 5–7 show the variation of $''(0)$, $g'(0)$ and $-\theta'(0)$ magnetic parameter M against copper solid volume fraction ϕ_{Cu}. As ϕ_{Cu} grows, the critical point of M_c shifts to the left, assisting in the separation of the boundary layer. $M_{c1} = 0.4877$, $M_{c2} = 0.34892$, and $M_{c3} = 0.2225$ referred to critical points of M for $\phi_{Cu} = 0.01$, 0.05, and 0.1. As a result, the dual-branch representation is possible for $M \geq M_{ci}$ where $i = 1, 2, 3$; however, no branch exists for $M < M_{ci}$. The variation in $f''(0)$ and $-\theta'(0)$ get dominant change against ϕ_{Cu} in the upper branch for a fixed value of M, while the reversal phenomenon can be seen in the bottom branch. Furthermore, as the magnetic field is increased, the skin friction coefficient $g'(0)$ decreases by maintaining constant values of ϕ_{Cu} in the upper branch while slower trend is predicted in the lower branch.

The influences of positive constant n on $f''(0)$, $g'(0)$, and $-\theta'(0)$ is reported in Figures 8 and 9The obtained results are prepared in view of stretching/shrinking parameter (λ). A lower observation of $f''(0)$for stretching constant is noted. In

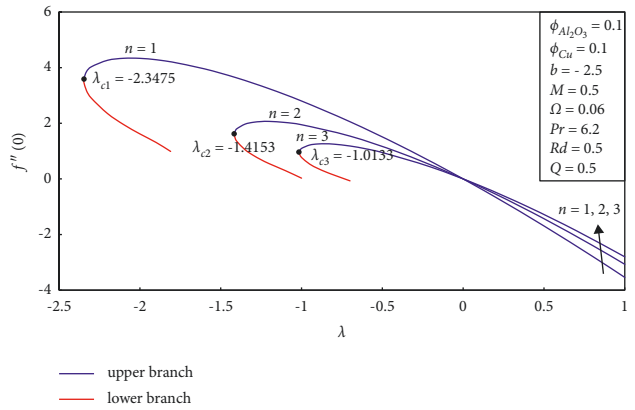

FIGURE 9: Impact of λ on $f''(0)$ for fixed values of n.

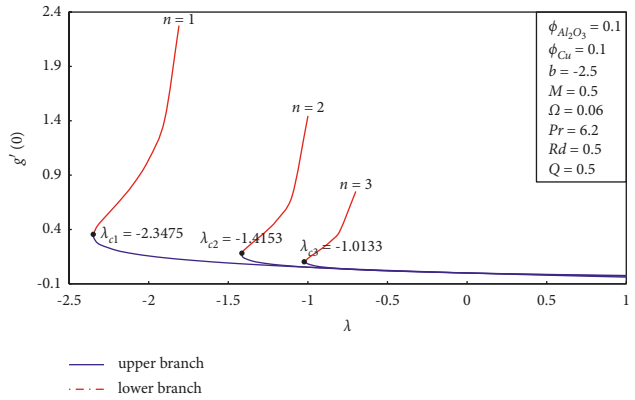

FIGURE 10: Impact of λ on $g'(0)$ for fixed values of n.

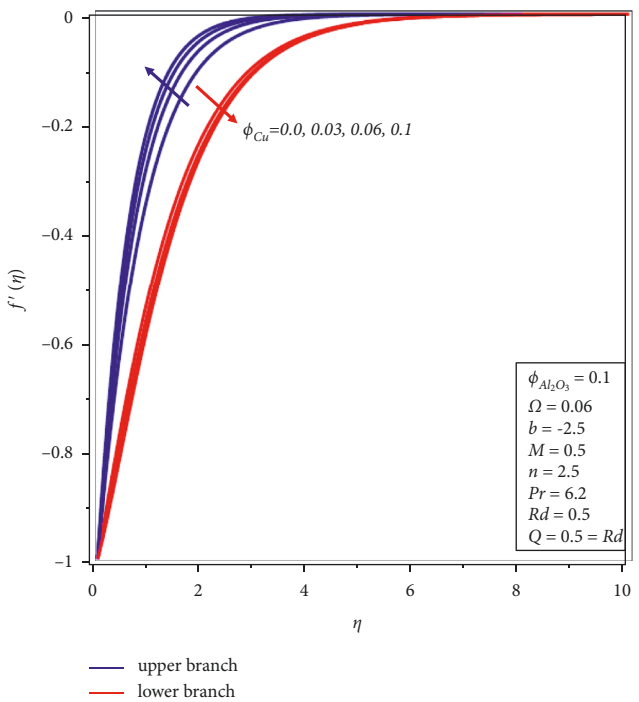

FIGURE 11: Variation of $f'(\eta)$ against η for various values of ϕ_{Cu}.

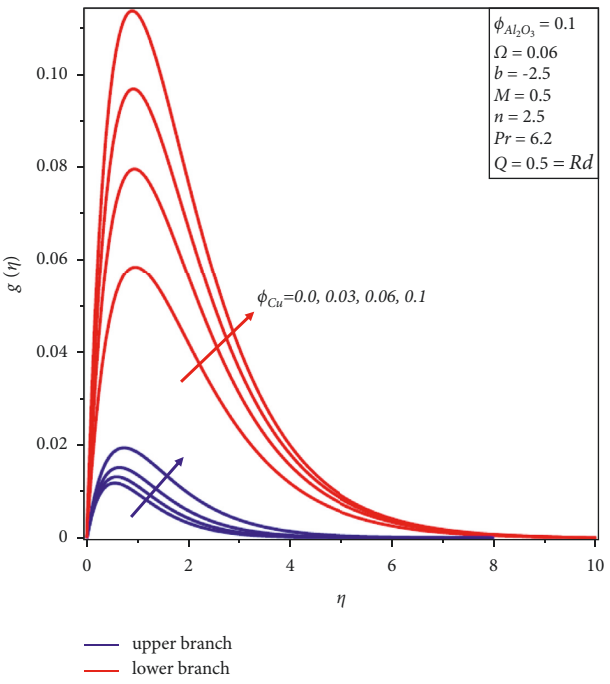

FIGURE 12: Variation of $g(\eta)$ against η for various values of ϕ_{Cu}.

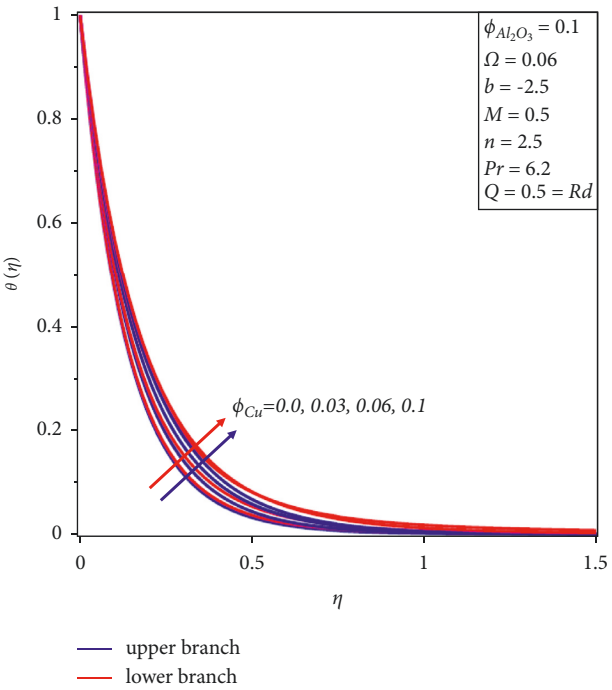

FIGURE 13: Variation of $\theta(\eta)$ against η for various values of ϕ_{Cu}.

upper zone, upon increasing λ, the change in $g'(0)$ is declining while $g'(0)$ increases. The thermal boundary layer separation is greater for linear stretching as compared to nonlinear case. Moreover, the heat transfer rate for stretching case is more progressive as compared to shrinking case. From Figure 10, a declining change in $f''(0)$ is observed for greater λ.

Figures 11–13 show the effect of copper solid volume fraction ϕ_{Cu} on velocity profiles $f'(\eta)$ and $g(\eta)$ in the x-

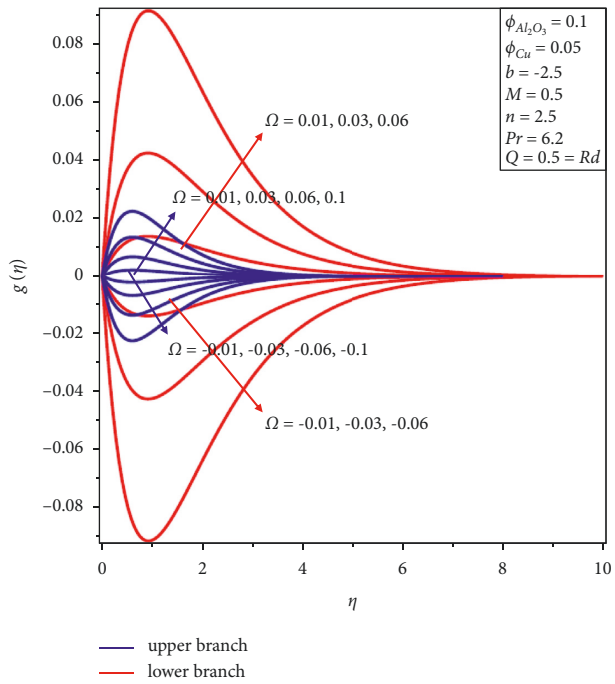

FIGURE 14: Variation of $g(\eta)$ against η for various values of Ω.

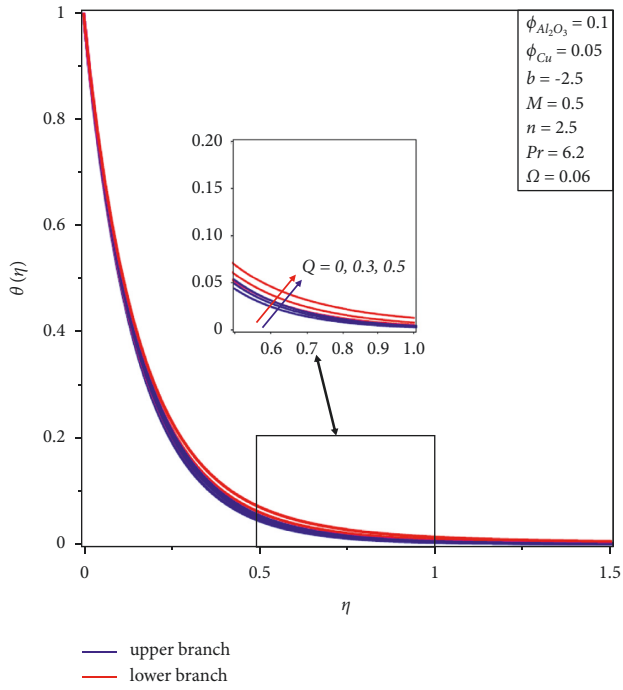

FIGURE 15: Variation of $\theta(\eta)$ against η for various values of Q.

and y-directions, as well as a temperature profile $\theta(\eta)$. Different profiles in both branches fulfill the far-field BCs $\eta \longrightarrow \infty$ for various values of ϕ_{Cu} and hence validate the obtained numerical results. In Figure 11, the field of velocity decreases as parameter ϕ_{Cu} increases in the upper surface while contradictory results are noted in the lower branch. This is because the volume fraction slows the velocity of the fluid, which reduces the thickness of the momentum layer and, as a result, the velocities in the x-direction. On the other hand, when ϕ_{Cu} rises, velocity rate increases in the y-direction for both branches (refer to Figure 12). Furthermore, as expected, heat transfer rate gets arisen for copper solid volume percentage ϕ_{Cu} rises in both branches.

The graphical outcomes for rotation constant Ω parameter on velocity along y-directions ($g(\eta)$) have been worked out in Figure 14. The solution has a symmetrical nature. When the

Table 4: The values of ε_1 for various values of ϕ_{Cu} and b when $\lambda = -1$, $M = 0.5$, $n = 2.5, Pr = 6.2$, $R\,d = Q = 0.5$.

ϕ_{Cu}	b	ε_1	
		Upper branch	Lower branch
0.01	−3	2.2281	−2.2827
	−2.5	1.9924	−1.9001
0.03	−3	2.6295	−2.8547
	−2.5	2.1824	−2.4373
0.05	−3	2.8626	−3.0626
	−2.5	2.25463	−2.4515

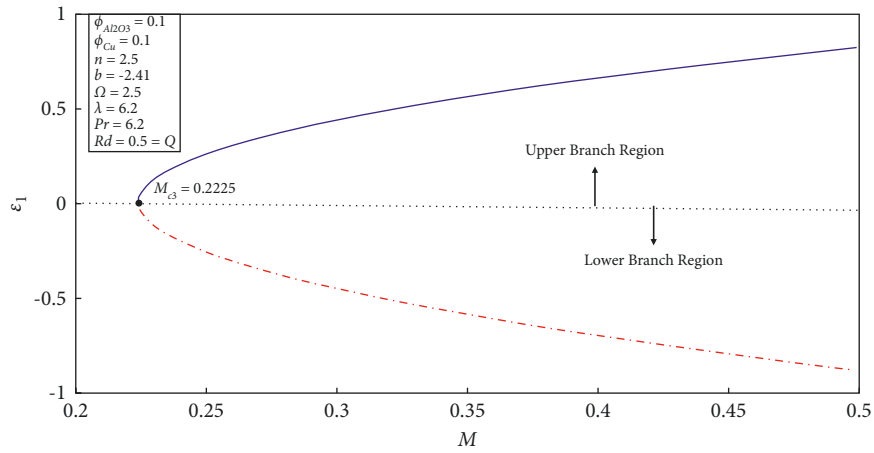

Figure 16: The values of ε_1 for various values of M.

value of Ω is positive, velocity increases in both branches. When the value of Ω is negative, the velocity of the hybrid nanofluid decreases. It is also discovered that when $-0.06 \leq \Omega \leq 0.06$, two branches are possible. Figure 15 shows the effect of heat sink/source parameter on temperature profiles. It has been observed that temperature of hybrid nanofluid increases in both solutions when the parameter Q increases. This enhancement is due to external heat source. This aids in the formation of the thermal boundary layer thickness.

It is well justified fact that upon existing of different solution branches, the importance of stability analysis cannot be denied identifying the more realistically branch. Usually, the upper branch is referred to the physical branch as it meets with the boundary assumptions. However, the stability of lower branch is also importance and can be observed via stability procedure. After carefully noticing, it is claimed that upper branch is more stable in view of ε_1. The positive sign of ε_1 ensures that stability of branch and reflects the decay and growth results. The negative values of ε_1 show that the branch is unstable. Both positive and negative values of ε_1 upper and lower branches are presented via Table 4. Figure 16 shows the lower numerical values of eigenvalue for upper and lower surface branches.

5. Conclusions

In a rotating hybrid nanofluid, the laminar steady boundary flow on a stretching/shrinking sheet was investigated. The governing PDEs were numerically solved in *bvp4c* using the well-known collocation approach known as the 3-stage-Lobatto-3a method. Numerical results for various values of physical application parameters have been graphically presented and thoroughly analyzed. The values of $\sqrt{Re}C_{fx}$ and $\sqrt{Re}C_{fy}$ are compared to published publications in order to validate the obtained numerical results, which show a positive agreement. In the precise range of the magnetic, suction, and shrinking/stretching parameters, dual branches have been discovered. The following are a few key points from the current study:

(i) For suction case, the heat transfer rate is larger as compared to injection phenomenon in the upper branch.

(ii) In upper branch, no significance change in y-directional velocity is observed while declining change in velocity is noticed for lower branch.

(iii) The presence of external heat source enhanced the heat transfer rate in both branches. However, the increment in heat transfer is relatively larger in the upper branch.

(iv) No dual branches exist outside the magnetic parameter and stretching/shrinking constant.

(v) Upon increasing the copper nanoparticle volume fraction, the enhancement in temperature rate is measured.

(vi) The fluctuation in thermal boundary layer is more progressive for linear stretching instead of nonlinear case.

Nomenclature

Al_2O_3:	Alumina
T_∞:	Ambient temperature
Cu:	Copper
f', g:	Dimensionless velocity
M:	Hartmann number
b:	Injunction/suction parameter
N_{ux}:	Local Nusselt number
Re_x:	Local Reynolds number
B:	Magnetic field
$w_w(x)$ (m/s):	Mass flux of velocity
Pr:	Prandtl number
C_{fx}, C_{fy}:	Skin friction coefficient
$T:(K)$:	Temperature
Q:	Sink/source parameter
T_w:	Variable temperature at the sheet
u, v, w:	(m/s) Velocity components
$u_w(x)$ (m/s):	Velocity of surface
H_2O:	Water
$\tilde{\Omega}$:	Angular velocity
ρ_{hnf}:	Density
θ:	Dimensionless temperature
μ_{hnf}:	Dynamic viscosity
σ_{hnf}:	Electrical conductivity
$(c_p)_{hnf}$:	Heat capacity
ε_1:	Smallest eigenvalue
τ:	Stability transformed variable
λ:	Stretching/shrinking parameter
k_{hnf}:	Thermal conductivity,
η:	Transformed variable
ε:	Unknown eigenvalue.

Data Availability

All data are given in the paper.

Conflicts of Interest

The authors declare that they have no conflicts of interest.

References

[1] S. U. Choi, *Enhancing thermal Conductivity of Fluids with Nanoparticles (No. ANL/MSD/CP-84938*, Argonne National Lab, IL (United States), 1995.

[2] M. Turkyilmazoglu, "Fully developed slip flow in a concentric annuli via single and dual phase nanofluids models," *Computer Methods and Programs in Biomedicine*, vol. 179, Article ID 104997, 2019.

[3] M. K. Nayak, I. S. Oyelakin, A. J. Chamkha, S. 4 Mondal, and P. Sibanda, "Three-dimensional rotating flow of an Oldroyd-B nanofluid with relaxation-retardation viscous dissipation," *Journal of Nanofluids*, vol. 10, pp. 408–419, 2021.

[4] M. d. F. M. d. Basir, M. Bilal, R. Choudhary, J. Mackolil, B. Mahanthesh, and K. S. Nisar, "Numerical and Sensitivity Analysis of MHD Bioconvective Slip Flow of Nanomaterial with Binary Chemical Reaction and Newtonian heating," *Heat Transfer Asian Research*, vol. 50, pp. 5439–5466, 2021.

[5] S. Ahmad, M. N. Khan, S. Nadeem, A. Rehman, H. Ahmad, and R. Ali, "Impact of Joule Heating and Multiple Slips on a Maxwell Nanofluid Flow Past a Slendering Surface," *Communications in Theoretical Physics*, vol. 74, no. (1), 2021.

[6] S. Nadeem, W. Fuzhang, F. M. Alharbi et al., "Numerical computations for Buongiorno nano fluid model on the boundary layer flow of viscoelastic fluid towards a nonlinear stretching sheet," *Alexandria Engineering Journal*, vol. 61, pp. 1769–1778, 2022.

[7] H. Vaidya, K. V. P. I. Tlili, O. D. Makinde et al., "Mixed convective nanofluid flow over a non linearly stretched Riga plate," *Case Studies in Thermal Engineering*, vol. 24, Article ID 100828, 2021.

[8] H. Wang, M. Pang, Y. Diao, and Y. Zhao, "Heat transfer characteristics and flow features of nanofluids in parallel flat minichannels," *Powder Technology*, vol. 402, Article ID 117321, 2022.

[9] A. H. Abdelaziz, W. M. E. l. Maghlany, A. A. E. l. Din, and M. A. Alnakeeb, "Mixed convection heat transfer utilizing Nanofluids ionic Nanofluids and hybrid nanofluids in a horizontal tube," *Alexandria Engineering Journal*, vol. 61, pp. 9495–9508, 2022.

[10] A. S. Sabu, A. Wakif, S. Areekara, A. Mathew, and N. A. Shah, "Significance of nanoparticles' shape and thermo-hydrodynamic slip constraints on MHD alumina-water nanoliquid flows over a rotating heated disk," *The passive control approach, International Communications in Heat and Mass Transfer*, vol. 129, Article ID 105711, 2021.

[11] O. Ojjela, O. Ojjela, P. K. Kambhatla, and F. Mebarek-Oudina, "Shape effect of MoS$$_2$$ nanoparticles on entropy generation and heat transport in viscoelastic boundary layer flow," *Pramana*, vol. 95, no. 4, p. 182, 2021.

[12] J. Dong, Q. Zheng, C. Xiong, E. Sun, and J. Chen, "Experimental investigation and application of stability and thermal characteristics of SiO2-ethylene-glycol/water nanofluids," *International Journal of Thermal Sciences*, vol. Volume 176, Article ID 107533, 2022.

[13] S. Sivasankaran and M. Bhuvaneswari, "Numerical study on influence of water based hybrid nanofluid and porous media on heat transfer and pressure loss," *Case Studies in Thermal Engineering*, vol. 34, Article ID 102022, 2022.

[14] N. Acharya, "Finite element analysis on the hydrothermal pattern of radiative natural convective nanofluid flow inside a square enclosure having nonuniform heated walls," *Heat Transfer Asian Research*, vol. 51, no. 1, pp. 323–354, 2022.

[15] H. Mondal and P. K. Kundu, "Spectral approach to study the entropy generation of radiative mixed convective couple stress fluid flow over a permeable stretching cylinder," *Part C: Journal of Mechanical Engineering Science*, vol. 235, no. 15, 2021.

[16] N. Acharya, "Spectral simulation to investigate the effects of active passive controls of nanoparticles on the radiative nanofluidic transport over a spinning disk," *J. Thermal Sci. Eng. Appl*, vol. 13, no. 3, Article ID 031023, 2021.

[17] A. Shafiq, S. A. Lone, T. N. Sindhu, Q. M. A. l. Mdallal, and G. Rasool, "Statistical modeling for bioconvective tangent hyperbolic nanofluid towards stretching surface with zero mass flux condition," *Scientific Reports*, vol. 11, Article ID 13869, (2021).

[18] T. Hayat, A. Shafiq, and A. Alsaedi, "Effect of Joule heating and thermal radiation in flow of third grade fluid over radiative surface," *PLoS One*, vol. 9, no. 1, 2014.

[19] S. Ahmad, M. Ashraf, and K. Ali, "Bioconvection due to gyrotactic microbes in a nanofluid flow through a porous medium," *Heliyon*, vol. 6, Article ID e05832, 2020.

[20] U. Nazir, M. Sohail, M. B. Hafeez, M. Krawczuk, S. Askar, and S. Wasif, "An inclination in thermal energy using nanoparticles with casson liquid past an expanding porous surface," *Energies*, vol. 14, no. 21, p. 7328, 2021.

[21] B. Mahanthesh, N. S. Shashikumar, B. J. Gireesha, and I. L. Animasaun, "Effectiveness of Hall current and exponential heat source on unsteady heat transport of dusty TiO2-EO nanoliquid with nonlinear radiative heat," *Journal of Computational Design and Engineering*, vol. 6, pp. 551–561, 2019.

[22] Kh. Hosseinzadeh, So. Roghani, A. R. Mogharrebi, A. Asadi, M. Waqas, and D. D. Ganji, "Investigation of cross-fluid flow containing motile gyrotactic microorganisms and nanoparticles over a three-dimensional cylinder," *Alexandria Engineering Journal*, vol. 59, no. 5, pp. 3297–3307, Oct. 2020.

[23] T. Armaghani, M. S. Sadeghi, A. M. Rashad et al., "MHD mixed convection of localized heat source/sink in an Al_2O_3-Cu/water hybrid nanofluid in L-shaped cavity," *Alexandria Engineering Journal*, vol. 60, pp. 2947–2962, 2021.

[24] T. N. Sindhu and A. Atangana, "Reliability analysis incorporating exponentiated invers," *Weibull distribution and inverse power law*, vol. 37, no. 6, pp. 2399–2422, 2021.

[25] G. Sowmya, B. J. Gireesha, I. L. Animasaun, and N. A. Shah, "Significance of buoyancy and Lorentz forces on water-conveying iron(III) oxide and silver nanoparticles in a rectangular cavity mounted with two heated fins: heat transfer analysis," *Journal of Thermal Analysis and Calorimetry*, vol. 144, pp. 2369–2384, (2021.

[26] L. S. Sundar, V. Punnaiah, M. K. Singh, A. M. B. Pereira, and A. C. M. Sousa, "Solar energy absorbed thermosyphon flat plate collector analysis using Cu/H_2O nanofluid – an experimental study," *Energy and Climate Change*, vol. Volume 2, Article ID 100028, 2021.

[27] S. Akhtar, L. B. McCash, S. Nadeem, S. Saleem, and A. Issakhov, "Convective heat transfer for Peristaltic flow of SWCNT inside a sinusoidal elliptic duct," *Science Progress*, vol. 104, no. 2, pp. 1–17, 2021.

[28] M. R. Eid and F. Mabood, "Entropy analysis of a hydromagnetic micropolar dusty carbon NTs-kerosene nanofluid with heat generation: Darcy–Forchheimer scheme," *Journal of Thermal Analysis and Calorimetry*, 2020.

[29] A. Shahid, M. M. Bhatti, O. A. Bég, I. L. Animasaun, and K. Javid, "Spectral computation of reactive bi-directional hydromagnetic non-Newtonian convection flow from a stretching upper parabolic surface in non-Darcyporous medium," *International Journal of Modern Physics B*, vol. 35, Article ID 2150294, (2021).

[30] J. K. Madhukesh, R. Naveen Kumar, R. J. Punith Gowda et al., "Numerical simulation of AA7072-AA7075/water-based hybrid nanofluid flow over a curved stretching sheet with Newtonian heating: a non-Fourier heat flux model approach," *Journal of Molecular Liquids*, vol. 335, p. 116103, 2021.

[31] N. Acharya, "On the flow patterns and thermal control of radiative natural convective hybrid nanofluid flow inside a square enclosure having various shaped multiple heated obstacles," *The European Physical Journal Plus*, vol. 136, p. 889, 2021.

[32] S. A. Devi and S. S. Devi, "Numerical investigation of hydromagnetic hybrid Cu–Al2O3/water nanofluid flow over a permeable stretching sheet with suction," *Int J of Nonl Sci and Numerical Simulation*, vol. 17, no. 5, pp. 249–257, 2016.

[33] S. S. Devi and S. A. Devi, "Numerical investigation of three-dimensional hybrid Cu–Al2O3/water nanofluid flow over a stretching sheet with effecting Lorentz force subject to Newtonian heating," *Canadian Journal of Physics*, vol. 94, no. 5, pp. 490–496, 2016.

[34] L. A. Lund, Z. Omar, and I. Khan, "Darcy-Forchheimer porous medium effect on rotating hybrid nanofluid on a linear shrinking/stretching sheet," *International Journal of Numerical Methods for Heat and Fluid Flow*, 2021.

[35] Y. Y. Teh and A. Ashgar, "Three dimensional MHD hybrid nanofluid flow with rotating stretching/shrinking sheet and Joule heating," *CFD Letters*, vol. 13, no. 8, pp. 1–19, 2021.

[36] K. Zaimi, A. Ishak, and I. Pop, "Stretching surface in rotating viscoelastic fluid," *Applied Mathematics and Mechanics*, vol. 34, no. 8, pp. 945–952, 2013.

[37] S. Ahmad, S. Nadeem, and Rehman, "Aysha; mathematical analysis of thermal energy distribution in a hybridized mixed convective flow," *Journal of Nanofluids*, vol. 10, no. 2, pp. 222–231, 2021.

Hindawi
Mathematical Problems in Engineering
Volume 2022, Article ID 6279498, 16 pages
https://doi.org/10.1155/2022/6279498

Research Article

Effect of Diffusion-Thermo on MHD Flow of a Jeffrey Fluid Past an Exponentially Accelerated Vertical Plate with Chemical Reaction and Heat Generation

Ahmad Shafique,[1] Zaib Un Nisa,[2] Muhammad Imran Asjad,[3] Mudassar Nazar,[1,4] and Fahd Jarad[5,6,7]

[1]*Centre for Advanced Studies in Pure and Applied Mathematics, Bahauddin Zakariya University, Multan, Pakistan*
[2]*Department of Mathematics, University of Education Lahore Multan Campus, Multan, Pakistan*
[3]*Department of Mathematics, University of Management and Technology Lahore 54770, Pakistan*
[4]*School of Mathematical Sciences, University of Science and Technology of China, Hefei, Anhui, China*
[5]*Department of Mathematics, Cankaya University, 06790 Etimesgut, Ankara, Turkey*
[6]*Department of Mathematics, King Abdulaziz University, Saudi Arabia*
[7]*Department of Medical Research, China Medical University, Taichung 40402, Taiwan*

Correspondence should be addressed to Fahd Jarad; fahd@cankaya.edu.tr

Received 10 January 2022; Accepted 19 February 2022; Published 24 May 2022

Academic Editor: Arshad Riaz

In many flow phenomenons of fluid with medium molecular weight, the energy flux is effected due to the inhomogeneity of concentration of mass. This contribution of the concentration to the energy flux is considered as diffusion-thermo effect or Dufour effect. In this research article the diffusion-thermo effect is addressed for the magnetohydrodynamics (MHD) flow of Jeffrey's fractional fluid past an exponentially accelerated vertical plate with generalized thermal and mass transports through a porous medium. For the generalization of the thermal and mass fluxes the constant proportional Caputo (CPC) fractional derivative is utilized. The governing of this generalized flow are reduced to non-dimensional forms and then solved semi analytically by Laplace transform. In additions the physical aspects of flow and material parameters especially the effect of *Du* and fractional parameters are discussed by sketching the graphs. From the graphical illustration, it is concluded that in the presence of Dufour effect flow speeds up. Moreover, a comparison between fractionalized and ordinary velocity fields is also drawn and it is also observed that fractional model with constant proportional derivative is of the more decaying nature as compare to the model contracted with classical Caputo and Caputo fractional derivatives.

1. Introduction

The non-Newtonian fluids posses the diverse nature from Newtonian fluids due to their complex rheological properties. Now a days the study of non-Newtonian becomes a popular research area due to its scientific and technological applications in the processing industry, and biological sciences, like making of plastic sheets, lubricant's performance and motion of biological fluid. There are several non-Newtonian fluid models have been presented to demonstrate the distinction between Newtonian and non-Newtonian fluids but the Jeffrey fluid model is more efficient to demonstrate attribute of stress relaxation for memory time scale (the relaxation of time). Mohd-Zin et al. [1] studied the porosity effect on unsteady MHD free convection flow of Jeffrey fluid past an oscillating vertical plate with ramped wall temperature. Bajwa et al. [2] solved a problem of transient flow of Jeffrey fluid semi-analytically over permeable wall. Asgir et al. [3] discussed the heat transfer analysis of channel flow of MHD Jeffrey fluid with porosity.

The model on Jeffrey fluid be simplest and most popular. Some of the work on Jeffrey fluid are of Das [4] and Qasim [5]. Ali et al. [6] discussed the magnetohydrodynamic fluctuating free convection flow of incompressible electrically conducting viscoelastic fluid in a porous medium in the presence of a pressure gradient. Shah et al. [7] worked on the new semi analytical technique for the solution of fractional Order Navier Stokes equation.

The fractional derivative is the generalization of ordinary derivative by taking the non-integer order of differentiation. Due its generalized property the fractional derivative becomes a potent tool to describe the heat and mass transfer phenomenons and has attained the attention by researchers. Chandra [8] present the MHD flow for Jeffrey fluid past an inclined porous plate by applying Laplace transform method. Jameel et al. [9] obtain the analytic solutions for the incompressible unsteady flow of fractionalized MHD Jeffrey fluid over an accelerating porous plate with linear slip effect by using Caputo fractional derivative. Abro et al. [10] obtain the solution of Jeffrey fluid flow acquired by non-singular kernel (Caputo-Fabrizio) using integral transform technique. During the last decade, different generalized fractional derivatives have appeared in the literature that are derivatives of Caputo, Caputo-Fabrizio, Atangana-Baleanu [11, 12]. Jawad et al. [13] observed the behavior of Caputo time fractional model based on generalized Fourier's and Fick's laws for Jeffrey Nano fluid. Siddique et al. [14] studied the unsteady double convection flow of a magnetohydrodynamics (MHD) differential-type fluid flow in the presence of Dufour effect, Newtonian heating, and heat source over an infinite vertical plate with fractional mass diffusion and thermal transports.

Sandeep et al. [15] discussed the behavior of momentum and heat transfer on Jeffrey, Maxwell and Oldroyd-B nanofluids over a stretching surface in the presence of transverse magnetic field, non-uniform heat source/sink. A magnetohydrodynamic Jeffrey fluid flow with thermal and mass transfer on an infinitely rotating upright cone investigated by Saleem et al. [16]. Sulochana et al. [17] solved a problem of a MHD radiative Casson fluid flow numerically over a wedge to analyze the heat and molecular transfer. A bio convective nanoliquid flow with the effect of second order slip and chemical reaction between the parallel plates studied by Acharya et al. [18]. The radiative couple stress fluid and chemically reactive nanofluid over a stretched cylinder with magnetic effect analyzed by Acharya et al. [19, 20]. Riaz et al. [21] obtained the solution of peristaltic flow of Prandtl fluid by using homotopy perturbation method. The role of hybrid nanoparticles in thermal performance of peristaltic flow of Eyring-Powell fluid model have discussed by Riaz et al. [22].

Different types of fractional operators has discussed by Yuri-Luchko [23]. Baleanu et al. [24] presented a new fractional operator combining proportional Caputo and solve different kind of example with CPC derivative. Chu et al. [25] worked on fractional model of Second grade fluid induced by generalized thermal and molecular fluxes with constant proportional Caputo. Siddique et al. [26] analyzed the blood liquor model fractionalized with constant proportional Caputo fractional derivative and Dolat et al. [27] investigate a fractional model of MHD viscous fluid with heat transfer by using the constant proportional Caputo fractional derivative.

The purpose of this article is to utilized the Constant proportional Caputo fractional derivative for the investigation of diffusion-thermo effect on MHD flow of Jeffrey fluid past an exponentially accelerated vertical plate in the presence of chemical reaction, and heat generation through a porous medium with generalized heat and mass fluxes. Constant proportional Caputo fractional derivative is considered for the generalization of constitutive equations for heat and mass fluxes. Initially, the proposed governing equations are reduced to non-dimensional form then solved semi analytically via Laplace transform. The physical aspects of flow regarding involved parameters are also discussed by sketching some graphs for velocity field of Jeffrey fluid. Moreover the obtained result for velocity with CPC will compare with ordinary result by sketching the graphs.

2. Mathematical Model

The flow of Jeffrey fluid is studied in the presence of MHD by considering the diffusion-thermo effect through a porous media. The rectangular coordinates system is oriented in such a way that the x^*-axis is pointing along the plate in the vertical direction and y_2^*-axis is pointing normal to the plate as shown in Figure 1. At the time $t_2^* = 0^+$ the system with the plate and fluid is suppose to be at rest, at the temperature T_∞^* with concentration C_∞^*. However, for the time $t_2^* > 0$, the plate suppose to be moves with exponential velocity $Ue^{at_2^*}$ in its own plane. The plate's temperature as well as concentration of the fluid raised to T_w^* and C_w^* respectively. Magnetic field effect is also considered normally with a constant strength β_0. Energy flux due to concentration gradient is also considered. In view of above assumptions, the Jeffrey fluid flow model with Boussinesq's approximation appears in the following form [3, 13, 28]

$$\frac{\partial u_1(y_2^*, t_2^*)}{\partial t_2^*} = \frac{\nu}{1+\lambda_1}\left(1 + \lambda_2 \frac{\partial}{\partial t_2^*}\right)\frac{\partial^2 u_1(y_2^*, t_2^*)}{\partial {y_2^*}^2} - \frac{\sigma\beta_0^2}{\rho}u_1(y_2^*, t_2^*) - \frac{\mu\phi}{\rho K_1}u_1(y_2^*, t_2^*) + g\beta_{T_1^*}(T_1^* - T_\infty^*) + g\beta_{C_1^*}(C_1^* - C_\infty^*). \tag{1}$$

Thermal Eq. is

$$\rho C_p \frac{\partial T_1^*(y_2^*, t_2^*)}{\partial t_2^*} = -\frac{\partial q_1^*(y_2^*, t_2^*)}{\partial y_2^*} + Q_1 T(T_1^* - T_\infty^*) - \frac{\rho K_T D_m}{DC_S} \frac{\partial J_1^*}{\partial y_2^*}. \tag{2}$$

Fourier's Law states that [29]

$$q_1^*(y_2^*, t_2^*) = -K_2 \frac{\partial T_1^*(y_2^*, t_2^*)}{\partial y_2^*}. \tag{3}$$

Diffusion Eq. is

$$\frac{\partial C_1^*(y_2^*, t_2^*)}{\partial t_2^*} = -\frac{\partial J_1^*(y_2^*, t_2^*)}{\partial y_2^*} - K_3(C_1^* - C_\infty^*). \tag{4}$$

Fick's Law states that, $J_1^*(y_2^*, t_2^*)$ is written as [30]

$$J_1^*(y_2^*, t_2^*) = -D \frac{\partial C_1^*(y_2^*, t_2^*)}{\partial y_2^*}. \tag{5}$$

The initial as well as boundary conditions of the flow problem are [20]

$$\begin{aligned} u_1(y_2^*, t_2^*) &= 0, \\ T_1^*(y_2^*, t_2^*) &= T_\infty^*, \\ C_1^*(y_2^*, t_2^*) &= C_\infty^*, \\ y_2^* &> 0, \\ t_2^* &= 0, \end{aligned} \tag{6}$$

$$\begin{aligned} u_1(0, t_2^*) &= U e^{a_1 t_2^*}, \\ T_1^*(0, t_2^*) &= T_w^*, \\ C_1^*(0, t_2^*) &= C_w^*, \\ a_1 &> 0, t_2^* > 0, \end{aligned} \tag{7}$$

$$\begin{aligned} u_1(y_2^*, t_2^*) &\longrightarrow 0, \\ T_1^*(y_2^*, t_2^*) &\longrightarrow 0, \\ C_1^*(y_2^*, t_2^*) &\longrightarrow 0, \\ y_2^* &\longrightarrow \infty, t_2^* > 0. \end{aligned} \tag{8}$$

The dimensionless form of the flow parameters are

$$\begin{aligned} v &= \frac{u_1}{U}, \\ t &= \frac{U^2 t_2^*}{\nu}, \\ Q &= \frac{Q_1 \nu}{U^2 \rho C_p}, \\ y &= \frac{U y_2^*}{\nu}, \\ \lambda &= \frac{U^2 \lambda_2}{\nu}, \\ J_1 &= \frac{J_1^*}{J}, \\ q_1 &= \frac{q_1^*}{q}, \\ Du &= \frac{\rho K_T D_m J}{UDC_S C_p (T_w - T_\infty)}, \\ Gm &= \frac{g\nu\beta_{C_1^*}(C_w^* - C_\infty^*)}{U^3}, \\ Gr &= \frac{g\nu\beta_{T_1^*}(T_w^* - T_\infty^*)}{U^3}, \\ M &= \frac{\beta_0^2 \sigma \nu}{\rho U^2}, \\ R &= \frac{K_3 \nu}{U^2}, \\ K &= \frac{\mu\phi\nu}{\rho U^2 K_1}, \\ C &= \frac{C_1^* - C_\infty^*}{C_w^* - C_\infty^*}, \\ T &= \frac{T_1^* - T_\infty^*}{T_w^* - T_\infty^*}, \\ a &= \frac{a_1 \nu}{U^2}. \end{aligned} \tag{9}$$

Using non-dimensional variables of equation (9) into equations (1-8), we have

$$\frac{\partial v(y,t)}{\partial t} = (1+\lambda_1)^{-1}\left(1 + \lambda\frac{\partial}{\partial t}\right)\frac{\partial^2 v(y,t)}{\partial y^2} + GrT(y,t) + GmC(y,t) - \left(M + \frac{1}{K}\right)v(y,t),$$

$$\frac{\partial T(y,t)}{\partial t} = -n_2 \frac{\partial q_1(y,t)}{\partial y} + QT(y,t) - Du\frac{\partial J_1}{\partial y} - m_1 \frac{\partial T}{\partial y} = q_1,$$

$$\frac{\partial C(y,t)}{\partial t} = -n_3 \frac{\partial J_1(y,t)}{\partial y} - RC(y,t) - n_1 \frac{\partial C}{\partial y} = J_1,$$

$$v(y,t) = 0,$$

$$T(y,t) = 0,$$

$$C(y,t) = 0, \quad y > 0, t = 0,$$

$$v(0,t) = e^{at},$$

$$T(0,t) = C(0,t) = 1, \quad a > 0, t > 0,$$

$$v(y,t) = T(y,t) = C(y,t) \longrightarrow 0, y \longrightarrow \infty, \tag{10}$$

$$n_2 = \frac{q(T_w - T_\infty)^{-1}}{U\rho C_p},$$

$$n_3 = \left(\frac{(C_w - C_\infty)U}{J}\right)^{-1},$$

$$n_1 = \frac{DU}{(C_w - C_\infty)^{-1} J\nu},$$

$$m_1 = \frac{K_2 U}{(T_w - T_\infty)^{-1} q\nu},$$

where Pr, λ, K, Sc, R, and M represent the Prandtl number, Jeffrey parameter, non-dimensional permeability, Schmidt number, chemical reaction, and magnetic parameter respectively.

3. Generalization of Model

Eq. (10) can be written as

$$\frac{\partial v(y,t)}{\partial t} = \left[\frac{1}{1+\lambda_1} + \frac{\lambda}{1+\lambda_1}\frac{\partial}{\partial t}\right]\frac{\partial^2 v(y,t)}{\partial y^2} - (M + 1/K)(y,t) + \mathrm{Gr}T(y,t) + \mathrm{Gm}C(y,t), \tag{11}$$

Fractional form of Fourier's law [25, 31] is used to generalize Eq. (3) in dimensionless form

$$q_1 = -m_1^{CPC} D_t^{\gamma} \frac{\partial T(y,t)}{\partial y}, \quad 1 \geq \gamma > 0. \tag{12}$$

Fractional form of Fick's Law [25] is used to generalize Eq. (5) in dimensionless form

$$J_1 = -n_1^{CPC} D_t^{\alpha} \frac{\partial C(y,t)}{\partial y}, \quad 1 \geq \alpha > 0. \tag{13}$$

Using equation (12) into (2), and (3) into (3), we get

$$\frac{\partial T(y,t)}{\partial t} = n_2 \frac{\partial}{\partial y}\left(m_1^{\mathrm{CPC}} D_t^{\gamma} \frac{\partial T(y,t)}{\partial y}\right) + QT(y,t) + Du\frac{\partial}{\partial y}\left[n_1^{\mathrm{CPC}} D_t^{\alpha} \frac{\partial C}{\partial y}\right], \tag{14}$$

$$\frac{\partial C(y,t)}{\partial t} = n_3 \frac{\partial}{\partial y}\left[n_1^{CPC} D_t^{\alpha} \frac{\partial C(y,t)}{\partial y}\right] - RC(y,t). \tag{15}$$

Equations (14) and (15) can be written as

$$\frac{\partial T(y,t)}{\partial t} = \frac{1}{\mathrm{Pr}}\, {}^{CPC}D_t^{\gamma} \frac{\partial^2 T(y,t)}{\partial y^2} + QT(y,t) + \mathrm{Dun}_1^{\mathrm{CPC}} D_t^{\alpha} \frac{\partial^2 C}{\partial y^2}, \tag{16}$$

$$\frac{\partial C(y,t)}{\partial t} = \frac{1}{Sc}\, {}^{CPC}D_t^{\alpha} \frac{\partial^2 C(y,t)}{\partial y^2} - RC(y,t). \tag{17}$$

where ${}^{CPC}D_t^{\alpha} f(y,t)$ indicates the CPC fractional derivative of $f(y,t)$ [24] as

$$ {}^{CPC}D_t^{\alpha} f(y,t) = \frac{1}{\Gamma(1-\alpha)} \int_0^t \left(K_1(\alpha) f(y,\tau) + K_0(\alpha) f\prime(y,\tau)(t-\tau) \right)^{-\alpha} d\tau. \tag{18} $$

4. Solution of Problem

The formulated initial and boundary value value problem can be solved by means of the Laplace transform method.

4.1. Concentration Field. (17) be solved via Laplace transform for concentration species as

$$ s\overline{C}(y,s) = Sc^{-1}\left(\frac{k_1(\alpha)}{s} + k_0(\alpha) \right) s^{\alpha}(y,s) - \mathrm{R}\overline{C}(y,s), \tag{19} $$

with

$$ \overline{C}(0,s) = \frac{1}{s}, \quad \overline{C}(y,s) \longrightarrow 0, y \longrightarrow \infty. \tag{20} $$

Put (20) into (19), and result is

$$ \overline{C}(y,s) = \frac{1}{s} e^{-y\sqrt{\frac{(R+s)}{Sc^{-1}(K_1(\alpha)/s + K_0(\alpha))s^{\alpha}}}}. \tag{21} $$

This is complicated to solve analytically. Algorithm [32, 33] is used to derive the numerical result of (21).

4.2. Sherwood Number. The local coefficient of the rate of mass transfer is define in term of Sherwood number, and define by the following relation

$$ Sh = \left. \frac{\partial C}{\partial y} \right|_{y=0} = -L^{-1}\left[\left. \frac{\partial \overline{C}}{\partial y} \right|_{y=0} \right] = L^{-1}\left[\frac{1}{s} \sqrt{\frac{(R+s)}{Sc^{-1}(K_1(\alpha)/s + K_0(\alpha))s^{\alpha}}} \right]. \tag{22} $$

4.3. Temperature Field. (16) be solved via Laplace transform for temperature profile as

$$ s\overline{T}(y,s) = \mathrm{Pr}^{-1}\left(\frac{k_1(\gamma)}{s} + k_0(\gamma) \right) s^{\gamma} \frac{\partial^2 \overline{T}(y,s)}{\partial y^2} + Q\overline{T}(y,s) + n_1 \mathrm{Du}\left(\frac{k_1(\alpha)}{s} + k_0(\alpha) \right) s^{\alpha} \frac{\partial^2 \overline{C}(y,s)}{\partial y^2}, \tag{23} $$

with

$$ \overline{T}(0,s) = \frac{1}{s}, \quad \overline{T}(y,s) \longrightarrow 0, y \longrightarrow \infty. \tag{24} $$

Put (24) into (23), and result is

$$ \overline{T}(y,s) = \frac{1}{s} e^{-y\sqrt{\frac{(s-Q)}{\mathrm{Pr}^{-1}(K_1(\gamma)/s + K_0(\gamma))s^{\gamma}}}} + \frac{n_1 Du(R+s)}{\left(\mathrm{Pr}^{-1}(R+s)/(K_1(\alpha)/s + K_0(\alpha))s^{\alpha} - Sc^{-1}(s-Q)/(K_1(\gamma)/s + K_0(\gamma))s^{\gamma} \right)(k_1(\gamma) + sk_0(\gamma))s^{\gamma}} \times \left(e^{-y\sqrt{\frac{(s-Q)s}{\mathrm{Pr}^{-1}(K_1(\gamma)/s + K_0(\gamma))s^{\gamma}}}} - e^{-y\sqrt{\frac{(R+s)}{Sc^{-1}(K_1(\alpha)/s + K_0(\alpha))s^{\alpha}}}} \right). \tag{25} $$

This is complicated to solve analytically. Algorithm [32, 33] is used to derive the numerical result of (25).

4.4. Nusselt Number. The local coefficient of the rate of heat transfer is define in term of Nusselt number as

$$ Nu = \left. \frac{\partial T}{\partial y} \right|_{y=0} = -L^{-1}\left[\left. \frac{\partial \overline{T}}{\partial y} \right|_{y=0} \right] = L^{-1}\left[\frac{1}{s} \frac{(s-Q)}{\mathrm{Pr}^{-1}(K_1(\gamma)/s + K_0(\gamma))s^{\gamma}} + \frac{n_1 Du(R+s)}{\left(\mathrm{Pr}^{-1}(R+s)/(K_1(\alpha)/s + K_0(\alpha))s^{\alpha} - Sc^{-1}(s-Q)/(K_1(\gamma)/s + K_0(\gamma))s^{\gamma} \right)(k_1(\gamma) + sk_0(\gamma))s^{\gamma}} \times \left(\sqrt{\frac{(s-Q)s}{\mathrm{Pr}^{-1}(K_1(\gamma)/s + K_0(\gamma))s^{\gamma}}} - \sqrt{\frac{(R+s)}{Sc^{-1}(K_1(\alpha)/s + K_0(\alpha))s^{\alpha}}} \right) \right]. \tag{26} $$

4.5. Velocity field. (11) be solved via Laplace transform for velocity field as

$$s\overline{v}(y,t) = \left(1+\lambda_1\right)^{-1}(1+\lambda s)\frac{\partial^2\overline{v}(y,t)}{\partial y^2} - [(M+1/K)\overline{v}(y,t) - \mathrm{Gr}\overline{T}(y,t) - \mathrm{Gm}\overline{C}(y,t)], \tag{27}$$

with

$$\overline{v}(0,s) = (s-a)^{-1}, \quad \overline{v}(y,s) \longrightarrow 0, y \longrightarrow \infty. \tag{28}$$

Put (28) into (27), we get

$$\begin{aligned}\overline{v}(y,s) = {} & \frac{1}{s-a}e^{-y\sqrt{\frac{(s+M+1/K)(1+\lambda_1)}{1+\lambda s}}} \\ & + \frac{\left[\mathrm{Gr}/s + n_1\mathrm{DuGr}(R+s)/\left(\mathrm{Pr}^{-1}(R+s)/\left(K_1(\alpha)/s+K_0(\alpha)\right)s^{\alpha} - \mathrm{Sc}^{-1}(s-Q)/\left(K_1(\gamma)/s+K_0(\gamma)\right)s^{\gamma}\right)\left(k_1(\gamma)+sk_0(\gamma)\right)s^{\gamma}\right]}{\mathrm{Pr}(s-Q)(1+\lambda s)/\left(K_1(\gamma)/s+K_0(\gamma)\right)s^{\gamma}(1+\lambda_1) - (s+M+1/K)} \\ & \cdot\left(e^{-y\sqrt{\frac{(s+M+1/K)(1+\lambda_1)}{1+\lambda s}}} - e^{-y\sqrt{\frac{(s-Q)}{\mathrm{Pr}^{-1}\left(K_1(\gamma)/s+K_0(\gamma)\right)s^{\gamma}}}}\right) + \\ & \frac{\mathrm{Gm}/s - n_1\mathrm{DuGr}(R+s)/\left(\mathrm{Pr}^{-1}(R+s)/\left(K_1(\alpha)/s+K_0(\alpha)\right)s^{\alpha} - \mathrm{Sc}^{-1}(s-Q)/\left(K_1(\gamma)/s+K_0(\gamma)\right)s^{\gamma}\right)\left(k_1(\gamma)+sk_0(\gamma)\right)s^{\gamma}}{\mathrm{Sc}(R+s)(1+\lambda s)/\left(K_1(\alpha)/s+K_0(\alpha)\right)s^{\alpha}(1+\lambda_1) - (s+M+1/K)} \\ & \cdot\left(e^{-y\sqrt{\frac{(s+M+1/K)(1+\lambda_1)}{1+\lambda s}}} - e^{-y\sqrt{\frac{(R+s)}{\mathrm{Sc}^{-1}\left(K_1(\alpha)/s+K_0(\alpha)\right)s^{\alpha}}}}\right).\end{aligned} \tag{29}$$

This is complicated to solve analytically. Algorithm [32, 33] is used to derive the numerical result of (29).

4.6. Skin Friction. The expression of skin friction is define by using (29) as

$$\begin{aligned}\tau = \frac{\partial u}{\partial y}|_{y=0} = -L^{-1}\left[\frac{\partial\overline{u}}{\partial y}|_{y=0}\right] = L^{-1}\Bigg[& \frac{1}{s-a}\sqrt{\frac{(s+M+1/K)(1+\lambda_1)}{1+\lambda s}} \\ & + \frac{\mathrm{Gr}/s + n_1\mathrm{DuGr}(R+s)/\left(\mathrm{Pr}^{-1}(R+s)/\left(K_1(\alpha)/s+K_0(\alpha)\right)s^{\alpha} - \mathrm{Sc}^{-1}(s-Q)/\left(K_1(\gamma)/s+K_0(\gamma)\right)s^{\gamma}\right)\left(k_1(\gamma)+sk_0(\gamma)\right)s^{\gamma}}{\mathrm{Pr}(s-Q)(1+\lambda s)/\left(K_1(\gamma)/s+K_0(\gamma)\right)s^{\gamma}(1+\lambda_1) - (s+M+1/K)} \\ & \times\left(\sqrt{\frac{(s+M+1/K)(1+\lambda_1)}{1+\lambda s}} - \sqrt{\frac{(s-Q)}{\mathrm{Pr}^{-1}\left(K_1(\gamma)/s+K_0(\gamma)\right)s^{\gamma}}}\right)\end{aligned}$$

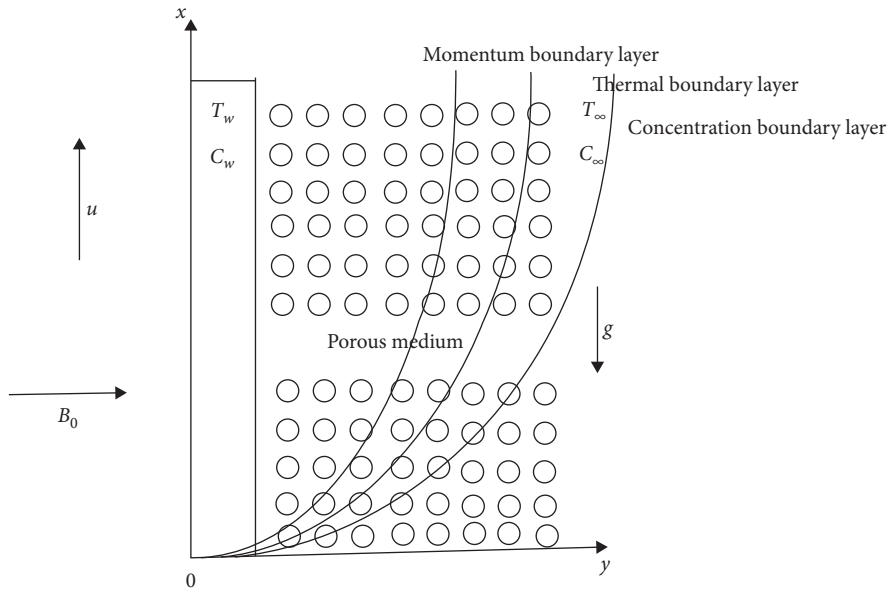

Figure 1: Physical model.

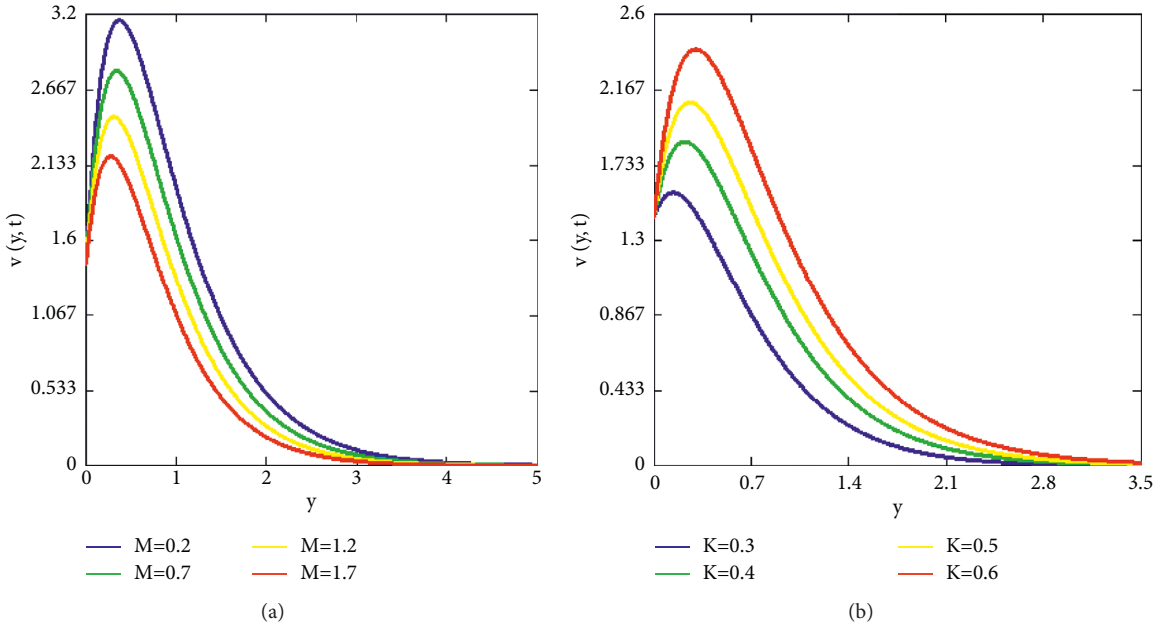

Figure 2: (a) Velocity profile $v(y,t)$ for parameter M at $R=3.2$, $Q=4$, Gr = 14, Gm = 8, Du = 0.4, Sc = 2.5, Pr = 6, and $K=2$. (b) Velocity profile $v(y,t)$ for parameter K at $R=3.2$, $Q=4$, Gr = 14, Gm = 8, $M=4$, Sc = 2.5, Pr = 6, and Du = 0.4.

$$+\frac{\mathrm{Gm}/s-n_1\mathrm{DuGr}\,(R+s)/\left(\mathrm{Pr}^{-1}\,(R+s)/\left(K_1\,(\alpha)/s+K_0\,(\alpha)\right)s^{\alpha}-\mathrm{Sc}^{-1}\,(s-Q)/\left(K_1\,(\gamma)/s+K_0\,(\gamma)\right)s^{\gamma}\right)\left(k_1\,(\gamma)+sk_0\,(\gamma)\right)s^{\gamma}}{\mathrm{Sc}\,(R+s)\,(1+\lambda s)/\left(K_1\,(\alpha)/s+K_0\,(\alpha)\right)s^{\alpha}\left(1+\lambda_1\right)-(s+M+1/K)}$$
$$\times\left(\sqrt{\frac{(s+M+1/K)\,(1+\lambda_1)}{1+\lambda s}}-\sqrt{\frac{(R+s)}{\mathrm{Sc}^{-1}\,(K_1\,(\alpha)/s+K_0\,(\alpha))s^{\alpha}}}\right)\Bigg]. \tag{30}$$

5. Results and Discussion

In this article the diffusion-thermo effect is investigated for the magnetohydrodynamics (MHD) flow of Jeffrey's fractional fluid past an exponentially accelerated vertical plate with generalized thermal and mass transports through a porous medium. The semi-analytical results for the concentration, temperature, and velocity fields are obtained.

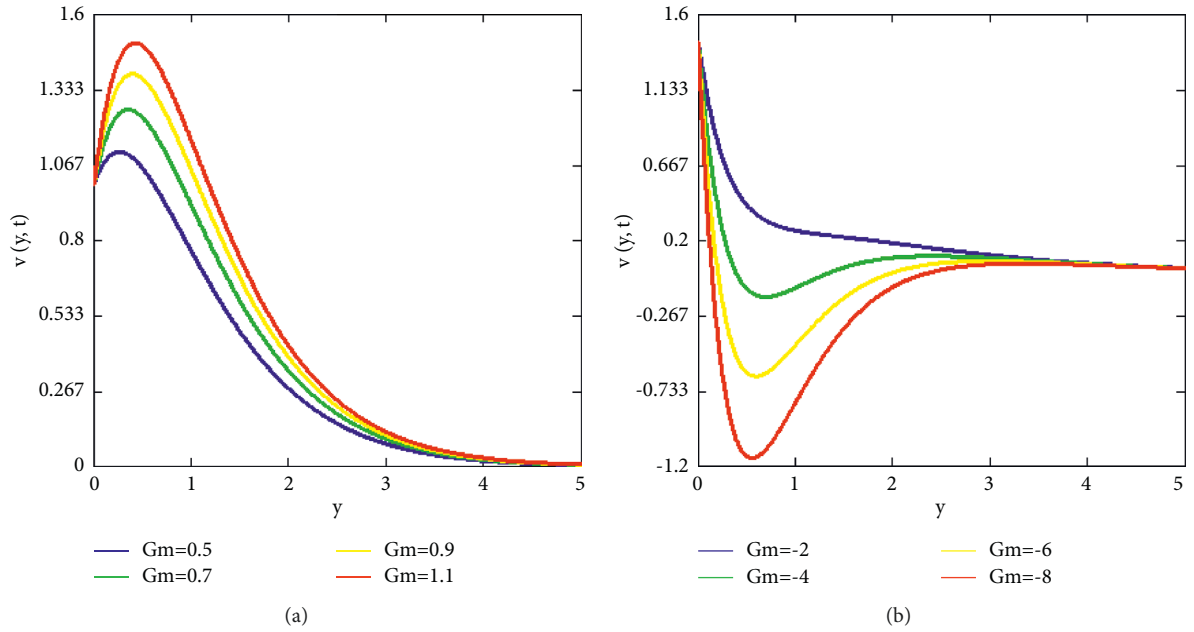

Figure 3: (a) Velocity profile $v(y,t)$ for parameter Gm at $R=3.2$, $Q=4$, Gr = 14, Du = 0.4, $M=4$, Sc = 2.5, Pr = 6, and $K=2$. (b) Velocity profile $v(y,t)$ for parameter Gm at $R=3.2$, $Q=4$, Gr = 14, Du = 0.4, $M=4$, Sc = 2.5, Pr = 6, and $K=2$.

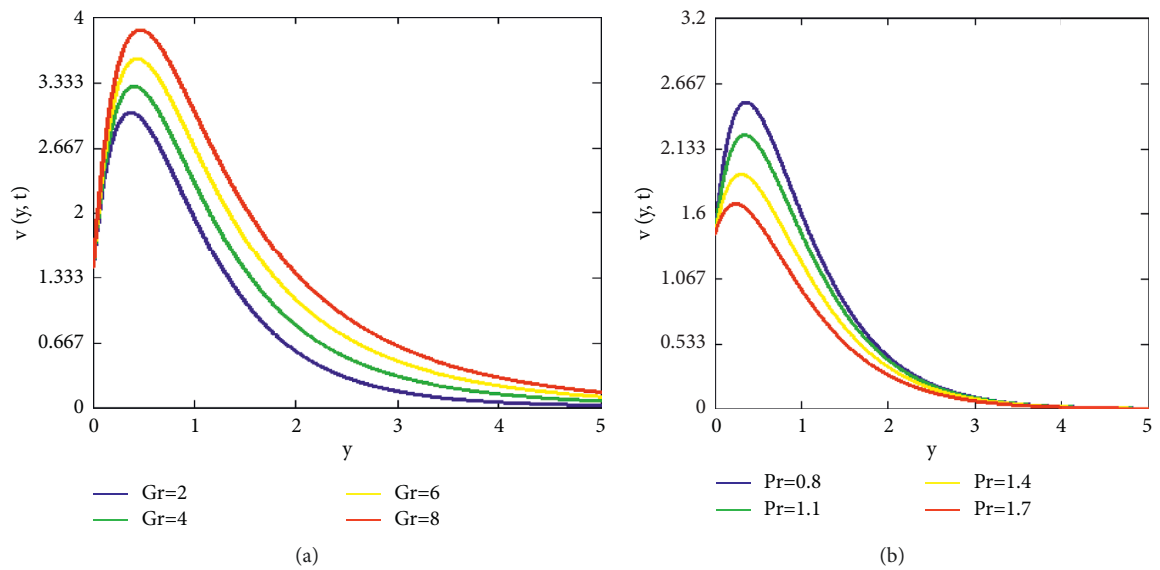

Figure 4: (a) Velocity profile $v(y,t)$ for parameter Gr at $R=3.2$, $Q=4$, Gm = 8, $M=4$, Sc = 2.5, Pr = 6, and $K=2$. (b) Velocity profile $v(y,t)$ for parameter Pr at $R=3.2$, $Q=4$, Gr = 14, Gm = 8, $M=4$, Sc = 2.5, Du = 0.4, and $K=2$.

Moreover to see the physical effect of involved parameters, the concentration, temperature, and velocity fields are postured by some graphs.

Velocity profile is sketched in the Figure 2(a) to twilight the influence magnetic field over the fluid velocity and it is observed that fluid slows down for greater values of M. In the presence of magnetic field a retarding force is created which oppose the fluid motion as depicted in Figure 2(a). The effect of porosity parameter K on fluid flow is defected in Figure 2(b) and it is noted that the fluid motion enhance with increasing value of K. The larger value of K refers to the less Darcy resistance to the flow that is why flow speeds up with increasing value of K. The influence of mass Gm on fluid velocity $v(y,t)$ is illustrate in Figures 3(a) and 3(b). It is noted that fluid motion increases as values of Gm increasing. Physically higher values of Gm refers the higher concentration gradients and greater the buoyancy force and more current in flow domain so velocity increases. Figure 4(a) represent the result of Gr on fluid velocity $v(y,t)$. The fluid motion rises up with maximizing the values of Gr, and it represents the more impact of thermal buoyancy force as compare to the viscous effect. Therefore maximizing the values of Gr refers the higher temperature gradient due to which

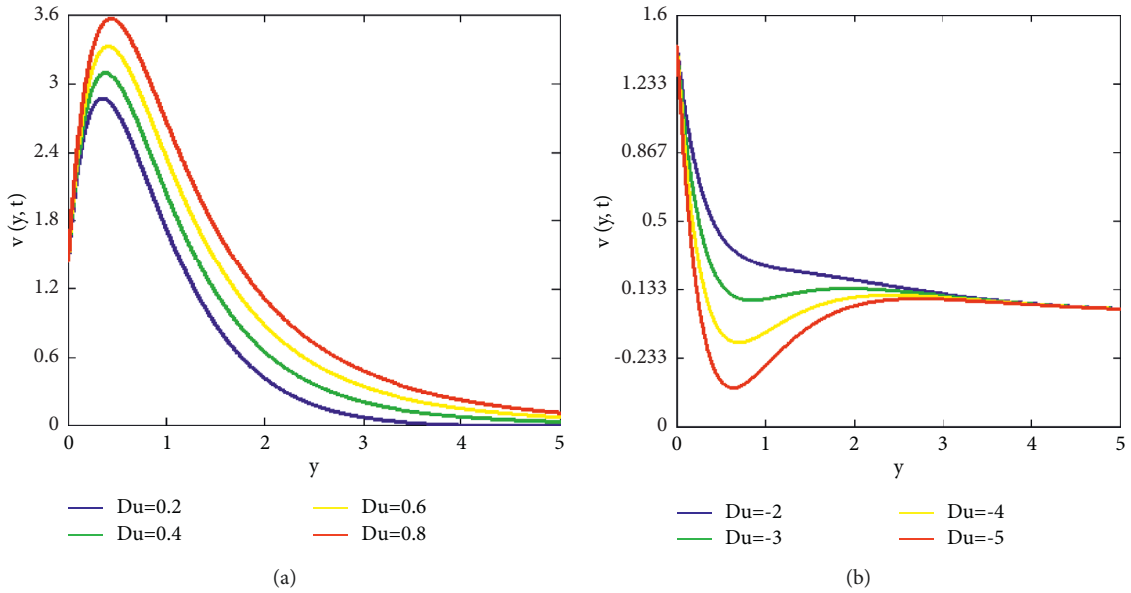

FIGURE 5: (a) Velocity profile $v(y,t)$ for parameter Du at $R = 3.2$, $Q = 4$, Gr = 14, Gm = 8, $M = 4$, Sc = 2.5, Pr = 6, and $K = 2$. (b) Velocity profile $v(y,t)$ for parameter Du at $R = 3.2$, $Q = 4$, Gr = 14, Gm = 8, $M = 4$, Sc = 2.5, Pr = 6, and $K = 2$.

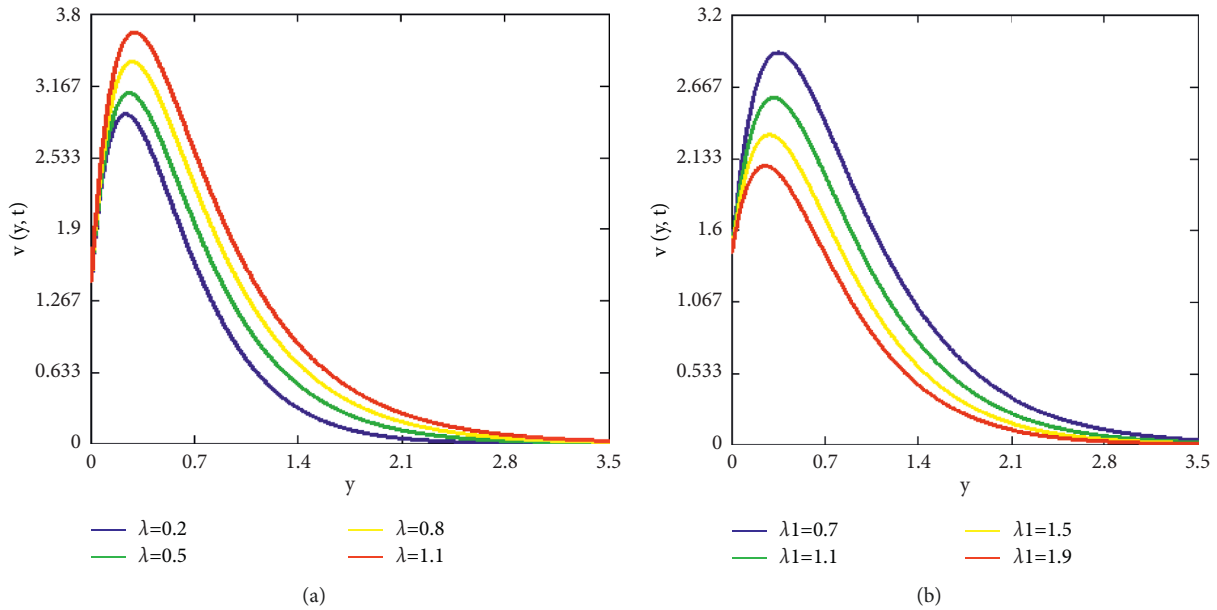

FIGURE 6: (a) Velocity profile $v(y,t)$ for heat generation parameter λ at $R = 3.2$, Q = 4, Gr = 14, Gm = 8, $M = 4$, Sc = 2.5, Pr = 6, and $K = 2$. (b) Velocity profile $v(y,t)$ for chemical reaction parameter λ_1 at $R = 3.2$, $Q = 4$, Gr = 14, Gm = 8, $M = 4$, Sc = 2.5, Pr = 6, and $K = 2$.

velocity field rises. The impact of Pr for velocity field is presented in Figure 4(b).

The diffusion-thermo or Dufour effect (Du) over the velocity field are discussed in the Figures 5(a) and 5(b). An enhancing flow pattern is observed due to the increasing variations of the Du. The concentration gradient give a contribute to the temperature gradient which creates an additional energy flux in the flow domain. Therefore an increasing value of the Du refer to the more energy flux which generates the more flow current that is why the flow speeds up with increasing value of Du. Moreover the negative values refer to the opposite direction of the additional energy flux therefore more negativity of Du generates the more opposite flow current in the flow domain.

Figures 6(a) and 6(b) are drawn to see impact of Jeffrey parameters λ and λ_1 over velocity field $v(y,t)$ respectively. As parameter λ refer to the viscosity of the fluid therefore fluid velocity falls due to the increasing value of λ and the parameter λ_1 refers to the elasticity of the fluid material so fluid speed up with increasing value λ_1. The influence of heat generation on $v(y,t)$ is reported in Figure 7(a). An increasing value of R decreases the fluid velocity as shown in Figure 7(b). The impact of Sc on $v(y,t)$ is illustrate in Figure

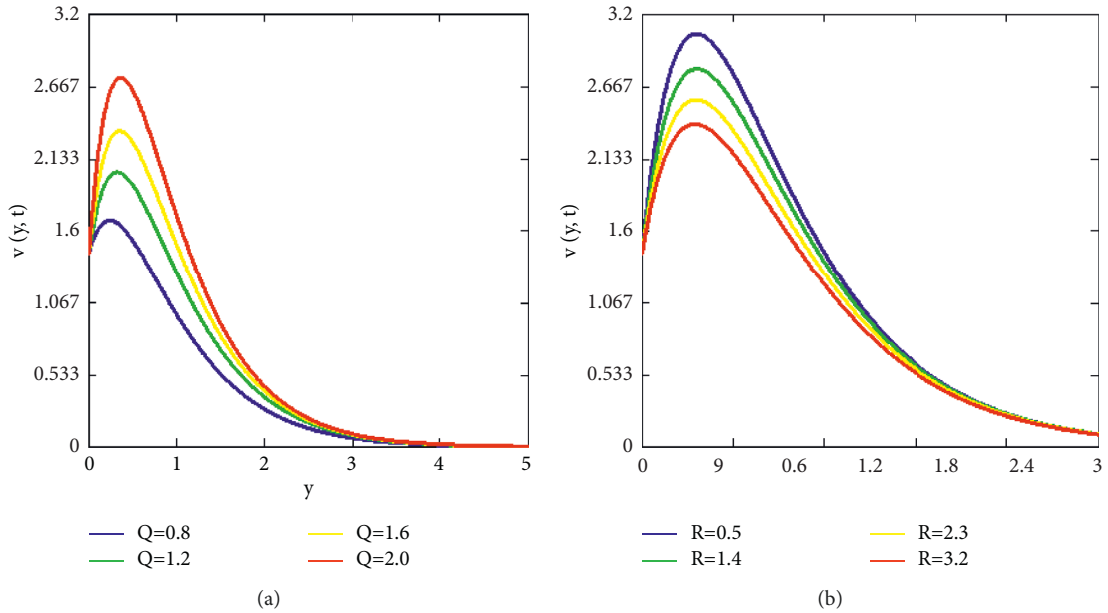

FIGURE 7: (a) Velocity profile $v(y,t)$ for heat generation parameter Q at $R = 3.2$, Du = 0.4, Gr = 14, Gm = 8, $M = 4$, Sc = 2.5, Pr = 6, and $K = 2$. (b) Velocity profile $v(y,t)$ for chemical reaction parameter R at $Q = 4$, Du = 0.4, Gr = 14, Gm = 8, $M = 4$, Sc = 2.5, Pr = 6, and $K = 2$.

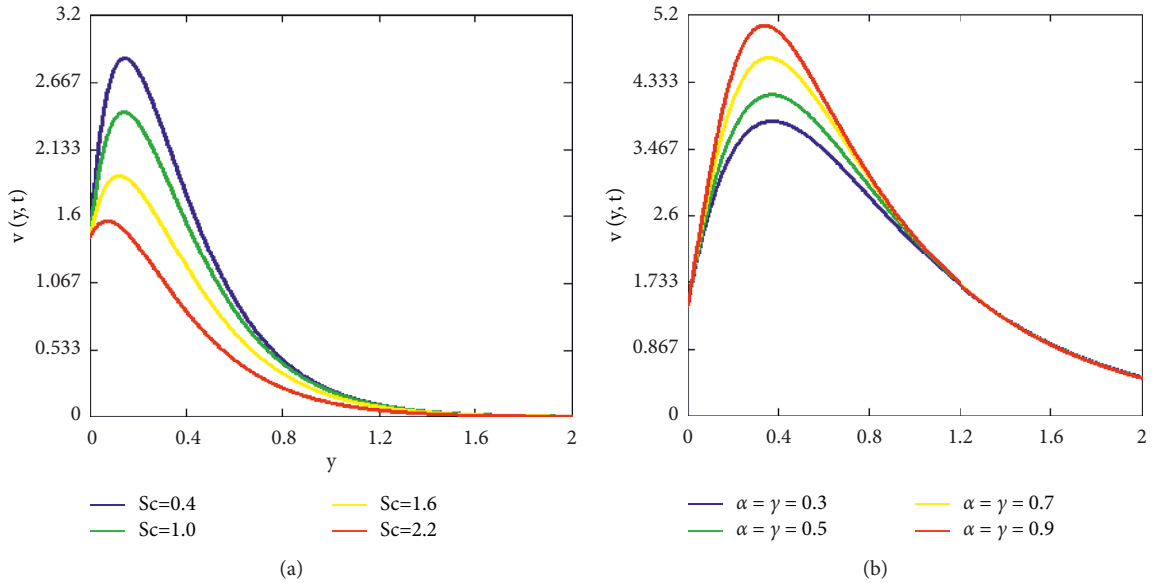

FIGURE 8: Velocity profile $v(y,t)$ for parameter Sc at $R = 3.2$, $Q = 4$, Gr = 14, Gm = 8, $M = 4$, Du = 0.4, Pr = 6, and $K = 2$. (b) Velocity profile $v(y,t)$ for fractional parameters at $Q = 4$, Du = 0.4, Gr = 14, Gm = 8, M = 4, R = 3.2, Du = 0.4, Pr = 6, and $K = 2$.

8(a). Here, maximizing the values of Sc slow down the fluid motion due to decay of molecular diffusion. It is analyzed that motion of fluid increases with raising values of $\alpha = \gamma$ as depicted in Figure 8(b). The graphical behavior of Du, Pr, Q, and t on $T(y,t)$ are shown in Figures 9(a), 9(b), 10(a) as well as 10(b) respectively. Figures illustrate that temperature reduces by exceeding the values of Du, and Pr, and temperature increases by exceeding the values of Q and t. The impacts of Schmidt number Sc as well as chemical reaction R on $C(y,t)$ are present in Figures 11(a) as well as 11(b) respectively. Figures 12(a) and 12(b) represent the comparison of velocity and temperature distribution of present work with Naseem [20] respectively. If we take fractional parameters $\alpha = \gamma \longrightarrow 1, = \lambda = \lambda_1 = M = \text{Gm} = \text{Du} = Q = 0$, $1/K \longrightarrow 0, 1/\gamma \longrightarrow 0$ and $f(t) = e^{at_2^*}$ in Naseem [28], the velocity fields are identical that shows the validity of this present work. Moreover the comparison of present work with other fractional derivatives Caputo and Caputo Fabrizio used in Nazar et al. [34] and Nadeem et al. [35] respectively in the absence of K, Q, Gm, R, Du are shown in Figure 12(c). If we put $\alpha = 1$ the fluid curves are identical as shown in Figure 12(d). From the figures, it is concluded that Jeffrey fluid with CPC fractional derivative is the best choice to enhance the fluid motion. Figures 13(a) and 13(b)

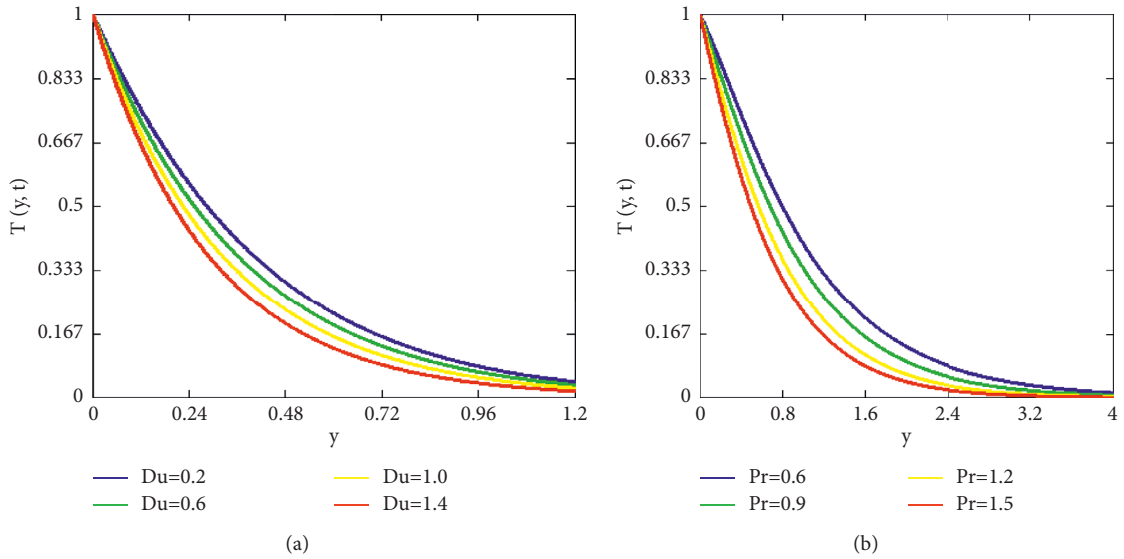

Figure 9: (a) Temperature profile $T(y,t)$ for parameter Du. (b) Temperature profile $T(y,t)$ for Pr.

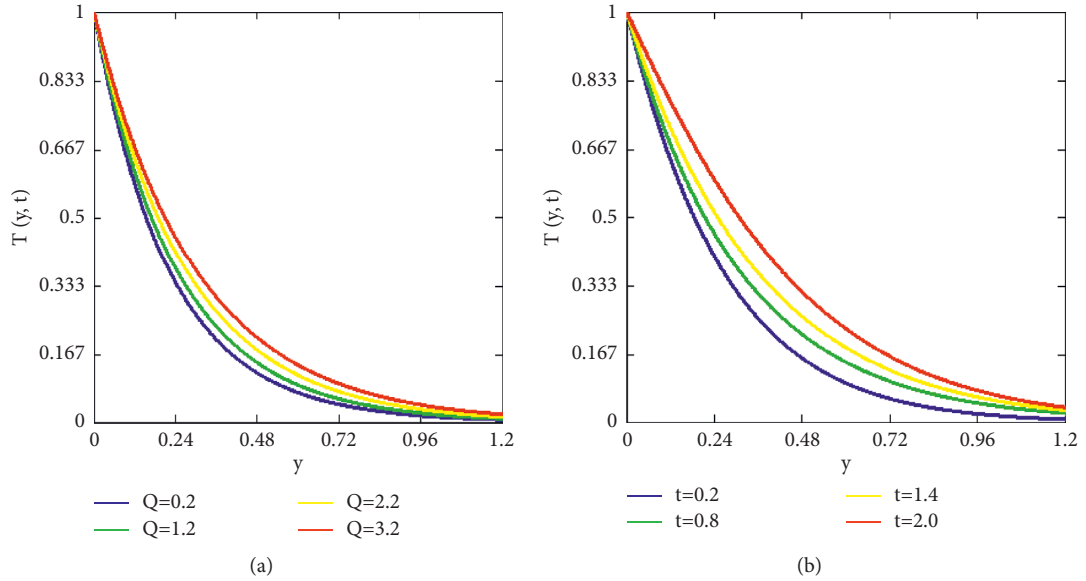

Figure 10: Temperature profile $T(y,t)$ for parameter Q. (b) Temperature profile $T(y,t)$ for t.

represent the authenticity of inversion algorithms for temperature and concentration distributions. The velocity distributions overlap which shows the authenticity of inversion algorithms as presented in Figure 14. Skin friction, rate of heat and mass transfer can be enhanced by increasing the values of fractional parameter and presented in table 1.

- With decreasing fractional parameter values, the velocity distribution slows down.
- Thermal buoyancy forces accelerate the fluid velocity.
- Fluid velocity reduces as Schmidt number Sc, chemical reaction R, and magnetic parameter M rises.
- The fluid velocity increased for larger values of Jeffrey parameter as well as fractional parameter.
- The temperature distribution increases by the smaller values of Prandtl number Pr.

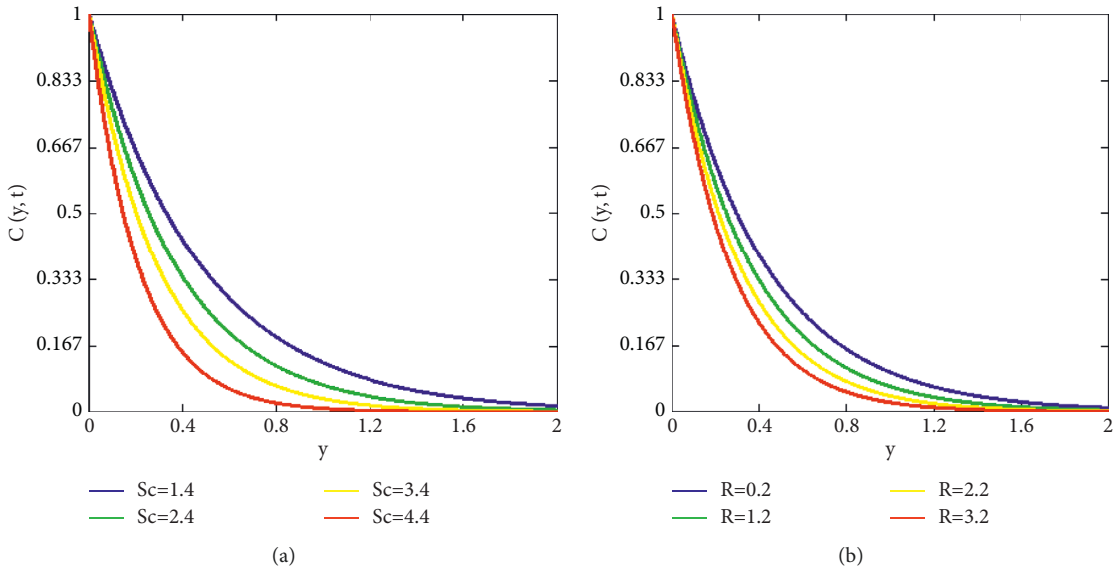

Figure 11: (a) Concentration profile $C(y,t)$ for parameter Sc. (b) Concentration profile $C(y,t)$ for parameter R.

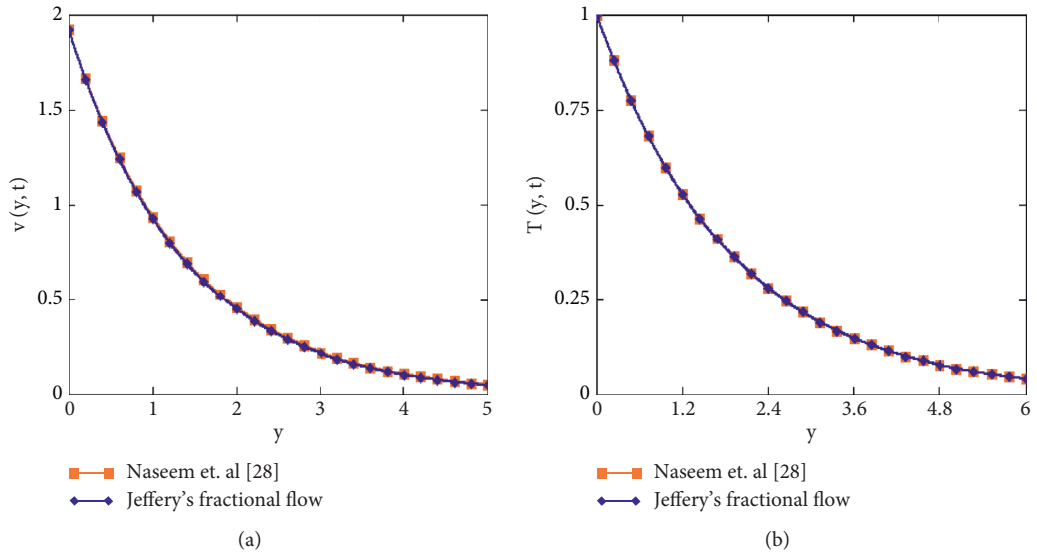

Figure 12: Continued.

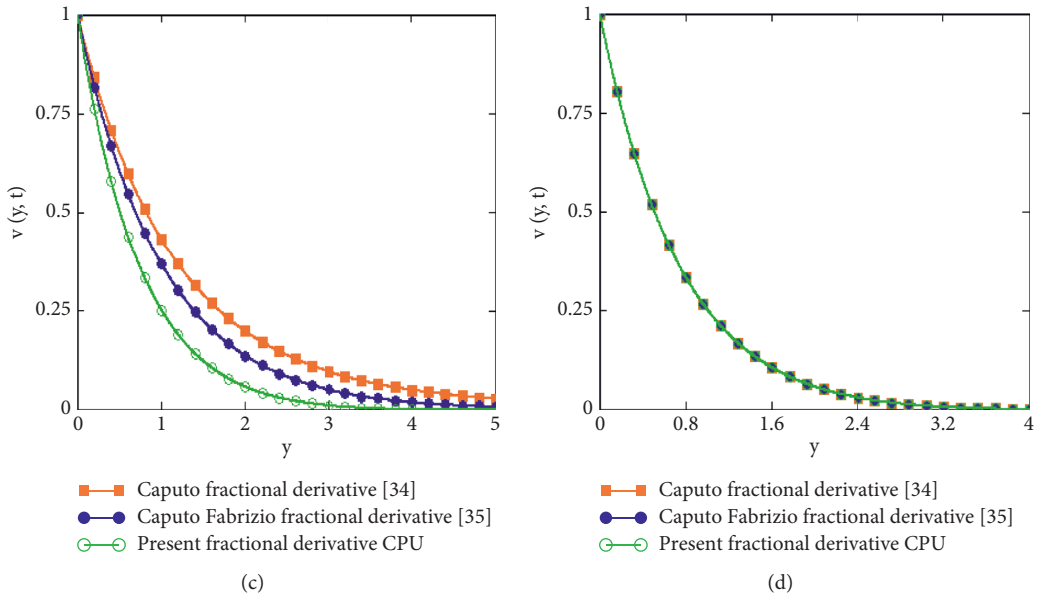

Figure 12: (a) Velocity distribution for comparison of our work with Naseem [28] as $\alpha = \gamma \to 0, \lambda = \lambda = M = Gm = Du = Q = 0, 1/K \to 0, 1/\gamma \to 0$. (b) Temperature for comparison of our work with Naseem [28] as $\alpha = \gamma \to 1$, $Gm = Du = Q = 0$. (c) Comparisons between different fractional derivatives $\alpha = 0.5$ (d) Comparisons between different fractional derivatives $\alpha \to 1$.

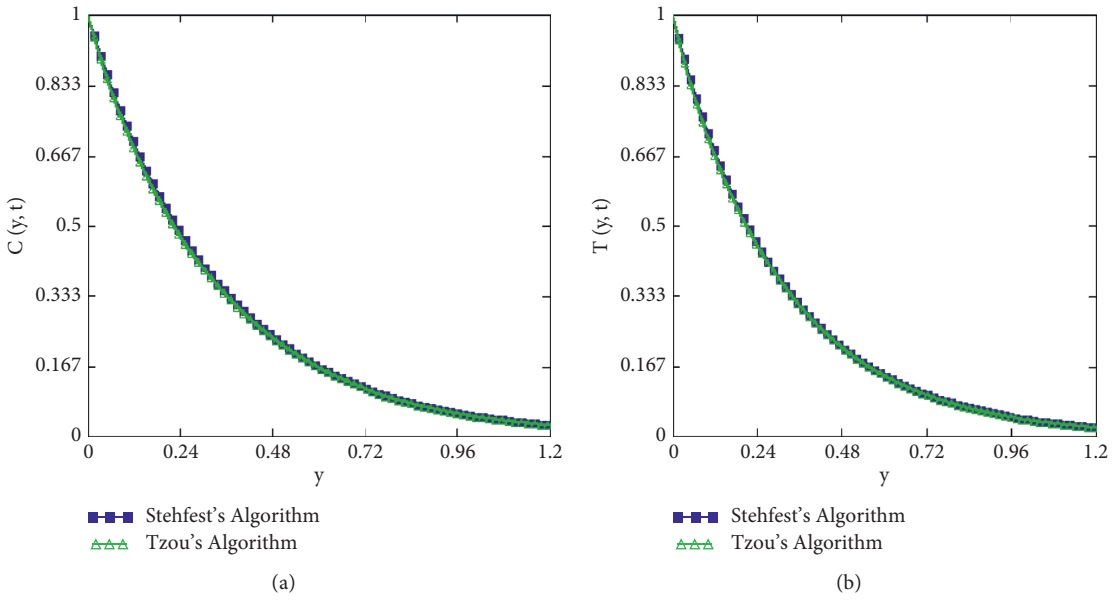

Figure 13: (a) Concentration obtained by Stehfest's and Tzou's algorithms. (b) Temperature obtained by Stehfest's and Tzou's algorithms.

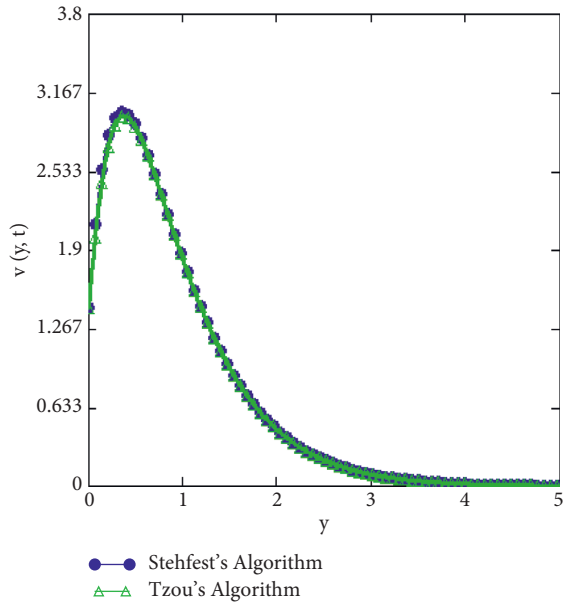

Figure 14: Velocity obtained by Stehfest's and Tzou's algorithms.

Table 1: Effect of α on skin friction, Nusselt number, and Sherwood number.

Fractional Parameter	skin friction	Nusselt number	Sherwood number
0.1	1.458 939 71	1.363 328 25	1.293 234 41
0.2	1.469 733 54	1.376 590 53	1.306 809 85
0.3	1.480 812 22	1.389 919 45	1.320 272 42
0.4	1.492 212 41	1.403 398 90	1.333 699 19
0.5	1.503 987 04	1.417 120 90	1.347 160 76
0.6	1.516 206 97	1.431 188 59	1.360 720 51
0.7	1.528 970 61	1.445 719 09	1.374 431 12
0.8	1.542 413 61	1.460 842 28	1.388 325 48
0.9	1.556 732 82	1.476 693 47	1.402 406 85
0.99	1.572 220 17	1.493 394 87	1.416 634 77

- The concentration distribution decreases for greater values of Schmidt number Sc.
- The concentration distribution decreases by exceeding the values of chemical reaction R.

6. Conclusions

The Magnetohydrodynamics flow model of Jeffrey's fractional fluid model has been considered with the effect of magnetic field in the porous regime. Heat generation, and radiation are also consider with effect of chemical reaction in the flow domain. This flow model is solved analytically and results for velocity, temperature, and concentration fields are constructed by using Laplace transform. Further different graphs of optimising fields are plotted to highlight the influence parameters. The key outcomes of this flow model are:

Nomenclature

v: : fluid velocity, $[ms^{-1}]Sr$: Soret number
Gr: : Thermal Grashof number, $[\beta T_w]Gm$: Mass Grashof number, $[\beta T_w]Nu$: Nusselt number
Sc: : Schmidt number
λ: : Jeffrey parameter
g: acceleration due to gravity, $[ms^{-2}]C_p$: Specific heat at a constant pressure, $[jkg^{-1}K^{-1}]T$: Temperature of fluid, $[K]T_w$: Fluid temperature at plate, $[K]T_\infty$: Fluid temperature far away from the plate, $[K]C$: Concentration of fluid, $[kgm^{-3}]C_w$: Concentration level at plate, $[kgm^{-3}]C_\infty$: Concentration of the fluid far away from the plate, $[kgm^{-3}]s$: Laplace transform parameter
ρ: Fluid density, $[kgm^{-3}]\alpha$: Fractional parameter
ν: Kinematic viscosity, $[m^2s^{-1}]\beta_T$: Volumetric Coefficient of thermal expansion, $[K^{-1}]\beta_C$: Volumetric Coefficient of mass expansion, $[m^3kg^{-1}]$.

Data Availability

The data used to support the findings of this study are included within the article.

Additional Points

With decreasing fractional parameter values, the velocity distribution slows down. Thermal buoyancy forces accelerate the fluid velocity. Fluid velocity reduces as Schmidt number Sc, chemical reaction R, and magnetic parameter M rise. The fluid velocity increased for larger values of Jeffrey parameter as well as fractional parameter. The temperature distribution increases by the smaller values of Prandtl

number Pr. The concentration distribution decreases for greater values of Schmidt number Sc. The concentration distribution decreases by exceeding the values of the chemical reaction R.

Conflicts of Interest

The authors declare that they have no conflicts of interest.

References

[1] N. A. Mohd Zin, A. Q. Mohamad, I. Khan, and S. Shafie, "Porosity effect on unsteady MHD free convection flow of Jeffrey fluid past an oscillating vertical plate with ramped wall temperature," *Malaysian Journal of Fundamental and Applied Sciences*, vol. 13, pp. 49–59, 2017.

[2] S. Bajwa, S. Ullah, I. Khan, and M. Fayz-Al-Asad, "Transient flow of Jeffrey fluid over a permeable wall," *Mathematical Problems in Engineering*, vol. 2021, pp. 1–9, Article ID 9999949, 2021.

[3] M. Asgir, A. A. Zafar, A. M. Alsharif, M. B. Riaz, and M. Abbas, "Special function form exact solutions for Jeffery fluid: an application of power law kernel," *Advances in Difference Equations*, pp. 1–18, 2021.

[4] K. Das, "Influence of slip and heat transfer on MHD peristaltic flow of a Jeffrey fluid in an inclined asymmetric porous channel," *Indian Journal of Mathematics*, vol. 54, pp. 19–45, 2012.

[5] M. Qasim, "Heat and mass transfer in a Jeffrey fluid over a stretching sheet with heat source/sink," *Alexandria Engineering Journal*, vol. 52, no. 4, pp. 571–575, 2013.

[6] F. Ali, M. Khan, and M. Gohar, "Magnetohydrodynamic fluctuating free convection flow of Second-grade fluid flow in a porous medium," *Mathematical Problems in Engineering*, vol. 2021, pp. 1–13, 2021.

[7] N. A. Shah, M. Areshi, J. D. Chung, and K. Nonlaopon, "The new semianalytical technique for the solution of fractional-order Navier-Stokes equation," *Journal of Function Spaces*, vol. 2021, pp. 1–13, 2021.

[8] K. V. Chandra, "Laplace transform solution of unsteady MHD Jeffrey fluid flow past vertically inclined porus plate," *Frontiers in Heat and Mass Transfer*, pp. 1–6, 2021.

[9] M. Jamil and A. Haleem, "MHD fractionalized Jeffrey fluid over an accelerated slipping porous plate," *Nonlinear Engineering*, vol. 9, no. 1, pp. 273–289, 2020.

[10] K. A. Abro, I. A. Abro, S. M. Almani, and I. Khan, "On the thermal analysis of magnetohydrodynamic Jeffery fluid via modern non integer order derivative," *Journal of King Saud University Science*, vol. 31, no. 4, pp. 973–979, 2019.

[11] A. Atangana, A. Akgul, and K. M. Owolabi, "Analysis of fractal fractional differential equations," *Alexandria Engineering Journal*, vol. 59, pp. 1–18, 2020.

[12] A. Atangana and J. F. Gómez-Aguilar, "Numerical approximation of Riemann-Liouville definition of fractional derivative: from Riemann-Liouville to Atangana-Baleanu," *Numerical Methods for Partial Differential Equations*, vol. 34, no. 5, pp. 1502–1523, 2018.

[13] J. Ahmad, F. Ali, S. Murtaza, and I. Khan, "Caputo time fractional model based on generalized Fourier's and Fick's laws for Jeffrey Nano fluid: applications in automobiles," *Mathematical Problems in Engineering*, vol. 2021, pp. 1–12, Article ID 4611656, 2021.

[14] I. Siddique, S. Ayaz, and F. Jarad, "Dufour effect on transient MHD double convection flow of fractionalized second-grade fluid with caputo-fabrizio derivative," *Complexity*, vol. 2021, pp. 1–21, 2021.

[15] N. Sandeep and C. Sulochana, "Momentum and heat transfer behaviour of Jeffrey, Maxwell and Oldroyd-B nanofluids past a stretching surface with non-uniform heat source/sink," *Ain Shams Engineering Journal*, vol. 9, no. 4, pp. 517–524, 2018.

[16] S. Saleem, M. M. Al-Qarni, S. Nadeem, and N. Sandeep, "Convective heat and mass transfer in magneto Jeffrey fluid flow on a rotating cone with heat source and chemical reaction," *Communications in Theoretical Physics*, vol. 70, no. 5, p. 534, 2018.

[17] C. Sulochana, S. R. Aparna, and N. Sandeep, "Heat and mass transfer of magnetohydrodynamic Casson fluid flow over a wedge with thermal radiation and chemical reaction," *Heat Transfer*, vol. 50, no. 4, pp. 3704–3721, 2021.

[18] N. Acharya, R. Bag, and P. K. Kundu, "Unsteady bioconvective squeezing flow with higher-order chemical reaction and second-order slip effects," *Heat Transfer*, vol. 50, no. 6, pp. 5538–5562, 2021.

[19] N. Acharya, H. Mondal, and P. K. Kundu, "Spectral approach to study the entropy generation of radiative mixed convective couple stress fluid flow over a permeable stretching cylinder," vol. 235, pp. 2692–2704, 2021.

[20] N. Acharya, S. Maity, and P. K. Kundu, "Differential transformed approach of unsteady chemically reactive nanofluid flow over a bidirectional stretched surface in presence of magnetic field," *Heat Transfer*, vol. 49, no. 6, pp. 3917–3942, 2020.

[21] A. Riaz, S. Nadeem, R. Ellahi, and N. S. Akbar, "The influence of wall flexibility on unsteady peristaltic flow of Prandtl fluid in a three dimensional rectangular duct," *Applied Mathematics and Computation*, vol. 241, pp. 389–400, 2014.

[22] A. Riaz, R. Ellahi, and S. M. Sait, "Role of hybrid nanoparticles in thermal performance of peristaltic flow of Eyring-Powell fluid model," *Journal of Thermal Analysis and Calorimetry*, vol. 143, no. 2, pp. 1021–1035, 2021.

[23] Yuri-Luchko, "Book on fractional integrals and derivatives: "true" versus "false," *Mathematics*, pp. 1–283, 2021.

[24] D. Baleanu, A. Fernandez, and A. Akgül, "On a fractional operator combining proportional and classical differintegrals," *Mathematics*, vol. 8, no. 3, p. 360, 2020.

[25] Y. M. Chu, M. Ahmad, M. I. Asjad, and D. Baleanu, "Fractional model of Second grade fluid induced by generalized thermal and molecular fluxes with constant proportional Caputo," *Thermal Science*, vol. 25, pp. 1–6, 2021.

[26] I. Siddique and A. Akgul, "Analysis of blood liquor model via nonlocal and singular constant proportional Caputo hybrid differential operator," *Mathematical Methods in the Applied Sciences*, pp. 1–17, 2021.

[27] D. khan, P. Kumam, and W. Watthayu, "A novel comparative case study of entropy generation for natural convection flow of proportional.Caputo hybrid and Atangana baleanu fractional derivative," *Scientific Reports*, vol. 11, pp. 1–11, 2021.

[28] A. Naseem, "General solution of Casson fluid past a vertical plate subject to the time dependent velocity with constant wall temperature," *Open Journal of Mathematical Analysis*, vol. 2(2018), no. 1, pp. 47–65, 2018.

[29] G. B. Arfken, D. F. Griffing, D. C. Kelly, and J. Priest, "Instructional aids to accompany university physics," *International Edition University Physics*, pp. 1–905, 1984.

[30] D. R. Poirier and G. H. Geifer, *Transport Phenomena in Materials Processing*, pp. 1–660, Springer, Berlin/Heidelberg, Germany, 2016.

[31] J. Hristov, "Transient heat diffusion with a non-singular fading memory from the cattaneo constitutive equation with Jeffrey's kernel to the Caputo-fabrizio time fractional derivative," *Thermal Science*, vol. 20, pp. 557–562, 2016.

[32] D. Y. Tzou, *Macro to Microscale Heat Transfer, the Lagging Behavior*, pp. 01–339, Taylor & Francis, Washington, District of Columbia, 1997.

[33] H. Stehfest, "Algorithm 368: numerical inversion of Laplace transforms [D5]," *Communications of the ACM*, vol. 13, no. 1, pp. 47–49, 1970.

[34] M. Nazar, M. Ahmad, M. A. Imran, and N. A. Shah, "Double convection of heat and mass transfer flow of mhd generalized Second grade fluid over an exponentially accelerated infinite vertical plate with heat absorption," *Journal of Mathematical Analysis*, vol. 8, pp. 28–44, 2017.

[35] N. A. Sheikh, F. Ali, I. Khan, and M. Saqib, "A modern approach of Caputo-Fabrizio time-fractional derivative to MHD free convection flow of generalized second-grade fluid in a porous medium," *Neural Computing & Applications*, vol. 30, no. 6, pp. 1865–1875, 2018.

Hindawi
Mathematical Problems in Engineering
Volume 2022, Article ID 3091897, 13 pages
https://doi.org/10.1155/2022/3091897

Research Article

Insights of Heat and Mass Transfer in Magneto-Mixed Convective Sisko Nanofluid over a Wedge with Viscous Dissipation

Yogesh Dadhich,[1] **Reema Jain**,[1] **and Sonam Gyeltshen**[2]

[1]*Department of Mathematics and Statistics, Manipal University Jaipur, Rajasthan 303007, India*
[2]*Department of Humanities and Management, Jigme Namgyel Engineering College, Royal University of Bhutan, Dewathang, Bhutan*

Correspondence should be addressed to Reema Jain; reemajain197@gmail.com and Sonam Gyeltshen; sonamgyeltshen@jnec.edu.bt

Received 7 March 2022; Revised 19 April 2022; Accepted 21 April 2022; Published 23 May 2022

Academic Editor: Arshad Riaz

The current analysis provides the important insights of Sisko nanofluid flow over a wedge with thermal radiation and viscous dissipation effects. The Buongiorno nanofluid model, which includes Brownian movement and thermophoresis, is taken into consideration. Momentum, temperature, and nanoparticle concentration equations are used to simulate the current problem. The suitable similarity variables are applied to the governing partial differential equations (PDEs) which yield the dimensionless ordinary differential equations (ODEs). The MATLAB function bvp4c has been used to resolve the resulting ODEs. The attributes of various flow parameters on the transfer rate of mass, heat, temperature, velocity, and nanoparticle concentration have been explored. The pressure gradient parameter boosts the mass transfer and velocity. Moreover, mixed convection leads to the decrement in thermal and nanoparticle concentration boundary layer. The obtained numerical findings are compared to published results in the literature by considering the particular cases to validate the current study and are seen to be in perfect accord.

1. Introduction

In aerodynamics, geothermal systems, and many other fields, convective flow across a wedge has been discussed extensively. The flow over a wedge is significant because each wedge angle generates a distinct pressure profile, providing insight into boundary layer behaviour in a variety of conditions. Skan [1] was the first to propose a flow arrangement on the wedge. Since then, many researchers have investigated wedge and produced several useful discoveries, including Yih [2], Sattar [3], Turkyilmazoglu [4], Raju and Sandeep [5], Kudenatti et al. [6], Awaludin et al. [7], and many others. Khan and Pop [8] investigated the problem of steady boundary layer flow of nanofluid past a stretchy wedge. For solving the governing system, they employed the implicit finite-difference technique. Rajagopal et al. [9] extended the problem of flow field across a wedge to the problem of non-Newtonian fluid, where fluid of a second grade is examined. Many more studies of the flow field across a wedge were then investigated [10–12]. The steady 2D magnetohydrodynamic wedge flow of micropolar fluid in the presence of fluctuating wall temperature was explored by Ishaq et al. [13]. The boundary layer flows particularly for non-Newtonian fluids over stretched surfaces have been widely discussed by the researchers [14–18]. The Sisko fluid model [19] is one of the most essential models among non-Newtonian fluid models since it accurately describes a few non-Newtonian fluids. It may be assessed as a broad view of Newtonian and power-law fluids. Dadhich and Jain [20] examined some important characteristics of the fluid flow over an exponential surface in the Sisko model. The Falkner–Skan wedge flow of a power-law fluid through a porous material was studied by several researchers, including Kim [21]. Munir et al. [22] investigated convective heat transfer in Sisko nanofluid past a wedge. They applied the unique similarity transformations for converting the physical system. The boundary layer flow of a power-law fluid past a porous stretching wedge was studied by Postelnicu and Pop [23]. Das et al. [24] investigated how different fluid characteristics affect nanofluid flow over a wedge. The flow study was done with the effect of surface slip in account. The wedge flow of a power-law fluid in a porous medium was analyzed by Hassanien et al. [25]. Khan and Shahzad [26] explored Sisko fluid's Falkner–Skan boundary layer movement.

Bano et al. [27] used analytical methods to investigate the stretching wedge of Casson fluid with varied effects.

Enhancement of heat transfer is essential in improving performances and compactness of electronic devices. Usual cooling agents (water, oil, etc.) have relatively small thermal conductivities, and therefore heat transfer is not very efficient. Thus, to augment thermal characteristics, very small size particles (nanoparticles) were added to fluids forming the so-called nanofluids. These suspensions of nanoparticles in fluids have physical and chemical properties depending on the concentration and the shape of particles. It is observed that adding a little amount of nanoparticles to a base fluid increases the thermal conductivity of the fluid significantly. Loganathan et al. [28] investigated 3D flow of viscoelastic nanofluid over an bidirectional stretched surface. They applied the homotopy analysis method and concluded that heat as well as mass transportation is significantly affected by Brownian motion and thermophoresis. Wakif et al. [29] examined the impact of heat and mass transfer mechanisms on convective motion near a heated extending sheet embedded horizontally in a bi-phasic medium containing a certain volume fraction of alumina nanoparticles (Al_2O_3) dispersed completely in a micropolar fluidic medium containing 60% ethylene glycol ($C_2H_6O_2$) ($C_2H_6O_2$ *EG*) and 40% pure water (H_2O). Ashraf et al. [30], using the extended differential quadrature approach, quantitatively investigated the peristaltic flow of a blood-based nanofluid. After completing the thorough literature review, the authors observed that no attempt has been made to fully comprehend the transportation of heat and mass in the Sisko model with suspended nanoparticles over a wedge including viscous dissipation effect. Bhatti and Abdelsalam [31] investigated the peristaltically driven movement of Carreau fluid in a symmetric channel under the effect of a generated and applied magnetic field. They used the tantalum (Ta) and gold (Au) nanoparticles in the hybrid nanofluid with thermal radiation effects. Lubrication theory is used to complete the mathematical framework.

High-temperature plasmas, glass manufacturing, and liquid metal fluids all benefit from heat transfer analysis of boundary layer flow with radiation. These transport phenomena difficulties are particularly non-linear when linked with thermal convection processes. Thermal radiation alters the temperature distribution in the boundary layer at high temperatures, which impacts heat transfer at the wall. Multiphysical radiative-convective fluxes have been the subject of a number of research studies [32–35].

The purpose of this analysis is to examine the magneto-mixed convective Sisko nanofluid over a wedge with viscous dissipation. We extended Sisko nanofluid over a wedge from Macha et al. [36]. But we introduce new similarity variables [22, 26] for constructing a mathematical model. The governing partial differential equations are changed into non-linear ordinary differential equations, which are numerically solved by applying MATLAB bvp4c solver. The obtained numerical findings are compared to published results in the literature by considering the particular cases to validate the current study and are seen to be in perfect accord. The current issue has not yet been published in the scientific literature, and it is important to polymeric manufacturing processes and nuclear waste simulations, to the best of the authors' knowledge.

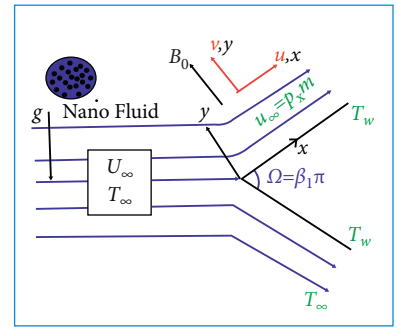

Figure 1: Geometry of physical model.

2. Flow Analysis

In the presence of heat source, radiated laminar flow of Sisko nanofluid is investigated. Heat and mass transport phenomena are considered and discussed. The flow is steady and two-dimensional as illustrated in Figure 1. Rectangular coordinate system is used, where x-axis and y-axis are aligned alongside and perpendicular to wedge surface, respectively. Free stream velocity is considered as u_∞ where $u_\infty(x) = Px^m$ (P is a positive constant). The wedge angle $\Omega = \pi\beta_1$ where $\beta_1 = 2m/m + 1$. Besides, it is assumed that temperature T and nanoparticle fraction C take constant values T_w and C_w, respectively, on the surface of wedge. The ambient temperature and concentration are denoted by T_∞ and C_∞, respectively. A uniform magnetic field B0 is imposed transverse to the wedge surface.

Based on these assumptions, equations for conservation of mass, momentum, thermal energy, and nanoparticle concentration for Sisko nanofluids can be stated as [12, 18, 20]

$$\frac{\partial u}{\partial x} + \frac{\partial v}{\partial y} = 0, \tag{1}$$

$$\begin{aligned} u\frac{\partial u}{\partial x} + v\frac{\partial u}{\partial y} = u_\infty \frac{\mathrm{d}u_\infty}{\mathrm{d}x} + \frac{\epsilon_1}{\rho}\frac{\partial^2 u}{\partial y^2} - \frac{\epsilon_2}{\rho}\frac{\partial}{\partial y}\left(-\frac{\partial u}{\partial y}\right)^n \\ - \frac{\sigma {B_0}^2 u}{\rho} + g\beta(T - T_\infty)\sin\left(\frac{\Omega}{2}\right) \\ + g\beta^*(C - C_\infty)\sin\left(\frac{\Omega}{2}\right), \end{aligned} \tag{2}$$

$$\begin{aligned} u\frac{\partial T}{\partial x} + v\frac{\partial T}{\partial y} = \frac{k}{(\rho C_p)_f}\frac{\partial^2 T}{\partial y^2} + \tau\left[D_B\frac{\partial C}{\partial y}\frac{\partial T}{\partial y} + \frac{D_T}{T_\infty}\left(\frac{\partial T}{\partial y}\right)^2\right] \\ - \frac{1}{(\rho C_p)_f}\frac{\partial q_r}{\partial y} + \frac{Q}{(\rho C_p)_f}(T - T_\infty) \\ + \frac{\mu}{(\rho C_p)_f}\left(\frac{\partial u}{\partial y}\right)^2 + \frac{\sigma {B_0}^2 u^2}{(\rho C_p)_f}, \end{aligned} \tag{3}$$

$$u\frac{\partial C}{\partial x} + v\frac{\partial C}{\partial y} = D_B\frac{\partial^2 C}{\partial y^2} + \frac{D_T}{T_\infty}\frac{\partial^2 T}{\partial y^2}. \tag{4}$$

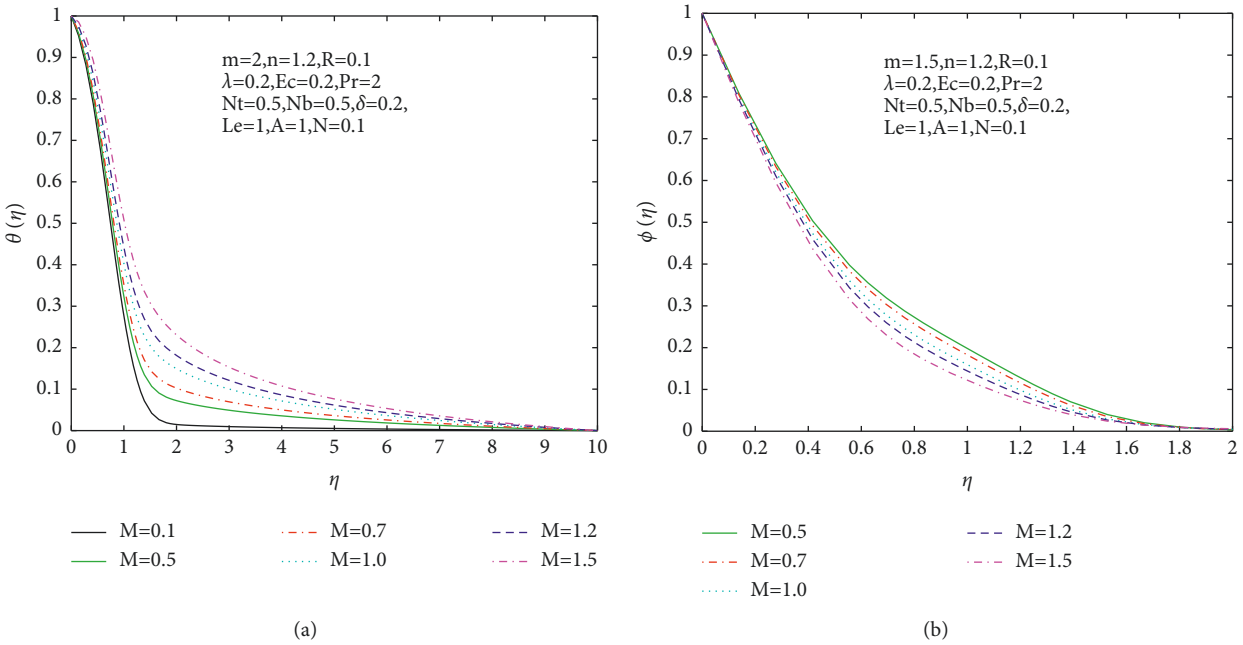

Figure 2: (a) θ Vs M. (b) Φ Vs M.

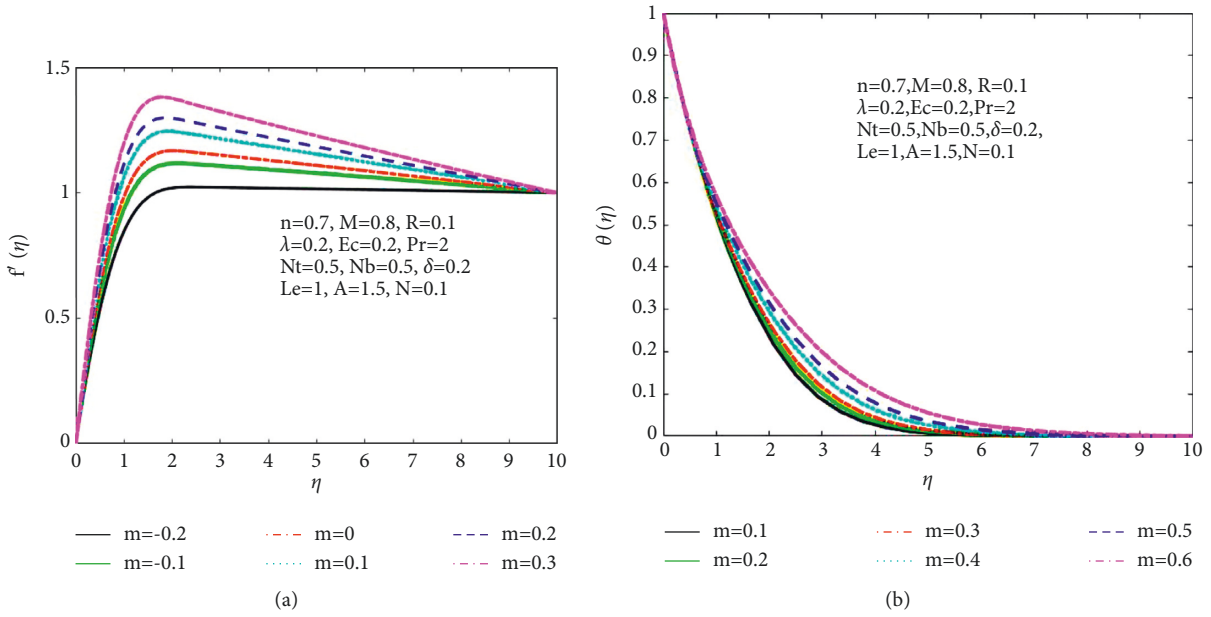

Figure 3: (a) f' Vs m. (b) θ Vs m.

The boundary conditions are

$$\text{at } y = 0: u = 0; v = 0; T = T_w; C = C_w, \tag{5}$$

$$\text{at } y \longrightarrow \infty: u = u_\infty = Px^m, v \longrightarrow 0, T \longrightarrow T_\infty, C \longrightarrow C_\infty. \tag{6}$$

Here ϵ_1, ϵ_2, and $n(>0)$ are material constants; $\alpha_f = k/\rho C_p$ is the thermal diffusivity; ϑ is the kinematic viscosity; C_p is the specific heat of the fluid; k is the thermal conductivity; $\tau = (\rho C_p)_p/(\rho C_p)_f$ is the proportion of the heat capacity of nanoparticles to that of the base fluid; D_B is the Brownian diffusion; D_T is the thermophoretic diffusion; and q_r is the radiative heat flux.

The following non-dimensional variables are proposed [22, 26]:

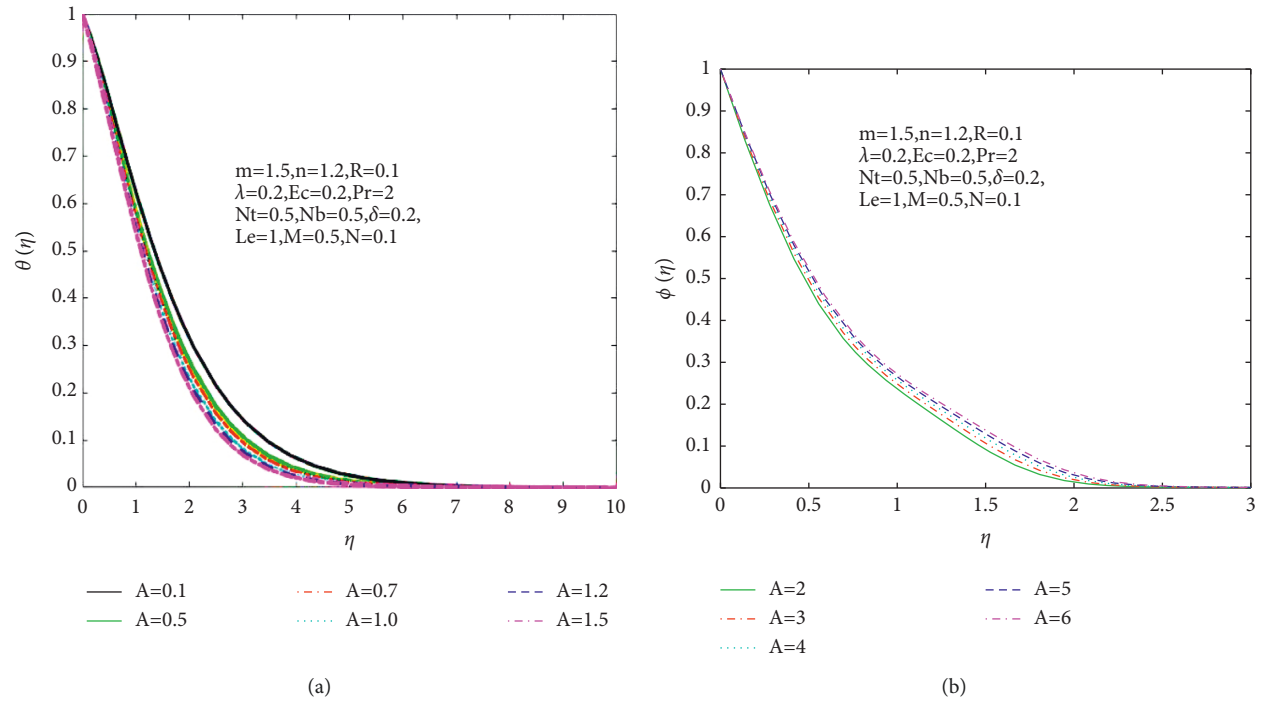

Figure 4: (a) θ Vs A. (b) Φ Vs A.

$$\eta = \frac{y}{x}(\mathrm{Re}_b)^{1/(n+1)},$$
$$u = u_\infty f'(\eta),$$
$$v = -u_\infty (\mathrm{Re}_b)^{-1/(n+1)}[(m+1)f - \eta f'], \quad (7)$$
$$\theta(\eta) = \frac{T - T_\infty}{T_w - T_\infty},$$
$$\phi(\eta) = \frac{C - C_\infty}{C_w - C_\infty}.$$

The Rosseland diffusion flux model can be defined as follows:

$$q_r = -\frac{4\sigma^*}{3k^*}\frac{\partial T^4}{\partial y}. \quad (8)$$

Usually, T^4 is expressed as a linear function of temperature, and applying Taylor's expansion (ignoring higher-order terms), it takes the form

$$T^4 = 4T_\infty^3 - 3T_\infty^4. \quad (9)$$

The following set of ODEs may be obtained by using (7), (8), and (9) in equations (2)–(6):

$$Af''' + n(-f'')^{n-1}f''' + Mf' - mf'^2 + (m+1)ff'' + m + \lambda\{\theta + N\phi\}\sin\left(\frac{\Omega}{2}\right) = 0,$$
$$\left(1 + \frac{4R}{3}\right)\theta'' + P_r\left[(m+1)f\theta' + N_b\theta'\phi' + N_t\theta'^2\right] + \delta P_r\theta + MP_rE_cf'^2 + E_cf''^2 = 0,$$
$$\phi'' + P_rL_e(m+1)f\phi' + \left(\frac{N_t}{N_b}\right)\theta'' = 0. \quad (10)$$

Transformed boundary conditions are

$$\text{at } \eta = 0:\ f(\eta) = 0, f'(\eta) = 0, \theta(\eta) = 1, \phi(\eta) = 1,$$
$$\text{at } \eta \longrightarrow \infty:\ f'(\eta) = 1, f(\eta) = 1, \theta(\eta) = 0, \phi(\eta) = 0. \quad (11)$$

Here prime implies the differentiation with respect to η, and the non-dimensional terms are described as

$$M = \frac{\sigma B_0^2 x}{\rho u_\infty}; P_r = \frac{\vartheta}{\alpha_f}; N_b = \frac{\tau D_B(C_w - C_\infty)}{\vartheta};$$
$$N_t = \frac{\tau D_T(T_w - T_\infty)}{\vartheta T_\infty}; L_e = \frac{\alpha_f}{D_B}; R = \frac{4\sigma^* T_\infty^3}{k^* k},$$
$$\delta = \frac{Qx}{\rho c_p u_\infty}; E_c = \frac{(u_\infty)^2}{(c_p)_f(T_w - T_\infty)}; \mathrm{Re}_a = \frac{\rho x u_\infty}{\epsilon_1}; \quad (12)$$
$$R_{e_b} = \frac{\rho x(u_\infty)^{(2-n)}}{\epsilon_2}; A = \frac{(\mathrm{Re}_b)^{2/(n+1)}}{\mathrm{Re}_a},$$
$$N = \frac{\beta^*(C_w - C_\infty)}{\beta(T_w - T_\infty)}; \lambda = \frac{G_{r_x}}{(\mathrm{Re}_x)^2}; G_{r_x} = \frac{g\beta(T_w - T_\infty)x^3}{4\vartheta^2}.$$

2.1. Coefficients of Heat and Mass Transport. The main goal of this study is to figure out what factors are important to engineers when they deal with heat and nanoparticle mass transfer. The engineering interests of the physical quantities are defined below: local Nusselt number $N_{u_x} = (xq_w/k(T_w - T_\infty))_{y=0}$ and local nanofluid Sherwood number is given by $Sh_x = (xq_w/D_B(C_w - C_\infty))_{y=0}$; where $q_w = -k(\partial T/\partial y)_{y=0}$ is wall heat flux. Using above-mentioned transformations, these

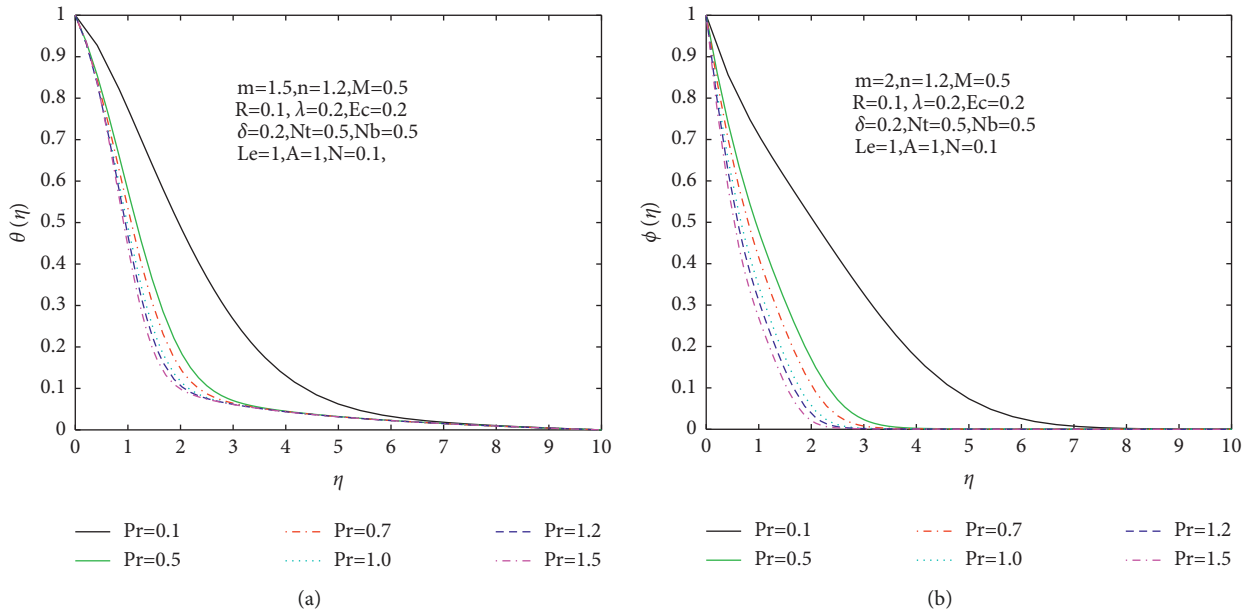

Figure 5: (a) θ Vs Pr. (b) Φ Vs Pr.

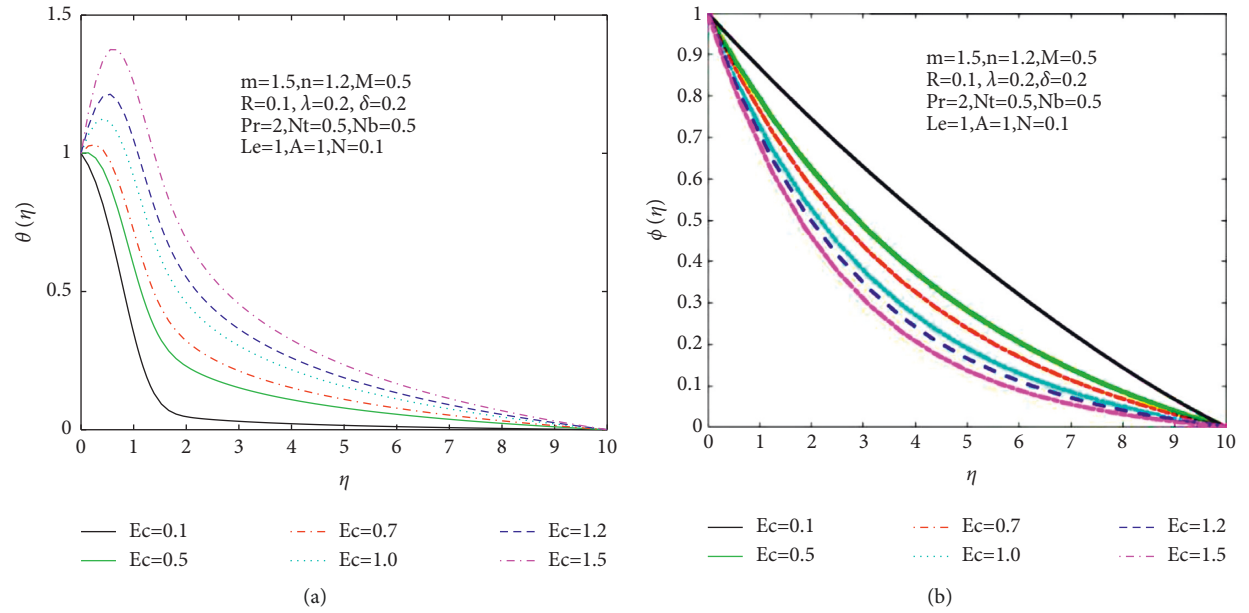

Figure 6: (a) θ Vs *Ec*. (b) Φ Vs *Ec*.

parameters will reduce to $(\mathrm{Re}_b)^{-1/(n+1)} N_{u_x} = -(1 + 4R/3)\theta'(0)$ and $(\mathrm{Re}_b)^{-1/(n+1)} Sh_x = -\phi'(0)$.

3. Numerical Computation

The above-mentioned system of non-linear ODEs along with boundary conditions is solved by applying MATLAB bvp4c code. Thus, the system is converted to first-order ODEs using the mathematical algorithm which is appended below ((13)–(29)). "Boundary conditions defined at infinity are addressed by fixing it at a finite value, for example, $\eta_\infty = 10$ implies that variable is confined in $0 \le \eta \le 10''$. Calculations are performed numerically using an interval $\Delta\eta = 0.01$, 10^{-3} is a convergent criterion to repeated and attain the numeric solution.

$$f = g_1, \tag{13}$$

$$f' = g_2, \tag{14}$$

$$f'' = g_3, \tag{15}$$

$$f''' = g_3', \tag{16}$$

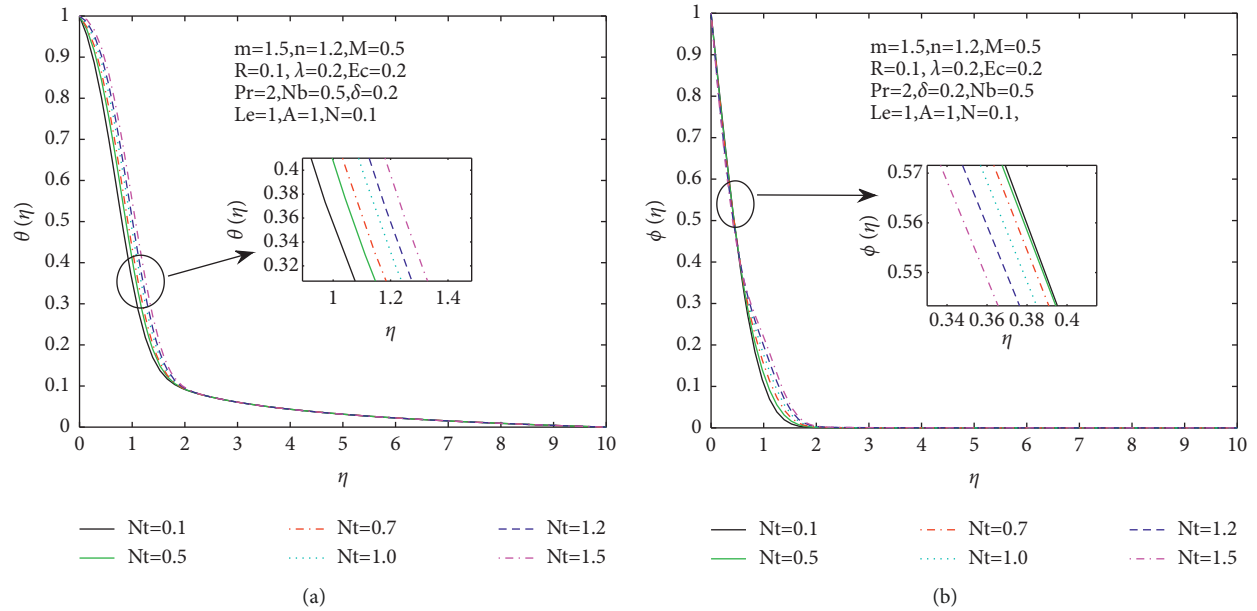

Figure 7: (a) θ Vs N_t. (b) Φ Vs N_t.

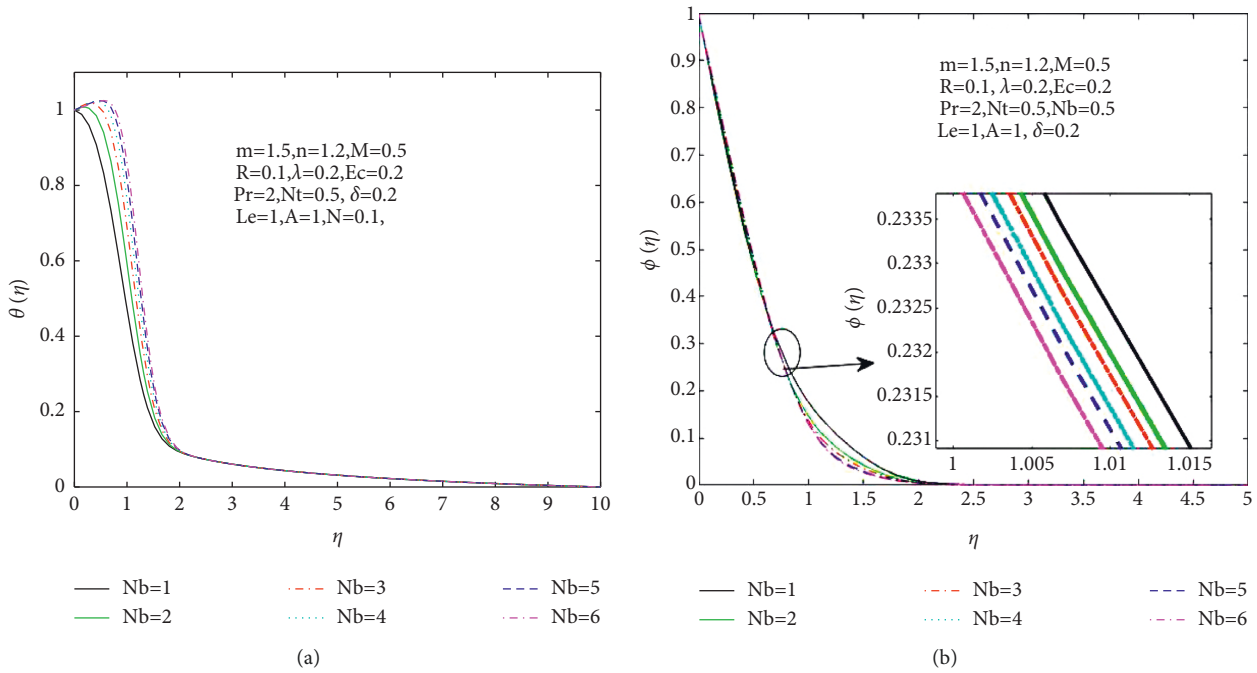

Figure 8: (a) θ Vs N_b. (b) Φ Vs N_b.

$$\theta = g_4, \tag{17}$$

$$\theta' = g_5, \tag{18}$$

$$\theta'' = g_5', \tag{19}$$

$$\phi = g_6, \tag{20}$$

$$\phi' = g_7, \tag{21}$$

$$\phi'' = g_7', \tag{22}$$

$$f''' = \frac{g_2{}^2 m - M g_2 - m - (m+1) g_1 g_3 - \lambda \{g_4 + N g_6\} \sin(\Omega/2)}{A + (-1)^{n-1} n (g_3)^{n-1}}, \tag{23}$$

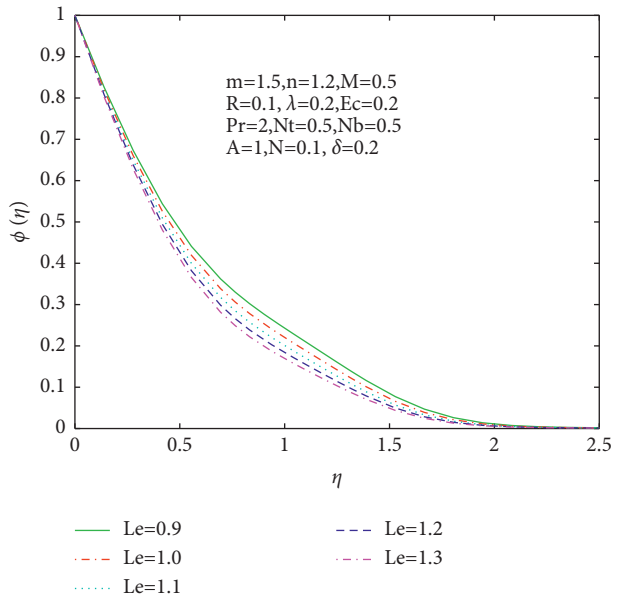

Figure 9: Φ Vs *Le*.

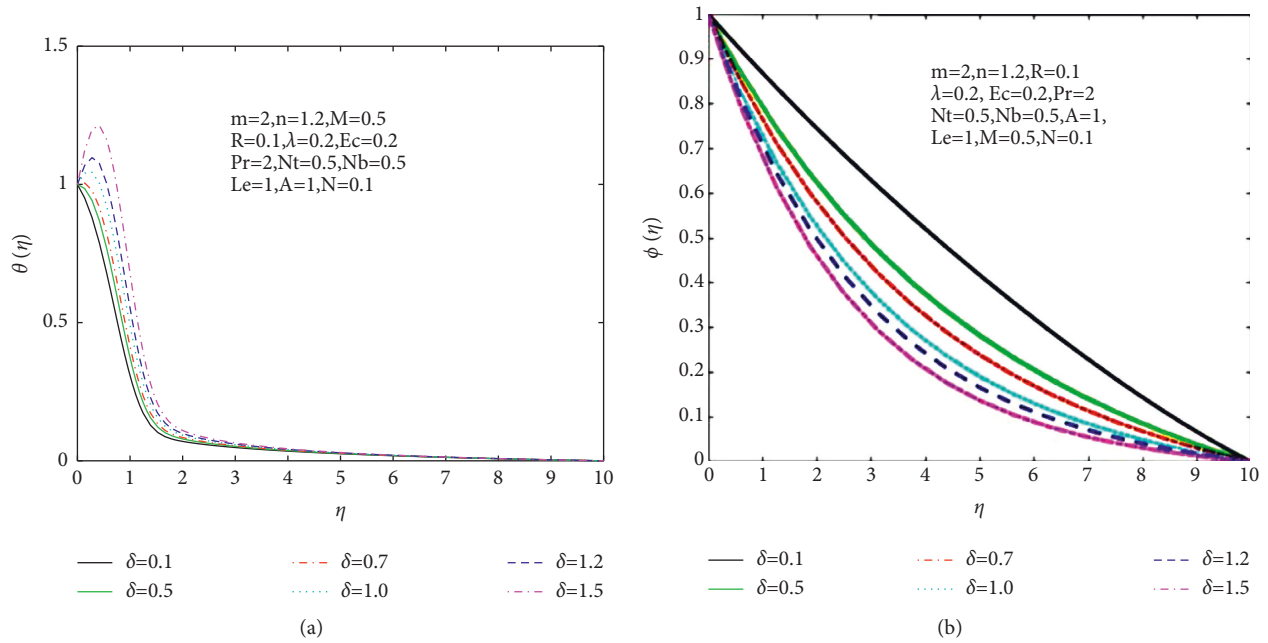

Figure 10: (a) θ Vs δ. (b) Φ Vs δ.

$$\theta'' = g_5{}' = \frac{\left[P_r(m+1)g_1g_5 + \delta P_r g_4 + E_c(g_3)^2 + MP_rE_cg_2^2 + P_r\left(N_bg_5g_7 + N_tg_5^2\right)\right]}{-(1+4R/3)}, \tag{24}$$

$$\phi'' = g_7' = -\left[P_rL_e(m+1)g_1g_7 + \frac{N_t}{N_b}{}'g_5\right]. \tag{25}$$

Using boundary conditions:

$$g_0(1) = 0, g_0(2) = 0, g_0(4) - 1 = 0, g_0(6) - 1 = 0, \tag{26}$$

$$g_1(2) - 1 = 0, g_1(1) - 1 = 0, g_1(4) = 0, g_1(6) = 0. \tag{27}$$

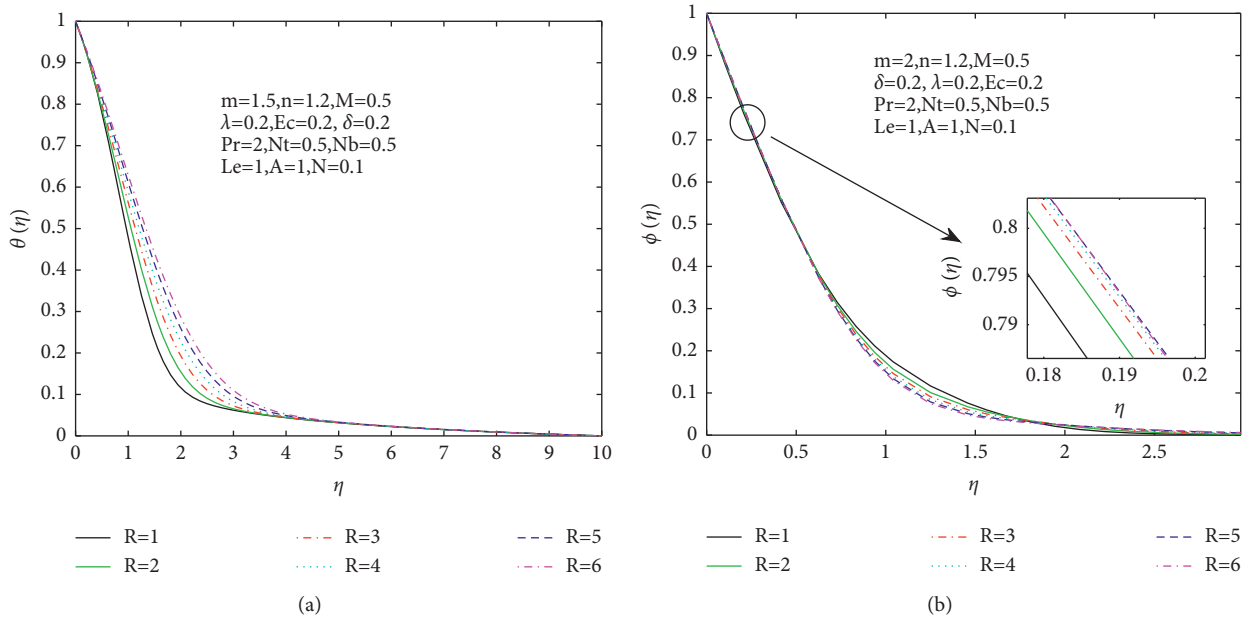

Figure 11: (a) θ vs R. (b) Φ Vs R.

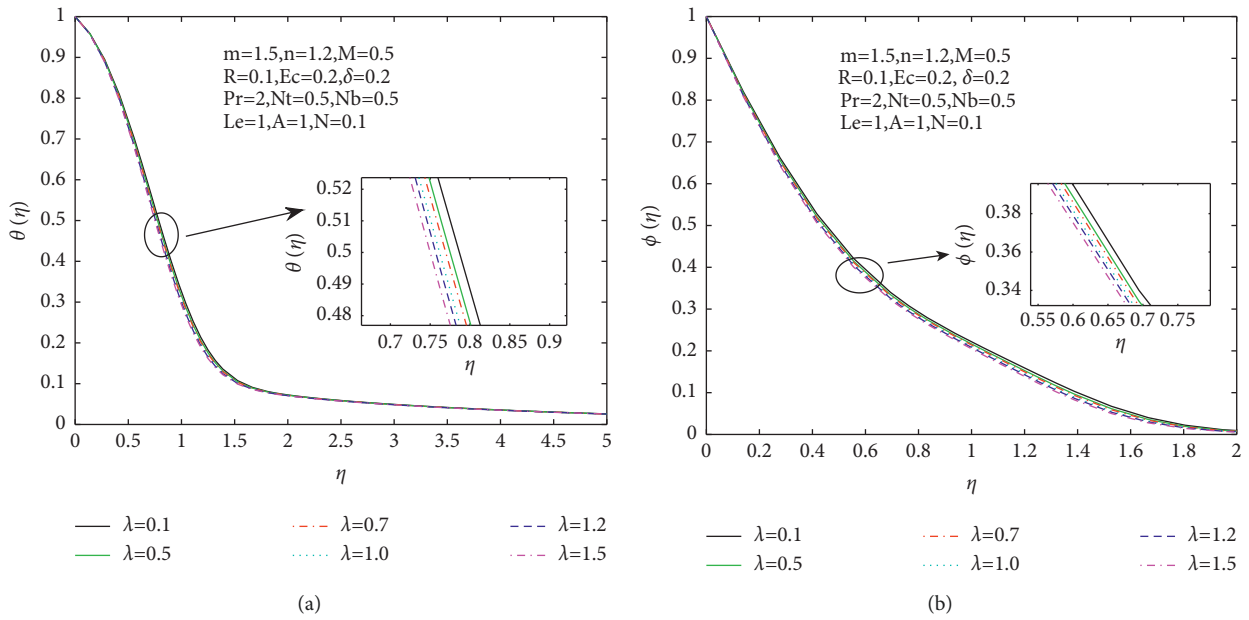

Figure 12: (a) θ Vs λ. (b) Φ Vs λ.

4. Result and Discussion

In this section, the impact of numerous physical parameters on temperature and concentration is demonstrated. The fixed values of physical parameters are $m = 1, M = 0.8, n = 1, R = 0.1, Ec = 0.2, A = 1, N = 0.1, Nb = 0.5, Nt = 0.5, Le = 1, \lambda = 0.2, \delta = 0.2$. These findings are summarized in Figures 2–17 and Tables 1 and 2. Figures 2(a) and 2(b) illustrate the graphs of temperature (θ) and concentration (ϕ) for different M. As strength of magnetic field is increased, it increases resistive force. Therefore, additional heat is produced which causes high temperature and concentration of nanoparticles decreases. The impact of m on fluid flow and heat is represented by Figures 3(a) and 3(b). This variation is due to m, which is associated with pressure gradient. Increasing values of m indicate a promising pressure gradient which improves the flow. Fluid temperature is also influenced by wedge angle. Figures 4(a) and 4(b) demonstrate the effect of A (material parameter) on θ and ϕ. Due to the fact that the material parameter has an inverse relationship with consistency index b (fluid's viscosity). As A increases, fluid viscosity decreases which causes less resistance for the fluid

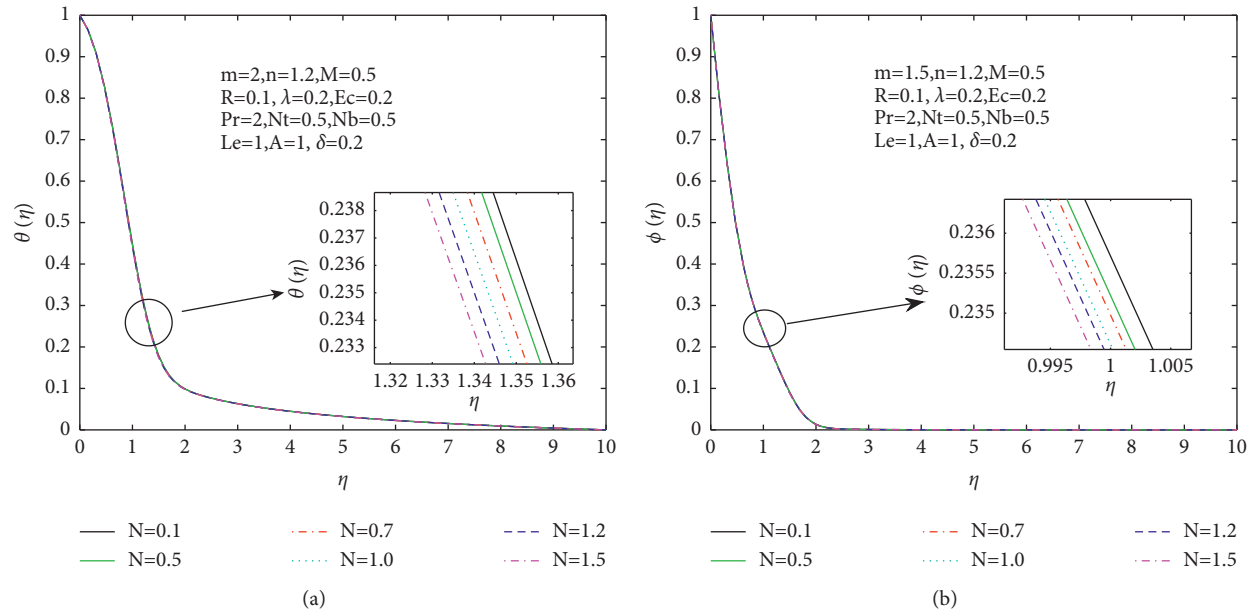

Figure 13: (a) θ Vs N. (b) Φ Vs N.

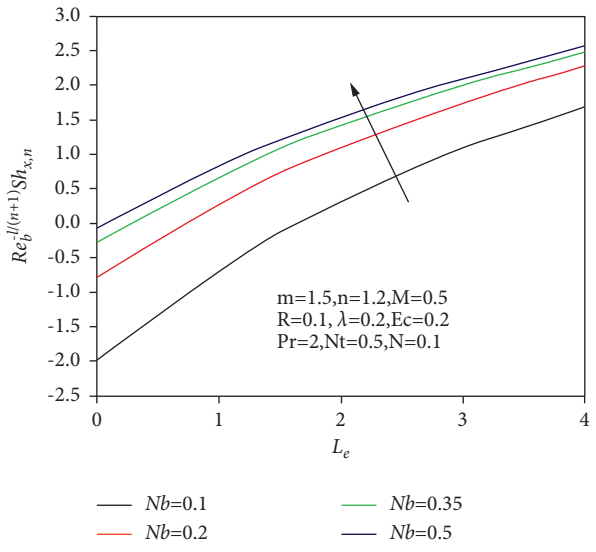

Figure 14: Change in $-\phi'(0)$ with L_e and N_b.

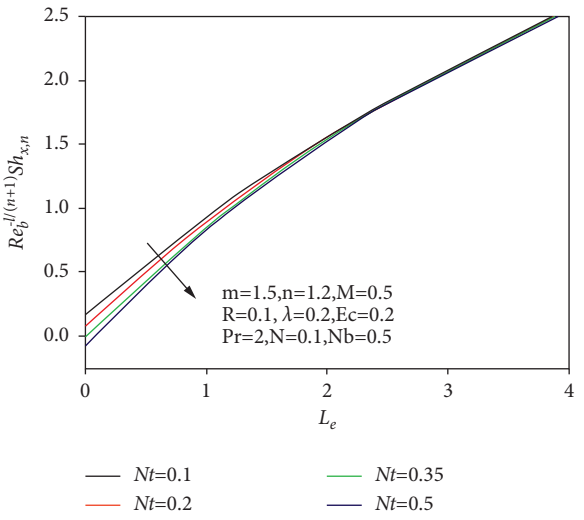

Figure 15: Change in $-\phi'(0)$ withL_e and N_t.

to move, and this increases the fluid velocity. As a result, an increase in material parameter A results in a decay of the temperature profile and a rise in concentration.

Figures 5(a) and 5(b) illustrate the influence of Pr on the distribution of heat and nanoparticle concentrations, respectively. The graph demonstrates that when Pr grows, the temperature of the fluid drops. Since Pr is inversely proportional to thermal diffusivity. Consequently, the temperature drops and the nanoparticle concentration is also reduced as Pr rises. The change in temperature and concentration as Ec varies is exhibited in Figures 6(a) and 6(b). It explains that increase in Ec enhances the temperature of fluid. As energy is accumulated in fluid due to frictional heating, nanoparticle concentration decreases. Figures 7(a) and 7(b) depict the effect of N_t on θ and ϕ. Growing N_t causes particles to move more quickly, raising the fluid temperature. Furthermore, when N_t increases, the nanoparticle concentration nearest to the surface drops and rises away from it. As N_t increases, more particles are expelled off the heated surface, causing the concentration to increase. Additionally, as seen in Figures 8(a) and 8(b), the parameter N_b has an effect on the temperature and concentration of nanoparticles. With increasing N_b values, the concentration of nanoparticles in fluid falls.

Figure 9 shows a shift in concentration as Le increases. Evidently, ϕ reduces as Le increases. This is because Le has an inverse relationship with D_B, which is associated with N_b. Thus, an increase in Le lowers the thermal diffusivity, causing a decrease in the speed in boundary layer area. Figures 10(a) and 10(b) illustrate temperature and concentration patterns for different δ (which is >0). By

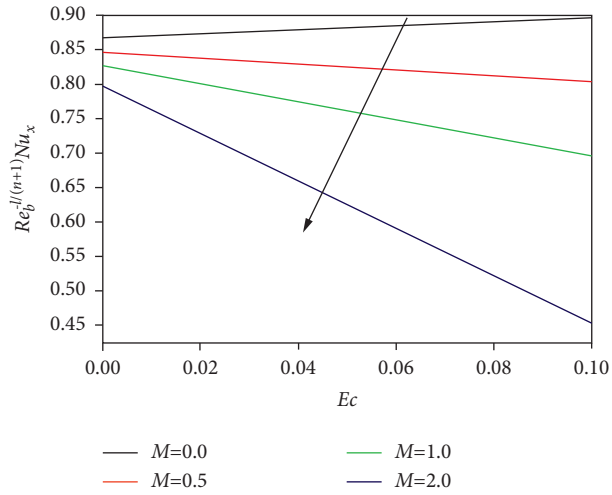

Figure 16: Change in $-\theta'(0)$ with M and Ec.

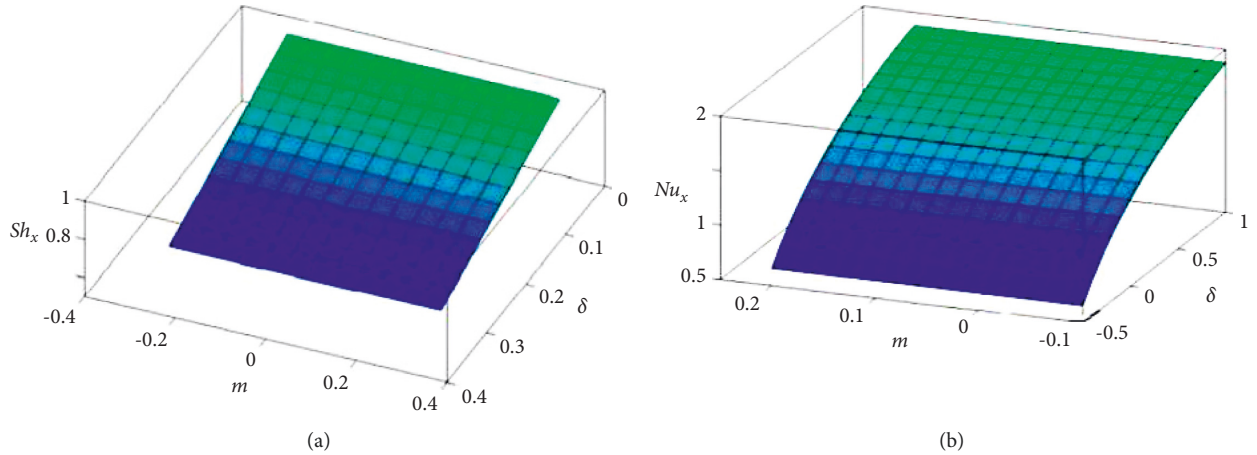

Figure 17: (a) 3D plot of $(\mathrm{Re}_b)^{-1/(n+1)}Sh_x$ for m and δ. (b) 3D plot of $(\mathrm{Re}_b)^{-1/(n+1)}N_{u_x}$ for m and δ.

Table 1: Comparative study of $f''(0)$ and $-\theta'(0)$ of $M = 0.5$, $Ec = 0.2$, $R = 0.1$, and $A = 1$.

m	Gaffar et al. [37]		Current study	
	$\mathbf{f}''(0)$	$-\theta'(0)$	$\mathbf{f}''(0)$	$-\theta'(0)$
0.1	0.4914	0.2083	0.4900	0.2292
0.2	0.5589	0.2122	0.5569	0.2362
0.3	0.6259	0.2162	0.6213	0.2376
0.4	0.6917	0.2202	0.6901	0.2426

enhancing δ, the temperature scales are increased but reduction is observed in concentration values. Consequently, the concentration decreases. A similar trend is observed for temperature and concentration when R increases as shown in Figures 11(a) and 11(b). High values of R result in a higher temperature of fluid.

Figures 12(a) and 12(b) indicate temperature and concentration profiles with different λ. Clearly, it is concluded that increment in λ causes the decline in fluid's temperature and similar behaviour is observed for the concentration. Likewise, the increasing values of N reduce both temperature and concentration as depicted in Figures 13(a) and 13(b). Figure 14 shows that increment in L_e causes decay in concentration profile. Hence, nanofluid's Sherwood number $-\phi'(0)$ is enhanced. Instead, Figure 15 reveals that the nanofluid's Sherwood number decreases with N_t. Also, Figure 16 shows the diminishing tendency of local Nusselt number as Ec and M increase. Figures 17(a) and 17(b) show that heat and mass transfer rates increase as m increases. Increasing δ values cause a decrease in heat transfer while mass transfer increases.

Table 1 compares the local skin friction and Nusselt number for different m, and it is pretty evident that the conclusions of the current analysis are consistent with those of other researchers. Table 2 shows the variation of heat and mass transfer rate with respect to change in m, N, Pr, λ, and δ. It is perceived that heat transfer rate shows an increasing behaviour when the values of all the parameters are rising; however, when δ is increasing, the heat transfer rate is decreasing. Also, the rate of mass transfer enhances with the increase of the value of m.

Table 2: Nu_x and Sh_x for various values of m, N, Pr, λ, and δ taking $n = 1.2$, $M = 0.5$, $Ec = 0.2$, $R = 0.1$, and $A = 1$.

m	N	Pr	λ	δ	$(\mathrm{Re}_b)^{-1/(n+1)}\mathbf{N_{u_x}}$ (heat transfer rate)	$(\mathrm{Re}_b)^{-1/(n+1)}\mathbf{Sh_x}$ (mass transfer rate)
0.2	0.1	0.7	0.2	0.2	0.2362	0.3235
	0.5				0.2372	0.3265
	1.0				0.2383	0.3295
	0.5	0.5	0.2		0.2321	0.3251
		1.0			0.2431	0.3249
		2.0			0.2659	0.3245
	0.1	0.7	0.1		0.2336	0.3261
			0.2		0.2362	0.3335
			0.5		0.2384	0.3392
0.2	0.1	0.7	0.2		0.2362	0.3235
0.3					0.2373	0.3398
0.4					0.2426	0.3531
0.2	0.1	0.7	0.2	0.0	0.2726	0.3235
				0.2	0.2362	0.3236
				0.4	0.2203	0.3342

5. Conclusion

In the present work, analysis of heat and mass transfer in the Sisko model with suspended nanoparticles over a wedge including viscous dissipation effect is investigated. The effects of the wedge angle parameter, nanoparticle volume fraction, radiation, heat generation/absorption, and other variables are explored and presented graphically. For many physical parameters, numerical values of rate of heat and mass transport are provided, and noteworthy aspects are explained in depth. The obtained numerical findings are compared to published results in the literature by considering the particular cases to validate the current study and are seen to be in perfect accord. The following is a summary of the key findings of this study:

(i) The higher values of pressure gradient parameter (m) lead to the rising phenomena in the velocity profile.

(ii) While a material parameter (A) is increased, the temperature profile decays and the concentration rises.

(iii) Prandtl and Schmidt numbers affect mass concentration reversely.

(iv) Thermal and solutal boundary layers are declined due to the augmentation in mixed convection parameter (λ).

(v) Increasing values of magnetic field and Eckert number will produce a diminishing behaviour in heat transfer rate.

(vi) Mass transfer rate is more pronounced for higher values of pressure gradient parameter.

Abbreviations

A: Material parameter (dimensionless)
B_0: Magnetic field strength (kg $s^{-2}A^{-1}$)
C: Concentration (kg m^{-3})
C_∞: Ambient concentration (kg m^{-3})
C_w: Sheet concentration (kg m^{-3})
c_p: Specific heat (J kg^{-1} K^{-1})
D_B: Coefficient of Brownian diffusion (m^2 s^{-1})
D_T: Coefficient of thermophoretic diffusion (m^2 s^{-1})
E_c: Eckert number (dimensionless)
k: Thermal conductivity (W m^{-1} K^{-1})
L_e: Lewis parameter (dimensionless)
m: Pressure gradient parameter
M: Magnetic field parameter (dimensionless)
N: Concentration to thermal buoyancy ratio parameter
N_b: Brownian diffusion parameter (dimensionless)
N_t: Thermophoresis parameter (dimensionless)
Nu_x: Local Nusselt number (dimensionless)
P_r: Prandtl number (dimensionless)
q_r: Radiative heat flux (Wm^{-2})
R: Radiation parameter (dimensionless)
Re_a, Re_b: Local Reynolds numbers (dimensionless)
Sh_x: Sherwood number (dimensionless)
T: Fluid temperature (K)
T_w: Sheet temperature (K)
T_∞: Ambient fluid temperature (K)
u, v: Velocity components (m s^{-1})
x, y: Cartesian coordinates (m)
G_{r_x}: Local Grashof number (dimensionless)
α_f: Thermal diffusivity (m^2s^{-1})
β: Coefficient of thermal expansion (K^{-1})
β^*: Coefficient of concentration expansion
β_1: Wedge angle parameter
δ: Heat source/sink parameter (dimensionless)
η: Similarity parameter (dimensionless)
θ: Temperature similarity function (dimensionless)
ϕ: Concentration similarity function (dimensionless)
λ: Mixed convection parameter (dimensionless)
ϑ: Kinematic viscosity (m^2s^{-1})
ρ: Density (kg m^{-1})
τ: Ratio of the effective heat capacity
σ: Electrical conductivity (S m)
f: Fluid phase
∞: Ambient condition
w: Surface condition.

Data Availability

No data were used to support this study.

Conflicts of Interest

The authors declare that there are no conflicts of interest.

Authors' Contributions

All authors contributed equally to this work. All authors have read and approved the final version of the manuscript.

References

[1] F. Skan, "Philosophical," *Magazine*, vol. 12, pp. 865–896, 1931.

[2] K. A. Yih, "Uniform suction/blowing effect on forced convection about a wedge: uniform heat flux," *Acta Mechanica*, vol. 128, no. 3-4, pp. 173–181, 1998.

[3] M. A. Sattar, "A local similarity transformation for the unsteady twodimensional hydrodynamic boundary layer equations of a flow past a wedge," *International Journal of Applied Mathematics and Mechanics*, vol. 7, pp. 15–28, 2011.

[4] M. Turkyilmazoglu, "Slip flow and heat transfer over a specific wedge: an exactly solvable Falkner-Skan equation," *Journal of Engineering Mathematics*, vol. 92, no. 1, pp. 73–81, 2015.

[5] C. S. K. Raju and N. Sandeep, "Nonlinear radiative magnetohydrodynamic Falkner-Skan flow of Casson fluid over a wedge," *Alexandria Engineering Journal*, vol. 55, no. 3, pp. 2045–2054, 2016.

[6] R. B. Kudenatti, S. R. Kirsur, A. L. Nargund, and N. M. Bujurke, "Similarity solutions of the MHD boundary layer flow past a constant wedge within porous media," *Mathematical Problems in Engineering*, vol. 2017, Article ID 1428137, 11 pages, 2017.

[7] I. S. Awaludin, A. Ishak, and I. Pop, "On the stability of MHD boundary layer flow over a stretching/shrinking wedge," *Scientific Reports*, vol. 8, no. 1, pp. 13622–13628, 2018.

[8] W. A. Khan and I. Pop, "Boundary layer flow past a wedge moving in a nanofluid," *Mathematical Problems in Engineering*, vol. 20137 pages, Article ID 637285, 2013.

[9] K. R. Rajagopal, A. S. Gupta, and T. Y. Na, "A note on the falkner-skan flows of a non-Newtonian fluid," *International Journal of Non-linear Mechanics*, vol. 18, no. 4, pp. 313–320, 1983.

[10] M. J. Martin and I. D. Boyd, "Falkner-Skan flow over a wedge with slip boundary conditions," *Journal of Thermophysics and Heat Transfer*, vol. 24, no. 2, pp. 263–270, 2010.

[11] K.-L. Hsiao, "MHD mixed convection for viscoelastic fluid past a porous wedge," *International Journal of Non-linear Mechanics*, vol. 46, no. 1, pp. 1–8, 2011.

[12] M. M. Rahman, M. A. Al-Lawatia, I. A. Eltayeb, and N. Al-Salti, "Hydromagnetic slip flow of water based nanofluids past a wedge with convective surface in the presence of heat generation (or) absorption," *International Journal of Thermal Sciences*, vol. 57, pp. 172–182, 2012.

[13] A. Ishak, R. Nazar, and I. Pop, "MHD Boundary-layer flow of a micropolar fluid past a wedge with variable wall temperature," *Acta Mechanica*, vol. 196, no. 1-2, pp. 75–86, 2008.

[14] T. Hayat, R. Sajjad, T. Muhammad, A. Alsaedi, and R. Ellahi, "On MHD nonlinear stretching flow of Powell-Eyring nanomaterial," *Results in Physics*, vol. 7, pp. 535–543, 2017.

[15] K. Loganathan, S. Sivasankaran, M. Bhuvaneswari, and S. Rajan, "Second-order slip, cross-diffusion and chemical reaction effects on magneto-convection of Oldroyd-B liquid using Cattaneo-Christov heat flux with convective heating," *Journal of Thermal Analysis and Calorimetry*, vol. 136, no. 1, pp. 401–409, 2019.

[16] R. S. Saif, T. Hayat, R. Ellahi, T. Muhammad, and A. Alsaedi, "Stagnation-point flow of second grade nanofluid towards a nonlinear stretching surface with variable thickness," *Results in Physics*, vol. 7, pp. 2821–2830, 2017.

[17] T. Hayat, R. S. Saif, R. Ellahi, T. Muhammad, and B. Ahmad, "Numerical study for Darcy-Forchheimer flow due to a curved stretching surface with Cattaneo-Christov heat flux and homogeneous-heterogeneous reactions," *Results in Physics*, vol. 7, pp. 2886–2892, 2017.

[18] Y. Dadhich, R. Jain, A. R. Kaladgi, M. Alwetaishi, A. Afzal, and C. A. Saleel, "Thermally radiated Jeffery fluid flow with nanoparticles over a surface of varying thickness in the influence of heat source," *Case Studies in Thermal Engineering*, vol. 28, no. 1, Article ID 101549, 2021.

[19] A. W. Sisko, "The flow of lubricating greases," *Industrial and Engineering Chemistry*, vol. 50, no. 12, pp. 1789–1792, 1958.

[20] Y. Dadhich and R. Jain, "Numerical solution of magnetohydrodynamic flow and heat transfer of sisko fluid over an exponential stretching sheet," *Journal of Physics: Conference Series*, vol. 1504, no. 1, Article ID 012005, 2020.

[21] Y. J. Kim, "The Falkner-Skan wedge flows of power-law fluids embedded in a porous medium," *Transp Porous Media*, vol. 44, no. 2, pp. 267–279, 2001.

[22] A. Munir, A. Shahzad, and M. Khan, "Convective flow of Sisko fluid over a wedge with viscous dissipation," *Journal of the Brazilian Society of Mechanical Sciences and Engineering*, vol. 38, no. 2, pp. 581–587, 2016.

[23] A. Postelnicu and I. Pop, "Falkner-Skan boundary layer flow of a power-law fluid past a stretching wedge," *Applied Mathematics and Computation*, vol. 217, no. 9, pp. 4359–4368, 2011.

[24] K. Das, N. Acharya, and P. K. Kundu, "Influence of variable fluid properties on nanofluid flow over a wedge with surface slip," *Arabian Journal for Science and Engineering*, vol. 43, no. 5, pp. 2119–2131, 2018.

[25] I. A. Hassanien, A. A. Abdullah, and R. S. R. Gorla, "Flow and heat transfer in a power-law fluid over a nonisothermal stretching sheet," *Mathematical and Computer Modelling*, vol. 28, no. 9, pp. 105–116, 1998.

[26] M. Khan and A. Shahzad, "Falkner-Skan boundary layer flow of a Sisko Fluid," *Zeitschrift für Naturforschung A*, vol. 67, no. 8-9, pp. 469–478, 2012.

[27] N. Bano, B. B. Singh, and S. R. Sayyed, "MHD heat transfer flow of Casson fluid with velocity and thermal slips over a stretching wedge in the presence of thermal radiation," *Diffusion Foundations*, vol. 26, pp. 1–22, 2020.

[28] K. Loganathan, N. Alessa, and S. Kayikci, "Heat transfer analysis of 3-D viscoelastic nanofluid flow over a convectively heated porous Riga plate with Cattaneo-Christov double flux," *Frontiers in Physics*, vol. 9, 2021.

[29] A. Wakif, M. Zaydan, A. Ali Saleh, T. Muhammad, and R. Sehaqui, "New insights into the dynamics of alumina-(60% ethylene glycol + 40% water) over an isothermal stretching sheet using a renovated Buongiorno's approach: a numerical GDQLLM analysis," *International Communications in Heat and Mass Transfer*, vol. 133, Article ID 105937, 2022.

[30] M. U. Ashraf, M. Qasim, A. Wakif, M. I. Afridi, and I. L. Animasaun, "A generalized differential quadrature algorithm for simulating magnetohydrodynamic peristaltic flow of blood-based nanofluid containing magnetite nanoparticles: a physiological application," *Numerical Methods for Partial Differential Equations*, vol. 38, pp. 666–692, 2022.

[31] M. M. Bhatti and S. I. Abdelsalam, "Bio-inspired Peristaltic Propulsion of Hybrid Nanofluid Flow with Tantalum (Ta) and Gold (Au) Nanoparticles under Magnetic Effects," *Waves in Random and Complex Media*, 2021.

[32] N. Acharya, "Spectral quasi linearization simulation on the radiative nanofluid spraying over a permeable inclined

spinning disk considering the existence of heat source/sink," *Applied Mathematics and Computation*, vol. 411, Article ID 126547, 2021.

[33] K. Loganathan and S. Rajan, "An entropy approach of Williamson nanofluid flow with Joule heating and zero nanoparticle mass flux," *Journal of Thermal Analysis and Calorimetry*, vol. 141, no. 6, pp. 2599–2612, 2020.

[34] Z. Sabir, A. Imran, M. Umar et al., "A numerical approach for 2-D sutterby fluid-flow bounded at a stagnation point with an inclined magnetic field and thermal radiation impacts," *Thermal Science*, vol. 25, pp. 1975–1987, 2021.

[35] K. Loganathan, K. Mohana, M. Mohanraj, P. Sakthivel, and S. Rajan, "Impact of third-grade nanofluid flow across a convective surface in the presence of inclined Lorentz force: an approach to entropy optimization," *Journal of Thermal Analysis and Calorimetry*, vol. 144, no. 5, pp. 1935–1947, 2020.

[36] M. Madhu, C. S. Reddy, and N. Kishan, "Magnetohydrodynamic flow and heat transfer to Sisko nanofluid over a wedge," *International Journal of Fluid Mechanics Research*, vol. 44, no. 1, pp. 1–13, 2017.

[37] S. A. Gaffar, V. R. Prasad, and E. Keshava Reddy, "Mixed convection boundary layer flows of a non-Newtonian Jeffrey's fluid from a non-isothermal wedge," *Ain Shams Engineering Journal*, vol. 8, no. 2, pp. 145–162, 2017.

Hindawi
Mathematical Problems in Engineering
Volume 2022, Article ID 9732083, 16 pages
https://doi.org/10.1155/2022/9732083

Research Article

Nonlinear Mixed Convective Bidirectional Dynamics of Double Stratified Radiative Oldroyd-B Nanofluid Flow with Heat Source/Sink and Higher-Order Chemical Reaction

Iftikhar Ahmad,[1] Muhammad Faisal,[1] K. Loganathan,[2] Muhammad Zaheer Kiyani,[1] and Ngawang Namgyel[3]

[1]*Department of Mathematics, Azad Jammu & Kashmir University, Muzaffarabad 13100, Pakistan*
[2]*Department of Mathematics and Statistics, Manipal University Jaipur, Jaipur 303007, Rajasthan, India*
[3]*Jigme Namgyel Engineering College, Royal University of Bhutan, Dewathang, Bhutan*

Correspondence should be addressed to Muhammad Faisal; muhammad.faisal@ajku.edu.pk, K. Loganathan; loganathankaruppusamy304@gmail.com, and Ngawang Namgyel; ngawangnamgyel@jnec.edu.bt

Received 29 December 2021; Revised 27 January 2022; Accepted 22 April 2022; Published 23 May 2022

Academic Editor: Mohsan Hassan

Little is known in the literature about the concept of nonuniform heat source/sink and higher-order chemical reaction for the dynamics of Oldroyd-B nanoparticles. Therefore, the present article addresses the nonuniform heat source/sink and higher-order chemical reaction features in nonlinear mixed convection bidirectional MHD dynamics of Oldroyd-B nanoparticles with thermal radiation aspects through porous space. Stratification effects for both the temperature and concentration setups are also used in the mathematical model with the significance of random movement and thermodiffusion of nanoparticles. Shape-preserving transformations have been employed to convert the transport equations into solvable forms. An innovative analytical tactic, namely, homotopy analysis method, has been adopted to find the solution of the modeled problem. Behaviors of pertinent parameters on thermal and concentration profiles have been discussed through various graphs. Inspection of heat/mass transport against appropriate varieties of pertinent parameters has been made and explained physically. Thermal profile is augmented with the higher estimations of space and temperature-dependent heat source/sink links. Concentration profile is diminished with the augmentation of higher-order chemical reaction parameter. Sherwood number is improved with the estimation of $0 \le \beta_t \le 100$ and is reduced with the growth of $0 \le \beta_c \le 100$. Nusselt number is declined with the upgraded amounts of $0 \le N_b \le 3$ and $0 \le N_t \le 5$.

1. Introduction

Rheology of non-Newtonian fluids is based on their multiphase nature, and they have got great importance on account of their wide spread involvement in industrial and technological applications. Shear-thinning, shear thickening, and viscoelasticity are the main characteristics of non-Newtonian liquids. These characteristics are described by nonlinear relationship between shear force and shearing deformation. Several models of non-Newtonian materials have been suggested, like Maxwell, Jeffery, and Oldroyd-B models. An Oldroyd-B model is a rate type non-Newtonian material having relaxation and retardation time effects.

Thermal energy has a significant role in almost every field of science, engineering, industries, biomedicine, plant processing, transports, power houses, generating stations, and many others. The effectiveness of all the above cited applications is greatly dependent upon thermal conductivity of the fluids involved in the heat interchanging processes. Many fluids like water, ethylene, and oil bear the restrictions in applications due to low thermal conductivity. Hence, nanoparticles of average size of about 1–100 nm are inserted into the base fluid to augment the thermophysical and concentration circumstances of the fluid, and the obtained colloidal suspension is regarded as nanofluid. The novel attributes of nanofluids make them positively functional in

the numerous applications of heat transference along with microelectronics, energy cells, and domiciliary refrigeration and heating equipment, in disintegrating and cracking units, machining, hybrid powered engines, medications, and heat exchange units. Choi and Eastman [1] firstly proposed the term nanofluid through a permeable prolonging sheet along with consumption/injection. Then, Xuan and Li [2] extended the concept of nanofluids by proposing that fluids with solidified particles of metalloid and polymeric origin in a base fluid can also be termed as nanofluids. Buongiorno [3] formulated a mathematical tool for the analysis of convective transference in nanofluids with the consideration of Brownian movement and thermal diffusion properties. Copper, titanium, silicon, aluminum, zinc, magnesium, and graphene oxide are the best well-known particulates used for the development of nanofluids, while water, oil, glycol, and ethylene are the most regular working liquids.

Boundary-layer flows through stretching surfaces have been considered in studies because of their countless applications from household practices to aerospace such as in industries, irrigation waterways, environmental production, aerodynamics, sports, enhancement of heat transference, enhancement of mixing, transport of species, formation of rubber and plastic sheets, and fiber glass manufacturing. Boundary-layer flow produced by continuous elongation of obstacle was primarily studied by Sakiadis [4]. Crane [5] introduced the development of boundary-layer stream through stretching of surface and found exact solutions for the flow field. The bidirectional flow caused as a result of linearly plane bidirectional stretching of sheet was studied by Wang [6]. Ariel [7] deduced approximate analytical and numerical solutions of bidirectional steady flow over an elongating sheet. Sajid and Hayat [8] premeditated the aspects of thermal deposition and heat transportation in the boundary-layer dynamics of a viscid fluid influenced by an exponential elongation of obstacle. An analysis of the motion of a nanofluid produced by stretching of surface using connective model was developed by Khan and Pop [9].

Bhattacharyya and Layek [10] investigated the effects of chemically receptive solute convergence in magnetohydrodynamic boundary-layer stream. Ahmad et al. [11] continued the work accomplished by Liu and Anderson [12] by estimating the Darcy resistance impact and applied magnetic field. Stratification is a predominant phenomenon which has gained remarkable consideration because of its inclusion in the geophysical flows such as waterways, within lakes, oceans, ground-water supplies, warm energy stockpiling frameworks, and so on. A lot of researchers experimented with stratification with different effects. Ibrahim and Makinde [13] considered the doubly stratified boundary-regime flow of nanomaterials through an upright plate. Loganathan et al. [14] inspected the effect of second-order slip in a convective dynamic of an Oldroyd-B material with the aspects of chemical reaction and thermal radiation. Sandeep and Reddy [15] studied magnetohydrodynamic (MHD) flow having double stratified and cross diffusion aspects for an Oldroyd-B fluid. Waqas et al. [16] described the features of mixed convection progression of an Oldroyd-B nanomaterial via accumulating the impact of heat creation as well as heat/mass stratification.

The notion of heat production/consumption is convenient in many practices including heat disposal of atomic fuel wreckage, underground removal of radiative garbage substances, food storages, and disconnecting materials in packed bed reactors. In this way, nanocomposites have a capacity to assemble incident radiation. Turkyilmazoglu and Pop [17] explored the concurrent effects of heat and mass transport with thermal radiation through an unsteady nanomaterial progression. Rashidi et al. [18] analyzed the effect of second law of thermodynamics in magnetohydrodynamic dynamics of nanoliquid over a revolving disk. Moradi et al. [19] performed an analysis to check the effects of nanoparticles in Jeffery–Hamel flow. Makinde et al. [20] analyzed the buoyancy-driven dynamics of nanoliquid near a stagnated domain with connective boundary conditions. Mahanthesh et al. [21] worked toward approximate solution for the dynamics of an Oldroyd-B material with the significance of thermal deposition and heat consumption/generation impacting upon a nonlinearly expanding obstacle.

The subject of fluid motion with the involvement of porous medium has developed significantly in many fields of science and engineering like flow through water rocks, skin pronouncement, liquid purification processes, chemical trash, crude oil production, porous insulation, grain storage, mastic transport modeling, and underground removal of atomic waste. The interdependence of the voids in a porous medium permits certain liquids to flow through material. Ghosh and Sana [22] studied the time dependent dynamics of an Oldroyd-B material influenced by reformed sine pulses. Mukhopadhyay [23] considered and studied the time dependent heat transference and mixed connective dynamics produced by a penetrable stretching obstacle. The magnetohydrodynamic dynamics of tiny-sized nanoparticles passed over a permeable wedge is scrutinized by Kandasamy et al. [24]. Tripathy et al. [25] analyzed the impact of chemical reaction on magnetohydrodynamic free connective sheet over an upright moving plate through permeable material. Ali et al. [26] presented the analytical solution for flowing fluid through exponential stretching of permeable surface including heat flux in permeable medium utilizing homotopy analysis method (HAM). Goud [27] introduced the magnetohydrodynamic flow through an upright appendicular plate including radiation and chemical reaction effects through a permeable medium. Some more impactful scientific contributions related to the bidirectional dynamics of nanofluids with various mechanical and thermal aspects have been made by some researchers [28–36].

The above literature survey reveals that the study of non-Newtonian nanofluid performs a vital role in the industrial and engineering advancements. Moreover, a huge gap regarding the combined study of nonlinear aspects of mixed convection, chemical reaction, and heat consumption/generation is found during literature review. Hence, the novelty of present exploration is to discuss the steady dynamics of 3D radiative non-Newtonian (Oldroyd-B) nanofluid with the nonlinear aspects of mixed convection, chemical reaction, and heat source/sink. Additionally, significance of porous medium, magnetohydrodynamics, and double stratification has been addressed to

achieve the thermal engineering relevancy of the mathematical model. To the best of our knowledge, no such attempt has been made previously. Mathematical modeling of the physical model has been completed with the help of boundary-layer approximations and basic laws of fluid dynamics. With the functionality of similarity transformations, transport equations have been converted into one parameter family of solvable equations based on the physical domain. Analytical analysis of the mathematical model has been presented by following the procedure of homotopy analysis method [37–44]. Some more solution techniques (Keller-Box method, Lie group analysis, etc.) have also been offered by some researchers/scholars [45–50], but here preference is given to homotopy analysis method because of its compatibility with the modeled problem. Finally, the obtained outcomes have been discussed physically with the support of various charts and tables against the fluctuating choices of involved parameters.

2. Model Development

An incompressible, doubly stratified, and three-dimensional steady dynamic of radiative Oldroyd-B magneto-nanomaterial impacting upon an expanding obstacle through porous space is considered with the nonlinear aspects of mixed convection, chemical reaction, and heat consumption/generation. Effects of random motion and thermodiffusion of nanoparticles have also been provided via Buongiorno nanofluid model. The Lorentz force is perpendicular to the xy-plane, whereas gravitational force is parallel to the x-direction. Influence of chemical reaction has been included in the nanoparticle mass transport equation, whereas radiation effects have been involved in the heat equation of the nanofluid. The expansion velocity along x-direction is explained as $u_w = ax$, whereas expansion velocity along the y-direction is elaborated as $v_w = by$. The relations for wall and free stream temperatures are settled according to the rule of thermal stratification, whereas the relations for wall and free stream nanoparticle mass concentration are established according to the regulation of solutal stratification. The graphical abstract of the present investigation is presented via Figure 1. The governing equations for the present analysis supported by [16, 22, 27, 31, 32, 44] are composed as

$$\frac{\partial u}{\partial x}+\frac{\partial v}{\partial y}+\frac{\partial w}{\partial z}=0, \tag{1}$$

$$\begin{aligned} u\frac{\partial u}{\partial x}+v\frac{\partial u}{\partial x}+w\frac{\partial u}{\partial z}+\lambda_1\left(\begin{array}{c} u^2\dfrac{\partial^2 u}{\partial x^2}+v^2\dfrac{\partial^2 u}{\partial y^2}+w^2\dfrac{\partial^2 u}{\partial z^2} \\ +2uv\dfrac{\partial^2 u}{\partial x\partial y}+2vw\dfrac{\partial^2 u}{\partial y\partial z}+2uw\dfrac{\partial^2 u}{\partial x\partial z}\end{array}\right), \\ =\vartheta\frac{\partial^2 u}{\partial z^2}+\vartheta\lambda_2\left(\begin{array}{c} u\dfrac{\partial^3 u}{\partial x\partial z^2}+v\dfrac{\partial^3 u}{\partial x\partial z^2}+w\dfrac{\partial^3 u}{\partial z^3} \\ -\dfrac{\partial u}{\partial x}\dfrac{\partial^2 u}{\partial z^2}-\dfrac{\partial u}{\partial y}\dfrac{\partial^2 u}{\partial z^2}-\dfrac{\partial u}{\partial z}\dfrac{\partial^2 w}{\partial z^2}\end{array}\right), \\ +g\left[\alpha_1\left(T-T_\infty\right)+\alpha_2\left(T-T_\infty\right)^2\right] \\ +g\left[\alpha_3\left(C-C_\infty\right)+\alpha_4\left(C-C_\infty\right)^2\right]-\frac{\mu_f\phi_1}{\rho_f p_1}u-\frac{\sigma B^{\circ 2}}{\rho_f}\left(u+\lambda_1 w\frac{\partial u}{\partial z}\right), \end{aligned} \tag{2}$$

$$\begin{aligned} u\frac{\partial v}{\partial x}+v\frac{\partial v}{\partial y}+w\frac{\partial v}{\partial z}+\lambda_1\left(\begin{array}{c} u^2\dfrac{\partial^2 v}{\partial x^2}+v^2\dfrac{\partial^2 v}{\partial y^2}+w^2\dfrac{\partial^2 v}{\partial z^2} \\ +2uv\dfrac{\partial^2 v}{\partial x\partial y}+2vw\dfrac{\partial^2 v}{\partial y\partial z}+2uv\dfrac{\partial^2 v}{\partial x\partial z}\end{array}\right), \\ =\vartheta\frac{\partial^2 v}{\partial z^2}+\vartheta\lambda_2\left(\begin{array}{c} u\dfrac{\partial^3 v}{\partial x\partial z^2}+v\dfrac{\partial^3 v}{\partial x\partial z^2}+w\dfrac{\partial^3 v}{\partial z^3} \\ -\dfrac{\partial v}{\partial x}\dfrac{\partial^2 v}{\partial z^2}-\dfrac{\partial v}{\partial y}\dfrac{\partial^2 v}{\partial z^2}-\dfrac{\partial v}{\partial z}\dfrac{\partial^2 w}{\partial z^2}\end{array}\right), \\ -\frac{\mu_f\phi_1}{\rho_f p_1}v-\frac{\sigma B^{\circ 2}}{\rho_f}\left(v+\lambda_1 w\frac{\partial v}{\partial z}\right), \end{aligned} \tag{3}$$

$$u\frac{\partial T}{\partial x}+v\frac{\partial T}{\partial y}+w\frac{\partial T}{\partial z}=\alpha_m\frac{\partial^2 T}{\partial z^2}$$
$$+\frac{(\rho c)_p}{(\rho c)_f}\left(D_B\left(\frac{\partial T}{\partial z}\frac{\partial C}{\partial z}\right)+\frac{D_T}{T_\infty}\left(\frac{\partial T}{\partial z}\right)^2\right)-\frac{1}{(\rho c)_f}\frac{\partial q_r}{\partial z}+\frac{q'''}{(\rho c)_f}, \tag{4}$$

$$u\frac{\partial C}{\partial x}+v\frac{\partial C}{\partial y}+w\frac{\partial C}{\partial z}=D_B\frac{\partial^2 C}{\partial z^2}+\frac{D_T}{T_\infty}\left(\frac{\partial^2 T}{\partial z^2}\right)$$
$$-\left[k_{c1}(C-C_\infty)+k_{c2}(C-C_\infty)^2\right]. \tag{5}$$

Here, $q''' = (ku_w/x\vartheta)[A^*(T_w - T_\infty)f' + B^*(T - T_\infty)]$.

The relevant boundary conditions supported by [15, 16, 44] are

$$u = u_w, v = v_w, w = 0, T = T_w, C = C_w \text{ at } z = 0,$$
$$u \longrightarrow 0, v \longrightarrow 0, T \longrightarrow T_\infty, C \longrightarrow C_\infty \text{ as } z \longrightarrow \infty. \tag{6}$$

Using the relation of Rosseland approximation, radiative heat-flux q_r is determined as (see [48]) $q_r = -(4\sigma^*/3K^*)(\partial T^4/\partial z)$ with $T^4 \cong 4T_\infty^3 T - 3T_\infty^4$.

Here, x, y, and z describe the space coordinates; u, v, and w express parts of velocity in the direction of x, y, and z, respectively; λ_1 and λ_2 are used to represent relaxation time and retardation time, respectively; $\vartheta = (\mu_f/\rho_f)$ denotes kinematic viscosity with μ_f as dynamic viscosity and ρ_f as density; g represents the gravitational acceleration; α_1 exhibits the involvement of linear thermal expansion; α_2 represent involvement of nonlinear thermal expansion; α_3 and α_4 depict, respectively, linear and nonlinear concentration coefficients; σ^* denotes Stefan–Boltzmann constant; B_0 stands for magnetic field strength with electrical conductivity σ; ϕ_1 is used to express the porosity constant; p_1 the permeability constant; T is the temperature, C is the concentration of nanoparticles; $\alpha_m = (k/(\rho c)_f)$ denotes the thermal diffusivity with thermal conductivity k; and D_B and D_T are the symbols of random and thermodiffusion coefficients of nanocomposites, respectively. Efficient heat capability of nanoparticles and efficient heat capability of the fluid are symbolized by $(c)_p$ and $(c)_f$, respectively; k_{c1} and k_{c2} represent the first- and second-order chemical reaction parameters, respectively; q_r is thermal deposition; q''' is nonuniform heat consumption/absorption; T_w is temperature at the surface; T_∞ denotes the ambient temperature; and C_w and C_∞ serve as nanoparticle concentrations at the obstacle and far from the obstacle. Here, the expansion velocities, temperature, and nanoparticle mass concentration at the surface are described as (see [15, 16, 44])

$$\begin{aligned} u_w(x) &= ax,\\ v_w(y) &= by,\\ T_w(x) &= T_{\infty,0} + M_1 x,\\ C_w(x) &= C_{\infty,0} + N_1 x,\\ T_\infty(x) &= T_{\infty,0} + A_1 x,\\ C_\infty(x) &= C_{\infty,0} + B_1 x. \end{aligned} \tag{7}$$

Here, $a, b, A_1, B_1, M_1, N_1, T_{\infty,0}$, and $C_{\infty,0}$ are dimensional constants.

We utilize the accompanying similarity transformations supported by [37, 38, 44] as follows:

$$\left.\begin{aligned} &u = axf'(\eta), v = ayg'(\eta) \quad w = -(a\vartheta)^{1/2}(f+g), \eta = \left(\frac{a}{\vartheta}\right)^{1/2} z\\ &\theta(\eta) = \frac{T - T_{\infty,0}}{T} - \frac{A_1 x}{T} \quad \Delta T = T_w(x) - T_{\infty,0} = M_1 x\\ &\phi(\eta) = \frac{C - C_{\infty,0}}{C} - \frac{B_1 x}{C} \quad \Delta C = C_w(x) - C_{\infty,0} = N_1 x \end{aligned}\right\}. \tag{8}$$

Via using the above-mentioned local similarity set, (1) is straightforwardly fulfilled and simplified forms of (2-5) are mentioned below:

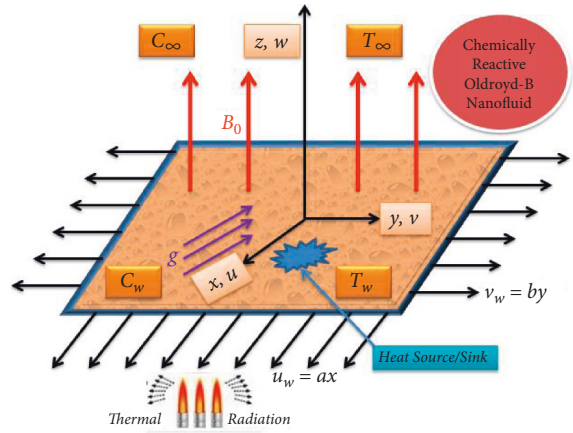

Figure 1: Graphical abstract of the mathematical model.

$$f''' + \left(1 + M^2\beta_1\right)(f+g)f'' - f'^2 + \beta_1\left[2(f+g)f'f'' - (f+g)^2 f'''\right], \\ + \beta_2\left[2(f''+g'')f'' - (f+g)f^{iv}\right] - \left(\delta + M^2\right)f' + \lambda\left[(1+\beta_t\theta)\theta + N^*(1+\beta_c\phi)\phi\right] = 0, \tag{9}$$

$$g''' + \left(1 + M^2\beta_1\right)(f+g)g'' - g'^2 + \beta_1\left[2(f+g)g'g'' - (f+g)^2 g'''\right], \\ + \beta_2\left[2(f''+g'')g'' - (f+g)g^{iv}\right] - \left(\delta + M^2\right)g' = 0, \tag{10}$$

$$\left(1 + \frac{4}{3}R_d\right)\theta'' + \Pr\left[(f+g)\theta' - (\theta+\varepsilon_t)f' + N_b\theta'\phi' + N_t\theta'^2\right] + A^*(1-\varepsilon_t)f' + B^*\theta = 0, \tag{11}$$

$$\phi'' + \Pr Le\left[(f+g)\phi' - (\phi+\varepsilon_s)f' - \gamma(1+k_c\phi)\phi\right] + \frac{N_t}{N_b}\theta'' = 0. \tag{12}$$

The boundary conditions are confined as

$$\begin{aligned} f &= 0, \\ g &= 0, \\ f' &= 1, \\ g' &= \alpha, \\ \theta &= 1 - \varepsilon_t, \\ \phi &= 1 - \varepsilon_s \text{ at } \eta = 0, \end{aligned} \tag{13}$$

$$\begin{aligned} f' &\longrightarrow 0, \\ g' &\longrightarrow 0, \\ f'' &\longrightarrow 0, \\ g'' &\longrightarrow 0, \\ \theta &\longrightarrow 0, \\ \phi &\longrightarrow 0, \text{ as } \eta \longrightarrow \infty. \end{aligned} \tag{14}$$

In the above-mentioned equations, f' and g' are the dimensionless velocities along x- and y-direction, respectively; θ and ϕ are the dimensionless temperature and concentration, respectively; $\beta_1 = \lambda_1 a$ and $\beta_2 = \lambda_2 a$ are the Deborah numbers corresponding to relaxation and retardation times, respectively; $\beta_t = (\alpha_2/\alpha_1)T$ and $\beta_c = (\alpha_4/\alpha_3)C$ indicate the nonlinear convection constraints for temperature and concentration, respectively; $M^2 = (\sigma B^{\circ}{}_2/\rho_f a)$ is the magnetic constraint; $\delta = (\vartheta\phi_1/p_1 a)$ is used to express the porosity constraint; $N^* = (\lambda^*/\lambda)$ stands for buoyancy ratio parameter; $\lambda = (Gr/Re_x^2)$ and $\lambda^* = (Gr^*/Re_x^2)$ denote the mixed convective parameters for thermal and concentration setups, respectively; $Le = (\alpha_m/D_B)$ is the Lewis number; $Pr = (\vartheta/\alpha_m)$ signifies the Prandtl number; $N_b = ((\rho c)_p/(\rho c)_f)(D_B\Delta C/\vartheta)$ denotes the random movement involvement; $N_t = ((\rho c)_p/(\rho c)_f)(D_T\Delta T/\vartheta T_\infty)$ corresponds to thermo-diffusion parameter; A^* and B^* denote, respectively, the quantities of space-dependent and temperature-dependent heat consumption/generation; $\gamma = (k_{c1}/a)$ is the rate of chemical reaction; $k_c = (k_{c2}/k_{c1})C$ is the dimensionless chemical reaction parameter; $R_d = (4T_\infty^3\sigma^*/kk^*)$ represents radiation parameter; k^* represents the Rosseland mean absorption constant; $\alpha = (b/a)$ is the expansion ratio parameter; $\varepsilon_t = (A_1/M_1)$ and $\varepsilon_s = (B_1/N_1)$ are the representatives of the heat and mass stratified parameters, respectively; and prime represents differentiation taking η as an independent similarity variable.

The amount of mass transference is presented by local Sherwood number Sh_x while the amount of heat

transference is described by local Nusselt number Nu_x, and these numbers can be expressed in the form of Reynolds number $Re_x = (u_w x/\vartheta)$ as below:

$$\begin{aligned} Sh_x &= -\frac{x}{(C_w - C_\infty)}\frac{\partial C}{\partial z}\Big|_{z=0}, \\ &= -(Re_x)^{(1/2)}\phi'(0), \\ Nu_x &= -\frac{x}{(T_w - T_\infty)}\left(\frac{\partial T}{\partial z} - \frac{q_r}{k}\right)\Big|_{z=0}, \\ &= -(Re_x)^{(1/2)}\left(1 + \frac{4}{3}R_d\right)\theta'(0). \end{aligned} \tag{15}$$

3. Homotopic Series Solution

This section deals with the series solutions of the mathematical modeled dimensionless equations (9)–(12) based on boundary restrictions via (8) and (9) with the procedure of homotopy analysis method (HAM). For this purpose, primary guesses are approximated in accordance with boundary conditions (8) and (9) and are shown as

$$\begin{aligned} f_0(\eta) &= 1 - e^{-\eta}, \\ g_0(\eta) &= \alpha(1 - e^{-\eta}), \\ \theta_0(\eta) &= (1 - \varepsilon_t)e^{-\eta}, \\ \phi_0(\eta) &= (1 - \varepsilon_c)e^{-\eta}. \end{aligned} \tag{16}$$

The linear operators are denoted by $\mathscr{L}_f, \mathscr{L}_g, \mathscr{L}_\theta$, and $\mathscr{L}_\phi$ as follows:

$$\begin{aligned} \mathscr{L}_f &= f''' - f', \\ \mathscr{L}_g &= g''' - g', \\ \mathscr{L}_\theta &= \theta'' - \theta', \\ \mathscr{L}_\phi &= \phi'' - \phi', \\ &\left.\begin{aligned} \mathscr{L}_f[C_1 + C_2 e^{\eta} + C_3 e^{-\eta}] = 0 \quad \mathscr{L}_g[C_4 + C_5 e^{\eta} + C_6 e^{-\eta}] = 0 \\ \mathscr{L}_\theta[C_7 e^{\eta} + C_8 e^{-\eta}] = 0 \qquad \mathscr{L}_\phi[C_9 e^{\eta} + C_{10} e^{-\eta}] = 0 \end{aligned}\right\}, \end{aligned} \tag{17}$$

$$\begin{aligned} (1-P)\mathscr{L}_f\left[\widehat{f}(\eta,P) - f_0(\eta)\right] &= P\hbar_f \mathscr{N}_f[\widehat{f}(\eta,P), \widehat{g}(\eta,P), \widehat{\theta}(\eta,P), \widehat{\phi}(\eta,P)], \\ (1-P)\mathscr{L}_g\left[\widehat{g}(\eta,P) - g_0(\eta)\right] &= P\hbar_g \mathscr{N}_g[\widehat{f}(\eta,P), \widehat{g}(\eta,P), \widehat{\theta}(\eta,P), \widehat{\phi}(\eta,P)], \\ (1-P)\mathscr{L}_\theta\left[\widehat{\theta}(\eta,P) - \theta_0(\eta)\right] &= P\hbar_\theta \mathscr{N}_\theta[\widehat{f}(\eta,P), \widehat{g}(\eta,P), \widehat{\theta}(\eta,P), \widehat{\phi}(\eta,P)], \\ (1-P)\mathscr{L}_\phi\left[\widehat{\phi}(\eta,P) - \phi_0(\eta)\right] &= P\hbar_\phi \mathscr{N}_\phi[\widehat{f}(\eta,P), \widehat{g}(\eta,P), \widehat{\theta}(\eta,P), \widehat{\phi}(\eta,P)]. \end{aligned}$$

In the above relations, $\hbar_f$, $\hbar_g$, $\hbar_\theta$, and $\hbar_\phi$ are auxiliary constraints, whereas $\mathscr{N}_f$, $\mathscr{N}_g$, $\mathscr{N}_\theta$, and $\mathscr{N}_\phi$ serve as nonlinear operators, and P is the embedding parameter. The BCs (boundary conditions) in the coding language can be expressed as

$$\left.\begin{aligned} &\widehat{f}(0,P) = 0,\ \widehat{f}'(0,P) = 1,\ \widehat{f}'(\infty,P) = 0,\ \widehat{g}(0,P) = 0,\ \widehat{g}'(0,P) = \alpha, \\ &\widehat{g}'(\infty,P) = 0,\ \widehat{\theta}(0,P) = 1 - \varepsilon_t,\ \widehat{\theta}(\infty,P) = 0,\ \widehat{\phi}(0,P) = 1 - \varepsilon_c,\ \widehat{\phi}(\infty,P) = 0 \end{aligned}\right\}, \tag{18}$$

$$\begin{aligned} \mathscr{N}_f[\widehat{f}(\eta,P), \widehat{g}(\eta,P), \widehat{\theta}(\eta,P), \widehat{\phi}(\eta,P)] &= \frac{\partial^3 \widehat{f}}{\partial \eta^3} + \left(1 + M^2 * \beta_1\right)(\widehat{f} + \widehat{g})\frac{\partial^2 \widehat{f}}{\partial \eta^2} - \left(\frac{\partial \widehat{f}}{\partial \eta}\right)^2, \\ +\beta_1\left(2(\widehat{f} + \widehat{g})\frac{\partial \widehat{f}}{\partial \eta}\frac{\partial^2 \widehat{f}}{\partial \eta^2} - (\widehat{f} + \widehat{g})^2\frac{\partial^3 \widehat{f}}{\partial \eta^3}\right) + \beta_2\left(2\left(\frac{\partial^2 \widehat{f}}{\partial \eta^2} + \frac{\partial^2 \widehat{g}}{\partial \eta^2}\right)\frac{\partial^2 \widehat{f}}{\partial \eta^2} - (\widehat{f} + \widehat{g})\frac{\partial^4 \widehat{f}}{\partial \eta^4}\right) - \left(\delta + M^2\right)\frac{\partial \widehat{f}}{\partial \eta}, \\ +\lambda\left[\left(\left(1 + \beta_t\widehat{\theta}\right)\widehat{\theta} + N^*\left(1 + \beta_t\widehat{\phi}\right)\widehat{\phi}\right)\right], \end{aligned} \tag{19}$$

$$\mathcal{N}_g[\widehat{f}(\eta,P),\widehat{g}(\eta,P),\widehat{\theta}(\eta,P),\widehat{\phi}(\eta,P)] = \frac{\partial^3\widehat{g}}{\partial\eta^3} + \left(1+M^2\beta_1\right)(\widehat{f}+\widehat{g})\frac{\partial^2\widehat{g}}{\partial\eta^2} - \left(\frac{\partial\widehat{g}}{\partial\eta}\right)^2,$$
$$+\beta_1\left(2(\widehat{f}+\widehat{g})\frac{\partial\widehat{g}}{\partial\eta}\frac{\partial^2\widehat{g}}{\partial\eta^2} - (\widehat{f}+\widehat{g})^2\frac{\partial^3\widehat{g}}{\partial\eta^3}\right) + \beta_2\left(2\left(\frac{\partial^2\widehat{f}}{\partial\eta^2}+\frac{\partial^2\widehat{g}}{\partial\eta^2}\right)\frac{\partial^2\widehat{g}}{\partial\eta^2} - (\widehat{f}+\widehat{g})\frac{\partial^4\widehat{g}}{\partial\eta^4}\right) - \left(\delta+M^2\right)\frac{\partial\widehat{g}}{\partial\eta}, \tag{20}$$

$$\mathcal{N}_\theta[\widehat{f}(\eta,P),\widehat{g}(\eta,P),\widehat{\theta}(\eta,P),\widehat{\phi}(\eta,P)] = \left(1+\frac{4}{3}R_d\right)\frac{\partial^2\widehat{\theta}}{\partial\eta^2} + Pr(\widehat{f}+\widehat{g})\frac{\partial\widehat{\theta}}{\partial\eta},$$
$$-Pr\left(\widehat{\theta}+\varepsilon_t\right)\frac{\partial\widehat{f}}{\partial\eta} + Pr*N_b\frac{\partial\widehat{\theta}}{\partial\eta}\frac{\partial\widehat{\phi}}{\partial\eta} + Pr*N_t\left(\frac{\partial\widehat{\theta}}{\partial\eta}\right)^2 + A^*\left(1-\varepsilon_t\right)\frac{\partial\widehat{f}}{\partial\eta} + B^*\widehat{\theta}, \tag{21}$$

$$\mathcal{N}_\phi[\widehat{f}(\eta,P),\widehat{g}(\eta,P),\widehat{\theta}(\eta,P),\widehat{\phi}(\eta,P)] = \frac{\partial^2\widehat{\phi}}{\partial\eta^2} + Le*Pr(\widehat{f}+\widehat{g})\frac{\partial\widehat{\phi}}{\partial\eta},$$
$$-Le*Pr\left(\widehat{\phi}+\varepsilon_c\right)\frac{\partial\widehat{f}}{\partial\eta} - Le*Pr*\gamma\widehat{\phi} - Le*Pr*\gamma*k_c\widehat{\phi}^2 + \left(\frac{N_t}{N_b}\right)\frac{\partial^2\widehat{\theta}}{\partial\eta^2}, \tag{22}$$

$$\mathcal{L}_f\left[f_m(\eta) - \chi_m f_{m_{-1}}(\eta)\right] = \hbar_f R_f^m(\eta), \tag{23}$$

$$\mathcal{L}_g\left[g_m(\eta) - \chi_m g_{m_{-1}}(\eta)\right] = \hbar_g R_g^m(\eta), \tag{24}$$

$$\mathcal{L}_\theta\left[\theta_m(\eta) - \chi_m\theta_{m_{-1}}(\eta)\right] = \hbar_\theta R_\theta^m(\eta), \tag{25}$$

$$\mathcal{L}_\phi\left[\phi_m(\eta) - \chi_m\phi_{m_{-1}}(\eta)\right] = \hbar_\phi R_\phi^m(\eta), \tag{26}$$

$$\begin{aligned} f_m(0) &= f_m'(0), \\ &= f_m'(\infty), \\ &= 0, \\ g_m(0) &\\ &= g_m'(\infty), \\ &= 0, \end{aligned} \tag{27}$$

$$\begin{aligned} \theta_m(0) &= \theta_m(\infty), \\ &= 0, \\ \phi_m(0) &= \phi_m(\infty), \\ &= 0, \end{aligned} \tag{28}$$

$$R_f^m(\eta) = f_{m-1}''(\eta) + \left(1+M^2\beta_1\right)\sum_{k=0}^{m-1}\left(f_{m-1-k}f_k'' + g_{m-1-k}f_k''\right) - \sum_{k=0}^{m-1}\left(f_{m-1-k}' + f_k'\right),$$
$$+2\beta_1\sum_{k=0}^{m-1}f_{m-1-k}\sum_{l=0}^{k}f_{k-1}'f_l'' + 2\beta_1\sum_{k=0}^{m-1}g_{m-1-k}\sum_{l=0}^{k}f_{k-1}'f_l'' - \beta_1\sum_{k=0}^{m-1}f_{m-1-k}''\sum_{l=0}^{k}f_{k-1}f_l,$$
$$-\beta_1\sum_{k=0}^{m-1}f_{m-1-k}''\sum_{l=0}^{k}g_{k-1}g_l - \sum_{k=0}^{m-1}f_{m-1-k}''\sum_{l=0}^{k}g_{k-1}f_l + 2\beta_1\sum_{k=0}^{m-1}f_{m-1-k}''f_k'' + 2\beta_1\sum_{k=0}^{m-1}g_{m-1-k}''f_k'', \tag{29}$$
$$-\beta_2\sum_{k=0}^{m-1}f_{m-1-k}f_k''' - \beta_2\sum_{k=0}^{m-1}g_{m-1-k}f_k''' - \left(\delta+M^2\right)f_{m-1}(\eta),$$
$$+\lambda\left(\theta_{m-1}(\eta) + \beta_t\sum_{k=0}^{m-1}\theta_{m-1-k}\theta_k + N*\phi_{m-1}(\eta) + N**\beta_c\sum_{k=0}^{m-1}\phi_{m-1-k}\phi_k\right),$$

$$\begin{aligned}\widehat{R}_g^m(\eta) = {} & g''_{m-1}(\eta) + \left(1 + M^2\beta_1\right)\sum_{k=0}^{m-1}\left(f_{m-1-k}g''_k + g_{m-1-k}g''_k\right) - \sum_{k=0}^{m-1} g_{m_{-1-k}}{}'g'_k, \\ & +2\beta_1\sum_{k=0}^{m-1} f_{m-1-k}\sum_{l=0}^{k} g_{k-l}{}'g''_l + 2\beta_1\sum_{k=0}^{m-1} g_{m-1-k}\sum_{l=0}^{k} g_{k-l}g''_l - m, \\ & \beta_1\sum_{k=0}^{m-1} g''_{m-1-k}\sum_{l=0}^{k} f_{k-1}f_l - \beta_1\sum_{k=0}^{m-1} g''_{m-1-k}\sum_{l=0}^{k} g_{k-1}f + 2\beta_1\sum_{k=0}^{m-1} g_{m-1-k}{}''\sum_{l=0}^{k} g_{k-1}g_l +, \\ & 2\beta_1\sum_{k=0}^{m-1} f''_{m-1-k}g''_k + 2\beta_1\sum_{k=0}^{m-1} g''_{m-1-k}g''_k - \beta_2\sum_{k=0}^{m-1} f_{m-1-k}g'''_k - \beta_2\sum_{k=0}^{m-1} g_{m-1-k}g'''_k - \left(\delta + M^2\right)g_{m-1}(\eta),\end{aligned} \tag{30}$$

$$\begin{aligned}\widehat{R}_\theta^m(\eta) = {} & \left(1 + \frac{4}{3}R_d\right)\theta''_{m-1}(\eta) + Pr\sum_{k=0}^{m-1}\left(f_{m-1-k}\theta'_k + g_{m-1-k}\theta'_k\right) - Pr\sum_{k=0}^{m-1} f_{m-1-k}{}'\theta'_k, \\ & -Pr * \varepsilon_t f_{m-1}{}'(\eta) + Pr * N_t\sum_{k=0}^{m-1}\theta_{m-1-k}{}'\theta'_k + Pr * N_b\sum_{k=0}^{m-1}\phi_{m-1-k}{}'\theta'_k + A^*\left(1 - \varepsilon_t\right)f_{m-1}{}'(\eta) + B^*\theta_{m-1}(\eta),\end{aligned} \tag{31}$$

$$\begin{aligned}\widehat{R}_\phi^m(\eta) = {} & \phi''_{m-1}(\eta) + Le * Pr\sum_{k=0}^{m-1}\left(f_{m-1-k}\phi'_k + g_{m-1-k}\phi'_k\right) - Le * Pr\sum_{k=0}^{m-1} f'_{m_{-1-k}}\phi_k, \\ & -Le * Pr * \varepsilon_c * f_{m-1}{}'(\eta) - Le * Pr * \gamma * \phi_{m-1}(\eta) - \gamma * Le * Pr * k_c\sum_{k=0}^{m-1}\phi_{m-1-k}\phi_k + \left(\frac{N_t}{N_b}\right)\theta''_{m-1}(\eta),\end{aligned} \tag{32}$$

$$\chi_m = \begin{cases} 0, & m \le 1, \\ 1, & m > 1. \end{cases} \tag{33}$$

The general solutions f_m, g_m, θ_m, and ϕ_m of (23)–(26) with regard to particular solutions $f_m^*, g_{m'}^*\theta_m^*, \phi_m^*$ are expressed by

$$f_m(\eta) = f_m^*(\eta) + C_1 + C_2e^{\eta} + C_3e^{-\eta}, \tag{34}$$

$$g_m(\eta) = g_m^*(\eta) + C_4 + C_5e^{\eta} + C_6e^{-\eta}, \tag{35}$$

$$\theta_m(\eta) = \theta_m^*(\eta) + C_7e^{\eta} + C_8e^{-\eta}, \tag{36}$$

$$\phi_m(\eta) = \phi_m^*(\eta) + C_9e^{\eta} + C_{10}e^{-\eta}. \tag{37}$$

The general constants $C_i\,(i = 1 - 10)$ in the above equations are calculated by applying boundary conditions and are stated as

$$\left.\begin{aligned} & C_1 = C_2 = C_5 = C_7 = C_9, C_3 = \frac{\partial f_m^*(\eta)}{\partial\eta}|_{\eta=0} && C_1 = -C_3 - f_m^*(0), C_6 = \frac{\partial g_m^*(\eta)}{\partial\eta}|_{\eta=0} \\ & C_4 = -C_6 - g_m^*(0), \; C_1 = -C_3 - f_m^*(0) && C_8 = -\theta_m^*(0), C_{10} = -\phi_m^*(0) \end{aligned}\right\}. \tag{38}$$

4. Convergence Analysis

The admissible range for unknown boundary restrictions is the first task to obtain the solution via homotopy analysis method. This range can be traced by identifying those portions of curves lying exactly parallel to the horizontal axis as sketched in Figure 2. The solid-green line curve expresses $f''(0)$ with admissible range of $-0.7 \le \hbar_f \le -0.1$. The admissible range for the curve of $g''(0)$ is $-0.8 \le \hbar_g \le -0.1$, and it is depicted by the black dashed line. Similarly, the admissible ranges of $\theta'(0)$ and $\phi'(0)$ are estimated as $-0.6 \le \hbar_\theta \le -0.1$ and $-0.4 \le \hbar_\phi \le -0.1$, and they are represented by red and blue curves, respectively. For convenience, throughout the analysis we have chosen $\hbar_f = \hbar_g = \hbar_\phi = \hbar_\theta = -0.3 = \hbar$. Hence, the convergence table for appropriate amounts of emerging parameters is generated, and the corresponding results are shown through Table 1. Table 1 illustrates that at least sixty-four orders of approximation are needed to obtain the missing boundary conditions for $\theta(\eta)$ and $\phi(\eta)$, whereas at least seventy orders of approximation are required to attain the momentum boundary conditions. To maintain the convergence and

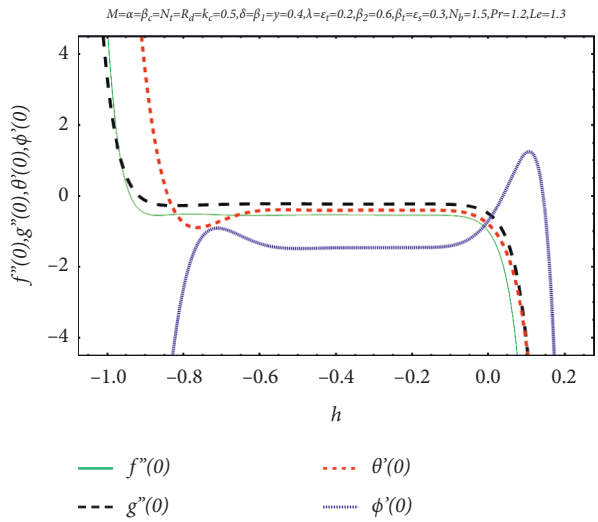

Figure 2: Estimation of convergent region via $\hbar$-curve sketching.

Table 1: Convergence check of series solutions by considering different orders of deformation m when $\hbar = -0.3$ with the values of involved parameters kept the same as Figure 1.

m	$-f''(0)$	$-g''(0)$	$-\theta'(0)$	$-\phi'(0)$
1	0.67180	0.33000	0.60480	0.99566
8	0.54487	0.22133	0.41078	1.45734
16	0.54294	0.22897	0.40751	1.45982
22	0.54220	0.22546	0.41026	1.46269
28	0.54556	0.22697	0.40922	1.45788
34	0.54160	0.22788	0.40893	1.46162
40	0.54399	0.22506	0.41025	1.46070
46	0.54236	0.22702	0.41048	1.46132
52	0.54311	0.22688	0.41057	1.46149
58	0.54286	0.22697	0.41065	1.46158
64	0.54292	0.22692	0.41067	1.46159
70	0.54288	0.22695	0.41067	1.46159
80	0.54288	0.22695	0.41067	1.46159

stability of the solution, the numbers of approximations are increased up to eight.

5. Results and Discussion

This section describes the graphical illustrations of temperature fluctuation, concentration fluctuation, local Nusselt number, and local Sherwood number under the consequences of important involved parameters. Figure 3 explains the impact of thermal stratification parameter $0 \le \varepsilon_t \le 1$ on dimensionless temperature fluctuation when the similarity variable is increased from $\eta = 0$ to $\eta = 4$ with the constant choices of other involved parameters. Maximum temperature fluctuation occurs at $\varepsilon_t = 0$, minimum temperature fluctuation is achieved at $\varepsilon_t = 1$, and thermal stratification phenomenon is generated for $0 < \varepsilon_t < 1$. Temperature profile is reduced with the improvement in the choice of ε_t. Physically, higher choice of ε_t develops the ambient temperature and reduces the temperature at the surface. As a result, the temperature profile is reduced. The thickness of thermal layer is improved with the improvement in the value of the similarity variable. Figure 4 illustrates the trend of solutal stratification parameter $0 \le \varepsilon_s \le 1$ on dimensionless concentration fluctuation when the similarity variable is increased from $\eta = 0$ to $\eta = 1.8$ with the fixed amounts of other influential parameters. Maximum concentration is achieved at $\varepsilon_s = 0$, minimum concentration is obtained at $\varepsilon_s = 1$, and solutal stratification phenomenon is traced for $0 < \varepsilon_s < 1$. Concentration setup is diminished with the higher estimation of ε_s. The physical reason behind this outcome is the downfall of nanoparticle concentration at the wall and improvement of nanoparticle concentration away from the stretching device. Concentration layer thickness is also increased with the improvement of the similarity variable.

Figure 5 indicates the role of space-dependent heat source/sink parameter $-1.5 \le A^* \le 1.5$ in dimensionless temperature fluctuation with the increase of the similarity variable from $\eta = 0$ to $\eta = 8$. Minimum temperature is attained for heat consumption case, $-1.5 \le A^* < 0 - 1.5 \le A^* < 0$; maximum temperature is achieved for heat generation case, $0 < A^* \le 1.50 < A^* \le 1.5$; and moderate temperature is reached in the absence of heat

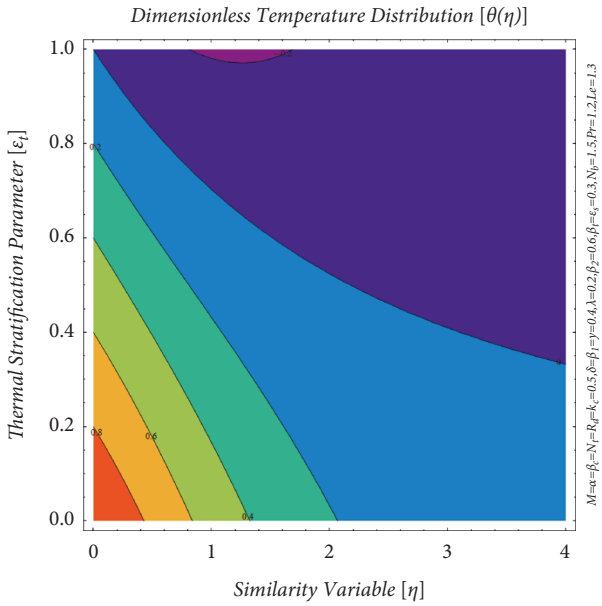

Figure 3: Interference of ε_t on thermal layer $\theta(\eta)$.

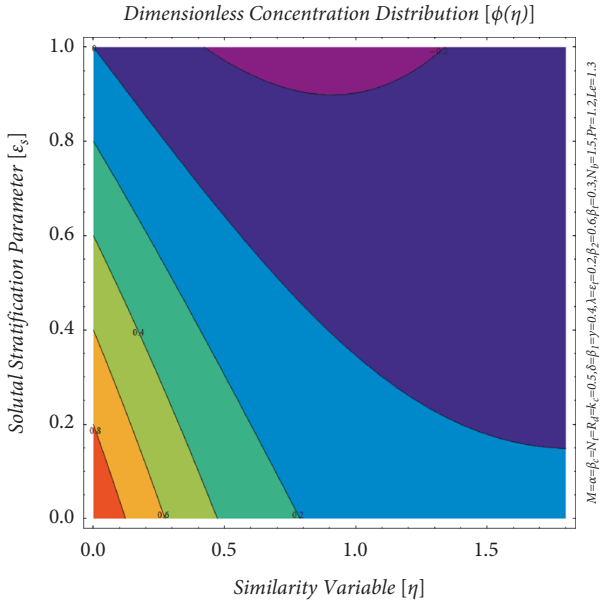

Figure 4: Interference of ε_s on concentration layer $\phi(\eta)$.

generation/consumption, $A^* = 0$. Mathematically, A^* is involved as a multiple of velocity profile $f'(\eta)$ in (7); therefore, the velocity profile also increases with the higher estimation of A^*, and hence temperature profile is improved. Therefore, it is called space-dependent heat source/sink influence on thermal profile. The thickness of thermal layer is also improved with the growth of the similarity variable. Figure 6 illuminates the potential of temperature-dependent heat source/sink parameter $-1.5 \le B^* \le 1.5$ on dimensionless temperature fluctuation with the growth of the similarity variable from $\eta = 0$ to $\eta = 8$. Minimal temperature is accomplished for heat ingestion case, $-1.5 \le B^* < 0 - 1.5 \le B^* < 0$; maximal temperature is realized for heat production case, $0 < B^* \le 1.50 < B^* \le 1.5$; and modest temperature is touched in the nonappearance of heat production/consumption, $B^* = 0$. Precisely, B^* is involved as a multiple of $\theta(\eta)$ in (7); therefore, the thermal profile is also augmented with the greater estimation of B^*, and hence it is called temperature-dependent heat source/sink influence on thermal profile. The depth of thermal layer is also enriched with the progress of similarity variable. Figure 7 establishes the connection between dimensionless concentration fluctuation and chemical reaction parameter $0 \le k_c \le 20$ with the growth of the similarity variable up to $\eta = 3.2$. Decreasing trend in concentration fluctuation is observed with the growth in the estimation of k_c, maximal concentration is achieved for smaller values of k_c, and minimal concentration is generated for greater estimations of k_c. Physically, higher estimation of k_c increases the second-order chemical reaction and reduces the first-order chemical reaction at the same time. As an outcome, negative trend in the concentration profile is attained. The thickness of concentration layer is also developed with the improvement in the similarity variable. Figure 8 explores the effect of thermal radiation parameter $0 \le R_d \le 4$ on thermal fluctuation with the evolution of the similarity variable from $\eta = 0$ to $\eta = 7$. A huge improvement in the thermal fluctuation is attained with the intensification in R_d. Maximal temperature is measured for higher R_d, and minimal temperature is obtained for basic/lower R_d. The thickness of thermal layer is also improved and it is found to be higher for the middle values of R_d. Physically, radiation is basically the transference of energy in the form of electromagnetic waves. More electromagnetic waves are produced with the improvement of R_d, and hence dominant temperature fluctuation is observed when R_d reaches maximal estimation. Figure 9(a) deals with the relationship between relaxation time Deborah number $0 \le \beta_1 \le 10$ and temperature distribution for the similarity variable $0 \le \eta \le 7$. Here, thermal environment is upgraded with the higher estimation of β_1. Basically, β_1 is generated in the momentum equation due to the inclusion of Oldroyd-B nanoparticles and defined as the product of expansion rate a and the relaxation time λ_1. Hence, higher estimation of β_1 enhances the value of λ_1 as well as the expansion rate. As an outcome, improvement in thermal setup is noticed with the upgraded width of thermal layer. Figure 9(b) shows the effect of β_1 on concentration fluctuation. Concentration is tremendously promoted with the advanced values of β_1. Physically, upgraded value of β_1 enhances the expansion rate that increases the movement of Oldroyd-B nanoparticles, and so concentration setup is boosted. Figure 10(a) establishes the link between retardation time Deborah number $0 \le \beta_2 \le 4$ and thermal fluctuation for the similarity variable $0 \le \eta \le 4$. At this time, thermal environment is degraded with the refined approximation of β_2. Fundamentally, β_2 involves in the momentum equation due to the presence of Oldroyd-B nanoparticles and is defined as the mathematical product of the stretching rate a and the retardation time λ_2. Therefore, estimation of β_2 augments the value of λ_2 as well as the expansion rate. As a conclusion, reduction in thermal setup is perceived with the

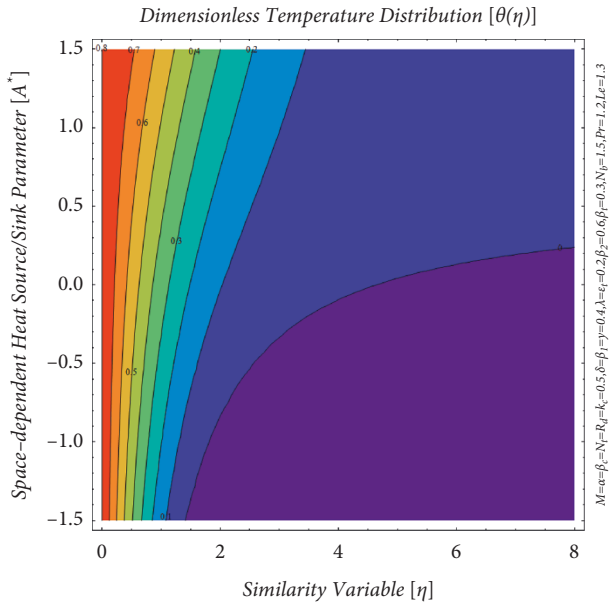

Figure 5: Interference of A^* on thermal layer $\theta(\eta)$.

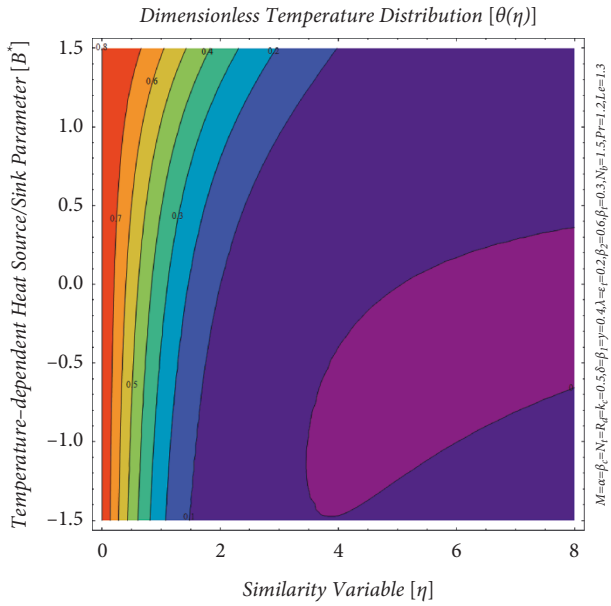

Figure 6: Interference of B^* on thermal layer $\theta(\eta)$.

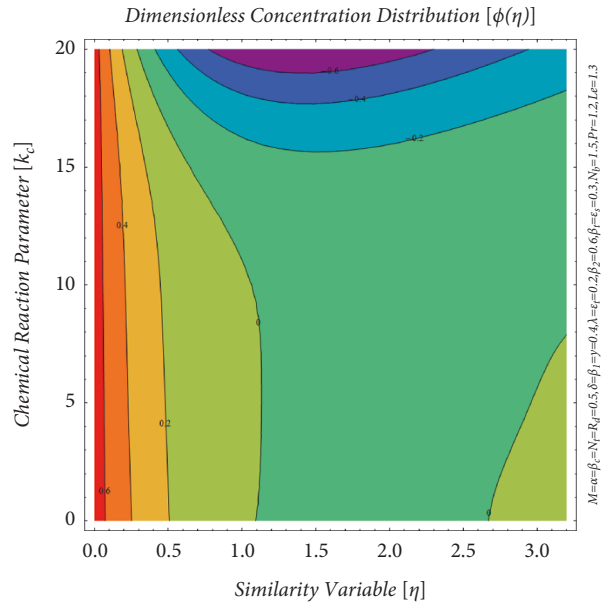

Figure 7: Interference of k_c on concentration layer $\phi(\eta)$.

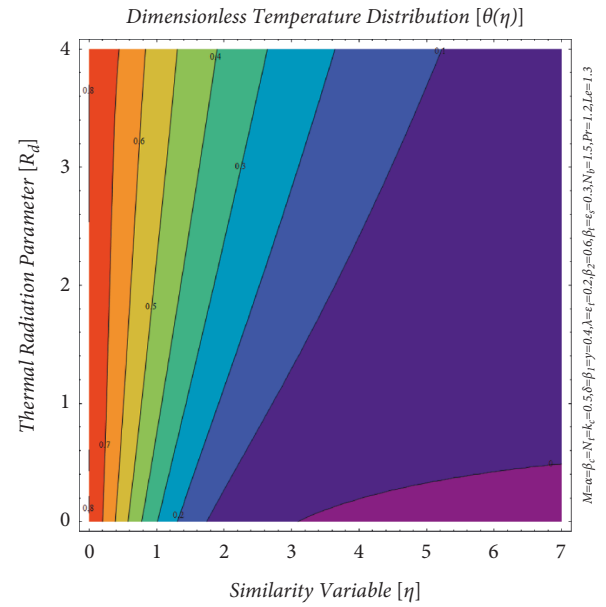

Figure 8: Interference of R_d on thermal layer $\theta(\eta)$.

progressive width of thermal stream. Figure 10(b) illustrates the influence of β_2 on concentration flux. Concentration is enormously decreased with the advancement of β_2. Actually, improved value of β_2 develops the retardation rate, and so concentration setup is reduced.

Nusselt number measures the rate of heat transference whereas Sherwood number measures the rate of mass transference from hot region to cold region. Figure 11 describes the rate of heat transport with the combined inspiration of random motion $0 \le N_b \le 3$ and thermodiffusion $0 \le N_t \le 5$ parameters. Rate of heat transport is declined with the upgraded amounts of these parameters related to the nanofluid. Maximal rate of heat transport is measured for smaller amounts of these nanoparticle parameters, whereas minimal rate of heat transport is attained for greater amounts of N_b and N_t. Maximum value of Nusselt number is approximated as 1.2, whereas minimum value of Nusselt number is estimated as 0.3 for the adopted ranges of Brownian and thermodiffusion parameters. Physically, a higher value of N_b enhances the Brownian diffusion coefficient, and a higher value of N_t enhances the thermodiffusion coefficient, whereas kinematic viscosity of Oldroyd-B nanofluid is reduced with the escalation of these parameters. As a whole, these physical changes are the main

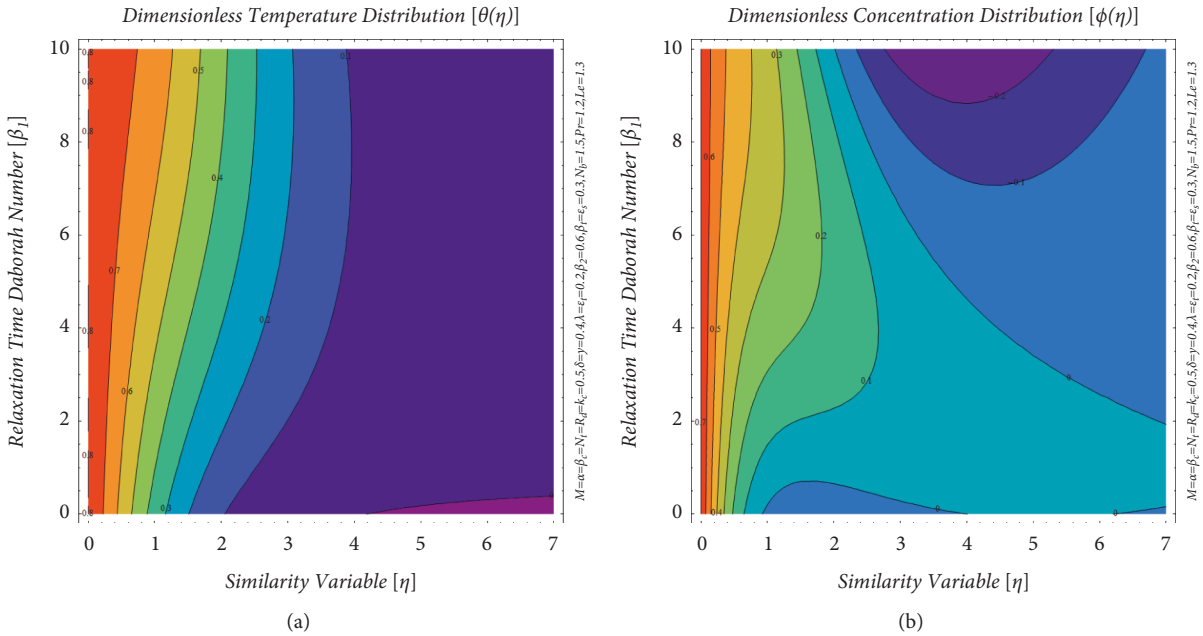

(a) (b)

Figure 9: (a) Interference of β_1 on thermal layer $\theta(\eta)$. (b) Interference of β_t on concentration layer $\phi(\eta)$.

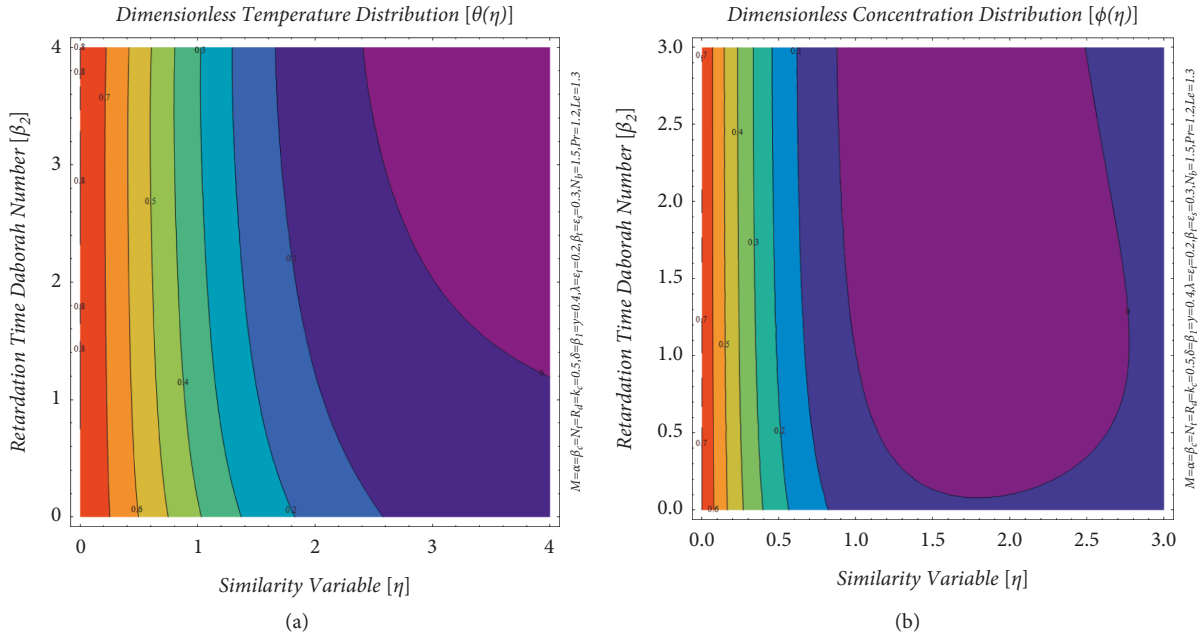

(a) (b)

Figure 10: (a) Interference of β_2 on thermal layer $\theta(\eta)$. (b) Interference of β_2 on concentration layer $\phi(\eta)$.

causes for the reduction of heat transport. Figure 12 shows the rate of mass transport with the collective stimulation of random motion $0 \le N_b \le 1$ and thermodiffusion $0 \le N_t \le 6$ parameters. Rate of mass transport is degenerated with the progress in the amount of N_t, whereas it is improved with the advancement in the amount of N_b. Highest rate of mass transport is stated for smaller choice of N_t and higher choice of N_b. Maximum value of Sherwood number is formulated as 1.4, whereas minimum value of Sherwood number is predicted as −0.4 for the implemented ranges of Brownian and thermodiffusion factors. Physically, a higher value of N_b enhances the heat capacity induced by nanoparticles, and a higher value of N_t develops the temperature difference, whereas density of Oldroyd-B nanofluid is upgraded with the intensification of these forces. Overall, these physical variations are the main reasons for the improvement of Sherwood number with the positive tendency in N_b and reduction of Sherwood number with the positive

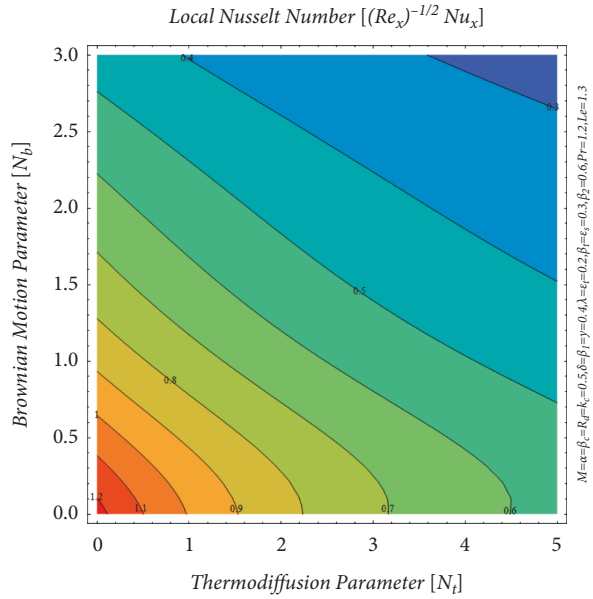

Figure 11: Nusselt number in the view of N_b and N_t.

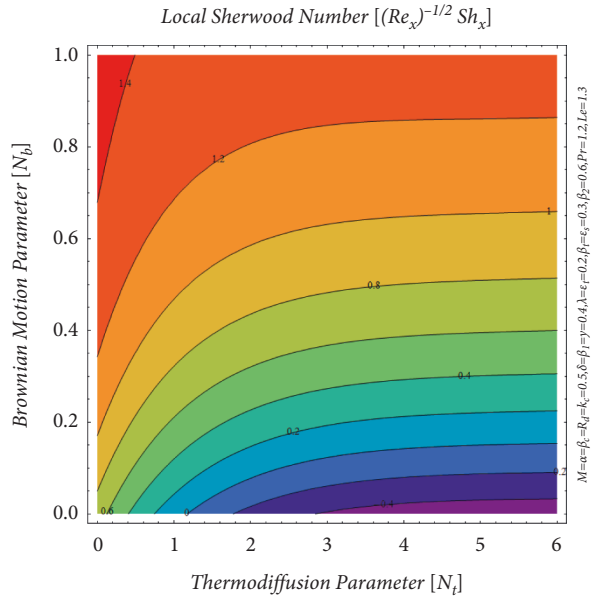

Figure 12: Sherwood number in the view of N_b and N_t.

approach of N_t. Figure 13(a) indicates the rate of heat transport with the communal effect of thermal convection parameter $0 \le \beta_t \le 100$ and concentration convection parameter $0 \le \beta_c \le 100$. The maximum value of heat transport is reported as 0.84 for smaller communal effect of convection parameters, whereas the minimum value of heat transport is calculated as 0.7 for larger communal effect of convection parameters. Nusselt number is reduced with the higher estimation of β_c, and it is improved with the growth of β_t. On the other hand, Figure 13(b) explains the rate of mass transport with the combined effect of convection parameters. Sherwood number is improved with the estimation of β_t, and it is reduced with the growth of β_c. Maximum mass transport is observed at the right top of the figure and minimal mass transport is noticed at the left bottom of the figure. Physically, thermal convection parameter depends on the temperature difference, and thermal environment is reduced with its escalation; hence, rate of heat transport is improved. Moreover, concentration convection parameter relies on the concentration difference, and thermal environment is boosted with its growth; hence, rate of heat transport is reduced for this situation.

Table 2 is arranged to compare the present outcomes with the previously published work in the absence of

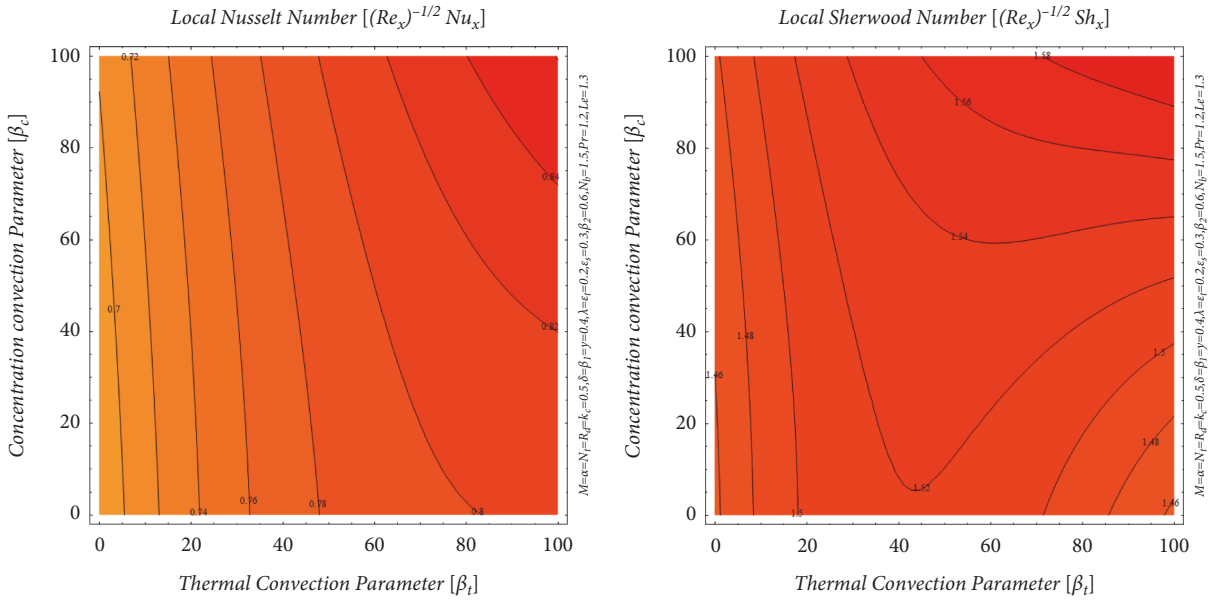

(a) (b)

Figure 13: (a) Nusselt number in the view of β_t and β_c. (b) Sherwood number in the view of β_t and β_c.

Table 2: Comparison establishment with the previously published report of Azeem Khan et al. [44] for $\delta = M = \lambda = \beta_t = \beta_c = A^* = \varepsilon_t = \varepsilon_s = R_d = \gamma = k_r = 0$.

α	Pr	B^*	N_b	N_t	Le	Present outcomes		Published outcomes [44]	
						$-\theta'(0)$	$-\phi'(0)$	$-\theta'(0)$	$-\phi'(0)$
0.0	1.2	0.2	0.1	0.1	1.0	0.351853	0.474210	0.351853	0.474210
0.3						0.509837	0.482838	0.509837	0.482838
0.4						0.549438	0.488939	0.549438	0.488939
0.5	1.0					0.513728	0.430930	0.513728	0.430930
	1.1					0.551238	0.463216	0.551238	0.463216
	1.3					0.617393	0.527723	0.617393	0.527723
		0.0				0.757208	0.356670	0.757208	0.356670
		0.1				0.676907	0.422143	0.676907	0.422143
		0.4				0.335390	0.690221	0.335390	0.690221
			0.2			0.540514	0.683362	0.540514	0.683362
			0.3			0.497586	0.745281	0.497586	0.745281
			0.4			0.456841	0.775726	0.456841	0.775726
				0.2		0.575795	0.199343	0.575795	0.199343
				0.4		0.505394	0.277762	0.505394	0.277762
				0.5		0.480757	0.464410	0.480757	0.464410
					0.8	0.591165	0.352548	0.591165	0.352548
					0.9	0.588200	0.426414	0.588200	0.426414
					1.1	0.583427	0.560578	0.583427	0.560578

porosity, magnetic environment, dual stratifications, radiation, chemical reaction, and space-dependent heat source/sink factors. The reduced results for thermal and concentration gradients are best matched with the previously published report by Khan et al. [47] via homotopy analysis method.

6. Conclusions

The significance of higher-order chemical reaction and nonuniform heat source/sink influence on the dynamics of Oldroyd-B nanoparticles have been analytically investigated in this contribution. For physical relevancy, thermal radiation, mixed convection, and double stratification have also been incorporated in the bidirectional flow of the nanoliquid with the help of Buongiorno nanofluid model. Chief findings/outcomes of the ongoing exploration are listed below:

(i) Level of heat exposure is improved with the intensification in thermal stratification parameter ε_t, whereas level of mass exposure is reduced with

the improvement in solutal stratification parameter ε_s.

(ii) Level of mass exposure is developed with the higher selections of Brownian motion N_b and chemical reaction k_r parameters, whereas level of heat exposure is condensed with the escalation in the choices of heat source/sink parameters A^*&B^* and radiation factor R_d.

(iii) Nusselt and Sherwood numbers are decreased with greater amounts of concentration convection parameter, whereas opposite trend is noticed for thermal convection parameter.

(iv) Higher estimations of Brownian and thermodiffusion parameters reduce the rate of heat transport.

(v) Temperature and concentration profiles are reduced with the positive tendency of retardation time Deborah number β_2, and opposite trends are detected for relaxation time Deborah number β_1.

Finally, the outcomes obtained through this investigation are helpful in the improvement of thermal instruments. This mathematical model has some applications in biomedicine and chemical and mechanical engineering like coating a sheet with nanomaterial, paper production process, and treatment of cancer.

Data Availability

The raw data supporting the conclusion of this paper will be made available by the corresponding author without undue reservation.

Conflicts of Interest

The authors declare that they have no conflicts of interest.

Authors' Contributions

All authors contributed equally to this work and read and approved the final version of the paper.

References

[1] S. U. Choi and J. A. Eastman, "Enhancing thermal Conductivity of Fluids with Nanoparticles," in *Proceedings of the 1995 International mechanical engineering congress and exhibition*, Argonne National Lab., IL (United States), San Francisco, CA, USA, November 1995.

[2] Y. Xuan and Q. Li, "Heat transfer enhancement of nanofluids," *International Journal of Heat and Fluid Flow*, vol. 21, no. 1, pp. 58–64, 2000.

[3] J. Buongiorno, "Convective transport in nanofluids," *Journal of Heat Transfer*, vol. 128, no. 3, pp. 240–250, 2006.

[4] B. C. Sakiadis, "Boundary-layer behavior on continuous solid surfaces: I. Boundary-layer equations for two-dimensional and axisymmetric flow," *AIChE Journal*, vol. 7, no. 1, pp. 26–28, 1961.

[5] L. J. Crane, "Flow past a stretching plate," *Zeitschrift für angewandte Mathematik und Physik ZAMP*, vol. 21, no. 4, pp. 645–647, 1970.

[6] C. Y. Wang, "The three-dimensional flow due to a stretching flat surface," *Physics of Fluids*, vol. 27, no. 8, pp. 1915–1917, 1984.

[7] P. D. Ariel, "Generalized three-dimensional flow due to a stretching sheet," *Zamm*, vol. 83, no. 12, pp. 844–852, 2003.

[8] M. Sajid and T. Hayat, "Influence of thermal radiation on the boundary layer flow due to an exponentially stretching sheet," *International Communications in Heat and Mass Transfer*, vol. 35, no. 3, pp. 347–356, 2008.

[9] W. A. Khan and I. Pop, "Boundary-layer flow of a nanofluid past a stretching sheet," *International Journal of Heat and Mass Transfer*, vol. 53, no. 11-12, pp. 2477–2483, 2010.

[10] K. Bhattacharyya and G. C. Layek, "Chemically reactive solute distribution in MHD boundary layer flow over a permeable stretching sheet with suction or blowing," *Chemical Engineering Communications*, vol. 197, no. 12, pp. 1527–1540, 2010.

[11] I. Ahmad, M. Ahmed, Z. Abbas, and M. Sajid, "Hydromagnetic flow and heat transfer over a bidirectional stretching surface in a porous medium," *Thermal Science*, vol. 15, no. 2, pp. 205–220, 2011.

[12] I. C. Liu and H. I. Andersson, "Heat transfer over a bidirectional stretching sheet with variable thermal conditions," *International Journal of Heat and Mass Transfer*, vol. 51, no. 15-16, pp. 4018–4024, 2008.

[13] W. Ibrahim and O. D. Makinde, "The effect of double stratification on boundary-layer flow and heat transfer of nanofluid over a vertical plate," *Computers & Fluids*, vol. 86, pp. 433–441, 2013.

[14] K. Loganathan, S. Sivasankaran, M. Bhuvaneswari, and S. Rajan, "Second-order slip, cross-diffusion and chemical reaction effects on magneto-convection of Oldroyd-B liquid using Cattaneo-Christov heat flux with convective heating," *Journal of Thermal Analysis and Calorimetry*, vol. 136, no. 1, pp. 401–409, 2019.

[15] N. Sandeep and M. G. Reddy, "MHDOldroyd-B fluid flow across a melting surface with cross diffusion and double stratification," *The European Physical Journal Plus*, vol. 132, no. 3, pp. 1–18, 2017.

[16] M. Waqas, M. Ijaz Khan, T. Hayat, and A. Alsaedi, "Stratified flow of an Oldroyd-B nanoliquid with heat generation," *Results in Physics*, vol. 7, pp. 2489–2496, 2017.

[17] M. Turkyilmazoglu and I. Pop, "Heat and mass transfer of unsteady natural convection flow of some nanofluids past a vertical infinite flat plate with radiation effect," *International Journal of Heat and Mass Transfer*, vol. 59, pp. 167–171, 2013.

[18] M. M. Rashidi, S. Abelman, and N. Freidooni Mehr, "Entropy generation in steady MHD flow due to a rotating porous disk in a nanofluid," *International Journal of Heat and Mass Transfer*, vol. 62, pp. 515–525, 2013.

[19] A. Moradi, A. Alsaedi, and T. Hayat, "Investigation of nanoparticles effect on the jeffery-hamel flow," *Arabian Journal for Science and Engineering*, vol. 38, no. 10, pp. 2845–2853, 2013.

[20] O. D. Makinde, W. A. Khan, and Z. H. Khan, "Buoyancy effects on MHD stagnation point flow and heat transfer of a nanofluid past a convectively heated stretching/shrinking sheet," *International Journal of Heat and Mass Transfer*, vol. 62, pp. 526–533, 2013.

[21] B. Mahanthesh, B. J. Gireesha, S. A. Shehzad, F. M. Abbasi, and R. S. R. Gorla, "Nonlinear three-dimensional stretched flow of an Oldroyd-B fluid with convective condition, thermal radiation, and mixed convection," *Applied Mathematics and Mechanics*, vol. 38, no. 7, pp. 969–980, 2017.

[22] A. K. Ghosh and P. Sana, "On hydromagnetic flow of an Oldroyd-B fluid near a pulsating plate," *Acta Astronautica*, vol. 64, no. 2-3, pp. 272–280, 2009.

[23] S. Mukhopadhyay, "Effects of slip on unsteady mixed convective flow and heat transfer past a porous stretching surface," *Nuclear Engineering and Design*, vol. 241, no. 8, pp. 2660–2665, 2011.

[24] R. Kandasamy, I. Muhaimin, and A. K. Rosmila, "The performance evaluation of unsteady MHD non-Darcy nanofluid flow over a porous wedge due to renewable (solar) energy," *Renewable Energy*, vol. 64, pp. 1–9, 2014.

[25] R. S. Tripathy, G. C. Dash, S. R. Mishra, and S. Baag, "Chemical reaction effect on MHD free convective surface over a moving vertical plate through porous medium," *Alexandria Engineering Journal*, vol. 54, no. 3, pp. 673–679, 2015.

[26] A. Ali, H. Zaman, M. Z. Abidin, and S. I. A. Shah, "Analytic solution for fluid flow over an exponentially stretching porous sheet with surface heat flux in porous medium by means of homotopy analysis method," *American Journal of Computational Mathematics*, vol. 05, no. 02, pp. 224–238, 2015.

[27] B. S. Goud, "MHD flow past a vertical oscillating plate with radiation and chemical reaction in porous medium-finite difference method," *International Journal of Emerging Trends in Engineering Research*, vol. 5, no. 11, pp. 32–35, 2017.

[28] M. Faisal, I. Ahmad, and T. Javed, "Numerical assessments of prescribed heat sources on unsteady 3D flow of Williamson nanoliquid through porous media," *Special Topics & Reviews in Porous Media - An International Journal*, vol. 12, no. 2, pp. 71–92, 2021.

[29] P. Besthapu, R. U. Haq, S. Bandari, and Q. M. Al-Mdallal, "Mixed convection flow of thermally stratified MHD nanofluid over an exponentially stretching surface with viscous dissipation effect," *Journal of the Taiwan Institute of Chemical Engineers*, vol. 71, pp. 307–314, 2017.

[30] I. Ahmad, M. Faisal, and T. Javed, "Unsteady rotating flow of nanofluid with prescribed thermal aspects," *International Journal of Modern Physics C*, vol. 32, no. 7, pp. 1–18, 2021.

[31] T. S. Karthik, K. Loganathan, A. N. Shankar et al., "Zero and nonzero mass flux effects of bioconvective viscoelastic nanofluid over a 3D riga surface with the swimming of gyrotactic microorganisms," *Advances in Mathematical Physics*, vol. 2021, Article ID 9914134, 13 pages, 2021.

[32] T. Hayat, M. Z. Kiyani, I. Ahmad, and A. Alsaedi, "Double stratified radiative flow of an Oldroyd-B nanofluid with nonlinear convection," *Applied Mathematics and Mechanics*, vol. 40, no. 12, pp. 1861–1878, 2019.

[33] I. Ahmad, M. Faisal, and T. Javed, "Dynamics of copper-water nanofluid with the significance of prescribed thermal conditions," *Heat Transfer*, vol. 50, no. 5, pp. 4248–4263, 2021.

[34] M. Faisal, I. Ahmad, and T. Javed, "Keller-Box simulation for nonzero and zero mass fluxes of nanofluid flow impinging over a bi-directional stretching sheet: an unsteady mathematical model," *International Journal of Modern Physics C*, vol. 32, no. 4, Article ID 2150052, 2021.

[35] G. Sarojamma, R. Vijaya Lakshmi, K. Sreelakshmi, and K. Vajravelu, "Dual stratification effects on double-diffusive convective heat and mass transfer of a sheet-driven micropolar fluid flow," *Journal of King Saud University Science*, vol. 32, no. 1, pp. 366–376, 2020.

[36] D. Srinivasacharya and O. Surender, "Effect of double stratification on mixed convection boundary layer flow of a nanofluid past a vertical plate in a porous medium," *Applied Nanoscience*, vol. 5, no. 1, pp. 29–38, 2015.

[37] I. Ahmad, I. Khurshid, M. Faisal, T. Javed, and Z. Abbas, "Mixed convective flow of an Oldroyd-B nanofluid impinging over an unsteady bidirectional stretching surface with the significances of double stratification and chemical reaction," *SN Applied Sciences*, vol. 2, no. 9, pp. 1–14, 2020.

[38] K. Loganathan, K. Mohana, M. Mohanraj, P. Sakthivel, and S. Rajan, "Impact of third-grade nanofluid flow across a convective surface in the presence of inclined Lorentz force: an approach to entropy optimization," *Journal of Thermal Analysis and Calorimetry*, vol. 144, no. 5, pp. 1935–1947, 2020.

[39] M. Faisal, I. Ahmad, and T. Javed, "Dynamics of MHD tangent hyperbolic nanofluid with prescribed thermal conditions, random motion and thermo-migration of nanoparticles," *Journal of Dispersion Science and Technology*, pp. 1–15, 2021.

[40] K. Loganathan and S. Rajan, "An entropy approach of Williamson nanofluid flow with Joule heating and zero nanoparticle mass flux," *Journal of Thermal Analysis and Calorimetry*, vol. 141, pp. 2599–2612, 2020.

[41] I. Ahmad, M. Faisal, and T. Javed, "Magneto-nanofluid flow due to bidirectional stretching surface in a porous medium," *Special Topics & Reviews in Porous Media - An International Journal*, vol. 10, no. 5, pp. 457–473, 2019.

[42] T. Hayat, T. Muhammad, S. A. Shehzad, M. S. Alhuthali, and J. Lu, "Impact of magnetic field in three-dimensional flow of an Oldroyd-B nanofluid," *Journal of Molecular Liquids*, vol. 212, pp. 272–282, 2015.

[43] I. Ahmad, M. Faisal, and T. Javed, "Unsteady flow of Walters-B magneto-nanofluid over a bidirectional stretching surface in a porous medium with heat generation," *Special Topics & Reviews in Porous Media - An International Journal*, vol. 12, no. 3, pp. 49–70, 2021.

[44] W. Azeem Khan, M. Khan, and R. Malik, "Three-dimensional flow of an Oldroyd-B nanofluid towards stretching surface with heat generation/absorption," *PLoS One*, vol. 9, no. 8, Article ID e105107, 2014.

[45] I. Ahmad, M. Faisal, T. Javed, and I. L. Animasaun, "Insight into the relationship between unsteady Cattaneo-Christov double diffusion, random motion and thermo-migration of tiny particles," *Ain Shams Engineering Journal*, vol. 13, 2021.

[46] S. Asghar, M. Jalil, M. Hussan, and M. Turkyilmazoglu, "Lie group analysis of flow and heat transfer over a stretching rotating disk," *International Journal of Heat and Mass Transfer*, vol. 69, pp. 140–146, 2014.

[47] M. Turkyilmazoglu, "Nanoliquid film flow due to a moving substrate and heat transfer," *The European Physical Journal Plus*, vol. 135, no. 10, pp. 1–13, 2020.

[48] I. Ahmad, M. Faisal, T. Javed, A. Mustafa, and M. Z. Kiyani, "Numerical investigation for mixed convective 3D radiative flow of chemically reactive Williamson nanofluid with power law heat/mass fluxes," *Ain Shams Engineering Journal*, vol. 13, 2021.

[49] J. A. Khan, M. Mustafa, T. Hayat, M. Turkyilmazoglu, and A. Alsaedi, "Numerical study of nanofluid flow and heat transfer over a rotating disk using Buongiorno's model," *International Journal of Numerical Methods for Heat and Fluid Flow*, vol. 27, no. 1, pp. 221–234, 2017.

[50] M. Turkyilmazoglu, "On the transparent effects of Buongiorno nanofluid model on heat and mass transfer," *The European Physical Journal Plus*, vol. 136, no. 4, pp. 1–15, 2021.

Hindawi
Mathematical Problems in Engineering
Volume 2022, Article ID 5759671, 17 pages
https://doi.org/10.1155/2022/5759671

Research Article

Entropy Minimization on Sutterby Nanofluid past a Stretching Surface with Swimming of Gyrotactic Microorganisms and Nanoparticles

F. Ali,[1] **K. Loganathan**,[2,3] **E. Prabu**,[4] **S. Eswaramoorthi**,[5] **M. Faizan**,[1] **A. Zaib**,[1] **and Dinesh Kumar Chaudhary**[6]

[1]*Department of Mathematical Sciences, Federal Urdu University of Arts, Sciences & Technology, Gulshan-e-Iqbal, Karachi 75300, Pakistan*
[2]*Department of Mathematics and Statistics, Manipal University Jaipur, Jaipur-303007, Rajasthan, India*
[3]*Research and Development Wing, Live4Research, Tiruppur 638106, Tamilnadu, India*
[4]*Department of Mathematics, Erode Arts and Science College, Erode, Tamilnadu, India*
[5]*Department of Mathematics, Dr. N. G. P. Arts and Science College, Coimbatore, Tamilnadu, India*
[6]*Department of Physics Amrit Campus, Tribhuvan University, Kathmandu, Nepal*

Correspondence should be addressed to K. Loganathan; loganathankaruppusamy304@gmail.com and Dinesh Kumar Chaudhary; din.2033@gmail.com

Received 19 December 2021; Revised 22 February 2022; Accepted 1 March 2022; Published 10 May 2022

Academic Editor: Ahmed Zeeshan

This analysis examines the flow of Sutterby nanofluid having bioconvection due to a stretching sheet and heated convective boundary condition. The heat sink/source was imposed in terms of the energy equation. The entropy minimization is also considered. Through the appropriate transformation of the system of nonlinear PDE's setting, the existing problem has altered into nonlinear ODEs and then numerically utilized via the bvp4c method. The numerical values of skin friction, Nusselt number, Sherwood number, and motile density profiles are revealed in a tabular form. In comparison, other governing variables on velocity, temperature, concentration, and bioconvection are seen through various plots and discussed. For example, increment in the Deborah number of heat flux depreciated in temperature distribution while opposite observation was carried out for heat source and sink parameter. Moreover, it has also been investigated that the shear-thinning fluid is entirely reverse to that of the shear thickening fluid. Further, the increase in the magnetic number accelerates in the Bejan number and irreversibility ratio. Finally, the comparison has been made with previous literature and found an excellent agreement.

1. Introduction

The non-Newtonian fluid flow past the stretching surface has massive features in science and engineering technology. Various kinds of non-Newtonian fluid models are paid widely remarkable attention due to their outstanding features such as polymers solution, multiple types of engine oil, and paint. The power-law model has been achieved by the rheological properties of complex fluids such as oil and polymer solution. Sutterby fluid model [1, 2] validates the phenomenon of pseudoplastic and dilatants and obtains comprehensive mathematical expression. The hyperbolic tangent flow with the Dufour effect due to stretching surface was attempted by Gangadhar et al. [3]. MHD flow of Sutterby fluid in a Darcy surface has been conducted by Bilal et al. [4]. The thermal behavior of Sutterby nanomaterial with stratification is discussed by Nazeer and others [5]. Khan et al. [6] described Sutterby nanofluid over a rotating disk. The combined effect of heat and mass transfer in the MHD flow of Sutterby nanoliquid due to stretching cylinder is deliberated by Sohail and Naz [7]. Rehman and others [8] reported the thermal stratification phenomenon on the Sutterby nanofluid with zero mass flux

condition. The significance of heat and mass transfer on Sutterby nanofluid past a wedge surface was discussed by Usman and others. [9]. Bhatti [10] et al. reported the chemically reactive mass transport mechanism on the Jeffrey fluid model in the presence of extrinsic magnetic impact discussed in this paper. A permeable material is used to move the fluid. The mathematical modeling of momentum and concentration equations is done via Lie group transformations. Loganathan et al. [11] conducted a steady flow of thermal analysis of Oldroyd-B flow under second-order slip and cross-diffusion effects.

In the last few decades, nanofluid established the contemplation of numerous researchers because of their various industrial and mechanical engineering applications. It is also observed that heat transport fluids efficiently depend on their physical distinctiveness, such as thermal conductivity. There are a few base fluids containing water, oil, ethylene, and many more that have less conductivity. As a result, such types of liquids have deprived heat transfer phenomena. So, enhancing their thermal conductivity needs to be an important problem to receive the views of recent scholars. The word nanofluid was employed by [12], which showed thermal performance. Later, to augment the thermal properties of nanofluid, Buongiorno [13] added two main features of nanoliquid, namely, Brownian movement and thermophoretic. The MHD flow of micropolar nanomaterial between two rotating surfaces has been designed by Islam et al. [14]. Nonlinear radiation, swimming microorganisms, and nanoparticles with a 3D bioconvective viscoelastic nanofluid flow across a heated Riga surface were studied by Karthik et al. [15]. Ijaz et al. [16] studied the radiative flow of Sisko nanofluid over a stretching rotating circle with entropy generation. The impact of nanofluid characteristics and heat exchange inside a twisted tube over a revolving disk is pointed out by Alempour et al. [17]. The research by Abo-Elkhair et al. [18] looks at the effects of magnetic force and nonlinear thermal radiation on hybrid bio-nanofluid flow in a peristaltic channel under the influence of a high and low Reynolds number applied magnetic field. Sabir et al. [19] introduced the influence of thermal radiative on Sutterby nanofluid by using Cattaneo-Christov heat near the stagnation point. Ali and Zaib [20] studied time-dependent Eyring-Powell comprising nanoliquid due to convective conditions. Khan et al. [21] looked at the effect of heat and mass transport on third-grade nanofluid due to heat convectively stretching sheet. Ibrahim and Makinde [22] considered the power-law nanofluid over convective boundary conditions near the stagnation point. Bhatti et al. [23] address the nanofluid flow and microbe swimming across parallel rotating circular plates separated by a limited distance and containing a porous media.

In the past few years, numerous analyses into energy creation in various fluid stream conditions have been taken out by investigators' attention on the entropy generation. Many investigators are stimulated by recognizing the features of entropy production in liquid flow and some applications such as heat pumps, fire engines, air conditioners, and many more. The entropy production minimization had been coined by Bejan [24]. Later, the impact of entropy production on the Sutterby nanofluid past a stretching surface near the stagnation point was discovered by Azhar et al. [25]. Hayat et al. [26] discussed the MHD peristaltic flow of Sutterby nanofluid and entropy generation. Loganathan et al. [27] examined the third-grade nanofluid flow over a stretching plate with entropy generation. They found that, for the higher thermal relaxation time parameter, the entropy production and Bejan number profiles show the opposite impact. Furthermore, the radiation constant, Biot number, suction/injection constant, Hartmann number, and Brinkman number all improve the system's entropy. Yousaf and others [28] explained the influence of entropy optimization and motile density of Williamson nanofluid past an inclined sheet. Makinde and Tshehla [29] deliberated the mixed convective flow of nanoliquid in an entropy minimization and mass suction/injection. Loganathan and Rajan [30] presented the Williamson nanofluid flow with zero mass flux and Joule heating impacts. They also found the entropy generation of the problem. Afridi et al. [31] considered Newtonian flow for entropy minimization induced by the thermal radiative flow. Inside the cavity, the entropy production of fluid flow with the permeable surface is scrutinized by Alsabery [32].

Sutterby fluid [1, 2] is one of the very important non-Newtonian fluids which shows the modeled equations of high polymer aqueous solution. The current analysis is dedicated to inspecting the entropy production on bioconvection for the flow of Sutterby fluid because a heated convective sheet is examined. Thermal radiation, heat sink/source, Brownian motion, and thermophoresis are also considered. The main aim of this study is that the non-Newtonian Sutterby fluid is selected to examine the rheological properties of shear-thinning/thickening with the effect of thermal radiation and microorganism. The similarity conversion is used to alter the nonlinear PDE into ODE to solve modeled equations. The numerical solution of these modeled equations has been produced via BVP4c in Matlab. To investigate the behavior of velocity, temperature, concentration, and motile density, they are plotted against numerous variables. The numerical computation is displayed in the form of figures and tables. Manufacturing of rubber and plastic sheets, melt-spinning, glass-fiber manufacturing, and metallic plate cooling systems are some of the beneficial uses of this sort of inquiry. Also, the Bejan number is used to estimate entropy generation in power engineering and aeronautical propulsion to forecast the smartness of the overall system.

1.1. Mathematical Formulation. The incompressible, laminar, time-dependent flow of Sutterby nanomaterial past stretching sheet subject to the convective condition and entropy production is examined. The stretching sheet velocity is $U_w(x,t) = ax/1 - \gamma t$. The mathematical modeling of the physical problem is designed with coordinate (x, y) with velocity component $(\hat{u}, \hat{v})$ taken in x- and y-axis (see Figure 1). The mathematical formulation for Sutterby nanofluid in a steady flow is taken in [25], and it converted to be unsteady in the following flow equations.

$$\frac{\partial \hat{u}}{\partial x} + \frac{\partial \hat{v}}{\partial y} = 0, \tag{1}$$

$$\frac{\partial \hat{u}}{\partial t} + \hat{u}\frac{\partial \hat{u}}{\partial x} + \hat{v}\frac{\partial \hat{u}}{\partial y} = \frac{\mu_0}{\rho}\left[\frac{\partial^2 \hat{u}}{\partial y^2} + \frac{mB^2}{2}\left(\frac{\partial \hat{u}}{\partial y}\right)^2 \frac{\partial^2 \hat{u}}{\partial y^2}\right] - \frac{\sigma}{\rho}B_0^2 \hat{u}, \tag{2}$$

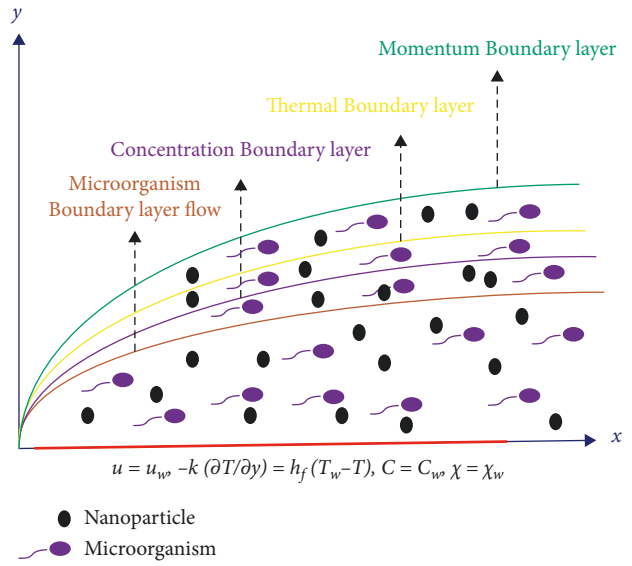

Figure 1: Physical model.

$$\frac{\partial \widehat{T}}{\partial t}+\widehat{u}\frac{\partial \widehat{T}}{\partial x}+v\frac{\partial \widehat{T}}{\partial y}=\frac{k}{\rho C_p}\left(\frac{\partial^2 \widehat{T}}{\partial y^2}\right)+\tau\left(D_B\frac{\partial \widehat{C}}{\partial y}\frac{\partial \widehat{T}}{\partial y}+\frac{D_T}{\widehat{T}_\infty}\left(\frac{\partial \widehat{T}}{\partial y}\right)^2\right)-\frac{1}{\rho C_p}\frac{\partial q_r}{\partial y}+\frac{Q_0}{\rho C_p}\left(\widehat{T}-\widehat{T}_\infty\right), \tag{3}$$

$$\frac{\partial \widehat{C}}{\partial t}+\widehat{u}\frac{\partial \widehat{C}}{\partial x}+\widehat{v}\frac{\partial \widehat{C}}{\partial y}=D_B\frac{\partial^2 \widehat{c}}{\partial y^2}+\frac{D_T}{\widehat{T}_\infty}\left(\frac{\partial^2 \widehat{T}}{\partial y^2}\right)-\kappa_0\left(\widehat{C}-\widehat{C}_\infty\right), \tag{4}$$

$$\frac{\partial \widehat{\chi}}{\partial t}+\widehat{u}\frac{\partial \widehat{\chi}}{\partial x}+\widehat{v}\frac{\partial \widehat{\chi}}{\partial y}+\frac{bW_c}{\left(\widehat{C}_w-\widehat{C}_\infty\right)}\frac{\partial}{\partial y}\left(\widehat{\chi}\frac{\partial \widehat{C}}{\partial y}\right)=D_m\frac{\partial^2 \widehat{\chi}}{\partial y^2}. \tag{5}$$

With boundary condition,

$$\widehat{u}=U_w(x,t),\ \widehat{v}=0,\ -k\frac{\partial \widehat{T}}{\partial y}=h(t)\left(\widehat{T}_w-\widehat{T}_\infty\right),$$

$$\widehat{C}=\widehat{C}_w,\widehat{\chi}=\widehat{\chi}_w\ \ y=0,$$

$$\widehat{u}\longrightarrow 0,\ \widehat{T}\longrightarrow\widehat{T}_\infty,\ \widehat{C}\longrightarrow\widehat{C}_\infty,\widehat{\chi}\longrightarrow\widehat{\chi}_\infty\ at\ \ y\longrightarrow\infty. \tag{6}$$

In equation (2), m shows three conditions. If $m<0$, then it shows pseudoplastic or represents fluid with decreasing viscosity; if $m>0$, it demonstrates the dilatant or fluid with increasing viscosity; if $m=0$, it reflects the Newtonian fluid.

The Rosseland approximation is crucial in thermal radiative heat flow. The Rosseland approximation requires an optically thick medium and radiation that travels only a short distance before being scattered or absorbed. As a result, a simplified model for the Radiative Transfer Equation (RTE) based on the Rosseland approximation is provided as follows:

$$q_r=\frac{4\sigma_1}{3k*}\frac{\partial \widehat{T}^4}{\partial y}=-\frac{16\sigma^*}{3k^*}\widehat{T}^3\frac{\partial \widehat{T}^4}{\partial y}, \tag{7}$$

where $\widehat{T}^4$ can be expanded as follows:

$$\widehat{T}^4\cong 4\widehat{T}_\infty^3\widehat{T}-3\widehat{T}_\infty^4. \tag{8}$$

Replacing equation (7) into equation (8),

$$q_r=\frac{16\sigma*T_\infty^3}{3k*}\frac{\partial \widehat{T}}{\partial y}. \tag{9}$$

Similarity expressions are

$$\left.\begin{aligned}&\widehat{u}=\frac{ax}{1-\gamma t}f'(\eta),\ \widehat{v}=-\sqrt{\frac{av}{1-\gamma t}}f(\eta),\ \eta=\sqrt{\frac{a}{v(1-\gamma t)}}y,\\&\theta=\frac{\widehat{T}-\widehat{T}_\infty}{\widehat{T}_w-\widehat{T}_\infty},\phi=\frac{\widehat{C}-\widehat{C}_\infty}{\widehat{C}_w-\widehat{C}_\infty},N=\frac{\widehat{\chi}-\widehat{\chi}_\infty}{\widehat{\chi}_w-\widehat{\chi}_\infty},\end{aligned}\right\} \tag{10}$$

$$f'''+ff''-f'^2-A\left(f'+\frac{\eta}{2}f''\right)+\frac{1}{2}m\delta\mathrm{Re}f''^2f'''+Mf'=0, \tag{11}$$

$$\theta''\left(1+\frac{4}{3}Rd\right)-\Pr\frac{1}{2}\eta A\theta'+\Pr Nt\theta'^2+\Pr Nb\theta'\phi'+\Pr\varepsilon\theta=0, \tag{12}$$

$$\phi''+Sc\left(f\phi'\right)-\frac{1}{2}\eta ScA\phi'+\left(\frac{Nb}{Nt}\right)\theta''-Sc\kappa\phi=0, \tag{13}$$

$$N''-Pe\left[\phi''(N+\varpi)+\phi'N'\right]-Lb\left(\frac{1}{2}\eta AN'+fN'\right)=0. \tag{14}$$

The converted boundary conditions are

$$\left.\begin{aligned}&f(0)=0,f'(0)=1,\theta'(0)=-Bi+Bi(\theta(0)),\phi(0)=1\\&f'(\infty)=0,\theta(\infty)=0,\phi(\infty)=0,N(\infty)=0.\end{aligned}\right. \tag{15}$$

The Reynolds number ($\mathrm{Re}=ax^2/v$), Deborah number ($\delta=B^2a^2/v$), magnetic parameter ($M=\sigma B_0^2/\rho a$), unsteady parameter ($A=\gamma/a$), heat source parameter (ε), radiation parameter ($R\,d=(4\sigma^*T_\infty^3)/(kk^*)$), Prandtl number ($\Pr=v/\alpha$), Brownian motion parameter ($Nb=\tau D_B(\widehat{C}_w-\widehat{C}_\infty)/v$), thermophoresis parameter ($Nt=\tau D_T(\widehat{T}_w-\widehat{T}_\infty)/\widehat{T}_\infty v$), Schmidt number ($Sc=v/D_B$), Biot number ($Bi=d/k\sqrt{v/a}$), microorganisms concentration ($\varpi=\widehat{\chi}_\infty/\widehat{\chi}_m-\widehat{\chi}_\infty$), Bioconvection Peclet number ($Pe=bW_c/D_m$). Bioconvection Lewis number ($Lb=v/D_m$) are shown.

2. Engineering Interest Quantities

$$C_{fx} = \frac{\tau_w}{\rho u_w^2},\ Nu_x = \frac{xq_w}{k\left(\widehat{T}_w - \widehat{T}_\infty\right)},$$
$$Sh_x = \frac{xq_m}{D_b\left(\widehat{C}_w - \widehat{C}_\infty\right)}, \tag{16}$$
$$Nn = \frac{xq_n}{D_m\left(\widehat{\chi}_w - \widehat{\chi}_\infty\right)}.$$

Shear wall τ_w, heat q_w, mass q_m, and motile density q_n have been displayed as

$$\tau_w = -\mu_0\left[\frac{\partial \widehat{u}}{\partial y} + \frac{m}{6}\mathrm{Re}\ \delta\left(\frac{\partial \widehat{u}}{\partial y}\right)^3\right]_{y=0}$$
$$q_w = -k\left(\frac{\partial \widehat{T}}{\partial y}\right)\Big|,\ q_m = -k\left(\frac{\partial \widehat{C}}{\partial y}\right)\Big|_{y=0},$$
$$q_n = -D_m\left(\frac{\partial \widehat{\chi}}{\partial y}\right)\Big|_{y=0}. \tag{17}$$

In the use of (10) and (17),

$$C_f \mathrm{Re}_x^{0.5} = \left[f''(0) + \frac{m}{6}\delta\,\mathrm{Re}\left(f''(0)\right)^3\right],$$
$$\frac{Nu_x}{Re_x^{1/2}} = -\theta'(0)\left[1 + \frac{4}{3}Rd\right],$$
$$\frac{Sh_x}{Re_x^{1/2}} = -\phi'(0), \frac{Nn}{Re_x^{1/2}} = -N'(0). \tag{18}$$

3. Entropy Generation Analysis

The entropy production rate (S_G) for the Sutterby fluid [25] under magnetic field, thermal radiation, and diffusion effect can be written as

$$S_G = \frac{k}{\widehat{T}_0}\left(\left[\frac{\partial \widehat{T}}{\partial x}\right]^2 + \left[\frac{\partial \widehat{T}}{\partial y}\right]^2 + +\frac{16\sigma^* \widehat{T}_\infty^3}{3kk^*}\left(\frac{\partial \widehat{T}}{\partial y}\right)^2\right) + \frac{\mu}{\widehat{T}_\infty}\left(\frac{\partial \widehat{u}}{\partial y}\right)^2\left[1 + \frac{m\mathrm{Re}\delta}{6}\left(\frac{\partial \widehat{u}}{\partial y}\right)^2\right] + \frac{RD_m}{\widehat{C}_\infty}\left(\frac{\partial \widehat{C}}{\partial y}\right)^2$$
$$+ \frac{RD_m}{\widehat{T}_\infty}\left(\frac{\partial T}{\partial y}\right)\left(\frac{\partial \widehat{C}}{\partial y}\right) + \frac{RD_m}{\widehat{\chi}_\infty}\left(\frac{\partial \widehat{\chi}}{\partial y}\right)^2 + \frac{RD_m}{\widehat{T}_\infty}\left(\frac{\partial \widehat{\chi}}{\partial y}\right)\left(\frac{\partial \widehat{T}}{\partial y}\right) + \frac{\sigma B_0^2}{\widehat{T}_\infty}u^2. \tag{19}$$

The dimensionless entropy generation number is expressed as

$$Ns = (1 + R\ d)\theta'^2 + Re\frac{Br}{\Pi}\left[1 + \frac{m\mathrm{Re}\delta}{3}(f'')^2\right](f'')^2 + \mathrm{Re}\left(\frac{\Gamma}{\Pi}\right)^2\phi'^2$$
$$+ \mathrm{Re}\left(\frac{\Gamma}{\Pi}\right)\phi'\theta' + Re\left(\frac{\xi}{\Pi}\right)^2 N'^2 + Re\left(\frac{\xi}{\Pi}\right)N'\theta' + \frac{Br}{\Pi}M\,f'^2. \tag{20}$$

The Bejan number (Be) is described as

$$Be = \frac{(1 + R\ d)\theta'^2 + \mathrm{Re}(\Gamma/\Pi)^2\phi'^2 + \mathrm{Re}(\Gamma/\Pi)\phi'\theta' + Re(\xi/\Pi)^2N'^2 + Re\ (\xi/\Pi)N'\theta'}{(1 + Rd)\theta'^2 + Re\ Br/\Pi\left[1 + m\mathrm{Re}\delta/3\left(f''\right)^2\right](f'')^2 + \mathrm{Re}(\Gamma/\Pi)^2\phi'^2 + \mathrm{Re}(\Gamma/\Pi)\phi'\theta' + Re(\xi/\Pi)^2N'^2 + Re(\xi/\Pi)N'\theta' + Br/\Pi M\,f'^2}. \tag{21}$$

3.1. Solution Methodology. To compute the numeric outcomes of formulated systems of ODEs (10)–(13) subject to boundary conditions equation (14) by bvp4c technique, the ODEs are renovated into first-order ODEs by assigning a new variable.

$$\left.\begin{aligned} &f = \Upsilon_1, f' = \Upsilon_2, f'' = \Upsilon_3, f''' = \Upsilon_3' \\ &\theta = \Upsilon_4, \theta' = \Upsilon_5, \theta'' = \Upsilon_5' \\ &\phi = \Upsilon_6, \phi' = \Upsilon_7, \phi'' = \Upsilon_7' \\ &N = \Upsilon_8, N' = \Upsilon_9, N'' = \Upsilon_9' \end{aligned}\right\}, \tag{22}$$

$$\Upsilon_3' = \frac{\left\{-\Upsilon_1\Upsilon_3 + (\Upsilon_2)^2 - M\Upsilon_2\right\}}{\left[1 + 1/2m\delta\ \mathrm{Re}\Upsilon_3^2\right]}, \tag{23}$$

$$\Upsilon_5' = \frac{\left[-\mathrm{Pr}\Upsilon_1\Upsilon_5 + \alpha\Upsilon_1\Upsilon_2\Upsilon_5 - \mathrm{Pr}\left(Nb\Upsilon_5\Upsilon_7 + Nt{\Upsilon_5}^2\right)\right]}{\left(1 + R\ d - \alpha\Upsilon^2\right)}, \tag{24}$$

$$\Upsilon_7' = -\left[ScSr\Upsilon_5' - Sc\Upsilon_1\Upsilon_5 + \Upsilon_5'\frac{Nt}{Nb} - Sc\ \kappa\Upsilon_6\right], \tag{25}$$

$$\Upsilon_9' = Pe\Upsilon_7'(\Upsilon + \varpi) - \Upsilon_7\Upsilon_9 + Lb\Upsilon_9. \tag{26}$$

The converted boundary condition is

$$\begin{aligned} &\Upsilon_1(0) = 0, \Upsilon_2(0) = 1, \Upsilon_5(0) = -\gamma\left(1 - \Upsilon_4(0)\right), \Upsilon_6(0) \\ &\quad = 1, \Upsilon_8(0) = 1 \\ &\Upsilon_2(\infty) = 0, \Upsilon_4(\infty) = 0, \Upsilon_6(\infty) = 0, \Upsilon_8(\infty) = 0. \end{aligned} \tag{27}$$

By using (27) with boundary conditions, the results are using a finite value for η_{max} .

$$\begin{aligned} &f\prime(\eta_{\max}) \longrightarrow 0, \theta(\eta_{\max}) \longrightarrow 0, \phi(\eta_{\max}) \\ &\quad \longrightarrow 0, N(\eta_{\max}) \longrightarrow 0. \end{aligned} \tag{28}$$

The step size is measured $\Delta\eta = 0.001$ and 10^{-6} is a convergent criterion to repeat and attain the numeric solution.

4. Result and Discussion

The current study involves the governing parameters on velocity $f'(\eta)$, temperature $\theta(\eta)$, concentration $\theta(\eta)$, density of motile microorganisms $N(\eta)$, entropy generation $Ns(\eta)$, and Bejan number $Be(\eta)$. Table 1 presents the code validation of $-\theta(0)$ for different Pr values. This validation provides that the result of our computation is an optimum one.

Figures 2(a)–2(d) delineate the different values of the Deborah number (δ) on velocity distribution $f'(\eta)$, temperature field $\theta(\eta)$, entropy generation $Ns(\eta)$, and Bejan number $Be(\eta)$. Figure 2(a) presents the larger value of the Deborah number (δ) results, the fluid velocity reduces for pseudoplastic flow $(m<0)$, and fluid velocity enhances as the Deborah number δ upsurges for the dilatant flow $(m<0)$. The Deborah number fluidity for scenarios when $m > 0$ and $m<0$ is represented. In both circumstances, increasing the value of the Deborah number results in the opposite behavior of the velocity fields. The flow of fluid accelerates as the Deborah number increases but decreases as the Deborah number increases in the form of the pseudoplastic fluid. Increases in the values of the Deborah number play an important part in refining elastic impacts, and as a result, dilatant fluids increase fluid flow; nevertheless, the pseudoplastic fluid exhibits quite different behavior. An increment in the value of the Deborah number as thermal layer thickness depreciates for pseudoplastic flow $(m<0)$ in Figure 2(b). Also, the temperature field $\theta(\eta)$ reduces with the increasing value of the Deborah number δ in the shear thickening fluid $(m<0)$. Figures 2(c) and 2(d) interestingly show that entropy production rate $Ns(\eta)$ enhances for dilatant $(m<0)$ and reduces for pseudoplastic $(m<0)$ through the escalation in the Deborah parameter δ while the Bejan number $Be(\eta)$ is an escalating function of the Deborah number (δ) for both pseudoplastic flow $(m<0)$ but reduces dilatant flow $(m<0)$. The plot of various values of power-law index parameter (m) is shown in Figures 3(a) and 3(b). In Figure 3(a), the velocity profile $f'(\eta)$ escalates as (m) rises. Moreover, the velocity profile $f'(\eta)$ is interpreted through (m=0, m<0, m>0). The Newtonian fluid $(m=0)$, pseudoplastics $(m<0)$, and dilatants fluid $(m<0)$ are analyzed. The Newtonian, shear-thinning, and shear-thickening fluid is described in Figure 3(b). The temperature profile $\theta(\eta)$ decays with a larger value of m. Figures 4(a)–4(d) display the behavior of unsteady variable A on $f'(\eta)$, $\theta(\eta)$, $Ns(\eta)$, and $Be(\eta)$. For both cases $m>0$ and $m<0$, Figures 4(a) and 4(b) represent that both velocity and temperature profiles decay due to greater value of A. Actually, the unsteady variable reduces the flow strength of velocity profile $f'(\eta)$ and temperature field $\theta(\eta)$. The reason behind this is that pseudoplastic and dilatant fluid was not affected on both profiles. Similar performance for $Ns(\eta)$ and $Be(\eta)$ was noted in Figures 4(c) and 4(d).

Figures 5(a)–5(d) depict the feature of (Re) for the velocity distribution $f'(\eta)$, temperature field $\theta(\eta)$, entropy generation $Ns(\eta)$, and Bejan number $Be(\eta)$. From Figure 5(a), the arising value of the Reynolds number (Re) diminishes the velocity profile $f'(\eta)$ for viscous force and velocity field augment due to the larger value of the Reynolds number for dilatant fluid. Figure 5(b) shows that a larger value of the Reynolds number (Re) causes a reduction in temperature profile for shear-thinning and temperature profile decreases as there is an increment in (Re). Figures 5(c) and 5(d) display that both entropy minimization and the Bejan number reduce and upsurge with the rise of the value of Re. The plots of the magnetic variable on the velocity and temperature profiles are exposed in Figure 6(a)–6(d). The velocity of the fluid grows with a mounting value of M while an opposite observation is noted for the temperature field for both $(m<0)$ and $(m<0)$. Physically, there is an increment in the strength of the magnetic field whereas resistive force turned down the velocity. From Figure 6(c), the entropy minimization increases with a larger magnitude

Table 1: Comparing of $-\theta(0)$ for the diverse value of the Prandtl number Pr.

Pr	Goyal and Bhargava [33] (FEM)	G. B. Chandra Mouli et al. [34]	Current solution
0.7	0.4539	0.45391616	0.456051151444
2	0.9113	0.91135768	0.911321182335
7	1.8954	1.89540326	1.895381877516
20	3.3539	3.35390035	3.353886926545

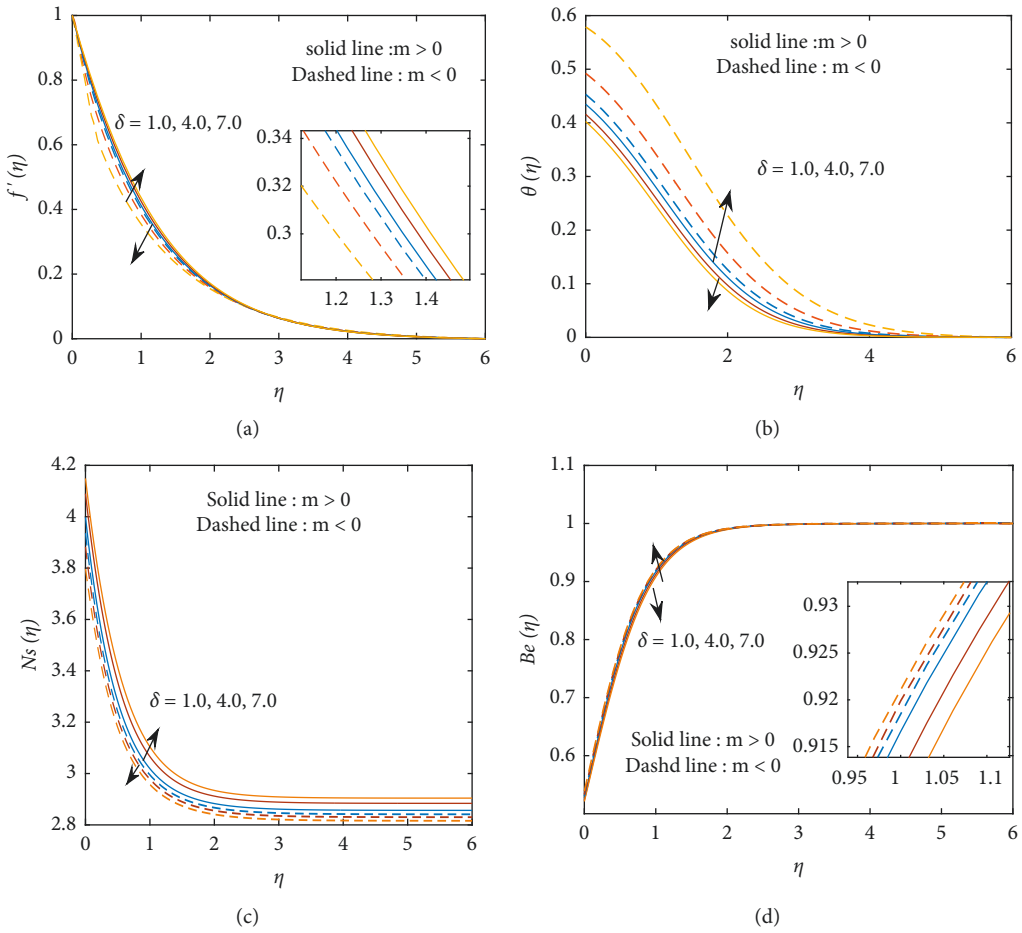

Figure 2: Impact of δ on (a) $f'(\eta)$, (b) $\theta(\eta)$, (c) $Ns(\eta)$, and (d) $Be(\eta)$.

of magnetic number for both cases pseudoplastic and dilatants whereas its opposite behavior is seen in Figure 6(d).

The view of (Nb) on temperature field $\theta(\eta)$ and concentration profile $\phi(\eta)$ is disseminated in Figures 7(a) and 7(b). The temperature profile $\theta(\eta)$ is enhanced with enhancing the value of the Brownian motion (Nb). An augment in the (Nb) causes an enhancement in the nanoparticle collision that results in an increment in fluid temperature. However, deceleration in the concentration field is observed in Figure 7(b). Figures 8(a) and 8(b) display thermophoretic estimation (Nt) on temperature $\theta(\eta)$ and concentration profiles $\theta(\eta)$. Larger values of (Nt) for both $\theta(\eta)$ and $\phi(\eta)$ have been intensified. Nanoparticles have dragged from hotter to cold surfaces. That is the reason of the increase in thermal and concentration profiles. The plots for the Prandtl (Pr) and Schmidt number (Sc) on temperature $\phi(\eta)$ and concentration profiles $\phi(\eta)$ are carried out in Figures 9(a) and 9(b). It can be shown from these figures that enlargement in the (Pr) causes a dazzling depreciation in the fluid temperature. The concentration profile reduces with a larger value of (Sc). Physically, the Schmidt number (Sc) is dependent on the proportion of momentum to mass diffusivity. By increasing the value of (Sc), momentum diffusivity increases as nanoparticle concentration declines. Figures 10(a) and 10(b) show the Biot number (Bi) and chemical reaction parameter (κ) on temperature and concentration profiles. The Biot number means the ratio of convection over conduction inside the boundary at the surface. The gradually growing value of values of the Biot number climbs the temperature distribution while similar behavior is observed for increasing value of κ on the concentration profile. The features of the Bioconvection Lewis number (Lb) and Peclet number (Pe) on motile

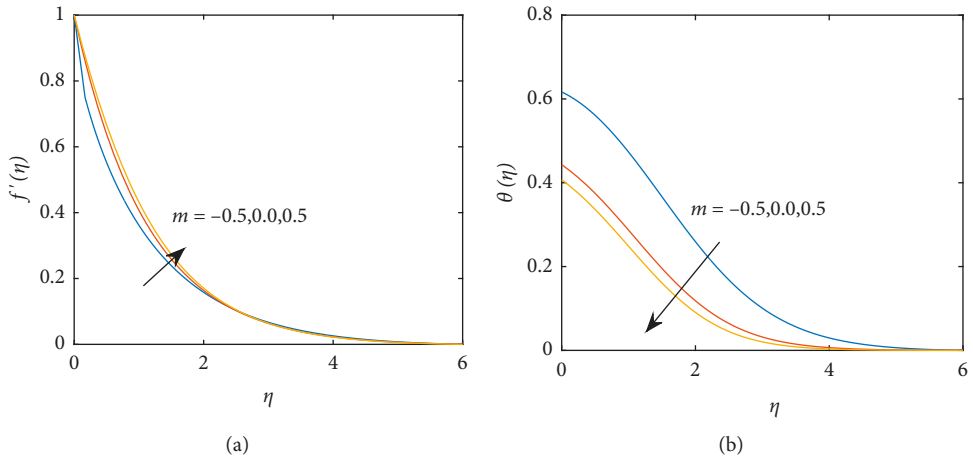

FIGURE 3: Impact of (m) on (a) $f'(\eta)$ and (b) $\theta(\eta)$.

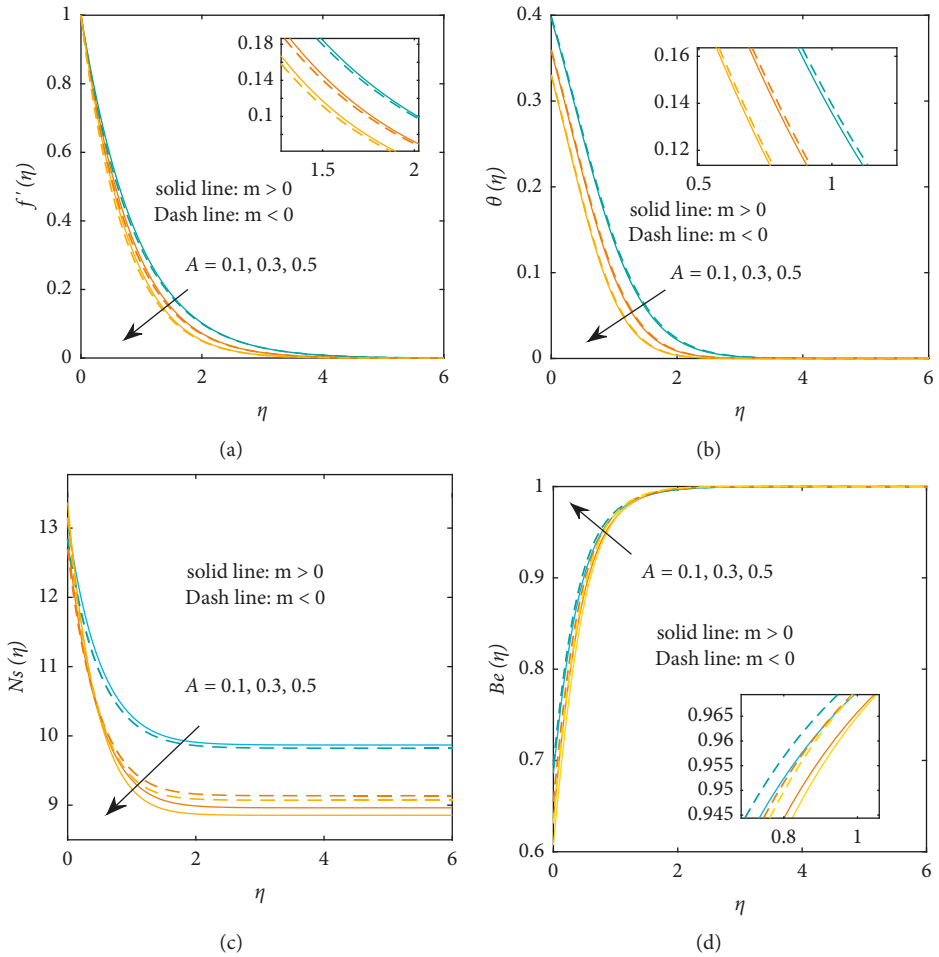

FIGURE 4: Impact of A on (a) $f'(\eta)$, (b) $\theta(\eta)$, (c) $Ns(\eta)$, and (d) $Be(\eta)$.

density microorganism $N(\eta)$ were seen in Figures 11(a) and 11(b). For the mounting value of (Lb) as the diffusivity microorganism upsurges, so, the density of motile microorganism has increased. Figure 11(b) shows the influence of the Peclet number on microorganism density that has been assumed. Enlarging the Peclet number climbs the movement of fluid particles. Due to this, microorganism density enhances as their concentration diminishes.

The impact of Re and δ on skin friction coefficient was presented in Figure 12 for dilatant and pseudo-plastic cases. In dilatant case, the surface drag force suppresses when enhancing the δ values, and it aggravates for increasing Re

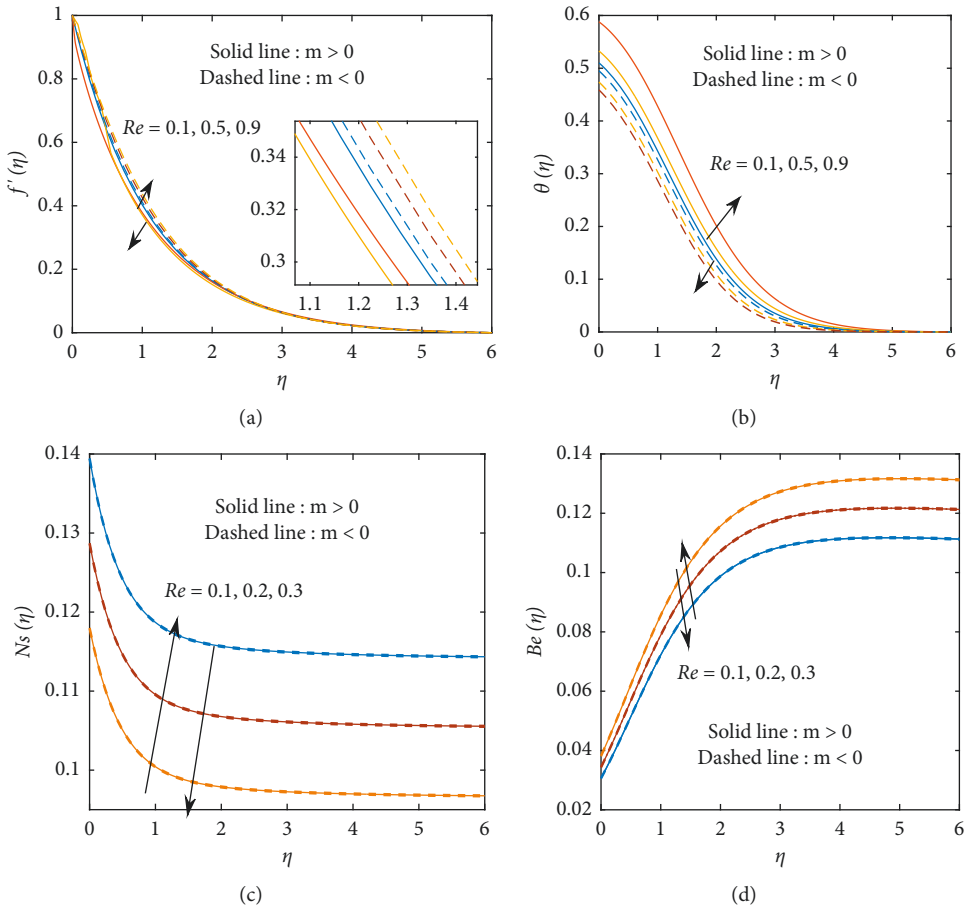

Figure 5: Impact of (Re) on (a) $f'(\eta)$, (b) $\theta(\eta)$, (c) $Ns(\eta)$, and (d) $Be(\eta)$.

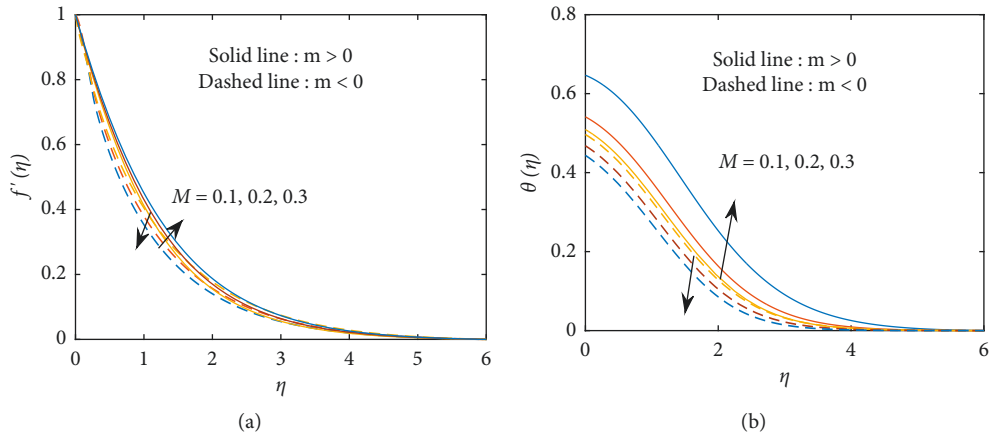

Figure 6: Continued.

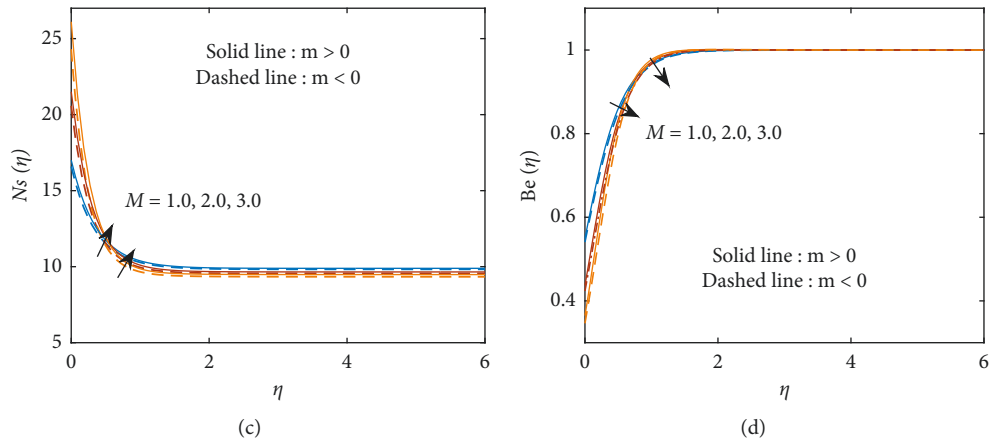

Figure 6: Impact of M on (a) $f'(\eta)$, (b) $\theta(\eta)$, (c) $Ns(\eta)$, and (d) $Be(\eta)$.

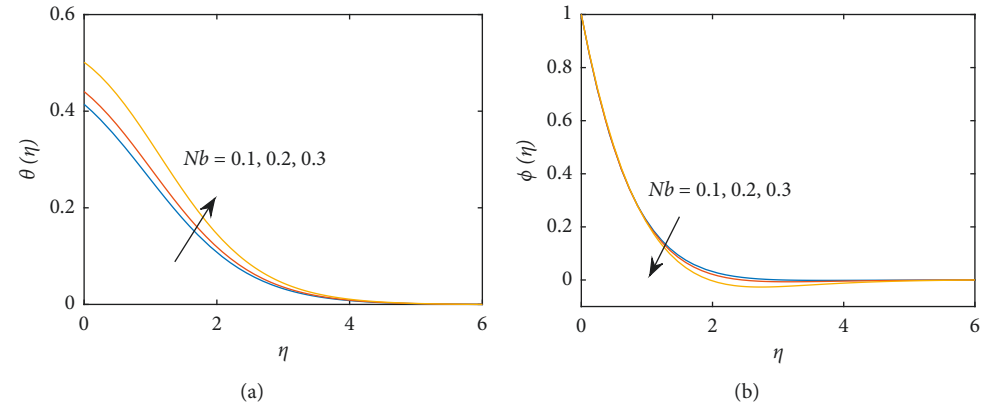

Figure 7: Impact of Nb on (a) $\theta(\eta)$ and (b) $\phi(\eta)$.

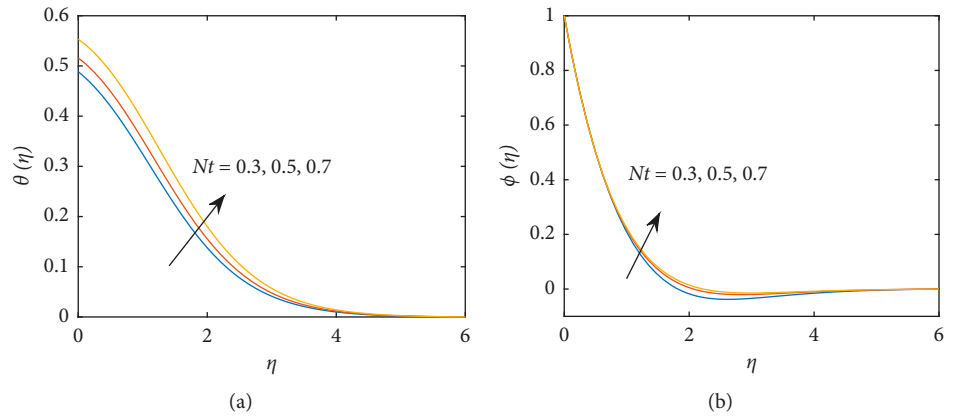

Figure 8: Impact of Nt on (a) $\theta(\eta)$ and (b) $\phi(\eta)$.

values and the opposite trend was obtained in pseudo-plastic case. Figure 13 illustrates the variations of Nu for different combinations of Nb and Rd. In small quantity of Nb, the heat transfer gradient upsurges when rising the Rd variations and the reverse trend was attained for higher quantity of Nb. The consequences of κ and Sc on Sherwood number is plotted in Figure 14. In Sc = 0.8, the Sherwood number enlarges for strengthening the κ values, and the Sherwood number is almost same for changing κ values at Sc = 0.9. In addition, the Sherwood number decays for raising the κ values at Sc = 1.0. Figure 15 gives the impact of Pe and Lb on motile density. It is detected from this figure that the motile density

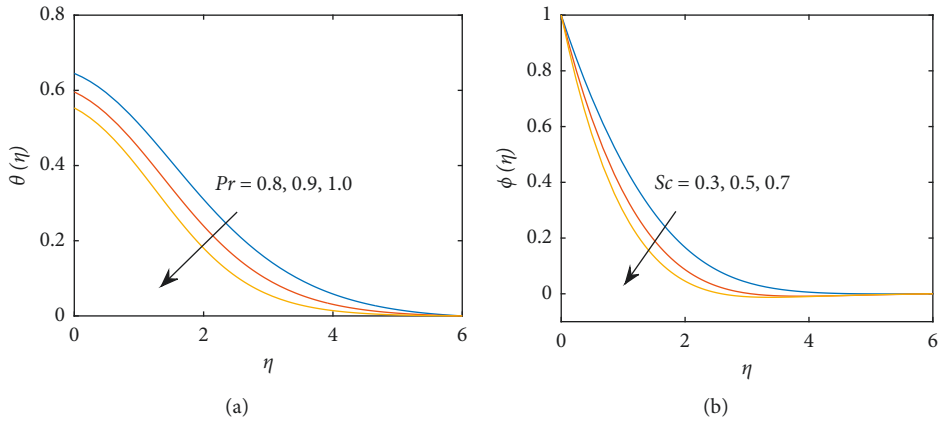

Figure 9: Impact of Pr on (a) $\theta(\eta)$ and (b) Sc on$\phi(\eta)$.

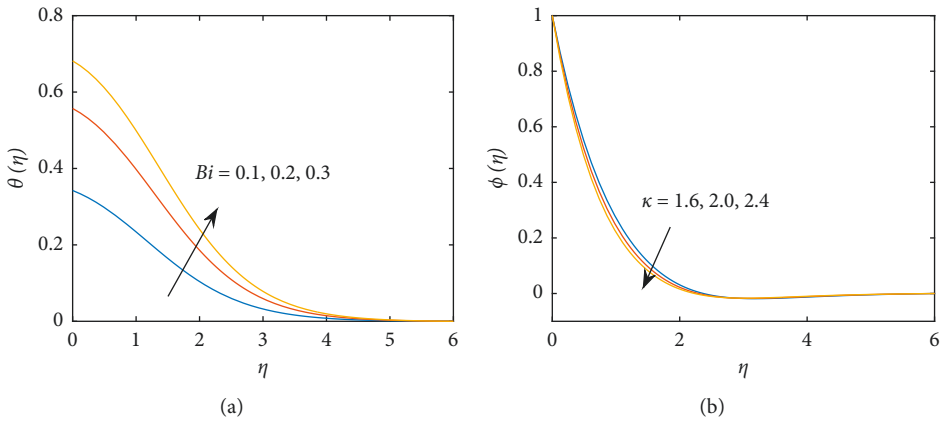

Figure 10: Impact of (a) Bi on $\theta(\eta)$ and (b) κ on $\phi(\eta)$.

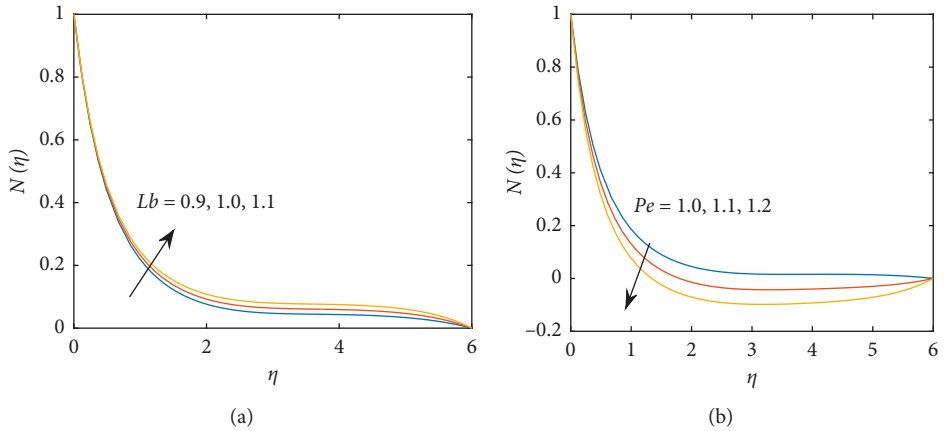

Figure 11: Impact of (a) Lb and (b) Pe on $N(\eta)$.

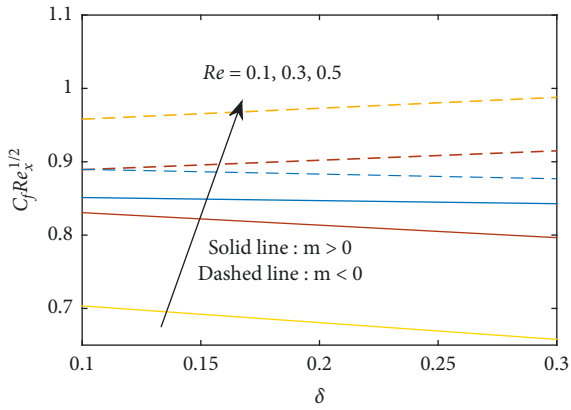

Figure 12: Impact of Re and δ versus skin friction.

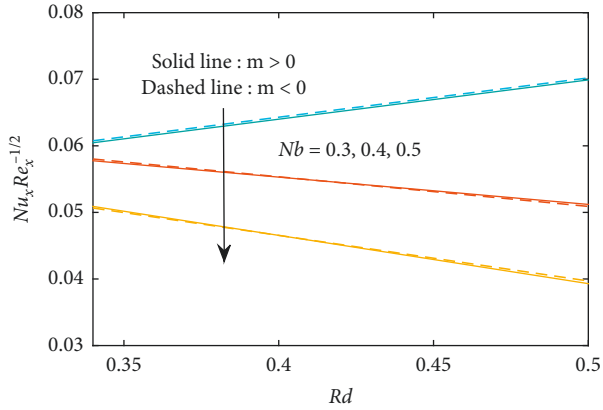

Figure 13: Impact of Rd and Nb versus the Nusselt number.

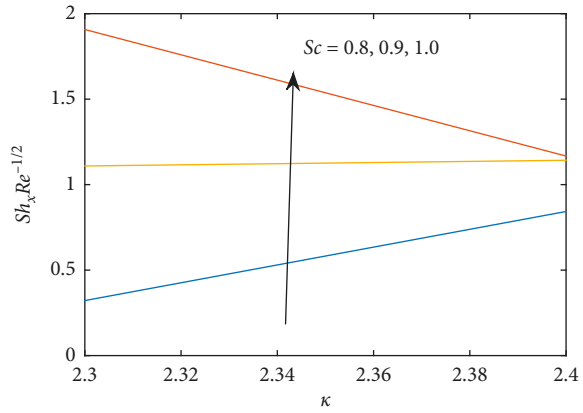

Figure 14: Impact of κ and Sc versus the Sherwood number.

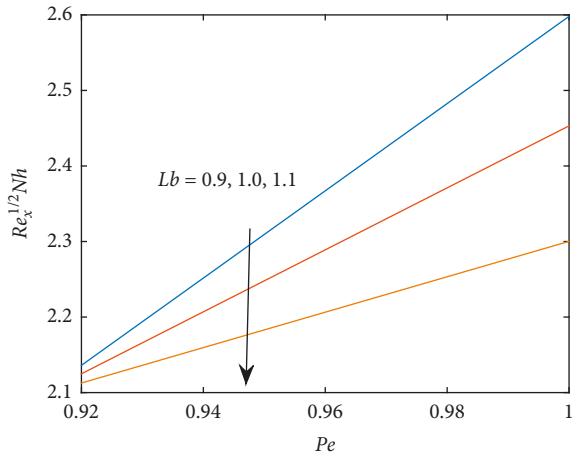

Figure 15: Impact of Lb and Pe versus the Motile density.

Table 2: Numerical simulation values of $\mathrm{Re}_x^{1/2}Cf_x$ with numerous variables Re, M, δ.

Re	δ	M	$\mathrm{Re}_x^{1/2}Cf_x$	
			$m=-0.5$	$m=0.5$
0.1	0.2	0.2	0.8896	0.8892
0.3			0.8768	0.9149
0.5			0.8638	0.9274
	0.4		0.8306	0.9580
	0.6		0.7965	0.9878
	0.7		0.7790	1.0024
		0.4	0.7035	0.8512
		0.5	0.6578	0.8428
		0.6	0.6943	0.8372

Table 3: Numerical values of $\mathrm{Re}_x^{-1/2}Nu_x$ with numerous variables of *Rd*, *Nb*, *Nt*, *Pr*, ε.

Rd	Nb	Nt	Pr	$\mathrm{Re}_x^{-1/2}\mathrm{Nu}_x$	
				$m=-0.5$	$m=0.5$
0.1	0.3	0.7	0.7	0.0594	0.0598
0.2				0.0612	0.0609
0.3				0.0668	0.0671
	0.4			0.0538	0.0534
	0.5			0.0393	0.0397
	0.6			0.0244	0.0248
		0.5		0.0581	0.0584
		0.4		0.0699	0.0702
		0.3		0.0793	0.0796
			0.7	0. 0824	0. 0825
			1.1	0.0984	0.0987

Table 4: Numerical values of $\mathrm{Re}_x^{-1/2}Sh_x$ with numerous variables of *Nb*, *Nt*, *Pr*, *Sc*.

Pr	Sc	κ	Nb	Nt	$\mathrm{Re}_x^{-1/2}Sh_x$
0.5		2.3	0.4	0.1	0.8429
0.6					0.3218
0.7					1.0624

Table 4: Continued.

Pr	Sc	κ	Nb	Nt	$\mathrm{Re}_x^{-1/2}Sh_x$
	0.8				1.9074
	0.9				1.1671
	1.0				1.0741
		2.4			1.1092
		2.5			1.1425
		2.6			1.1770
			0.3		1.1779
			0.4		1.1785
			0.5		1.1810
				0.2	1.4161
				0.3	1.4814
				0.4	1.4918

Table 5: Numerical values of $\mathrm{Re}_x^{-1/2}Nh_x$ with numerous variables of Nb, Pe, Lb, ϖ.

Lb	Pe	ϖ	Nb	$\mathrm{Re}_x^{-1/2}\mathrm{Nh}_x$
0.9	0.9	0.9	0.7	2.0658
1.				2.0428
1.1				2.0206
	1.0			2.3002
	1.			2.4351
	1.1			2.5981
		1.1		2.9703
		1.2		3.1641
		1.3		3.5637
			0.3	3.1072
			0.4	3.8628
			0.5	3.9162

Table 6: List of symbols.

Expression	Name	Unit
Re	Local Reynolds number	Dimensionless
t	Time	Sec
δ	Deborah number	Dimensionless
M	Magnetic parameter	Dimensionless
m	Power index number	Dimensionless
A	Unsteady parameter	Dimensionless
Nb	Brownian motion parameter	Dimensionless
Nt	Thermophoresis parameter	Dimensionless
Pr	Prandtl number	Dimensionless
$R\ d$	Radiation parameter	Dimensionless
Sc	Schmidt number	Dimensionless
Lb	Bioconvection Lewis number	Dimensionless
Pe	Bioconvection Peclet number	Dimensionless
ε	Heat source/sink parameter	Dimensionless
κ	Chemical reaction parameter	Dimensionless
C_f	Skin friction coefficient	Dimensionless
Nu_x	Nusselt number	Dimensionless
Sh_x	Sherwood number	Dimensionless
Nh_x	Microorganism density number	Dimensionless
f	Dimensionless velocity profile	Dimensionless
θ	Dimensionless temperature profile	Dimensionless
ϕ	Dimensionless concentration profile	Dimensionless
N	Dimensionless microorganism profile	Dimensionless
ϖ	Microorganism concentration difference parameter	Dimensionless
η	Similarity variable	Dimensionless

Table 6: Continued.

Expression	Name	Unit
$\widehat{u}, \widehat{v}$	Components of velocity along x, y direction	ms^{-1}
τ	Ratio of the effective heat capacity	Dimensionless
υ	Kinematic viscosity	m^2s^{-1}
a	Stretching rate	s^{-1}
ρ	Density	kgm^{-1}
C_p	Specific heat	$Jkg^{-1}K^{-1}$
D_B	Brownian diffusion coefficient	m^2s^{-1}
D_T	Thermophoretic diffusion coefficient	m^2s^{-1}
D_m	Microorganism's diffusion coefficient	m^2s^{-1}
B_o	Constant magnetic field	$kgs^{=2}A^{-1}$
$\widehat{C}$	Concentration	kgm^{-3}
$\widehat{C}_\infty$	Ambient concentration	kgm^{-3}
$\widehat{C}_w$	Surface concentration of nanoparticles	kgm^{-3}
k	Thermal conductivity	$mkgs^{-3}K^{-1}$
$\widehat{T}$	Temperature	K
$\widehat{T}_\infty$	Ambient temperature	K
$\widehat{T}_w$	Wall temperature	K
$h(t)$	Coefficient of heat transfer	$W\ m^{-2}K^{-1}$
$\widehat{\chi}$	Microorganism's profile	Dimensionless
$\widehat{\chi}_w$	Surface concentration of microorganisms	kgm^{-3}
$\widehat{\chi}_\infty$	Ambient concentration of microorganisms	kgm^{-3}
W_c	Maximum cell swimming speed	ms^{-1}
x, y	Cartesian coordinates	m
σ	Electrical conductivity	$S^3m^2\,kg^{-1}$
u_w	Velocity of the sheet	ms^{-1}
S_G	Local volumetric entropy generation rate	$Wm^{-3}K^{-1}$
Ns	Entropy generation	Dimensionless
Be	Bejan number	Dimensionless

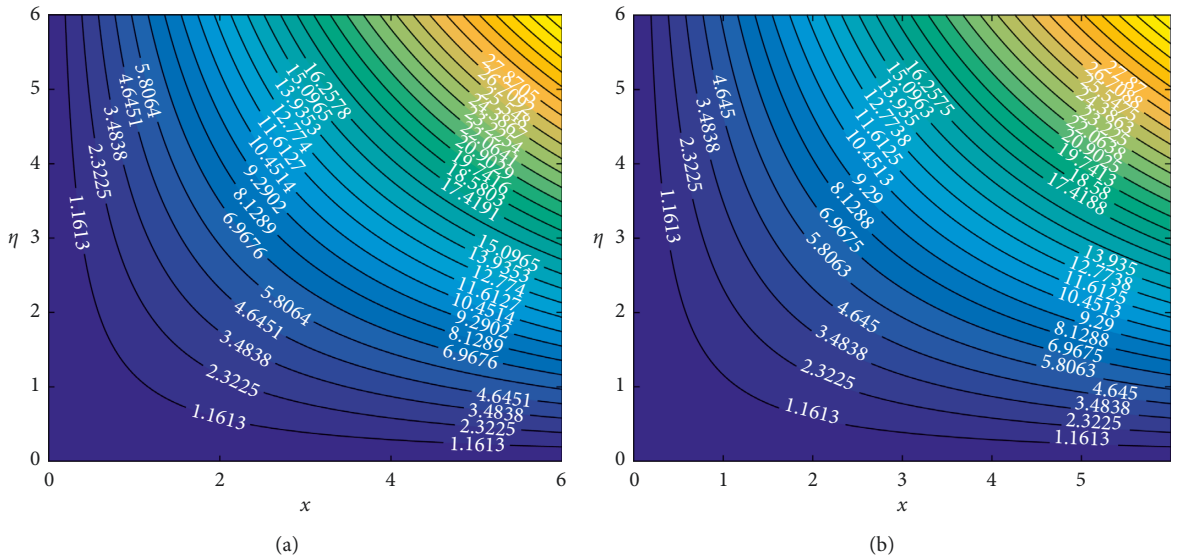

Figure 16: Streamlines for (a) Unsteady flow. (b) Steady flow.

escalates when escalating the vales of Pe and its downturns for enriching the Lb quantity.

Numerical estimation of drag friction for Re, δ and M has been shown in Table 2 for dilatant and pseudo-plastic cases. It is noticed that the drag friction diminishes when rising the Re & δ values in the pseudo-plastic case and it is elevated in the dilatant case. In Addition, the drag friction slumps for a higher quantity of M in both cases. Table 3 presents the numerical values of Rd, Nb, Nt, Pr on Nusselt number for $m = -0.5$ and $m = 0.5$. From this table we obtain Rd, Nt, Pr have an increasing tendency and the opposite behaviour is found for Nb in both cases. Table 4 provides the consequences of Pr, Sc, κ, Nb and Nt on the Sherwood number and found that the Sherwood number mounts when

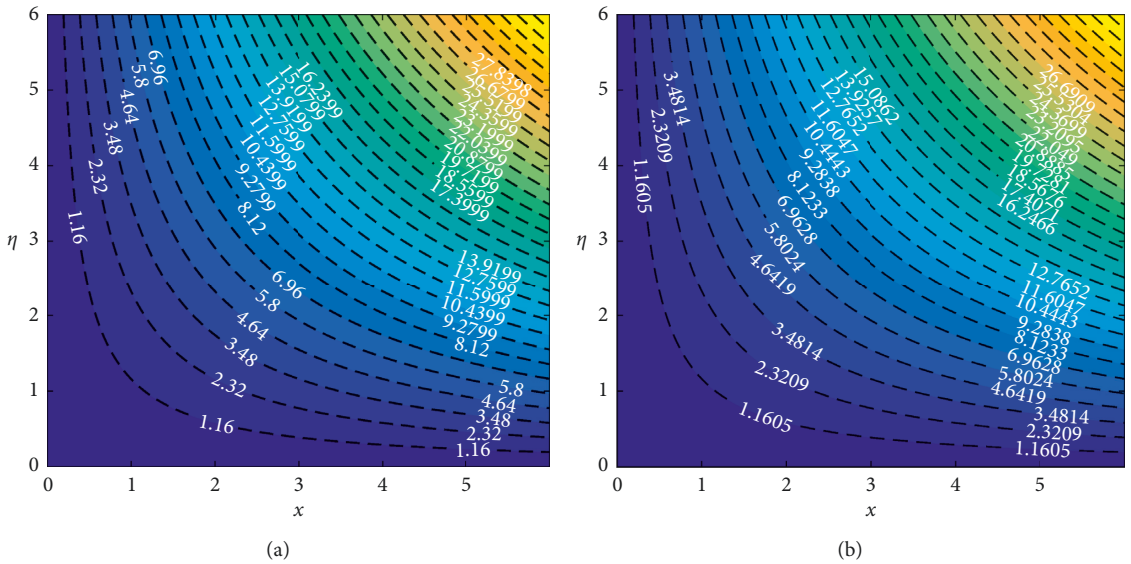

Figure 17: Streamline for (a) $m = -0.3$ and (b) $m = 0.3$.

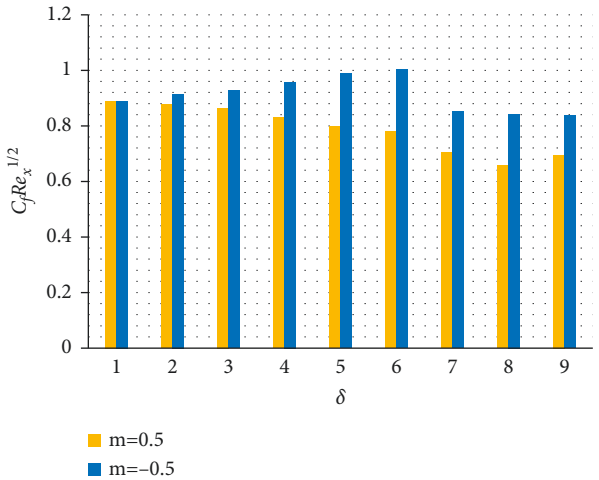

Figure 18: Bar graph for skin friction.

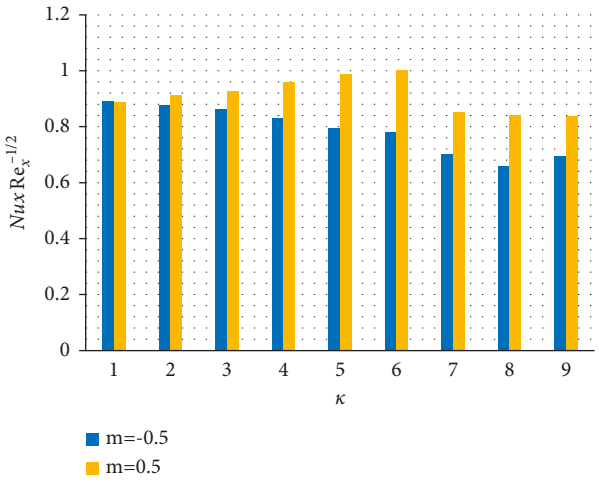

Figure 19: Bar graph for Nusselt number.

improving the Pr, κ, *Nb* and *Nt* values and its downfalls when larger quantity of Sc values. The impact of Le, Pe, ω and *Nb* on motile density was displayed in Table 5. It is seen that the motile density progress when elevating the Pe, ω and Nb values and it depresses when higher values of Le. Table 6 provides the list of symbols in our analysis. The flow line for steady flow 16(a), unsteady flow 16(b), pseudo-plastic 17(a) and dilatant 17(b) was presented in Figures 16(a), 16(b) and 17(a), 17(b). Figures 18 explains the skin friction coefficient for different values of δ for dilatant and pseudo-plastic cases. It is found that pseudo-plastic has a more pronounced than the dilatant case. The Nusselt number variations for different values of κ for dilatant and pseudo-plastic cases. It is seen that the higher heat transfer gradient attains in pseudo-plastic case than the dilatant case.

5. Conclusion

In this article, the influence of numerical simulation of MHD flow of Sutterby nanofluid with thermal radiation and heat source/sink has been investigated. Entropy production is also considered. The transmuted ODEs are obtained numerically through bvp4c. By this simulation, we have revealed the influence of emerging parameters on the flow of entropy generation and chemical reaction effects with thermal radiative for time-dependent MHD of Sutterby fluid past stretching surface. This investigation can be enlarged for Ree-Eyring fluid, Williamson fluid, and generalized fluid model. Some precise conclusions which have been produced from this research are given as follows.

(i) Velocity profile is reducing while temperature, entropy generation, and Bejan number accelerated due to the larger value of the Deborah number for $m < 0$.

(ii) The velocity of fluid mounted whereas temperature, entropy generation, and Bejan number declined due to the larger value of the Deborah number for $m > 0$.

(iii) A higher value in *Pr* causes the reduction in the temperature profile.

(iv) Increases in the Deborah number for heat flow result in a decrease in the temperature profile while increasing the heat source/sink parameter.

(v) Skin friction coefficient augments for ($m < 0$, $m > 0$) but reduced the Nusselt number.

Data Availability

The raw data supporting the conclusions of this article will be made available by the corresponding author without undue reservation.

Conflicts of Interest

The authors declare that they have no conflicts of interest.

Authors' Contributions

All authors listed have made a substantial, direct, and intellectual contribution to the work and approved it for publication.

References

[1] J. L. Sutterby, "Laminar converging flow of dilute polymer solutions in conical sections: Part I. Viscosity data, new viscosity model, tube flow solution," *AIChE Journal*, vol. 12, no. 1, pp. 63–68, 1966.

[2] R. L. Batra and M. Eissa, "Helical flow of a Sutterby model fluid," *Polymer - Plastics Technology & Engineering*, vol. 33, no. 4, pp. 489–501, 1994.

[3] K. Gangadhar, T. Kannan, N. S. L. V. Narasimharao, B. Rushi Kumar, and G. Sakthivel, "Thermo diffusion effects on MHD casson fluid flow over non-flatness stretching surface: keller box method," *International Journal of Ambient Energy*, vol. 42, no. 4, pp. 374–382, 2018.

[4] S. Bilal, M. Sohail, R. Naz, and M. Y. Malik, "Dynamical and optimal procedure to analyse the exhibition of physical attribute imparted by Sutterby magneto nano fluid in Darcy medium yield by axially stretched cylinder," *Canadian Journal of Physics*, vol. 98, 2019.

[5] R. Saif-ur-Rehman, N. A.Mir, M. Farooq et al., "Analysis of thermally stratified flow of Sutterby nanofluid with zero mass flux condition," *Journal of Materials Research and Technology*, vol. 9, no. 2, pp. 1631–1639, 2020.

[6] M. I. Khan, H. Waqas, U. Farooq, S. U. Khan, Y.-M. Chu, and S. Kadry, "Assessment of bioconvection in magnetized Sutterby nanofluid configured by a rotating disk: a numerical approach," *Modern Physics Letters B*, vol. 35, no. 12, Article ID 2150202, 2021.

[7] M. Sohail and R. Naz, "Modified heat and mass transmission models in the magnetohydrodynamic flow of Sutterby nanofluid in stretching cylinder," *Physica A: Statistical Mechanics and Its Applications*, vol. 549, Article ID 124088, 2020.

[8] R. Su, N. A. Mir, M. S. Alqarni, M. Farooq, and M. Y. Malik, "Analysis of heat generation/absorption in thermally stratified Sutterby fluid flow with Cattaneo-Christov theory," *Microsystem Technologies*, vol. 25, pp. 3365–3373, 2020.

[9] L. P. Usman and A. Ghaffari, "Heat and mass transfer in a steady flow of Sutterby nanofluid over the surface of a stretching wedge," *Physica Scripta*, vol. 96, Article ID 065003, 2021.

[10] M. M. Bhatti, S. Jun, C. M. Khalique, A. Shahid, L. Fasheng, and M. S. Mohamed, "Lie group analysis and robust computational approach to examine mass transport process using Jeffrey fluid model," *Applied Mathematics and Computation*, vol. 421, Article ID 126936, 2022.

[11] K. Loganathan, S. Sivasankaran, M. Bhuvaneswari, and S. Rajan, "Second-order slip, cross-diffusion and chemical reaction effects on magneto-convection of Oldroyd-B liquid using Cattaneo-Christov heat flux with convective heating," *Journal of Thermal Analysis and Calorimetry*, vol. 136, no. 1, pp. 401–409, 2019.

[12] S. U. S. Choi, "Enhancing thermal conductivity of fluids with nanoparticles," in *Proceedings of the 1995 ASME International Mechanical Engineering Congress and Exposition*, vol. 231, pp. 99–103, San Francisco, January 1995.

[13] J. Buongiorno, "Convective transport in nanofluids," *Journal of Heat Transfer*, vol. 128, no. 3, pp. 240–250, 2006.

[14] S. Islam, A. Khan, W. Deebani, E. Bonyah, N. A. Alreshidi, and Z. Shah, "Influences of Hall current and radiation on MHD micropolar non-Newtonian hybrid nanofluid flow between two surfaces," *AIP Advances*, vol. 10, Article ID 055015, 2020.

[15] T. S. Karthik, K. Loganathan, A. N. Shankar et al., "Zero and nonzero mass flux effects of bioconvective viscoelastic nanofluid over a 3D Riga surface with the swimming of gyrotactic microorganisms," *Advances in Mathematical Physics*, vol. 2021, Article ID 9914134, 2021.

[16] M. Ijaz, M. Ayub, and H. Khan, "Entropy generation and activation energy mechanism in nonlinear radiative flow of Sisko nanofluid: rotating disk," *Heliyon*, vol. 5, p. e01863, Article ID e01863, 2019.

[17] S. M. Alempour, A. A. Abbasian Arani, and M. M. Najafizadeh, "Numerical investigation of nanofluid flow characteristics and heat transfer inside a twisted tube with elliptic cross section," *Journal of Thermal Analysis and Calorimetry*, vol. 140, no. 3, pp. 1237–1257, 2020.

[18] R. E. Abo-Elkhair, M. M. Bhatti, and K. S. Mekheimer, "Magnetic force effects on peristaltic transport of hybrid bio-nanofluid (Au Cu nanoparticles) with moderate Reynolds number: an expanding horizon," *International Communications in Heat and Mass Transfer*, vol. 123, Article ID 105228, 2021.

[19] Z. Sabir, A. Imran, M. Umar et al., "A numerical approach for 2-D Sutterby fluid-flow bounded at a stagnation point with an inclined magnetic field and thermal radiation impacts," *Thermal Science*, vol. 25, pp. 1975–1987, 2021.

[20] F. Ali and A. Zaib, "Unsteady flow of an Eyring-Powell nanofluid near stagnation point past a convectively heated stretching sheet," *Arab Journal of Basic and Applied Sciences*, vol. 26, no. 1, pp. 215–224, 2019.

[21] W. A. Khan, J. R. Culham, and O. D. Makinde, "Combined heat and mass transfer of third-grade nanofluids over a convectively-heated stretching permeable surface," *Canadian Journal of Chemical Engineering*, vol. 93, no. 10, pp. 1880–1888, 2015.

[22] W. Ibrahim and O. Makinde, "Magnetohydrodynamic stagnation point flow of a power-law nanofluid towards a convectively heated stretching sheet with slip," *Proceedings of the Institution of Mechanical Engineers - Part E: Journal of Process Mechanical Engineering*, vol. 230, no. 5, pp. 345–354, 2016.

[23] M. M. Bhatti, M. B. Arain, A. Zeeshan, R. Ellahi, and M. H. Doranehgard, "Swimming of Gyrotactic Microorganism in MHD Williamson nanofluid flow between rotating circular plates embedded in porous medium: application of thermal energy storage," *Journal of Energy Storage*, vol. 45, p. 103511, 2022.

[24] A. Bejan, "A study of entropy generation in fundamental convective heat transfer," *Journal of Heat Transfer*, vol. 101, no. 4, pp. 718–725, 1979.

[25] E. Azhar, Z. Iqbal, and E. N. Maraj, "Impact of entropy generation on stagnation-point flow of Sutterby nanofluid: a numerical analysis," *Zeitschrift für Naturforschung A*, vol. 71, no. 9, pp. 837–848, 2016.

[26] T. Hayat, Z. Nisar, A. Alsaedi, and B. Ahmad, "Analysis of activation energy and entropy generation in mixed convective peristaltic transport of Sutterby nanofluid," *Journal of Thermal Analysis and Calorimetry*, vol. 143, no. 3, pp. 1867–1880, 2021.

[27] K. Loganathan, K. Mohana, M. Mohanraj, P. Sakthivel, and S. Rajan, "Impact of third-grade nanofluid flow across a convective surface in the presence of inclined Lorentz force: an approach to entropy optimization," *Journal of Thermal Analysis and Calorimetry*, vol. 144, no. 5, pp. 1935–1947, 2020.

[28] T. A. Yusuf, F. Mabood, B. C. Prasannakumara, and I. E. Sarris, "Magneto-bioconvection flow of Williamson nanofluid over an inclined plate with gyrotactic microorganisms and entropy generation," *Fluid*, vol. 6, no. 3, p. 109, 2021.

[29] O. D. Makinde and M. S. Tshehla, "Irreversibility analysis of MHD mixed convection channel flow of nanofluid with suction and injection," *Global Journal of Pure and Applied Mathematics*, vol. 13, pp. 4851–4867, 2017.

[30] K. Loganathan and S. Rajan, "An entropy approach of Williamson nanofluid flow with Joule heating and zero nanoparticle mass flux," *Journal of Thermal Analysis and Calorimetry*, vol. 141, no. 6, pp. 2599–2612, 2020.

[31] M. I. Afridi and M. Qasim, "Entropy generation and heat transfer in boundary layer flow over a thin needle moving in a parallel stream in the presence of nonlinear Rosseland radiation," *International Journal of Thermal Sciences*, vol. 123, pp. 117–128, 2018.

[32] A. I. Alsabery, T. Tayebi, A. J. Chamkha, and I. Hashim, "Effect of rotating solid cylinder on entropy generation and convective heat transfer in a wavy porous cavity heated from below," *International Communications in Heat and Mass Transfer*, vol. 95, pp. 197–209, 2018.

[33] M. Goyal and R. Bhargava, "Boundary layer flow and heat transfer of viscoelastic nanofluids past a stretching sheet with partial slip conditions," *Applied Nanoscience*, vol. 4, no. 6, pp. 761–767, 2014.

[34] G. B. C. Mouli, K. Gangadhar, and B. H. S. Raju, "On spectral relaxation approach for Soret and Dufour effects on Sutterby fluid past a stretching sheet," *International Journal of Ambient Energy*, vol. 43, no. 1, pp. 500–507, 2019.

Hindawi
Mathematical Problems in Engineering
Volume 2022, Article ID 3098781, 10 pages
https://doi.org/10.1155/2022/3098781

Research Article

The Effects of Magneto-Radiative Parameters on the Heat Transfer Mechanism in H_2O Composed by Cu-Al_2O_3 Hybrid Nanomaterial: Numerical Investigation

Wahid Khan,[1] Umar Khan,[1] Adnan,[2] Basharat Ullah,[2] Naveed Ahmed,[3] Ilyas Khan,[4] Aisha M. Alqahtani,[5] and Md. Nur Alam[6]

[1]*Department of Mathematics and Statistics, Hazara University, Mansehra 21120, Pakistan*
[2]*Department of Mathematics, Mohi-ud-Din Islamic University, Nerian Sharif AJ&K 12080, Pakistan*
[3]*Department of Mathematics, Faculty of Sciences, HITEC University, Taxila Cantt 47070, Pakistan*
[4]*Department of Mathematics, College of Science Al-Zulfi, Majmaah University, Al-Majmaah 11952, Saudi Arabia*
[5]*Department of Mathematical Sciences, College of Science, Princess Nourah bint Abdulrahman University, P. O. Box 84428, Riyadh 11671, Saudi Arabia*
[6]*Department of Mathematics, Pabna University of Science & Technology, Pabna-6600, Bangladesh*

Correspondence should be addressed to Umar Khan; umar_jadoon4@yahoo.com, Adnan; adnan_abbasi89@yahoo.com, and Md. Nur Alam; nuralam.pstu23@gmail.com

Received 3 September 2021; Revised 10 November 2021; Accepted 30 March 2022; Published 4 May 2022

Academic Editor: Mohammadreza Safaei

The analysis of thermal performance in second generation of nanofluids (hybrid nanofluids) attained much attention of the researchers, scientists, engineers, and industrialists. These fluids have ultra-high thermal characteristics due to which their broad applications could be found in many areas of technological world. Therefore, a novel analysis regarding the heat transfer is conducted over a stretched surface by considering combined convection, thermal radiations, and magnetic field. The hybrid nanofluid is synthesized by Cu-Al_2O_3 guest hybrid-nanomaterial and host liquid H_2O. The hybrid flow model is solved numerically and decorated the results over the region of interest. It is drawn that the velocity drops by increasing the strength of Cu-Al_2O_3 fraction and applied Lorentz forces. Furthermore, the thermal performance of Cu-Al_2O_3/H_2O augmented against stronger thermal radiations, volumetric fraction, and magnetic field effects.

1. Introduction

Hybrid nanofluids are a new generation of nanofluids with ultra-high thermal performance than conventional nanofluids. Hybrid nanofluids are composed by binary mixture of nanoparticles of various metallic, nonmetallic, carbide, and CNT nanomaterials suspended in the host liquid. Thermal conductivity of the nanoparticles is an important part in the composition of nanofluids that improves the heat transport rate of the nanofluids significantly. The advancement in the nanofluids became very famous among the researchers and engineers due their superior heat transport mechanism. Thus, investigators and engineers paved their attention on such significant nanofluids and studies from different aspects. The nanofluids almost determined the problems of manufacturers and engineers about to huge amount of heat transfer for different manufacturing processes. Hence, the researchers investigated the influences of nanofluids on the flow characteristics under different conditions. The applications of these fluids are broadly found in medical, microelectronics, momentum, sailing buildings, microfluidics, civil engineering, for the detection of cancer cells in human bodies, paint industries, aerodynamics, chemical engineering and cooling of building, etc.

Keeping in view the broad applications of this new generation of the nanofluids, researchers paid much attention to investigate the flow characteristics more specifically thermal performance. Therefore, Takabi et al. [1]

worked on laminar convection flow of the nanofluid (composed by Cu-Al_2O_3) and discussed significant results regarding heat transport by altering various flow quantities. Takabi and Shoshouhmand [2] explained the heat transfer in the hybrid nanofluid (Cu-Al_2O_3/water). Suresh et al. [3] described the influence of hybrid nanofluid (Cu-Al_2O_3/water) in heat transference. Morain [4] organized an experimental study for thermal performance in the hybrid nanoliquid. They synthesized the fluid mixture by adding nanoadditives of Cu and aluminum oxides in the host liquid. They chose water as a host fluid and then performed the analysis over the synthesized hybrid nanoliquid. Suresh et al. [5] explored the influence of $Cu - Al_2O_3$/water hybrid nanofluids regarding the heat transfer. Another study for turbulent flow is conducted by Suresh et al. [6] by using the same hybrid nanoliquid. Some other imperative analysis on the heat transport mechanism in the hybrid nanoliquid under certain flow assumptions and conditions are reported in [7, 8].

Ahmad and Khan [9] examined the behaviour of heat and mass transfer in the fluid over a surface with elasticity characteristics and provided a comprehensive detail about the flow regimes. They analyzed the model numerically. Kumar and Bandari [10] worked in the melting temperature transference of nanofluid and stretching surface. The model comprised the effects of Brownian motion and thermophoresis and then investigated the alterations in the heat and mass transfer due to these physical parameters. Khan and Pop [11] organized and discussed a laminar flow over a stretchable surface and explored the flow characteristic over a semi-infinite domain. Mohimanianpour and Rashidi [12] performed the analysis of steady-state flow behaviour under boundary-layer approximation theory (BLAT) and discussed the results in brevity. They tackled the nonlinear problem via HAM and decorated the results. Bhargava et al. [13] studied combined convection effects in micropolar fluid. They modeled the problem over a porous surface which is stretchable.

The heat transfer can be described magnetic effect of flow over stretching sheet which is explained by Chakrabarti et al. [14]. Ahmad [15] designed a flow model under the impacts of magnetic field and unsteady effects. For mathematical investigation, they utilized quasi-linearization technique and performed the results. Rashidi et al. [16] reported the parametric study and optimization of entropy generation in unsteady MHD flow past a stretching rotational disk with particle swarm optimization (PSO) algorithm, HAM, and artificial neural network (ANN). Sheikholeslami et al. [17] worked on the Lattice Boltzmann method to study the magneto-hydrodynamic flow using Cu – water nanofluid. Fang [19] presented MHD flow above a nonlinearly affecting surface. Devi and Suriyakumar [20] combined the properties of magnetic field on the Blasius and Sakiadis flow composed by Cu and Al_2O_3 nanoparticles. The effects of flow parameters in the flow model on the velocity, high temperature, skin friction coefficient, and local heat transfer were explained comprehensively.

The second generation of nanofluids titled as hybrid nanofluid took much attention of the researchers and scientists due to their ultra-high thermal performance rate. These are extensively used in cooling systems and for other industrial and technological purposes. In the view of extensive uses of such fluids, Rashidi et al. [21] reported the energy transport mechanism in the hybrid nanofluid. The study is organized in lid driven cavity of square shaped. In ordered to enhance the energy efficiency, they plugged the influences of mixed convection on the square boundaries and reported the significant results regarding the heat transport mechanism. The analysis of non-Newtonian fluids has their own importance in various industries. In this regard, a study is conducted by Nazari et al. [22]. They reported that, by enhancing the volumetric fraction and Darcy number, the heat transport rate rises.

The investigation of two-phase nanofluid flow synthesized by hafnium nanoparticles in the presence of slip effects is discussed by Ellahi et al. [23]. The model is tackled analytically and plotted the results for particles phase and fluid phase with a comprehensive detail. A study regarding the heat transfer by considering multiple nanomaterials (MWCNTs, Cu, and Al_2O_3) in cavity is explored by Goodarzi et al. [24]. The results are obtained against various aspect ratios under the influence of natural convection and conductive heat transport. Mixed convection which is a combination of two physical phenomena known as natural and forced convection significantly alters the fluid behaviour and its temperature. In 2020, Yousefzadeh et al. [25] analyzed the fluid dynamics under the impacts of mixed convection by taking various heat transfer areas.

2. Description of the Problem

The study of heat transfer over a stretchable surface is organized for two different generation of the fluids known as nanofluid ($Cu–H_2O$) and hybrid nanofluid ($Cu–Al_2O_3–H_2O$). The sheet is situated in the Cartesian frame. The following assumptions are made during the analysis of aforementioned fluids:

(i) The flow is steady, laminar, and incompressible

(ii) The surface is stretchable in unidirectional

(iii) The flow is two dimensional

(iv) The guest nanomaterial (Cu-Al_2O_3) and the host liquid (H_2O) are thermally compatible

(v) The surface is maintained at temperature T_w and velocity U_w

(vi) The effects of thermal radiations, combined convection, and magnetic field are taken during the study

(vii) The surface is stretched with the velocity $Uw = ax$ and the temperature and velocity asymptotically vanish at extreme position of the surface

Figure 1 elaborates the flow configuration of the fluids.

The basic constitutive relations for the particular flow are described by the following equations [26]:

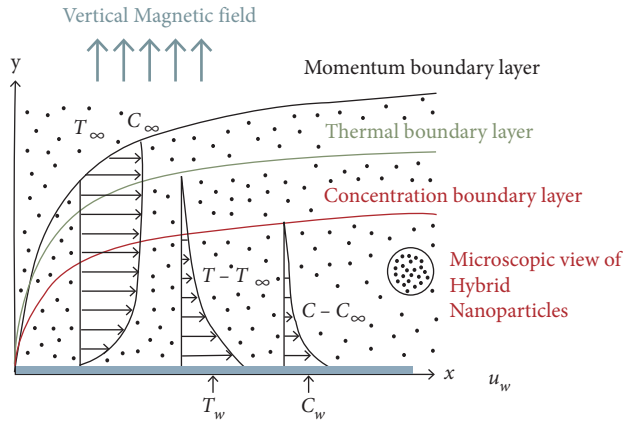

Figure 1: Flow configuration and geometrical coordinates.

$$\frac{\partial u}{\partial x} + \frac{\partial v}{\partial y} = 0, \tag{1}$$

$$\rho_{hnf}\left(u\frac{\partial u}{\partial x} + v\frac{\partial u}{\partial y}\right) = \mu_{hnf}\frac{\partial^2 u}{\partial y^2} + g(\rho\beta)_{hnf}(T - T_\infty) - \sigma_{hnf}B_0^2 u, \tag{2}$$

$$\left(\rho C_p\right)_{hnf}\left(u\frac{\partial T}{\partial x} + v\frac{\partial T}{\partial y}\right) = K_{hnf}\frac{\partial^2 T}{\partial y^2} - \frac{\partial q_r}{\partial y}. \tag{3}$$

Appropriate boundary conditions are presented as

$$\begin{aligned} &\text{at } y = 0,\\ &u = U_w = ax,\\ &v = v_0,\\ &T = T_w,\\ &\text{at } y \longrightarrow \infty. u \longrightarrow 0,\ T \longrightarrow T_\infty. \end{aligned} \tag{4}$$

For the particular flow configuration, the velocity components u, v and the stream function are defined as $u = \partial\psi/\partial y$ and $v = -\partial\psi/\partial x$ wherever ψ represents stream function. Hence, we get the values of u, v as below:

$$\begin{aligned} u &= axF'(\eta),\\ v &= -\sqrt{av_f}F(\eta). \end{aligned} \tag{5}$$

In equations (2) and (3), ρ_{hnf}, $(\rho C_p)_{hnf}$ symbolizes the density and heat capacity, μ_{hnf} denotes the dynamic viscosity, g represents the gravity acceleration, and β_{hnf} is thermal expansion. Now, for the hybrid nanofluids, the expression for ρ_{hnf}, $(\rho C_p)_{hnf}$, and $(\rho\beta)_{hnf}$ are reported as

$$\begin{aligned} \rho_{hnf} &= \left\{(1-\phi_2)(1-\phi_1)\rho_f + (1-\phi_2)\phi_1\rho_{s1}\right\} + \phi_2\rho_{s2},\\ \left(\rho C_p\right)_{hnf} &= (1-\phi_2)\left\{(1-\phi_1)\left(\rho C_p\right)_f + \phi_1\left(\rho C_p\right)_{s1}\right\} + \phi_2\left(\rho C_p\right)_{s2},\\ (\rho\beta)_{hnf} &= \left\{(1-\phi_1)(1-\phi_2)(\rho\beta)_f + \phi_1(1-\phi_2)(\rho\beta)_{s1}\right\} + \phi_2(\rho\beta)_{s2},\\ \frac{\sigma_{hnf}}{\sigma_{bf}} &= \frac{\sigma_{s2} + 2\sigma_{bf} - 2\phi_2\left(\sigma_{bf} - \sigma_{s2}\right)}{\sigma_{s2} + 2\sigma_{bf} + \phi_1\left(\sigma_{bf} - \sigma_{s2}\right)}. \end{aligned} \tag{6}$$

The dynamic viscosity and thermal conductivity of hybrid nanofluid are described as

$$\begin{aligned} \frac{\mu_{hnf}}{\mu_f} &= \frac{1}{(1-\phi_1)^{2.5}(1-\phi_2)^{2.5}},\\ K_{hnf} &= K_f\left[\frac{((K_{s2} + 2A_2) - \phi_2(A_2 - K_{s2}))}{((K_{s2} + 2A_2) + \phi_2(A_2 - K_{s2}))}\right],\\ A_2 &= \frac{\left(\left(K_{s1} + k_f\right) - 2\phi_1\left(K_f - K_{s1}\right)\right)}{\left(\left(K_{s1} + 2f\right) + \phi_1\left(K_f - K_{s1}\right)\right)}. \end{aligned} \tag{7}$$

Here, ϕ_1 and ϕ_2 represent the fraction factor of the used nanomaterials, respectively. Furthermore, K_f, K_{hnf} are the thermal conductivities of the host and hybrid nanoliquid, respectively. Suppose that the velocity and temperature of the stretching sheet are described as

$$\begin{aligned} U_w(x,0) &= ax,\\ T_w(x,0) &= T_\infty + bx, \end{aligned} \tag{8}$$

where a, b, and c are constants. The dimensionless stream function F and dimensionless temperature θ are described as

$$\begin{aligned} \eta &= \sqrt{\frac{a}{v_f}}y,\\ \psi &= \sqrt{av_f}\,xF(\eta),\\ \theta(\eta) &= \frac{T - T_\infty}{T_w - T_\infty},\\ q_r &= -\left(\frac{4\sigma^*}{3k^*}\right)\frac{\partial T^4}{\partial y}, \end{aligned} \tag{9}$$

where η represents the similarity variable. Furthermore, $\psi(x,y)$ is the stream function and q_r denotes the radiative heat flux. Finally, the following hybrid-nanoliquid flow model is obtained after incorporating the effective empirical correlations and similarity equations:

$$F'''(\eta) - (1-\phi_1)^{2.5}(1-\phi_2)^{2.5}\left[\left\{(1-\phi_2)\left((1-\phi_1)+\phi_1\frac{\rho_{s1}}{\rho_f}\right)+\phi_2\frac{\rho_{s2}}{\rho_f}\right\}\left\{(F'(\eta))^2 - F(\eta)F''(\eta)\right\}\right]$$

$$-(1-\phi_1)^{2.5}(1-\phi_2)^{2.5}\left\{\frac{\sigma_{s2}+2\sigma_{bf}-2\phi_2\left(\sigma_{bf}-\sigma_{s2}\right)}{\sigma_{s2}+2\sigma_{bf}+\phi_1\left(\sigma_{bf}-\sigma_{s2}\right)}\right\}, \tag{10}$$

$$MF'(\eta) + (1-\phi_1)^{2.5}(1-\phi_2)^{2.5}\left\{(1-\phi_2)\left((1-\phi_1)+\phi_1\frac{(\rho\beta)_{s1}}{(\rho\beta)_f}\right)+\phi_2\frac{(\rho\beta)_{s2}}{(\rho\beta)_f}\right\}\lambda\theta(\eta) = 0,$$

$$\frac{1}{\Pr}\frac{\left(K_{hnf}/K_{bf}+Rd\left(1+(\theta_w-1)\right)^3\right)}{\left(\rho C_p\right)_{hnf}}\theta''(\eta) + F(\eta)\theta'(\eta) = 0. \tag{11}$$

The transformed boundary conditions become

$$\begin{aligned} F(0) &= 0,\\ \theta(0) &= 1,\\ F'(0) &= 1,\\ F'(\eta) &\longrightarrow 0,\\ \theta(\eta) &\longrightarrow 0, \text{ at } \eta \longrightarrow \infty, \end{aligned} \tag{12}$$

$$\begin{aligned} C_f &= \frac{2U_w^{-2}\tau_w}{\rho_f},\\ Nu_x &= \frac{xq_w\left(T_w - T_\infty\right)^{-1}}{K_f}. \end{aligned} \tag{13}$$

Here, Re is denoted the Reynolds number, Gr is denoted the Grashof number, and λ represents the buoyancy parameter given by the following expressions:

$$\begin{aligned} Re_x &= U_w x v_f^{-1},\\ Gr_x &= g\beta_f\left(T_w - T_\infty\right)v_f^{-2}x^3,\\ \lambda &= Gr_x Re_x^{-2}. \end{aligned} \tag{14}$$

Moreover, $Pr = v_f/\propto_f$ denotes Prandtl number and $M = \sigma_f B_0^2/a\rho_f$ is the magnetic interaction parameter for the hybrid nanofluids. The skin friction coefficient is symbolized C_f and heat transfer capacity that, said in the Nusselt number Nu_x, explains the following.Wherever τ_w is represented the shear stresses and heat flux is denoted q_w,

$$\begin{aligned} \tau_w &= \mu_{hnf}\left(\frac{\partial u}{\partial y}\right)_{y=0},\\ q_w &= -K_{hnf}\left(\frac{\partial T}{\partial y}\right)_{y=0}. \end{aligned} \tag{15}$$

Applying transformation in the nondimensional expressions, we obtained the following expressions:

$$\begin{aligned} C_f Re_x^{1/2} &= 2\left((1-\phi_1)^{-2.5}(1-\phi_2)^{-2.5}\right)F''(0),\\ \frac{Nu_x}{Re_x^{1/2}} &= -\left(\frac{K_{hnf}}{K_{bf}}\right)\theta'(0). \end{aligned} \tag{16}$$

3. Mathematical Analysis

Many physical phenomena can be modeled as a system of highly coupled nonlinear differential equations over a bounded or semi-infinite regions. Actually, such models are very tedious due to high nonlinearity and impossible to tackle in the form of closed solution. However, numerical techniques are reliable under such circumstances. Therefore, RK technique and its coupling with the shooting method is applied on the model under consideration. The model is described in (10) and (11) along with conditions defined over the surface and away from it given in equation (12). Actually, aforementioned technique works for the system of first-order ODEs. In this regard, firstly, we fixed the following transformations to get the desired system:

$$\left(y_1, y_2, y_3, y_4, y_5, y_6\right) = \left(F, F'', F''', \theta, \theta', \theta''\right). \tag{17}$$

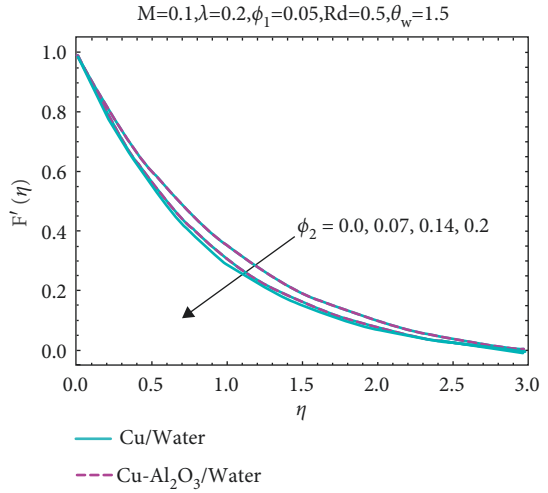

Figure 2: Effect of ϕ_2.

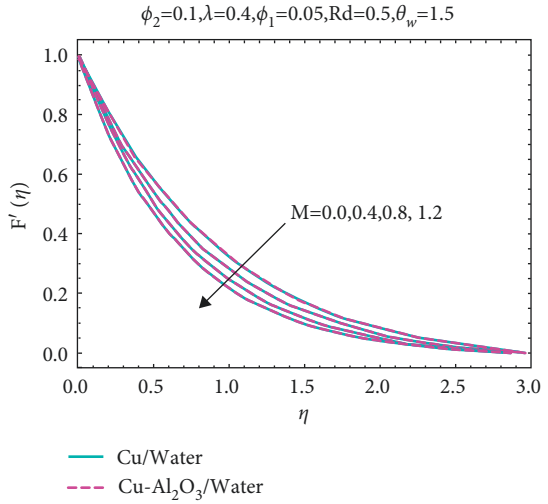

Figure 3: Effect of M.

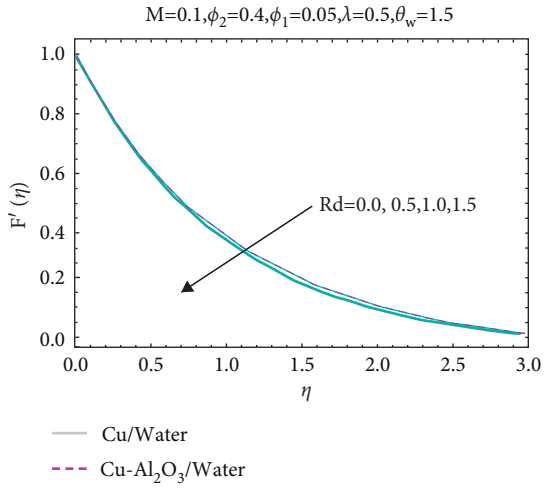

Figure 4: Effect of Rd.

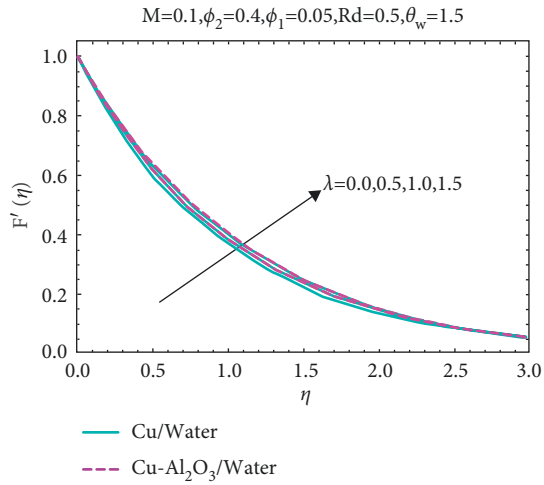

Figure 5: Effect of λ.

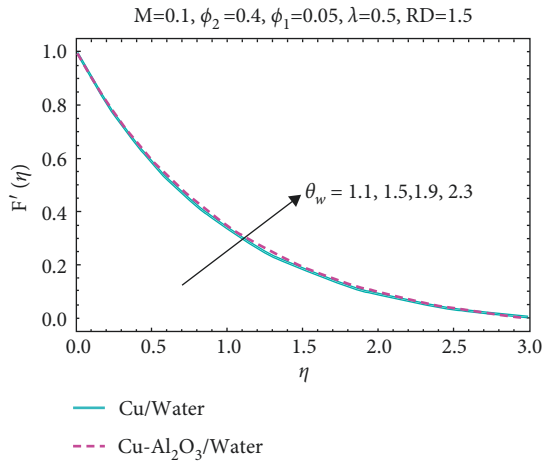

Figure 6: Effect of. θ_w

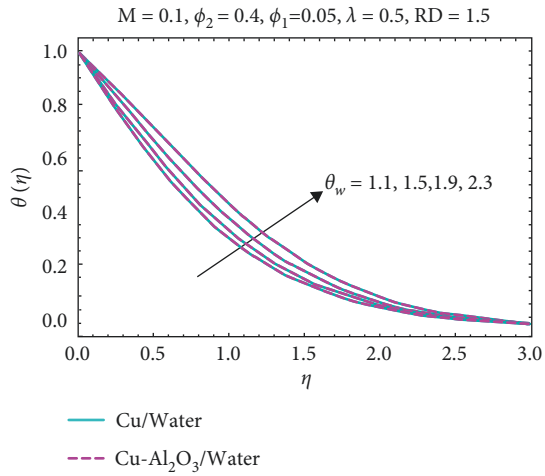

Figure 7: Effect of θ_w.

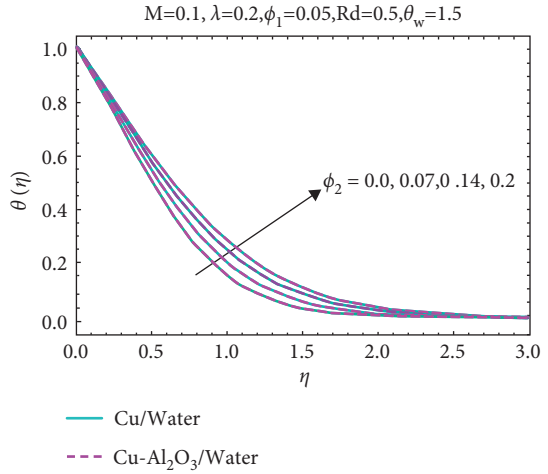

Figure 8: Effect of ϕ_2.

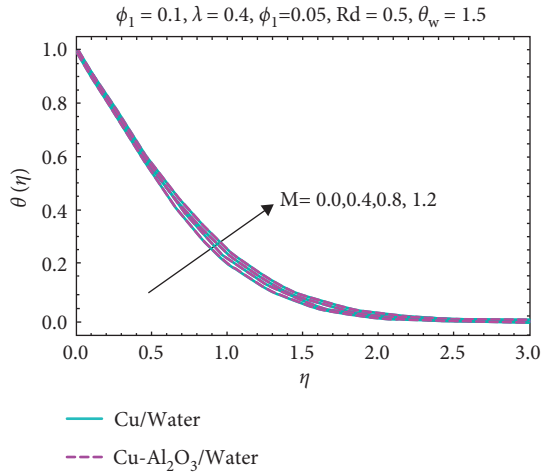

Figure 9: Effect of M.

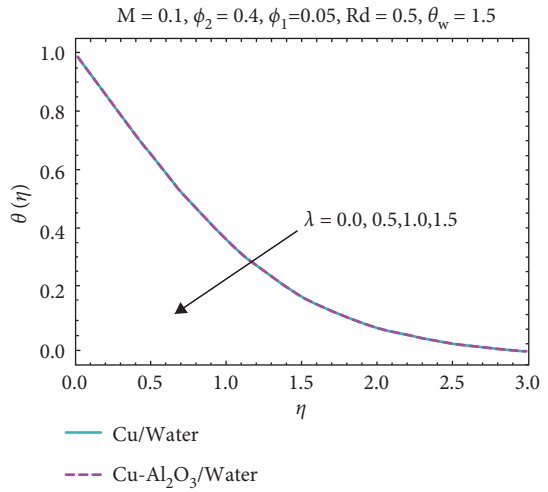

Figure 10: Effect of. λ.

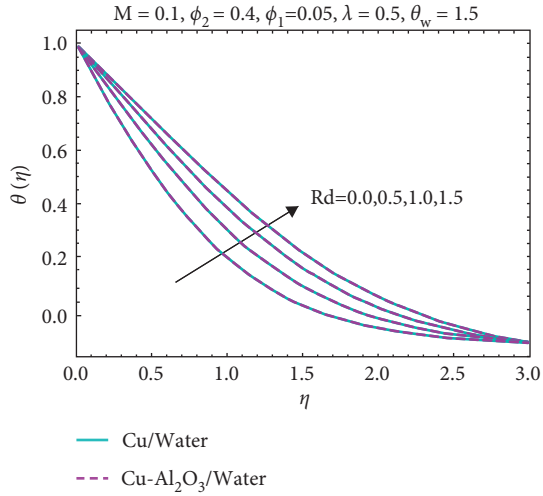

Figure 11: Effect of Rd.

By inducing these transformations in the hybrid model defined in (10) and (11), the following version is obtained:

$$y_2' = (1-\phi_1)^{2.5}(1-\phi_2)^{2.5}\left[\left\{(1-\phi_2)\left((1-\phi_1)+\phi_1\frac{\rho_{s1}}{\rho_f}\right)+\phi_2\frac{\rho_{s2}}{\rho_f}\right\}.\left\{(y_1')^2 - y_1 y_2'\right\}\right] + (1-\phi_1)^{2.5}(1-\phi_2)^{2.5}\left(\frac{\sigma_{s2}+2\sigma_{bf}-2\phi_2(\sigma_{bf}-\sigma_{s2})}{\sigma_{s2}+2\sigma_{bf}+\phi_1(\sigma_{bf}-\sigma_{s2})}My_1' - \left\{(1-\phi_2)\left((1-\phi_1)+\phi_1\frac{(\rho\beta)_{s1}}{(\rho\beta)_f}\right)+\phi_2\frac{(\rho\beta)_{s2}}{(\rho\beta)_f}\right\}\lambda y_4\right), \tag{18}$$

$$y_5' = -\frac{\left\{(1-\phi_1)(1-\phi_2)+\phi_1(1-\phi_2)(\rho C_p)_{s1}/(\rho C_p)_f+\phi_2(\rho C_p)_{s2}/(\rho C_p)_f\right\}}{\left(K_{hnf}/K_{bf}+Rd\left(1+(\theta_w-1)\right)^3\right)}Pr\{y_1 y_1'\}. \tag{19}$$

The model described in (18) and (19) is a desired system on which the proposed numerical technique is applicable. For said purpose, MATHEMATICA 10.0 code is generated for the model and plotted the results for the preeminent flow quantities.

4. Results and Discussion

This section is fixed to explore the results for the velocity and temperature behaviour of the hybrid as well conventional nanofluid. The results are decorated against the various preeminent flow parameters over the desired region.

M is Magnetic parameter, λ is the buoyancy parameter, and Rd is the radiation parameter. Measure two dissimilar kinds of nanoparticles, Cu and Al_2O_3. The boundary-layer viscosity rises with the rise in velocity gradient and the temperature gradient. Performances of resistance force such as density and thickness of the hybrid nanofluid; as a result, the particle viscosity and speed rise by the growth in other production follow. The volume of nanoparticles increases the thermal conductivity rises, as the case of this is increases temperature.

Figure 2 shows the influence of ϕ_2 on mix nanoparticles $Cu - Al_2O_3/H_2O$ in the velocity profile.

At that time, velocity decreases as the volume fraction increases. The presence of dense nanoparticles info to other weakening the velocity boundary-layer thickness.

Figure 3 represents the velocity profile which the magnetic parameter effect of hybrid nanofluid. Because of the description, velocity of hybrid nanofluid decreases with the varying of M. It obviously proves that right angles' attractive field plays with the transportation occurrences. It is main indication that the great oppositions continuously particles of fluid, which effect to viscosity produced in hybrid nanofluid. Figure 4 presents the velocity profile; the increase of Rd is an increase in the velocity of hybrid nanofluid. Because the viscosity and density decrease in the cause of this is increase the velocity of hybrid nanofluid. Figure 4 shows that the velocity of hybrid nanoparticles increases as the Rd vary. We can say that if varying Rd, then the stretching sheet of the nanoparticles and velocity is abtained. Figures 5 and 6 show that the varying λ and θ_w increase the velocity of hybrid nanofluid $Cu - Al_2O_3/H_2O$. The boundary-layer thickness will be increased.

Table 1: Thermophysical possessions of water hybrid nanofluids in addition nanoparticles [3, 5, 6].

Properties	Pure water H_2O	Alumina (Al_2O_3)	Copper (Cu)
$\rho(kg/m^3)$	997.1	3970	8933
$C_p(J/kgk)$	4179	765	385
k $(Wm^{-1}k^{-1})$	0.6130	40	401
$\beta \times 10^5 k^{-1}$	21	0.850	1.670
$\sigma(s/m)$	5.5×10^{-6}	3.5×10^6	59.6×10^6

Figures 7 and 8 appear that the temperature profiles θ_w and ϕ_2 are varying; then, the heat transfer increases. $\theta_w > 1$ Then, the given solution is nonlinear and plot will nonlinear plot. In this case, the solution of equation is nonlinear. Figure 8 calculates the thermal conductivity increases, and therefore, the thermal boundary-layer thickness rises, as the nanoparticle volume fraction increases. This case is in submission with the main proposes of using hybrid nanofluid and furthermore approves by physical performance; after the size increase of nanoparticles, then k_{hnf} and thermal boundary-layer viscosity rise. Figure 9 shows temperature circulation, and the heat transfer rises with rise in the attractive factor due to description; the temperature boundary-layer thickness rises. It observably shows that the right angles attractive field be pitted against the moving occurrences.

Figure 10 shows that decreasing of buoyancy parameter changes the hotness transfer of the hybrid nanoparticles which represent the temperature profile; however, increasing λ, the heat decreasing because the thermal conductivity is reduction. If thermal conductivity reduced, then thermal boundary layer reduced as well. Figure 11 clearly describes that the radiation *Rd* increases as well as increasing the heat transfer. Table 1 presents the thermophysical values of the base liquid and nanoparticles.

5. Conclusions

This work reported the study of heat transport phenomena in Cu-Al_2O_3/H_2O hybrid nanofluid by taking the effects of thermal radiations, magnetic field, and varying volumetric fraction. The flow situation is modeled over a stretched surface via similarity equations. The resultant hybrid model is accommodated via numerical technique and furnished the results against the parameters. Form the analysis, it is examined that [18]

(i) The velocity of Cu-Al_2O_3/H_2O declines against higher volumetric fraction of Cu-Al_2O_3 and stronger Lorentz forces

(ii) The fluid temperature significantly augmented for θ_w, and it vanishes asymptotically far from the surface

(iii) The velocity rises due to mixed convection effects λ, and it opposes the fluid temperature.

(iv) Thermal radiations worked as catalysis in the study regarding thermal transport which prominently played positive role

Data Availability

The study is based on numerical technique and no data were used in findings of the study.

Conflicts of Interest

The authors declare that they have no conflicts of interest.

Acknowledgments

Princess Nourah bint Abdulrahman University Researchers Supporting Project number (PNURSP2022R52), Princess Nourah bint Abdulrahman University, Riyadh, Saudi Arabia.

References

[1] B. Takabi, A. M. Gheitaghy, and P. Tazraei, "Hybrid water-based suspension of Al_2O_3 and Cu nanoparticles on laminar convection effectiveness," *Journal of ThermoPhysics and Heat Transfer*, vol. 30, no. 3, pp. 1–10. In press, 2015.

[2] B. Takabi and H. Shokouhmand, "Effects of Al2O3-Cu/water hybrid nanofluid on heat transfer and flow characteristics in turbulent regime," *International Journal of Modern Physics C*, vol. 26, no. 4, Article ID 1550047, 2015.

[3] S. Suresh, K. P. Venkitaraj, P. Selvakumar, and M. Chandrasekar, "Effect of Al2O3-Cu/water hybrid nanofluid in heat transfer," *Experimental Thermal and Fluid Science*, vol. 38, pp. 54–60, 2012.

[4] G. G. Momin, "Experimental investigation of mixed convection with Al_2O_3/H_2O& hybrid nanofluid in inclined tube for laminar flow," *International Journal of Scientific & Technology Research*, vol. 2, pp. 195–202, 2013.

[5] S. Sureh, K. Venkitaraj, p. Selvakumar, and M. Chandrasekar, "Effect of $Cu - Al_2O_3/H_2O$ hybrid nanofluid in heat transfer," *Experimental Thermal and Fluid Science*, vol. 38 9, pp. 54–60, 2012.

[6] S. Suresh, K. P. Venkitaraj, M. S. Hameed, and J. Sarangan, "Turbulent heat transfer and pressure drop characteristics of dilute water based Al_2O_3, Cu hybrid nanofluids," *Journal of Nano science and Nanotechnology*, vol. 14, Article ID 25632572, 2014.

[7] S. Suresh, K. P. Venkitaraj, P. Selvakumar, and M. Chandrasekar, "Synthesis of Al2O3-Cu/water hybrid nanofluids using two step method and its thermo physical properties," *Colloids and Surfaces A: Physicochemical and Engineering Aspects*, vol. 388, no. 1-3, pp. 41–48, 2011.

[8] B. Takabi and S. Salehi, "Augmentation of the heat transfer performance of a sinusoidal corrugated enclosure by employing hybrid nanofluid," *Advances in Mechanical Engineering*, vol. 6, Article ID 147059, 2014.

[9] R. Ahmad and W. A. Khan, "Unsteady heat and mass transfer magnetohydrodynamic (MHD) nanofluid flow over a stretching sheet with heat source-sink using quasi-linearization technique," *Canadian Journal of Physics*, vol. 93, no. 12, pp. 1477–1485, 2015.

[10] K. Kishore and S. Bandari, "Melting heat transfer in boundary layer stagnation-point flow of a nanofluid towards a stretching-shrinking sheet," *Canadian Journal of Physics*, vol. 92, no. 12, pp. 1703–1708, 2014.

[11] W. A. Khan and I. Pop, "Boundary-layer flow of a nanofluid past a stretching sheet," *International Journal of Heat and Mass Transfer*, vol. 53, no. 11-12, pp. 2477–2483, 2010.

[12] M. M. Rashidi and S. A. Mohimanian Pour, "Analytic approximate solutions for unsteady boundary-layer flow and heat transfer due to a stretching sheet by homotopy analysis method," *Nonlinear Analysis Modelling and Control*, vol. 15, no. 1, pp. 83–95, 2010.

[13] R. Bhargava, L. Kumar, and H. S. Takhar, "Finite element solution of mixed convection micropolar flow driven by a porous stretching sheet," *International Journal of Engineering Science*, vol. 41, no. 18, pp. 2161–2178, 2003.

[14] A. Chakrabarti and A. S. Gupta, "Hydromagnetic flow and heat transfer over a stretching sheet," *Quarterly of Applied Mathematics*, vol. 37, no. 1, pp. 73–78, 1979.

[15] M. M. Rashidi, M. Ali, N. Freidoonimehr, and F. Nazari, "Parametric analysis and optimization of entropy generation in unsteady MHD flow over a stretching rotating disk using artificial neural network and particle swarm optimization algorithm," *Energy*, vol. 55, pp. 497–510, 2013.

[16] T. Hayat, M. Awais, and A. Alsaedi, "Magnetohydrodynamic stretched flow of maxwell fluid in presence of homogeneous-heterogeneous chemical reactions by three different approaches," *Journal of Computational and Theoretical Nanoscience*, vol. 11, no. 4, pp. 953–957, 2014.

[17] T. Fang, "Magneto hydrodynamic viscous flow over a nonlinearly moving sur-face closed-form solutions," *Eur. Phys. J. Plus*, vol. 129, pp. 1–18, 2014.

[18] K. Vajravelu, "Hydromagnetic convection at a continuous moving surface," *Acta Mechanica*, vol. 72, no. 3-4, pp. 223–232, 1988.

[19] M. M. Rashidi, M. Sadri, and M. A. Sheremet, "Numerical simulation of hybrid nanofluid mixed convection in a lid-driven square cavity with magnetic field using high-order compact scheme," *Nanomaterials*, vol. 11, 2021.

[20] S. Nazari, R. Ellahi, M. M. Sarafraz, M. R. Safaei, A. Asgari, and O. A. Akbari, "Numerical study on mixed convection of a non-Newtonian nanofluid with porous media in a two lid-driven square cavity," *Journal of Thermal Analysis and Calorimetry*, vol. 140, no. 3, pp. 1121–1145, 2020.

[21] R. Ellahi, F. Hussain, S. A. Abbas, M. M. Sarafraz, M. Goodarzi, and M. S. Shadloo, "Study of two-phase newtonian nanofluid flow hybrid with hafnium particles under the effects of slip," *Inventions*, 2020.

[22] H. Goodarzi, O. A. Akbari, M. M. Sarafraz, M. M. Karchegani, M. R. Safaei, and G. A. S. Shabani, "Numerical simulation of natural convection heat transfer of nanofluid with Cu, MWCNT, and Al2O3 nanoparticles in a cavity with different aspect ratios," *Journal of Thermal Science and Engineering Applications*, vol. 11, Article ID 061020, 2019.

[23] S. Yousefzadeh, H. Rajabi, N. Ghajari, M. M. Sarafraz, O. A. Akbari, and M. Goodarzi, "Numerical investigation of mixed convection heat transfer behavior of nanofluid in a cavity with different heat transfer areas," *Journal of Thermal Analysis and Calorimetry*, vol. 140, no. 6, pp. 2779–2803, 2020.

[24] N. S. Wahid, N. M. Arifin, N. S. Khashi, I. Pop, N. Bachok, and M. E. H. Hafidzuddin, "MHD mixed convection flow of a hybrid nanofluid past a permeable vertical flat plate with thermal radiation effect," *Alexandria Engineering Journal*, vol. 140, p. 378, 2020.

Hindawi
Mathematical Problems in Engineering
Volume 2022, Article ID 1603529, 18 pages
https://doi.org/10.1155/2022/1603529

Research Article

Development of New Correlations and Parametric Optimization in Nanofluid Flow through Protruded Roughened Square Channel

Sunil Kumar,[1] **Gaurav Gupta**,[1] **Fairouz Tchier**,[2] **Qin Xin**,[3] **Anil Kumar**,[4] **and Faria Ahmed Shami**[5]

[1]*Yogananda School of Artificial Intelligence Computers and Data Science, Shoolini University, Solan 173229, Himachal Pradesh, India*
[2]*Department of Mathematics, King Saud University, Riyadh, Saudi Arabia*
[3]*Faculty of Science and Technology, University of the Faroe Islands, Tórshavn, Faroe Islands*
[4]*Department of Mechanical Engineering, University of Petroleum and Energy Studies, Dehradun 248007, India*
[5]*Bangabandhu Sheikh Mujibur Rahman Science and Technology University, Bihar Sharif, Bangladesh*

Correspondence should be addressed to Faria Ahmed Shami; fariashami@bsmrstu.edu.bd

Received 29 November 2021; Revised 13 February 2022; Accepted 24 February 2022; Published 6 April 2022

Academic Editor: Mohammadreza Safaei

This study discusses the optimization of heat-transfer parameters in nanofluid flow through a rough square surface channel including a protruded rib compound transverse pattern using response surface methodology (RSM). Flow and geometrical characteristics are optimized, resulting in optimal flow friction and heat transfer performances. The comparison of RSM's estimated values to experimentally observed values was abandoned. The results demonstrate that the RSM-calculated values agree with the observed values and are within the 5.5 percent uncertainty limitations. Statistical correlations for Nusselt number and friction factor have been developed as functions of protrusion transverse rib height, protrusion transverse rib diameter, *X*-axis pitch, *Y*-axis pitch, and Reynolds number. These correlations have been found to predict the values within the error limits of ±8.9% and ±8.7%, respectively. On the basis of correlations developed for Nusselt number and friction factor, an attempt has been made to compare the thermohydraulic performance of protruded roughened square channel.

1. Introduction

Energy conservancy is one of the indispensable issues of the twenty-first century, and it will absolutely be a challenge among the hugest difficulties sooner rather than later. Thus, researchers, engineers, and scientists are significantly trying to address this imperative concern [1].

Utilization of nanofluids (NFs) is one of the approaches to enhance heat transfer (HT), as traditional fluids, like, engine oil, ethylene glycol, and water have moderately low heat transfer rate (HTR) [2, 3]. Turbulence promoters and numerous geometrical shapes of the rib-groove duct are commonly used, since they cause stream division and reattachment, thus breaking the laminar viscous layer and causing enhanced heat transfer [4, 5].

Al-Shamani et al. [6] explored the turbulent flow of water-based Al_2O_3, SiO_2, and ZnO NFs with 1–4% volumes fractions (φ) and 25–70 nm nanoparticle diameter (dnp) through rib-groove duct. Studies reveal that the SiO_2-H_2O NF has a maximum heat transfer coefficient (HTC) in correlation with the other NFs. Kamali and Ali-Reja [7] and Kumar et al. [8] examined turbulent flow in a square conduit with four ribs' shapes. The outcomes showed that inter-rib distribution affected HTC. Lauriat [9] numerically and experimentally explored whereas Nguyen et al. [10] explored by experimentation the HT behavior of Al2O3-H_2O NF and found that the HTC increases up to 40% as compared to the base fluid.

Hussein et al. [11] numerically and experimentally investigated water-based NFs (CuO-H_2O, Al_2O_3-H_2O, TiO_2-H_2O) for φ that varied from 0 to 2%. The improvement of HT was about 47.3% (CuO), 49% (Al_2O_3), and 45.2% (TiO_2) over pure water. Ahmed and Yusoff [12] concluded that in comparison to the base fluid, Al_2O_3-H_2O NF showed an

improvement of 45.7% in HTC at 3 vol. % and Ren = 16,000. Mahian et al. [13] calculated HTC for φ up to 4% and dnp of 25 nm to four different NFs including CuO-H_2O, Al_2O_3-H_2O, TiO_2-H_2O, and SiO_2-H_2O. Findings indicated that Al_2O_3-H_2O NF had the highest HTC at $\varphi = 0.4\%$. Wen and Ding [14], and Singh and Sarao [15] experimentally found that with an increase in number such as Reynolds Re_n the Nusselt (Nu) and friction factor (f) of Al_2O_3-H_2O NF, heat exchanger improves over the base fluid H_2O.

Sundar et al. [16] determined convective HTC for a fully developed turbulent NF flow and found a 31.10% increment in Nu at $\varphi = 0.3\%$. Suresh et al. [17] noticed an improvement of 14.25% in flow friction at $\varphi = 0.1\%$ for Cu-Al_2O_3-H_2O NF flow at a volume flow rate of 2.24×10^{-5} m^3/s. Pak and Cho [18] experimentally observed enhancement in HTC compared to the H_2O for Al_2O_3 and TiO_2 NFs for Ren that ranges from 104 to 105 and φ varies from 0% to 3%. Ho et al. [19] investigated the HTC of Al_2O_3 nanoparticles whose φ varies from 0.1% to 4% in the square duct of various sizes. They proposed a HT correlation showing that improvement in HTC does not exist if φ is larger than 2% and also found around 18% improvement in HTC for the largest area duct.

Li and Peterson [20] experimentally investigated HT characteristics of Al_2O_3-H_2O NF of 25 nm dnp with φ ranging from 0.5% to 6%. A large deterioration percentage in the HTC was observed when φ increases. Ho et al. [21] suggested Nu correlations for the four different models based on two formulas for $\leq \varphi \leq 4\%$, and results confirmed a strong impact about uncertainties related to formulas adopted on the HT characteristics. Correlation formulas for Nu and f given by Sundar et al. [16]; Suresh et al. [17]; Pak and Cho [18]; Maïga et al. [22]; Petukhov [23]; Dittus and Boelter [24]; Duangthongsuk and Wongwises [25]; Madhesh et al. [26]; and Gnielinski [27] are listed in Table 1. Moreover, there are many numerical and experimental studies on heat exchanger using mono and hybrid nanofluids that have also been carried out by different researchers [28–32] and they revealed that the thermal characteristics of nanofluids are found to be higher and better for heat transfer application in comparison to the base fluid.

2. The RSM (Response Surface Methodology)

RSM, an assortment of mathematical/statistical technique, which is helpful for the analysis and modeling of issues, was a reaction of interest that is inspired by design parameters to optimize the boundaries of design on the ideal estimation of the response function, which is the primary goal. Working with the RSM involves the following 3 main steps [33, 34]:

(1) Choosing the design or model matrix.

(2) Selecting the number of the control factors and responses and accordingly entering the data.

(3) Analyzing the responses and conformation of the results.

The optimal set of experimental parameters can be discovered by RSM that delivers a most extreme or least estimation of response and expresses immediate and intelligent impacts of parameters over 2D and 3D plots. The quantitative relation between responses and input variables is translated as follows [33, 34]:

$$\mathbf{z} = \mathbf{f}\left(\mathbf{x}_1, \mathbf{x}_2, \mathbf{x}_3, \mathbf{x}_4, \ldots\ldots\ldots \mathbf{x}_n\right) \pm \boldsymbol{\varepsilon}, \tag{1}$$

where z is the response, whereas $\mathbf{x}_1, \mathbf{x}_2, \mathbf{x}_3, \mathbf{x}_4, \ldots\ldots\ldots \mathbf{x}_n$ are the input variables, and ε is the fitting error. The approximation projected using the cubic model of $\mathbf{f}$ is as follows:

$$\begin{aligned} f = a_0 &+ \sum_{i=1}^{n} a_i x_i + \sum_{i<j}^{n} a_{ij} x_i x_j + \sum_{i=1}^{n} a_i x_i^2 + \sum_{i<j}^{n} a_{ij} x_i^2 x_j \\ &+ \sum_{i<j}^{n} a_{ij} x_i x_j^2 + \sum_{i=1}^{n} a_i x_i^3 + \varepsilon, \end{aligned} \tag{2}$$

where $\mathbf{a_i}$ is the linear/quadratic and cubic effects of $\mathbf{x_i}$ and between $\mathbf{x_i}$ and $\mathbf{x_j}$ [33, 34].

From literature review, it has been found that there has been no study carried out on thermal performance enhancement of heat exchanger using nanofluid with combined protruded roughened square channel. In other words, the novelty of this study is to study the influence of the combined effect of both nanofluid and protruded roughened square channel. The primary objectives of the current analysis include the following: to optimize the operating parameters, i.e., nanoparticle concentration $(0.01 \leq \varphi \leq 0.04)$, nanoparticle diameter $(30 \leq \mathbf{d_{np}} \leq 45)$, stream-wise pitch $(1.4 \leq \mathbf{X_{axis}}/\mathbf{d_{print}} \leq 2.6)$, span-wise pitch $(1.4 \leq \mathbf{Y_{axis}}/\mathbf{d_{print}} \leq 2.6)$, ratio of print diameter $(0.83 \leq \mathbf{e_{rib}}/\mathbf{d_{print}} \leq 1.67)$, and Reynolds number $(4000 \leq \mathbf{Re_{num}} \leq 18000)$ using RSM, and to develop statistical correlations for Nusselt number $(\mathbf{Nu_{rough}})$ and friction factor $(\mathbf{f_{rough}})$ in terms of operating parameters.

3. Experimental Details and Preparation of Nanofluid

The experimental setup used for assessing Nu_{rough} and f_{rough} characteristics of the nanofluid flow constitutes a square duct having length of 340 mm, width of 10 mm, and height of 10 mm [1]. A schematic diagram of the experimental setup is presented in Figure 1, consisting of a test section with an installed heater, inlet and outlet sections, a reservoir tank, a circulating pump, a condenser, a U-tube manometer, and a control valve. The test section length is 108 mm, the outlet section is 32 mm, and the inlet section is 200 mm, which are selected using ASHRAE standard [35] to ensure completely built flow in the test section. The upper wall of the test section was heated by an electric heater providing a constant heat flux of 10 kW/m^2. A 10 liter reservoir tank of working fluid was mounted in between the 0.75 kW circulating pump and the 1 kW cooling capacity condenser. The fluid was forced to the inlet section and then to the test section to get a fully developed flow before entering the test section. The flow meter was connected between the pump and the inlet section for measuring the flow rates. A T-type thermocouple was used for taking down the temperature reading with the help of data acquisition. A total of 11 thermocouples were

Table 1: Correlation formulas for Nu and f for different flow regimes.

Researchers	Correlations	Description
Sundar et al. [16]	$Nu = 0.215Re^{0.8}Pr^{0.5}(1+\varphi)^{0.78}$ $f = 0.3108Re^{-0.245}(1+\varphi)^{0.42}$	$3000 < Re < 22000$ $0 < \varphi < 0.3\%$ $4.50 < Pr < 6.13$
Suresh et al. [17]	$\mathrm{Nu} = (0.31(\mathrm{RePr})^{0.68}(1+\varphi)^{95.73})$ $f = (26.44Re^{-0.8737}(1+\varphi)^{156.23})$	$700 < Re < 2300$; $\varphi = 0.1\%$
Pak and Cho [18]	$Nu = 0.021\,Re^{0.8}Pr^{0.5}$	$10^4 \le Re \le 10^5$ $6.54 \le Pr \le 12.33$
Maïga et al. [22]	$Nu = 0.085Re^{0.71}Pr^{0.35}$	$10^4 \le Re \le 5X10^5$ $6.6 \le Pr \le 13.9$
Petukhov [23]	$Nu = (RePr(f/8)/1.07 + 12.7(f/8)^{0.5}(Pr^{0.66}-1))$ $f = (1.82\log Re - 1.64)^{-2}$	$10^4 \le Re \le 5X10^5$ $0.5 \le Pr \le 2000$
Dittus and Boelter [24]	$Nu = \begin{cases} 0.024Re^{0.8}Pr^{0.4} \text{ for heating} \\ 0.024Re^{0.8}Pr^{0.3} \text{ for cooling} \end{cases}$	$2500 \le Re \le 1.24X10^5$ $0.7 \le Pr \le 120$
Duangthongsuk and Wongwises [25]	$Nu = 0.074Re^{0.707}Pr^{0.385}\varphi^{0.074}$	$3000 < Re < 18000$ $0 \le \varphi \le 2.0\%$
Madhesh et al. [26]	$\mathrm{Nu} = 0.012\mathrm{RePr}^{0.333}(\varphi)^{0.032}$	$4000 < \mathrm{Re} < 8000$ $0.15 < \varphi < 2.0\%$
Gnielinski [27]	$Nu = ((f/8)(Re-1000)Pr/1 + 12.7(f/8)^{0.5}(Pr^{0.66}-1))$ $f = 0.079Re^{-1/4}$	$2300 \le Re \le 5X10^5$ $0.5 \le Pr \le 10^6$

attached, out of which 08 were placed on the heated wall, 01 at the inlet, and 02 at the outlet to measure the temperature. When the fluid flow was in a steady-state condition, the pressure drop across the test section, temperature at the inlet and outlet of the test section, and wall temperature of the test section were recorded [1].

The four different volume concentrations of (Al_2O_3/H_2O) nanofluids were chosen as the sample, then dissolved in 100 ml of distilled water in each case, and then prepared in 4 different clean glass jars. The initial step is to blend Al_2O_3 nanoparticles in base fluid and the deionized water. The pH is one of the most important parameters, which effect the colloidal stability of oxide nanoparticles, so the pH value of nanofluid is tweaked about to 5.0. In the second step, Al_2O_3 nanoparticles were mixed with deionized water by an ultrasonic disrupter and homogenized for 2 days. The schematic of the practical setup is shown in Figure 1. The operating parameters are defined by protrusion transverse rib height (e_{rib}), protrusion transverse rib diameter (d_{print}), X-axis pitch (X_{axis}), and Y-axis pitch (Y_{axis}) of protrusions transverse rib as shown in Figure 2 [1]. The different processing parameters are determined using equations as presented in Table 2 [1, 4, 7–10] and the control factors, which touch the performance of heat exchanger and are considered in experimentation and optimization are tabulated in Table 3.

4. Validation and Uncertainty Analysis of Investigational Data

The $\mathbf{Nu_{smooth}}$ and $\mathbf{f_{smooth}}$ values are calculated from investigational data for smooth square surface duct, which have been equated with the data obtained from the Dittus-Boelter correlation (3) and (4) [1, 10, 24].

Dittus-Boelter correlation equation [24] of $\mathbf{Nu_{smooth}}$ for smooth surface square is as follows:

$$\mathbf{Nu_{smooth}} = 0.023\mathbf{Re_{num}^{0.8}Pr_{num}^{0.4}}. \quad (3)$$

Blasius correlation equation of $\mathbf{f_{smooth}}$ for smooth surface square is given as follows:

$$\mathbf{f_{smooth}} = 0.079\mathbf{Re_{num}^{-0.25}}. \quad (4)$$

For divergence of investigational and the projected data of $\mathbf{Nu_{smooth}}$ and $\mathbf{f_{smooth}}$ as a function of $\mathbf{Re_{num}}$, it is evidently illustrated that median (average) deviations of $\mathbf{Nu_{smooth}}$ and $\mathbf{f_{smooth}}$ were within 5%, which shows that experimental approach is acceptable and validates the experimental approach [1].

The uncertainty measurement of various quantities has been evaluated by using computation of uncertainty procedure given by Coleman and Glenn [36] and is in control limits, and the uncertainties values are calculated for $\mathbf{Re_{num}}$, $\mathbf{Nu_{rough}}$, and $\mathbf{f_{rough}}$, which are estimated as ±5.37%, ± 6.18%, and ±5.89%, respectively [1].

5. Results

To envisage the impacts of Reynolds number, nanoparticle concentration, nanoparticle diameter, transverse protrusion ribs on HT, and friction factor in a smooth square channel through an experimental/modeling analysis were used. The experimental data and modeling data (RSM) collected for various stream and roughness parameters have been discussed below.

5.1. ANOVA Analysis for Nusselt Number ($\mathbf{Nu_{rough}}$). The results of RSM model used for Nusselt number ($\mathbf{Nu_{rough}}$) are presented in Tables 4–7 in the form of ANOVA. The value of (Prob. > F) for used model is not more than 0.05 ($\alpha = 0.05$ or 95% confidence). Table 4 presents ANOVA test results for $\mathbf{Nu_{rough}}$ before elimination. The value 2690.10 of model F indicates the model significance. P-values less than 0.05 suggest that model terms are significant. In this case, A, B, C, D, E, F, AB, AC, AD, AE, AF, A^2, D^2, E^2, F^2, AE^2, D^3, E^3, and F^3 are significant model terms. Values higher than 0.1 suggest insignificance of model terms. Table 5 shows ANOVA test results of adequacy for $\mathbf{Nu_{rough}}$ before elimination. The predicted R-square of 0.9980 is in acceptable arrangement with the adjusted R-square of 0.9986, i.e., the difference is less than 0.2. A ratio greater than 4 is required

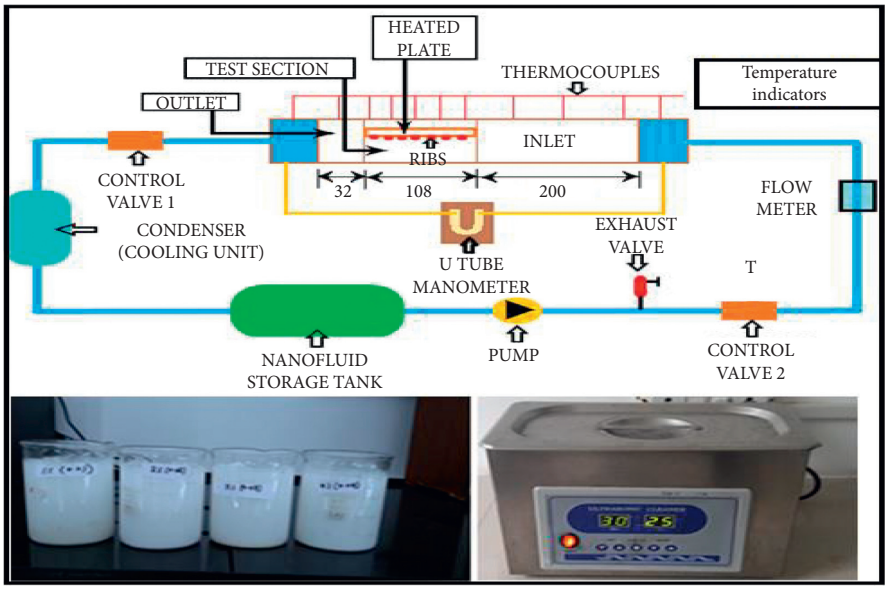

Figure 1: Experimental setup.

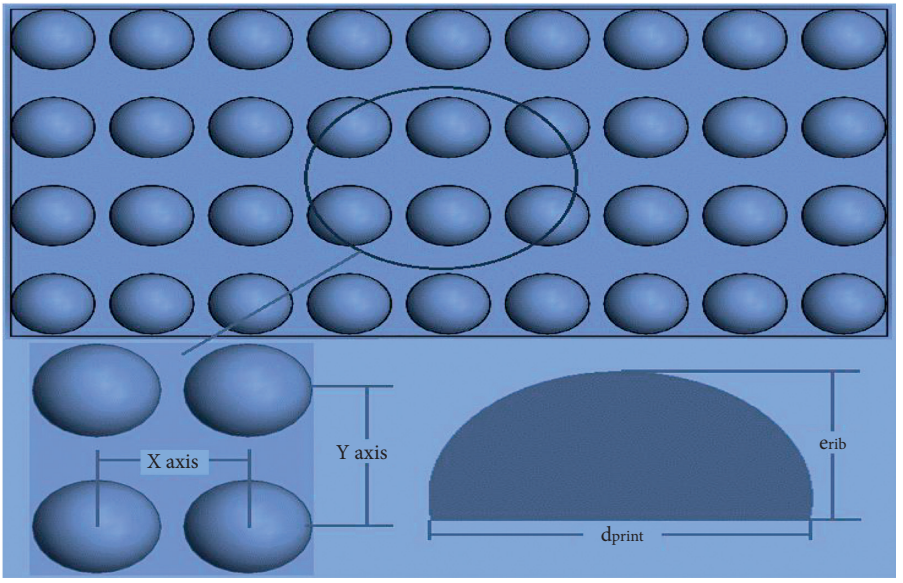

Figure 2: Rib shape parameters.

Table 2: The governing equations for processing essential parameters [1, 4, 7–10].

S. No	Parameter	Symbol	Governing equation
1	Power supplied to the heater	Q_{in}	$Q_{in} = I \times V$
2	Heat gain by fluid	Q_{out}	$Q_{out} = \dot{m} c_p (T_o - T_i)$
3	Heat transfer coefficient	h_t	$h_t = (Q_{\text{out}}/A_p (T_{pw} - T_f))$
4	Reynolds number	Re_{num}	$Re_{\text{num}} = (\rho_{nf} u_m D_h/\mu_{nf})$
5	Nusselt number	Nu_{rough}	$Nu_{\text{rough}} = (h_t D_h/k_{nf})$
6	Friction factor	f_{rough}	$f_{\text{rough}} = (2D_h \Delta p/\rho_{nf} L_t u_m^2)$

Table 3: Control factors.

Control factor	Range
A: Reynolds number, ($\mathrm{Re}_{\mathrm{num}}$)	6000–18000
B: nanoparticle concentration, (φ)	0.01–0.04
C: nanoparticle diameter (d_{np})	30–45
D:stream-wise pitch ($X_{\mathrm{axis}}/d_{\mathrm{print}}$)	1.40–2.60
E: span-wise pitch, ($Y_{\mathrm{axis}}/d_{\mathrm{print}}$)	1.40–2.60
F: proportion of protrusion height and print diameter ($e_{\mathrm{rib}}/d_{\mathrm{print}}$)	0.83–1.67

for adequacy precision measures. In this study, the adequacy precision ratio of 198.166 suggests an adequate signal. Thus, the model can be utilized to circumnavigate the design space.

In Table 6, ANOVA test results for $\mathbf{Nu_{rough}}$ after backward elimination are tabulated. The value 4219.54 of model F indicates the model significance. There is only a 0.01% chance that an F-value of this large could occur due to noise. *P*-values less than 0.05 suggest that model terms are significant. In this case, A, B, C, D, E, F, AB, AC, AD, AE, AF, A^2, D^2, E^2, F^2, A^2F, AD^2, AE^2, D^3, E^3, and F^3 are significant model terms. Values higher than 0.1 suggest insignificance of model terms. Table 6 shows ANOVA test results of adequacy for $\mathbf{Nu_{rough}}$ after backward elimination. The predicted R-square of 0.9980 is in acceptable arrangement with the adjusted R-square of 0.9986, i.e., the difference is less than 0.2. A ratio greater than 4 is required for adequacy precision measures. In this study, the adequacy precision ratio of 247.519 suggests an adequate signal and the model can be used to circumnavigate the design space. After backward elimination process, the ultimate cubic equation of $\mathbf{Nu_{rough}}$ in proportion to coded and actual factors is equated in (5) and (6), respectively, as follows:

Equation of $\mathbf{Nu_{rough}}$ in terms of coded factors is as follows:

$$\begin{aligned}\mathbf{Nu_{rough}} = {} & 109.44 + 65\mathbf{A} + 8.46\mathbf{B} - 7.87\mathbf{C} - 16.98\mathbf{D} - 17.72\mathbf{E} - 48.30\mathbf{F} + 2.79\mathbf{AB} - 2.07\mathbf{AC} - 2.10\mathbf{AD} - 3.01\mathbf{AE} \\ & - 2.14\mathbf{AF}7.35\mathbf{A}^2 - 6.07\mathbf{D}^2 - 6.71\mathbf{E}^2 - 6.03\mathbf{F}^2 + 1.50\mathbf{A}^2\mathbf{F} - 2.25\mathbf{AD}^2 - 2.91\mathbf{AE}^2 + 12.08\mathbf{D}^3 + 12.01\mathbf{E}^3 + 44.39\mathbf{F}^3.\end{aligned} \tag{5}$$

Equation of $\mathbf{Nu_{rough}}$ in terms of actual factors is as follows:

$$\begin{aligned}\mathbf{Nu_{rough}} = {} & -1950.51957 + 0.010555\mathbf{Re_{num}} + 272.00413\boldsymbol{\varphi} - 0.615097\mathbf{d_{np}} + 676.44264\left(\frac{\mathbf{X_{axis}}}{\mathbf{d_{print}}}\right) \\ & + 669.11935\left(\frac{\mathbf{Y_{axis}}}{\mathbf{d_{print}}}\right) + 2795.76986\left(\frac{\mathbf{e_{rib}}}{\mathbf{d_{print}}}\right) + 0.026551\mathbf{Re_{num}} \times \boldsymbol{\varphi} - 0.000039\mathbf{Re_{num}} \times \mathbf{d_{np}} \\ & + 0.003069\mathbf{Re_{num}} \times \left(\frac{\mathbf{X_{axis}}}{\mathbf{d_{print}}}\right) + 0.003906\mathbf{Re_{num}} \times \left(\frac{\mathbf{Y_{axis}}}{\mathbf{d_{print}}}\right) - 0.002328\mathbf{Re_{num}} \times \left(\frac{\mathbf{e_{rib}}}{\mathbf{d_{print}}}\right) \\ & - 2.4093 \times 10^{-07}\left(\mathbf{Re_{num}}\right)^2 - 342.56189\left(\frac{\mathbf{X_{axis}}}{\mathbf{d_{print}}}\right)^2 - 339.465\left(\frac{\mathbf{Y_{axis}}}{\mathbf{d_{print}}}\right)^2 - 2281.053\left(\frac{\mathbf{e_{rib}}}{\mathbf{d_{print}}}\right)^2 \\ & + 7.276\left(\mathbf{Re_{num}}\right)^2 \times \left(\frac{\mathbf{e_{rib}}}{\mathbf{d_{print}}}\right) - 0.0009\mathbf{Re_{num}} \times \left(\frac{\mathbf{X_{axis}}}{\mathbf{d_{print}}}\right)^2 - 0.0012\mathbf{Re_{num}} \times \left(\frac{\mathbf{Y_{axis}}}{\mathbf{d_{print}}}\right)^2. \\ & + 55.917\left(\frac{\mathbf{X_{axis}}}{\mathbf{d_{print}}}\right)^3 + 55.592\left(\frac{\mathbf{Y_{axis}}}{\mathbf{d_{print}}}\right)^3 + 599.182\left(\frac{\mathbf{e_{rib}}}{\mathbf{d_{print}}}\right)^3.\end{aligned} \tag{6}$$

5.2. ANOVA Analysis for Friction Factor ($\mathbf{f_{rough}}$). The results of the RSM model used for friction factor ($\mathbf{f_{rough}}$) are presented in Tables 8–11 in the form of ANOVA. Value of "Prob. > F" for used model is not more than 0.05 ($\alpha = 0.05$ or 95% confidence). Table 8 presents the ANOVA test results for $\mathbf{f_{rough}}$ before elimination. The value 6411.73 of model F

Table 4: ANOVA test results for Nusselt number (before exclusion).

From where	Squared sum	Squared mean	f value	Freedom degree	(Prob. > F)	
Model	2.652 E+05	8036.97	2690.10	33	<0.0001	Significant
A	4052.13	4052.13	1356.31	1	<0.0001	
B	81.63	81.63	27.32	1	<0.0001	
C	59.91	59.91	20.05	1	<0.0001	
D	428.39	428.39	143.39	1	<0.0001	
E	449.51	449.51	150.46	1	<0.0001	
F	1775.65	1775.65	594.34	1	<0.0001	
AB	87.33	87.33	29.23	1	<0.0001	
AC	40.66	40.66	13.61	1	0.0004	
AD	29.71	29.71	9.94	1	0.0022	
AE	64.25	64.25	21.50	1	<0.0001	
AF	48.89	48.89	16.36	1	0.0001	
A^2	49.38	49.38	16.53	1	<0.0001	
B^2	0.0028	0.0028	0.0009	1	0.9756	
C^2	4.28	4.28	1.43	1	0.2345	
D^2	253.69	253.69	84.91	1	<0.0001	
E^2	306.90	306.90	102.72	1	<0.0001	
F^2	178.64	178.64	59.79	1	<0.0001	
A^2B	0.4267	0.4267	0.1428	1	0.7063	
A^2C	3.94	3.94	1.32	1	0.2535	
A^2D	4.08	4.08	1.37	1	0.2454	
A^2E	0.7722	0.7722	0.2585	1	0.6124	
A^2F	8.20	8.20	2.74	1	0.1010	
AB^2	7.11	7.11	2.38	1	0.1263	
AC^2	2.15	2.15	0.7213	1	0.3979	
AD^2	8.93	8.93	2.99	1	0.0871	
AE^2	17.45	17.45	5.84	1	0.0176	
AF^2	6.61	6.61	2.21	1	0.1403	
A^3	6.43	6.43	2.15	1	0.1457	
B^3	1.54	1.54	0.5156	1	0.4745	
C^3	3.51	3.51	1.18	1	0.2811	
D^3	209.08	209.08	69.98	1	<0.0001	
E^3	206.80	206.80	69.22	1	<0.0001	
F^3	1414.79	1414.79	473.55	1	<0.0001	
Residual	280.84	2.99		94		
Cor total	2.655 E+05			127		

Table 5: ANOVA test results of adequacy for Nusselt number (before elimination).

Standard deviation	Mean	C.V. %	R-Square	Adjusted R-square	Predicted R-square	Precision in terms of adequacy
1.73	117.04	1.48	0.9989	0.9986	0.9980	198.1663

indicates that model is significant. P-values less than 0.0500 indicate that model terms are significant. In this ,case A, B, C, D, E, F, AB, AC, AD, AE, A^2, B^2, D^2, E^2, F^2, A^2B, AB^2, AD^2, A^3, D^3, E^3, and F^3 are significant model terms. Values higher than 0.1 suggest insignificance of model terms. Table 9 shows ANOVA test results of adequacy for $\mathbf{f_{rough}}$ before elimination. The predicted R-square of 0.9989 is in acceptable arrangement with the adjusted R-square of 0.9992, i.e., the difference is less than 0.2. A ratio greater than 4 is required for adequacy precision measures. In this study, the adequacy precision ratio of 366.2616 suggests an adequate signal. Thus, the model can be utilized to circumnavigate the design space.

Table 10 presents ANOVA test results for $\mathbf{f_{rough}}$ after backward elimination. The value 6987.87 of model F indicates that the model is significant. There is only a 0.01% chance that an F-value this large could occur due to noise. P-values less than 0.05 suggest that the model terms are significant. In this case, A, B, C, D, E, F, AB, AC, AD, AE, A^2, B^2, D^2, E^2, F^2, A^2B, AB^2, AD^2, A^3, D^3, E^3, and F^3 are significant model terms. Values higher than 0.1 suggest insignificance of model terms. Table 11 shows ANOVA test results of adequacy for $\mathbf{f_{rough}}$ after backward elimination. The predicted R-square of 0.9989 is in acceptable arrangement with the adjusted R-square of 0.9992, as difference is under 0.2. A ratio greater than 4 is required for adequacy precision measures. In this study, the adequacy precision ratio of 382.149 suggests an adequate signal and the model can be used to circumnavigate the design space. After backward elimination process, the ultimate cubic equation

Table 6: Test results ANOVA for Nusselt number (after backward exclusion).

From where	Squared sum	Squared mean	f value	Freedom degree	(Prob. > F)	
Model	2.652E + 05	12627.80	4219.54	21	<0.0001	Significant
A	18576.07	18576.07	6207.14	1	<0.0001	
B	1494.37	1494.37	499.34	1	<0.0001	
C	1293.46	1293.46	432.21	1	<0.0001	
D	525.43	525.43	175.57	1	<0.0001	
E	572.38	572.38	191.26	1	<0.0001	
F	1801.29	1801.29	601.89	1	<0.0001	
AB	97.76	97.76	32.67	1	<0.0001	
AC	54.09	54.09	18.07	1	<0.0001	
AD	35.17	35.17	11.75	1	0.0009	
AE	72.52	72.52	24.23	1	<0.0001	
AF	67.35	67.35	22.50	1	<0.0001	
A^2	419.55	419.55	140.19	1	<0.0001	
D^2	263.66	263.66	88.10	1	<0.0001	
E^2	321.46	321.46	107.41	1	<0.0001	
F^2	209.34	209.34	69.95	1	<0.0001	
A^2F	15.63	15.63	5.22	1	0.0243	
AD^2	17.80	17.80	5.95	1	0.0164	
AE^2	29.89	29.89	9.99	1	0.0021	
D^3	232.76	232.76	77.78	1	<0.0001	
E^3	230.06	230.06	76.87	1	<0.0001	
F^3	1411.28	1411.28	471.57	1	<0.0001	
Residual	317.23	2.99		106		
Cor total	2.655E + 05			127		

of $\mathbf{f_{rough}}$ in proportion to coded and actual factors is equated in equations (7) and (8), respectively, as follows:

Equation of $\mathbf{f_{rough}}$ in terms of coded factors is as follows:

$$\begin{aligned}\mathbf{f_{rough}} &= 0.122 - 0.033\mathbf{A} + .008\mathbf{B} - 0.007\mathbf{C} - 0.019\mathbf{D} - 0.024\mathbf{E} - 0.041\mathbf{F} - 0.0012\mathbf{AB}\\ &+ 0.0015\mathbf{AC} + 0.0012\mathbf{AD} + 0.0007\mathbf{AE} + 0.0035\mathbf{A}^2 + 0.0008\mathbf{B}^2 - 0.0057\mathbf{D}^2 - 0.009\mathbf{E}^2\\ &- 0.0124\mathbf{F}^2 + 0.0008\mathbf{A}^2\mathbf{B} + 0.0009\mathbf{AB}^2 + 0.0015\mathbf{AD}^2 - 0.0008\mathbf{A}^3 + 0.0123\mathbf{D}^3 + 0.017\mathbf{E}^3 + 0.0374\mathbf{F}^3.\end{aligned} \tag{7}$$

Equation of $\mathbf{f_{rough}}$ in terms of actual factors is as follows:

$$\begin{aligned}\mathbf{f_{rough}} &= -1.8878 - 5.338\times10^{-06}\mathbf{Re_{num}} + 0.9541\times\boldsymbol{\varphi} - 0.0012\times\mathbf{d_{np}} + 0.\frac{7381\times\mathbf{X_{axis}}}{\mathbf{d_{print}}}\\ &+ 1.0035\times\frac{\mathbf{Y_{axis}}}{\mathbf{d_{print}}} + 2.4439\times\frac{\mathbf{e_{rib}}}{\mathbf{d_{print}}} - 0.00006\times\mathbf{Re_{num}}\times\boldsymbol{\varphi} + 2.8066\times\mathbf{Re_{num}}\times\mathbf{d_{np}} - 2.0893\\ &\times10^{-06}\mathbf{Re_{num}}\times\frac{\mathbf{X_{axis}}}{\mathbf{d_{print}}} + 1.6869\times10^{-06}\mathbf{Re_{num}}\times\frac{\mathbf{Y_{axis}}}{\mathbf{d_{print}}} + 1.173\times10^{-10}(\mathbf{Re_{num}})^2\\ &- 3.1043(\boldsymbol{\varphi})^2 - 0.3636\left(\frac{\mathbf{X_{axis}}}{\mathbf{d_{print}}}\right)^2 - 0.498\left(\frac{\mathbf{Y_{axis}}}{\mathbf{d_{print}}}\right)^2 - 1.9638\left(\frac{\mathbf{e_{rib}}}{\mathbf{d_{print}}}\right)^2 + 1.0939\times10^{-09}(\mathbf{Re_{num}})^2\\ &\times(\boldsymbol{\varphi}) + 0.0006\mathbf{Re_{num}}\times(\boldsymbol{\varphi})^2 + 5.9369\times10^{-07}\mathbf{Re_{num}}\times\left(\frac{\mathbf{X_{axis}}}{\mathbf{d_{print}}}\right)^2 - 2.2293\times10^{-15}(\mathbf{Re_{num}})^3\\ &+ 0.0569\left(\frac{\mathbf{X_{axis}}}{\mathbf{d_{print}}}\right)^3 + 0.07883\left(\frac{\mathbf{Y_{axis}}}{\mathbf{d_{print}}}\right)^3 + 0.5049\left(\frac{\mathbf{e_{rib}}}{\mathbf{d_{print}}}\right)^3.\end{aligned} \tag{8}$$

Table 7: ANOVA test results of adequacy for Nusselt number (after backward elimination).

Standard deviation	Mean	C.V. %	R-square	Adjusted R-square	Predicted R-square	Precision in terms of adequacy
1.73	117.04	1.48	0.9988	0.9986	0.9980	247.5188

Table 8: ANOVA test results for f_{rough} (before elimination).

Source	Sum of square	Mean square	f-Value	Degree of freedom	Prob. > F	
Model	0.0866	0.0036	6411.73	24	<0.0001	Significant
A	0.0019	0.0019	3396.67	1	<0.0001	
B	0.0007	0.0007	1331.67	1	<0.0001	
C	0.0008	0.0008	1441.61	1	<0.0001	
D	0.0005	0.0005	878.07	1	<0.0001	
E	0.0009	0.0009	1531.32	1	<0.0001	
F	0.0014	0.0014	2402.01	1	<0.0001	
AB	0.0000	0.0000	34.09	1	<0.0001	
AC	0.0000	0.0000	59.28	1	<0.0001	
AD	0.0000	0.0000	21.74	1	<0.0001	
AE	4.715E-06	4.715E-06	8.38	1	0.0046	
AF	5.986E-07	5.986E-07	1.06	1	0.3047	
A^2	0.0001	0.0001	141.99	1	<0.0001	
B^2	3.048E-06	3.048E-06	5.42	1	0.0219	
C^2	5.826E-07	5.826E-07	1.04	1	0.3112	
D^2	0.0002	0.0002	368.99	1	<0.0001	
E^2	0.0005	0.0005	918.19	1	<0.0001	
F^2	0.0008	0.0008	1489.90	1	<0.0001	
A^2B	3.779E-06	3.779E-06	6.72	1	0.0109	
AB^2	2.548E-06	2.548E-06	4.53	1	0.0357	
AD^2	9.848E-06	9.848E-06	17.51	1	<0.0001	
A^3	3.023E-06	3.023E-06	5.37	1	0.0224	
D^3	0.0002	0.0002	341.70	1	<0.0001	
E^3	0.0004	0.0004	663.45	1	<0.0001	
F^3	0.0010	0.0010	1772.41	1	<0.0001	
Residual	0.0001	5.625E-07		103		
Cor total	0.0866			127		

Table 9: ANOVA test results of adequacy for f_{rough} (before elimination).

Standard deviation	Mean	C.V. %	R-Square	Predicted R-square	Adjusted R-square	Precision in terms of adequacy
0.0008	0.1286	0.5830	0.9993	0.9989	0.9992	366.2616

Table 10: ANOVA test results for f_{rough} (after backward elimination).

Source	Sum of square	Mean square	f-Value	Degree of freedom	Prob. > F	
Model	0.0866	0.0039	6987.87	22	<0.0001	Significant
A	0.0026	0.0026	4656.67	1	<0.0001	
B	0.0008	0.0008	1459.54	1	<0.0001	
C	0.0008	0.0008	1439.34	1	<0.0001	
D	0.0006	0.0006	1021.21	1	<0.0001	
E	0.0010	0.0010	1770.77	1	<0.0001	
F	0.0014	0.0014	2398.82	1	<0.0001	
AB	0.0000	0.0000	33.16	1	<0.0001	
AC	0.0000	0.0000	61.53	1	<0.0001	
AD	0.0000	0.0000	20.90	1	<0.0001	
AE	4.221E-06	4.221E-06	7.50	1	0.0073	
A^2	0.0001	0.0001	141.86	1	<0.0001	
B^2	4.021E-06	4.021E-06	7.14	1	0.0087	
D^2	0.0002	0.0002	401.80	1	<0.0001	
E^2	0.0006	0.0006	990.57	1	<0.0001	

Table 10: Continued.

Source	Sum of square	Mean square	f-Value	Degree of freedom	Prob. > F
F^2	0.0009	0.0009	1532.65	1	<0.0001
A^2B	3.779E-06	3.779E-06	6.71	1	0.0109
AB^2	3.046E-06	3.046E-06	5.41	1	0.0220
AD^2	9.275E-06	9.275E-06	16.47	1	<0.0001
A^3	3.023E-06	3.023E-06	5.37	1	0.0224
D^3	0.0002	0.0002	396.66	1	<0.0001
E^3	0.0004	0.0004	762.45	1	<0.0001
F^3	0.0010	0.0010	1778.15	1	<0.0001
Residual	0.0001	5.631E-07		105	
Cor Total	0.0866			127	

Table 11: ANOVA test results of adequacy for f_{rough} (after backward elimination).

Standard deviation	Mean	C.V. %	R-Square	Adjusted R-square	Predicted R-square	Precision in terms of adequacy
0.0008	0.1286	0.5833	0.9993	0.9992	0.9989	382.149

5.3. Heat and Fluid Flow. Experimental results of different nanoparticle concentration, particle diameter, and protruded roughness parameters on $\mathbf{Nu_{rough}}$ and $\mathbf{f_{rough}}$ in a square duct are presented here. The nanoparticle concentration (φ) of 1%–4% and particle diameter of 30 nm–45 nm are considered in this section. Figure 3(a) represents the $\mathbf{Nu_{rough}}$ with different values of φ and $\mathbf{Re_{num}}$. The other geometrical and NF flow parameters are fixed, such as $\mathbf{d_{np}} = 30\mathbf{nm}$, $(\mathbf{X_{axis}}/\mathbf{d_{print}}) = 1.8$ $(\mathbf{Y_{axis}}/\mathbf{d_{print}}) = 1.8$ and $(\mathbf{e_{rib}}/\mathbf{d_{print}}) = 1.67$. Modeling results show that the $\mathbf{Nu_{rough}}$ increases as φ and $\mathbf{Re_{num}}$ increase. Also when the values of φ are 0.02, 0.03 and 0.04, $\mathbf{Nu_{rough}}$ significantly enhanced around 1.075, 1.150, and 1.225 times for $\mathbf{Re_{num}}$ of 4000 and 1.053, 1.098, and 1.14 times for $\mathbf{Re_{num}}$ equal to 18000, when compared to the φ value of 0.01. Figure 3(b) exemplifies the value of $\mathbf{f_{rough}}$ with different values of φ and $\mathbf{Re_{num}}$. The other geometrical and NF flow parameters are fixed, such as $\mathbf{d_{np}} = 30\mathbf{nm}$, $(\mathbf{X_{axis}}/\mathbf{d_{print}}) = 1.8$ $(\mathbf{Y_{axis}}/\mathbf{d_{print}}) = 1.8$ and $(\mathbf{e_{rib}}/\mathbf{d_{print}}) = 1.67$. The RSM results are found that the $\mathbf{f_{rough}}$ values increase with increase in the values of the φ. In the protruded rib and φ cases, the $\mathbf{f_{rough}}$ distributions with the φ of 0.02, 0.03, and 0.04 significantly enhanced approximately around 1.039, 1.078, and 1.127 times for $\mathbf{Re_{num}}$ value of 4000 and 1.047, 1.094, and 1.188 for $\mathbf{Re_{num}}$ equal to 18000, respectively, when compared to the φ value of 0.01. This increment is due to the increase in the Prandtl number and thermal conductivity of nanofluid. It is also observed that nanoparticle concentration $\varphi = 0.04$ has the best heat transfer rate followed by 0.03, 0.02, and 0.01.

Figure 4(a) demonstrates the value of $\mathbf{Nu_{rough}}$ with different values of $\mathbf{d_{np}}$ and $\mathbf{Re_{num}}$. The other geometrical and NF flow parameters were fixed, such as $\varphi = 0.04$, $(\mathbf{X_{axis}}/\mathbf{d_{print}}) = 1.8$ $(\mathbf{Y_{axis}}/\mathbf{d_{print}}) = 1.8$ and $(\mathbf{e_{rib}}/\mathbf{d_{print}}) = 1.67$. Modeling results are found that the $\mathbf{Nu_{rough}}$ increases with decrease in the values of $\mathbf{d_{np}}$ and increase in $\mathbf{Re_{num}}$. When the $\mathbf{d_{np}}$ values are 30 nm, 35 nm, and 40 nm, $\mathbf{Nu_{rough}}$ significantly enhanced around 1.195, 1.122, and 1.049 times for $\mathbf{Re_{num}}$ of 4000 and 1.110, 1.072, and 1.039 times for $\mathbf{Re_{num}}$ of 18000 while compared to the $\mathbf{d_{np}}$ value of 45 nm. Figure 4(b) exemplifies the value of $\mathbf{f_{rough}}$ with different values of $\mathbf{d_{np}}$ and $\mathbf{Re_{num}}$. The other geometrical and NF flow parameters were fixed, such as $\varphi = 0.04$, $(\mathbf{X_{axis}}/\mathbf{d_{print}}) = 1.8$ $(\mathbf{Y_{axis}}/\mathbf{d_{print}}) = 1.8$ and $(\mathbf{e_{rib}}/\mathbf{d_{print}}) = 1.67$. Modeling results show that the $\mathbf{f_{rough}}$ increases with the decrease in $\mathbf{d_{np}}$ and $\mathbf{Re_{num}}$. Also while the $\mathbf{d_{np}}$ values are 30 nm, 35 ,nm and 40 nm, $\mathbf{f_{rough}}$ significantly enhanced around 1.106, 1.070, and 1.066 times for $\mathbf{Re_{num}}$ of 4000 and 1.109, 1.071, and 1.032 times for $\mathbf{Re_{num}}$ of 18000 when compared to the $\mathbf{d_{np}}$ of 45 nm. The 30 nm nanoparticle diameter has the highest heat transfer coefficient. This is because of Brownian motion and good thermal conductivity of nanofluid at smaller nanoparticle diameter.

Figure 5(a) illustrates the value of $\mathbf{Nu_{rough}}$ for different values of $(\mathbf{e_{rib}}/\mathbf{d_{print}})$ and $\mathbf{Re_{num}}$. The other geometrical and NF flow parameters were fixed, such as $(\mathbf{X_{axis}}/\mathbf{d_{print}}) = 1.8$, $(\mathbf{Y_{axis}}/\mathbf{d_{print}}) = 1.8$, $\mathbf{d_{np}} = 30\mathbf{nm}$ and $\varphi = 0.04$. Modeling results are found that the $\mathbf{Nu_{rough}}$ increases with the increase in the values of $(\mathbf{e_{rib}}/\mathbf{d_{print}})$ up to 1.0 and then increases beyond this, and the value of $\mathbf{Nu_{rough}}$ starts decreasing with $\mathbf{Re_{num}}$. It also shows that when values of $(\mathbf{e_{rib}}/\mathbf{d_{print}})$ are 0.83, 0.87, 1.0, and 1.25, $\mathbf{Nu_{rough}}$ significantly enhanced around 1.102, 1.224, 1.306, and 1.143 times for $\mathbf{Re_{num}}$ of 4000 and 1.048, 1.118, 1.160, and 1.080 times for $\mathbf{Re_{num}}$ of 18000, when compared to the $\mathbf{e_{rib}}/\mathbf{d_{print}}$ of 1.67. Figure 5(b) exemplifies the value of $\mathbf{f_{rough}}$ with different values of $\mathbf{e_{rib}}/\mathbf{d_{print}}$ and $\mathbf{Re_{num}}$. The other geometrical and NF flow parameters were fixed, such as $(\mathbf{X_{axis}}/\mathbf{d_{print}}) = 1.8$, $(\mathbf{Y_{axis}}/\mathbf{d_{print}}) = 1.8$, $\mathbf{d_{np}} = 30\mathbf{nm}$ and $\varphi = 0.04$. Modeling results concluded that the $\mathbf{f_{rough}}$ increases with the decrease in the values of $\mathbf{e_{rib}}/\mathbf{d_{print}}$ and $\mathbf{Re_{num}}$. It also shows that when the $(\mathbf{e_{rib}}/\mathbf{d_{print}})$ values are 0.83, 0.87, 1.0, and 1.25, $\mathbf{f_{rough}}$ significantly enhanced around 1.046, 1.127, 1. 156, and 1.093 times for $\mathbf{Re_{num}}$ value of 4000 and 1.079, 1.257, 1.306, and 1.168 times for $\mathbf{Re_{num}}$ value of 18000 when compared with the $(\mathbf{e_{rib}}/\mathbf{d_{print}})$ value of 1.67.

Figure 6(a) illustrates the value of $\mathbf{Nu_{rough}}$ with different values of $(\mathbf{Y_{axis}}/\mathbf{d_{print}})$ and $\mathbf{Re_{num}}$. The other geometrical and NF flow parameters were fixed, such as $(\mathbf{X_{axis}}/\mathbf{d_{print}}) = 1.8$, $(\mathbf{e_{rib}}/\mathbf{d_{print}}) = 1.0$, $\mathbf{d_{np}} = 30\mathbf{nm}$ and $\varphi = 0.04$. Modeling results found that the values of $\mathbf{Nu_{rough}}$

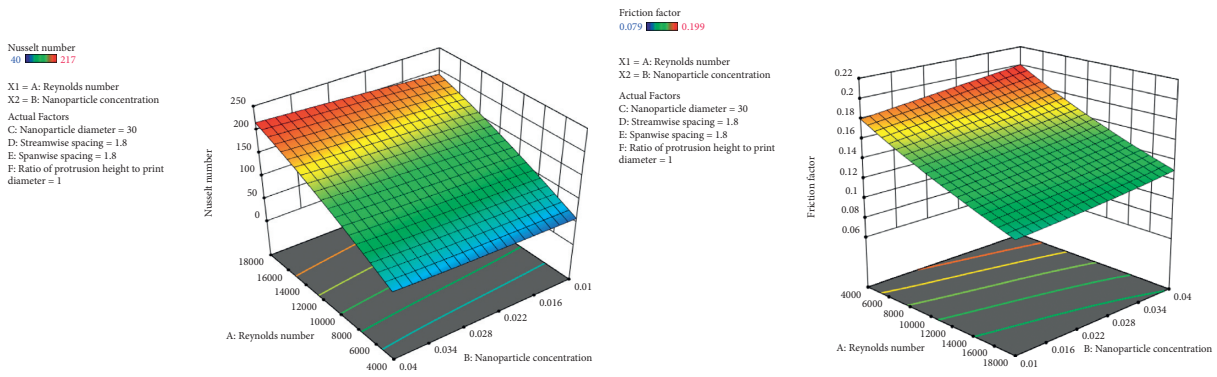

(a) (b)

FIGURE 3: (a) Variation of Nu_{rough} with φ and Re_{num}. (b) Variation of f_{rough} with φ andRe_{num}.

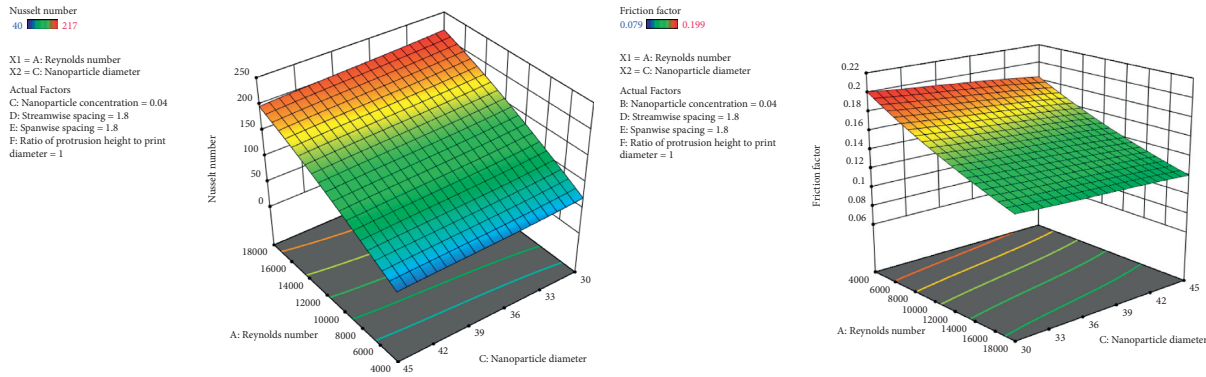

(a) (b)

FIGURE 4: (a) Variation of Nu_{rough} with d_{np} and Re_{num}. (b) Variation of f_{rough} with d_{np} andRe_{num}.

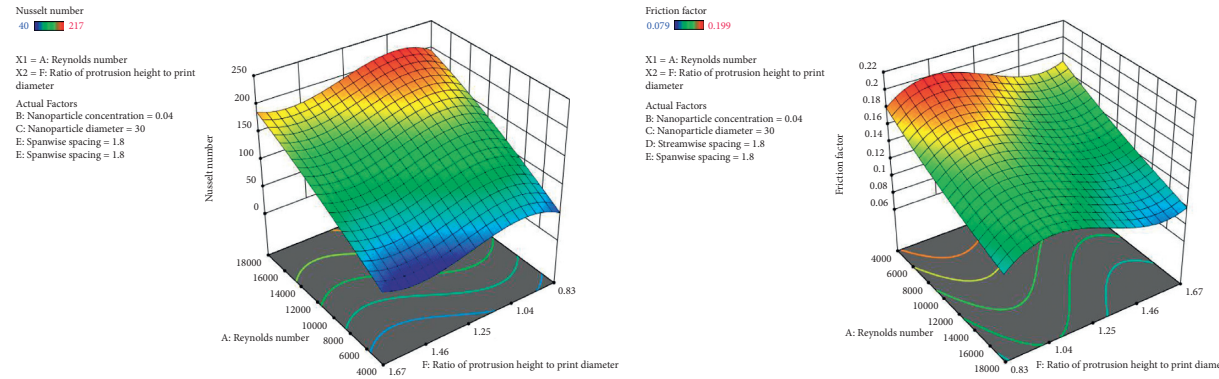

(a) (b)

FIGURE 5: (a) Variation of Nu_{rough} with $(e_{\text{rib}}/d_{\text{print}})$ and Re_{num}. (b) Variation of f_{rough} with $(e_{\text{rib}}/d_{\text{print}})$ and Re_{num}.

increase with the increase in the value of $(\mathbf{Y_{axis}/d_{print}})$ up to 1.8, beyond this any increase in the value of $(\mathbf{Y_{axis}/d_{print}})$, $\mathbf{Nu_{rough}}$ starts decreasing with $\mathbf{Re_{num}}$. Also, when $(\mathbf{Y_{axis}/d_{print}})$ is equal to 1.4, 1.8, and 2.2, $\mathbf{Nu_{rough}}$ significantly enhanced around 1.150, 1.225, and 1.075 times for $\mathbf{Re_{num}}$ value of 4000 and 1.098, 1.141, and 1.053 times for $\mathbf{Re_{num}}$ value of 18000 when compared to the $\mathbf{Y_{axis}/d_{print}}$ value of 2.6. Figure 6(b) exemplifies the value of $\mathbf{f_{rough}}$ with different values of $(\mathbf{Y_{axis}/d_{print}})$ and $\mathbf{Re_{num}}$. The other geometrical and NF flow parameters were fixed, such as $(\mathbf{X_{axis}/d_{print}}) = 1.8$, $(\mathbf{e_{rib}/d_{print}}) = 1.0$, $\mathbf{d_{np}} = 30\mathbf{nm}$ and $\varphi = 0.04$. Modeling results found that the $\mathbf{f_{rough}}$ increases with the increase in the values of $(\mathbf{Y_{axis}/d_{print}})$ from 1.4 to 1.8 and subsequently any increase in $(\mathbf{Y_{axis}/d_{print}})$, and the $\mathbf{f_{rough}}$

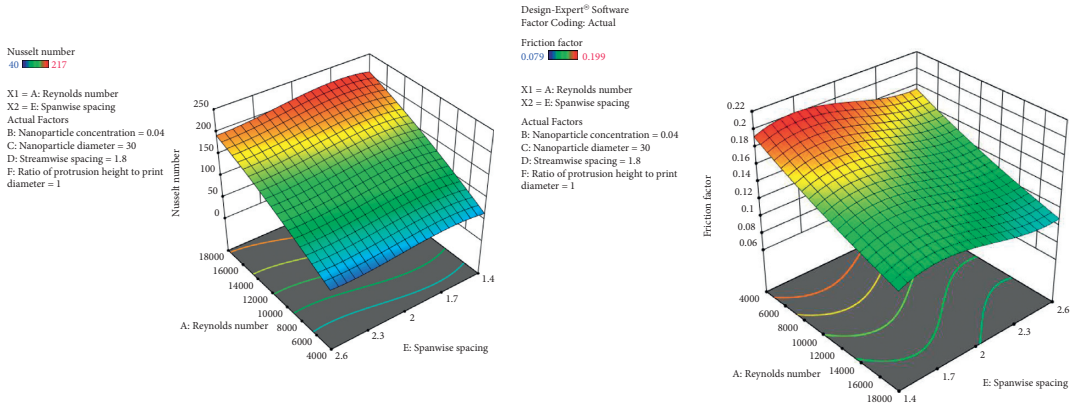

(a) (b)

FIGURE 6: (a) Variation of Nu_{rough} with $(Y_{\text{axis}}/d_{\text{print}})$ and Re_{num}. (b) Variation of f_{rough} with $(Y_{\text{axis}}/d_{\text{print}})$ and Re_{num}.

starts decreasing with the increase in $\mathbf{Re_{num}}$. While the $(\mathbf{Y_{axis}/d_{print}})$ values are 1.4, 1.8, and 2.2, $\mathbf{f_{rough}}$ significantly enhanced around 1.115, 1.,170 and 1.057 times for $\mathbf{Re_{num}}$ value of 4000 and 1.151, 1.278, and 1.075 times for $\mathbf{Re_{num}}$ value of 18000 when compared to the $(\mathbf{Y_{axis}/d_{print}})$ of 2.6.

Figure 7(a) represents the value of $\mathbf{Nu_{rough}}$ at different values of $\mathbf{X_{axis}/d_{print}}$ and $\mathbf{Re_{num}}$. The other geometrical and NF flow parameters were fixed, such as $(\mathbf{Y_{axis}/d_{print}}) = 1.8$, $(\mathbf{e_{rib}/d_{print}}) = 1.0, \mathbf{d_{np}} = 30\mathbf{nm}$ and $\varphi = 0.04$. Modeling results are found that the $\mathbf{Nu_{rough}}$ increases with increase in the values of $(\mathbf{X_{axis}/d_{print}})$ up to 1.8 and then increases beyond this, and $\mathbf{Nu_{rough}}$ starts decreasing with $\mathbf{Re_{num}}$. While the $(\mathbf{X_{axis}/d_{print}})$ values are 1.4, 1.8, and 2.2, $\mathbf{Nu_{rough}}$ significantly enhanced around 1.121, 1.195, and 1.048 times for $\mathbf{Re_{num}}$ value of 4000 and 1.072, 1.114, and 1.039 times for $\mathbf{Re_{num}}$ value of 18000 when compared to the $(\mathbf{X_{axis}/d_{print}})$ value of 2.6. Figure 7(b) exemplifies the value of $\mathbf{f_{rough}}$ at different values of $(\mathbf{X_{axis}/d_{print}})$ and $\mathbf{Re_{num}}$. The other geometrical and NF flow parameters were fixed, such as $\mathbf{X_{axis}/d_{print}} = 1.8, \mathbf{e_{rib}/d_{print}} = 1.0, \mathbf{d_{np}} = 30\mathbf{nm}$ and $\varphi = 0.04$. Modeling results are found that the $\mathbf{f_{rough}}$ values increase with the increase in the values of $(\mathbf{X_{axis}/d_{print}})$ up to 1.8 and then increases beyond this value, and $\mathbf{f_{rough}}$ starts decreasing with the increase in the values of $\mathbf{Re_{num}}$. While the $(\mathbf{X_{axis}/d_{print}})$ values are 1.4, 1.8, and 2.2, $\mathbf{f_{rough}}$ significantly enhanced around 1.099, 1.135, and 1.046 times for $\mathbf{Re_{num}}$ value of 4000 and 1.120, 1.160, and 1.045 times for Reynolds number value of 18000 when compared to the $(\mathbf{X_{axis}/d_{print}})$ value of 2.6. The deviation in $\mathbf{Nu_{rough}}$ and $\mathbf{f_{rough}}$ was because of turbulence, persuaded by the rapidity of $\mathbf{Al_2O_3/H_2O}$. Lesser $(\mathbf{X_{axis}/d_{print}})$ and $(\mathbf{Y_{axis}/d_{print}})$ values, greater is the velocity of $(\mathbf{Al_2O_3/H_2O})$ nanofluid and less significant is the area of disruption downstream of the transverse with combined protruded roughened square channel. Figure 8(a) and 8(b) show the comparison of predicted values of the $\mathbf{Nu_{rough}}$ and $\mathbf{f_{rough}}$ with that experimental values. The experimental and predicted values are in good considerate with each other, which assures the correctness of the information generated.

6. Correlations for $\mathbf{Nu_{rough}}$ and $\mathbf{f_{rough}}$

As referenced above, the analytical methods are not available for the prediction of $\mathbf{Nu_{rough}}$ and $\mathbf{f_{rough}}$ of NF flow through square duct protruded with combined transverse rib; hence, statistical correlations based on experimental data have been developed for $\mathbf{Nu_{rough}}$ and $\mathbf{f_{rough}}$ of NF flow through square duct protruded with combined transverse rib. The developed correlation is useful for the researchers working in this field in predicting $\mathbf{Nu_{rough}}$ and $\mathbf{f_{rough}}$ of a heat exchanger at any specifically required values of variable parameters.

6.1. Correlations for $\mathbf{Nu_{rough}}$. The earlier explained effects of various geometrical parameters on $\mathbf{Nu_{rough}}$ reveal that $\mathbf{Nu_{rough}}$ monotonously increases with the rise in $\mathbf{Re_{num}}$ and strongly depends upon operating parameters ϕ, $\mathbf{d_{np}}$, $(\mathbf{X_{axis}/d_{print}})$, $(\mathbf{Y_{axis}/d_{print}})$, and $(\mathbf{e_{rib}/d_{print}})$ and the $\mathbf{Re_{num}}$. The $\mathbf{Nu_{rough}}$ equation for this dependence can be written as follows:

$$\mathbf{Nu_{rough}} = \mathbf{Nu_{rough}}\left(\mathbf{Re_{num}}, \phi, \mathbf{d_{np}}, \left(\frac{\mathbf{X_{axis}}}{\mathbf{d_{print}}}\right), \left(\frac{\mathbf{Y_{axis}}}{\mathbf{d_{print}}}\right), \left(\frac{\mathbf{e_{rib}}}{\mathbf{d_{print}}}\right)\right). \tag{9}$$

Figure 9(a) represents the plotted $\mathbf{Nu_{rough}}$ against various $\mathbf{Re_{num}}$ and curve fitting using regression analysis through the data point. The resulted regression relation is as follows:

$$\mathbf{Nu_{rough}} = \mathbf{A_o Re_{num}^{0.864}}. \tag{10}$$

Here, $\mathbf{A_0}$ is dependent on $\mathbf{d_{np}}$, $(\mathbf{X_{axis}/d_{print}})$, $(\mathbf{Y_{axis}/d_{print}})$ **an d** $(\mathbf{e_{rib}/d_{print}})$. To correlate $\mathbf{A_0}$ and ϕ, $\mathbf{ln}(\mathbf{A_0})$ is plotted on a log-log scale against $\mathbf{ln}(\phi)$ and other fixed roughness parameters. The Figure 9(b) shows relationship of $\mathbf{ln}(\mathbf{A_0})$ with $\mathbf{ln}(\phi)$, and regression relation is as follows:

$$\mathbf{Nu_{rough}} = \mathbf{B_o Re_{num}^{0.864}}(\boldsymbol{\varphi})^{0.64}\mathbf{exp}\left(0.065\mathbf{ln}(\boldsymbol{\varphi})^2\right). \tag{11}$$

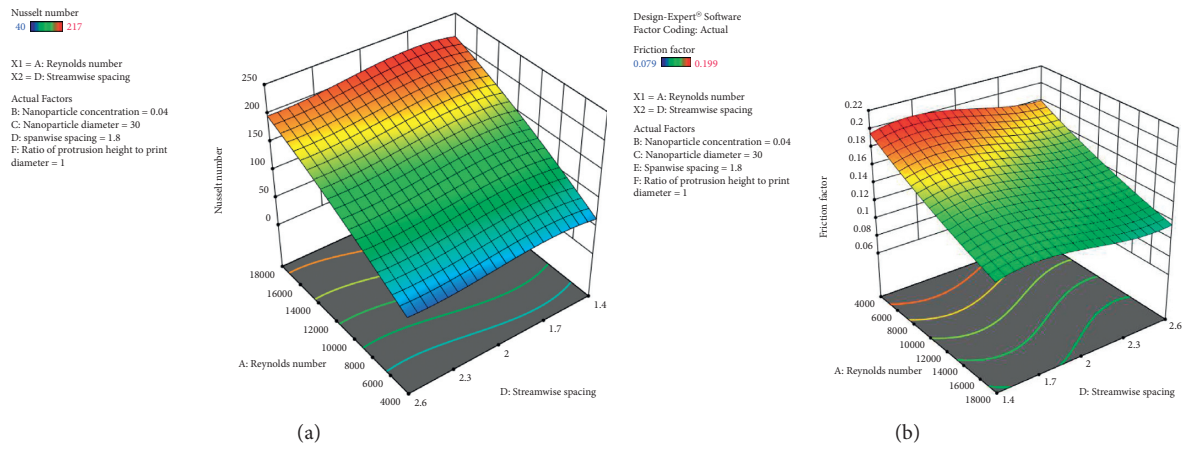

FIGURE 7: (a) Variation of Nu_{rough} with $(X_{\text{axis}}/d_{\text{print}})$ and Re_{num}. (b) Variation of f_{rough} with $(X_{\text{axis}}/d_{\text{print}})$ and Re_{num}.

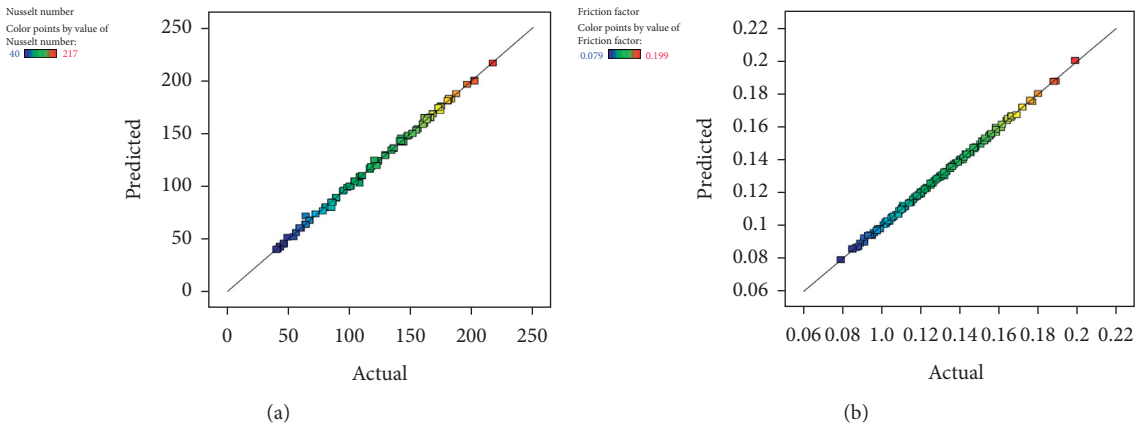

FIGURE 8: Experimental results vs RSM results. (a)Nu_{rough}. (b)f_{rough} (average deviation is ±5.5%).

The constant $\mathbf{B}_0$, which depends on $\mathbf{d_{np}}$, $(\mathbf{X_{axis}/d_{print}})$, $(\mathbf{Y_{axis}/d_{print}})$ **an d** $(\mathbf{e_{rib}/d_{print}})$, is plotted between $\mathbf{B}_0$ and $\mathbf{d_{np}}$, and fitting curve is represented in Figure 9(c). The relation between these parameters is as follows:

$$\mathbf{Nu_{rough}} = \mathbf{C}_0\mathbf{Re}_{\mathbf{num}}^{0.864}(\boldsymbol{\varphi})^{0.64}\mathbf{exp}\left(0.065\mathbf{ln}(\boldsymbol{\varphi})^2\right) \cdot \left(\mathbf{d_{np}}\right)^{0.784}\mathbf{exp}\left(-0.168\left(\ln\left(\mathbf{d_{np}}\right)^2\right)\right). \tag{12}$$

The plot between $\mathbf{ln}(\mathbf{C_o})$ and $\mathbf{ln}(\mathbf{Y_{axis}/d_{print}})$ in Figure 9(d) shows the effect of $(\mathbf{Y_{axis}/d_{print}})$. Thus, the parameters selected yield $\mathbf{Nu_{rough}}$ that is expressed as follows:

$$\mathbf{Nu_{rough}} = \mathbf{D}_0\left(\mathbf{Re_{num}}\right)^{0.864}(\boldsymbol{\varphi})^{0.64}\mathbf{exp}\left(0.065\mathbf{ln}(\boldsymbol{\varphi})^2\right)\left(\mathbf{d_{np}}\right)^{0.784} \cdot \mathbf{exp}\left(-0.168\mathbf{ln}\left(\mathbf{d_{np}}\right)^2\right)\left(\frac{\mathbf{Y_{axis}}}{\mathbf{d_{print}}}\right)^{0.848} \cdot \mathbf{exp}\left(-0.168\mathbf{ln}\left(\mathbf{Y_{axis}/d_{print}}\right)^2\right). \tag{13}$$

The data generated from the equation have been plotted between $\mathbf{ln}(\mathbf{D}_0)$ and $\mathbf{ln}(\mathbf{X_{axis}}/\mathbf{d_{print}})$ in Figure 9(e) to show the effect of $(\mathbf{X_{axis}}/\mathbf{d_{print}})$. The curve fitting yields $\mathbf{Nu_{rough}}$ that is expressed as follows:

$$\mathbf{Nu_{rough}} = \mathbf{E}_0(\mathbf{Re_{num}})^{0.864}(\boldsymbol{\varphi})^{0.64}\mathbf{exp}\left(0.065\ \ln\ (\boldsymbol{\varphi})^2\right)\left(\mathbf{d_{np}}\right)^{0.784}\mathbf{exp}\left(-0.168\ \ln\ \left(\mathbf{d_{np}}\right)^2\right) \cdot \left(\frac{\mathbf{Y_{axis}}}{\mathbf{d_{print}}}\right)^{0.848}\mathbf{exp}\left(-0.168\mathbf{ln}\left(\frac{\mathbf{Y_{axis}}}{\mathbf{d_{print}}}\right)^2\right)\mathbf{exp}\left(-1.01\mathbf{ln}\left(\mathbf{X_{axis}}/\mathbf{d_{print}}\right)^2\right). \tag{14}$$

The data generated from the equation have been plotted between $\mathbf{ln}(\mathbf{E}_0)$ and $\mathbf{ln}(\mathbf{e_{rib}}/\mathbf{d_{print}})$ in Figure 9(f) to show the effect of $(\mathbf{e_{rib}}/\mathbf{d_{print}})$. The curve fitting by incorporating all the parameters yields final $\mathbf{Nu_{rough}}$ correlation that is expressed as follows:

$$\mathbf{Nu_{rough}} = 0.054(\mathbf{Re_{num}})^{0.864}(\boldsymbol{\varphi})^{0.64}\mathbf{exp}\left(0.065\ \ln\ (\boldsymbol{\varphi})^2\right)\left(\mathbf{d_{np}}\right)^{0.784} \times \mathbf{exp}\left(-0.168\mathbf{ln}\left(\mathbf{d_{np}}\right)^2\right)\left(\frac{\mathbf{Y_{axis}}}{\mathbf{d_{print}}}\right)^{0.848}\mathbf{exp}\left(-0.168\mathbf{ln}\left(\frac{\mathbf{Y_{axis}}}{\mathbf{d_{print}}}\right)^2\right) \times \left(\frac{\mathbf{X_{axis}}}{\mathbf{d_{print}}}\right)^{1.046}\mathbf{exp}\left(-1.01\mathbf{ln}\left(\frac{\mathbf{X_{axis}}}{\mathbf{d_{print}}}\right)^2\right)\left(\frac{\mathbf{e_{rib}}}{\mathbf{d_{print}}}\right)^{0.235} \times \mathbf{exp}\left(-1.393\mathbf{ln}\left(\frac{\mathbf{e_{rib}}}{\mathbf{d_{print}}}\right)^2\right). \tag{15}$$

6.2. Correlation for $\mathbf{f_{rough}}$. The effects of various geometrical parameters on $\mathbf{f_{rough}}$ discussed earlier for various $\mathbf{Re_{num}}$ show dependence of $\mathbf{f_{rough}}$ on parameters such as ϕ, $\mathbf{d_{np}}$, $(\mathbf{X_{axis}}/\mathbf{d_{print}})$, $(\mathbf{Y_{axis}}/\mathbf{d_{print}})$, $(\mathbf{e_{rib}}/\mathbf{d_{print}})$, and $\mathbf{Re_{num}}$ and can be written as follows:

$$\mathbf{f_{rough}} = \mathbf{f_{rough}}\left(\mathbf{Re_{num}}, \phi, \mathbf{d_{np}}, \left(\frac{\mathbf{X_{axis}}}{\mathbf{d_{print}}}\right), \left(\frac{\mathbf{Y_{axis}}}{\mathbf{d_{print}}}\right), \left(\frac{\mathbf{e_{rib}}}{\mathbf{d_{print}}}\right)\right). \tag{16}$$

Figure 10(a) represents the plotted $\mathbf{f_{rough}}$ against various $\mathbf{Re_{num}}$ and curve fitting using regression analysis through the data point. The resulted regression relation is as follows:

$$\mathbf{f_{rough}} = \mathbf{A_o}\mathbf{Re_{num}^{-0.282}}. \tag{17}$$

Constant $\mathbf{A}_0$ is reliant on parameters φ, $\mathbf{d_{np}}$, $(\mathbf{X_{axis}}/\mathbf{d_{print}})$, $(\mathbf{Y_{axis}}/\mathbf{d_{print}})$, and $(\mathbf{e_{rib}}/\mathbf{d_{print}})$. The functional relationship between $\mathbf{A}_0$ and φ is determined by plotting data values of $\mathbf{ln}(\mathbf{A}_0)$ against the values of $\mathbf{ln}(\varphi)$, as shown in Figure 10(b) through given relation.

$$\mathbf{f_{rough}} = \mathbf{B_o}\mathbf{Re_{num}^{-0.282}}(\phi)^{0.542}\mathbf{exp}\left(0.057\mathbf{ln}(\boldsymbol{\varphi})^2\right). \tag{18}$$

The constant $\mathbf{B}_0$ depends on φ, $\mathbf{d_{np}}$, $(\mathbf{X_{axis}}/\mathbf{d_{print}})$, $(\mathbf{Y_{axis}}/\mathbf{d_{print}})$, and $(\mathbf{e_{rib}}/\mathbf{d_{print}})$. The log-log data plotted between $\mathbf{B}_0$ and $\mathbf{d_{np}}$ get the fitting curve as shown in Figure 10(c), which relates between these two parameters as follows:

$$\mathbf{f_{rough}} = \mathbf{C_o}\mathbf{Re_{num}^{-0.282}}(\boldsymbol{\varphi})^{0.542}\mathbf{exp}\left(0.057\mathbf{ln}(\boldsymbol{\varphi})^2\right) \cdot \left(\mathbf{d_{np}}\right)^{1.32}\mathbf{exp}\left(-0.219\ \ln\ \left(\mathbf{d_{np}}\right)^2\right). \tag{19}$$

Similarly constant $\mathbf{C}_0$ depends on $(\mathbf{X_{axis}}/\mathbf{d_{print}})$, $(\mathbf{Y_{axis}}/\mathbf{d_{print}})$, and $(\mathbf{e_{rib}}/\mathbf{d_{print}})$. The data plotted between $\mathbf{B}_0$ and $\mathbf{d_{np}}$ get the fitting curve as shown in log-log plot in Figure 10(d), which relates between these two parameters as follows:

$$\mathbf{f_{rough}} = \mathbf{D}_0\mathbf{Re_{num}^{-0.282}}(\phi)^{0.542}\mathbf{exp}\left(0.057\mathbf{ln}(\boldsymbol{\varphi})^2\right)\left(\mathbf{d_{np}}\right)^{1.32} \cdot \mathbf{exp}\left(-0.219\mathbf{ln}\left(\mathbf{d_{np}}\right)^2\right) \cdot \left(\frac{\mathbf{Y_{axis}}}{\mathbf{d_{print}}}\right)^{1.103}\mathbf{exp}\left(-1.065\ \ln\ \left(\frac{\mathbf{Y_{axis}}}{\mathbf{d_{print}}}\right)^2\right). \tag{20}$$

The data generated from the equation have been plotted between $\mathbf{ln}(\mathbf{D}_0)$ and $\mathbf{ln}(\mathbf{X_{axis}}/\mathbf{d_{print}})$ in Figure 10(e) to show the effect of $(\mathbf{X_{axis}}/\mathbf{d_{print}})$. The curve fitting yields $\mathbf{f_{rough}}$ that is expressed as follows:

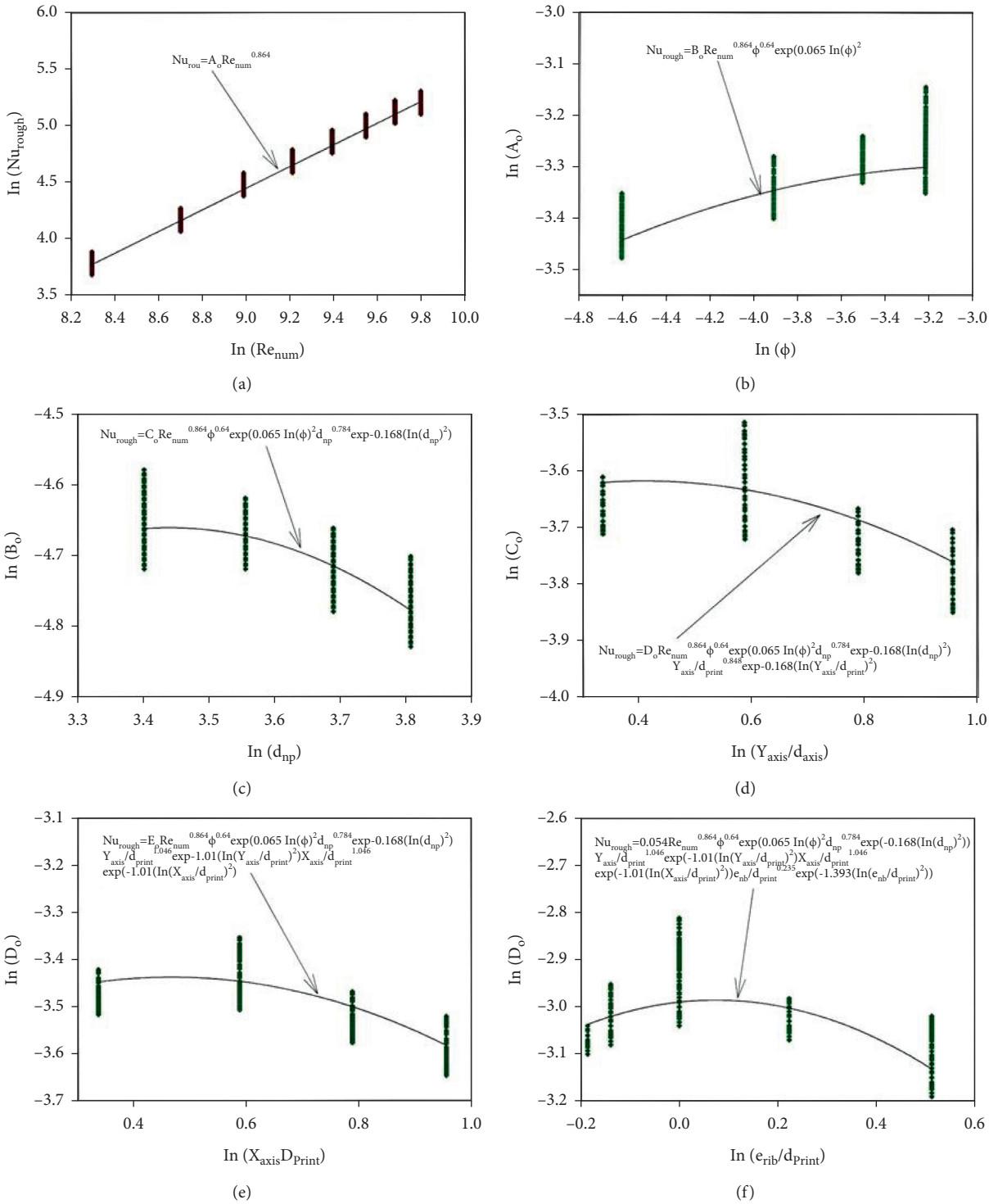

FIGURE 9: (a) Plot of $\ln(Nu_{\text{rough}})$ as a function of $\ln(\text{Re}_{\text{num}})$ for all the experimental data. (b) Plot of $\ln(A_o)$ as a function of $\ln(\phi)$. (c) Plot of $\ln(B_o)$ as a function of $\ln(\text{d}_{\text{np}})$. (d) Plot of $\ln(C_o)$ as a function of $\ln(Y_{\text{axis}}/d_{\text{print}})$. (e) Plot of $\ln(C_o)$ as a function of $\ln(X_{\text{axis}}/d_{\text{print}})$). (f) Plot of $\ln(E_o)$ as a function of $\ln(e_{\text{rib}}/d_{\text{print}})$.

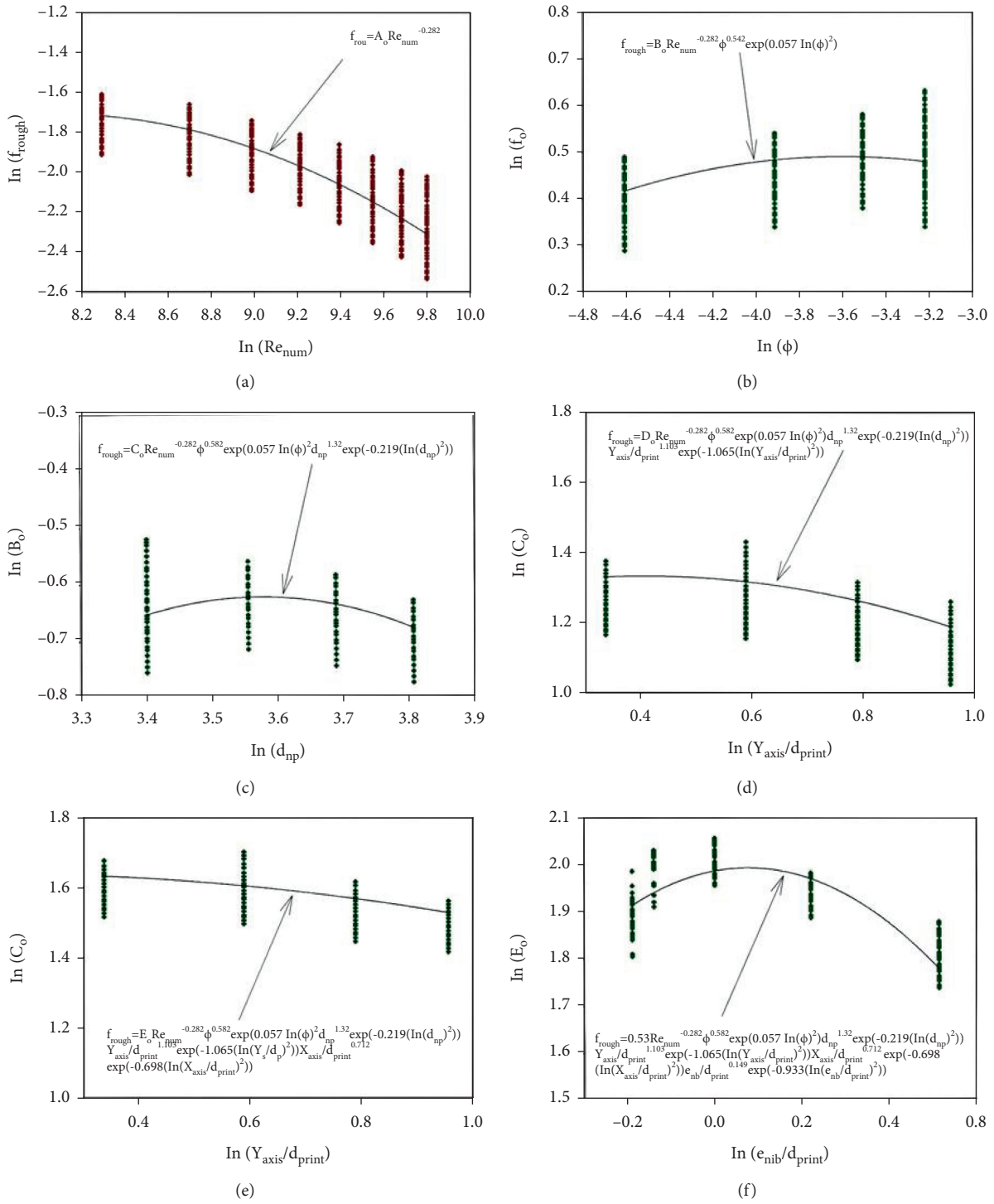

FIGURE 10: (a) Plot of $\ln(f_{\text{rough}})$ as a function of $\ln(\text{Re}_{\text{num}})$ for all the experimental data. (b) Plot of $\ln(A_o)$ as a function of $\ln(\phi)$. (c) Plot of $\ln(B_o)$ as a function of $\ln(\text{d}_{\text{np}})$. (d) Plot of $\ln(C_o)$ as a function of $\ln(Y_{\text{axis}}/d_{\text{print}})$. (e) Plot of $\ln(D_o)$ as a function of $\ln(X_{\text{axis}}/d_{\text{print}})$. (f) Plot of $\ln(C_o)$ as a function of $\ln(e_{\text{rib}}/d_{\text{print}})$.

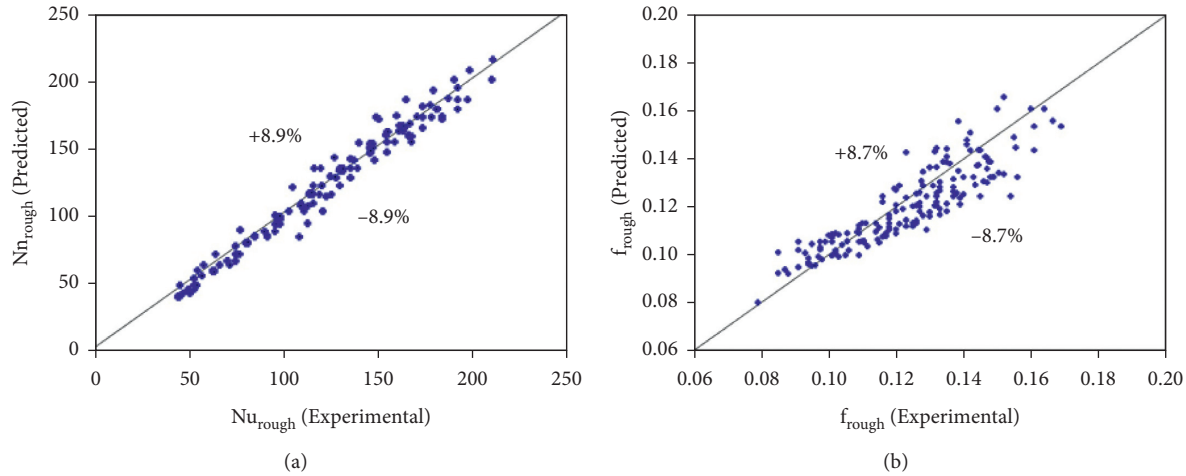

FIGURE 11: (a) Comparison of experimental and predicted data of Nu_{rough}. (b) Comparison of experimental and predicted values of f_{rough}.

$$\mathbf{f_{rough}} = \mathbf{E_0}\left(\mathbf{Re_{num}}\right)^{-0.282}(\boldsymbol{\varphi})^{0.542}\exp\left(0.057\ln(\boldsymbol{\varphi})^2\right)\cdot\left(\mathbf{d_{np}}\right)^{1.32}\exp\left(-0.219\ln\left(\mathbf{d_{np}}\right)^2\right)\left(\frac{\mathbf{Y_{axis}}}{\mathbf{d_{print}}}\right)^{1.103}\exp\cdot\left(-1.065\ln\left(\frac{\mathbf{Y_{axis}}}{\mathbf{d_{print}}}\right)^2\right)\times\exp\left(-0.698\ln\left(\frac{\mathbf{X_{axis}}}{\mathbf{d_{print}}}\right)^2\right)\left(\frac{\mathbf{X_{axis}}}{\mathbf{d_{print}}}\right)^{0.712}. \tag{21}$$

Finally after all the parameters are incorporated as shown in the Figure 10(f), the final correlation for $\mathbf{f_{rough}}$ is given as follows:

$$\mathbf{f_{rough}} = 0.53\left(\mathbf{Re_{num}}\right)^{-0.282}(\boldsymbol{\varphi})^{0.542}\exp\left(0.057\ln(\boldsymbol{\varphi})^2\right)\left(\mathbf{d_{np}}\right)^{1.32}\times\exp\left(-0.219\ln\left(\mathbf{d_{np}}\right)^2\right)\cdot\left(\frac{\mathbf{Y_{axis}}}{\mathbf{d_{print}}}\right)^{1.103}\exp\left(-1.065\ln\left(\frac{\mathbf{Y_{axis}}}{\mathbf{d_{print}}}\right)^2\right)\times\exp\left(-0.698\ln\left(\frac{\mathbf{X_{axis}}}{\mathbf{d_{print}}}\right)^2\right)\left(\frac{\mathbf{X_{axis}}}{\mathbf{d_{print}}}\right)^{0.712}\left(\frac{\mathbf{e_{rib}}}{\mathbf{d_{print}}}\right)^{0.149}\times\exp\left(-0.933\ln\left(\mathbf{e_{rib}}/\mathbf{d_{print}}\right)^2\right). \tag{22}$$

The Figure 11(a) displays the comparison of predicted values and experimental values of $\mathbf{Nu_{rough}}$ and shows maximum ±8.9% deviation. Also, the average absolute deviation in $\mathbf{Nu_{rough}}$ is found to be 4.82%. Similarly, Figure 11(b) displays the comparison of predicted values and experimental values of $\mathbf{f_{rough}}$ and shows maximum ±8.7% deviation. Also, the average absolute deviation in $\mathbf{f_{rough}}$ is found to be 4.53%. Therefore, it can be concluded that correlations developed in this work can predict the values of $\mathbf{Nu_{rough}}$ and $\mathbf{f_{rough}}$ with reasonable accuracy.

7. Conclusions

In this study, the parametric optimization and development of new correlations on heat transfer and flow friction for the turbulent regime of Al_2O_3-water-based nanofluid

flow in transverse with combined protrusion rib square duct have been discussed, and the following conclusions can be drawn:

(i) The maximum value of Nu_{rough} was found to be 217, which was found at design parameters values: φ of 4%, d_{np} of 30 nm, (X_{axis}/d_{print}) of 1.8, (Y_{axis}/d_{print}) of 1.8, ratio of (e_{rib}/d_{print}) 1.0, and Re_{num} of 18000.

(ii) The maximum value of f_{rough} was found to be 0.132, which was found at design parameters values: φ of 4%, d_{np} of 30 nm, (X_{axis}/d_{print}) of 1.8, (Y_{axis}/d_{print}) of 1.8, ratio of (e_{rib}/d_{print}) 1.0 and Re_{num} of 4000.

(iii) Because of the decrease in reattachment spacing with the increment in Re_{num}, the Nu_{rough} increases, whereas the f_{rough} decreases for all upsides of examined parameters.

(iv) The comparison of experimental values and predicted values of RSM model was carried out, and it was seen that the RSM predicted values are as per the experimental values in the in the uncertainties scope of ±5.5%, which shows a decent acceptance between the experimental results and developed RSM model results.

(v) The developed correlations for Nu_{rough} and f_{rough} were found to predict the values of Nu_{rough} and f_{rough} with good accuracy and absolute percentage deviation of 4.82% and 4.53%, respectively.

Data Availability

The data used to support the findings of the study are included within the article.

Conflicts of Interest

The authors declare that there are no conflicts of interest regarding the publication of this article.

Acknowledgments

This research was supported by the researchers with the supporting project number (RSP-2021/401) and the King Saud University, Riyadh, Saudi Arabia.

References

[1] S. Kumar, A. D. Kothiyal, M. S. Bisht, A. Kumar, and K. Anil, "Effect of nanofluid flow and protrusion ribs on performance in square channels: an experimental investigation," *Journal of Enhanced Heat Transfer*, vol. 26, no. 1, pp. 75–100, 2019.

[2] H. K. Bizhaem and A. Abbassi, "Numerical study on heat transfer and entropy generation of developing laminar nanofluid flow in helical tube using two-phase mixture model," *Advanced Powder Technology*, vol. 28, no. 9, pp. 2110–2125, 2017.

[3] B. Souayeh, N. Ben-Cheikh, and B. Ben-Beya, "Effect of thermal conductivity ratio on flow features and convective heat transfer," *Particulate Science & Technology*, 2016.

[4] S. Kumar and A. Kumar, "A comprehensive review on the heat transfer and nanofluid flow characteristics in different shaped channels," *International Journal of Ambient Energy*, vol. 42, no. 3, pp. 345–361, 2021.

[5] R. Kumar, R. Kumar, S. Kumar et al., "Impact of artificial roughness variation on heat transfer and friction characteristics of solar air heating system," *Alexandria Engineering Journal*, vol. 61, no. 1, pp. 481–491, 2022.

[6] A. N. Al-Shamani, K. Sopian, H. A. Mohammed, S. Mat, M. H. Ruslan, and A. M. Abed, "Enhancement heat transfer characteristics in the channel with Trapezoidal rib-groove using nanofluids," *Case Studies in Thermal Engineering*, vol. 5, pp. 48–58, 2015.

[7] R. Kamali and A. R. Binesh, "The importance of rib shape effects on the local heat transfer and flow friction characteristics of square ducts with ribbed internal surfaces," *International Communications in Heat and Mass Transfer*, vol. 35, no. 8, pp. 1032–1040, 2008.

[8] S. Kumar, M. Shandilya, A. Chauhan, R. Maithani, and A. Kumar, "Experimental analysis of zinc oxide/water/ethylene glycol-based nanofluid in a square duct roughened with inclined ribs," *Journal of Enhanced Heat Transfer*, vol. 27, no. 8, pp. 687–709, 2020.

[9] G. Lauriat, "On the uses of classical or improved heat transfer correlations for the predictions of convective thermal performances of water-Al2O3 nanofluids," *Applied Thermal Engineering*, vol. 129, pp. 1039–1057, 2018.

[10] C. T. Nguyen, R. Gilles, G. Christian, and N. Galanis, "Heat transfer enhancement using Al2O3-water nanofluid for an electronic liquid cooling system," *Applied Thermal Engineering*, vol. 27, no. 8–9, pp. 1501–1506, 2007.

[11] T. Hussein, S. N. Kazi, and A. Badarudin, "Turbulent heat transfer to separation nanofluid flow in annular concentric pipe," *International Journal of Thermal Sciences*, vol. 117, pp. 14–25, 2017.

[12] H. E. Ahmed, M. Z. Yusoff, M. N. A. Hawlader, M. I. Ahmed, B. H. Salman, and A. S. Kerbeet, "Turbulent heat transfer and nanofluid flow in a triangular duct with vortex generators," *International Journal of Heat and Mass Transfer*, vol. 105, pp. 495–504, 2017.

[13] O. Mahian, A. Kianifar, A. Z. Sahin, and S. Wongwises, "Performance analysis of a minichannel-based solar collector using different nanofluids," *Energy Conversion and Management*, vol. 88, pp. 129–138, 2014.

[14] D. Wen and Y. Ding, "Experimental investigation into convective heat transfer of nanofluids at the entrance region under laminar flow conditions," *International Journal of Heat and Mass Transfer*, vol. 47, no. 24, pp. 5181–5188, 2004.

[15] P. G. Singh and T. Sarao, "Experimental analysis of heat transfer and friction factor in plate heat exchanger with different orientations using Al2O3 nanofluids," *International Journal of Engineering*, vol. 29, pp. 1450–1458, 2016.

[16] L. S. Sundar, M. K. Singh, A. C. M. Sousa, and M. Sousa, "Enhanced heat transfer and friction factor of MWCNT-Fe3O4/water hybrid nanofluids," *International Communications in Heat and Mass Transfer*, vol. 52, pp. 73–83, 2014.

[17] S. Suresh, K. P. Venkitaraj, P. Selvakumar, and M. Chandrasekar, "Effect of Al2O3-Cu/water hybrid nanofluid in heat transfer," *Experimental Thermal and Fluid Science*, vol. 38, pp. 54–60, 2012.

[18] B. C. Pak and Y. I. Cho, "Hydrodynamic and heat transfer study of dispersed fluids with submicron metallic oxide particles," *Experimental Heat Transfer*, vol. 11, no. 2, pp. 151–170, 1998.

[19] C. J. Ho, L. C. Wei, and Z. W. Li, "An experimental investigation of forced convective cooling performance of a

microchannel heat sink with Al2O3/water nanofluid," *Applied Thermal Engineering*, vol. 30, no. 2–3, pp. 96–103, 2010.

[20] C. H. Li and G. P. Peterson, "Experimental studies of natural convection heat transfer of Al2O3/DI water nanoparticle suspensions (nanofluids)," *Advances in Mechanical Engineering*, 2010.

[21] C. J. Ho, W. K. Liu, Y. S. Chang, and C. C. Lin, "Natural convection heat transfer of alumina-water nanofluid in vertical square enclosures: an experimental study," *International Journal of Thermal Sciences*, vol. 49, no. 8, pp. 1345–1353, 2010.

[22] C. T. N. Maïga, S. B. Maïga, N. Galanis, G. Roy, T. Maré, and M. Coqueux, "Heat transfer enhancement in turbulent tube flow using Al2O3 nanoparticle suspension," *International Journal of Numerical Methods for Heat and Fluid Flow*, vol. 16, pp. 275–292, 2006.

[23] B. S. Petukhov, "Heat transfer and friction in turbulent pipe flow with variable physical properties," *Advances in Heat Transfer*, vol. 6, pp. 503–564, 1970.

[24] F. W. Dittus and L. M. K. Boelter, "Heat transfer in automobile radiators of the tubular type," *International Communications in Heat and Mass Transfer*, vol. 12, no. 1, pp. 3–22, 1985.

[25] W. Duangthongsuk and S. Wongwises, "Heat transfer enhancement and pressure drop characteristics of TiO2-water nanofluid in a double-tube counter flow heat exchanger," *International Journal of Heat and Mass Transfer*, vol. 52, no. 8, pp. 2059–2067, 2009.

[26] D. Madhesh, R. Parameshwaran, and S. Kalaiselvam, "Experimental investigation on convective heat transfer and rheological characteristics of Cu-TiO2 hybrid nanofluids," *Experimental Thermal and Fluid Science*, vol. 52, pp. 104–115, 2014.

[27] V. Gnielinski, "New equations for heat and mass transfer in turbulent pipe and channel flow," *International Chemical Engineering*, vol. 16, no. 2, pp. 359–368, 1976.

[28] S. Dinarvand, M. Nademi Rostami, R. Dinarvand, and I. Pop, "Improvement of drug delivery micro-circulatory system with a novel pattern of CuO-Cu/blood hybrid nanofluid flow towards a porous stretching sheet," *International Journal of Numerical Methods for Heat and Fluid Flow*, vol. 29, no. 11, pp. 4408–4429, 2019.

[29] M. E. Yazdi, M. Aghamajidi, S. Dinarvand, and I. Pop, "Tiwari-Das nanofluid model for magnetohydrodynamics (MHD) naturalconvective flow of a nanofluid adjacent to a spinning down-pointing vertical cone," *Propulsion and Power Research*, vol. 7, no. 1, pp. 78–90, 2018.

[30] S. Dinarvand, "Nodal/saddle stagnation-point boundary layer flow of CuO-Ag/water hybrid nanofluid: a novel hybridity model," *Microsystem Technologies*, vol. 25, no. 7, pp. 2609–2623, 2019.

[31] S. M. Mousavi, M. N. Rostami, M. Yousefi, S. Dinarvand, I. Pop, and M. A. Sheremet, "Dual solutions for Casson hybrid nanofluid flow due to a stretching/shrinking sheet: a new combination of theoretical and experimental models," *Chinese Journal of Physics*, vol. 71, pp. 574–588, 2021.

[32] S. Dinarvand and M. Nademi Rostami, "An innovative mass-based model of aqueous zinc oxide-gold hybrid nanofluid for von Kármán's swirling flow," *Journal of Thermal Analysis and Calorimetry*, vol. 138, no. 1, pp. 845–855, 2019.

[33] M. Malika and S. S. Sonawane, "Statistical modelling for the Ultrasonic photodegradation of Rhodamine B dye using aqueous based Bi-metal doped TiO2 supported montmorillonite hybrid nanofluid via RSM," *Sustainable Energy Technologies and Assessments*, vol. 44, Article ID 100980, 2021.

[34] I. D. J. Azzawi and a. Al-damook, "Multi-objective optimum design of porous triangular chamber using RSM," *International Communications in Heat and Mass Transfer*, vol. 130, Article ID 105774, 2022.

[35] American Society of Heating Refrigerating and Air-Conditioning Engineers Inc, *ASHRAE Handbook - Heating, Ventilating, and Air-Conditioning Applications*, American Society of Heating Refrigerating and Air-Conditioning Engineers Inc, Atlanta, Georgia, USA, SI Edition, 2015.

[36] H. W. Coleman and W. S. Glenn, *Experimentation, Validation, and Uncertainty Analysis for Engineers*, Wiley, Hoboken, NJ, USA, Third Edition, 2009.

Hindawi
Mathematical Problems in Engineering
Volume 2022, Article ID 4148401, 13 pages
https://doi.org/10.1155/2022/4148401

Research Article

Effects of Homogeneous-Heterogeneous Reactions on Maxwell Ferrofluid in the Presence of Magnetic Dipole along a Stretching Surface: A Numerical Approach

W. Tahir,[1] Nesreen Althobaiti,[2] N. Kousar,[1] Sharifah E. Alhazmi,[3] S. Bilal,[1] and A. Riaz[4]

[1]*Department of Mathematics, AIR University, Sector E-9 Islamabad, Pakistan*
[2]*Department of Mathematics and Statistics, College of Science, Taif University, Taif 21944, Saudi Arabia*
[3]*Mathematics Department, Al-Qunfudah University College, Umm Al-Qura University, Mecca, Saudi Arabia*
[4]*Department of Mathematics, Division of Science and Technology, University of Education, Lahore 54770, Pakistan*

Correspondence should be addressed to A. Riaz; arshad-riaz@ue.edu.pk

Received 28 November 2021; Revised 21 January 2022; Accepted 2 February 2022; Published 8 March 2022

Academic Editor: Mohammad Yaghoub Abdollahzadeh Jamalabadi

The document is presented to investigate momentum and thermal attributes of Maxwell liquid flow over a stretchable surface by inducting ferrite particles along with taking account of homogeneous-heterogeneous reactions. Two types of ferrite particles, namely, nickel zinc ferrite ($NiZnFe_2O_4$) and magnetite ferrite (Fe_3O_4), are considered and non-Newtonian fluid represented by Maxwell model is decided as base fluid blood is used. To elaborate effective use of ferrite particles, magnetization is provided by placing a single dipole. Heat transfer aspects are estimated through Cattaneo-Christov model, which includes thermal relaxation phenomena. The governing equations are changed into ODEs setup by obliging suitable variables. Subsequently, a solution is attained numerically by implementing shooting and RK methods jointly. The impact of involved pertinent parameters on associated momentum and thermal profiles is analyzed in graphical and tabular manner. It is measured that large intensity of homogeneous reaction weakens the concentration field, while ferrohydrodynamic interaction declines the flow velocity.

1. Introduction

In heat and mass transfer analysis, researchers have shown prodigious attention due to their superb industries and engineering utilizations common in freezing nuclear reactor, exchanger of heat, refrigerator, etc. The most frequently used Fourier's [1] law illustrates heat and mass transfer mechanism in a given medium. Fourier's law yields temperature field of parabolic type, which implies that heat transport has infinite speed and initial disturbance, notifying all over the medium. To solve this difficulty in the heat transfer paradox, Fourier's law needs modifications. Fourier's law is remodeled involving thermal inertial aspects by Cattaneo [2] in 1948. After that Christov [3] gave new formulation possessing Oldroyd's derivative of upper-convected to maintain the invariance, which is renowned as Cattaneo-Christov model. Straughan [4] manifested singularity of the solutions heeded for most popular Cattaneo-Christov equations. Diffusive aspects in the motion of nanoliquids were pondered by Hayat et al. [5] with handling Cattaneo-Christov model. Sandeep et al. [6] commence latest model of Kinetic viscosity in the stagnant flow with the help of interior heat source. Flow of Ag-ethylene glycol mixed convective nanofluid was studied by Muhammad et al. [7] with centered heated cavity. He showed comparison between two popular models and found higher rank of heat transferring in case of classical heat flux model instead of Cattaneo-Christov formulation. Khan and Alzahrani [8] measured the transportation of heat in Jeffry fluid by employing double diffusive model. By taking account of generalized Cattaneo-Christov scheme, Ijaz and Ayub [9] studied the novel features of nonlinearly convective movement of Maxwell nanofluid convinced by inclined cylinder. The variable thermophysical attributes of squeezing Newtonian liquid

were probed by Farooq et al. [10] by encompassing Cattaneo-Christov double diffusive law. Heat flux with modified heat flux model for flow past over a cone and a wedge with nonuniformly provided heat source/sink was examined by Anantha Kumar et al. [11], in which they anticipated that excessive heat transfer occurred in case of cone as compared to wedge.

The studies relevant to non-Newtonian fluids have acquired honorable consideration in recent time due to their tremendous utilization in industrial products. Single constitutive equation failed to describe such fluids; hence, to illustrate non-Newtonian fluids, diverse models have been recommended. Amidst them, differential type and rate type gained popular attention. Maxwell fluid lies in the division of rate type viscoelastic model, which includes the special factors of fluid relaxation time. The scrutiny of transportation of heat over prolonged surface has received fabulous importance owning to its abounding application in chemical and constructing process adding polymer processing, metal casting, ejection of copper lead, paper production and many more. Sakiadis flow generated due to the motion of Maxwell liquid over moving flat plate was planned by Sadeghy et al. [12]. The usage of boundary layer equation is obtained from 2-dimensional flow in the case of Maxwell fluid utilized by Harris [13]. With the implementation of finite difference method, Kumari and Nath [14] depicted Maxwell fluid in mixed convection stagnation point flow to enumerate numerical solution of boundary value problem. Noor [15] deliberated the thermophoresis effects in Maxwell hydrodynamic passed over a vertical covering. The impact of stretching sheet in stagnant flow of Maxwell liquid is detailed by Hayat et al. [16], obtaining series solution based on homotopy. Effect of exterior temperature in the existence of heat source/sink Mukhopadhay [17] summarized the 2-dimensional MHD non-Newtonian Maxwell fluid with unsteady case progress over an elongated sheet. In 2D steady flow of an upper-convected incompressible Maxwell liquid was analyzed under the consequences of MHD and thermal radiation by Subhas Abel et al. [18]. Mustafa [19] compared two types as numerical and homotopy solutions in the way of rotating flow in Maxwell fluid. Sequel of thermal radiation in the nomination of stagnation point flow of Maxwell liquid flopping in extendable sheet was checked by Mushtaq et al. [20]. Kara et al. [21] studied the dependence of pressure on relaxation time and viscosity in the flow of Maxwell liquid. Saleem and Sulochana [22] studied theoretical analysis of upper-convected Maxwell liquid flow by incorporating modified Fourier heat model. Magnetically affected flow of nonviscous liquid over a stretched surface with diffusion was examined by Kumaran et al. [23].

Due to this fact, finding of heat-mass transfer the effects of reacting chemical plays a significance role due to its distinct engineering appeal like procedure of food, hydrometallurgical industry, ceramics formulations, yield meditation utilizing freezing, etc. Chemical reaction divided either homogeneous or heterogeneous built upon where they exist in quantity of the fluid, or they exist on the surfaces of catalytic. When transport of reactions and catalyst is in the same/distinct phase, reactions are termed as homogeneous/heterogeneous. Basically, occurrence of homogeneous reaction is normally in the complete given phase, whereas the confined region, or within the boundary of phase, the heterogeneous reaction takes place. In viscous fluid flow, Merkin [24] explored the homogeneous and heterogeneous reactions. He utilized cubic autocatalysis for the case of homogeneous reaction and also heterogeneous reactions in catalyst surface. He also concludes that homogeneous and heterogeneous rate parameters could build multiple solutions. Equal diffusivities in case of homogeneous and heterogeneous reactions are detailed by Chaudhary and Merkin [25]. They also attained the valid solution for larger and smaller values of δ. They concluded that, for smaller δ, the homogeneous reactions become more extensive mechanism. In a stagnation point, the flow with regard to an elongated surface is examined by Bachok et al. [26]. In his paper, they discussed that, with fluid having smaller kinetic viscosity, a boundary layer is obtained in such case when extending velocity is less as compared to speed of free-stream and also inverted-boundary layer attained when elongated velocity shoots up free stream velocity. Flow of nanofluid bounded by porous stretchable flow with homogeneous and heterogeneous reactions takes place as announced by Kameswaran et al. [27]. They discussed the steady state of this system when auto catalyst and same diffusion coefficients of reactants are used. Homogeneous-heterogeneous reactions are taken by Hayat et al. [28] in the exploration of unfreezing heat in stretched flow of carbon nanotubes. They revealed that the temperature dispersal diminishes immediately as radiation parameter augmented. Imtiaz et al. [29] revealed the outturn of heterogeneous and homogeneous reactions in the study of MHD flow occurring in curved elongated surface. They observed that enhancement in curvature parameter fluid velocity also is enhanced. Also, enhancements occur in surface heat transmission for sizeable Prandtl number. Hayat et al. [30] scrutinized Cattaneo-Christov heat flux effects in the liquid flow by taking into account the Jeffery fluid model with the utilization of heterogeneous and homogeneous reactions. They concluded that for immense variation in strength of homogeneous reaction parameter concentration decreases, it is spiral in case of heterogeneous reaction parameter. Some recent developments on analysis of heat and flow attributes of liquids in multiple physical domain along with consideration of heterogenous-homogenous reactions are enclosed in refs [31–34].

In 1965, Stephen [35] is the first one who invented ferrofluid. These fluids lie in the category of magnetic fluid carrying very low viscosity, which is manufactured by mixing deeply potent colloidal suspension of refine magnetic particles in to the nonregulating carrier fluid. Ferrofluid became strongly magnetized due to the attendance of magnetic field. An astonishing and appealing attribute of ferromagnetism upon temperature is its credence on magnetization and this thermomagnetic coupling assemble ferromagnetic fluid functioning in distinct practical applications in [36–39]. Odenbach [40] performed the reliability of normal liquids with suspension of ferrite particles in special and medical lines. Shliomis [41] marked the influence of magnetization on ferrofluid viscosity and regulated it by

the cooperation of reversible thermodynamic law. By supplying radiative heat energy, Rani Titus [42] performed thermal analysis on ferromagnetic fluid, which is moving over extendable sheet. Appliance of variable surface temperature over nonlinear stretched sheet with the attendance of nonuniform magnetic field in ferrofluid is characterized by Bognar [43]. He expressed that, with increment in ferromagnetic parameter or power law exponent, the skin friction multiplier decreases, while esteem of heat transfer is shot out. In the flow of ferrofluid, the variable strength of magnetic dipole prompt due to magnetic domain was examined by Anderson and Valnes [44]. They conclude that, as compared to hydrodynamics case, primary effects of magnetic field diminished the fluid motion. Majeed et al. [45] enhanced the heat transfer effects in ferromagnetic fluid stream over extended sheet. In his paper, they discussed the different aspects of boundary conditions such as prescribed heat flux and prescribed surface temperature. Incorporation of three distinct ferrite particles in carrier fluid was discussed by Nadeem et al. [46] who also discussed in detail the heat transfer phenomena with the utilization of convective heat transfer coefficient. They conclude with the Nusselt number intimate swelling behavior with respect to broad solid volume fraction. The results of convective flow of ferrofluid slipped in curved prolonged belt in the occupancy of magnetic dipole were exposed by Imtiaz et al. [47]. They described that, due to enhancement in radiation parameter and Biot number, temperature also is enhanced. Microscopic rotational attributes of magnetic nanoparticles in side ferrofluid are examined by Hussanan et al. [48]. They also mentioned that the profile near the flow domain accelerates and then decreases in the presence of mass transfer parameter.

The motivation of this work is to analyze the impact of Maxwell ferrofluid by inducing ferrite particles (Nickel Zinc and Magnetite ferrite) due to its vast applications in medical and industrial sciences. The phenomenon underlines the utilization of the study being related to the curing of cancer disease. This effort is not done so far and will definitely provide direction to researchers. Here, blood is considered as represented by Maxwell model, and flow is considered over a linearly stretched surface by incorporating modified version of Fourier heat flux model along with assumption of heterogenous-homogenous reactions. A numerical investigation for the problem taken has been developed by using bvp4c tool. The results are validated through tabular justification made with the existing literature.

2. Mathematical Formulation

Let us assume electrically nonconducting two-dimensional incompressible Maxwell ferromagnetic fluid (base fluid Blood with suspended two ferrite particles Nickel Zinc Ferrite and Magnetite Ferrite) over a linearly elongated surface (Figure 1) with stretching velocity $U_w(x)$. Dipole is placed at y-axis at a distance c from the sheet, T_w is the wall temperature, Curie temperature is T_c and temperature away from the sheet is T_∞. Also, we have taken that $T_w < T_c$, fluid having no capability of being magnetization. The thermophysical properties of the fluid and particles are mentioned in Table 1.

The Ferro particles and base fluid are assumed to be in thermal equilibrium. The model for momentum and energy equation is utilized by Muhammad and Nadeem [49] with the addition of Maxwell fluid and Cattaneo-Christov heat flux model. Also Chaudhary and Merkin [25] proposed the following form for heterogeneous and homogeneous reactions:

$$\begin{aligned} A + 2B &\longrightarrow 3B, \quad \text{rate} = k_c a b^2, \\ A &\longrightarrow B, \quad \text{rate} = k_s a. \end{aligned} \tag{1}$$

Using boundary layer approximation, the constitutive equations are as follows:

$$\frac{\partial u}{\partial x} + \frac{\partial v}{\partial y} = 0, \tag{2}$$

$$\left(u\frac{\partial u}{\partial x} + v\frac{\partial u}{\partial y}\right) + \lambda_a\left(u^2\frac{\partial^2 u}{\partial x^2} + v^2\frac{\partial^2 u}{\partial y^2} + 2uv\frac{\partial^2 u}{\partial x\,\partial y}\right) = \frac{\mu_0}{\rho_{nf}}M\frac{\partial H}{\partial x} + \frac{\mu_{nf}}{\rho_{nf}}\frac{\partial^2 u}{\partial y^2}, \tag{3}$$

$$\begin{aligned} \left(u\frac{\partial T}{\partial x} + v\frac{\partial T}{\partial y}\right) + \lambda_c\left(u\frac{\partial u}{\partial x}\frac{\partial T}{\partial x} + v\frac{\partial v}{\partial y}\frac{\partial T}{\partial y} + u\frac{\partial v}{\partial x}\frac{\partial T}{\partial y} + v\frac{\partial u}{\partial y}\frac{\partial T}{\partial x} + 2uv\frac{\partial^2 T}{\partial x\,\partial y} + u^2\frac{\partial^2 T}{\partial x^2} + v^2\frac{\partial T^2}{\partial y^2}\right) \\ + \frac{\mu_0 T}{(\rho c_p)_{nf}}\left(u\frac{\partial H}{\partial x} + v\frac{\partial H}{\partial y}\right)\frac{\partial M}{\partial T} = \frac{k_{nf}}{(\rho C_p)_{nf}}\frac{\partial^2 T}{\partial y^2}, \end{aligned} \tag{4}$$

$$u\frac{\partial a}{\partial x} + v\frac{\partial a}{\partial y} = D_A\frac{\partial^2 a}{\partial y^2} - k_c a b^2, \tag{5}$$

$$u\frac{\partial b}{\partial x} + v\frac{\partial b}{\partial y} = D_B\frac{\partial^2 a}{\partial y^2} + k_c a b^2, \tag{6}$$

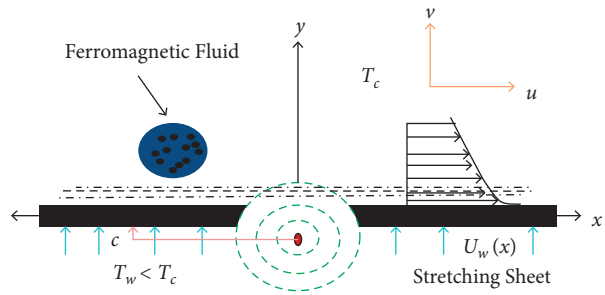

Figure 1: Geometric configuration.

Table 1: Thermophysical properties of blood, nickel zinc ferrite and magnetite ferrite.

Thermo-physical properties	ρ (kg/m^3)	C_p (J/kgK)	k (W/mK)
Blood	1060.0	3770	0.52
Nickel zinc ferrite	4800	710	6.3
Magnetite ferrite	5180	670	9.7

where M is the magnetization, and H is the magnetic field, μ_0 is characterized as magnetic permeability, μ_{nf} is defined as dynamic viscosity, λ_a represents relaxation parameter, λ_c expresses thermal relaxation time of heat flux, k_1 and k_2 are the diffusion rates, and the respective diffusion coefficients are D_A and D_B.

The boundary constraints are as follows:

$$\begin{aligned} u(0) &= U_w = Sx, \\ v(0) &= 0, \\ T(0) &= T_w, \\ D_A \frac{\partial a}{\partial y}(0) &= k_s a(0), \\ D_B \frac{\partial a}{\partial y}(0) &= -k_s a(0), \\ |u|_{y\longrightarrow\infty} &\longrightarrow 0, \\ |T|_{y\longrightarrow\infty} &\longrightarrow T_\infty = T_c, \\ |a|_{y\longrightarrow\infty} &\longrightarrow a_0, \\ |b|_{y\longrightarrow\infty} &\longrightarrow 0. \end{aligned} \tag{7}$$

Anderson and Valnes [44] showed that there is linear connection between temperature and magnetization:

$$M = K(T_c - T). \tag{8}$$

For finding the similarity solutions of equations (3)–(6) along with boundary conditions given in equation (7), the following transformations are used:

$$\begin{aligned} \psi(\eta,\xi) &= \frac{\mu_f}{\rho_f}\eta f(\xi), \\ \theta(\eta,\xi) &= \frac{T_c - T}{T_c - T_w} = \theta_1(\xi) + \eta^2\theta_2(\xi), \end{aligned} \tag{9}$$

$$\begin{aligned} a &= a_0 g(\xi), \\ b &= a_0 h(\xi), \\ \xi &= y\left(\frac{\rho_f S}{\mu_f}\right)^{1/2}, \\ \eta &= x\left(\frac{\rho_f S}{\mu_f}\right)^{1/2}. \end{aligned} \tag{10}$$

Express the velocity components, which govern the flow problem as

$$\begin{aligned} u &= Sx f'(\xi), \\ v &= -\left(Sv_f\right)^{1/2} f(\xi). \end{aligned} \tag{11}$$

By substitution of equations (8)–(11) into equations (3)–(6), we obtain the following system of nonlinear ODEs as

$$\left(\frac{1}{(1-\phi)^{2.5}\left(1-\phi+\phi\left(\rho_s/\rho_f\right)\right)}-\alpha_a f^2\right)f'''-f'^2+ff''+2\alpha_a ff'f''-\frac{2\beta\theta_1}{(\xi+\gamma)^4\left(1-\phi+\phi\left(\rho_s/\rho_f\right)\right)}=0, \tag{12}$$

$$\left(\frac{k_{nf}/k_f}{\left(1-\phi+\phi\left(\left(\rho C_p\right)_s/\left(\rho C_p\right)_f\right)\right)}-\alpha_c \mathrm{Pr} f^2\right)\theta_1''+\mathrm{Pr}\left(f\theta_1'-\alpha_c ff'\theta_1'\right)+\frac{2\lambda\beta f\left(\xi-\theta_1\right)}{(\xi+\gamma)^3}=0, \tag{13}$$

$$\begin{aligned}\left(\frac{k_{nf}/k_f}{\left(1-\phi+\phi\left(\left(\rho C_p\right)_s/\left(\rho C_p\right)_f\right)\right)}-\mathrm{Pr}\alpha_c f^2\right)\theta_2''-\mathrm{Pr}\left(\begin{array}{c}2f'\theta_2-f\theta_2'-2\alpha_c ff''\theta_2\\+4\alpha_c f'^2\theta_2-3\alpha_c ff'\theta_2\end{array}\right)\\-\lambda\beta\left(\theta_1-\varepsilon\right)\left(\frac{2f'}{(\xi+\gamma)^4}+\frac{4f}{(\xi+\gamma)^5}\right)+\frac{2\lambda\beta f\theta_2}{(\xi+\gamma)^3}=0,\end{aligned} \tag{14}$$

$$\frac{1}{S_c}g''+fg'-k_1gh^2=0, \tag{15}$$

$$\frac{\delta_1}{S_c}h''+fh'+k_1gh^2=0. \tag{16}$$

The associated boundary conditions (7) take the form

$$\begin{aligned}f(\xi)&=0,\\ f'(\xi)&=1,\\ \theta_1(\xi)&=1,\\ \theta_2(\xi)&=0,\\ g'(\xi)&=k_2 g(\xi),\\ \delta h'(\xi)&=-k_2 g(\xi)\text{at }\xi=0,\\ f'(\xi)&\longrightarrow 0,\\ \theta_1(\xi)&\longrightarrow 0,\\ \theta_2(\xi)&\longrightarrow 0,\\ g(\xi)&=1,\\ h(\xi)&=0,\text{when }\xi\longrightarrow\infty,\end{aligned} \tag{17}$$

where ε is the Curie temperature, β represents ferrohydrodynamic interaction parameter, Pr is the Prandtl number, α_a is the Deborah number, α_c is denoted as nondimensional thermal relaxation parameter, λ indicates viscous dissipation parameter, S_c shows Schmidt number, and k_1 and k_2 are the strength of homogeneous and heterogeneous reaction parameters.

$$\begin{aligned}\varepsilon&=\frac{T_\infty}{T_c-T_w},\\ \beta&=\frac{\gamma\mu_o K\left(T_c-T_w\right)\rho}{2\pi\mu^2},\\ \mathrm{Pr}&=\frac{\nu}{\alpha},\\ \lambda&=\frac{S\mu^2}{\rho k\left(T_c-T_w\right)},\\ \gamma&=\sqrt{\frac{S\rho c^2}{\mu}},\\ \alpha_a&=\lambda_a S,\\ \alpha_c&=\lambda_c S,\\ S_c&=\frac{\nu_f}{D_A},\\ k_1&=\frac{k_c a_0^2}{S},\\ k_2&=\frac{k_s}{D_A}\sqrt{\frac{\nu_f}{S}}.\end{aligned} \tag{18}$$

In most applications, it is expected that diffusion rate of chemical species A and B be of comparable size, which makes us make further assumptions that diffusion coefficients D_A and D_B are equal and about to take $\delta = 1$. In this case, we can write

$$g(\xi) + h(\xi) = 1. \tag{19}$$

The equations (15) and (16) reduce to the following form:

$$\frac{1}{S_c} g'' + f g' - k_1 g (1 - g)^2 = 0, \tag{20}$$

subject to the following B.Cs:

$$\begin{aligned} g'(\xi) &= k_2 g(\xi), \\ \xi &\longrightarrow 0, \\ g(\xi) &= 1, \\ \xi &\longrightarrow \infty. \end{aligned} \tag{21}$$

The physical quantities of interests are

$$\begin{aligned} C_f &= \frac{-2\tau_w}{\rho_{nf} U_w^2}, \\ \mathrm{Nu}_x &= \frac{x q_w}{k_f (T_c - T_w)}, \end{aligned} \tag{22}$$

with surface shear stress and surface heat flux being

$$\begin{aligned} \tau_w &= \mu_{nf} \left(\frac{\partial u}{\partial y} \right)|_{y=0}, \\ q_w &= -k_{nf} \left(\frac{\partial T}{\partial y} \right)|_{y=0}. \end{aligned} \tag{23}$$

The dimensionless expressions of equation (21) are attained

$$\begin{aligned} \frac{1}{2} \mathrm{Re}_x^{1/2} C_f &= \frac{1}{(1 - \phi)^{2.5}} f''(0), \\ \mathrm{Re}_x^{-1/2} N_{ux} &= \frac{k_{nf}}{k_f} \left(\theta_1'(0) + \eta^2 \theta_2(\xi) \right), \end{aligned} \tag{24}$$

where $\mathrm{Re}_x = (Sx^2/\nu_{nf})$.

3. Solution Procedure

This segment is presented to disclose attributes of Maxwell liquid by inducing two different types of the ferrite particles investigated. PDEs obtained in the process of mathematical formulation are turned out into a set of nonlinear ODEs with the usage of similarity transforms, and then these equations are handled numerically by using Runge-Kutta and shooting method. In shooting method, the formulated boundary-value problems are figured out in the form of initial value problems by choosing appropriate finite values of ξ (say ξ_∞). Initially, the equations (12)–(14) and (20) are converted in first-order system by selecting the set of new variables. For solving the current system with the support of shooting method, one must need the guess of missing values, which will hit the boundary conditions at every end. The acquired solution is valid or not relying upon velocity, temperature, and concentration profiles. Profiles are needed to approach boundary conditions at $\xi = \xi_\infty$ asymptotically.

To transform boundary-value problems defined in equations (12)–(14), and (20) into initial value problems, suppose that

$$(y_1, y_2, y_3, y_4, y_5, y_6, y_7, y_8, y_9 = f, f', f'', \theta_1, \theta_1', \theta_2, \theta_2' g, g'). \tag{25}$$

Subjecting these values, our system will become

$$y_1' = y_2, \tag{26}$$

$$y_2' = y_3, \tag{27}$$

$$y_3' = \left[\frac{1}{\left(1/(1 - \phi)^{2.5} * \left(1 - \phi + \phi \rho_s / \rho_f \right) \right) - \alpha_a y_{2/1}} \right] \left[y_2^2 - y_2 y_3 + y_2^2 - 2\alpha_a y_1 y_2 y_3 + \frac{2\beta y_4}{\left((\xi + \gamma)^4 * \left(1 - \phi + \phi \rho_s / \rho_f \right) \right)} \right], \tag{28}$$

$$y_4' = y_5, \tag{29}$$

$$y_5' = \left(\frac{\left(1 - \phi + \phi \left(\rho C_p \right)_s / \left(\rho C_p \right)_f \right)}{k_{nf}/k_f} - \frac{1}{\mathrm{Pr} \alpha_c y_1^2} \right) \left(\mathrm{Pr} \left(\alpha_c y_1 y_2 y_3 - y_1 y_5 \right) - \frac{2\lambda\beta y_1 \left(y_4 - \varepsilon \right)}{(\xi + \gamma)^3} \right), \tag{30}$$

$$y_4' = y_5, \tag{31}$$

$$y_7' = \left(\frac{\left(1-\phi+\phi\left(\rho C_p\right)_s/\left(\rho C_p\right)_f\right)}{k_{nf}/k_f} - \frac{1}{\Pr\alpha_1^2 y_1^2}\right)\left(\Pr\left(2y_2y_6 - y_1y_6 - 2\alpha y_1y_3y_6 + 4\alpha y_2y_6 - 3\alpha y_1y_2y_6\right)\right.$$
$$\left. + \lambda\beta\left(y_4-\varepsilon\right)\left(\frac{2y_2}{(\xi+\gamma)^4} + \frac{4y_1}{(\xi+\gamma)^5}\right) - \frac{2\lambda\beta y_1y_6}{(\xi+\gamma)^3}\right), \tag{32}$$

$$y_8' = y_9, \tag{33}$$

$$y_9' = -S_c\left(y_1y_7 - k_1\left(y_6\left(1-y_6^2\right)^2\right)\right), \tag{34}$$

with prescribed conditions

$$\begin{aligned} y_1(0) &= 0,\\ y_2(0) &= 1,\\ y_3(0) &= \omega_1 \text{ (unknown initial condition)},\\ y_4(0) &= 1,\\ y_5(0) &= \omega_2 \text{ (unknown initial condition)},\\ y_6(0) &= 0,\\ y_7(0) &= \omega_3 \text{ (unknown initial condition)},\\ y_9(0) &= k_2 y_8(0),\\ y_{10}(0) &= \omega_4 \text{ (unknown initial condition)}. \end{aligned} \tag{35}$$

As we are employing RK method in association with shooting scheme, so we required fulfilment of boundary conditions at infinity. The important factor here is to select ξ_∞ values. The ξ_∞ estimation is selected to opposite estimation of the limit at ξ_∞ for specified set of variables. The procedure is repeated until we obtain convergent solution with in an acceptable limit, i.e., 10^{-5}.

4. Graphical Analysis

In this section, we have explained the impact of flow variables on associated profiles.

4.1. Impact Physical Parameters on Velocity Profile. Figures 2–5 represent change in velocity profile against ferrohydrodynamic interaction (β), Deborah number (α_a), thermal relaxation parameter (α_c) and Prandtl number (Pr). Variation in velocity field against ferrohydrodynamic parameter (β) is probed in Figure 2. By increasing (β) velocity profile delineates is observed. The reason behind this fact is that by incrementing (β) interaction between magnetic field and particles also increases and more solid particles attracted towards magnetic field also due to presence of Lorentz forces velocity that is reduced. Also, momentum boundary layer decreases in case of Magnetite ferrite (Fe_2O_4) because magnetite ferrite more magnetized as compared to Nickel Zinc Ferrite so more attracted towards the magnetic field and velocity slow down quickly as compared to Nickel Zinc ferrite. Figure 3 interprets the velocity profile against Deborah number (α_a). It is monitored that with elongation in (α_a) fluid velocity decelerates. As Deborah number characterizes the fluidity of materials, so when we enhance (α_a) the fluid behaves like solid, and more viscosity is inherited, which reduces the velocity distribution. Figure 4 discusses the behavior of velocity distribution against thermal relaxation parameter (α_c). It is observed that by increasing (α_c) velocity increases because by increasing thermal relaxation parameter (α_c) momentum of fluid increases and an outcome average kinetic energy increases, which uplifts velocity. It is also focused that uplifting profile of velocity seemed in case of Magnetite ferrite (Fe_2O_4). Plot for momentum distribution against Prandtl number (Pr) is scrutinized in Figure 5. Positive trend in velocity found against (Pr). Since (Pr) shows the ratio of momentum to thermal diffusivities, so with increment in (Pr) the momentum diffusivities are enhanced, and fluid velocity profile exceeded, which is higher in case of Magnetite ferrite (Fe_2O_4) as compared to Nickel Zinc ferrite ($NiZnFe_2O_4$).

4.2. Impact Physical Parameters on Temperature Profile. Temperature profile against ferrohydrodynamic interaction (β), Deborah number (α_a), thermal relaxation parameter (α_c) and Prandtl number (Pr) is observed in Figures 6–9. Figure 6 describes the influence of ferrohydrodynamic interaction (β) on temperature field. This parameter shows interlink between the motion of fluid and action of active magnetic field. It is observed that increment in (β) elevates the frictional heating in the fluid layer, which is directly accountable for the augmentation in temperature profile. The augmented profile of temperature was observed in case of Magnetite ferrite (Fe_2O_4). Figure 7 accomplished the effects of α_a on temperature profile. It is observed that higher Deborah number expresses higher relaxation time, which protests fluid motion and is responsible of generating heat and increasing thermal boundary layer thickness. Figure 8 displays the inverse connection between thermal relaxation parameter (α_c) and temperature field. As soon as we increase α_c the decorum of temperature field demolished, because materials particles require exciting time to confer energy to their neighboring particles. Here, it is noticed that lower temperature is built in case Magnetite ferrite (Fe_2O_4). Sketch of temperature field with escalating values of Prandtl number can be seen in Figure 9. Escalating values of Prandtl number decline temperature profile, which concludes that, physically, Prandtl number contains the expression of

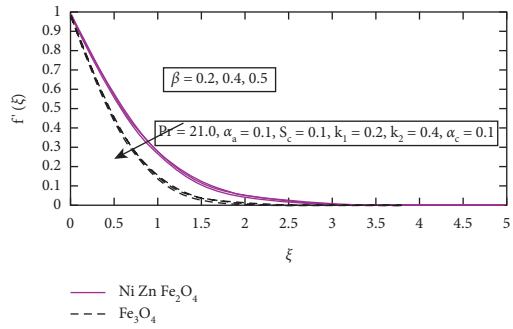

Figure 2: Velocity field with fluctuation in β.

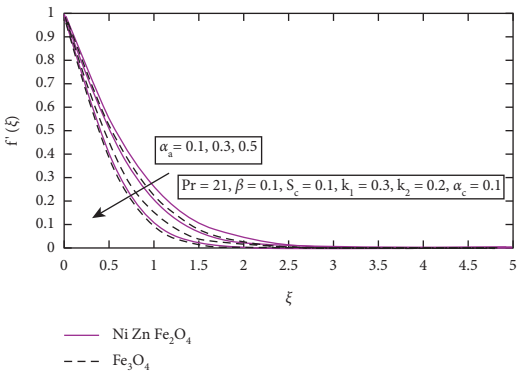

Figure 3: Velocity field with fluctuation in α_a.

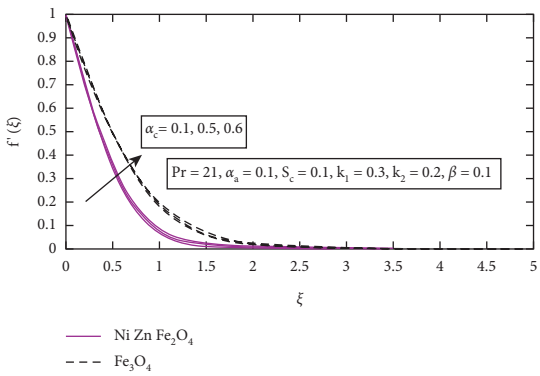

Figure 4: Velocity field with fluctuation in α_c.

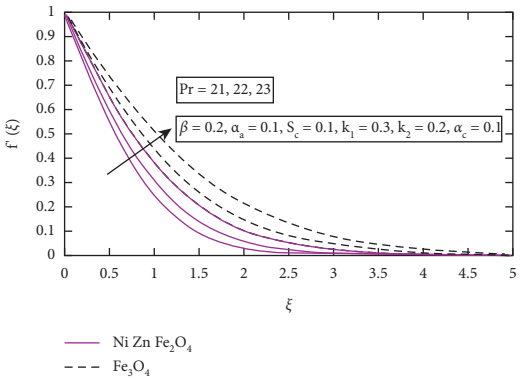

Figure 5: Velocity field with fluctuation in Pr.

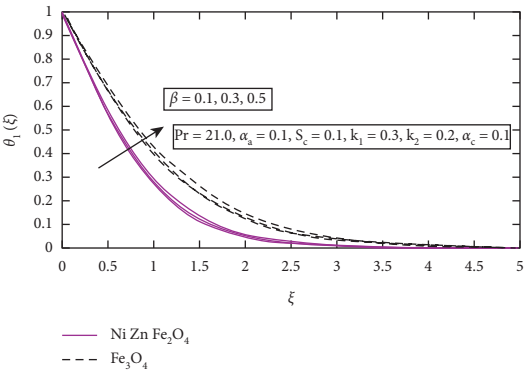

Figure 6: Thermal field with fluctuation in β.

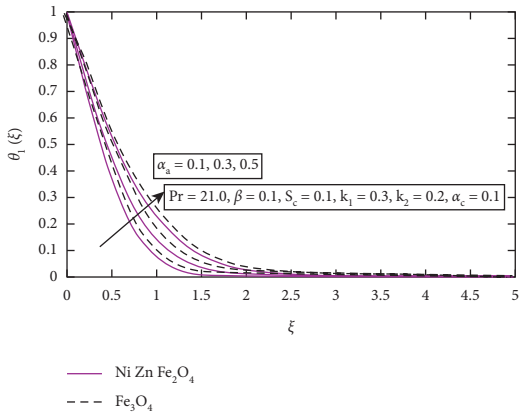

Figure 7: Thermal field with fluctuation in α_a.

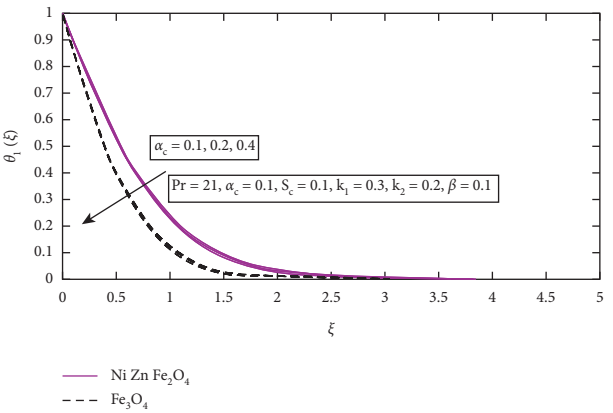

Figure 8: Thermal field with fluctuation in α_c.

momentum diffusivity to thermal diffusivity, due to which it is obvious that as Prandtl number varies, thermal diffusivity is going to be decreased, which means diffused heat slow.

4.3. Impact Physical Parameters on Concentration Profile. The behavior of Schmidt number (S_c) on concentration field is depicted in Figure 10. Schmidt number shows identical behavior against concentration field. As in case of Schmidt number, there is a ratio between momentum and mass diffusivity, so for advancement (S_c) corresponds to

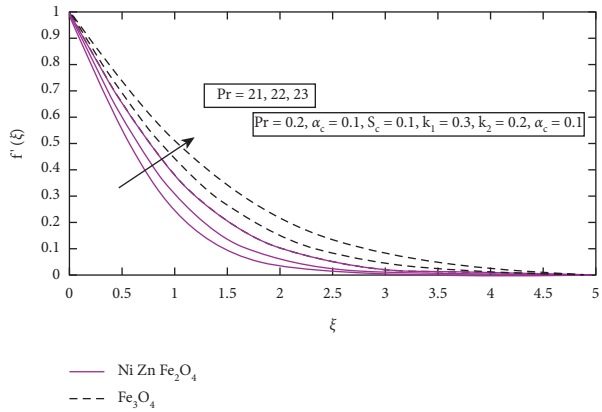

Figure 9: Thermal field with fluctuation in Pr.

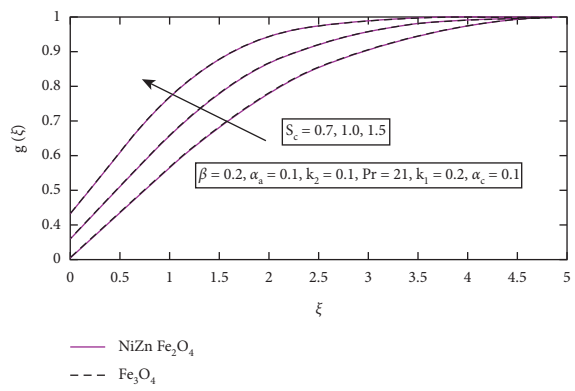

Figure 10: Concentration field with fluctuation in S_c.

reduction in diffusivity and as consequence the concentration field is enhanced. Figure 11 discloses the relation between strength of homogeneous reaction parameter (k_1) and concentration field, which is quite opposite as compared to Schmidt number. From the figure, it is obvious that inclination in (k_1) results in declination in concentration field. This kind of behavior is due to the fact that during homogeneous reaction the reactants are consumed. Graph of concentration field against different values of strength of heterogeneous reaction parameter (k_2) is shown in Figure 12. It is concluded that magnifying values of strength of heterogeneous parameter reduce concentration field. Also, it is perceived that in both graphs 4.10 and 4.11 higher concentration field is achieved by Nickel Zinc ferrite $(NiZnFe_2O_4)$.

4.4. Impact Physical Parameters on Skin Friction Parameter and Nusselt Number. Graphical results between ferrohydrodynamic interaction (β), Prandtl number (Pr) and skin friction coefficient are taken out in Figure 13. It is delineated that progressive attribute occurred in case of ferrohydrodynamic interaction (β) whereas reverse response is observed in case of Prandtl number (Pr) against skin friction. This situation arises because due to enhancing Prandtl number, the number rate of transferring momentum also increases due to increasing kinetic energy, which in term

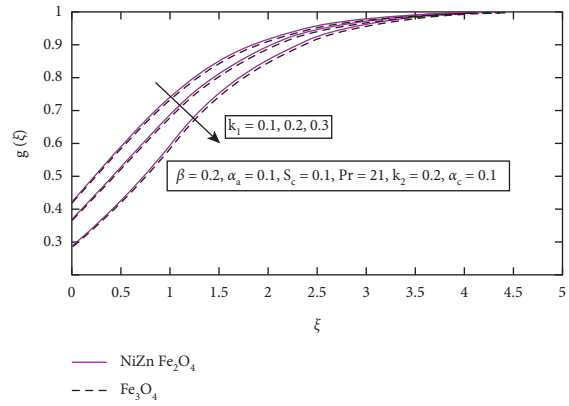

Figure 11: Concentration field with fluctuation in k_1.

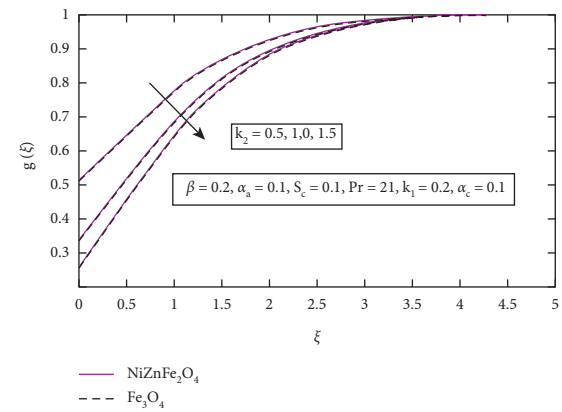

Figure 12: Concentration field with fluctuation in k_2.

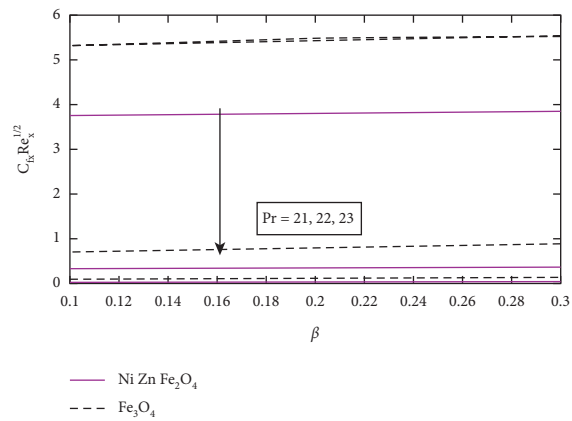

Figure 13: Skin friction coefficient with fluctuation in β and Pr.

reduces skin friction at wall. Figure 14 shows the direct relation between ferrohydrodynamic interaction (β), Prandtl number (Pr) and heat transfer coefficient. It is inferred that, by broadening Prandtl number (Pr), Nusselt number also blooms. Physically, we can explain this phenomenon as by increasing Prandtl number momentum diffusivity also magnifies, which give rise to kinetic energy and convective heat transfer rate which is responsible of augmenting Nusselt number. Expanding profile seemed to occur in case of Magnetite ferrite (Fe_2O_4) because thermal

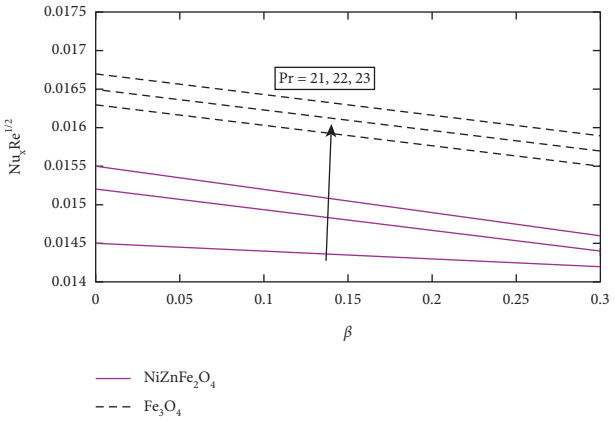

Figure 14: Nusselt number with fluctuation in β and Pr.

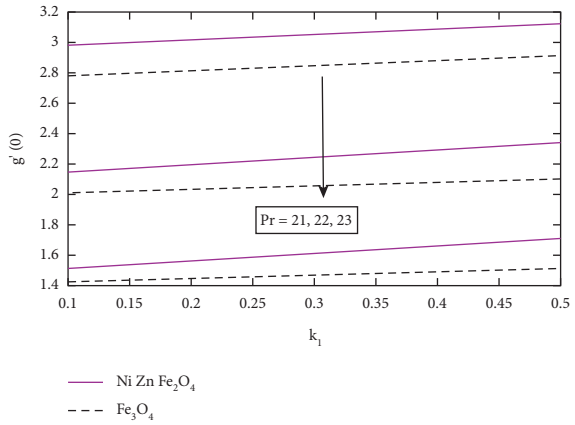

Figure 15: Mass flux coefficient with fluctuation in k_1 and S_c.

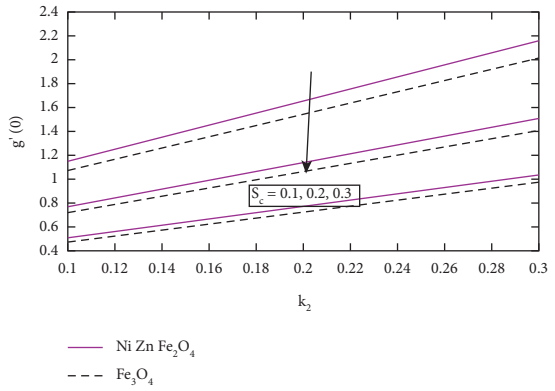

Figure 16: Mass flux coefficient with fluctuation in k_2 and S_c.

conductivity of Magnetite ferrite is higher as compared to Nickel Zinc ferrite. Variation in mass flux coefficient $(g'(0))$ against strength of homogeneous parameter and Schmidt number (S_c) is evaluated in Figure 15. It is depicted that by increasing strength of homogeneous parameter (k_1) change in mass distribution with in flow domain is enhanced, whereas contrary behavior is depicted in case of up surging magnitude of Schmidt number (S_c). Incrementing amplitude of Sherwood number $(g'(0))$ at wall against strength of homogeneous parameter (k_1) justified that by augmenting (k_1) homogeneous mixture is generated and accumulation of particles takes place which as an outcome raises the concentration magnitude. In addition Schmidt number (S_c) is the ratio of momentum to mass diffusivity so, by increasing Schmidt number (S_c) momentum of fluid molecules raises and concentration field reduces. Hence, it is divulged that magnitude of $(g'(0))$ is more in case of Nickel Zinc ferrite. Elevation in strength of heterogeneous reaction and Schmidt number (S_c) against mass flux coefficient is interrogated in Figure 16. The figure shows that strength of heterogeneous reaction parameter (k_2) upgrades the mass flux coefficient, while a contrasting behavior is noticed in case of Schmidt number (S_c). This mechanism is explained as in case of incrementing strength of heterogeneous reaction (k_2), the heterogeneous reaction give rise to and accretion of particles held, which in turn increases mass flux coefficient. Also (S_c) contain inverse relation with mass diffusivity so when we augmented (S_c) mass flux reduces. The skin friction coefficient, Nusselt number and mass flux coefficient are displayed in tabulated form with increasing values of ferrohydrodynamic interaction (β), Prandtl number (Pr), strength of homogeneous and heterogeneous parameters (k_1 and k_2) and Schmidt number (S_c). In Table 2 it is observed that by increasing ferrohydrodynamic interaction parameter, skin friction increases whereas contrary effect is observed in case of increasing values of Prandtl number. Enhancement in skin friction is observed against ferrohydrodynamic interaction (β) due to the generation of excessive resistive forces between molecules of fluid. In addition it is worthy to mention that skin friction is more increases in case of Nickel Zinc ferrite as compared to Magnetite ferrite.

Table 2: Values of $f''(0)$ by altering values of β and Pr.

($NiZnFe_2O_4$) β	Pr	$f''(0)$
0.1		0.0336
0.3	9	0.0628
0.5		1.1335
	10	0.2473
0.1	11	0.2290
	12	0.2120
(Fe_2O_4)		
0.1		0.0296
0.3	9	0.0625
0.5		1.1261
	10	0.2625
0.1	11	0.2479
	12	0.2349

In Table 3 magnifying values of Prandtl number (Pr) cause enhancement in $(-\theta'(0))$ as perceived. Table 4 represents the response of strength of homogeneous and heterogeneous parameters (k_1 and k_2) against $(g'(0))$. Table 5 shows that our present work shows excellent agreement with Rashidi and Noor results that increasing Pr number also increases Nusselt number. Table 6 shows the grid independence test for different values of tolerance by taking $\beta = 0.1$, $\lambda = 0.01$, $\gamma = 1.0$, Pr = 21 It suggests that, by reducing tolerance, Nusselt number and Skin friction show convergent behavior.

Table 3: Observations of $(-\theta'(0))$ by altering values of β and Pr.

$(NiZnFe_2O_4)$ β	Pr	$(-\theta'(0))$
0.1		0.0204
0.2	4	0.0079
0.3		0.0074
	4	0.0204
0.1	6	0.0769
	8	1.7286
(Fe_2O_4)		
0.1		0.3577
0.2	4	0.3378
0.3		0.3143
	4	0.3577
0.1	6	0.7002
	8	2.3027

Table 4: Obtained values of $g'(0)$ by altering values of k_1, k_2 and S_c.

$(NiZnFe_2O_4)$ k_1	k_2	S_c	$g'(0)$
0.1			2.9764
0.3		0.1	3.0462
0.5			3.1204
		0.1	2.9764
0.1		0.2	2.1425
		0.3	1.5128
	0.1		1.1437
	0.3	0.1	2.1586
	0.5		2.6197
		0.1	1.1437
	0.1	0.2	0.7627
		0.3	0.5016
(Fe_2O_4)			
0.1			2.7774
0.3		0.1	2.8425
0.5			2.9103
		0.1	2.7774
0.1		0.2	2.0094
		0.3	1.4266
	0.1		1.0682
	0.3	0.1	2.0151
	0.5		2.4450
		0.1	1.0682
	0.1	0.2	0.7165
		0.3	0.4748

Table 5: Agreement of results for heat flux coefficient by considering $\beta = \lambda = \varepsilon = \alpha_c, \alpha_a, S_c, k_1$ and $k_2 = 0$.

Pr	Rashidi [50]	OHAM results $Re_x^{-1/2}X^{-1}Nu_x$ Muhammad and Nadeem [49]	BVph2-midpoint $Re_x^{-1/2}X^{-1}Nu_x$ Muhammad and Nadeem [49]	Present work
0.72	0.808631	0.808641	0.808639	0.808637
1.0	1.000000	1.000000	1.000000	1.000000
3.0	1.923682	1.923690	1.923672	1.923669
4.0	—	2.003170	2.003162	2.003160
5.0	—	2.329810	2.329871	2.329869
8.0	—	—	2.541990	2.541992

Table 6: Grid independence.

ζ	Nusselt number	Skin friction
10^{-2}	1.9475	0.5523
10^{-4}	1.9471	0.5514
10^{-6}	1.9471	0.5514

5. Conclusion

Current communication explicates phenomenon of Maxwell ferro liquid flow over a linear stretching sheet with heterogenous-homogenous reactions. The impact of important parameters related to flow problem like the strength of chemical reaction parameters (k_1 and k_2), ferro hydrodynamic interaction (β), Schmidt number (S_c), Deborah number (α_a), and thermal relaxation time (α_c) is graphically analyzed for momentum, thermal and concentration fields as well as for skin friction and heat flux coefficients. Significant observations are deliberated as follows:

(i) Ferrohydrodynamic interaction parameter β cut down the velocity profile while accelerating temperature field and concentration field.

(ii) Variation in Deborah number α_a declined velocity profile whereas boosting temperature field.

(iii) Intensifying thermal relaxation parameter α_c results in declination in temperature profile.

(iv) By augmenting, Prandtl number shows flourishing behavior towards velocity and shrinkage in temperature profile.

(v) Growing values of Schmidt number S_c generate reduction in concentration in field.

(vi) Strength of homogeneous reaction parameter k_1 weakens concentration field [51].

Data Availability

Data can be obtained upon request to the authors.

Conflicts of Interest

The authors declare that there are no conflicts of interest.

Authors' Contributions

W. Tahir has done the drafting, Nesreen Althobaiti has presented the validity of the results, N. Kousar has produced the solutions and graphs, Sharifah E. Alhazmi has helped in conceptualization and language improvement, S. Bilal has done the methodology, and A. Riaz has supervised and improved the results.

References

[1] J. B. J. Fourier, *Théorieanalytique de la chaleur Paris*, 1822.

[2] C. Cattaneo, "Sulla conduzionedelcalore, AttiSemin," *Mat Fis Univ Modena Reggio Emilia*, vol. 3, pp. 83–101, 1948.

[3] C. I. Christov, "On frame indifferent formulation of the Maxwell-Cattaneo model of finite-speed heat conduction," *Mechanics Research Communications*, vol. 36, no. 4, pp. 481–486, 2009.

[4] B. Straughan, "Thermal convection with the Cattaneo-Christov model," *International Journal of Heat and Mass Transfer*, vol. 53, no. 1-3, pp. 95–98, 2010.

[5] T. Hayat, T. Muhammad, A. Alsaedi, and B. Ahmad, "Three-dimensional flow of nanofluid with Cattaneo-Christov double diffusion," *Results in Physics*, vol. 6, pp. 897–903, 2016.

[6] N. Sandeep, O. K. Koriko, and I. L. Animasaun, "Modified kinematic viscosity model for 3D-Casson fluid flow within boundary layer formed on a surface at absolute zero," *Journal of Molecular Liquids*, vol. 221, pp. 1197–1206, 2016.

[7] N. Muhammad, S. Nadeem, and A. Issakhov, "Finite volume method for mixed convection flow of Ag-ethylene glycol nanofluid flow in a cavity having thin central heater," *Physica A: Statistical Mechanics and Its Applications*, vol. 537, p. 122738, 2020.

[8] M. I. Khan and F. Alzahrani, ""Transportation of heat through Cattaneo-Christov heat flux model in non-Newtonian fluid subject to internal resistance of particles"," *Applied Mathematics and Mechanics*, vol. 41, pp. 1157–1166, 2010.

[9] M. Ijaz and M. Ayub, "Nonlinear convective stratified flow of Maxwell nanofluid with activation energy," *Heliyon*, vol. 5, no. e01121, p. 31, 2019.

[10] M. Farooq, S. Ahmad, M. Javed, and A. Anjum, "Analysis of Cattaneo-Christov heat and mass fluxes in the squeezed flow embedded in porous medium with variable mass diffusivity," *Results in Physics*, vol. 7, pp. 3788–3796, 2017.

[11] K. Anantha Kumar, J. V. Sugunamma, and N. Sandeep, "Magnetohydrodynamic Cattaneo-Christov flow past a cone and a wedge with variable heat source/sink," *Alexandria Engineering Journal*, vol. 57, no. 1, pp. 435–443, 2018.

[12] K. Sadeghy, A.-H. Najafi, and M. Saffaripour, "Sakiadis flow of an upper-convected Maxwell fluid," *International Journal of Non-linear Mechanics*, vol. 40, no. 9, pp. 1220–1228, 2005.

[13] J. Harris, *"Rheology and non-newtonian flow"*, Longman, London, 1977.

[14] M. Kumari and G. Nath, "Steady mixed convection stagnation-point flow of upper convected Maxwell fluids with magnetic field," *International Journal of Non-linear Mechanics*, vol. 44, no. 10, pp. 1048–1055, 2009.

[15] N. F. M. Noor, "Analysis for MHD flow of a Maxwell fluid past a vertical stretching sheet in the presence of thermophoresis and chemical reaction," *World Acad. Sci., Eng. Technol*, vol. 64, pp. 1019–1023, 2012.

[16] T. Hayat, Z. Abbas, and M. Sajid, "MHD stagnation-point flow of an upper-convected Maxwell fluid over a stretching surface," *Chaos, Solitons & Fractals*, vol. 39, no. 2, pp. 840–848, 2009.

[17] S. Mukhopadhyay, "Heat transfer analysis of the unsteady flow of a Maxwell fluid over a stretching surface in the presence of a heat source/sink," *Chinese Physics Letters*, vol. 29, no. 5, p. 054703, 2012.

[18] M. Subhas Abel, J. V. Tawade, and M. M. Nandeppanavar, "MHD flow and heat transfer for the upper-convected Maxwell fluid over a stretching sheet," *Meccanica*, vol. 47, no. 2, pp. 385–393, 2012.

[19] M. Mustafa, "Cattaneo-Christov heat flux model for rotating flow and heat transfer of upper-convected Maxwell fluid," *AIP Advances*, vol. 5, no. 4, p. 047109, 2015.

[20] A. Mushtaq, M. Mustafa, T. Hayat, and A. Alsaedi, "Effects of thermal radiation on the stagnation-point flow of upper-convected Maxwell fluid over a stretching sheet," *Journal of Aerospace Engineering*, vol. 27, no. 4, p. 04014015, 2014.

[21] S. Kara, V. Prusa, and K. V. Rajagopal, ""On Maxwell fluids with relaxation time and viscosity depending on the pressure"," *International Journal of Non-linear Mechanics*, vol. 46, pp. 819–827, 2011.

[22] N. Sandeep and C. Sulochana, "Momentum and heat transfer behaviour of Jeffrey, Maxwell and Oldroyd-B nanofluids past a stretching surface with non-uniform heat source/sink," *Ain Shams Engineering Journal*, vol. 9, no. 4, pp. 517–524, 2018.

[23] G. Kumaran, N. Sandeep, and M. E. Ali, "Computational analysis of magnetohydrodynamic Casson and Maxwell flows over a stretching sheet with cross diffusion," *Results in Physics*, vol. 7, pp. 147–155, 2017.

[24] J. H. Merkin, "A model for isothermal homogeneous-heterogeneous reactions in boundary-layer flow," *Mathematical and Computer Modelling*, vol. 24, no. 8, pp. 125–136, 1996.

[25] M. A. Chaudhary and J. H. Merkin, "A simple isothermal model for homogeneous-heterogeneous reactions in boundary-layer flow. II Different diffusivities for reactant and autocatalyst," *Fluid Dynamics Research*, vol. 16, no. 6, pp. 335–359, 1995.

[26] N. Bachok, A. Ishak, and I. Pop, "On the stagnation-point flow towards a stretching sheet with homogeneous-heterogeneous reactions effects," *Communications in Nonlinear Science and Numerical Simulation*, vol. 16, no. 11, pp. 4296–4302, 2011.

[27] P. K. Kameswaran, S. Shaw, P. Sibanda, and P. V. S. N. Murthy, "Homogeneous-heterogeneous reactions in a nanofluid flow due to a porous stretching sheet," *International Journal of Heat and Mass Transfer*, vol. 57, no. 2, pp. 465–472, 2013.

[28] T. Hayat, Z. Hussain, A. Alsaedi, and B. Ahmad, "Heterogeneous-homogeneous reactions and melting heat transfer effects in flow with carbon nanotubes," *Journal of Molecular Liquids*, vol. 220, pp. 200–207, 2016.

[29] M. Imtiaz, T. Hayat, A. Alsaedi, and A. Hobiny, "Homogeneous-heterogeneous reactions in MHD flow due to an unsteady curved stretching surface," *Journal of Molecular Liquids*, vol. 221, pp. 245–253, 2016.

[30] T. Hayat, S. Qayyum, M. Imtiaz, and A. Alsaedi, "Impact of cattaneo-christov heat flux in jeffrey fluid flow with homogeneous-heterogeneous reactions," *Plos One*, vol. 11, no. 2, p. e0148662, 2016.

[31] T. Hayat, Z. Hussain, T. Muhammad, and A. Alsaedi, "Effects of homogeneous and heterogeneous reactions in flow of nanofluids over a nonlinear stretching surface with variable surface thickness," *Journal of Molecular Liquids*, vol. 221, pp. 1121–1127, 2016.

[32] M. Sajid, S. A. Iqbal, M. Naveed, and Z. Abbas, "Effect of homogeneous-heterogeneous reactions and magnetohydrodynamics on Fe 3 O 4 nanofluid for the Blasius flow with thermal radiations," *Journal of Molecular Liquids*, vol. 233, pp. 115–121, 2017.

[33] A. Tanveer, T. Hayat, A. Alsaedi, and B. Ahmad, "Mixed convective peristaltic flow of Sisko fluid in curved channel with homogeneous-heterogeneous reaction effects," *Journal of Molecular Liquids*, vol. 233, pp. 131–138, 2017.

[34] T. Hayat, Z. Hussain, A. Alsaedi, and M. Mustafa, "Nanofluid flow through a porous space with convective conditions and heterogeneous-homogeneous reactions," *Journal of the Taiwan Institute of Chemical Engineers*, vol. 70, pp. 119–126, 2017.

[35] P. S. Stephen, "Low viscosity magnetic fluid obtained by the colloidal suspension of magnetic particles," 1965.

[36] W. Voit, D. K. Kim, W. Zapka, M. Muhammed, and K. V. Rao, "Magnetic behavior of coated superparamagnetic iron oxide nanoparticles in ferrofluids," *MRS Proceedings*, vol. 676, 2001.

[37] R. E. Rosensweig, "Magnetic fluids," *Annual Review of Fluid Mechanics*, vol. 19, 1987.

[38] A. C. Eringen and G. A. Maugin, *"Electrodynamics of Continua II": Fluids and Complex Media*, Springer, New York, 1990.

[39] J. R. L. Bailey and J. Magn and Magn, "Mater," vol. 2, p. 178, 1983.

[40] S. Odenbach, ""Magnetic fluids–suspensions of magnetic dipoles and their magnetic control"," *Journal of Physics: Condensed Matter*, vol. 15, 2003.

[41] M. I. Shliomis, "Ferrohydrodynamics: testing a third magnetization equation&quot," *Physical Review*, vol. 64, no. 6, 2001.

[42] L. S. Rani Titus, "Heat transfer in ferrofluid flow over a stretching sheet with radiation," *International Journal of Engineering Research and Technology*, vol. 3, pp. 2278–0181, 2014.

[43] G. Bongar, "Ferrofluid Flow in the presence of magnetic field above stretching Sheet," *Tribology in industry*, vol. 41, pp. 426–432, 2019.

[44] H. I. Andersson and O. A. Valnes, "Flow of a heated ferrofluid over a stretching sheet in the presence of a magnetic dipole," *Acta Mechanica*, vol. 128, no. 1-2, pp. 39–47, 1998.

[45] A. Majeed, A. Zeeshan, and R. Ellahi, "Unsteady ferromagnetic liquid flow and heat transfer analysis over a stretching sheet with the effect of dipole and prescribed heat flux," *Journal of Molecular Liquids*, vol. 223, pp. 528–533, 2016.

[46] S. Nadeem, S. Ahmad, and N. Muhammad, "Analysis of ferrite nanoparticles in liquid," *Pramana - Journal of Physics*, vol. 94, 2020.

[47] M. Imtiaz, T. Hayat, and A. Alsaedi, "Convective flow of ferrofluid due to a curved stretching surface with homogeneous-heterogeneous reactions," *Powder Technology*, vol. 310, pp. 154–162, 2017.

[48] A. Hussanan, M. Z. Salleh, and I. Khan, "Microstructure and inertial characteristics of a magnetite ferrofluid over a stretching/shrinking sheet using effective thermal conductivity model," *Journal of Molecular Liquids*, vol. 255, pp. 64–75, 2018.

[49] N. Muhammad and S. Nadeem, "Ferrite nanoparticles Ni-ZnFe2O4, Mn- ZnFe2O4 and Fe2O4 in the flow of ferromagnetic nanofluid," *The European Physical Journal Plus*, vol. 132, 2017.

[50] M. M. Rashidi, N. Vishnu Ganesh, A. K. Abdul Hakeem, B. Ganga, and G. Lorenzini, "Influences of an effective Prandtl number model on nano boundary layer flow of γ Al2O3-H2O and γ Al2O3-C2H6O2 over a vertical stretching sheet," *International Journal of Heat and Mass Transfer*, vol. 98, pp. 616–623, 2016.

[51] S. Saleem, M. Awais, S. Nadeem, N. Sandeep, and M. T. Mustafa, "Theoretical analysis of upper-convected Maxwell fluid flow with Cattaneo-Christov heat flux model," *Chinese Journal of Physics*, vol. 55, no. 4, pp. 1615–1625, 2017.

Hindawi
Mathematical Problems in Engineering
Volume 2022, Article ID 5289401, 18 pages
https://doi.org/10.1155/2022/5289401

Research Article

Flow Analysis of Two-Layer Nano/Johnson–Segalman Fluid in a Blood Vessel-like Tube with Complex Peristaltic Wave

A. Zeeshan,[1] **A. Riaz**,[2] **Faris Alzahrani**,[3] **and A. Moqeet**[1]

[1]*Department of Mathematics & Statistics, FBAS, International Islamic University Islamabad, H-10, Islamabad, Pakistan*
[2]*Department of Mathematics, Division of Science and Technology, University of Education, Lahore 54770, Pakistan*
[3]*Department of Mathematics, Faculty of Sciences, King Abdulaziz University, P. O. Box 80203, Jeddah 21589, Saudi Arabia*

Correspondence should be addressed to A. Zeeshan; ahmad.zeeshan@iiu.edu.pk

Received 17 November 2021; Revised 6 January 2022; Accepted 15 January 2022; Published 25 February 2022

Academic Editor: Ali Ahmadian

Biologically inspired micropumps using the phenomena of peristalsis are highly involved in targeted drugging in pharmacological engineering. This study analyzed theoretically the transport of two immiscible fluids in a long flexible tube. The core region contains Johnson–Segalman non-Newtonian fluid, while the peripheral region is saturated by nanofluid. It is assumed that Darcy's porous medium is encountered close to the walls of the tube. A complex peristaltic wave is transmitted on the compliant wall which induces the flow. Equations of continuity, momentum, energy, and nanoparticle concentration are used in modelling the problem. The modelled problem for both the regions, i.e., core and peripheral regions are developed with the assumptions of long wavelength and creeping flow. Temperature, velocity, and shear stress at the interface are assumed to be equal. The system of equations is solved analytically. The graphical results for different involving parameters are displayed and thoroughly discussed. It is received that the heat transfer goes inverse with fluid viscosity in the peripheral region, but opposite measurements are obtained in the core region. This theoretical model may be considerable in some medical mechanisms such as targeted drug delivery, differential diagnosis, and hyperthermia. Moreover, no study on non-Newtonian nanofluid is reported yet for the two-layered flow system, so this study will give a good addition in the literature of biomedical research.

1. Introduction

The transport of fluid in a channel or tube due to contraction and relaxation of flexible walls are known as peristalsis. It can be observed naturally in the human body for the transport of food, some blood vessels, movement of spermatozoa and ovum in reproductive track, and many other body systems. Phenomena inspired scientists and leads to many biomedical instruments and other transport techniques in machines such as a heart-lung machine and PDMS peristaltic micropump [1, 2]. Other than biomedical devices, it can be employed in devices such as sanitary transport.

Latham [3] experimentally elaborated the phenomena, leading to numerous investigations [4–8] allocated in the domain of peristaltic flow for different flow geometries and under various assumptions. Jaffrin and Shapiro [9] initiated the study of peristaltic transport with low Reynold's number approximation. Most recently, Zeeshan et al. [10] investigated the rheological features of nanofluid in a rectangular duct driven by a complex peristaltic wave. The effect of electrophoresis was focused and the analytic solution is found. They revealed that the change in amplitude ratios of complex waves affects the flow positively, that is, more bolus are observed. Tripathi et al. [11] theoretically studied the transport phenomena of a nanofluid due to complex peristaltic transportation with effects of electro-osmosis. The analysis focuses on nanofluids, and they observe the effects of the rise in Joule's heating, thermophoresis, Brownian motion, Grashoff number, etc. Javid et al. [12] described the peristaltic propulsion of viscous fluid in a channel with a complex wave. They used numerical simulations to evaluate the results. The evaluation further focused on magnetohydrodynamics which enhances the worth of study. Furthermore, Tripathi et al. [13] added electrodynamical effects with

a couple stress fluids in ocular flow. Bhatti et al. [14] argued two-phase flow in a channel with a compliant wall.

Usually, in biological systems, such as the ureter, oesophagus, or small veins, it became apparent that the walls are lubricated with a film of fluid. These fluids may be different in nature rheologically and continuously pumped out. Recently, some researchers [15, 16] have shown experimentally that the blood flux in tiny veins has an outer stratum made of plasma (which is usually Newtonian fluid), whereas an inner stratum called core possesses red blood (usually modelled as non-Newtonian fluid). The fluid rheologies may vary in different transport ducts of the human body. The study motivated some recent literature in physiological flow two-layer immiscible fluids' flow analysis.

Maybe, the first mathematical analysis in this domain was performed by Srivastava and Srivastava [17] back in 1982. They considered both Newtonian fluids with different viscosities and compared the results with experimental results of Weinberg et al. [18].

Misra and Pandey [19] then use the model for the transport of blood in small blood vessels. They use the Casson model for core region flow and Newtonian fluid close to the wall. They concluded the denser the peripheral fluid is, the higher the flow rate of the core region is.

More recently, Vajravelu and Saravana [20] examined the two-layered fluid model with non-Newtonian Jeffery fluid in the core region, and Newtonian fluid is taken close to walls in a channel with heat transfer and fluid slip effects. Ali et al. [21] worked on peristaltic transport in an axisymmetric tube with FENE-P fluid in the core region. They focused on electro-osmosis effects. Again, Ali et al. [22] reported similar flow with Ellis fluid in the core region. Rajashekhar et al. [23] assumed the Herschel–Bulkley model for the flow in the core region of so-called blood flow. Tripathi et al. [11] worked on Bingham and power-law fluid in a channel. The results are extended for three-layer fluids by Tripathi et al. [24] and were reported in 2017.

Mathematical simulations of many biologically inspired systems are developed and produced effect outputs in finding the cure or histories of many biologically inspired systems. Since decades, these models and simulation are vital in reducing animal experimentation [25–29]. So, major contributions of the current work can be overviewed as

(i) This article endures some novel applications of the flow of two-layer fluid in a flexible tube.

(ii) The complex peristaltic wave travels along the surface of the tube. As described by Dobrolyubov and Douchy [30] that the geometric form of a peristaltic wave in the intestine is complex most of the time, therefore, this study is an effort to describe flow as close to the real physiological problem as possible.

(iii) The two-layer flow of nanofluid and Johnson–Segalman fluid in the flexible tube with a compliant wall is evaluated analytically along with the effects of the partial porous medium and catheter.

The creeping flow and long-wavelength approximation are assumed and perturbation is employed to evaluate the solution. Structure of the investigation is arranged as follows. Section 2 discusses the mathematical modelling of the whole phenomenon through geometrical description and derivations of the quantitative expressions from main physical laws. Section 3 suggests the methodology of the solution to handle the obtained systems of equations. In Section 4, results are revealed in the form of graphs and tables and discussed with profound depth. Lastly, a few significant conclusions are drawn from the recent investigation and are furnished in Section 5.

2. Theory and Mathematical Model

2.1. Geometry of the Problem. An infinitely long circular axisymmetric co-centric cylinder, as illustrated in Figure 1, is the area of interest in current communication. Furthermore, a complex sinusoidal wave travels along z-axis on the outer cylinder which is passing through the centre of pipe along with wavelength λ, speed of wave c, amplitudes b_i, and the pipe radius a_0. The inner pipe has a radius of a_ϵ and is considered stationary. The motion of wave on a flexible wall is mathematically defined as

$$R_0(z,t) = \pm a_0 \pm b_1 \cos\left[\frac{2\pi}{\lambda}(z-ct)\right] \pm b_2 \cos\left[\frac{4\pi}{\lambda}(z-ct)\right]. \tag{1}$$

Mathematically inner cylinder can be represented as

$$R_\epsilon(z,t) = a_\epsilon. \tag{2}$$

Here, z designates the direction of propagation of the wave, i.e., parallel to the z-axis. The outer cylinder is kept at a temperature T_1, while the inner cylinder is at a temperature $T_0 < T_1$ The core region is also assumed to be saturated by non-Newtonian Johnson–Segalman fluid. While region close to the outer pipe wall is porous and is saturated by Newtonian nanofluid. Both the fluids are immiscible and separated at

$$R(z,t) = a_1. \tag{3}$$

2.2. Porous Media. A porous medium is a space defined by solid with void space uniformly distributed in the whole region, which allows fluid to transport but with some resistive force called Darcy's forces. These mediums help to uphold the heat in porous systems. The application and usage of porous media in engineering can be underlined in various fields such as petroleum engineering, rock and soil mechanics, hydrogeology, and, more recently, in bioengineering and biology. Many scientists have established their interest in considering heat transfer biologically inspired flow in permeable domains [31–35].

The basic feature of the porous medium is porosity which can be defined as the ratio of the volume of free space

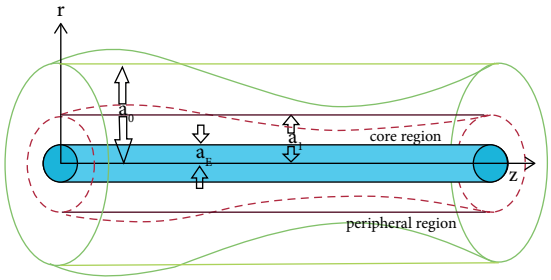

Figure 1: Geometry of the problem.

to the volume of the full body. Usually, the value of porosity is 0.45, with dense materials and compact structure; it reduces to 0.25 and so.

The velocity V of fluid flow hinges on permeability and pressure gradient as defined by the modified Darcy equation:

$$-\frac{dp}{dy} = \alpha\mu V + \beta\rho V^2. \tag{4}$$

Here, the coefficient α defines loss due to friction generated by the viscosity of fluid and shape of a porous medium. The inertial parameter β incorporates loss in inertial due to bend in porous spaces and other factors; it is proportional to ρV2.

The modified Darcy equation is universal relation and defines fluid flow in porous spaces.

At a low Reynolds number, the inertial term in equation (1) can be neglected and becomes

$$-\frac{dp}{dy} = \frac{\mu}{K}V. \tag{5}$$

Here, $K = 1/\alpha$ is known as the Darcy permeability.

2.3. Nanofluids. A solid-liquid suspension is engineered in such a way that nanosized particles are uniformly distributed and do not agglomerate in a base fluid. These nanosized particles are usually oxides and carbides of metal or carbon nanotubes. Base fluid can be any liquid that is oils or water with low thermal conductivity. These fluids exhibit enhanced thermal conductivity which makes it imperative to gain knowledge of the rheology of nanofluid before its usage. Application of these fluids is in solar energy storage, microelectronics, fuel cells, pharmaceutical process, hybrid engines, chillers, and other machines related to heat transfer. Nanofluids also show special properties with the magnetic field, acoustics and ultrasound, etc. [36–40].

Mathematical models of this fluid was described by Buongiorno [41]. He observed an abnormal increase in thermal conductivity, viscosity, and heat transfer rate coefficient. It is due to the nanofluid property of the thermophoresis and Brownian motion.

If J is diffusion mass flux of the nanoparticle w.r.t. fluid velocity, then it can be written as the sum of Brownian motion and thermophoresis; if no external force is applied,

$$-\frac{1}{\rho}\nabla\cdot\mathbf{J} = \frac{\partial\varphi}{\partial t} + \mathbf{V}\cdot\nabla\varphi = \nabla\cdot\left[\mathbf{D_B}\nabla\varphi + \mathbf{D_B}\frac{\nabla T}{T}\right], \tag{6}$$

where φ is the concentration of nanoparticles and D_B and DT are due to the slip velocity of particles caused by Brownian motion and thermophoresis. The energy equations for nanofluids are

$$\rho c\left[\frac{\partial\mathbf{T}}{\partial t} + \mathbf{V}\cdot\nabla\mathbf{T}\right] = -\nabla\cdot\mathbf{q} + h_p\nabla\cdot\mathbf{J}. \tag{7}$$

Neglecting radiative heat transfer, q can be calculated as the conduction heat flux, c is heat capacity, and h_p is specific enthalpy.

2.4. Constitutive Equation of Johnson–Segalman Fluid. The Johnson–Segalman fluid [42] defines nonmonotonically related shear stress and rate of shear for some values of the parameter of material. Spurt is an example of the property of this model.

Johnson and Segalman initially suggested an integral approach to the model, but rate type form can be derived. Considering appropriate parameters, the mathematical form of Johnson Segalman fluid [43] can be written as

$$\begin{aligned} S + \lambda\left(\begin{array}{c}\dfrac{DS}{Dt} + S(W - a\ D) + \\ \\ (W - a\ D)^T S\end{array}\right) &= 2\mu\ D, \\ T &= -2\mu\ D + S, \\ \sigma &= -pI + T. \end{aligned} \tag{8}$$

Here, $W = 1/2[L - L^T]$ is skew-symmetric and $D = 1/2[L - L^T]$ is symmetric part of velocity gradient, D/Dt is material derivative, λ is relaxation time, and a is called slip coefficient. The special case of this model can be achieved if

(a) $a = 1$: it becomes Olyroyd-B model

(b) $a = 1$ and $\mu = 0$: Maxwell model

(c) $\lambda = 0$: Newtonian fluid

2.5. Flow Problem. Modelling of flow in fluid transport problems usually involves four equations each, i.e.,

(i) Continuity equation as a consequence of the law of conservation of mass

(ii) Momentum equation due to law of conservation of momentum

(iii) Energy equation as defined by the law of conservation of energy

(iv) Nanoparticle concentration equation

In current communication, these equations are divided into two regions so-called core and the peripheral region.

The core region is saturated with Johnson–Segalman fluid and the porous peripheral region is filled with a nanofluid.

2.5.1. Peripheral Region

$$\left(\frac{\partial C}{\partial t}+\overline{u}\frac{\partial C}{\partial \overline{z}}+w\frac{\partial C}{\partial r}\right)=D_b\left(\frac{\partial^2 C}{\partial \overline{z}^2}+\frac{\partial^2 C}{\partial \overline{r}^2}+\frac{1}{\overline{r}}\frac{\partial C}{\partial \overline{r}}\right)+\frac{D_t}{T_0}\left(\frac{\partial^2 T}{\partial \overline{z}^2}+\frac{\partial^2 T}{\partial \overline{r}^2}+\frac{1}{\overline{r}}\frac{\partial T}{\partial \overline{r}}\right),$$

$$\rho c_p\left(\frac{\partial T}{\partial t}+\overline{u}\frac{\partial T}{\partial \overline{z}}+w\frac{\partial \overline{v}}{\partial r}\right)=k\left(\frac{\partial^2 T}{\partial \overline{z}^2}+\frac{\partial^2 T}{\partial \overline{r}^2}+\frac{1}{\overline{r}}\frac{\partial T}{\partial \overline{r}}\right),$$

$$+\mu\left(2\left(\left(\frac{\partial u}{\partial \overline{r}}\right)^2+\left(\frac{\partial w}{\partial \overline{z}}\right)^2\right)+\left(\frac{\partial u}{\partial z}+\frac{\partial w}{\partial r}\right)^2\right),$$

$$+\tau\begin{pmatrix} D_b\left(\frac{\partial C}{\partial \overline{r}}\frac{\partial T}{\partial \overline{r}}+\frac{\partial C}{\partial \overline{z}}\frac{\partial T}{\partial \overline{z}}\right)+ \\ \\ \frac{D_t}{T}\left(\left(\frac{\partial T}{\partial \overline{r}}\right)^2+\left(\frac{\partial T}{\partial \overline{z}}\right)^2\right)\end{pmatrix}, \tag{9}$$

$$-\frac{\mu}{K}w+\rho g\beta\left(T-T_0\right)+\rho g\beta\left(C-C_0\right),$$

$$\rho\left(\frac{\partial w}{\partial t}+\overline{u}\frac{\partial w}{\partial \overline{z}}+w\frac{\partial w}{\partial r}\right)=-\frac{\partial \overline{p}}{\partial z}+\mu\left(\frac{\partial^2 w}{\partial \overline{z}^2}+\frac{\partial^2 w}{\partial \overline{r}^2}+\frac{1}{\overline{r}}\frac{\partial w}{\partial \overline{r}}\right),$$

$$\rho\left(\frac{\partial \overline{u}}{\partial t}+\overline{u}\frac{\partial \overline{u}}{\partial \overline{z}}+w\frac{\partial \overline{u}}{\partial r}\right)=-\frac{\partial \overline{p}}{\partial r}+\mu\left(\frac{\partial^2 \overline{u}}{\partial \overline{z}^2}+\frac{\partial^2 \overline{u}}{\partial \overline{r}^2}+\frac{1}{\overline{r}}\frac{\partial \overline{u}}{\partial \overline{r}}\right),$$

$$\frac{\partial \overline{u}}{\partial \overline{z}}+\frac{1}{\overline{r}}\frac{\partial\left(w\overline{r}\right)}{\partial \overline{r}}=0.$$

2.5.2. Core Region

$$\frac{\partial \overline{u}}{\partial \overline{z}}+\frac{1}{\overline{r}}\frac{\partial\left(w\overline{r}\right)}{\partial \overline{r}}=0, \tag{10}$$

$$\rho\left(\frac{\partial \overline{u}}{\partial t}+\overline{u}\frac{\partial \overline{u}}{\partial \overline{z}}+w\frac{\partial \overline{u}}{\partial r}\right)=-\frac{\partial \overline{p}}{\partial \overline{r}}+\mu\left(\frac{\partial^2 \overline{u}}{\partial \overline{z}^2}+\frac{\partial^2 \overline{u}}{\partial \overline{r}^2}+\frac{1}{\overline{r}}\frac{\partial \overline{u}}{\partial \overline{r}}\right)+\left(\frac{\partial S_{\overline{rz}}}{\partial \overline{z}}+\frac{S_{\overline{rr}}}{\overline{r}}+\frac{\partial S_{\overline{rr}}}{\partial \overline{r}}-\frac{S_{\theta\theta}}{\overline{r}}\right), \tag{11}$$

$$\rho\left(\frac{\partial w}{\partial t}+\overline{u}\frac{\partial w}{\partial \overline{z}}+w\frac{\partial w}{\partial r}\right)=-\frac{\partial \overline{p}}{\partial \overline{z}}+\mu\left(\frac{\partial^2 w}{\partial \overline{z}^2}+\frac{\partial^2 w}{\partial \overline{r}^2}+\frac{1}{\overline{r}}\frac{\partial w}{\partial \overline{r}}\right)+\left(\frac{\partial S_{\overline{zz}}}{\partial \overline{z}}+\frac{S_{\overline{zr}}}{\overline{r}}+\frac{\partial S_{\overline{zr}}}{\partial \overline{r}}\right), \tag{12}$$

$$\rho c_p\left(\frac{\partial T}{\partial t}+\overline{u}\frac{\partial T}{\partial \overline{z}}+w\frac{\partial T}{\partial r}\right)=k\left(\frac{\partial^2 T}{\partial \overline{z}^2}+\frac{\partial^2 T}{\partial \overline{r}^2}+\frac{1}{\overline{r}}\frac{\partial T}{\partial \overline{r}}\right)+S_{rr}\frac{\partial u}{\partial r}+S_{rz}\frac{\partial u}{\partial z}+S_{zr}\frac{\partial w}{\partial r}+S_{zz}\frac{\partial w}{\partial z}. \tag{13}$$

Using the dimensionless parameters,

$$\left.\begin{aligned} r* &= \frac{r}{R_0}, z^* = \frac{z}{\lambda}, w^* = \frac{w}{c}, u^* = \frac{u}{c\delta}, t^* = \frac{ct}{\lambda}, \\ \mathrm{Re} &= \frac{\rho a c}{\mu}, \delta = \frac{a}{\lambda}, H = \frac{T - T_0}{T_1 - T_0}, M = \frac{C - C_0}{C_1 - C_0}, \\ G_r &= \frac{\rho_f g \alpha a^2}{\mu_f c} T_0, p^* = \frac{a^2 p}{\mu_f c \lambda}, \phi_1 = \frac{b_1}{a_0}, \phi_2 = \frac{b_2}{a_0}. \end{aligned}\right\} \quad (14)$$

Employing nondimensional variables in equations (11)–(19) and using long wavelength and low Reynolds number approximation, the equations for peripheral and core region become as follows.

2.5.3. Peripheral Region in Dimensionless Form

$$0 = \frac{\partial \overline{p}}{\partial r}, \quad (15)$$

$$0 = -\frac{\partial \overline{p}}{\partial z} + \left(\frac{\partial^2 w_1}{\partial \overline{r}^2} + \frac{1}{\overline{r}}\frac{\partial w_1}{\partial \overline{r}}\right) - Da\left(w_1 + 1\right) + GrH_1 + BrM_1, \quad (16)$$

$$0 = \frac{\partial^2 H_1}{\partial \overline{r}^2} + \frac{1}{\overline{r}}\frac{\partial H_1}{\partial \overline{r}} + Br\left(\left(\frac{\partial w_1}{\partial r}\right)^2\right) + N_b\left(\frac{\partial M_1}{\partial \overline{r}}\frac{\partial H_1}{\partial \overline{r}}\right) + N_t\left(\left(\frac{\partial H_1}{\partial \overline{r}}\right)^2\right), \quad (17)$$

$$0 = N_b\left(\frac{\partial^2 M_1}{\partial \overline{r}^2} + \frac{1}{\overline{r}}\frac{\partial M_1}{\partial \overline{r}}\right) + N_t\left(\frac{\partial^2 H_1}{\partial \overline{r}^2} + \frac{1}{\overline{r}}\frac{\partial H_1}{\partial \overline{r}}\right). \quad (18)$$

2.5.4. Core Region in Dimensionless Form

$$0 = \frac{\partial \overline{p}}{\partial \overline{r}} \quad (19)$$

$$0 = -\frac{\partial \overline{p}}{\partial z} + \frac{\partial^2 w_2}{\partial \overline{r}^2} + \frac{1}{\overline{r}}\frac{\partial w_2}{\partial \overline{r}} + \frac{S_{\overline{zr}}}{\overline{r}} + \frac{\partial S_{\overline{zr}}}{\partial \overline{r}}, \quad (20)$$

$$0 = \frac{\partial^2 H_2}{\partial \overline{r}^2} + \frac{1}{\overline{r}}\frac{\partial H_2}{\partial \overline{r}} + Br\left(S_{zr}\frac{\partial w_2}{\partial r}\right), \quad (21)$$

$$Srr = We(1 + a)S_{zr}\frac{\partial w_2}{\partial r}, Szz = -We(1 - a)S_{zr}\frac{\partial w_2}{\partial r}, Srz = \frac{\eta/\mu_r \partial w_2/\partial r}{1 + We^2\left(1 - a^2\right)\left(\partial w_2/\partial r\right)^2}. \quad (22)$$

2.5.5. Boundary Conditions

$$r_2 = 1 + \phi_1 \cos 2\,\pi(z - t) + \phi_2 \cos 4\,\pi(z - t),$$

$$\begin{cases} w_1 = -1,\ H_1 = 0,\ @r = r_\epsilon \\ w_1 = w_2,\ H_1 = H_2,\ M = 0, \\ \dfrac{\eta/\mu_r \partial w_2/\partial r}{1 + We^2\left(1 - a^2\right)\left(\partial w_2/\partial r\right)^2} = \partial w_1/\partial r, \partial \mathrm{H}_1/\partial r = \dfrac{\partial H_2}{\partial r}, \quad @\, r = r_1 \\ w_2 = -1,\ H_2 = 1,\ M = 1,\ @\, r = r_2 \end{cases} \quad (23)$$

In addition to these constraints, we are also imposing the condition of compliant walls [14, 44, 45] on the outer surface which is defined as the continuity of stress at $r = r_2$:

$$\frac{\mathrm{d}p}{\mathrm{d}z} = E_1\frac{\partial^3 r_2}{\partial z^3} + E_2\frac{\partial^3 r_2}{\partial t^2 \partial z} + E_3\frac{\partial^2 r_2}{\partial t\,\partial z}. \quad (24)$$

By taking the Wissenburg number very small, i.e., $O(We^2)$, we get the following results from equation (18)–(21) and B.Cs. (22):

$$
\begin{aligned}
0 &= \frac{\partial \overline{p}}{\partial \overline{r}},\\
0 &= -\frac{\partial \overline{p}}{\partial z} + \left(1 + \frac{\eta}{\mu_r}\right)\frac{\partial^2 w_2}{\partial \overline{r}^2} + \frac{1}{\overline{r}}\left(1 + \frac{\eta}{\mu_r}\right)\frac{\partial w_2}{\partial \overline{r}},\\
0 &= \frac{\partial^2 H_2}{\partial \overline{r}^2} + \frac{1}{\overline{r}}\frac{\partial H_2}{\partial \overline{r}} + Br\frac{\eta}{\mu_r}\left(\frac{\partial w_2}{\partial r}\right)^2,\\
&\begin{cases}
w_1 = -1,\ H_1 = 0,\ atr = r_\epsilon\\
w_1 = w_2,\ H_1 = H_2,\ C = 0,\\
\dfrac{\eta}{\mu_r}\dfrac{\partial w_2}{\partial r} = \dfrac{\partial w_1}{\partial r},\ \dfrac{\partial H_1}{\partial r} = \dfrac{\partial H_2}{\partial r} \quad atr = r_1,\\
w_2 = -1,\ H_2 = 1,\ C = 1,\ atr = r_2.
\end{cases}
\end{aligned}
\tag{25}
$$

3. Solution Method

Mathematical modelling of the whole problem discussed above suggests that the two systems (peripheral and core regions) of coupled equations (21)–(27) are to be solved along with the coupled boundary limitations defined in equation (25). The system of the core region has been solved by an exact method, and the results are elaborated underneath:

$$
\begin{aligned}
H_2 &= C_6 + \frac{1}{4}\left(-\frac{C_{15}Brr^2\eta\left(C_{15}r^2\mu_r + 16C_1(\eta + \mu_r)\right)}{16(\eta + \mu_r)^2} + 4C_5 Log[r] - \frac{2BrC_1^2\eta Log[r]^2}{\mu_r}\right),\\
w_2 &= \frac{r^2\mu_r}{4(\eta + \mu_r)}C_{15} + C_2 + C_1 Log[r].
\end{aligned}
\tag{26}
$$

On the contrary, the system of the peripheral region cannot be solved exactly, so we adopted the scheme of perturbation (HPM) [46–48] in which the same linear operator is chosen for velocity, heat, and energy functions, i.e., $\mathscr{H} = \partial^2/\partial r^2 + 1/r\partial/\partial r$. After using the routine calculation of HPM, the final solutions have been composed in subsequent forms:

$$
\begin{pmatrix}
768C_{14}Nb + 3BrC_{15}r^2\begin{pmatrix} 32C_3(Nb + Nt) \\ +(Nb + 3Nt)G_1r^2 \end{pmatrix} + \\
\frac{1}{Log[r2] - Log[r\varepsilon]}\times \\
\begin{pmatrix}
128\,(\,(Nbt - nNqt)Log[r]^3(C_7Nb + \\
\left(BrC_3{}^2 + C_7{}^2Nt\right) \\
(Log[r_2] - Log[r_\varepsilon]) \\
+3Log[r]^2(C_7NbNt - \\
\left(C_{11}(Nb - Nt) - Nt\left(BrC_3^2 + C_7^2Nt\right)\right) \\
(Log[r_2] - Log[r_\varepsilon])) - 6NbLog[r_\varepsilon] + \\
6NbLog[r]1 + (C_{13}Log[r_2] \\
-C_{13}Log[r_\varepsilon])
\end{pmatrix}
\end{pmatrix}
$$

$$
\begin{aligned}
M_1 &= \frac{1}{768Nb}\times,\\
H_1 &= C_{12} + C_8 - \frac{1}{64}BrC_{15}r^2\left(16C_3 + C_{15}r^2\right) + \left(C_{11} + C_7\right)Log[r] + \frac{1}{2}Log[r]^2\\
&\quad \left(-BrC_3{}^2 + C_7\left(-C_7Nt + \frac{Nb}{-Log[r_2] + Log[r_\varepsilon]}\right)\right),\\
&\quad + \frac{r^2\begin{pmatrix} -\left(\left(-1 + C_3 - C_4\right)Da + \left(-C_7 + C_8\right)Gr\right)\\ \left(Log[r_2] - Log[r_\varepsilon]\right) + Br\left(1 + Log[r_\varepsilon]\right)\end{pmatrix}}{4\left(Log[r_2] - Log[r_\varepsilon]\right)} + \frac{1}{4}r^2Log[r]\left(C_3Da - C_7Gr + \frac{Br}{-Log[r_2] + Log[r_\varepsilon]}\right),\\
w_1 &= C_{10} + C_4 + \frac{C_{15}r^2}{4} + \frac{1/64Da\ C_{15}}{r^4} + C_3Log[r] + C_9Log[r],
\end{aligned}
\tag{27}
$$

where the constants C_n, $n = 1, 2, 3, \ldots 14$, are found by using B.Cs. (26) and are written in Appendix.

4. Results and Discussion

This section involves some graphical discussion based on the theoretical data achieved in the preceding section where we have collected analytical readings of observable sections of the study along with the compliant walls' phenomenon. To deal with this, we have captured some graphs of obtained analytical statistics of velocity, temperature, nanoparticles' fraction, and stream functions. Figures 2–8 reflect the sketches for the velocity field, Figures 9–13 for temperature, Figures 13–19 for nanoparticles, and Figures 20–23 for streamlines. Above mentioned graphs contain the behaviour of said profiles for both the peripheral and core regions. From these plots, we imagine that how a quantity varies against the including factor theoretically, and its matching with the physical aspects are also being stated.

4.1. Velocity Variation. Figure 2 contemplates the impact of the viscosity ratio parameter μ_r on the curves of velocity function w plotted along the radial coordinate r. After viewing this figure, we can state that velocity is showing direct variance with the rising impact of the said parameter. It is also to be mentioned here that blue lines carry the information of the peripheral portion while red lines convey the core region data. It is also noted that the peripheral region gives more parabolic curves than the core region and the velocity gets maximum in the central slab. On the contrary, the core region contains the more flatter curves which predict that velocity varies linearly with the radial coordinate and becomes minimum at the walls. Figure 3 depicts the variation of velocity for the parameter E_1 which accounts for mass per unit area. It can be started from the said graph that velocity is varying in increasing fashion when we increase the values of the factor E_1. It is also noted that very smooth and similar behaviour can be concluded in both regions. From Figures 4 and 5, we can visualize the effects of viscous damping force E_2 and flexure rigidity of the walls E_3, respectively, on the velocity envelop. It is found here that velocity is minimum at the static walls due to no slip at the boundaries, but it goes large in the middle lump of the domain between the peripheral and core regions. From Figure 6, it can be estimated that Brinkman number Br exerts a direct impact on velocity in the peripheral region, but the core region experiences no difference in velocity with the variation of the said factor which can be observed by a single bold red line in the figure. Figure 7 reveals the behaviour of fluid velocity under the variation of Darcy's number Da, and it can be suggested here that, in the peripheral region, velocity curves are suppressed with the increasing amount of Darcy's number, but on the core side, we receive no variance which suggests that porosity factors are only present on the outside walls and not on the inner surface of the channel. This variation can be physically justified as that due to pores on the peripheral region velocity of the fluid gets decreased as some molecules are resisted by the porous wall and gets sucked into the boundary causing the reduction in the flow speed. Figure 8 shows that velocity is depending on Grashof number Gr directly in the peripheral region, but there is no effect of the said factor in a core region which shows that the nanoparticles contribute significantly only in the mainstream of the flow.

4.2. Thermal Exchange. Figure 9 implies the variation of temperature distribution profile H under the variation of Brinkman number Br along the radial axis. It is measured from this plot that temperature goes direct with the Brinkman number. It is physically found from the graph that when we provide a large value to the Brinkman number, the heat is transferred to a large extent in the peripheral region, but in the core region, the variation remains direct but consistent. It is also found that maximum thermal exchange is reported at $r = 0 \cdot 3$, and then, after that, it starts decreasing throughout the domain. Figure 10 suggests that fluid dynamic viscosity factor η imposes inverse impact on the profile of temperature difference in the peripheral region which can be found in the graph through blue curves, but red curves are showing that, in the core region, heat is transferred at a very small rate which depicts that there is a very slight impact of fluid dynamic viscosity features in the core region regarding a change in temperature. When we look at Figure 11, we approach the fact that the Johnson–Segalman

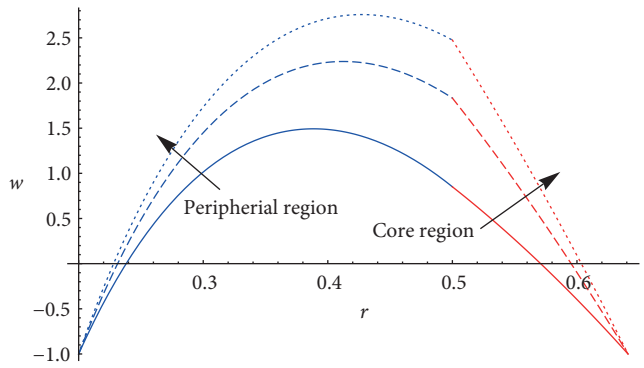

Solid line $\mu_r = 0.1$
Dashed line $\mu_r = 0.2$
Dotted line $\mu_r = 0.3$

Figure 2: Variation in velocity vs. radius of pipe for both fluids with changes in μ_r.

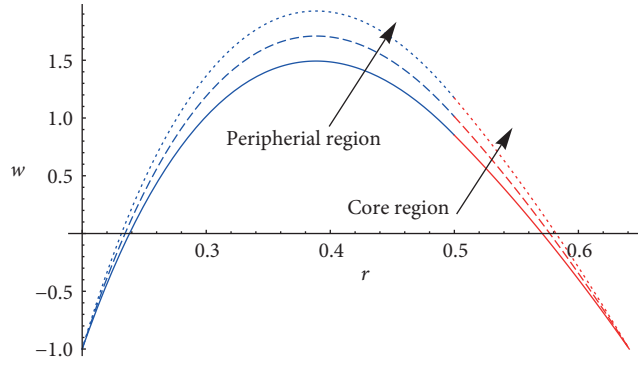

Solid line $E_1 = 0.1$
Dashed line $E_1 = 0.2$
Dotted line $E_1 = 0.3$

Figure 3: Variation in velocity vs. radius of pipe for both fluids with changes in E_1.

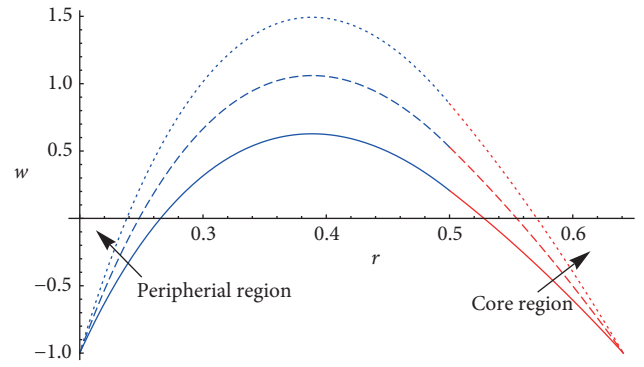

Solid line $E_2 = 0.5$
Dashed line $E_2 = 0.7$
Dotted line $E_2 = 0.9$

Figure 4: Variation in velocity vs. radius of pipe for both fluids with changes in E_2.

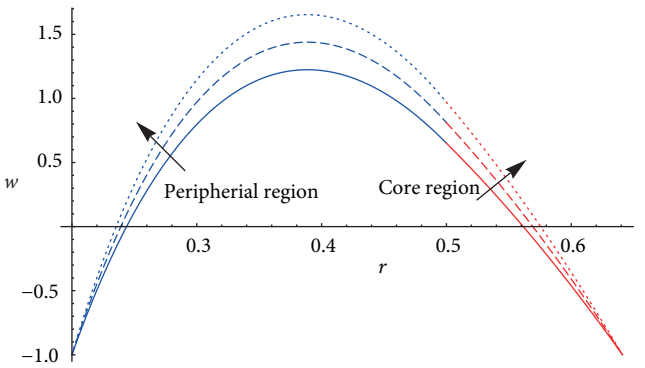

Solid line $E_3 = 0.1$
Dashed line $E_3 = 0.5$
Dotted line $E_3 = 0.9$

Figure 5: Variation in velocity vs. radius of pipe for both fluids with changes in E_3.

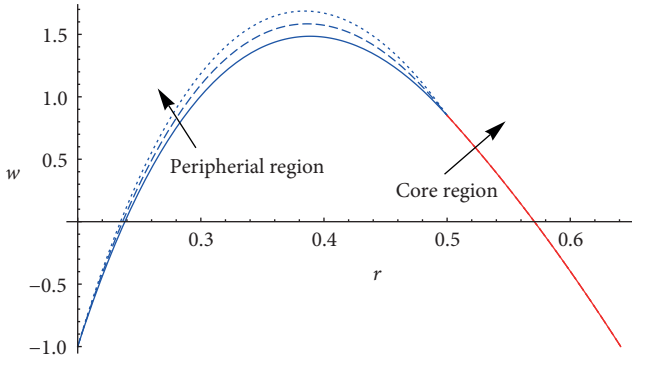

Bold line Br = 0.5
Dashed line Br = 5.0
Dotted line Br = 10

Figure 6: Variation in velocity vs. radius of pipe for both fluids with changes in Br.

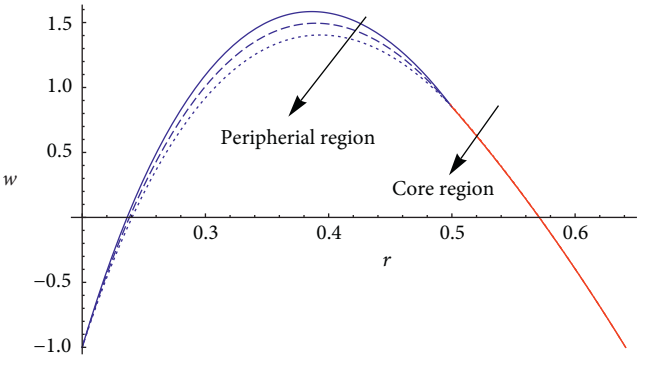

Solid line Da = 0.1
Dashed line Da = 4
Dotted line Da = 8

Figure 7: Variation in velocity vs. radius of pipe for both fluids with changes in Da.

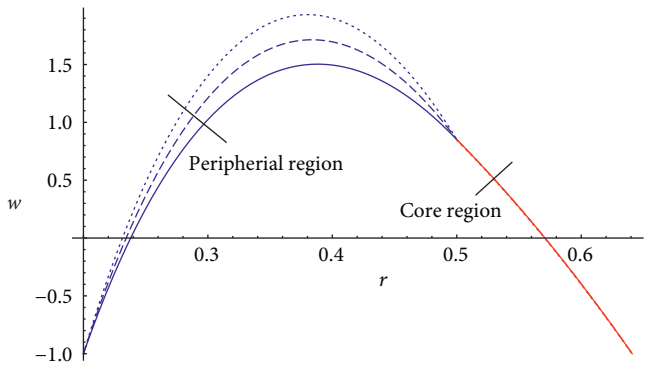

Solid line Gr = 0.10
Dashed line Gr = 05
Dotted line Gr = 10

Figure 8: Variation in velocity vs. radius of pipe for both fluids with changes in Gr.

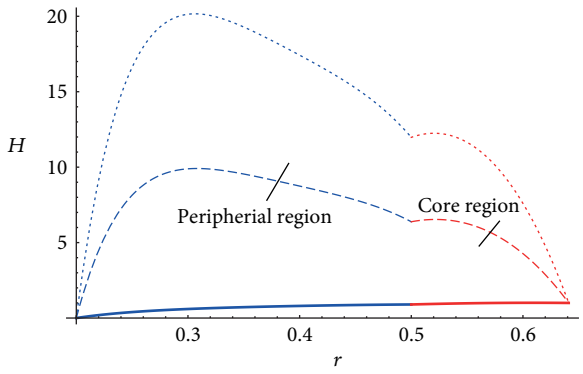

Bold line Br = 0.1
Dashed line Br = 5.0
Dotted line Br = 10

Figure 9: Variation in temperature vs. radius of pipe for both fluids with changes in Br.

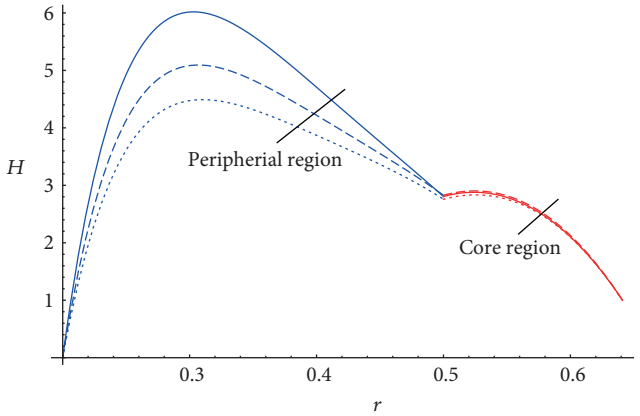

Bold line $\eta = 0.2$
Dashed line $\eta = 0.3$
Dotted line $\eta = 0.4$

Figure 10: Variation in temperature vs. radius of pipe for both fluids with changes in η.

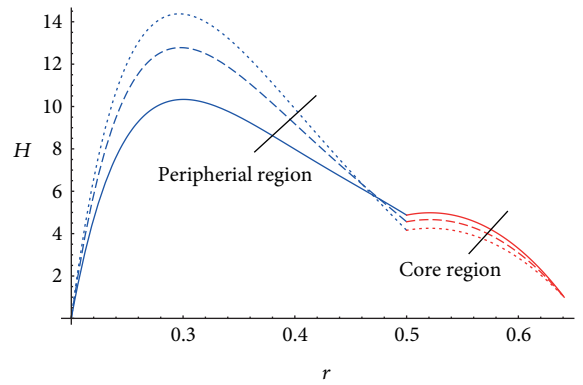

Solid line $\mu_r = 0.3$
Dashed line $\mu_r = 0.5$
Dotted line $\mu_r = 0.7$

Figure 11: Variation in temperature vs. radius of pipe for both fluids with changes in μ_r.

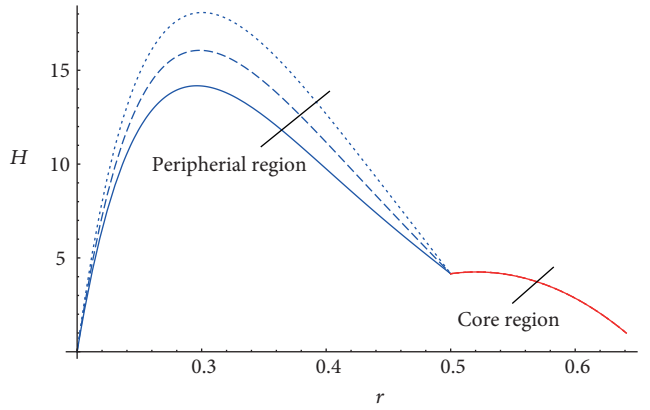

Bold line Nb = 0.3
Dashed line Nb = 5.0
Dotted line Nb = 10

Figure 12: Variation in temperature vs. radius of pipe for both fluids with changes in Nb.

fluid's variable viscosity μ_r is contributing to heat transfer indirect manner especially in the peripheral region which is in the region adjacent to the core region; also, in the whole core region, it puts inverse pressure on the thermal profile but at a lesser rate which results in decreasing the thermal transfer intensity. Figures 12 and 13 display the effects of Brownian diffusion Nb and thermophoresis diffusion Nt, accordingly on the heat exchange features. From both graphs, we receive almost the similar characteristics that are heat transfer curves rising in the peripheral region against both the factors, but there is no contribution of these two parameters in the core region as we have neglected their effects in the considered flow problem in the core region.

4.3. Nanoparticles' Phenomenon. As in the modelling section, we have considered the nanoparticles' phenomenon only in the core region, so we will here discuss the behaviour of nanoparticles' distribution only in the peripheral region.

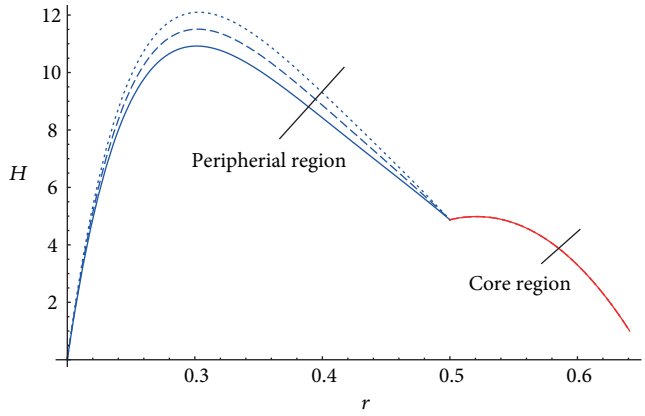

Bold line Nt = 0.3
Dashed line Nt = 0.5
Dotted line Nt = 0.7

Figure 13: Variation in temperature vs. radius of pipe for both fluids with changes in Nt.

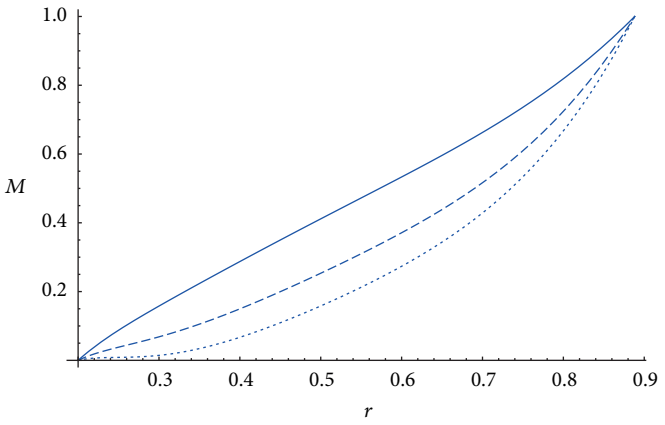

Solid line Br = 0.05
Dashed line Br = 0.10
Dotted line Br = 0.13

Figure 14: Variation in nanoparticles' concentration vs. radius of pipe for both fluids with changes in Br.

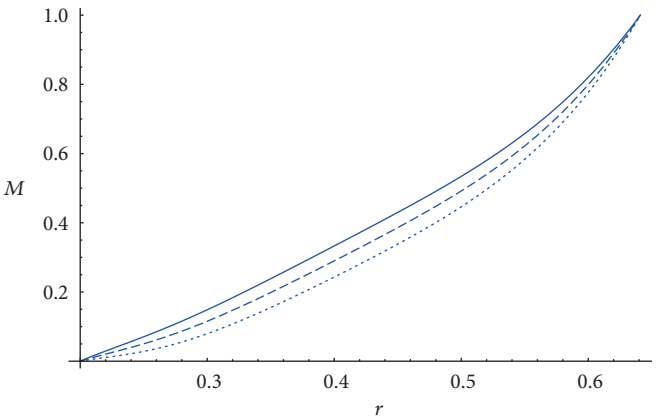

Solid line $E_1 = 0.1$
Dashed line $E_1 = 0.2$
Dotted line $E_1 = 0.3$

Figure 15: Variation in nanoparticles' concentration vs. radius of pipe for both fluids with changes in E_1.

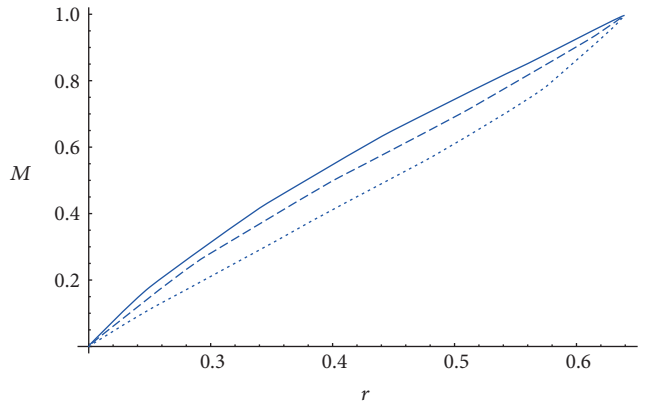

Solid line $E_2 = 0.1$
Dashed line $E_2 = 0.4$
Dotted line $E_2 = 0.7$

Figure 16: Variation in nanoparticles' concentration vs. radius of pipe for both fluids with changes in E_2.

Figure 14 discloses the effects of Brinkman number Br on the profile of nanoparticles' distribution M. It is noted here that Brinkman constant pushes back the nanoparticles' distribution. From Figure 15, it is concluded that rise in mass per unit factor E_1 results in decreasing nanoparticles' distribution which means that increase in mass of the compliant walls puts an inverse impact on the distribution of nanoparticles. The same behaviour is measured in front of viscous damping forces E_2 and flexure rigidity of the compliant walls E_3 which can be found in Figures 16 and 17, orderly, which implies the resistive effects of compliant walls on the nanoparticles' profile. From Figure 18, we can judge that viscosity μ_r shows inverse relation with the nanoparticles' flow rate, but in the domain $r > 0 \cdot 55$, almost constant characteristics are noted regarding the magnitude of nanoparticles' volume fraction. When we look at Figure 19, we come to the statement that Brownian diffusion factor Nb is directly proportional to the profile of M, but on the contrary, thermophoresis parameter Nt reflects opposite readings which can be visualized in Figure 20.

4.4. Streamlines' Discussion. Streamlines have been unveiled to discuss the flow sketches under the effects of some considerable features of the study. In Figure 21, the circulating bolus mechanism has been included for the factor E_1, and we have obtained that there are four portions, namely, 1st, 2nd, 3rd, and 4th quadrants taken in anticlockwise directions to discuss the flow pattern. In the first quadrant, the bolus volume increases for the value of $E_1 < 1$, but for $E_1 > 1$, the size is decreased, while in the 2nd portion, the size is continuously increasing. On the contrary, the 3rd and 4th quadrants reveal that bolus dimensions are decreasing. It is concluded here that an increase in mass/unit area of the

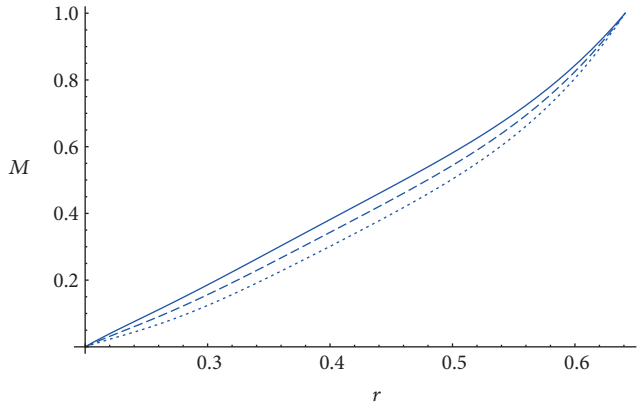

Solid line $E_3 = 0.1$
Dashed line $E_3 = 0.5$
Dotted line $E_3 = 0.9$

FIGURE 17: Variation in nanoparticles' concentration vs. radius of pipe for both fluids with changes in E_3.

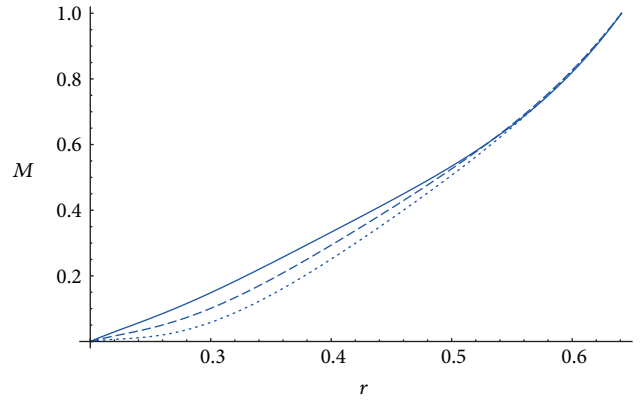

Solid line $\mu_r = 0.1$
Dashed line $\mu_r = 0.2$
Dotted line $\mu_r = 0.3$

FIGURE 18: Variation in nanoparticles' concentration vs. radius of pipe for both fluids with changes in μ_r.

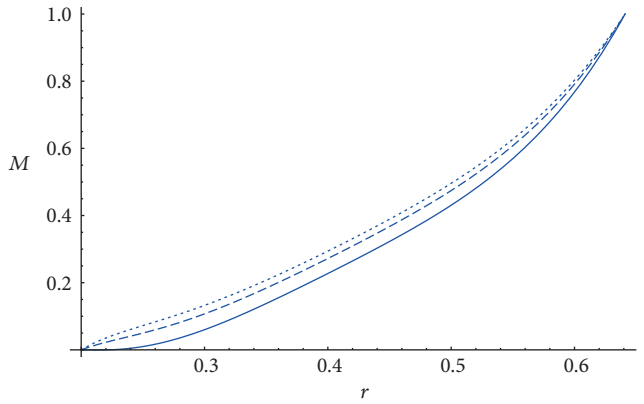

Solid line Nb = 0.5
Dashed line Nb = 0.7
Dotted line Nb = 0.9

FIGURE 19: Variation in nanoparticles' concentration vs. radius of pipe for both fluids with changes in *Nb*.

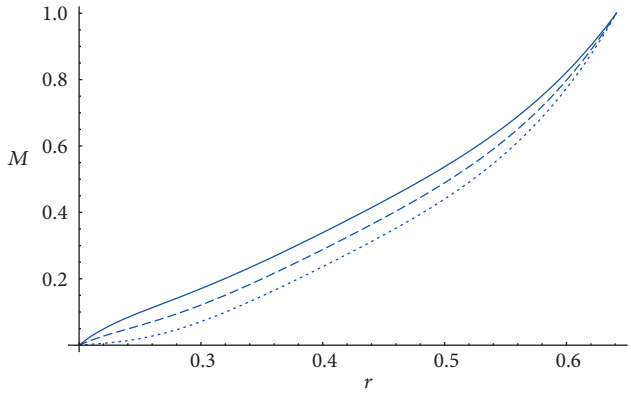

Solid line Nt = 0.1
Dashed line Nt = 0.2
Dotted line Nt = 0.3

Figure 20: Variation in nanoparticles' concentration vs. radius of pipe for both fluids with changes in Nt.

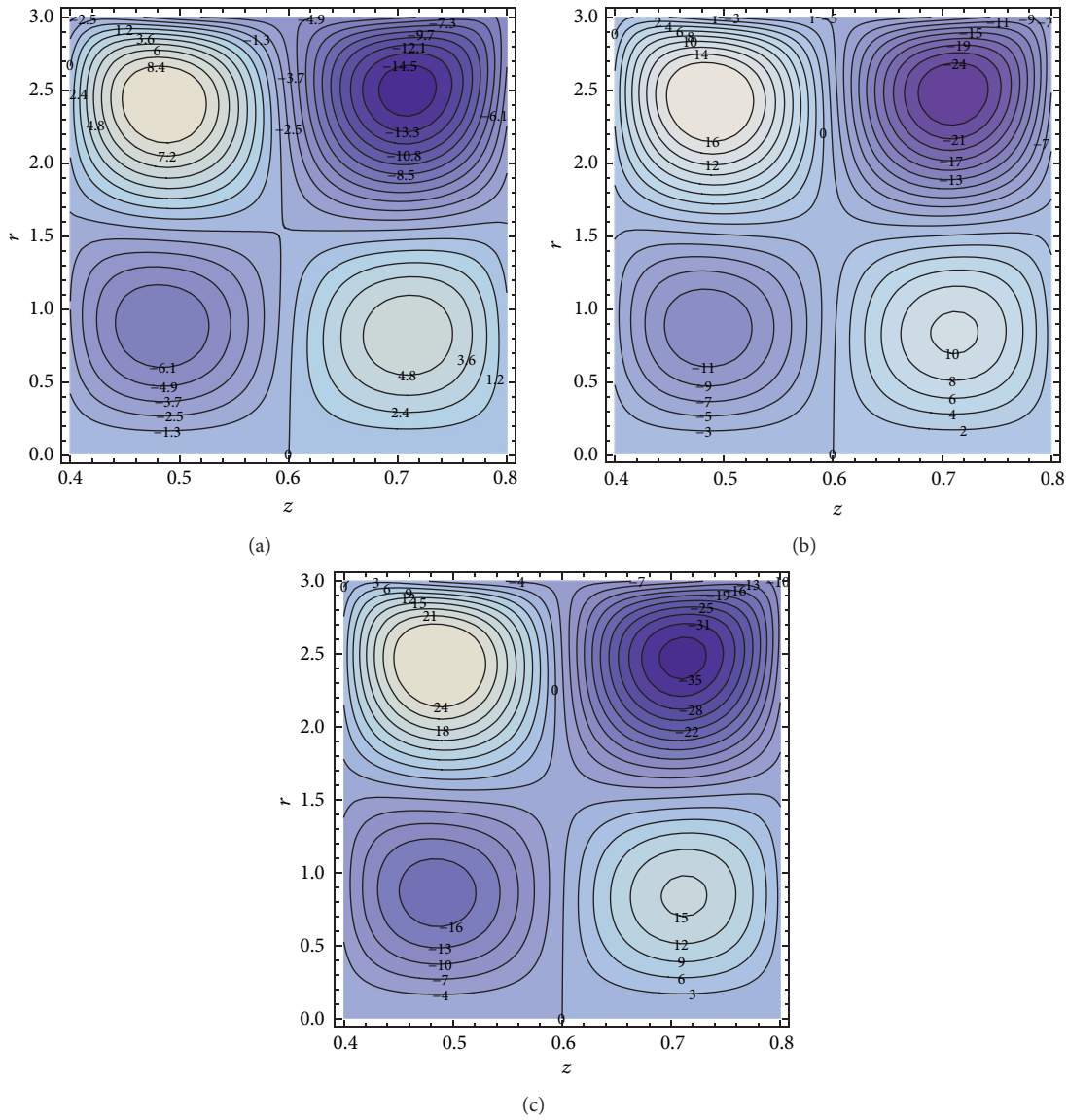

Figure 21: Variation in streamlines with E_1.

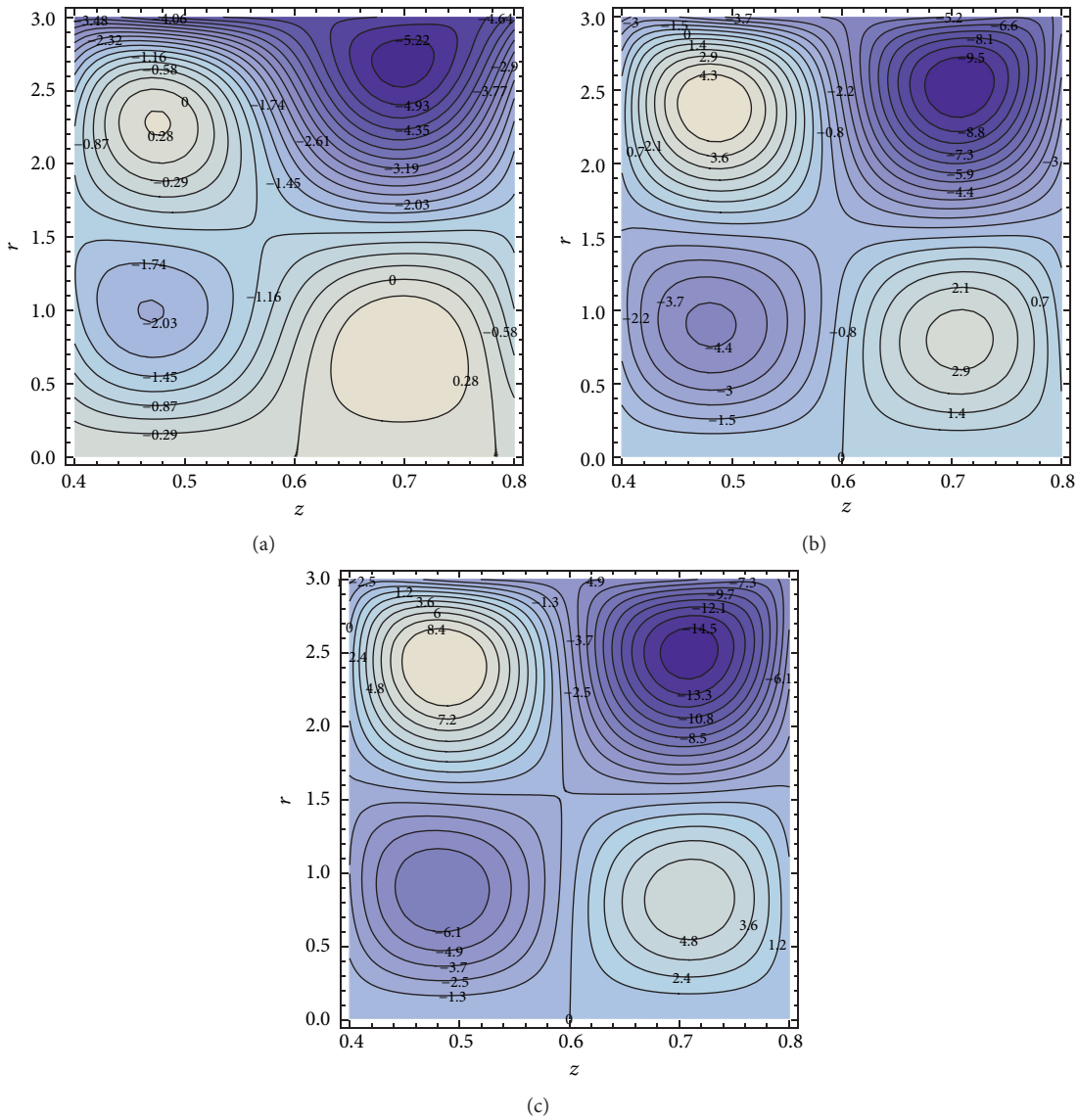

Figure 22: Variation in streamlines with E_2.

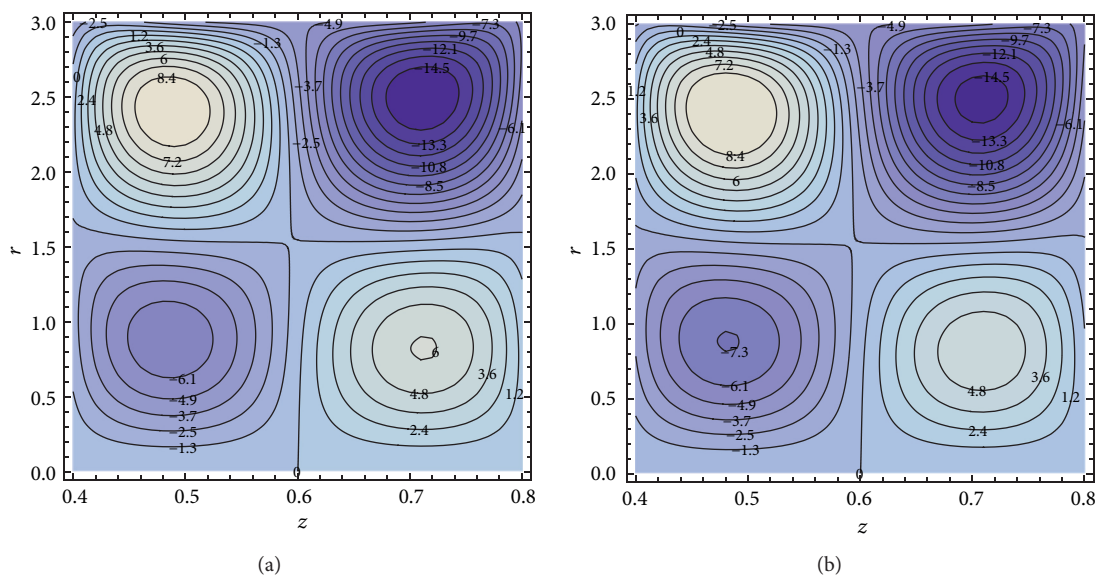

Figure 23: Continued.

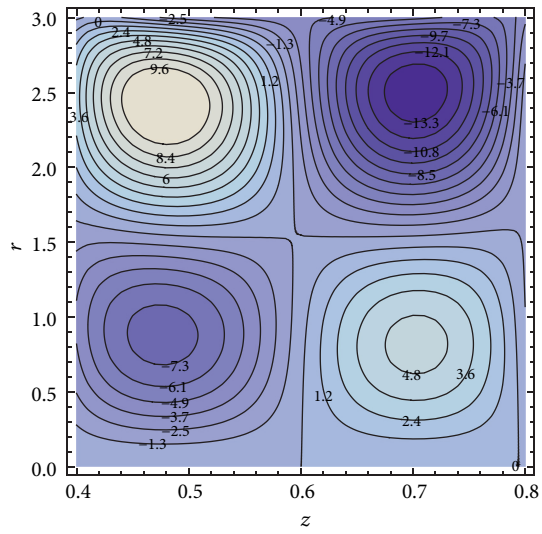

(c)

Figure 23: Variation in streamlines with E_3.

compliant walls puts pressure on the flow and in-response flow gets faster resulting decrease in the size of the boluses. Figure 22 describes the variation of stream boluses by the increasing variety of viscous damping force E_2. It can be decided here that most of the size of the space of the circulating contours is increasing, resulting in decrease in the flow rate which may be due to the large viscous damping forces pressure producing large boluses due to the lesser speed of the fluid. Figure 23 directs that in the 1st and 3rd quadrant, more boluses are produced with relatively lesser sizes for $E_3 < 1$, but for $E_3 > 1$, the situation is the opposite. On the contrary, the boluses in the rest of the quadrants are broken with a large magnitude of the parameter resulting in a decrease in the number of contours.

5. Concluding Remarks

Currently, we have discovered the theoretical analysis of the bi-layered flow of Johnson–Segalman/nanofluid with peristaltic phenomenon through an infinitely long circular axis-symmetric co-centric cylinder having flexible outer walls under the constraints of long wavelength and low Reynolds number. The flow has been observed in two layers, namely, peripheral and core regions. The unknown quantities of the core region have been achieved by exact solutions, but the peripheral region has been tackled by HPM. The developed analytic solutions have been sketched on Mathematica and discussed descriptively. From the above whole study, we collected the following important points:

(i) The velocity is an increasing function of fluid viscosity μ_r in both the regions, but the profile is much flatter in the core region as compared to the peripheral region, depicting the result that fluid viscosity affects the flow speed significantly in the peripheral region than the core region.

(ii) It is finalized that compliant walls are executing the same sort of effect on the flow characteristics in both the peripheral and core portions, and overall, the flow speeds up due to walls' compliance.

(iii) It should be added that velocity is enhanced due to the large intensity of Brinkman number and Grashof number which is not in the case of wall's porosity effects.

(iv) It can be stated that the Brinkman number increases the rate of thermal transfer in both the regions.

(v) It can also be placed here that the heat transfer rate is decreasing with increasing fluid viscosity η in the peripheral region.

(vi) It is found that nanoparticles' distribution goes backwards due to compliant walls, fluid's viscosity, Brinkman number, and thermophoresis factor but moves forward by the Brownian diffusion.

(vii) Due to the large mass per unit area of the compliant walls, the circulating contours are squeezed.

More research on the topic can be made by taking different types of nanoparticles and by considering their affective properties; also, the effects of magnetic field and electro-osmotic mechanism can be described in future. The study can be made by inclusion of electro-osmotic effects as well.

Appendix

A. List of Coefficients

$$C_1 = \frac{C_{15}\mu_r\left(-r_1{}^2\eta - r_2{}^2\mu_r + r_\varepsilon{}^2(\eta+\mu_r) + 2r_1{}^2\mu_r(Log[r_1] - Log[r_\varepsilon])\right)}{4(\eta+\mu_r)((\eta-\mu_r)Log[r_1] + \mu_r Log[r_2] - \eta Log[r_\varepsilon])}, \tag{A.1}$$

$$C_2 = \frac{1}{4}\left(-4 - \frac{C_{15}r_2^2\mu_r}{\eta+\mu_r} + \frac{C_{15}\mu_r Log[r_2]\left(r_1{}^2\eta + r_2{}^2\mu_r - r_\varepsilon{}^2(\eta+\mu_r) + 2r_1{}^2\mu_r(-Log[r_1] + Log[r_\varepsilon])\right)}{(\eta+\mu_r)((\eta-\mu_r)Log[r_1] + \mu_r Log[r_2] - \eta Log[r_\varepsilon])}\right), \tag{A.2}$$

$$C_3 = \frac{C_{15}\left(\eta\left(-r_1{}^2\eta - r_2{}^2\mu_r + r_\varepsilon{}^2(\eta+\mu_r)\right) + 2r_1{}^2\mu_r{}^2(\mathrm{Log}[r_1] - \mathrm{Log}[r_2])\right)}{4(\eta+\mu_r)((\eta-\mu_r)\mathrm{Log}[r_1] + \mu_r\mathrm{Log}[r_2] - \eta\mathrm{Log}[r_\varepsilon])}, \tag{A.3}$$

$$C_4 = \frac{1}{4}\left(-4 - C_{15}r_\varepsilon{}^2 + \frac{C_{15}\left(\eta\left(r_1{}^2\eta + r_2{}^2\mu_r - r_\varepsilon{}^2(\eta+\mu_r)\right) + 2r_1{}^2\mu_r{}^2(-\mathrm{Log}[r_1] + \mathrm{Log}[r_2])\right)\mathrm{Log}[r_\varepsilon]}{(\eta+\mu_r)((\eta-\mu_r)\mathrm{Log}[r_1] + \mu_r\mathrm{Log}[r_2] - \eta\mathrm{Log}[r_\varepsilon])}\right), \tag{A.4}$$

$$C_5 = \begin{pmatrix} \mu_r\left(16\left(4 + BrC_1C_{15}\left(-r_1^2 + r_2^2\right)\right)\eta^2 + \begin{pmatrix} 128 - BrC_{15}(r_1 - r_2)(r_1 + r_2) \\ \left(16C_1 + C_{15}\left(r_1^2 + r_2^2\right)\right) \end{pmatrix}\eta\mu_r + 64\mu_r^2\right) + \\ 4Br\eta(8C_1^2(\eta+\mu_r)^2 Log[r_1]^2 + 8C_1^2(\eta+\mu_r)^2 Log[r_2]^2 - C_{15}r_1^2\mu_r\left(C_{15}r_1^2\mu_r + 8C_1(\eta+\mu_r)\right)\mathrm{Log}[r_\varepsilon]\mathrm{Log}[r_1], \\ \left(C_{15}r_1^2\mu_r\left(C_{15}r_1^2\mu_r + 8C_1(\eta+\mu_r)\right) - \frac{16C_1^2}{\left(64\mu_r(\eta+\mu_r)^2(\mathrm{Log}[r_2] - \mathrm{Log}[r_\varepsilon])\right)}\right. \end{pmatrix} \tag{A.5}$$

$$C_6 = 1 + \frac{Br\eta Log[r_2]^2 C_1^2}{2\mu_r} + \frac{r_2^2 Br\eta C_1 C_{15}}{4(\mu_r+\eta)} + \frac{r_2^4\mu_r Br\eta C_{15}^2}{64(\mu_r+\eta)^2} + Log[r_2]\left(-r_1\left(\frac{Br\eta Log[r_1]C_1^2}{r_1\mu_r} + \frac{r_1 Br\eta C_1 C_{15}}{2(\mu_r+\eta)} + \frac{r_1^3\mu_r Br\eta C_{15}^2}{16(\mu_r+\eta)^2}\right) + \frac{\left(-(-Log[r_1] + Log[r_2])\left(Br\eta Log[r_1]C_1^2/r_1\mu_r + r_1 Br\eta C_1C_{15}/2(\mu_r+\eta) + r_1^3\mu_r Br\eta C_{15}^2/16(\mu_r+\eta)^2\right) - \left(\begin{matrix} -1 + Br\eta Log[r_1]^2C_1^2/2\mu_r - Br\eta Log[r_2]^2C_1^2/2\mu_r + r_1^2 Br\eta C_1C_{15}/4(\mu_r+\eta) - \\ r_2^2 Br\eta C_1C_{15}/4(\mu_r+\eta) + r_1^4\mu_r Br\eta C_{15}^2/64(\mu_r+\eta)^2 - r_2^4\mu_r Br\eta C_{15}^2/64(\mu_r+\eta)^2 \end{matrix}\right)/r_1\right)}{(-Log[r_2]/r_1 + Log[r_\epsilon]/r_1)}, \tag{A.6}$$

$$C_7 = -\frac{\left(\begin{matrix} -(-Log[r_1] + Log[r_2])\left(Br\eta Log[r_1]C_1^2/r_1\mu_r + r_1 Br\eta C_1C_{15}/2(\mu_r+\eta) + r_1^3\mu_r Br\eta C_{15}^2/16(\mu_r+\eta)^2\right) - \\ \left(\begin{matrix} -1 + Br\eta Log[r_1]^2C_1^2/2\mu_r - Br\eta Log[r_2]^2C_1^2/2\mu_r + r_1^2 Br\eta C_1C_{15}/4(\mu_r+\eta) - \\ r_2^2 Br\eta C_1C_{15}/4(\mu_r+\eta) + r_1^4\mu_r Br\eta C_{15}^2/64(\mu_r+\eta)^2 - r_2^4\mu_r Br\eta C_{15}^2/64(\mu_r+\eta)^2 \end{matrix}\right)/r_1 \end{matrix}\right)}{-Log[r_2]/r_1 + Log[r_\varepsilon]/r_1}, \tag{A.7}$$

$$C_8 = \frac{Log[r_\epsilon]\left(\begin{matrix} -(-Log[r_1] + Log[r_2])\left(Br\eta Log[r_1]C_1^2/r_1\mu_r + r_1 Br\eta C_1C_{15}/2(\mu_r+\eta) + r_1^3\mu_r Br\eta C_{15}^2/16(\mu_r+\eta)^2\right) - \\ \left(\begin{matrix} -1 + Br\eta Log[r_1]^2C_1^2/2\mu_r - Br\eta Log[r_2]^2C_1^2/2\mu_r + r_1^2 Br\eta C_1C_{15}/4(\mu_r+\eta) - \\ r_2^2 Br\eta C_1C_{15}/4(\mu_r+\eta) + r_1^4\mu_r Br\eta C_{15}^2/64(\mu_r+\eta)^2 - r_2^4\mu_r Br\eta C_{15}^2/64(\mu_r+\eta)^2 \end{matrix}\right)/r_1 \end{matrix}\right)}{-Log[r_2]/r_1 + Log[r_\epsilon]/r_1}, \tag{A.8}$$

$$C_9 = \frac{1}{64(Log[r_1] - Log[r_\varepsilon])(-Log[r_2] + Log[r_\varepsilon])} \cdot \left(\begin{matrix} 16(-r_1^2 Br Log[r_1] + (r_1 - r_\varepsilon)(r_1 + r_\varepsilon)(Br + Da\ Log[r_2]) + \left(r_1^2(Br - Da) + r_\varepsilon^2 Da\right)Log[r_\varepsilon] + (Log[r_2] - Log[r_\varepsilon]) \\ \left(16\left(Da\left(-r_1^2 + r_\varepsilon^2 + r_1^2 Log[r_1] - r_\varepsilon^2 Log[r_\varepsilon]\right)C_3 + (r_1 - r_\varepsilon)(r_1 + r_\varepsilon)Da\ C_4 + Gr\left(r_1^2 - r_\varepsilon^2 - r_1^2 Log[r_1] + r_\varepsilon^2 Log[r_\varepsilon]\right)C_7 + \left(-r_1^2 + r_\varepsilon^2\right)GrC_8\right) + \left(r_1^4 - r_\varepsilon^4\right)Da\ C_{15}\right) \end{matrix}\right), \tag{A.9}$$

$$C_9 = \frac{1}{64\left(Log[r_1] - Log[r_\varepsilon]\right)\left(-Log[r_2] + Log[r_\varepsilon]\right)} \cdot \Big(16\Big(-r_1^2 Log[r_\varepsilon]\left(Br + Da\ Log[r_2]\right) + (Br - Da)Log[r_\varepsilon]\Big) + Log[r_1]\Big(r_\varepsilon^2 Da\left(Log[r_2] - Log[r_\varepsilon]\right) + Br\Big(r_\varepsilon^2 + r_1^2 Log[r_\varepsilon]\Big)\Big)\Big) + \left(Log[r_2] - Log[r_\varepsilon]\right) \left(16\begin{pmatrix} Da\Big(-r_\varepsilon^2 Log[r_1] - \Big(r_1^2 + \Big(-r_1^2 + r_\varepsilon^2\Big)Log[r_1]\Big)Log[r_\varepsilon]\Big)C_3 + Da\Big(r_\varepsilon^2 Log[r_1] - r_1^2 Log[r_\varepsilon]\Big)C_4 \\ + Gr\Big(-r_1^2 Log[r_\varepsilon] + Log[r_1] + \Big(r_\varepsilon^2 + (r_1 - r_\varepsilon)(r_1 + r_\varepsilon)Log[r_\varepsilon]\Big)\Big)C_7 + Gr\Big(-r_\varepsilon^2 Log[r_1] + r_1^2 Log[r_\varepsilon]\Big)C_3 \end{pmatrix} + Da\Big(r_\varepsilon^4 Log[r_1] - r_1^4 Log[r_\varepsilon]\Big)C_{15}\Big), \tag{A.10}$$

$$C_{11} = \frac{\begin{pmatrix} -32\Big(Log[r_1]^2 - Log[r_\epsilon]^2\Big)\Big(NbC_7 + \left(Log[r_2] - Log[r_\epsilon]\right)\Big(BrC_3^2 + NtC_7^2\Big)\Big) + \\ 16(r_1 - r_\epsilon)(r_1 + r_\epsilon)Br\left(-Log[r_2] + Log[r_\epsilon]\right)C_3C_{15} + \Big(r_1^4 - r_\epsilon^4\Big)Br\left(-Log[r_2] + Log[r_\epsilon]\right)C_{15}^2 \end{pmatrix}}{64\left(Log[r_1] - Log[r_\epsilon]\right)\left(-Log[r_2] + Log[r_\epsilon]\right)}, \tag{A.11}$$

$$C_{12} = \frac{1}{64\left(Log[r_1] - Log[r_\varepsilon]\right)\left(-Log[r_2] + Log[r_\varepsilon]\right)} \cdot \begin{pmatrix} 32Log[r_1]\left(Log[r_1] - Log[r_\varepsilon]\right)Log[r_\varepsilon] \\ \Big(NbC_7 + \left(Log[r_2] - Log[r_\varepsilon]\right)\Big(BrC_3^2 + NtC_7^2\Big)\Big) + 16Br\left(Log[r_2] - Log[r_\varepsilon]\right) \\ \Big(-r_\varepsilon^2 Log[r_1] + r_1^2 Log[r_\varepsilon]\Big)C_3C_{15} + Br\left(Log[r_2] - Log[r_\varepsilon]\right)\Big(-r_\epsilon^4 Log[r_1] + r_1^4 Log[r_\varepsilon]\Big)C_{15}^2 \end{pmatrix}, \tag{A.12}$$

$$C_{13} = \frac{1}{768Nb\left(Log[r_2] - Log[r_\epsilon]\right)} \cdot \begin{pmatrix} 128Br\Big(-3NtLog[r_2]^2 + (-Nb + Nt)Log[r_2]^3 + Log[r_\epsilon]^2\left(3Nt + (Nb - Nt)Log[r_\epsilon]\right)\Big) \\ C_3^2 - 128\Big((Nb - Nt)Log[r_2]^2 + Log[r_2]\left(3Nt + (Nb - Nt)Log[r_\epsilon]\right) + Log[r_\epsilon]\left(3Nt + (Nb - Nt)Log[r_\epsilon]\right)\Big) \\ C_7\left(Nb + Nt\left(Log[r_2] - Log[r_\epsilon]\right)C_7\right) + 384\left(Nb - Nt\right)\Big(Log[r_2]^2 - Log[r_\epsilon]^2\Big) \\ C_{11} - 96\left(r_2 - r_\epsilon\right)\left(r_2 + r_\epsilon\right)Br\left(Nb + Nt\right)C_3C_{15} - 3\Big(r_2^4 - r_\epsilon^4\Big)Br\left(Nb + 3Nt\right)C_{15}^2 \end{pmatrix}, \tag{A.13}$$

$$C_{14} = -\frac{1}{768Nb\left(Log[r_2] - Log[r_\epsilon]\right)} \cdot \begin{pmatrix} 128BrLog[r_2]\left(Log[r_2] - Log[r_\epsilon]\right)Log[r_\epsilon]\left(-3Nt - \left(Nb - Nt\right)\left(Log[r_2] + Log[r_\epsilon]\right)\right) \\ C_3^2 - 128Log[r_2]Log[r_\epsilon]\left(3Nt + \left(Nb - Nt\right)\left(Log[r_2] + Log[r_\epsilon]\right)\right) \\ C_7\left(Nb + Nt\left(Log[r_2] - Log[r_\epsilon]\right)C_7\right) + 3\left(-Nb + Nt\right)\left(Log[r_2] - Log[r_\epsilon]\right)C_{11}) + \\ 96Br\left(Nb + Nt\right)\Big(r_\epsilon^2 Log[r_2] - r_2^2 Log[r_\epsilon]\Big)C_3C_{15} + 3Br\left(Nb + 3Nt\right)\Big(r_\epsilon^4 Log[r_2] - r_2^4 Log[r_\epsilon]\Big)C_{15}^2 \end{pmatrix}, \tag{A.14}$$

$$C_{15} = E_3\Big(4\pi^2\phi_1 Cos[2\pi(-t + z)] + 16\pi^2\phi_2 Cos[4\pi(-t + z)]\Big) + E_1\Big(8\pi^3\phi_1 Sin[2\pi(-t + z)] + 64\pi^3\phi_2 Sin[4\pi(-t + z)]\Big) + E_2\Big(8\pi^3\phi_1 Sin[2\pi[-t + z]] + 64\pi^3\phi_2 Sin[4\pi(-t + z)]\Big). \tag{A.15}$$

Data Availability

This is a theoretical study and there are no associated data. Numerical codes can be obtained from the corresponding author upon request.

Conflicts of Interest

The authors declare that they have no conflicts of interest.

References

[1] Y. C. Fung and C. S. Yih, "Peristaltic transport," *Journal of Applied Mechanics*, vol. 35, no. 4, pp. 669–675, 1968.

[2] K. R. Diller, "Modeling of bioheat transfer processes at high and low temperatures," *Advances in Heat Transfer*, vol. 22, pp. 157–357, 1992.

[3] T. W. Latham, *Fluid Motions in a Peristaltic Pump*, Doctoral dissertation, Massachusetts Institute of Technology, Massachusetts, USA, 1966.

[4] T. Hayat, N. Aslam, M. I. Khan, M. I. Khan, and A. Alsaedi, "Physical significance of heat generation/absorption and Soret effects on peristalsis flow of pseudoplastic fluid in an inclined channel," *Journal of Molecular Liquids*, vol. 275, pp. 599–615, 2019.

[5] Q. Afzal, S. Akram, R. Ellahi, S. M. Sait, and F. Chaudhry, "Thermal and concentration convection in nanofluids for peristaltic flow of magneto couple stress fluid in a nonuniform channel," *Journal of Thermal Analysis and Calorimetry*, vol. 144, no. 6, pp. 2203–2218, 2021.

[6] K. S. Mekheimer and Y. Abd elmaboud, "Peristaltic Transport through Eccentric Cylinders: Mathematical Model," *Applied Bionics and Biomechanics*, vol. 10, no. 1, pp. 19–27, 2013.

[7] Z. Nisar, T. Hayat, A. Alsaedi, and B. Ahmad, "Wall properties and convective conditions in MHD radiative peristalsis flow of Eyring–Powell nanofluid," *Journal of Thermal Analysis and Calorimetry*, vol. 144, no. 4, pp. 1199–1208, 2021.

[8] O. U. Mehmood, A. A. Qureshi, H. Yasmin, and S. Uddin, "Thermo-mechanical analysis of non Newtonian peristaltic mechanism: Modified heat flux model," *Physica A: Statistical Mechanics and Its Applications*, vol. 550, Article ID 124014, 2020.

[9] M. Y. Jaffrin and A. H. Shapiro, "Peristaltic pumping," *Annual Review of Fluid Mechanics*, vol. 3, no. 1, pp. 13–37, 1971.

[10] A. Zeeshan, A. Riaz, and F. Alzahrani, *Electrophoresis*, National Human Genome Research Institute, Mary land, USA, 2021.

[11] D. Tripathi, A. Sharma, and O. A. Bég, "Joule heating and buoyancy effects in electro-osmotic peristaltic transport of aqueous nanofluids through a microchannel with complex wave propagation," *Advanced Powder Technology*, vol. 29, no. 3, pp. 639–653, 2018.

[12] K. Javid, N. Ali, and Z. Asghar, "Numerical Simulation of The Peristaltic Motion of a Viscous Fluid Through a Complex Wavy Non-Uniform Channel With The Magneto-Hydrodynamic Effects," *Physica Scripta*, vol. 94, no. 11, Article ID 115226, 2019.

[13] D. Tripathi, R. Jhorar, O. A. Bég, and A. Kadir, "Electro-magneto-hydrodynamic peristaltic pumping of couple stress biofluids through a complex wavy micro-channela," *Journal of Molecular Liquids*, vol. 236, p. 358, 2017.

[14] M. M. Bhatti, R. Ellahi, A. Zeeshan, M. Marin, and N. Ijaz, "Numerical study of heat transfer and Hall current impact on peristaltic propulsion of particle-fluid suspension with compliant wall properties," *Modern Physics Letters B*, vol. 33, no. 35, Article ID 1950439, 2019.

[15] G. Bugliarello and J. Sevilla, "Velocity distribution and other characteristics of steady and pulsatile blood flow in fine glass tubes," *Biorheology*, vol. 7, no. 2, pp. 85–107, 1970.

[16] V. P. Srivastava, "A theoretical model for blood flow in small vessels," *Applications and Applied Mathematics: An International Journal (AAM)*, vol. 2, no. 1, p. 5, 2007.

[17] L. M. Srivastava and V. P. Srivastava, "Peristaltic transport of a two-layered model of physiological fluid," *Journal of Biomechanics*, vol. 15, no. 4, p. 257, 1982.

[18] S. L. Weinberg, E. C. Eckstein, and A. H. Shapiro, "An experimental study of peristaltic pumping," *Journal of Fluid Mechanics*, vol. 49, no. 3, p. 461, 1971.

[19] J. C. Misra and S. K. Pandey, "Peristaltic transport of blood in small vessels: Study of a mathematical model," *Computers & Mathematics with Applications*, vol. 43, no. 8-9, p. 1183, 2002.

[20] K. S. S. Vajravelu and R. Saravana, "Influence of velocity slip and temperature jump conditions on the peristaltic flow of a Jeffrey fluid in contact with a Newtonian fluid," *Applied Mathematics and Nonlinear Sciences*, vol. 2, no. 2, p. 429, 2017.

[21] N. Ali, S. Hussain, and K. Ullah, "Theoretical analysis of two-layered electro-osmotic peristaltic flow of FENE-P fluid in an axisymmetric tube," *Physics of Fluids*, vol. 32, no. 2, Article ID 023105, 2020.

[22] N. Ali, S. Hussain, K. Ullah, and O. A. Bég, "Mathematical modelling of two-fluid electro-osmotic peristaltic pumping of an Ellis fluid in an axisymmetric tube," *The European Physical Journal Plus*, vol. 134, p. 141, 2019.

[23] C. Rajashekhar, G. Manjunatha, K. V. Prasad, B. B. Divya, and H. Vaidya, "Peristaltic transport of two-layered blood flow using Herschel–Bulkley Model," *Cogent Engineering*, vol. 5, no. 1, Article ID 1495592, 2018.

[24] D. Tripathi, A. Borode, R. Jhorar, O. A. Bég, and A. K. Tiwari, "Computer modelling of electro-osmotically augmented three-layered microvascular peristaltic blood flow," *Microvascular Research*, vol. 114, pp. 65–83, 2017.

[25] S. Shubham, N. Jain, V. Gupta, S. Mohan, M. M. Ariffin, and A. Ahmadian, "Identify glomeruli in human kidney tissue images using a deep learning approach," *Soft Computing*, 2021.

[26] P. J. Cook, R. Doll, and S. A. Fellingham, "A mathematical model for the age distribution of cancer in man," *International Journal of Cancer*, vol. 4, no. 1, pp. 93–112, 1969.

[27] E. Ackerman, J. W. Rosevear, and W. F. McGuckin, "A Mathematical Model of the Glucose-tolerance test," *Physics in Medicine & Biology*, vol. 9, no. 2, p. 203, 1964.

[28] N. Jain, S. Jhunthra, H. Garg et al., "Prediction modelling of COVID using machine learning methods from B-cell dataset," *Results in physics*, vol. 21, Article ID 103813, 2021.

[29] V. Gupta, N. Jain, P. Katariya et al., "An Emotion Care Model using Multimodal Textual Analysis on COVID-19," *Chaos, Solitons & Fractals*, vol. 144, Article ID 110708, 2021.

[30] A. I. Dobrolyubov and G. Douchy, "Peristaltic Transport as the Travelling Deformation Waves," *Journal of Theoretical Biology*, vol. 219, no. 1, p. 55, 2002.

[31] I. Waini, A. Ishak, T. Groşan, and I. Pop, "Mixed convection of a hybrid nanofluid flow along a vertical surface embedded in a porous medium," *International Communications in Heat and Mass Transfer*, vol. 114, Article ID 104565, 2020.

[32] T. Hayat, F. Haider, A. Alsaedi, and B. Ahmad, "Unsteady flow of nanofluid through porous medium with variable characteristics," *International Communications in Heat and Mass Transfer*, vol. 119, Article ID 104904, 2020.

[33] A. Yasin, N. Ullah, S. Saleem, S. Nadeem, and A. Al-Zubaidi, "Impact of uniform and non-uniform heated rods on free convective flow inside a porous enclosure: Finite element analysis," *Physica Scripta*, vol. 96, no. 8, Article ID 085203, 2021.

[34] U. Nazir, M. A. Sadiq, and M. Nawaz, "Non-Fourier thermal and mass transport in hybridnano-Williamson fluid under chemical reaction in Forchheimer porous medium," *International Communications in Heat and Mass Transfer*, vol. 127, Article ID 105536, 2021.

[35] T. Abbas, B. Ahmad, A. Majeed, T. Muhammad, and M. Ismail, "Numerical Investigations of Radiative Flow of Viscous Fluid Through Porous Medium," *Journal of Magnetics*, vol. 26, no. 3, p. 277, 2021.

[36] S. Nadeem, N. Abbas, and M. Y. Malik, "Inspection of hybrid based nanofluid flow over a curved surface," *Computer Methods and Programs in Biomedicine*, vol. 189, Article ID 105193, 2020.

[37] A. Riaz, R. Ellahi, and S. M. Sait, "Role of hybrid nanoparticles in thermal performance of peristaltic flow of Eyring–Powell fluid model," *Journal of Thermal Analysis and Calorimetry*, vol. 143, pp. 1021–1035, 2021.

[38] T. Hayat, S. Qayyum, A. Alsaedi, and B. Ahmad, "Entropy generation minimization: Darcy-Forchheimer nanofluid flow due to curved stretching sheet with partial slip," *International Communications in Heat and Mass Transfer*, vol. 111, Article ID 104445, 2020.

[39] A. Riaz, R. Ellahi, S. M. Sait, and T. Muhammad, "Magnetized Jeffrey nanofluid with energy loss in between an annular part of two micro non-concentric pipes," *Energy Sources, Part A: Recovery, Utilization, and Environmental Effects*, pp. 1–20, 2020.

[40] A. Zeeshan, A. Majeed, M. J. Akram, and F. Alzahrani, "Numerical investigation of MHD radiative heat and mass transfer of nanofluid flow towards a vertical wavy surface with viscous dissipation and Joule heating effects using Keller-box method," *Mathematics and Computers in Simulation*, vol. 190, p. 1080, 2021.

[41] J. Buongiorno, "Convective Transport in Nanofluids," *Journal of heat transfer*, vol. 128, no. 3, pp. 240–250, 2006.

[42] M. W. Johnson and D. Segalman, "A model for viscoelastic fluid behavior which allows non-affine deformation," *Journal of Non-newtonian Fluid Mechanics*, vol. 2, no. 3, p. 255, 1977.

[43] Y. Wang, T. Hayat, and K. Hutter, "Peristaltic flow of a Johnson-Segalman fluid through a deformable tube," *Theoretical and Computational Fluid Dynamics*, vol. 21, no. 5, p. 369, 2007.

[44] A. Saleem, A. Qaiser, S. Nadeem, M. Ghalambaz, and A. Issakhov, "Physiological Flow of Non-Newtonian Fluid with Variable Density Inside a Ciliated Symmetric Channel Having Compliant Wall," *Arabian Journal for Science and Engineering*, vol. 46, no. 1, pp. 801–812, 2021.

[45] T. Hayat, M. Javed, and A. A. Hendi, "Peristaltic transport of viscous fluid in a curved channel with compliant walls," *International Journal of Heat and Mass Transfer*, vol. 54, no. 7-8, p. 1615, 2011.

[46] M. Kapoor, "Exact solution of coupled 1D non-linear Burgers' equation by using Homotopy Perturbation Method (HPM): A review," *Journal of Physics Communications*, vol. 4, no. 9, Article ID 095017, 2020.

[47] B. N. Kharrat and G. Toma, "Electronic Customer Relationship Management (E-CRM) and its Effect on Customer Retention of Selected E-Retail Companies in Lagos State, Nigeria," *Middle-East Journal of Scientific Research*, vol. 28, no. 2, p. 142, 2020.

[48] M. Qayyum and I. Oscar, "Least square homotopy perturbation method for ordinary differential equations," *Journal of Mathematics*, vol. 2021, Article ID 7059194, 16 pages, 2021.

Hindawi
Mathematical Problems in Engineering
Volume 2022, Article ID 1019810, 17 pages
https://doi.org/10.1155/2022/1019810

Research Article

An Application of Homotopy Perturbation Method to Fractional-Order Thin Film Flow of the Johnson–Segalman Fluid Model

Mubashir Qayyum,[1] **Farnaz Ismail**,[2] **Syed Inayat Ali Shah**,[2] **Muhammad Sohail**,[3] **Essam R. El-Zahar**,[4,5] **and K. C Gokul**[6]

[1]*Department of Sciences and Humanities, National University of Computer & Emerging Sciences FAST Lahore, Lahore, Pakistan*
[2]*Department of Mathematics, Islamia College University Peshawar, Peshawar, Pakistan*
[3]*Department of Applied Mathematics and Statistics, Institute of Space Technology, P.O. Box 2750, Islamabad, Pakistan*
[4]*Department of Mathematics, College of Science and Humanities in Al-Kharj, Prince Sattam Bin Abdulaziz University, P.O. Box 83, Al-Kharj 11942, Saudi Arabia*
[5]*Department of Basic Engineering Science, Faculty of Engineering, Menoufia University, Shebin El-Kom 32511, Egypt*
[6]*Department of Natural Sciences (Mathematics Group), Kathmandu University, Kathmandu, Nepal*

Correspondence should be addressed to K. C Gokul; gokul.kc@ku.edu.np

Received 31 December 2021; Revised 22 January 2022; Accepted 31 January 2022; Published 23 February 2022

Academic Editor: Arshad Riaz

Thin film flow is an important theme in fluid mechanics and has many industrial applications. These flows can be observed in oil refinement process, laser cutting, and nuclear reactors. In this theoretical study, we explore thin film flow of non-Newtonian Johnson–Segalman fluid on a vertical belt in fractional space in lifting and drainage scenarios. Modelled fractional-order boundary value problems are solved numerically using the homotopy perturbation method along with Caputo definition of fractional derivative. In this study, instantaneous and average velocities and volumetric flux are computed in lifting and drainage cases. Validity and convergence of homotopy-based solutions are confirmed by finding residual errors in each case. Moreover, the consequences of different fractional and fluid parameters are graphically studied on the velocity profile. Analysis shows that fractional parameters have opposite effects of the fluid velocity.

1. Introduction

Modelling and analysis of non-Newtonian fluids is an important and active research theme in industrial engineering. Food processing, paper production, blood flow analysis, and mud drilling are different applications areas of non-Newtonian fluids. These fluids are defined through a nonlinear relationship between rate of deformation and stress tensors, and therefore, it has several models in different scenarios. Johnson–Segalman fluid is one of the very significant fluid modals which have numerous engineering and industrial applications.

Thin film flow can be detected in different natural situations, for example, movement of raindrop on window glass, tears in the eyes, and lava flow. Industrial applications of such flows include oil refining, nuclear reactors, and laser cutting[1–4]. The initial work on thin film flow was carried out in [3] for Newtonian fluids, but this study has limitations and cannot be generalized for non-Newtonian fluids such as melted plastics, gels, pastes, honey, ketchup, and blood [5]. Siddiqui et al. examined thin film of different fluids including PTT (Phan-Thien and Tanner) and third and fourth grade fluids in [6–8]. Landau [9] and Stuart [10] extended these analyses to turbulence. Ullah et al. studied the film flow under slip conditions in generalized Maxwell fluids in [11]. Ruan et al. studied thin film from a distributed source on a vertical wall in [12]. Ahmad and Xu proposed an improved nanofluid model in thin film under the action of gravity in [13].

Fractional calculus has gained significant attention due to its striking application as a new modelling tool in a variety of fields, such as fluid dynamics, hydrology, system control theory, signal processing, physics, biology, and finance [14–20]. These fractional models are more appropriate for describing memory and transmissible properties of different materials than integral-order models. In the past few decades, various numerical techniques have been developed by different researchers for nonlinear BVPs. Wazwaz proposed the modified decomposition method (MDM) for BVPs in [21]. Noor and Mohyud-Din used VIM along with He's polynomials for the solution of higher order BVPs [22]. Liu et al. used the multiscale method for nanoparticle diffusion in sheared cellular blood flow in [23]. Jafari and Gejji used adomian decomposition for the solution of system of FDEs in [24]. Hashim et al. apply OHAM to fractional-order fuzzy differential equations in [22]. Rysak and Gregorczyk proposed DTM for fractional dynamical systems in [25]. Zada et al. apply NIM to fractional PDEs in [26]. Yaghouti used radial basis functions to different families of fractional differential equations in [27]. Al-Kuze et al. used spectral quasi-linearization and irreversibility analysis of magnetized cross-fluid flow [28].

In this study, we extend the theoretical study of thin film flow to fractional space in case of non-Newtonian Johnson–Segalman fluid since exact solutions of highly nonlinear fractional differential equations (FDEs) are not possible. The conventional approach is to use perturbation techniques in such scenarios, which again need small or large parameters. To avoid this, we utilize the well-known homotopy perturbation method (HPM) [29–33] along with fractional calculus for solution purpose. This method is effectively used by many scholars in [29–33]. Validation and convergence of the obtained numerical solutions are confirmed by means of finding residual errors. To the best of the authors' knowledge, the given problem has not been attempted before in fractional space.

2. Preliminaries

2.1. Fractional Calculus. Few basic definitions of fractional calculus are given below.

Definition 1. Let $f(t), t > 0$, be a real function in the space $C_\mu, \mu \in R$, if $\exists$ a real number $p > \mu \ni f(t) = t^p f_1(t)$, where $f_1(t) \in C(0, \infty)$, and it is in the space

$$C_\mu^m \Leftrightarrow f^m \in C_\mu, m \in N. \tag{1}$$

Definition 2. The Caputo fractional derivative D^α is defined as

$$D^\alpha f(t) = \frac{1}{\Gamma(m-\alpha)} \int_0^t (t-\tau)^{m-\alpha-1} f^m d\tau, \text{ for } m - 1 < \alpha < m, m \in N, t > 0. \tag{2}$$

Definition 3. $\alpha \geq 0$ order Riemann–Liouville fractional integration is defined as

$$J^\alpha f(t) = \frac{1}{\Gamma(\alpha)} \int_0^t (t-\tau)^{\alpha-1} f(\tau) d\tau, k - 1 < \alpha < k, \text{ and } k \in N. \tag{3}$$

2.2. Basic Equations. The basic equations of incompressible fluid of Johnson–Segalman fluid are

$$\operatorname{div} \mathscr{V} = 0, \tag{4}$$

$$\rho \frac{\mathrm{D}\mathscr{V}}{\mathrm{D}t} = \operatorname{div} \boldsymbol{\sigma} + \rho \mathbf{f}, \tag{5}$$

where $\mathscr{V}$ is the velocity vector, ρ is the constant density, $\mathbf{f}$ is the body force per unit mass, and σ is the Cauchy stress tensor, where

$$\boldsymbol{\sigma} = -p\mathbf{I} + \mathbf{T}, \tag{6}$$

$$\mathbf{T} = \mathbf{S} + 2\mu\mathbf{D}, \tag{7}$$

$$\mathbf{S} + m\left[(\mathbf{W} - a\mathbf{D})^T \mathbf{S} + \mathbf{S}(\mathbf{W} - a\mathbf{D}) + \frac{\mathrm{D}\mathbf{S}}{\mathrm{D}t} \right] = 2\mathbf{D}\eta. \tag{8}$$

3. Mathematical Formulation in Lifting Case

The belt is passing through the container filled with Johnson–Segalman fluid, and it is moving vertically with constant speed U_0. A uniform thickness δ of the thin film is taken up by the belt, but due to gravity fluid, it is draining down. Let pressure be assumed to be atmospheric, and the flow is uniform, steady, and laminar. Also, the x-axis is considered to be normal, while the y-axis is along the belt.

The boundary conditions are

$$\begin{aligned} x &= 0, \\ v &= U_0, \\ x &= \delta, \\ T_{xy} &= 0. \end{aligned} \tag{9}$$

Velocity is of the form

$$\mathscr{V} = (0,\ v(x),\ 0), \tag{10}$$

$$\mathbf{T} = \mathbf{T}(x) \text{ and } \mathbf{T}_{\mathbf{xz}}, \tag{11}$$

where the extra and shear stress tensor is $\mathbf{T} = \mathbf{T}(x)$ and $\mathbf{T}_{\mathbf{xz}}$, respectively.

Substitution of (8) in (3) and (4) shows that (3) is satisfied, while (4) has the form

$$0 = \frac{\mathrm{d}T_{\mathrm{xx}}}{\mathrm{d}x} + \rho f_1, \tag{12}$$

$$0 = \frac{\mathrm{d}T_{\mathrm{xy}}}{\mathrm{d}x} + \rho f_2, \tag{13}$$

where f_1 and f_2 are the components of body force.

Since gravitational force is in downward while y-axis is in upward directions, hence, (12) and (13) become

$$0 = \frac{dT_{xx}}{dx},$$
$$0 = \frac{dT_{xy}}{dx} - \rho g. \tag{14}$$

By using equations (8), (10), and (11) in (7), components of **S** are

$$S_{xx} = \frac{-\eta m(1-a)(dv/dx)^2}{1+m^2(1-a^2)(dv/dx)^2}, \tag{15}$$

$$S_{xy} = \frac{\eta dv/dx}{1+m^2(1-a^2)(dv/dx)^2} = S_{yx}, \tag{16}$$

$$S_{yy} = \frac{\eta m(1+a)(dv/dx)^2}{1+m^2(1-a^2)(dv/dx)^2}. \tag{17}$$

Using (15)–(17), stress tensor **T** in (6) is

$$T_{xx} = \frac{-\eta m(1-a)(dv/dx)^2}{1+m^2(1-a^2)(dv/dx)^2}, \tag{18}$$

$$T_{xy} = \mu\left(\frac{dv}{dx}\right) + \frac{\eta dv/dx}{1+m^2(1-a^2)(dv/dx)^2} = T_{yx}, \tag{19}$$

$$T_{yy} = \frac{\eta m(1+a)(dv/dx)^2}{1+m^2(1-a^2)(dv/dx)^2}. \tag{20}$$

Substituting T_{xy} in (14) gives

$$\frac{d}{dx}\left[\mu\left(\frac{dv}{dx}\right) + \frac{\eta dv/dx}{1+m^2(1-a^2)(dv/dx)^2}\right] = \rho g. \tag{21}$$

Boundary conditions become

$$\frac{dv}{dx} = 0 \text{ at } x = \delta, \tag{22}$$

$$v = U_0 \text{ at } x = 0. \tag{23}$$

Introduce nondimensional parameters as

$$x^* = \frac{x}{\delta}, v^* = \frac{v}{U_0} \text{ and } \varphi = \frac{\mu}{\mu+\eta}, \tag{24}$$

where φ is the ratios of viscosities. Equations (21)–(23) become

$$\frac{d}{dx}\left[\varphi\left(\frac{dv}{dx}\right) + \frac{(1-\varphi)dv/dx}{1+W_e^2(1-a^2)(dv/dx)^2}\right] = S_t. \tag{25}$$

$$\text{At } x = 1, \frac{dv}{dx} = 0. \tag{26}$$

$$\text{At } x = 0, \quad v = 1, \tag{27}$$

where $S_t = \rho g\delta^2/\mu_{\text{eff}}U_0$ and $W_e = mU_0/\delta$ are Stokes and Weissenberg numbers, respectively, and $\mu_{\text{eff}} = \mu + \eta$.

Simplification of equation (25) gives

$$\frac{d^2v}{dx^2} + W_e^4(1-a^2)^2\left[\varphi\frac{d^2v}{dx^2} - S_t\right]\left(\frac{dv}{dx}\right)^4 - W_e^2(1-a^2)\left(\frac{d^2v}{dx^2} + \varphi\frac{d^2v}{dx^2} + 2S_t\right)\left(\frac{dv}{dx}\right)^2 - S_t = 0, \tag{28}$$

with

$$\frac{dv}{dx} = 0 \text{ at } x = 1,$$
$$v = 1 \text{ at } x = 0. \tag{29}$$

Now, using definition of fractional calculus given in Section 2.1, the fractional form of equation (28) is

$$\frac{d^2v(x)}{dx^2} + W_e^4(1-a^2)^2\left[\varphi\frac{d^2v(x)}{dx^2} - S_t\right](D^\alpha v(x))^4 - W_e^2(1-a^2)\left[\frac{d^2v(x)}{dx^2} + \varphi\frac{d^2v(x)}{dx^2} + 2S_t\right](D^\alpha v(x))^2 - S_t = 0, \tag{30}$$

with

$$v(0) = 1, v'(1) = 0, 0 < \alpha < 1. \tag{31}$$

4. Homotopy Solution of Johnson–Segalman Fluid in the Lifting Case

Homotopy $\Omega \times [0,1] \longrightarrow \Re$ for (30) is

$$(1-p)\frac{d^2v(x)}{dx^2} + p\left[\frac{d^2v(x)}{dx^2} + W_e^4\left(1-a^2\right)^2\left[\varphi\frac{d^2v(x)}{dx^2} - S_t\right](D^\alpha v(x))^4\right.$$
$$\left. -W_e^2\left(1-a^2\right)\left[\frac{d^2v(x)}{dx^2} + \varphi\frac{d^2v(x)}{dx^2} + 2S_t\right](D^\alpha v(x))^2 - S_t\right] = 0. \tag{32}$$

Using (30) and (31), we obtain the following.

Zeroth-order problem:

$$v_0''(x) = 0, \quad v_0(0) = 1, v_0'(1) = 0. \tag{33}$$

First-order problem:

$$\begin{aligned} &-S_t - 2S_t W_e^2 (D^\alpha v_0(x))^2 + 2a^2 S_t W_e^2 (D^\alpha v_0(x))^2 - S_t W_e^4 (D^\alpha v_0(x))^4 \\ &+ 2a^2 S_t W_e^4 (D^\alpha v_0(x))^4 - a^4 S_t W_e^4 (D^\alpha v_0(x))^4 - W_e^2 (D^\alpha v_0(x))^2 v_0''(x) \\ &+ a^2 W_e (D^\alpha v_0(x))^2 v_0''(x) - W_e^2 \phi (D^\alpha v_0(x))^2 v_0''(x) + a^2 W_e^2 \phi (D^\alpha v_0(x))^2 v_0''(x) \\ &+ W_e^4 \phi (D^\alpha v_0(x))^4 v_0''(x) - 2a^2 W_e^4 \phi (D^\alpha v_0(x))^4 v_0''(x) + a^4 W_e^4 \phi (D^\alpha v_0(x))^4 v_0''(x) \\ &+ v_1''(x) = 0, v_1(0) = 0, v_1'(1) = 0. \end{aligned} \tag{34}$$

Second-order problem:

$$\begin{aligned} &W_e^2 (D^\alpha v_0(x))(D^\alpha v_1(x)) + 4a^2 S_t W_e^2 (D^\alpha v_0(x)) - 4S_t (D^\alpha v_1(x)) \\ &- 4S_t W_e^4 (D^\alpha v_0(x))^3 (D^\alpha v_1(x)) 8a^2 S_t W_e^4 (D^\alpha v_0(x))^3 (D^\alpha v_1(x)) \\ &- 4a^4 S_t W_e^4 (D^\alpha v_0(x))^3 (D^\alpha v_1(x)) - 2W_e^2 (D^\alpha v_0(x))(D^\alpha v_1(x)) v_0''(x) \\ &+ 2a^2 W_e^2 (D^\alpha v_0(x))(D^\alpha v_1(x)) v_0''(x) - 2W_e^2 \phi (D^\alpha v_0(x))(D^\alpha v_1(x)) v_0''(x) \\ &+ 2a^2 W_e^2 \phi (D^\alpha v_0(x))(D^\alpha v_1(x)) v_0''(x) + 4W_e^4 \phi (D^\alpha v_0(x))^3 (D^\alpha v_1(x)) v_0''(x) \\ &- 8a^2 W_e^4 \phi (D^\alpha v_0(x))^3 (D^\alpha v_1(x)) v_0''(x) + 4a^4 W_e^4 \phi (D^\alpha v_0(x))^3 (D^\alpha v_1(x)) v_0''(x) \\ &- W_e^2 (D^\alpha v_0(x))^2 v_1''(x) + a^2 W_e^2 (D^\alpha v_0(x))^2 v_1''(x) - W_e^2 \phi (D^\alpha v_0(x))^2 v_1''(x) \\ &+ a^2 W_e^2 \phi (D^\alpha v_0(x))^2 v_1''(x) + W_e^4 \phi (D^\alpha v_0(x))^4 v_1''(x) - 2a^2 W_e^4 \phi (D^\alpha v_0(x))^4 v_1''(x) \\ &+ a^4 W_e^4 \phi (D^\alpha v_0(x))^4 v_1''(x) + v_2''(x) = 0, v_2(0) = 0, v_2'(1) = 0. \end{aligned} \tag{35}$$

Similarly, we can find higher order problems and their solutions.

Third-order approximate solution, after applying Caputo definition and keeping $\alpha = 0.99, \phi = 0.1, S_t = 0.01$, $a = 0.01$, and $W_e = 0.1$ fixed, is

$$V(x) = 1 + \frac{1}{2}\left(-0.02t + 0.01x^2\right) + \left(0.0796711\left(-8.24342 \times 10^{-8} x^{2.98}\right.\right.$$
$$\left.\left. +1.23219 \times 10^{-7}\, x^4 - 8.24098 \times 10^{-8}\, x^5 + 2.04999 \times 10^{-8}\, x^6\right)\right)$$
$$x^{1.98}$$

$$+\left(0.0398355\left(-9.06776\times10^{-8}x^{2.98}+1.35541\times10^{-7}x^{4}\right.\right.$$
$$\left.\left.\frac{-9.06508\times10^{-8}x^{5}+2.25499\times10^{-8}x^{6}\right))}{x^{1.98}}. \tag{36}$$

The residual is denoted by R and is defined as

$$R=\frac{d^2V(x)}{dx^2}+W_e^4\left(1-a^2\right)^2\left[\varphi\frac{d^2V(x)}{dx^2}-S_t\right]\left(D^{\alpha}V(x)\right)^4$$
$$-W_e^2\left(1-a^2\right)\left[\frac{d^2V(x)}{dx^2}+\varphi\frac{d^2V(x)}{dx^2}+2S_t\right]\left(D^{\alpha}V(x)\right)^2-S_t. \tag{37}$$

5. Flow Rate and Average Velocity in the Lifting Case

Flow rate in this case is

$$Q=\frac{1}{6\left(15-16\alpha+4\alpha^2\right)\Gamma(4-\alpha)^2}(-3+2\alpha)\left(-\frac{1}{-7+2\alpha}\left(3\left(-1+a^2\right)S_t^3W_e^2(-3+\alpha)^2(-16+\alpha(25+\alpha(-13+2\alpha)))(3+\phi)\right)\right.$$
$$\left.-2(-3+S_t)(-5+2\alpha)\Gamma(4-\alpha)^2\right), \tag{38}$$

and average velocity is

$$\overline{V}=\frac{1}{6\left(15-16\alpha+4\alpha^2\right)\Gamma(4-\alpha)^2}(-3+2\alpha)\left(-\frac{1}{-7+2\alpha}\left(3\left(-1+a^2\right)S_t^3W_e^2(-3+\alpha)^2(-16+\alpha(25+\alpha(-13+2\alpha)))(3+\phi)\right)\right.$$
$$\left.-2(-3+S_t)(-5+2\alpha)\Gamma(4-\alpha)^2\right). \tag{39}$$

6. Mathematical Formulation in the Drainage Case

Let fluid be draining down due to gravity on the infinite stationary belt. Equations (4)–(8) become

$$0=\frac{dT_{xy}}{dx}+\rho g. \tag{40}$$

Using equation (19) in (14) gives the form

$$\frac{d}{dx}\left[\mu\left(\frac{dv}{dx}\right)+\frac{\eta dv/dx}{1+m^2\left(1-a^2\right)(dv/dx)^2}\right]=-\rho g, \tag{41}$$

with

$$\frac{dv}{dx}=0 \text{ at } x=\delta,$$
$$v=0 \text{ at } x=0. \tag{42}$$

Equation (40) in the dimensionless form is

$$\frac{d}{dx}\left[\frac{(1-\varphi)dv/dx}{1+W_e^2\left(1-a^2\right)(dv/dx)^2}+\varphi\left(\frac{dv}{dx}\right)\right]=-S_t. \tag{43}$$

$$\text{At } x=1,\frac{dv}{dx}=0,$$
$$\text{At } x=0,\quad v=0. \tag{44}$$

Simplification of (43) gives

$$\frac{d^2v}{dx^2}+W_e^4\left(1-a^2\right)^2\left[\varphi\frac{d^2v}{dx^2}+S_t\right]\left(\frac{dv}{dx}\right)^4$$
$$-W_e^2\left(1-a^2\right)\left(\frac{d^2v}{dx^2}+\varphi\frac{d^2v}{dx^2}-2S_t\right)\left(\frac{dv}{dx}\right)^2+S_t=0. \tag{45}$$

Three cases as fractional boundary value problems are obtained.

Table 1: Solution and residual error for α keeping $a = 0.1, W_e = 0.0\,1, S_t = 0.001$, and $\phi = 0.1$ fixed in lifting.

	$\alpha = 0.2$		$\alpha = 0.6$		$\alpha = 0.99$	
x	$V(x)$	Res error	$V(x)$	Res error	(x)	Res error
0.1	0.905	-8.76128×10^{-25}	0.905	-9.08606×10^{-24}	0.905	-6.59422×10^{-23}
0.2	0.82	-2.5981×10^{-24}	0.82	-1.45747×10^{-23}	0.82	-4.249×10^{-23}
0.3	0.745	-4.78151×10^{-24}	0.745	-1.74003×10^{-23}	0.745	-2.54931×10^{-23}
0.4	0.68	-7.11425×10^{-24}	0.68	-1.79924×10^{-23}	0.68	-1.41813×10^{-24}
0.5	0.625	-9.29068×10^{-24}	0.625	-1.69071×10^{-23}	0.625	-6.9968×10^{-24}
0.6	0.58	-1.10441×10^{-23}	0.58	-1.4743×10^{-23}	0.58	-3.0318×10^{-24}
0.7	0.545	-1.2179×10^{-23}	0.545	-1.20434×10^{-23}	0.545	-1.0542×10^{-24}
0.8	0.52	-1.25923×10^{-23}	0.52	-9.26204×10^{-24}	0.52	-2.52839×10^{-25}
0.9	0.505	-1.22773×10^{-23}	0.505	-6.71129×10^{-24}	0.505	-2.91563×10^{-27}
1.	0.5	-1.13159×10^{-23}	0.5	-4.57323×10^{-24}	0.5	1.0211×10^{-26}

Table 2: Solution and residual error for ϕ keeping $\alpha = 0.99, W_e = 0.01, S_t = 0.001$, and $a = 0.1$ fixed in lifting.

	$\phi = 0.1$		$\phi = 0.6$		$\phi = 0.9$	
x	$V(x)$	Res error	$V(x)$	Res error	$V(x)$	Res error
0.1	0.905	-6.59422×10^{-23}	0.905	-9.09923×10^{-23}	0.905	$-1.08443 \times 10{-}22$
0.2	0.82	-4.249×10^{-23}	0.82	-5.8628×10^{-23}	0.82	-6.98245×10^{-23}
0.3	0.745	-2.54931×10^{-23}	0.745	-3.51797×10^{-23}	0.745	-4.19438×10^{-23}
0.4	0.68	-1.41813×10^{-23}	0.68	-1.95548×10^{-23}	0.68	-2.32819×10^{-23}
0.5	0.625	-6.9968×10^{-24}	0.625	-9.6702×10^{-24}	0.625	-1.15297×10^{-23}
0.6	0.58	-3.0318×10^{-24}	0.58	-4.18483×10^{-24}	0.58	-4.96745×10^{-24}
0.7	0.545	-1.0542×10^{-24}	0.545	-1.45024×10^{-24}	0.545	-1.7253×10^{-24}
0.8	0.52	-2.52839×10^{-25}	0.52	-3.53713×10^{-25}	0.52	-4.20658×10^{-25}
0.9	0.505	-2.91563×10^{-27}	0.505	-1.76326×10^{-26}	0.505	-2.24163×10^{-26}
1.	0.5	1.0211×10^{-26}	0.5	5.3895×10^{-27}	0.5	9.2139×10^{-27}

Table 3: Solution and residual error for S_t keeping $\alpha = 0.98, W_e = 0.001, \phi = 0.1$, and $a = 0.1$ fixed in lifting.

	$S_t = 0.001$		$S_t = 0.01$		$S_t = 0.1$	
x	$V(x)$	Res error	$V(x)$	Res error	$V(x)$	Res error
0.1	0.999905	-7.23543×10^{-27}	0.99905	-6.29219×10^{-22}	0.9905	-6.30818×10^{-17}
0.2	0.99982	-3.63823×10^{-27}	0.9982	-4.18657×10^{-22}	0.982	-4.18849×10^{-17}
0.3	0.999745	-2.86435×10^{-27}	0.99745	-2.5807×10^{-22}	0.9745	-2.57976×10^{-17}
0.4	0.99968	$-1.51698^{*} \times 10^{-27}$	0.9968	-1.46438×10^{-22}	0.968	-1.46541×10^{-18}
0.5	0.999625	-8.70705×10^{-28}	0.99625	-7.53253×10^{-23}	0.9625	-7.52476×10^{-18}
0.6	0.99958	-4.61286×10^{-28}	0.9958	-3.40645×10^{-23}	0.958	-3.37798×10^{-18}
0.7	0.999545	-4.34662×10^{-28}	0.99545	-1.28478×10^{-23}	0.9545	-1.25942×10^{-18}
0.8	0.99952	-4.00347×10^{-29}	0.9952	-3.70343×10^{-24}	0.952	-3.64878×10^{-19}
0.9	0.999505	-1.66647×10^{-29}	0.99505	-1.07941×10^{-24}	0.9505	-8.14999×10^{-20}
1.	0.9995	9.95937×10^{-30}	0.995	-8.78476×10^{-26}	0.95	-8.71776×10^{-21}

Table 4: Solution and residual error for W_e keeping $\alpha = 0.95, S_t = 0.001, \phi = 0.1$, and $a = 0.1$ fixed in lifting.

	$W_e = 0.001$		$W_e = 0.01$		$W_e = 0.1$	
x	$V(x)$	Res error	$V(x)$	Res error	$V(x)$	Res error
0.1	0.905	-5.48732×10^{-27}	0.905	-5.51525×10^{-23}	0.905	-5.4982×10^{-19}
0.2	0.82	-3.75182×10^{-27}	0.82	-3.98956×10^{-23}	0.82	-3.98946×10^{-19}
0.3	0.745	-2.5638×10^{-27}	0.745	-2.63606×10^{-23}	0.745	-2.63525×10^{-19}
0.4	0.68	-1.17028×10^{-27}	0.68	-1.60262×10^{-23}	0.68	-1.6049×10^{-19}
0.5	0.625	-7.01495×10^{-28}	0.625	-8.9237×10^{-24}	0.625	-8.93613×10^{-20}
0.6	0.58	-4.80416×10^{-28}	0.58	-4.47664×10^{-24}	0.58	-4.46647×10^{-20}
0.7	0.545	-3.2225×10^{-28}	0.545	-1.95569×10^{-24}	0.545	-1.9563×10^{-20}
0.8	0.52	7.79×10^{-30}	0.52	-7.49229×10^{-25}	0.52	-7.37223×10^{-21}
0.9	0.505	1.3884×10^{-28}	0.505	-2.49356×10^{-25}	0.505	-2.42499×10^{-21}
1.	0.5	9.40717×10^{-29}	0.5	-6.13229×10^{-26}	0.5	-5.63892×10^{-22}

Table 5: Solution and residual error for α keeping $a = 0.1, W_e = 0.0\,1, S_t = 0.001$, and $\phi = 0.1$ fixed in Case 1 of drainage.

	$\alpha = 0.3$		$\alpha = 0.6$		$\alpha = 0.9$	
x	$V(x)$	Res error	$V(x)$	Res error	$V(x)$	Res error
0.1	0.000095	1.61655×10^{-24}	0.000095	9.08344×10^{-24}	0.000095	6.30751×10^{-23}
0.2	0.00018	4.16166×10^{-24}	0.00018	1.45689×10^{-23}	0.00018	4.18362×10^{-23}
0.3	0.000255	6.96312×10^{-24}	0.000255	1.73923×10^{-23}	0.000255	2.57623×10^{-23}
0.4	0.00032	9.57269×10^{-24}	0.00032	1.79837×10^{-23}	0.00032	1.46516×10^{-23}
0.5	0.000375	1.16444×10^{-23}	0.000375	1.6899×10^{-23}	0.000375	7.51521×10^{-24}
0.6	0.00042	1.29537×10^{-23}	0.00042	1.47362×10^{-23}	0.00042	3.40636×10^{-24}
0.7	0.000455	1.34057×10^{-23}	0.000455	1.20384×10^{-23}	0.000455	1.25929×10^{-24}
0.8	0.00048	1.30281×10^{-23}	0.00048	9.25865×10^{-24}	0.00048	3.70727×10^{-25}
0.9	0.000495	1.19467×10^{-23}	0.000495	6.70931×10^{-24}	0.000495	8.09182×10^{-26}
1.	0.0005	1.0354×10^{-23}	0.0005	4.57227×10^{-24}	0.0005	1.89895×10^{-26}

Table 6: Solution and residual error for ϕ keeping $\alpha = 0.98, W_e = 0.01, S_t = 0.001$, and $a = 0.1$ fixed for Case 1 of drainage.

	$\phi = 0.01$		$\phi = 0.1$		$\phi = 0.3$	
x	$V(x)$	Res error	$V(x)$	Res error	$V(x)$	Res error
0.1	0.000095	5.92844×10^{-23}	0.000095	6.30751×10^{-23}	0.000095	8.18541×10^{-23}
0.2	0.00018	3.93158×10^{-23}	0.00018	4.18362×10^{-23}	0.00018	5.42952×10^{-23}
0.3	0.000255	2.42117×10^{-23}	0.000255	2.57623×10^{-23}	0.000255	3.34316×10^{-23}
0.4	0.00032	1.37711×10^{-23}	0.00032	1.46516×10^{-23}	0.00032	1.90143×10^{-23}
0.5	0.000375	7.0636×10^{-24}	0.000375	7.51521×10^{-24}	0.000375	9.74926×10^{-24}
0.6	0.00042	3.20361×10^{-24}	0.00042	3.40636×10^{-24}	0.00042	4.41229×10^{-24}
0.7	0.000455	1.18469×10^{-24}	0.000455	1.25929×10^{-24}	0.000455	1.62912×10^{-24}
0.8	0.00048	3.49409×10^{-25}	0.00048	3.70727×10^{-25}	0.00048	4.82038×10^{-25}
0.9	0.000495	7.66394×10^{-26}	0.000495	8.09182×10^{-26}	0.000495	1.05556×10^{-25}
1.	0.0005	1.87118×10^{-26}	0.0005	1.89895×10^{-26}	0.0005	2.15706×10^{-24}

Table 7: Solution and residual error for S_t keeping $\alpha = 0.99, W_e = 0.01, \phi = 0.01$, and $a = 0.1$ fixed in Case 1 of drainage.

	$S_t = 0.001$		$S_t = 0.01$		$S_t = 0.1$	
x	$V(x)$	Res error	$V(x)$	Res error	$V(x)$	Res error
0.1	0.000095	5.82872×10^{-23}	0.000095	5.82511×10^{-18}	0.000095	$5.8252 \times 10--13$
0.2	0.00018	3.7525×10^{-23}	0.00018	3.75136×10^{-18}	0.00018	$3.75135 \times 10--13$
0.3	0.000255	2.24807×10^{-23}	0.000255	2.25476×10^{-18}	0.000255	$2.25477 \times 10--13$
0.4	0.00032	1.25172×10^{-23}	0.00032	1.24919×10^{-18}	0.00032	$1.2492 \times 10--13$
0.5	0.000375	6.177×10^{-24}	0.000375	6.22301×10^{-19}	0.000375	$6.22317 \times 10--14$
0.6	0.00042	2.69667×10^{-24}	0.00042	2.67581×10^{-19}	0.00042	$2.67572 \times 10--14$
0.7	0.000455	9.14662×10^{-25}	0.000455	9.26852×10^{-20}	0.000455	$9.2681 \times 10--15$
0.8	0.00048	2.38577×10^{-25}	0.00048	2.30937×10^{-20}	0.00048	$2.3095 \times 10--15$
0.9	0.000495	2.25046×10^{-26}	0.000495	3.77223×10^{-21}	0.000495	$3.76414 \times 10--16$
1.	0.0005	3.98217×10^{-27}	0.0005	1.84694×10^{-22}	0.0005	1.88184×10^{-17}

Table 8: Solution and residual error for γ keeping $S_t = 0.01, \phi = 0.1, W_e = 0.001$, and $a = 0.1$ fixed in Case 2 of drainage.

	$\gamma = 1.2$		$\gamma = 1.6$		$\gamma = 1.99$	
x	$V(x)$	Res error	$V(x)$	Res error	$V(x)$	Res error
0.1	$5.72659 \times 10--4$	-1.32727×10^{-18}	$1.75703 \times 10--4$	3.197×10^{-18}	$5.1638 \times 10--5$	1.29417×10^{-17}
0.2	$1.31563 \times 10--3$	-2.02422×10^{-18}	$5.3263 \times 10--3$	3.56035×10^{-18}	$2.05125 \times 10--4$	1.22623×10^{-17}
0.3	$2.14014 \times 10--3$	-1.98946×10^{-18}	$1.01899 \times 10--3$	3.88346×10^{-18}	$4.59664 \times 10--4$	1.24389×10^{-17}
0.4	$3.02251 \times 10--3$	-2.9885×10^{-19}	$1.61463 \times 10--3$	3.46852×10^{-18}	$8.14833 \times 10--4$	1.35961×10^{-17}
0.5	$3.95057 \times 10--3$	-1.84225×10^{-18}	$2.30744 \times 10--3$	3.68767×10^{-18}	$1.27034 \times 10--3$	1.31157×10^{-17}
0.6	$4.91675 \times 10--3$	-2.46976×10^{-18}	$3.08901 \times 10--3$	3.57668×10^{-18}	$1.82595 \times 10--3$	1.37891×10^{-17}
0.7	$5.91581 \times 10--3$	-2.09831×10^{-18}	$3.95307 \times 10--3$	3.36789×10^{-18}	$2.4815 \times 10--3$	1.30025×10^{-17}
0.8	$6.94391 \times 10--3$	-1.35899×10^{-18}	$4.89465 \times 10--3$	3.06616×10^{-18}	$3.23682 \times 10--3$	1.40449×10^{-17}
0.9	$7.99811 \times 10--3$	-5.26745×10^{-19}	$5.90971 \times 10--3$	4.003×10^{-18}	$4.09177 \times 10--3$	1.29653×10^{-17}
1.	$9.07604 \times 10--3$	-1.50223×10^{-18}	$6.99484 \times 10--3$	2.56045×10^{-18}	$5.04625 \times 10--3$	1.32103×10^{-17}

Table 9: Solution and residual error for α keeping $\gamma = 1.95, S_t = 0.001, \phi = 0.1, W_e = 0.01$, and $a = 0.1$ fixed in Case 3 of drainage.

	$\alpha = 0.3$		$\alpha = 0.7$		$\alpha = 0.99$	
x	$V(x)$	Res error	$V(x)$	Res error	$V(x)$	Res error
0.1	$5.87208 \times 10--6$	-9.076×10^{-20}	$5.87208 \times 10--6$	1.16701×10^{-19}	$5.87208 \times 10--6$	6.48938×10^{-21}
0.2	$2.26882 \times 10--5$	6.62623×10^{-20}	$2.26882 \times 10--5$	-3.50514×10^{-20}	$2.26882 \times 10--5$	-1.64872×10^{-19}
0.3	$5.0024 \times 10--5$	7.16925×10^{-20}	$5.0024 \times 10--5$	-5.38787×10^{-20}	$5.0024 \times 10--5$	-5.48153×10^{-20}
0.4	$8.76616 \times 10--5$	6.17061×10^{-20}	$8.76616 \times 10--5$	4.81294×10^{-20}	$8.76616 \times 10--5$	-2.07791×10^{-19}
0.5	$1.35451 \times 10--4$	-7.89358×10^{-20}	$1.35451 \times 10--4$	8.88535×10^{-20}	$1.35451 \times 10--4$	6.49314×10^{-20}
0.6	$1.9328 \times 10--4$	5.62103×10^{-20}	$1.9328 \times 10--4$	-8.1769×10^{-20}	$1.9328 \times 10--4$	-1.40755×10^{-20}
0.7	$2.61056 \times 10--4$	2.13652×10^{-20}	$2.61056 \times 10--4$	2.46311×10^{-19}	$2.61056 \times 10--4$	8.01669×10^{-21}
0.8	$3.38702 \times 10--4$	4.3926×10^{-20}	$3.38702 \times 10--4$	-3.74249×10^{-20}	$3.38702 \times 10--4$	-1.55483×10^{-19}
0.9	$4.26153 \times 10--4$	-1.25871×10^{-19}	$4.26153 \times 10--4$	-4.78429×10^{-20}	$4.26153 \times 10--4$	-1.57049×10^{-19}
1.	$5.2335 \times 10--4$	7.27423×10^{-20}	$5.2335 \times 10--4$	3.94566×10^{-20}	$5.2335 \times 10--4$	-5.88772×10^{-20}

Table 10: Solution and residual error for γ keeping $\alpha = 0.95, S_t = 0.001, \phi = 0.1, W_e = 0.01$, and $a = 0.1$ fixed in Case 3 of drainage.

	$\gamma = 1.2$		$\gamma = 1.6$		$\gamma = 1.99$	
x	$V(x)$	Res error	$V(x)$	Res error	$V(x)$	Res error
0.1	$5.72659 \times 10--4$	-8.85316×10^{-20}	$1.75703 \times 10--5$	-9.8013×10^{-20}	$5.1638 \times 10--6$	4.95955×10^{-21}
0.2	$1.31563 \times 10--4$	-1.35853×10^{-19}	$5.3263 \times 10--5$	-5.72227×10^{-20}	$2.0512 \times 10--5$	1.06505×10^{-20}
0.3	$2.14014 \times 10--4$	1.63841×10^{-20}	$1.01899 \times 10--4$	3.02498×10^{-22}	$4.5966 \times 10--5$	2.98796×10^{-20}
0.4	$3.02251 \times 10--4$	-1.77002×10^{-19}	$1.61463 \times 10--4$	2.74106×10^{-19}	$8.1483 \times 10--5$	8.85672×10^{-20}
0.5	$3.95057 \times 10--4$	6.75864×10^{-20}	$2.30744 \times 10--4$	-2.9077×10^{-20}	$1.2703 \times 10--4$	-1.25093×10^{-19}
0.6	$4.91675 \times 10--4$	-1.24341×10^{-19}	$3.08901 \times 10--4$	2.8962×10^{-19}	$1.8259 \times 10--4$	7.08777×10^{-21}
0.7	$5.91581 \times 10--4$	3.33152×10^{-20}	$3.95307 \times 10--4$	4.4664×10^{-20}	$2.4815 \times 10--4$	3.73471×10^{-20}
0.8	$6.94391 \times 10--4$	-5.4743×10^{-20}	$4.89465 \times 10--4$	-4.42716×10^{-20}	$3.2368 \times 10--4$	-2.48835×10^{-20}
0.9	$7.99811 \times 10--4$	-4.85706×10^{-20}	$5.90971 \times 10--4$	-1.45847×10^{-19}	$4.0917 \times 10--4$	1.10885×10^{-19}
1.	$9.07604 \times 10--4$	-2.09174×10^{-19}	$6.99484 \times 10--4$	1.98754×10^{-20}	$5.0462 \times 10--4$	2.57162×10^{-19}

Case 1

$$\frac{d^2v(x)}{dx^2} + W_e^4\left(1-a^2\right)^2\left[\varphi\frac{d^2v(x)}{dx^2} + S_t\right]\left(D^\alpha v(x)\right)^4 - W_e^2\left(1-a^2\right)\left[\frac{d^2v(x)}{dx^2} + \varphi\frac{d^2v(x)}{dx^2} - 2S_t\right]\left(D^\alpha v(x)\right)^2 + S_t = 0, \tag{46}$$

with

$$v(0) = 0, v'(1) = 0, 0 < \alpha < 1. \tag{47}$$

Case 2

$$D^\gamma v(x) + W_e^4\left(1-a^2\right)^2\left[\varphi D^\gamma v(x) + S_t\right]\left(\frac{dv(x)}{dx}\right)^4 - W_e^2\left(1-a^2\right)\left[D^\gamma v(x) + D^\gamma v(x) - 2S_t\right]\left(\frac{dv(x)}{dx}\right)^2 + S_t = 0. \tag{48}$$

$$v(0) = 0, v'(1) = 0, 1 < \gamma < 2. \tag{49}$$

Case 3. Here both first- and second-order derivatives are replaced by the noninteger order derivative as follows:

$$D^\gamma v(x) + W_e^4\left(1-a^2\right)^2\left[\varphi D^\gamma v(x) + S_t\right]\left(D^\alpha v(x)\right)^4 - W_e^2\left(1-a^2\right)\left[D^\gamma v(x) + D^\gamma v(x) - 2S_t\right]\left(D^\alpha v(x)\right)^2 + S_t = 0, \tag{50}$$

with

$$v(0) = 0, v(1) = 0, 1 < \gamma < 2, 0 < \alpha < 1. \tag{51}$$

7. Results and Discussion

In this paper, the fractional study of thin film flow of Johnson–Segalman fluid is carried out in lifting and drainage cases. The obtained boundary value problems are solved for different values of involved parameters and results mentioned in Tables 1–4 for lifting while Tables 5–10 in drainage situation. Tables 1 and 5 present solutions and corresponding errors for different α. Tables 2 and 6 show solutions along with errors for ϕ. Tables 3 and 7 show case solutions and errors for various S_t. Table 4 demonstrates solutions and errors for various W_e in the lifting case.

Tables 8–10 exhibit solutions and residual errors for different values of fractional parameters in Cases 2 and 3, respectively. Exploration of these tables confirms that solutions are consistent. Influence of different parameters on $V(x)$ in lifting and drainage cases are seen graphically. Figures 1–8show the effect of different parameters on $V(x)$

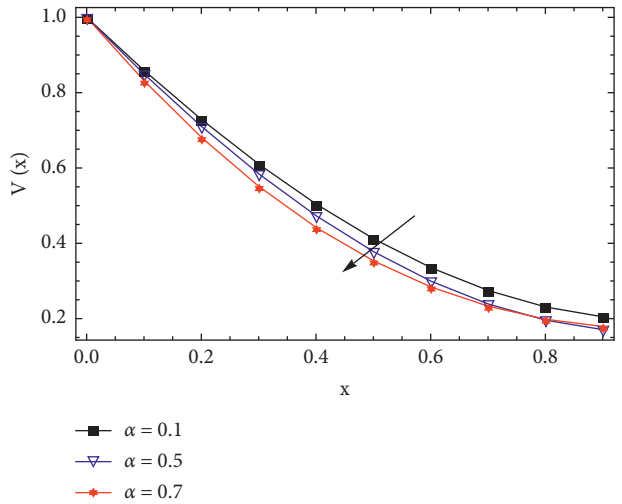

Figure 1: Effect of α on $V(x)$ for $a = 0.1, W_e = 1, S_t = 1$, and $\phi = 0.1$ fixed in the lifting case.

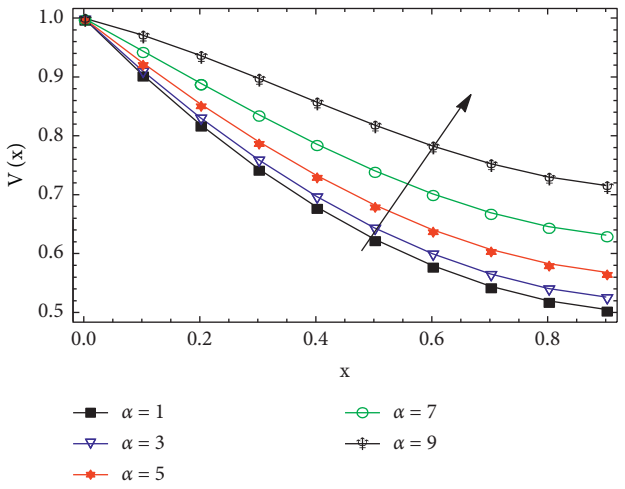

Figure 2: Effect of a on $V(x)$ for $\alpha = 0.95, S_t = 1, \phi = 0.01$, and $W_e = 0.1$ fixed in the lifting case.

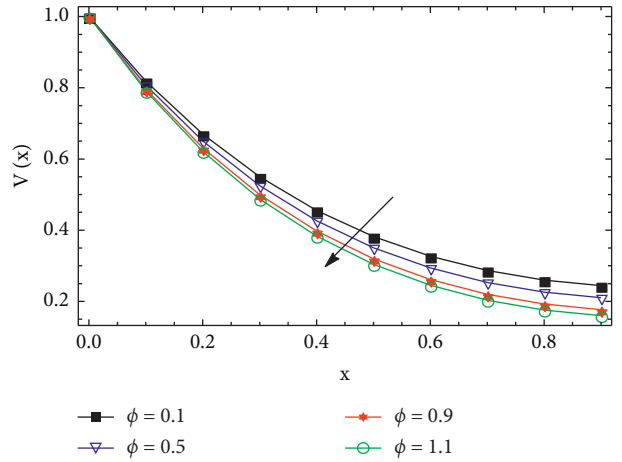

Figure 3: Effect of ϕ on $V(x)$ for $\alpha = 0.98, a = 0.1$, $W_e = 1$, and $S_t = 1$ fixed in the lifting case.

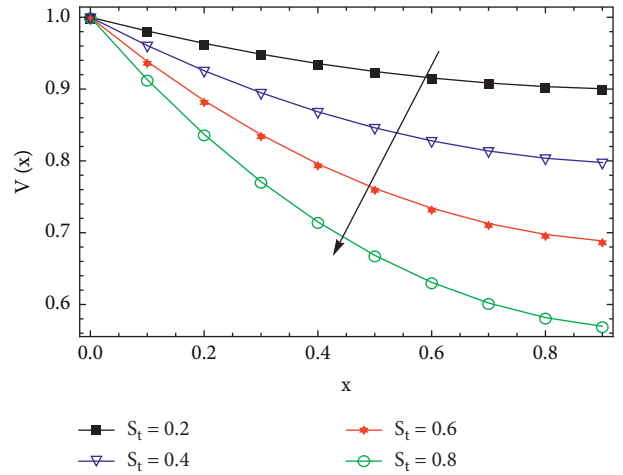

Figure 4: The effect of S_t on $V(x)$ for $\alpha = 0.95, a = 0.1$, $W_e = 1$, and $\phi = 0.1$ fixed in the lifting case.

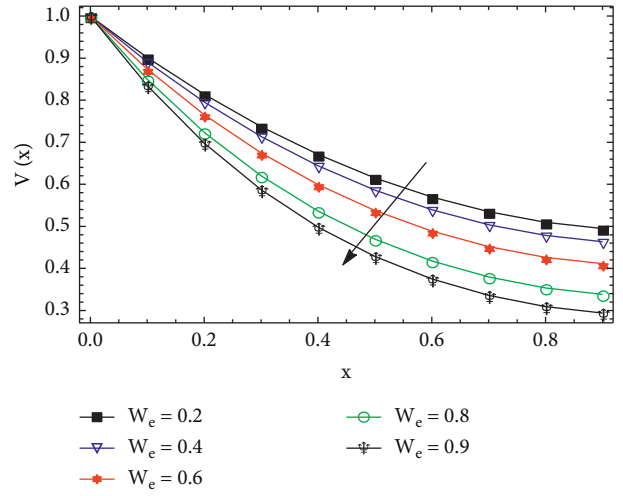

Figure 5: Effect of W_e on $V(x)$ for $\alpha = 0.98, a = 0.1, S_t = 1$, and $\phi = 0.1$ fixed in the lifting case.

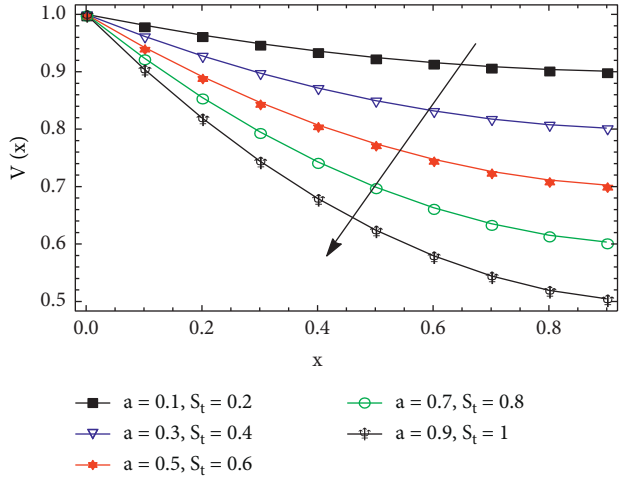

Figure 6: Effect of increasing S_t and a simultaneously on $V(x)$ for $\alpha = 0.99, W_e = 0.1$, and $\phi = 0.1$ fixed in the lifting case.

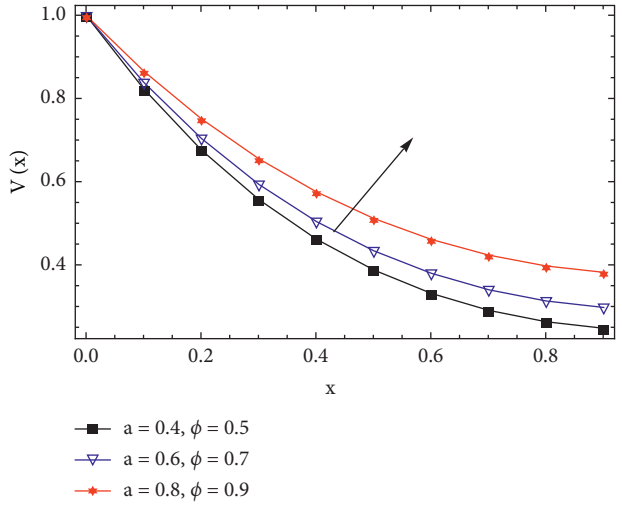

Figure 7: Effect of increasing ϕ and a simultaneously on $V(x)$ for $\alpha = 0.95, W_e = 1$, $S_t = 0.1$ fixed in the lifting case.

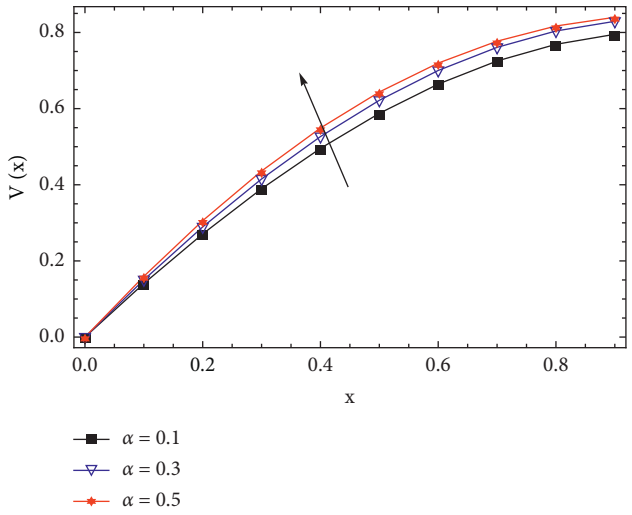

Figure 8: Effect of α on $V(x)$ for $a = 0.1, W_e = 1$, $S_t = 1$, and $\phi = 0.1$ fixed for Case 1 in the drainage case.

in the lifting case. Figure 1 shows the effect of α on $V(x)$. It is seen that increasing α reduces $V(x)$. Figure 2 shows effect of a on $V(x)$, showing that a has direct relationship with $V(x)$. Figures 3–5 depict the consequence of ϕ, S_t, and W_e on $V(x)$, respectively. It is observed that Weissenberg number is the dimensionless number while this parameter is used to measure the flow behavior into motion regarding particles. It is physically defined as ratio among viscous force and elastic force. Viscous force is enhanced against higher values of Weissenberg number, whereas higher viscous force brings a declination into motion of fluid particles. Momentum layers are also the reducing function versus implanted higher values of the Weissenberg number. It is seen that $V(x)$ has inverse relationship with mentioned parameters in all cases. Figure 6 indicates the impact of increasing a and S_t simultaneously on $V(x)$. It is observed that $V(x)$ decreases with an increase in a and S_t, and hence, S_t is a more

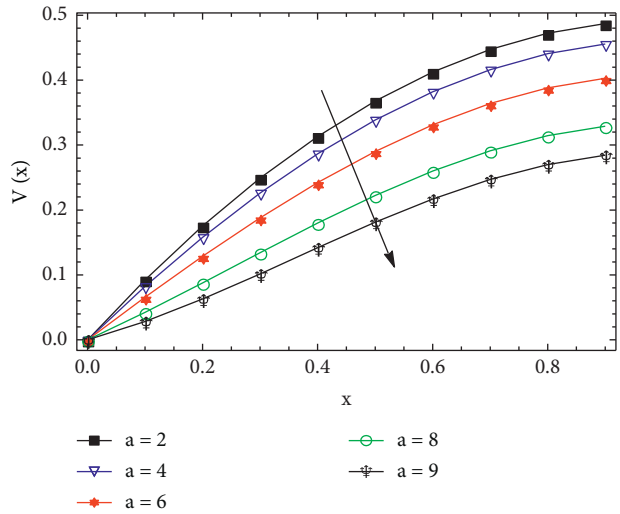

Figure 9: Effect of a on $V(x)$ for $\alpha = 0.95, W_e = 0.1$, $S_t = 1$, and $\phi = 0.01$ fixed for Case 1 in the drainage case.

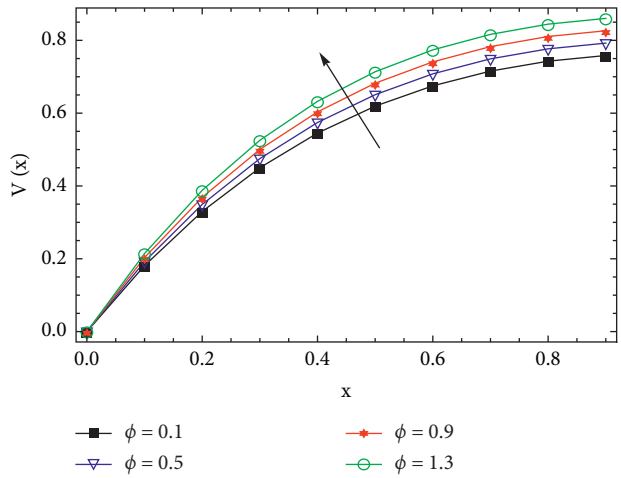

Figure 10: The effect of ϕ on $V(x)$ for $\alpha = 0.97, a = 0.1, W_e = 1$, and $S_t = 1$ fixed for Case 1 in the drainage case.

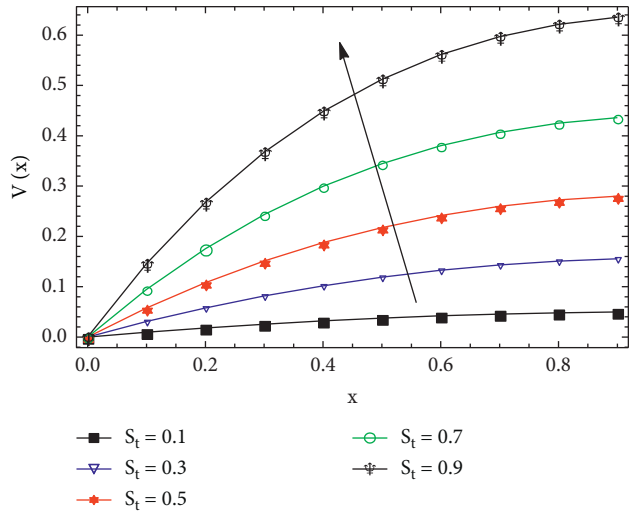

Figure 11: The effect of S_t on $V(x)$ for $\alpha = 0.95, a = 0.2, W_e = 1$, and $\phi = 0.1$ fixed for Case 1 in the drainage case.

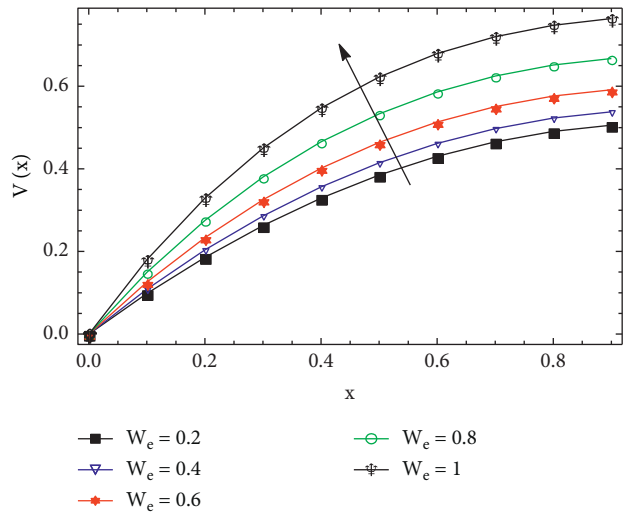

Figure 12: The effect of W_e on $V(x)$ for $\alpha = 0.95, a = 0.1$, $S_t = 1$, and $\phi = 0.1$ fixed for Case 1 in the drainage case.

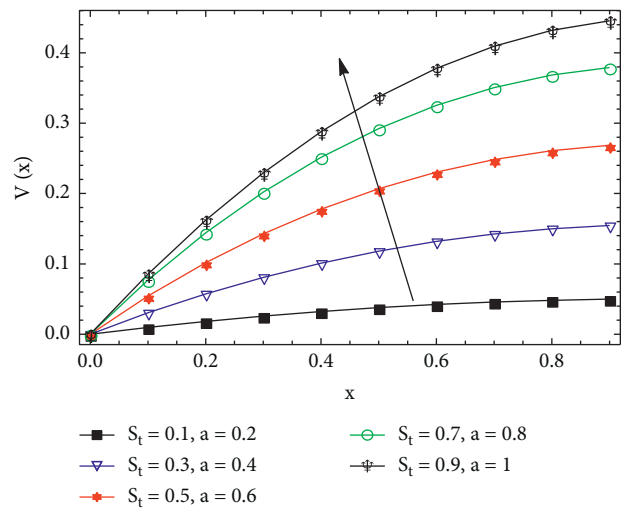

Figure 13: Effect of increasing S_t and a simultaneously on $V(x)$ for $\alpha = 0.95, W_e = 1$, and $\phi = 0.01$ fixed for Case 1 in the drainage case.

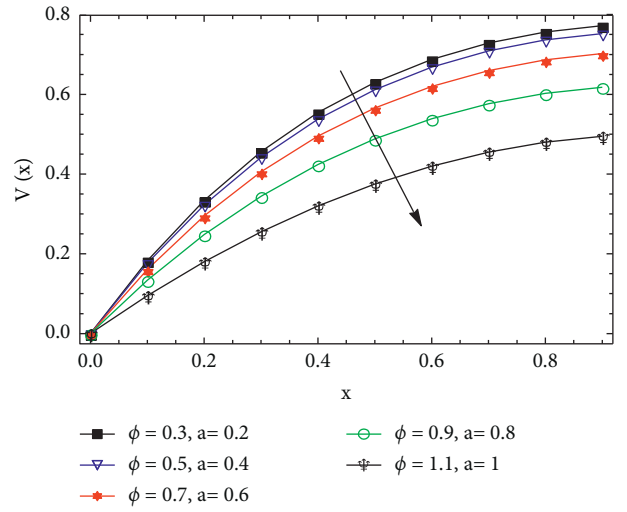

Figure 14: Effect of increasing ϕ and a simultaneously on $V(x)$ for $\alpha = 0.95, W_e = 1$, and $S_t = 1$ fixed for Case 1 in the drainage case.

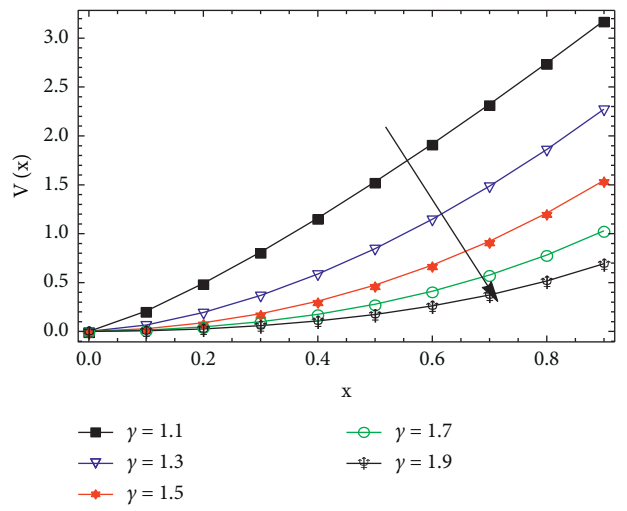

Figure 15: The effect of γ on $V(x)$ for $a = 0.1, W_e = 1$, $S_t = 1$, and $\phi = 0.1$ fixed for Case 2 in the drainage case.

influential parameter then a. Figure 7 shows the combine effect of a and ϕ. Motion into fluid particles is reduced versus higher impact of ratio of viscosity number. For higher values of ϕ make a declination into motion of fluid. So, fluid becomes more viscous and thick. It is seen that $V(x)$ increases with increase in a and ϕ, and hence, a is more influential than ϕ. Figures 8–14 show the effect of different parameters on $V(x)$ in Case 1 of drainage. Figure 8 depicts the effect of α on $V(x)$. It is seen that $V(x)$ has direct association with α. Figure 9 shows the impact of a on $V(x)$. It is seen that $V(x)$ has inverse association with a. Figures 10–12 show the effect of ϕ, S_t, and W_e on $V(x)$, respectively. It is realized that $V(x)$ has direct connection with these parameters. Figure 13 shows the combined effect of increasing S_t and a. It is observed that $V(x)$ increases with increase in S_t and a, and hence, S_t is more influential than a. Stoke number (S_t) is a dimensionless number. Physically, it is used to know characterization of fluid particles during the flow of fluid. Basically, it is defined as the ratio among characteristics time and characteristics time during the flow regarding particle. So, it is noticed that flow of particles is directly proportional against velocity of fluid. Furthermore, Figure 14 shows the effect of increasing ϕ and a on $V(x)$. Investigation shows that a is a more influential than ϕ. Figure 15 shows the effect of γ on $V(x)$ in Case 2 of drainage. It is seen that $V(x)$ has inverse association with γ. Figures 16 and 17 indicate the effect of α and γ on $V(x)$ in Case 3 of drainage. It is observed that α and γ exhibit opposite behaviors on $V(x)$ in this case. In addition to the above results, volumetric flow and average velocities are also computed in lifting and drainage cases.

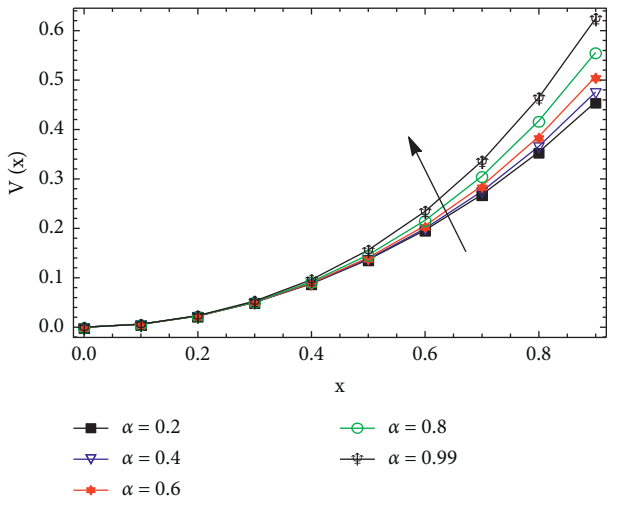

Figure 16: The effect of α on $V(x)$ for $\gamma = 1.95, a = 0.1, W_e = 1$, $S_t = 1$, and $\phi = 0.1$ fixed for Case 3 in the drainage case.

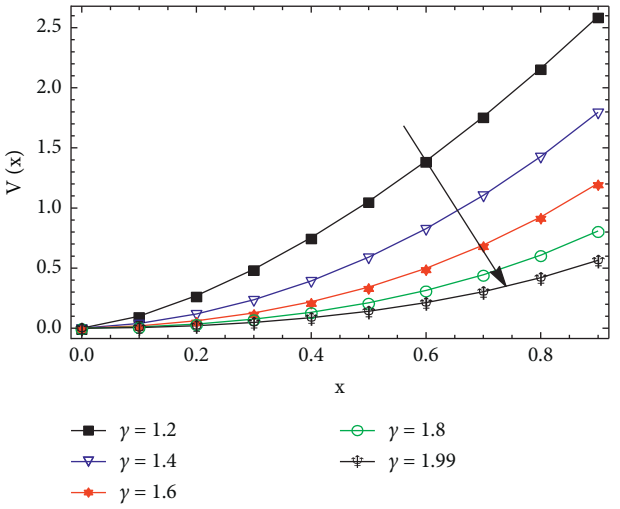

Figure 17: The effect of γ on $V(x)$ for $\alpha = 99, a = 0.1, W_e = 1$, $S_t = 1$, and $\phi = 0.1$ fixed for Case 3 in the drainage case.

8. Conclusions

In this study, thin film of Johnson–Segalman fluid flow is investigated in fractional space for the case of lifting and drainage. Solutions of boundary value problems are obtained using fractional calculus and HPM. Validity of obtained solutions is established through residual errors' computation. Few important results related to different parameters are established in the fractional space. It is comprehended that fractional parameter α has shown reverse effect in drainage and lifting. The study also discloses that fractional state Stokes and Weissenberg numbers showed similar effects on the fluid velocity in drainage and lifting cases. It is further seen that the Stokes number is the most influential parameter in both lifting and drainage situations. [34–39].

Nomenclature

Symbols

v:	Vector velocity
μ:	Kinematic viscosity
div:	Divergence
ρ:	Fluid density
σ:	Cauchy stress tensor
p:	Pressure
T:	Tensor
η:	Independent variable
g:	Gravitational force
f:	Body force
f_1, f_2:	Components of body force
$\alpha\gamma$:	Fractional parameters
C_μ:	Real number
x, y:	Space coordinates
T_{xx}, T_{xy}:	Components of tensor
ϕ:	Ratio of viscosities
S_t:	Stoke number
We:	Weissenberg number.

Appendix

A. Homotopy Solution in Case 1 of Drainage

Homotopy $\Omega \times [0,1] \longrightarrow \Re$, for equation (46), is

$$(1-p)\frac{d^2v(x)}{dx^2} + p\frac{d^2v(x)}{dx^2} + W_e^4\left(1-a^2\right)^2\left[\varphi\frac{d^2v(x)}{dx^2} + S_t\right]\left(D^\alpha v(x)\right)^4$$
$$-W_e^2\left(1-a^2\right)\left[\frac{d^2v(x)}{dx^2} + \varphi\frac{d^2v(x)}{dx^2} - 2S_t\right]\left(D^\alpha v(x)\right)^2 + S_t\Bigg] = 0. \quad (A.1)$$

Using (46) and (47), various order problems are obtained.

Zeroth-order problem:

$$v_0''(x) = 0,\ v_0(0) = 0, v_0'(1) = 0. \tag{A.2}$$

First-order problem:

$$\begin{aligned} &S_t + 2S_t W_e^2 \left(D^\alpha v_0(x)\right)^2 - 2a^2 S_t W_e^2 \left(D^\alpha v_0(x)\right)^2 + S_t W_e^4 \left(D^\alpha v_0(x)\right)^4 \\ &- 2a^2 S_t W_e^4 \left(D^\alpha v_0(x)\right)^4 + a^4 S_t W_e^4 \left(D^\alpha v_0(x)\right)^4 - W_e^2 \left(D^\alpha v_0(x)\right)^2 v_0''(x) \\ &+ a^2 W_e \left(D^\alpha v_0(x)\right)^2 v_0''(\mathrm{x}) - W_e^2 \phi \left(D^\alpha v_0(x)\right)^2 v_0''(x) - 2a^2 W_e^4 \phi \left(D^\alpha v_0(x)\right)^4 v_0''(x) \\ &+ a^2 W_e^2 \phi \left(D^\alpha v_0(x)\right)^2 v_0''(x) + W_e^4 \phi \left(D^\alpha v_0(x)\right)^4 v_0''(x) \\ &+ a^4 W_e^4 \phi \left(D^\alpha v_0(x)\right)^4 v_0''(x) + v_1''(x) = 0,\ v_1(0) = 0, v_1'(1) = 0. \end{aligned} \tag{A.3}$$

Second-order problem:

$$\begin{aligned} &4S_t W_e^2 \left(D^\alpha v_0(x)\right)\left(D^\alpha v_1(x)\right) - 4a^2 S_t W_e^2 \left(D^\alpha v_0(x)\right)\left(D^\alpha v_1(x)\right) \\ &+ 4S_t W_e^4 \left(D^\alpha v_0(x)\right)^3 \left(D^\alpha v_1(x)\right) - 8a^2 S_t W_e^4 \left(D^\alpha v_0(x)\right)^3 \left(D^\alpha v_1(x)\right) \\ &+ 4a^4 S_t W_e^4 \left(D^\alpha v_0(x)\right)^3 \left(D^\alpha v_1(x)\right) - 2W_e^2 \left(D^\alpha v_0(x)\right)\left(D^\alpha v_1(x)\right) v_0''(x) \\ &+ 2a^2 W_e^2 \left(D^\alpha v_0(x)\right)\left(D^\alpha v_1(x)\right) v_0''(x) - 2W_e^2 \phi \left(D^\alpha v_0(x)\right)\left(D^\alpha v_1(x)\right) v_0''(x) \\ &+ 2a^2 W_e^2 \phi \left(D^\alpha v_0(x)\right)\left(D^\alpha v_1(x)\right) v_0''(x) + 4W_e^4 \phi \left(D^\alpha v_0(x)\right)^3 \left(D^\alpha v_1(x)\right) v_0''(x) \\ &- 8a^2 W_e^4 \phi \left(D^\alpha v_0(x)\right)^3 \left(D^\alpha v_1(x)\right) v_0''(x) + 4a^4 W_e^4 \phi \left(D^\alpha v_0(x)\right)^3 \left(D^\alpha v_1(x)\right) v_0''(x) \\ &- W_e^2 \left(D^\alpha v_0(x)\right)^2 v_1''(x) + a^2 W_e^2 \left(D^\alpha v_0(\mathrm{x})\right)^2 v_1''(x) - W_e^2 \phi \left(D^\alpha v_0(x)\right)^2 v_1''(x) \\ &+ a^2 W_e^2 \phi \left(D^\alpha v_0(x)\right)^2 v_1''(\mathrm{x}) + W_e^4 \phi \left(D^\alpha v_0(x)\right)^4 v_1''(x) - 2a^2 W_e^4 \phi \left(D^\alpha v_0(x)\right)^4 v_1''(x) \\ &+ a^4 W_e^4 \phi \left(D^\alpha v_0(x)\right)^4 v_1''(x) + v_2''(x) = 0, v_2(0) = 0, v_2'(1) = 0. \end{aligned} \tag{A.4}$$

Similarly, we can find higher order problems and their solutions.

Third-order approximate solution after applying Caputo definition and keeping $\alpha = 0.99$, , $a = 0.01$, $\phi = 0.1$, $W_e = 0.1$, and $S_t = 0.01$ fixed is

$$\begin{aligned} V(x) = \frac{1}{2}\left(0.2\,\mathrm{x} - 0.1\,x^2\right) + \Big(0.0380982\,\big(0.000092534x^{2.96} - 0.000137786x^4 \\ \frac{+0.000092426x^5 - 0.0000228777x^6))}{x^{1.96}} + \Big(0.0761964\big(0.0000841218x^{2.96} \\ \frac{-0.00012526x^4 + 0.0000840236x^5 - 0.0000207979\,\mathrm{x}^6))}{x^{2.96}}. \end{aligned} \tag{A.5}$$

The residual is

$$R = \frac{d^2v(x)}{dx^2} + W_e^4\left(1-a^2\right)^2\left[\varphi\frac{d^2v(x)}{dx^2} + S_t\right]\left(D^\alpha v(x)\right)^4 - W_e^2\left(1-a^2\right)\left[\frac{d^2v(x)}{dx^2} + \varphi\frac{d^2v(x)}{dx^2} - 2S_t\right]\left(D^\alpha v(x)\right)^2 + S_t. \tag{A.6}$$

B. Homotopy Solution in Case 2 of Drainage

Homotopy $\Omega \times [0,1] \longrightarrow R$ for equation (48) is

$$(1-p)\frac{d^2v(x)}{dx^2} + p\left[D^\gamma v(x) + W_e^4\left(1-a^2\right)^2\left[\varphi D^\gamma v(x) + S_t\right]\left(\frac{dv(x)}{dx}\right)^4 - W_e^2\left(1-a^2\right)\left[D^\gamma v(x) + D^\gamma v(x) - 2S_t\right]\left(\frac{dv(x)}{dx}\right)^2 + S_t\right] = 0. \tag{B.1}$$

Using (48) and (49), we obtain the following.

Zeroth-order problem:

$$D^\gamma v_0(x) = 0, v_0(0) = 0, v_0'(1) = 0. \tag{B.2}$$

First-order problem:

$$\begin{aligned} &S_t + D^\gamma v_1(x) + 2S_t W_e^2\left(v_0'(x)\right)^2 - 2a^2 S_t W_e^2\left(V_0\right)'[t]^2 - W_e^2\left(D^\gamma v_0(x)\right)\left(v_0'(x)\right)^2 \\ &+ a^2 W_e^2\left(D^\gamma v_0(x)\right)\left(v_0'(x)\right)^2 - \phi W_e^2\left(D^\gamma v_0(x)\right)\left(v_0'(x)\right)^2 + a^2\phi W_e^2\left(D^\gamma v_0(x)\right)\left(v_0'(x)\right)^2 \\ &+ S_t W_e^4\left(v_0'(x)\right)^4 - 2a^2 S_t W_e^4\left(v_0'(x)\right)^4 + a^4 S_t W_e^4\left(v_0'(x)\right)^4 + \phi W_e^4\left(D^\gamma v_0(x)\right)\left(v_0'(x)\right)^4 \\ &- 2a^2\phi W_e^4\left(D^\gamma v_0(x)\right)\left(v_0'(x)\right)^4 + a^4\phi W_e^4 D^\gamma v_0(x)\left(v_0'(x)\right)^4 = 0, v_1(0) = 0, v_1'(1) = 0. \end{aligned} \tag{B.3}$$

Second-order problem:

$$\begin{aligned} &D^\gamma v_2(x) - W_e^2\left(D^\gamma v_1(x)\right)\left(v_0'(x)\right)^2 + a^2 W_e^2\left(D^\gamma v_1(x)\right)\left(v_0'(x)\right)^2 \\ &- \phi W_e^2\left(D^\gamma v_1(x)\right)\left(v_0'(x)\right)^2 + a^2\phi W_e^2\left(D^\gamma v_1(x)\right)\left(v_0'(x)\right)^2 + \phi W_e^4\left(D^\gamma v_1(x)\right)\left(v_0'(x)\right)^4 \\ &- 2a^2\phi W_e^4\left(D^\gamma v_1(x)\right)\left(v_0'(x)\right)^4 + a^4\phi W_e^4\left(D^\gamma v_1(x)\right)\left(v_0'(x)\right)^4 + 4S_t W_e^2\left(v_0'(x)\right)\left(v_1'(x)\right) \\ &- 4a^2 S_t W_e^2\left(v_0'(x)\right)\left(v_1'(x)\right) - 2W_e^2\left(D^\gamma v_0(x)\right)\left(v_0'(x)\right)\left(v_1'(x)\right) + 2a^2 W_e^2\left(D^\gamma v_0(x)\right)\left(v_0'(x)\right)\left(v_1'(x)\right) \\ &- 2\phi W_e^2\left(D^\gamma v_0(x)\right)\left(v_0'(x)\right)\left(v_1'(x)\right) + 2a^2\phi W_e^2\left(D^\gamma v_0(x)\right)\left(v_0'(x)\right)\left(v_1'(x)\right) \\ &+ 4S_t W_e^4\left(v_0'(x)\right)^3\left(v_1'(x)\right) - 8a^2 S_t W_e^4\left(v_0'(x)\right)^3\left(v_1'(x)\right) + 4a^4 S_t W_e^4\left(v_0'(x)\right)^3\left(v_1'(x)\right) + \\ &4\phi W_e^4\left(D^\gamma v_0(x)\right)\left(v_0'(x)\right)^3\left(v_1'(x)\right) - 8a^2\phi W_e^4\left(D^\gamma v_0(x)\right)\left(v_0'(x)\right)^3\left(v_1'(x)\right) \\ &+ 4a^4\phi W_e^4\left(D^\gamma v_0(x)\right)\left(v_0'(x)\right)^3\left(v_1'(x)\right) = 0, v_2(0) = 0, v_2'(1) = 0. \end{aligned} \tag{B.4}$$

Similarly, we can find higher order problems and their solutions.

Keeping $\gamma = 1.7$, $a = 0.1$, $S_t = 0.01, W_e = 0.00\,1$, and $\phi = 0.1$ fixed and using Caputo definition, the approximate solution is

$$V(x) = -0.00647381x^{1.7} - 6.77768 \times 10^{-13}x^{3.1}. \tag{B.5}$$

The residual is

$$R = D^{\gamma}V(x) + W_e^4\left(1-a^2\right)^2\left[\varphi D^{\gamma}V(x) + S_t\right]\left(\frac{\mathrm{d}V(x)}{\mathrm{d}x}\right)^4 - W_e^2\left(1-a^2\right)\left[D^{\gamma}V(x) + D^{\gamma}V(x) - 2S_t\right]\left(\frac{\mathrm{d}V(x)}{\mathrm{d}x}\right)^2 + S_t. \tag{B.6}$$

C. Homotopy Solution in Case 3 of Drainage

Homotopy $\Omega \times [0,1] \longrightarrow R$ for equation (50) is

$$(1-p)\frac{d^2v(x)}{\mathrm{d}x^2} + p\Big[D^{\gamma}v(x) + W_e^4\left(1-a^2\right)^2\left[\varphi D^{\gamma}v(x) + S_t\right]\left(D^{\alpha}v(x)\right)^4 - W_e^2\left(1-a^2\right)\left[D^{\gamma}v(x) + D^{\gamma}v(x) - 2S_t\right]\left(D^{\alpha}v(x)\right)^2 + S_t\Big] = 0. \tag{C.1}$$

Using (50) and (51), we obtain the following.
Zeroth-order problem:

$$D^{\gamma}v_0(x) = 0, v_0(0) = 0, v_0'(1) = 0. \tag{C.2}$$

First-order problem:

$$\begin{aligned} &S_t + 2S_tW_e^2\left(D^{\alpha}v_0(x)\right)^2 - 2a^2S_tW_e^2\left(D^{\alpha}v_0(x)\right)^2 + S_tW_e^4\left(D^{\alpha}v_0(x)\right)^4 \\ &- 2a^2S_tW_e^4\left(D^{\alpha}v_0(x)\right)^4 + a^4S_tW_e^4\left(D^{\alpha}v_0(x)\right)^4 - W_e^2\left(D^{\alpha}v_0(x)\right)^2\left(D^{\gamma}v_0(x)\right) \\ &+ a^2W_e^2\left(D^{\alpha}v_0(x)\right)^2\left(D^{\gamma}v_0(x)\right) - \phi W_e^2\left(D^{\alpha}v_0(x)\right)^2\left(D^{\gamma}v_0(x)\right) \\ &+ a^2\phi W_e^2\left(D^{\alpha}v_0(x)\right)^2\left(D^{\gamma}v_0(x)\right) + \phi W_e^4\left(D^{\alpha}v_0(x)\right)^4\left(D^{\gamma}v_0(x)\right) \\ &- 2a^2\phi W_e^4\left(D^{\alpha}v_0(x)\right)^4\left(D^{\gamma}v_0(x)\right) + a^4\phi W_e^4\left(D^{\alpha}v_0(x)\right)^4\left(D^{\gamma}v_0(x)\right) \\ &+ \left(D^{\gamma}v_1(x)\right) = 0, v_1(0) = 0, v_1'(1) = 0. \end{aligned} \tag{C.3}$$

Second-order problem:

$$\begin{aligned} &4S_tW_e^2\left(D^{\alpha}v_0(x)\right)\left(D^{\alpha}v_1(x)\right) - 4a^2S_tW_e^2\left(D^{\alpha}v_0(x)\right)\left(D^{\alpha}v_1(x)\right) \\ &+ 4S_tW_e^4\left(D^{\alpha}v_0(x)\right)^3\left(D^{\alpha}v_1(x)\right) - 8a^2S_tW_e^4\left(D^{\alpha}v_0(x)\right)^3\left(D^{\alpha}v_1(x)\right) \\ &+ 4a^4S_tW_e^4\left(D^{\alpha}v_0(x)\right)^3\left(D^{\alpha}v_1(x)\right) - 2W_e^2\left(D^{\alpha}v_0(x)\right)\left(D^{\alpha}v_1(x)\right)\left(D^{\gamma}v_0(x)\right) \\ &+ 2a^2W_e^2\left(D^{\alpha}v_0(x)\right)\left(D^{\alpha}v_1(x)\right)\left(D^{\gamma}v_0(x)\right) - 2\phi W_e^2\left(D^{\alpha}v_0(x)\right)\left(D^{\alpha}v_1(x)\right)\left(D^{\gamma}v_0(x)\right) \\ &+ 2a^2\phi W_e^2\left(D^{\alpha}v_0(x)\right)\left(D^{\alpha}v_1(x)\right)\left(D^{\gamma}v_0(x)\right) + 4\phi W_e^4\left(D^{\alpha}v_0(x)\right)^3\left(D^{\alpha}v_1(x)\right)\left(D^{\gamma}v_0(x)\right) \\ &- 8a^2\phi W_e^4\left(D^{\alpha}v_0(x)\right)^3\left(D^{\alpha}v_1(x)\right)\left(D^{\gamma}v_0(x)\right) + 4a^4\phi W_e^4\left(D^{\alpha}v_0(x)\right)^3\left(D^{\alpha}v_1(x)\right)\left(D^{\gamma}v_0(x)\right) - \frac{-b \pm \sqrt{b^2-4ac}}{2a} \end{aligned}$$

$$\cdot W_e^2\left(D^\alpha v_0(x)\right)^2\left(D^\gamma v_1(x)\right) + a^2 W_e^2\left(D^\alpha v_0(x)\right)^2\left(D^\gamma v_1(x)\right) - \phi W_e^2\left(D^\alpha v_0(x)\right)^2\left(D^\gamma v_1(x)\right)$$
$$+ a^2\phi W_e^2\left(D^\alpha v_0(x)\right)^2\left(D^\gamma v_1(x)\right) + \phi W_e^4\left(D^\alpha v_0(x)\right)^4\left(D^\gamma v_1(x)\right) - 2a^2\phi W_e^4\left(D^\alpha v_0(x)\right)^4\left(D^\gamma v_1(x)\right)$$
$$+ a^4\phi W_e^4\left(D^\alpha v_0(x)\right)^4\left(D^\gamma v_1(x)\right) + \left(D^\gamma v_2(x)\right) = 0, v_2(0) = 0, v_2'(1). \tag{C.4}$$

Similarly, we can find higher order problems and their solutions.

Approximate solution after applying Caputo definition and keeping $\alpha = 0.95$, $\phi = 0.1, W_e = 0.1$, $a = 0.1$, $S_t = 0.1$, and $\gamma = 1.99$ fixed is

$$V(x) = -0.0504625x^{1.99} - 2.39478 \times 10^{-6}x^{4.07}. \tag{C.5}$$

The residual is

$$R = D^\gamma V(x) + W_e^4\left(1-a^2\right)^2\left[\varphi D^\gamma V(x) + S_t\right]\left(D^\alpha V(x)\right)^4$$
$$- W_e^2\left(1-a^2\right)\left[D^\gamma V(x) + D^\gamma V(x) - 2S_t\right]\left(D^\alpha V(x)\right)^2 + S_t. \tag{C.6}$$

Flow rate and average velocity in the drainage case is

$$Q = \int_0^1 v(x)\mathrm{d}x,$$
$$Q = \frac{1}{6\left(15-16\alpha+4\alpha^2\right)\Gamma(4-\alpha)^2}\left(S_t(-3+2\alpha)\left(\frac{1}{-7+2\alpha}\left(3\left(-1+a^2\right)S_t^2W_e^2\right.\right.\right. \tag{C.7}$$
$$\left.\left.\left.\cdot(-3+\alpha)^2(-16+\alpha(25+\alpha(-13+2\alpha)))(3+\phi)\right)2(-5+2\alpha)\Gamma(4-\alpha)^2\right)\right).$$

For drainage problem, the average velocity $\overline{V}$ is

$$\overline{V} = \frac{1}{6\left(15-16\alpha+4\alpha^2\right)\Gamma(4-\alpha)^2}\left(S_t(-3+2\alpha)\left(\frac{1}{-7+2\alpha}\left(3\left(-1+a^2\right)S_t^2W_e^2(-3+\alpha)^2\right.\right.\right. \tag{C.8}$$
$$\left.\left.\left.\cdot(-16+\alpha(25+\alpha(-13+2\alpha)))(3+\phi)\right) + 2(-5+2\alpha)\Gamma(4-\alpha)^2\right)\right).$$

Data Availability

All the data used to support the findings of the study are given within the article.

Conflicts of Interest

The authors declare that they have no conflicts of interest to report regarding the present study.

References

[1] C. D. Denson, "The drainage of Newtonian liquids entrained on a vertical surface," *Industrial & Engineering Chemistry Fundamentals*, vol. 9, no. 3, pp. 443–448, 1970.

[2] S. B. G. O. Brien and L. W. Schwartz, "Theory and modeling of thin film flows," *Encyclopedia of Surface and Colloid Science*, pp. 5283–5297, 2002.

[3] H. Jeffreys, "The draining of a vertical plate," *Mathematical Proceedings of the Cambridge Philosophical Society*, vol. 26, no. 2, pp. 204-205, 1930.

[4] J. J. V. Rossum, "Viscous lifting and drainage of liquid," *Applied Scientific Research*, vol. 7, pp. 141–145, 1958.

[5] G. Astarita and G. Marrucci, *Principle of Non-newtonian Fluid Mechanics*, McGraw-Hill, London UK, 1974.

[6] A. M. Siddiqui, R. Mahmood, and Q. K. Ghori, "Homotopy perturbation method for thin film flow of a third grade fluid down an inclined plane," *Chaos, Solitons & Fractals*, vol. 35, no. 1, pp. 140–147, 2008.

[7] A. M. Siddiqui, R. Mahmood, and Q. K. Ghori, "Some exact solutions for the thin film flow of a PTT fluid," *Physics Letters A*, vol. 356, no. 4-5, pp. 353–356, 2006.

[8] A. M. Siddiqui, R. Mahmood, and Q. K. Ghori, "Homotopy perturbation method for thin film flow of a fourth grade fluid down a vertical cylinder," *Physics Letters A*, vol. 352, no. 4-5, pp. 404–410, 2006.

[9] L. D. Landau, "On the problem of turbulence," *Comptes Rendus de L'Academie des Sciences de L'URSS*, vol. 44, pp. 311–314, 1944.

[10] J. T. Stuart, "On the role of Reynolds stresses in stability theory," *Journal of the Aerospace Sciences*, vol. 23, pp. 86–88, 1956.

[11] S. Ullah, K. Akhtar, N. A. Khan, and A. Ullah, "Analysis of thin film flow of generalized Maxwell fluid confronting withdrawal and drainage on non-isothermal cylindrical surfaces," *Advances in Mechanical Engineering*, vol. 11, no. 10, pp. 1–19, 2019.

[12] Y. Raun, A. Nadim, and M. Chugunova, "Thin liquid film resulting from a distributed source on a vertical wall," arXiv: 1910.10810 [physics.flu-dyn], 2019.
[13] S. Ahmad and H. Xu, "Mixed convection in gravity-driven thin nano-liquid film flow with homogeneous–heterogeneous reactions," *Physics of Fluids*, vol. 32, Article ID 023604, 2020.
[14] I. Podlubny, *Fractional Differential Equations*, Academic Press, New York USA, 1999.
[15] M. Yavuz, T. A. Sulaiman, F. Usta, and H. Bulut, "Analysis and numerical computations of the fractional regularized long-wave equation with damping term," *Mathematical Methods in the Applied Sciences*, 2020.
[16] M. Yavuz and N. Sene, "Fundamental calculus of the fractional derivative defined with Rabotnov exponential kernel and application to nonlinear dispersive wave model," *Journal of Ocean Engineering and Science*, vol. 6, no. 2, pp. 196–205, 2021.
[17] M. Qayyum and H. Khan, "Behavioral study of unsteady squeezing flow through porous medium," *Journal of Porous Media*, vol. 19, no. 1, pp. 83–94, 2016.
[18] J. H. He, "The simpler, the better: analytical methods for nonlinear oscillators and fractional oscillators," *Journal of Low Frequency Noise, Vibration and Active Control*, vol. 38, no. 3-4, pp. 1252–1260, 2019.
[19] X. Su, W. Xu, W. Chen, and H. Yang, "Fractional creep and relaxation models of viscoelastic materials via a non-Newtonian time-varying viscosity: physical interpretation," *Mechanics of Materials*, vol. 140, p. 103222, 2020.
[20] M. Kamran Alam, M. T. Rahim, T. Haroon, S. Islam, and A. M. Siddiqui, "Solution of steady thin film flow of Johnson-Segalman fluid on a vertical moving belt for lifting and drainage problems using Adomian Decomposition Method," *Applied Mathematics and Computation*, vol. 218, no. 21, pp. 10413–10428, 2012.
[21] D. J. Hashim, A. F. Jameel, T. Y. Ying, A. K. Alomari, and N. R. Anakira, "Optimal homotopy asymptotic method for solving several models of first order fuzzy fractional IVPs," *Alexandria Engineering Journal*, vol. 61, no. 6, pp. 4931–4943, 2022.
[22] A. Rysak and M. Gregorczyk, "Differential transform method as an effective tool for investigating fractional dynamical systems," *Applied Sciences*, vol. 11, no. 15, p. 6955, 2021.
[23] J. H. He, "Application of homotopy perturbation method to nonlinear wave equations," *Chaos, Solitons & Fractals*, vol. 26, pp. 295–700, 2005.
[24] L. Zada, R. Nawaz, R. Nawaz, S. Ahsan, K. S. Nisar, and D. Baleanu, "New iterative approach for the solutions of fractional order inhomogeneous partial differential equations," *AIMS Mathematics*, vol. 6, no. 2, pp. 1348–1365, 2021.
[25] J.-H. He, "Approximate analytical solution for seepage flow with fractional derivatives in porous mediaflow with fractional derivatives in porous media," *Computer Methods in Applied Mechanics and Engineering*, vol. 167, no. 1-2, pp. 57–68, 1998.
[26] M. R. Yaghouti, M. Mazjini, and A. Zabihi, "Numerical solution of a family of fractional differential equations by use of RBF method," *World Applied Programming*, vol. 2, no. 2, pp. 88–96, 2012.
[27] Z. Liu, J. R. Clausen, R. R. Rao, and C. K. Aidun, "Nanoparticle diffusion in sheared cellular blood flow," *Journal of Fluid Mechanics*, vol. 871, pp. 636–667, 2019.
[28] W. Al-Kouz, C. S. Reddy, M. S Alqarni, B. Mahanthesh, and B. Mahanthesh, "Spectral quasi-linearization and irreversibility analysis of magnetized cross fluid flow through a microchannel with two different heat sources and Newton boundary conditions," *The European Physical Journal Plus*, vol. 136, no. 6, 2021.
[29] J.-H. He, "Homotopy perturbation technique," *Computer Methods in Applied Mechanics and Engineering*, vol. 178, no. 3-4, pp. 257–262, 1999.
[30] O. D. Makinde, M. T. Omojola, B. Mahanthesh et al., "Significance of buoyancy, velocity index and thickness of an upper horizontal surface of a paraboloid of revolution: the case of non-Newtonian carreau fluid," *Defect and Diffusion Forum*, vol. 387, pp. 550–561, 2018.
[31] S. Abbasbandy, "Homotopy perturbation method for quadratic Riccati differential equation and comparison with Adomian's decomposition method," *Applied Mathematics and Computation*, vol. 172, no. 1, pp. 485–490, 2006.
[32] R. Hilfer, *Applications of Fractional Calculus in Physics*, Academic Press, Orlando USA, 1999.
[33] J.-H. He and F.-Y. Ji, "Two-scale mathematics and fractional calculus for thermodynamics," *Thermal Science*, vol. 23, no. 4, pp. 2131–2133, 2019.
[34] B. R. Munson and D. F. Young, *Fundamentals of Fluid Mechanics*, John Wiley & Sons, New York USA, 1994.
[35] C. S. Yih, "Stability of parallel laminar flow with a free surface," *Proceedings of the Second U.S. National Congress of Applied Mechanics*, pp. 623–628, ASME, New York, 1995.
[36] S. P. Py Lin, "Finite amplitude side-band stability of a viscous film," *Journal of Fluid Mechanics*, vol. 63, no. 3, pp. 417–429, 1974.
[37] M. W. Jr Johnson and D. Segalman, "A model for viscoelastic fluid behavior which allows non-affine deformation," *Journal of Non-newtonian Fluid Mechanics*, vol. 2, no. 3, pp. 255–270, 1997.
[38] A. M. Wazwaz, "Approximate solutions to boundary value problems of higher order by the modified decomposition method," *Computers and Mathematics with Applications*, vol. 40, no. 6-7, pp. 679–691, 2000.
[39] M. A. Noor and S. T. Mohyud-Din, "Variational homotopy perturbation method for solving higher dimensional initial boundary value problems," *Mathematical Problems in Engineering*, vol. 2008, pp. 1–11, 2008.

Hindawi
Mathematical Problems in Engineering
Volume 2022, Article ID 9469164, 12 pages
https://doi.org/10.1155/2022/9469164

Research Article

Analysis of Hybrid Nanofluid Stagnation Point Flow over a Stretching Surface with Melting Heat Transfer

Muhammad Jawad,[1] **Ziad Khan**,[1] **Ebenezer Bonyah**,[2] **and Rashid Jan**[1]

[1]*Department of Mathematics, University of Swabi, Swabi 23561, Khyber Pakhtunkhwa, Pakistan*
[2]*Department of Mathematics Education, Akenten Appiah Menka University of Skills Training and Entrepreneurial Development, Kumasi, Ghana*

Correspondence should be addressed to Ebenezer Bonyah; ebbonya@gmail.com

Received 26 October 2021; Revised 31 December 2021; Accepted 8 January 2022; Published 3 February 2022

Academic Editor: Arshad Riaz

The behavior of hybrid nanofluid and stagnation point flow toward a stretched surface along with melting heat transfer, second-order slip, electric field, and magnetic field effect is investigated in this study. Hybrid nanoparticles alumina (Al_2O_3) and copper (Cu) are considered with the base fluids water (H_2O). The PDEs with corresponding boundary constraints are transformed into a set of nonlinear ODEs using similarities transformation. The set of nonlinear ODEs are analyzed analytically using semianalytical method HAM in Mathematica software. Dual solution is determined which relaying on the emerging parameters included magnetic field, volume fractions, electric field, dimensionless surface velocity slip factors, Eckert number, and Prandtl number. The results are shown in the velocity and temperature curves as well as skin friction coefficient and local Nusselt number. The analysis shows that velocity profile is an increasing function of slip parameter, electric field, while reducing function of magnetic field. Temperature profile is an increasing function of magnetic field parameter, electric field parameter, volume fraction parameter, and Eckert number, while reducing function of Prandtl number. The main outcomes are as follows that hybrid nanofluids are higher thermal properties as compared to conventional fluids. As a result, hybrid nanofluid has numerous uses in engineering cosmetics, automotive industry, home industry, for cancer treatment, food packaging, pharmaceuticals, fabrics, paper plastics, paints, ceramics, food colorants, and soaps as well.

1. Introduction

A conventional fluid like ethylene glycol and water has less value of thermal conductivity. Additions of nanosized particle improved thermal characteristics of ordinary fluids. Due to its exceptional thermophysical characteristic, a new class of fluids known as hybrid nanofluid is being used in a wide range of technical application. Hybrid nanofluids are advanced types of nanofluids that are made up of two distinct nanoparticles mixed together with a base fluid. Due to its thermal properties, hybrid nanofluids have become a new dawn for the young researcher and academics who have begun to explore hybrid nanofluids in solar energy. Mathematical modeling and its analysis contributed a lot to inspect natural phenomena in different fields of research [1–5]. The literature of heat absorption or generation of hybrid nanoparticles is rich, and many researchers contributed to study this phenomenon. Verma et al. [6] compute energy and energy efficiencies in flat plate solar collectors employing copper oxides (CuO)/MWCNTs (multiwall carbon nanotubes) and magnesium oxides (MgO)/MWCNTs nanofluid. Chen et al. [7] investigated the use of CuO/ATO (antimony-doped tin oxide) hybrid nanofluid in solar energy applications. The properties of MWCNTs-Ag/SiO_2 hybrid nanofluid in solar energy industry are investigated by Zeng et al. [8]. The authors selected these combinations due to greater absorption radiations of MWCNTs (multiwall carbon nanotubes). It is shown that multiwall carbon nanotubes (MWCNTs) are more efficient as compared to Ag/SiO_2. Xuan et al. [9] investigate the effect of

concentration on temperature using plasmonic hybrid nanofluid, namely, TiO_2-Ag/water in a solar energy absorption. The addition of nanoparticles to the refrigerant improved heat transmission and resulted in a high heat transfer coefficient for refrigeration systems. Viscosity and thermal conductivity are essential aspects to find out the performance of nanorefrigerants against ordinary water fluids. To test refrigeration system's performance, the researchers utilized different nanorefrigerants instead of traditional fluids. The efficiency of heating, ventilation, and air conditioning (HVAC) systems in refrigerant is improved by using nanoparticles. Different techniques are utilized for this motivation like ultrasonic agitation and magnetic force agitation. Experimental tests are performed by Bi et al. [10] to determine boiling heat transfer characteristics of R22 refrigerants along Al_2O_3 nanoparticle. According to findings, the inclusion of nanoparticles enhanced refrigerant heat transmission while reducing the size of bubbles that move rapidly along heat transfer surface. Ahmed and Elsaid [11] investigate characteristics of vapor compression refrigeration with chilled water air conditioning. The purpose of heat exchangers is to transfer heat from hot fluids to cool fluids, and the use of nanofluids in heat exchangers is a recent development. According to researchers and scientists, the thermal performance of heat exchangers may be considerably improved by improving thermal conductivity of base fluids. As a result, different fluids like nanofluids and hybrid nanofluids improve heat exchangers' thermal performance. Through the use of tabular heat exchanger, Madhesh and Kalaiselvam [12] studied heat transfer enhancement and rheological behavior of hybrid nanofluid. Allahyar et al. [13] performed tests using alumina-silver hybrid nanofluid to measure characteristics and pressure decrease in helical coil heat exchangers. The thermal managements of an automobile's engine are essential since it has a direct impact on its efficiency in terms of economy, materials selections, and pollution control. The addition of nanoparticles to engine oil increases vehicle performance as well as engine cooling.

Ali et al. [14] used alumina-TiO_2/oil hybrid nanofluid to investigate frictional power losses and wear rate in sliding contacts between piston ring and cylinder. By aggregating all research of a particular type of nanofluid, Sidik et al. [15] evaluated a study on motor oil cooling systems. Nanosize particle which is also cheap in cost and widely accessible may be employed in mineral oil, which increases dielectric characteristics of transformers and oil-based electrical components. Choi et al. [16] utilized Al_2O_3/AIN transformer oil-based nanofluid to improve thermal characteristic of oils. The use of nanoparticles in water-cooled nuclear reactors has potential to significantly enhance system performance in terms of economic costs and safety margins. The heat flux in fuel rod plays critical roles in determining the performance of nuclear reactors because of maximal heat flow. Boungiorno and Hu [17] observed nanofluids' essential heat flow and improved heat transfer in nuclear reactors. Mousavizadeh et al. [18] explore TiO_2/water nanofluid for evaluating heat transfer properties of the VVER-1000 nuclear reactors.

Nanotechnology used at cellular and molecular level has resulted in significant advancements in health care and life sciences [19]. In biomedical field, nanofluids and nanoparticles are frequently utilized. Nanoparticles adhere to tumor cells better than normal cells, and combining impact of radiation and hypothermia is related to heat created during the repair process as a result of radiation-induced DNA damage [20]. The primary goal of biomedical nanotechnology development is to efficiently monitor and regulate biological cell activity. Kleinstreuer et al. [21] developed biomicroelectronics mechanical systems for the first time. Nanofluids are now finding use in cancer imaging and medication administration because of their unique characteristics of nanoparticles. Iron-based nanoparticles and magnetic nanofluid are used for guiding tumors through magnet. As a consequence, cancer therapy can be improved and afflicted portions can be diagnosed without causing damage to healthy tissues. In comparison with other metal nanoparticles, magnetic nanoparticles are frequently utilized because they may be controlled by magnetic force [22]. Yan and Liu [23] conducted simulation on phase change bioheat transfer at cell levels to compare the temperatures of traditional cryosurgery with nanocryosurgery. Using Al_2O_3/water nanoparticle, Mansoury et al. [24] investigate the performance of parallel flow heat exchanger. The stagnation point flow in hybrid nanofluid across a shrinking cylinder along slip impact and viscous dissipation was researched by Ghazali et al. [25]. Alghamdi et al. [26] investigate hybrid nanofluid MHD flow containing the medicine through blood vessels. The movement of nanomaterial between two stretchy disks was investigated by Ijaz Khan and Alzahrani [27]. Gul et al. [28] studied hybrid nanoparticle flow in the conical gap between the cone and the surface of a spinning disk. Ghadikolaei et al. [29] investigate the thermophysical characteristics of $TiO_2 - Cu/H_2O$ hybrid nanoliquid using Lorentz force. The problems of heat transfer of aluminum oxide and copper hybrid nanoparticles are numerically studied by Tayebi and Chamkha [30]. Besides, Waini et al. [31] consider hybrid nanofluid flow and heat transfer over a permeable biaxial stretching/shrinking sheet. Moreover, the problems of a hybrid nanofluid flow with the influence of various emerging parameters are also considered by many researchers [32–36].

The aim of the present study is to investigate a steady two-dimensional boundary layer MHD hybrid nanofluid and stagnation point flow toward a stretching surface with melting heat transfer and second-order slip. Here, Al_2O_3 and Cu are considered as the hybrid nanofluid while H_2O as the base fluid. It is well known that it has numerous uses in engineering cosmetics, automotive industry, home industry, for cancer treatment, food packaging, pharmaceuticals, fabrics, paper plastics, paints, ceramics, food colorants, and soaps as well. Also, the comparison between HAM and NDSolve solution is computed for $f(\eta)$, $f'(\eta)$ and $\theta(\eta)$.

2. Mathematical Modeling

Here, we assume a steady two-dimensional boundary layer MHD hybrid nanofluid and stagnation point flow with melting heat transfer and second-order slip toward a stretching surface. The surface velocities and external flow of the stretching surface are, respectively, defined as $u_w(x) = \gamma x$, $u_e(x) = \omega x$ $(x) = \omega x$, where ω and γ are constants. The melting surface and ambient temperature are, respectively, represented by T_m and T_∞, where $T_m < T_\infty$. The governing equations and boundary conditions can be written in the following way (see Waini et al. [37] and Walelign et al. [38]):

$$\frac{\partial u}{\partial x} + \frac{\partial v}{\partial y} = 0, \tag{1}$$

$$u\frac{\partial u}{\partial x} + v\frac{\partial u}{\partial y} = u_e\frac{du_e}{dx} + \frac{\mu_{hnf}}{\rho_{hnf}}\frac{\partial^2 u}{\partial y^2} + \frac{\sigma_{hnf}}{\rho_{hnf}}\left(E_0B_0 - B_0^2(u_e - u)\right), \tag{2}$$

$$u\frac{\partial T}{\partial x} + v\frac{\partial T}{\partial y} = \frac{k_{hnf}}{\left(\rho C_p\right)_{hnf}}\frac{\partial^2 T}{\partial y^2} + \frac{\sigma_{hnf}}{\left(\rho C_p\right)_{hnf}} (uB_0 - E_0)^2 + \frac{Q_0}{\left(\rho C_p\right)_{hnf}}(T - T_\infty), \tag{3}$$

$$\begin{aligned} u &= u_w(x) + u_{slip}, \\ T &= T_m \\ at\ y &= 0; \\ u &\longrightarrow u_e(x), \\ T &\longrightarrow T_\infty \\ as\ y &\longrightarrow \infty, \end{aligned} \tag{4}$$

$$k_{hnf}\left(\frac{\partial T}{\partial y}\right)_{y=0} = \rho_{hnf}\left[L + c_s(T_m - T_0)\right]v(x,0). \tag{5}$$

Here, u and v represent the velocity term in the direction of x- and y-axes, respectively, and the temperature and latent heat of the hybrid nanofluid are indicated by T and L. Equation (5) shows the melting surface condition which is introduced by Roberts [39] in which c_s denotes heat capacity. Further, dynamic viscosity, thermal conductivity, heat capacity, and density of the hybrid nanofluid are represented, respectively, by μ_{hnf}, k_{hnf}, $(\rho C_p)_{hnf}$, and ρ_{hnf}.

Moreover, the slip velocity u_{slip} is introduced by [40] and defined as

$$u_{\text{slip}} = A\frac{\partial u}{\partial y} + B\frac{\partial^2 u}{\partial y^2}. \tag{6}$$

The similarity transformation of this study is defined as follows:

$$\begin{aligned} u &= \omega x f'(\eta), \\ v &= -\left(\omega \nu_f\right)^{1/2} f(\eta), \\ \theta(\eta) &= \frac{T - T_m}{T_\infty - T_m}, \\ \eta &= y\left(\frac{\omega}{\nu_f}\right)^{1/2}. \end{aligned} \tag{7}$$

Using equation (7) into equations (2)–(4), we get a set of nonlinear ODEs:

$$\frac{\mu_{hnf}}{\mu_f}f''' + ff'' - f'^2 + 1 + \frac{\sigma_{hnf}/\sigma_f}{\rho_{hnf}/\rho_f}M\left(E - (1 - f')\right) = 0, \tag{8}$$

$$\frac{1}{\Pr}\frac{k_{hnf}/k_f}{\left(\rho C_p\right)_{hnf}/\left(\rho C_p\right)_f}\theta' + f\theta' + \frac{\sigma_{hnf}/\sigma_f}{\left(\rho C_p\right)_{hnf}/\rho_f}MEc\left(f' - E\right) + \frac{\left(\rho C_p\right)_f}{\left(\rho C_p\right)_{hnf}}Q\theta = 0. \tag{9}$$

Dimensionless form of boundary conditions is as follows:

$$\begin{aligned} \Pr\frac{\rho_{hnf}}{\rho_f}f(0) + M_1\frac{k_{hnf}}{k_f}\theta'(0) &= 0, \\ f(0) = \lambda + \alpha f''(0) + \beta f'(0), \theta(0) &= 0, \\ f'(\eta) \longrightarrow 1, \theta(\eta) \longrightarrow 1, as\ \eta &\longrightarrow \infty. \end{aligned} \tag{10}$$

Here, prime represents differentiation in terms of η, ν_f is kinematic viscosity of the fluid, Pr is Prandtl number, λ is stretching parameter, $0 \le \alpha$ (first order) and $0 \ge \beta$ (second order) are the dimensionless velocity slip parameters, M_1 is melting parameter, E is electric parameter, M is magnetic parameter, and Ec is Eckert number, which is determined as follows:

$$\lambda = \frac{\gamma}{\omega},$$

$$\Pr = \frac{\left(\mu C_p\right)_f}{k_f},$$

$$\alpha = A\sqrt{\frac{\omega}{\nu_f}},$$

$$\beta = \frac{\omega B}{\nu_f},$$

$$M_1 = \frac{(T_\infty - T_m)(C_p)_f}{L + (T_m - T_0)c_s},$$
$$E = \frac{E_0}{\beta_0 \omega x},$$
$$M = \frac{\sigma \beta_0^2}{\rho_f \omega},$$
$$Ec = \frac{\omega x^2}{C_p \Delta T}. \tag{11}$$

3. Physical Quantities

Here, the subscripts hnf, nf, and f indicate hybrid nanofluids, nanofluids, and fluids, respectively, while the volume fraction of nanoparticles (Al_2O_3) and (Cu) are denoted by ϕ_1 and ϕ_2 and there solid components are represented by n_1 and n_2. The skin friction coefficient (C_f) and the local Nusselt number (Nu_x) are the most important physical variables in this problem that can be interpreted as follows:

$$C_f = \frac{\tau_w}{\rho_f (u_e)^2},$$
$$Nu_x = \frac{x q_w}{k_f (T_\infty - T_m)}. \tag{12}$$

Here, the symbol τ_w is shear stress of the stretching surface and q_w is the heat flux, which is described as follows:

$$\tau_w = \mu_{hnf} \left(\frac{\partial u}{\partial y}\right)_{y=0},$$
$$q_w = -k_{hnf} \left(\frac{\partial T}{\partial y}\right)_{y=0}. \tag{13}$$

Substituting equation (13) into equation (12), we get

$$C_f = \frac{\mu_{hnf}}{\rho_f (u_e)^2} \left(\frac{\partial u}{\partial y}\right)_{y=0},$$
$$Nu_x = -\frac{x k_{hnf}}{k_f (T_\infty - T_m)} \left(\frac{\partial T}{\partial y}\right)_{y=0}. \tag{14}$$

Using equations (7) and (14), we obtained

$$Re_x^{1/2} C_f = \frac{\mu_{hnf}}{\mu_f} f''(0),$$
$$Re_x^{1/2} Nu_x = -\frac{k_{hnf}}{k_f} \theta'(0). \tag{15}$$

Here, $Re_x = u_e x / \nu_f$ is the local Reynolds number.

4. HAM Solution

Optimal method is used for the solution procedure. The nonlinear ODEs (8) and (9) with boundary constraint (10) are solved through HAM. Mathematica program is accomplished for this process. The basic derivations of the modeled equations through HAM are detailed below.

$$\widehat{f}(\eta) = 1 - e^{-\eta},$$
$$\widehat{\Phi}(\eta) = e^{-\eta},$$
$$\widehat{\theta}(\eta) = e^{-\eta},$$
$$L_{\widehat{f}}(\widehat{f}) = \widehat{f}''',$$
$$L_{\widehat{\theta}}(\widehat{\theta}) = \widehat{\theta}''. \tag{16}$$

Linear operators $L_{\widehat{f}}$ and $L_{\widehat{\theta}}$ are signified as follows:

$$L_{\widehat{f}}\left(e_1 + e_2\eta + e_3\eta^2\right) = 0,$$
$$L_{\widehat{\theta}}(e_4 + e_5\eta) = 0. \tag{17}$$

The consistent nonlinear operator is appropriately chosen as $N_{\widehat{f}}$ and $N_{\widehat{\theta}}$ and recognized in system:

$$N_{\widehat{f}}[\widehat{f}(\zeta;\eta)] = \frac{\mu_{hnf}}{\mu_f}\widehat{f}_{\eta\eta\eta} + \widehat{f}\widehat{f}_{\eta\eta} - \widehat{f}_\eta^2 + 1 + \frac{\sigma_{hnf}/\sigma_f}{\rho_{hnf}/\rho_f} M\left(E - \left(1 - \widehat{f}_\eta\right)\right),$$
$$N_{\widehat{\theta}}[\widehat{f}(\zeta;\eta), \widehat{\theta}(\zeta;\eta)] = \frac{1}{\Pr} \frac{k_{hnf}/k_f}{(\rho C_p)_{hnf}/(\rho C_p)_f}\widehat{\theta}_{\eta\eta} + \widehat{f}\widehat{\theta}_\eta + \frac{\sigma_{hnf}/\sigma_f}{(\rho C_p)_{hnf}/\rho_f} MEc\left(\widehat{f}_\eta - E\right) + \frac{(\rho C_p)_f}{(\rho C_p)_{hnf}} Q\widehat{\theta}. \tag{18}$$

For equations (8) and (9), the 0^{th}-order system is written as follows:

$$(1-\zeta)L_{\widehat{f}}\left[\widehat{f}(\zeta;\eta) - \widehat{f}_0(\eta)\right] = p\hbar_{\widehat{f}} N_{\widehat{f}}[\widehat{f}(\zeta;\eta)],$$
$$(1-\zeta)L_{\widehat{\theta}}\left[\widehat{\theta}(\zeta;\eta) - \widehat{\theta}_0(\eta)\right] = p\hbar_{\widehat{\theta}} N_{\widehat{\theta}}[\widehat{f}(\zeta;\eta), \widehat{\theta}(\zeta;\eta)]. \tag{19}$$

BCs are as follows:

$$\Pr \frac{\rho_{hnf}}{\rho_f}\widehat{f}(\zeta;\eta)|_{\eta=0} + M\frac{k_{hnf}}{k_f}\frac{\partial\widehat{\theta}(\zeta;\eta)}{\partial\eta}|_{\eta=0} = 0,$$
$$\widehat{f}(0) = \lambda + \alpha\frac{\partial^2\widehat{f}(\zeta;\eta)}{\partial\eta^2}|_{\eta=0} + \beta\frac{\partial^2\widehat{f}(\zeta;\eta)}{\partial\eta^2}|_{\eta=0}, \widehat{\theta}(\zeta;\eta)|_{\eta=0} = 0,$$
$$\widehat{f}(\zeta;\eta)|_{\eta=\infty} \longrightarrow 1,\ \widehat{\theta}(\zeta;\eta)|_{\eta=\infty} \longrightarrow 1, as\ \eta \longrightarrow \infty. \tag{20}$$

The embedded constraint $\zeta \in [0,1]$ is utilized to control the solution convergence $\hbar_{\widehat{f}}$ and $\hbar_{\widehat{\theta}}$, when $\zeta = 0$ and $\zeta = 1$, and then we have the following:

$$\widehat{f}(1;\eta) = \widehat{f}(\eta),$$
$$\widehat{\theta}(1;\eta) = \widehat{\theta}(\eta). \tag{21}$$

For $\zeta = 0$, expand $\widehat{f}(\zeta;\eta)$ and $\widehat{\theta}(\zeta;\eta)$ through Taylor's expansion:

$$\widehat{f}(\zeta;\eta) = \widehat{f}_0(\eta) + \sum_{n=1}^{\infty} \widehat{f}_n(\eta)\zeta^n,$$
$$\widehat{\theta}(\zeta;\eta) = \widehat{\theta}_0(\eta) + \sum_{n=1}^{\infty} \widehat{\theta}_n(\eta)\zeta^n,$$
$$\widehat{f}_n(\eta) = \frac{1}{n!}\frac{\partial \widehat{f}(\zeta;\eta)}{\partial \eta}|_{p=0}, \tag{22}$$
$$\widehat{\theta}_n(\eta) = \frac{1}{n!}\frac{\partial \widehat{\theta}(\zeta;\eta)}{\partial \eta}|_{p=0}.$$

BCs are as follows:

$$\Pr\frac{\rho_{hnf}}{\rho_f}\widehat{f}(0) + M\frac{k_{hnf}}{k_f}\widehat{\theta}'(0) = 0,$$
$$\widehat{f}(0) = \lambda + \alpha\widehat{f}''(0) + \beta\widehat{f}''(0), \widehat{\theta}(0) = 0, \tag{23}$$
$$\widehat{f}'(\eta) \longrightarrow 1, \widehat{\theta}(\eta) \longrightarrow 1, as\, \eta \longrightarrow \infty$$

Now,

$$\mathfrak{R}_n^{\widehat{f}}(\eta) = \frac{\mu_{hnf}}{\mu_f}\widehat{f}''_{n-1} + \sum_{j=0}^{w-1}\widehat{f}_{w-1-j}\widehat{f}''_j - \widehat{f}'^2_{n-1} + 1$$
$$+ \frac{\sigma_{hnf}/\sigma_f}{\rho_{hnf}/\rho_f}M\left(E - \left(1 - \widehat{f}'_{n-1}\right)\right),$$
$$\mathfrak{R}_n^{\widehat{\theta}}(\eta) = \frac{1}{\Pr}\frac{k_{hnf}/k_f}{\left(\rho C_p\right)_{hnf}/\left(\rho C_p\right)_f}\widehat{\theta}''_{n-1} + \sum_{j=0}^{w-1}\widehat{f}_{w-1-j}\widehat{\theta}'_j$$
$$+ \frac{\sigma_{hnf}/\sigma_f}{\left(\rho C_p\right)_{hnf}/\rho_f}MEc\left(\widehat{f}'_{n-1} - E\right) + \frac{\left(\rho C_p\right)_f}{\left(\rho C_p\right)_{hnf}}Q\widehat{\theta}_{n-1}. \tag{24}$$

$$\chi_n = \begin{cases} 1, & \text{if } n > 1 \\ 0, & \text{if } n \le 1 \end{cases}. \tag{25}$$

5. Result and Discussion

The purpose of this section is to go through the physical factors of figures and tables, as well as to explain the true process behind the flow and temperature variations caused by physical variables M, Q, β, $\phi_1 = \phi_2$, Ec, and Pr. A set of nonlinear ODEs (8) and (9) along with boundary constraints (10) are solved analytically using semianalytical techniques HAM in Mathematica software. The computed numerical results of $f'(\eta)$ and $\theta(\eta)$ are achieved for different values of emerging parameters involved in the equations, like velocity slip parameter, magnetic field parameter, electric field parameter, volume fraction parameter, Eckert number, and Prandtl number. Graphical representation of physical flow model is shown in Figure 1 while graphical solution for velocity and temperature gradient is discussed in Figures 2–9. The velocity graphs for different values of M, β, and E are shown in Figures 2–4. It is seen from Figure 2 that $f'(\eta)$ decreased for increasing the values of M with other parameters is fixed. It is obvious that the magnetic field depends on Lorentz force, which is stronger for a larger magnetic field. Therefore, velocity profile declines with more magnetic field. The effect of slip parameter on $f'(\eta)$ is depicted in Figure 3. As we decrease the values of slip parameter as a result velocity profiles increase. Figure 4 shows that when the value of E increases velocity profile of hybrid nanofluids improves significantly. It is the fact that the Lorentz force increasing as a result of electric field acts as an accelerating force that reduces the frictional resistance which causes to change the streamlines far from the linear stretching sheet.

Temperature graphs for different values of emerging parameters M, E, Ec, Pr, and $\phi_1 = \phi_2$ are shown in Figures 5–9. Figure 5 indicates a comparative analysis of $\theta(\eta)$ for $(Al_2O_3 - Cu)/H_2O$ against different values of M. It is observed that temperature gradient rises with increasing values of M. Physically, this is due to the external magnetic field's retarding behavior, which generates an opposite Lorentz force, which suppresses momentum transfer and improves the thermal boundary layer's viscosity.

The impact of electric field parameter on $\theta(\eta)$ is shown in Figure 6. The temperature profile enhances with rise in the values of electric field. Due to Lorentz effect, the electric field accelerates fluid temperature and thermal boundary layers.

The graphical result of temperature gradient for $(Al_2O_3 - Cu)/H_2O$ against Eckert number (Ec) when $\phi_1 = \phi_2 = 0.03$, $\Pr = 6.4$, $E = 0.6$, and $M = 0.8$ is present in Figure 7. It is seen that the values of Ec enhance. Physically, Eckert number is the ratio of kinetic energy to the specific enthalpy difference between wall and fluid. Therefore, an increase in Eckert number causes the transformation of kinetic energy into internal energy by work that is done against the viscous fluid stresses. Due to this, increasing Ec enhances the temperature of the fluid. The effect of Pr on temperature field is shown in Figure 8. This happens basically because high values of Prandtl number relate to weak thermal diffusivity, which upshots in a thinner thermal boundary layer. As a matter of fact, intensification in the Prandtl number infers an upsurge in fluid viscosity, which consecutively causes deterioration in temperature distribution. Hence, Pr can be used to upturn the rate of cooling in flows. The influence of ϕ_1 and ϕ_2 (volume fractions of $Al_2O_3 + H_2O$ and Cu+ H_2O hybrid nanoparticles, respectively) on $\theta(\eta)$ is depicted in Figure 9. For both types of nanoparticles, it is discovered that the fluid temperature rises as $\phi_1 = \phi_2$ increases. The specific heat capacity of nanoliquid is physically reduced as the credit of $\phi_1 = \phi_2$ increases. Furthermore, it boosts nanoliquid thermal expansion; therefore, temperature field rises with the rise of $\phi_1 = \phi_2$.

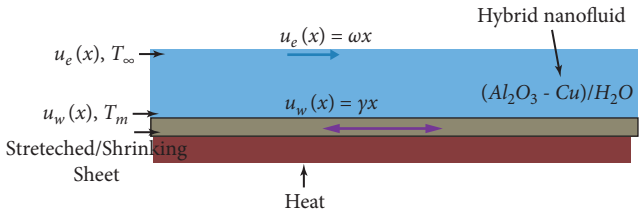

Figure 1: Graphical representation to illustrate the overall idea of the model.

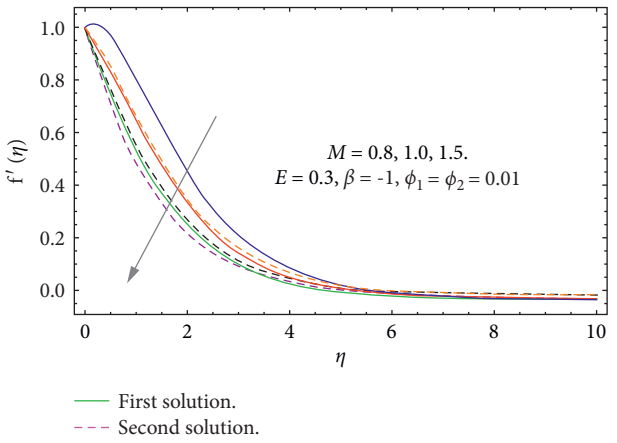

Figure 2: Velocity gradient corresponds to different values of M.

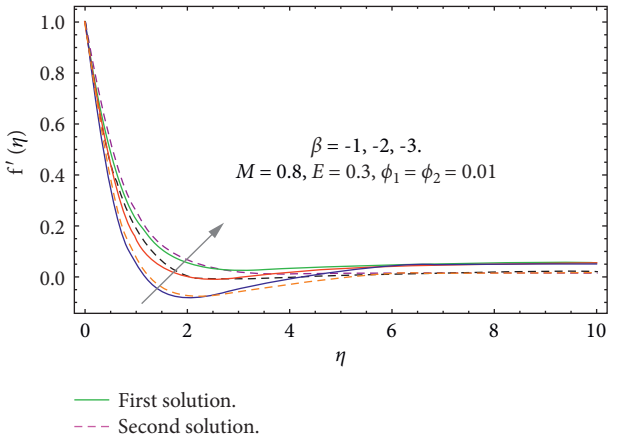

Figure 3: Velocity gradient corresponds to different values of β.

Thermophysical characteristics of nanofluid and hybrid nanofluid are defined in Table 1, while (Cu) thermophysical characteristics along with (Al_2O_3) and (H_2O) are given in Table 2. The numerical result of skin friction coefficient for different embedded parameters is presented in Table 3. We illustrate that the values of skin friction enhanced for more magnetic field and volume fraction. In fact, magnetic field produces more resistive type force against the fluid flow, and hybrid nanofluids have a higher density than ordinary fluids. Further, C_f declines, when values of E enhanced. It is seen that C_f also decreased as we decreased values of β. The numerical solution of local Nusselt number against various

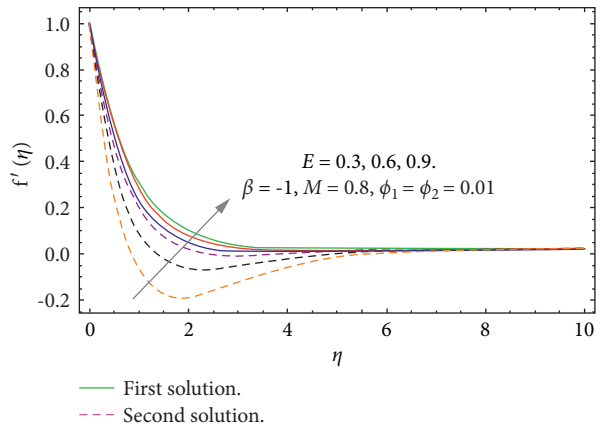

Figure 4: Velocity gradient corresponds to different values of E.

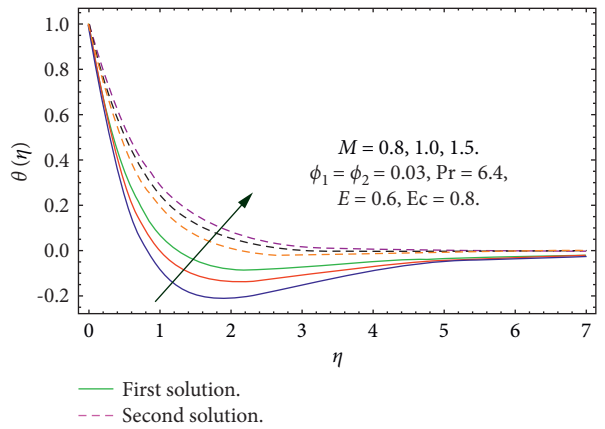

Figure 5: Temperature gradient corresponds to different values of M.

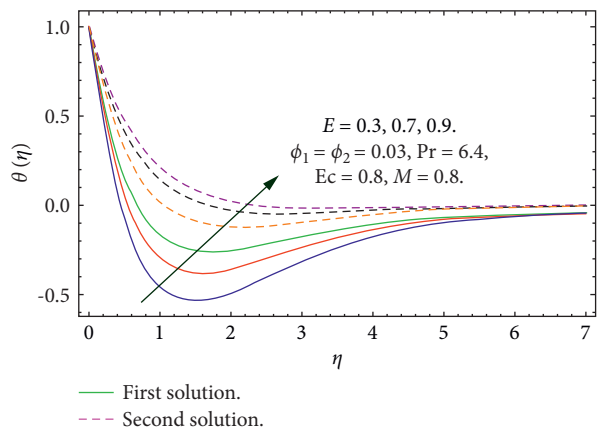

Figure 6: Temperature gradient corresponds to different values of E.

values of M, Q, E, Ec, Pr, and $\phi_1 = \phi_2$ is shown in Table 4. Increasing values of M, Q, E, Ec, and $\phi_1 = \phi_2$ boots up the Nusselt number while decreased for more values of Pr. Comparison between HAM and NDSolve solution for $f(\eta)$, $f'(\eta)$, and $\theta(\eta)$ is shown in Table 5. Hybrid nanofluid has

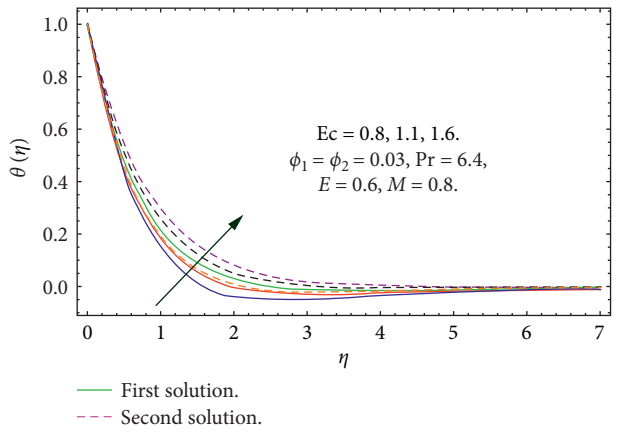

Figure 7: Temperature gradient corresponds to different values of Ec.

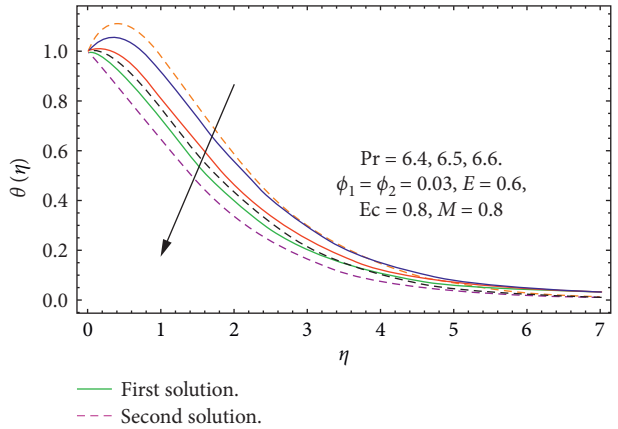

Figure 8: Temperature gradient corresponds to different values of Pr.

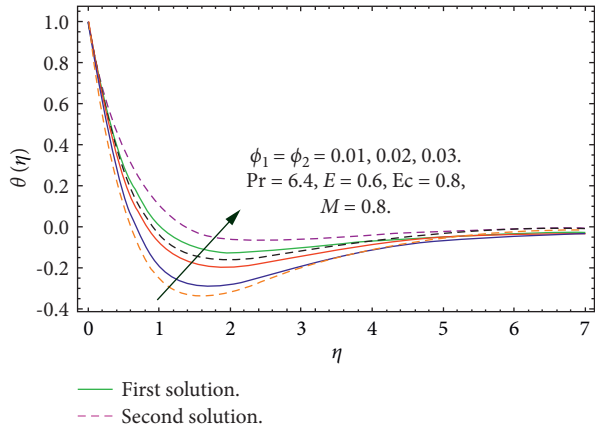

Figure 9: Temperature gradient corresponds to different values of $\phi_1 = \phi_2$.

Table 1: Applied models for thermophysical characteristics of nanofluid and hybrid nanofluid [41].

Thermophysical characteristics	Nanofluid	Hybrid nanofluid
Heat capacity	$(\rho C_p)_{nf} = (\rho C_p)_f(1-\phi_1) + (\rho C_p)_{n_1}\phi_1$	$(\rho C_p)_{hnf} = [(1-\phi_1)(\rho C_p)_f + \phi_1(\rho C_p)](1-\phi_2) + (\rho C_p)_{n_2}\phi_2$
Density	$\rho_{nf} = (1-\phi_1)\rho_f + \phi_1\rho_{n_1}$	$\rho_{hnf} = (1-\phi_1)[(1-\phi_1)\rho_f + \phi_1\rho_{n_1}] + \phi_2\rho_{n_2}$
Dynamic viscosity	$\mu_{nf} = \mu_f/(1-\phi_1)^{2.5}$	$\mu_{hnf} = \mu_f/(1-\phi_1)^{2.5}(1-\phi_2)^{2.5}$
Thermal conductivity	$k_{nf}/k_f = (k_{n_1} + 2k_f - 2\phi_1(k_f - k_{n_1}))/(k_{n_1} + 2k_f + \phi_1(k_f - k_{n_1}))$	$k_{hnf}/k_{nf} = (k_{n_2} + 2k_{nf} - 2\phi_2(k_{nf} - k_{n_2}))/(k_{n_2} + 2k_{nf} + \phi_2(k_{nf} - k_{n_2}))$

Table 2: Cu thermophysical characteristics along with Al_2O_3 and H_2O [42].

Thermophysical characteristics	Al_2O_3	Cu	H_2O
$\rho\,(kg/m^3)$	3970	8933	997.1
$C_p\,(J/kgK)$	765	385	4179
k (W/mK)	40	400	0.613
$\beta_1 \times 10^5\,(1/K)$	0.85	I.67	21

Table 3: Numerical solution of $Re_x^{1/2}C_f = \mu_{hnf}/\mu_f f''(0)$ for various values of M, E, β, and $\phi_1 = \phi_2$.

M	E	β	$\phi_1 = \phi_2$	$Re_x^{1/2}C_f = \mu_{hnf}/\mu_f f''(0)$	
				First solution	Second solution
0.8	0.3	−1.0	0.01	1.6213508	1.5142383
1.0				1.6543042	1.5735209
1.5				1.6650136	1.5910754
	0.3			1.2321081	1.1436517
	0.6			1.2205727	1.1252333
	0.9			1.2052157	1.1104628
		−1.0		1.1267062	1.0167801
		−2.0		1.1052316	0.8486314
		−3.0		1.0342501	0.6340932
			0.01	0.9236189	1.5159406
			0.02	1.4527824	1.8727814
			0.03	1.5348957	2.0302805

Table 4: Numerical solution of $Re_x^{-1/2}Nu_x = -k_{hnf}/k_f\theta'(0)$ for various values of M, Q, Pr, E, Ec, and $\phi_1 = \phi_2$.

M	Q	Pr	E	Ec	$\phi_1 = \phi_2$	$Re_x^{1/2}Nu_x = -k_{hnf}/k_f\theta'(0)$	
						First solution	Second solution
0.8	0.5	6.4	0.7	0.5	0.01	0.7874521	1.2542597
1.0						0.7663643	1.2345208
1.2						0.7586801	1.2169017
	0.5					1.1323406	1.1205636
	1.0					1.1052164	0.9021037
	1.5					1.0364381	0.8170671
		6.4				1.3484059	1.3482139
		6.5				1.4430045	1.3676202
		6.6				1.4773406	1.3755261
			0.2			1.1060213	2.4385033
			0.4			1.0705325	2.3635328
			0.6			0.8705766	2.3052406
				0.3		0.9609555	2.3310675
				0.7		0.9498006	2.3165059
				0.9		0.8779701	2.3008414
					0.01	1.5213907	1.0720828
					0.02	1.5028026	0.9721585
					0.03	1.5006208	0.9520008

Table 5: Comparison between HAM and NDSolve solution.

η	$f(\eta)$		$f'(\eta)$		$\theta(\eta)$	
	HAM	NDSolve	HAM	NDSolve	HAM	NDSolve
0	0	0	0.045639405	0.045639394	0.254	0.254
0.5	0.020450172	0.020450164	0.097702304	0.097702295	0.208120116	0.208120102
1.0	0.021416272	0.021416265	0.105158029	0.105158016	0.209405201	0.209405182

Table 5: Continued.

η	$f(\eta)$		$f'(\eta)$		$\theta(\eta)$	
	HAM	NDSolve	HAM	NDSolve	HAM	NDSolve
1.5	0.021750481	0.021750471	0.107420204	0.107420192	0.217165026	0.217165007
2.0	0.022067245	0.022067232	0.109330074	0.109330058	0.218410128	0.218410115
2.5	0.025150151	0.025150145	0.116018154	0.116018145	0.219040166	0.219040149
3.0	0.026948161	0.026948152	0.117341044	0.117341032	0.220512221	0.220512213
3.5	0.028320341	0.028320333	0.119318774	0.119318749	0.222096096	0.222096057
4.0	0.029670405	0.029670385	0.124631244	0.124631225	0.238425621	0.238425611
4.5	0.105450161	0.105450152	0.140581204	0.140581175	0.248059096	0.248059067
5.0	0.108250325	0.108250318	0.142054024	0.142054015	0.257521616	0.257521599
5.5	0.117261209	0.117261192	0.143486343	0.143486315	0.258049316	0.258049297
6.0	0.122631101	0.122631092	0.145783104	0.145783086	0.266089225	0.266089201
6.5	0.134707161	0.134707148	0.146435034	0.146435025	0.270104196	0.270104147
7.0	0.135707551	0.135707549	0.147049144	0.147049127	0.295086326	0.295086301
7.5	0.142720621	0.142720602	0.148220494	0.148220413	0.298138418	0.298138402

been found to be more efficient in increasing heat absorption or generation rates as compared to conventional fluids.

$$\begin{aligned} \phi_1 &= 0.01, \\ \phi_2 &= 0.01, \\ E &= 0.3, \\ Ec &= 1.1, \\ \Pr &= 6.4, \\ M &= 0.8, \\ Q &= 0.5. \end{aligned} \tag{26}$$

6. Conclusion

An analysis of the steady 2D boundary layer MHD stagnation point flow of hybrid nanofluid over a stretching/shrinking sheet is examined in this study. Electric field, second-order slip, and melting heat transfer are considered. The boundary layer governing equations are transformed to nonlinear ordinary differential equations using similarity transformations and then solved by HAM. Influence of several variables on velocity and temperature is scrutinized. Numerical outcomes of velocity gradient and heat transfer rates against various parameters are deliberated. Also, comparison between HAM and NDSolve solution is computed. Some significant aspects throughout this report skew our judgment on the following remarks:

(i) Increasing values of electric field enhanced $f'(\eta)$, while more magnetic field decreased $f'(\eta)$.

(ii) As we decrease the values of slip parameter as a result $f'(\eta)$ boots up while C_f declines.

(iii) More values of M, Q, E, Ec, and $\phi_1 = \phi_2$ enhanced temperature profile, while high Prandtl number Pr declines $\theta(\eta)$.

(iv) Skin friction boots up for more magnetic field and volume frictions while decreases as we increase electric field parameter.

(v) High values of M, Q, E, Ec, and $\phi_1 = \phi_2$ enhanced the local Nusselt number.

(vi) High estimation of Prandtl number reduces Nu_x.

(vii) In comparison with conventional fluids, hybrid nanofluids are quick agents for thermal analysis study, according to the findings.

(viii) The current findings are limited to the use of (Cu) and (Al_2O_3) nanoparticles in combination. Other researchers, on the additional hand, may expand the study to include other hybrid nanofluids or physical factors in order to obtain the desired result.

Notation

u: Velocity term with respect to x-axis
v: Velocity term with respect to y-axis
u_e: Free stream velocity (ms^{-1})
u_w: Surface velocity (ms^{-1})
$f(\eta)$: Dimensionless stream function
L: Latent heat of the fluid (Jkg^{-1})
C_p: Specific heat at constant pressure $(Jkg^{-1}K^{-1})$
k: Thermal conductivity $(Wm^{-1}K^{-1})$
c_s: Heat capacity of surface $(kgm^{-1}s^{-2})$
Pr: Prandtl number
Re_x: Local Reynolds number
Nu_x: Local Nusselt number
Ec: Eckert number
M: Magnetic parameter
E: Electric parameter
Q: Heat absorption parameter
β: Velocity slip parameter
ω, γ: Constant
T: Temperature of the fluid (K)
T_m: Surface temperature (K)
ρ: Density of fluid (kgm^{-3})
n_1: Solid component of (Al_2O_3)
μ: Dynamic viscosity of fluid $(kgm^{-1}s^{-1})$
θ: Dimensionless temperature
ρC_p: Heat capacity of fluid $(JK^{-1}m^{-3})$
ν: Kinematic viscosity of fluid (m^2s^{-1})

x, y: Cartesian coordinate
ψ: Stream function
τ_w: Shear stress
q_w: Heat flux
ϕ_1: Nanoparticles volume fraction for alumina (Al_2O_3)
ϕ_2: Nanoparticles volume fraction for copper (Cu)
f: Base fluids
nf: Nanofluids
hnf: Hybrid nanofluids
η: Similarity variable
n_2: Solid component of (Cu)
t: Time
T_0: Reference temperature (K)
T_∞: Ambient temperature (K).

Data Availability

No data were used to support this study.

Conflicts of Interest

The authors declare that they have no conflicts of interest.

References

[1] F. M. Alharbi, M. Naeem, M. Zubair, M. Jawad, W. U. Jan, and R. Jan, "Bioconvection due to gyrotactic microorganisms in couple stress hybrid nanofluid laminar mixed convection incompressible flow with magnetic nanoparticles and chemical reaction as carrier for targeted drug delivery through porous stretching sheet," *Molecules*, vol. 26, no. 13, Article ID 3954, 2021.

[2] S. M. Boulaaras, A. Choucha, M. Abdalla, K. Rajagopal, and S. A. Idris, "Blow-up of solutions for a coupled nonlinear viscoelastic equation with degenerate damping terms: without Kirchhoff term," *Complexity*, vol. 2021, no. 1, 9 pages, Article ID 6820219, 2021.

[3] S. Manaa, S. Boulaaras, H. Benseridi, M. Dilmi, and S. Alodhaibi, "Analysis for flow of an incompressible brinkman-type fluid in thin medium with friction," *Journal of Function Spaces*, vol. 2021, Article ID 5112840, 8 pages, 2021.

[4] H. M. Srivastava, R. Jan, A. Jan, W. Deebani, and M. Shutaywi, "Fractional-calculus analysis of the transmission dynamics of the dengue infection," *Chaos: An Interdisciplinary Journal of Nonlinear Science*, vol. 31, no. 5, Article ID 053130, 2021.

[5] S. M. Boulaaras, A. Choucha, A. Zara, M. Abdalla, and B. B. Cheri, "Global existence and decay estimates of energy of solutions for a new class of-Laplacian heat equations with logarithmic nonlinearity," *Journal of Function Spaces*, vol. 2021, Article ID 5558818, 11 pages, 2021.

[6] S. K. Verma, A. K. Tiwari, S. Tiwari, and D. S. Chauhan, "Performance analysis of hybrid nanofluids in flat plate solar collector as an advanced working fluid," *Solar Energy*, vol. 167, pp. 231–241, 2018.

[7] N. Chen, H. Ma, Y. Li et al., "Complementary optical absorption and enhanced solar thermal conversion of CuO-ATO nanofluids," *Solar Energy Materials and Solar Cells*, vol. 162, pp. 83–92, 2017.

[8] J. Zeng and Y. Xuan, "Enhanced solar thermal conversion and thermal conduction of MWCNT-SiO2/Ag binary nanofluids," *Applied Energy*, vol. 212, pp. 809–819, 2018.

[9] Y. Xuan, H. Duan, and Q. Li, "Enhancement of solar energy absorption using a plasmonic nanofluid based on TiO2/Ag composite nanoparticles," *RSC Advances*, vol. 4, no. 31, pp. 16206–16213, 2014.

[10] S.-S. Bi, L. Shi, and L.-L. Zhang, "Application of nanoparticles in domestic refrigerators," *Applied Thermal Engineering*, vol. 28, no. 14-15, pp. 1834–1843, 2008.

[11] M. S. Ahmed and A. M. Elsaid, "Effect of hybrid and single nanofluids on the performance characteristics of chilled water air conditioning system," *Applied Thermal Engineering*, vol. 163, Article ID 114398, 2019.

[12] D. Madhesh and S. Kalaiselvam, "Experimental study on heat transfer and rheological characteristics of hybrid nanofluids for cooling applications," *Journal of Experimental Nanoscience*, vol. 10, no. 15, pp. 1194–1213, 2015.

[13] H. R. Allahyar, F. Hormozi, and B. ZareNezhad, "Experimental investigation on the thermal performance of a coiled heat exchanger using a new hybrid nanofluid," *Experimental Thermal and Fluid Science*, vol. 76, pp. 324–329, 2016.

[14] M. K. A. Ali, H. Xianjun, L. Mai, C. Bicheng, R. F. Turkson, and C. Qingping, "Reducing frictional power losses and improving the scuffing resistance in automotive engines using hybrid nanomaterials as nano-lubricant additives," *Wear*, vol. 364-365, pp. 270–281, 2016.

[15] N. A. C. Sidik, M. N. A. W. M. Yazid, and R. Mamat, "A review on the application of nanofluids in vehicle engine cooling system," *International Communications in Heat and Mass Transfer*, vol. 68, pp. 85–90, 2015.

[16] C. Choi, H. S. Yoo, and J. M. Oh, "Preparation and heat transfer properties of nanoparticle-in-transformer oil dispersions as advanced energy-efficient coolants," *Current Applied Physics*, vol. 8, no. 6, pp. 710–712, 2008.

[17] J. Buongiorno and L.-W Hu, "Innovative technologies: two-phase heat transfer in water-based nanofluids for nuclear applications final report," Massachusetts Institute of Technology, Cambridge, MA, USA, No. DOE/ID/14765-8, 2009.

[18] S. M. Mousavizadeh, G. R. Ansarifar, and M. Talebi, "Assessment of the TiO2/water nanofluid effects on heat transfer characteristics in VVER-1000 nuclear reactor using CFD modeling," *Nuclear Engineering and Technology*, vol. 47, no. 7, pp. 814–826, 2015.

[19] B. Godin, J. H. Sakamoto, R. E. Serda, A. Grattoni, A. Bouamrani, and M. Ferrari, "Emerging applications of nanomedicine for the diagnosis and treatment of cardiovascular diseases," *Trends in Pharmacological Sciences*, vol. 31, no. 5, pp. 199–205, 2010.

[20] V. Sridhara, B. S. Gowrishankar, Snehalatha, and L. N. Satapathy, "Nanofluids-a new promising fluid for cooling," *Transactions - Indian Ceramic Society*, vol. 68, no. 1, pp. 1–17, 2009.

[21] C. Kleinstreuer, J. Li, and J. Koo, "Microfluidics of nano-drug delivery," *International Journal of Heat and Mass Transfer*, vol. 51, no. 23-24, pp. 5590–5597, 2008.

[22] D. Bica, L. Vékás, M. V. Avdeev et al., "Sterically stabilized water based magnetic fluids: synthesis, structure and properties," *Journal of Magnetism and Magnetic Materials*, vol. 311, no. 1, pp. 17–21, 2007.

[23] J.-F. Yan and J. Liu, "Nanocryosurgery and its mechanisms for enhancing freezing efficiency of tumor tissues," *Nanomedicine: Nanotechnology, Biology and Medicine*, vol. 4, no. 1, pp. 79–87, 2008.

[24] D. Mansoury, F. Ilami Doshmanziari, S. Rezaie, and M. M. Rashidi, "Effect of Al2O3/water nanofluid on

performance of parallel flow heat exchangers," *Journal of Thermal Analysis and Calorimetry*, vol. 135, no. 1, pp. 625–643, 2019.

[25] N. M. S. Ghazali, K. Abdul Hamid, S. K. Soid, A. S. A. Aziz, and Z. Md Ali, "Stagnation point flow in nanofluids over a shrinking cylinder with slip effect and viscous dissipation," *AIP Conference Proceedings*, vol. 2266, no. 1, Article ID 50003, 2020.

[26] W. Alghamdi, A. Alsubie, P. Kumam, A. Saeed, and T. Gul, "MHD hybrid nanofluid flow comprising the medication through a blood artery," *Scientific Reports*, vol. 11, no. 1, pp. 1–13, 2021.

[27] M. Ijaz Khan and F. Alzahrani, "Entropy optimized magnetohydrodynamics Darcy-Forchheimer second order velocity slip flow of nanomaterials between two stretchable disks," *Proceedings of the Institution of Mechanical Engineers - Part C: Journal of Mechanical Engineering Science*, vol. 234, no. 21, pp. 4190–4199, 2020.

[28] T. Gul, M. Bilal, W. Alghamdi, M. I. Asjad, and T. Abdeljawad, "Hybrid nanofluid flow within the conical gap between the cone and the surface of a rotating disk," *Scientific Reports*, vol. 11, no. 1, pp. 1–19, 2021.

[29] S. S. Ghadikolaei, M. Yassari, H. Sadeghi, K. Hosseinzadeh, and D. D. Ganji, "Investigation on thermophysical properties of Tio2-Cu/H2O hybrid nanofluid transport dependent on shape factor in MHD stagnation point flow," *Powder Technology*, vol. 322, pp. 428–438, 2017.

[30] T. Tayebi and A. J. Chamkha, "Free convection enhancement in an annulus between horizontal confocal elliptical cylinders using hybrid nanofluids," *Numerical Heat Transfer, Part A: Applications*, vol. 70, no. 10, pp. 1141–1156, 2016.

[31] I. Waini, A. Ishak, and I. Pop, "Hybrid nanofluid flow and heat transfer over a permeable biaxial stretching/shrinking sheet," *International Journal of Numerical Methods for Heat and Fluid Flow*, vol. 30, no. 7, pp. 3497–3513, 2019.

[32] T. Hayat, S. Nadeem, and A. U. Khan, "Rotating flow of Ag-CuO/H2O hybrid nanofluid with radiation and partial slip boundary effects," *The European Physical Journal E*, vol. 41, no. 6, Article ID 75, 2018.

[33] M. Subhani and S. Nadeem, "Numerical analysis of micropolar hybrid nanofluid," *Applied Nanoscience*, vol. 9, no. 4, pp. 447–459, 2019.

[34] N. S. Khashi'ie, N. Md Arifin, R. Nazar, E. H. Hafidzuddin, N. Wahi, and I. Pop, "Magnetohydrodynamics (MHD) axisymmetric flow and heat transfer of a hybrid nanofluid past a radially permeable stretching/shrinking sheet with Joule heating," *Chinese Journal of Physics*, vol. 64, pp. 251–263, 2020.

[35] N. A. Zainal, R. Nazar, K. Naganthran, and I. Pop, "MHD mixed convection stagnation point flow of a hybrid nanofluid past a vertical flat plate with convective boundary condition," *Chinese Journal of Physics*, vol. 66, pp. 630–644, 2020.

[36] E. H. Aly and I. Pop, "MHD flow and heat transfer near stagnation point over a stretching/shrinking surface with partial slip and viscous dissipation: hybrid nanofluid versus nanofluid," *Powder Technology*, vol. 367, pp. 192–205, 2020.

[37] I. Waini, A. Ishak, and I. Pop, "Melting heat transfer of a hybrid nanofluid flow towards a stagnation point region with second-order slip," *Proceedings of the Institution of Mechanical Engineers - Part E: Journal of Process Mechanical Engineering*, vol. 235, no. 2, pp. 405–415, 2021.

[38] T. Walelign, E. Haile, T. Kebede, and G. Awgichew, "Heat and mass transfer in stagnation point flow of maxwell nanofluid towards a vertical stretching sheet with effect of induced magnetic field," *Mathematical Problems in Engineering*, vol. 2021, Article ID 6610099, 2021.

[39] L. Roberts, "On the melting of a semi-infinite body of ice placed in a hot stream of air," *Journal of Fluid Mechanics*, vol. 4, no. 5, pp. 505–528, 1958.

[40] L. Wu, "A slip model for rarefied gas flows at arbitrary Knudsen number," *Applied Physics Letters*, vol. 93, no. 25, Article ID 253103, 2008.

[41] H. F. Oztop and E. Abu-Nada, "Numerical study of natural convection in partially heated rectangular enclosures filled with nanofluids," *International Journal of Heat and Fluid Flow*, vol. 29, no. 5, pp. 1326–1336, 2008.

[42] N. A. Zainal, R. Nazar, K. Naganthran, and I. Pop, "Unsteady stagnation point flow of hybrid nanofluid past a convectively heated stretching/shrinking sheet with velocity slip," *Mathematics*, vol. 8, no. 10, Article ID 1649, 2020.

Hindawi
Mathematical Problems in Engineering
Volume 2021, Article ID 1705736, 10 pages
https://doi.org/10.1155/2021/1705736

Research Article

Numerical Investigation for Radiative Transport in Magnetized Flow of Nanofluids due to Moving Surface

Hassan Waqas,[1] Shan Ali Khan,[1] Metib Alghamdi,[2] and Taseer Muhammad[2]

[1]*Department of Mathematics, Government College University Faisalabad, Layyah Campus, Layyah 31200, Pakistan*
[2]*Department of Mathematics, College of Sciences, King Khalid University, Abha 61413, Saudi Arabia*

Correspondence should be addressed to Taseer Muhammad; taseer_qau@yahoo.com

Received 10 August 2021; Revised 15 September 2021; Accepted 25 September 2021; Published 7 October 2021

Academic Editor: Ahmed Zeeshan

In this article, we examined the magnetized flow of ethylene glycol- (50 – 50%) water-based nanoliquids comprising molybdenum disulfide (MoS_2) across a stretching sheet. Flow properties were examined under the impacts of magnetic field and thermal radiation. The behavior of heat generation/absorption is also accounted. Similarity transformations are used on the system of PDEs to get nondimensional ODEs. The obtained nondimensional ODEs are solved with the help of the Runge–Kutta–Fehlberg method via computational software MATHEMATICA. The behavior of prominent parameters for velocity and thermal profiles is plotted graphically and discussed in detail. It is depicted that the temperature field is upgraded with increase in the heat generation/absorption parameter. Furthermore, a larger Schmidt number causes reduction in the concentration field. The current formulated model may be useful in biomedical engineering, biotechnology, nanotechnology, biosensors, crystal growth, plastic industries, and mineral and cleaning oil manufacturing.

1. Introduction

Nanofluids play an essential role in our daily life assisting innovations in industries such as HVAC, electronics, and automotive and mechanical engineering for efficient increase of heat energy of fluids and improving heat transmission in materials. Nanofluids are often characterized when nanoparticles are combined with some regular fluids. The use of a liquid with disseminated particles as a heat-transfer fluid has been around for a long time; nevertheless, owing to sedimentation of the dispersed particles, the traditional scattered fluids cannot be used. Nanofluids do not have the aforementioned drawbacks. The inclusion of nanoparticles (metals or their oxides) in very small-volume fractions significantly increases the heat proficiency of the base fluid. According to the conclusions of the first experiments on nanofluid heat capacity, nanofluids are observed to be heat-transfer fluids that are exceptionally reactive and can be utilized rather than water.

To improve the emphatically viable qualities of one another, an ideal mix of nanoparticles should be chosen. Keeping this in view, Suresh [1] first and foremost proposed the possibility of using half and half nanofluids to all the more likely improve the critical qualities of normal nanoparticles. An assortment of logical investigation distributions were obtained on the possibility of mixture nanofluids. Momin [2] provided an observational examination of convective and crossover nanoparticles for laminar streaming in tendency cylinders. Crossover nanofluids involve at least two kinds of nanoparticles having new thermophysical and compound aspects that are fit for upgrading power of thermal transportation inferable from synergic sway [3]. Tian et al. [4] discussed 2-D and 3-D executions and their impact on thermal sink viability of the MHD half-breed nanoparticle subject to slip and nonslip streams. Al-Hossainy et al. [5] reviewed the highest order rate of rotating reactants of single nanofluid ($PEG - H_2O/ZrO_2$) and hybrid nanofluid ($PEG - H_2O/ZrO_2 + MgO$) over the stretching surface. Roy et al. [6] assessed the transport of micropolar water-based hybrid nanoliquids through a stretchable surface. Effects of porous circle with powerful properties of stage

alter measure through PCM improved roundabout line all through nanofluid constrained convective in scattering working point is examined by Alizadeh et al. [7]. The outcomes of transport using water-based crossover nanoliquids with heat features were accounted by Fazeli et al. [8]. Kumar et al. [9] explored examination of thermal transport improvement observed because of the impact of significant liquid fluctuation qualities in the presence of radiation on cross-breed nanoliquids. Aziz et al. [10] discussed Powell–Eyring water-based cross-breed transport of nanoliquids with convective heat transmission under volumetric entropy improvement for the consistently flat penetrable extending sheet. Haider et al. [11] examined nanofluid transport in a Darcy–Forchheimer permeable space through a rotating plate. Few studies of hybrid nanoliquids with different geometries are provided in [12–18].

The influence of magnetic field on an electrical current-conductive liquid has an impact on boundary layer transport because of ionization. If the ionized liquid with the lower density is affected by a stronger electromagnetic field, then final conduction of the fluid decreases and, as a result, free-ion spiraling of electromagnetic field lines cause natural current in magnetic and electrical fields. This current is named as "Hall current." The magnetic field is considered highly important in a variety of nanofluid technologies and industrial applications. Several devices, such as motors, bearings, and magnetohydrodynamic devices, geophysical configurations, and chemical processes are intensely traumatized by the effect of magnetohydrodynamics magnetostrictive physical occurrences of fluids. Magnetohydrodynamics has numerous chemical and industrial manufacturing applications in the related industrial sectors where temperature disruptions exist. Usually, variations can fall below 350 degrees centigrade. Alfven in 1942 firstly proposed the concept of magnetohydrodynamics [19]. Kholshchevnik [20] in the nineteen century employed two combined cathodes in the magnetohydrodynamic generator to observe the impact of boundary current. Zainal et al. [21] noticed magnetohydrodynamic water-based mixture (Al_2O_3/H_2O) nanoliquid transport through a permeable extended/shrinked surface with quadratic velocity. Patil et al. [22] investigated attributes of magnetohydrodynamic Prandtl nanoliquid transport through an extending surface. Elayarani et al. [23] explored the numerical framework for 2-dimensional bioconvective Carreau nanoliquid, incorporating motile microorganisms with the electromagnetic field and slip features. Sabu et al. [24] considered magnetohydrodynamic (MHD) convection ferro-nanofluids (Fe_3O_4-water) transport through a channel. Saqib et al. [25] discussed MHD transport of a ferro-nanoliquid mixture in presence of radiation. Almakki et al. [26] assessed the magnetohydrodynamic micropolar-nanoliquid transport using an extending sheet. Yasmin et al. [27] developed magnetohydrodynamic Casson nanoliquid transport using the Brinkman framework. Few studies on magnetohydrodynamics (MHD) with hybrid nanoliquids can be seen in [28–34].

Thermal radiation moves at a pace equivalent to that of lighting. Effect of thermal radiation is an important part of the research due to its realistic engineering applications such as furnace construction, glass manufacturing, gas-cooled nuclear power plant construction, polymer manufacturing, and propelled systems. Firstly, Hunt in 1978 presented the concept of generating radiation by utilizing nanoparticles [35]. Siddiqa et al. [36] assessed convection in micropolar nanoliquids in the presence of thermal radiation. Magnetohydrodynamic (MHD) transport of nanoliquids through wedges was presented by Sreedevi et al. [37]. Malek et al. [38] analyzed numerical clarification of Rosseland relation for thermal radiation in improved essential capacities. Gireesha et al. [39] assessed nanomaterials of half and half nanofluid subject to convective conditions. Zainal et al. [40] addressed thermal transport properties of water-based nanoliquids under impacts of MHD and thermal radiation through a permeable moving sheet. Hayat et al. [41] examined the features of thermal radiation on 3-D flow of nanoliquids through carbon nanotubes. Eid et al. [42] explored the gold-blood nanofluid to improve the heat-transfer rate. Rana et al. [43] investigated the thermal radiation effects on nanoliquid flow by adopting the Buongiorno model. Khan et al. [44] investigated the entropy generation aspects on the Williamson nanofluid under the effects of a chemical reaction. Gireesha et al. [39] examined the thermal radiation impacts on hybrid nanoliquids. Khan et al. [45] explored the hybrid nanoliquid with entropy of the system.

Nanoparticles have the ability to expand surface area and thermal efficiency and engage fluid particles with one another in liquids. As a result, this phenomenon is crucial in industrial operations, as well as solar sources of energy and biomedical therapies. A nanofluid has recently been found to be important in a wide range of heat transmission techniques. Generator cooling, refrigeration, and heating in structures, circuit cooling, cooling systems, the coolant in cutting, and the coolant in machining, automotive cooling, and radioactive system cooling are few applications of nanofluids. Numerous researchers were inspired to use nanofluids to solve real-world heat transfer issues as a result of these relevant implementations. Motivated from the above survey of the literature, the novelty of the current study was to obtain the numerical solution of ethylene glycol- (50 – 50%) water-based nanoliquid flow containing molybdenum disulfide (MoS_2) through a stretched sheet. To fulfill this gap in the current analysis, we have considered the magnetized MoS_2-ethylene glycol- (50 – 50%) water-based nanoliquid with thermal radiation and heat source/sink configured with a stretching sheet. The system of PDEs is reduced to ODEs. The numerical outcomes are found with the Runge–Kutta–Fehlberg method using software MATHEMATICA. The outcomes of velocity, temperature, and concentration according to different variations of the involved parameters are dissected graphically. The effects of nanoparticle volume fraction, thermal radiation, and heat source/sink are valuable characteristics towards the novelty of the accounted model.

2. Mathematical Formulation

Consider the two-dimensional flow of the MoS_2-ethylene glycol- (50 – 50%) water-based nanoliquid over a stretching sheet. Let us assume the Cartesian coordinate (x, y) in such a way that x-axis is along the sheet and y-axis is perpendicular to it (see Figure 1). Here, molybdenum disulfide (MoS_2) is used as nanoparticles in ethylene glycol-water (50 – 50%) mixture. The impacts of thermal radiation and heat generation/absorption are considered. Let T_w and C_w be the surface temperature and concentration, respectively. The assumptions of the current analysis are as follows [46, 47]:

(i) Two-dimensional steady flow of nanofluid is developed

(ii) The flow is generated through a stretching surface

(iii) Heat-transfer improvement through MoS_2-ethylene glycol- (50 – 50%) water-based nanofluid is considered

(iv) Heat absorption/generation and thermal radiation are present

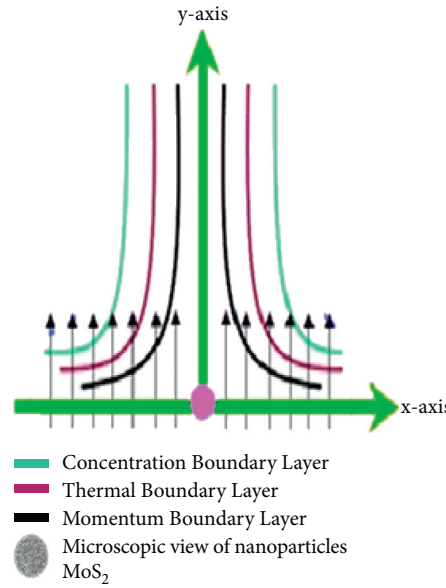

Figure 1: Physical view of the model.

The governing equations are [46, 48]

$$\begin{aligned}
&\partial_x u + \partial_y v = 0,\\
&u\partial_x u + v\partial_y u = \frac{\mu_{nf}}{\rho_{nf}}\partial_{yy} u - \frac{\sigma_{nf}}{\rho_{nf}} B_0^2 u,\\
&u\partial_x T + v\partial_y T = \frac{k_{nf}}{(\rho c_p)_{nf}}\partial_{yy} T - \frac{1}{(\rho c_p)_{nf}}\partial_y q_r + \frac{Q_0}{(\rho c_p)_{nf}}(T - T_0),\\
&u\partial_x C + v\partial_y C = D_m \partial_{yy} C.
\end{aligned} \tag{1}$$

The boundary conditions are [46, 48]

$$\begin{aligned}
u = U_w, v = 0, T = T_w = T_0 + Ax^{n+1}, C = C_w = C_0 + Bx^{n+1} \text{ at } y = 0,\\
u \longrightarrow 0, T \longrightarrow T_0, C \longrightarrow C_0 \text{ as } y \longrightarrow \infty.
\end{aligned} \tag{2}$$

Here, μ_{nf} denotes the nanofluid dynamic viscosity, ρ_{nf} denotes the density of nanofluid, $(\rho c_p)_{nf}$ denotes the nanofluid specific heat, σ_{nf} denotes the electric conductivity of nanofluid, T denotes the temperature, k_{nf} denotes the nanofluid thermal conductivity, T_0 denotes the temperature away from the surface, and C_0 denotes the concentration away from the surface.

We considered the following similarity variables [46]:

$$
\begin{aligned}
u &= C_1 C_2 x^{(2n+1)/3} f', \\
v &= -\left[\left(\frac{2+n}{3}\right) C_1 x \frac{n-1}{3} f + C_1 \xi x \frac{n-1}{3} f'\right], \\
\theta(\eta) &= \frac{T - T_0}{A x^{n+1}}, \\
g(\eta) &= \frac{C - C_0}{B x^{n+1}}, \\
\xi &= C_2 x \frac{n-1}{3} y, \\
C_1 &= \sqrt[4]{\frac{\sigma_T A \mu_f}{\rho_f^2}}, \\
C_2 &= \sqrt[4]{\frac{\sigma_T A \rho_f}{\mu_f^2}}, \\
A &= \frac{\Delta T}{x^{n+1}} 5, \\
B &= \frac{\Delta C}{x^{n+1}} 5.
\end{aligned}
\tag{3}
$$

The dimensionless system is defined by

$$
\frac{1}{\phi_1} f'''[\eta] + \frac{2+n}{3} f[\eta] f''[\eta] - \frac{2n+1}{3} f'^2[\eta] - \phi_2 M f'[\eta] = 0,
\tag{4}
$$

$$
\begin{aligned}
\phi_3 (1 + R\ d)\theta''[\eta] + \frac{2+n}{3} Pr f[\eta]\theta'[\eta] \\
- (1+n)\mathrm{Pr} f'[\eta]\theta[\eta] + Q\theta[\eta] = 0,
\end{aligned}
\tag{5}
$$

$$
g''[\eta] + \frac{2+n}{3} Sc f[\eta] g'[\eta] - (1+n) Sc f'[\eta] g[\eta] = 0,
\tag{6}
$$

$$
\begin{aligned}
f(0) &= 0, \\
f'(0) &= 1, \\
\theta(0) &= 1, \\
g(0) &= 1, \\
f'(\infty) &\longrightarrow 0, \\
\theta(\infty) &\longrightarrow 0, \\
g(\infty) &\longrightarrow 0.
\end{aligned}
\tag{7}
$$

The flow-controlling parameters and constant terms appearing in expressions (4–7) are listed as follows: magnetic parameter ($M = \sigma_f B_0^2 / C_1 C_2 \rho_f$); Prandtl number ($\mathrm{Pr} = \nu_f / \alpha_f$); Schmidt number ($Sc = \alpha / D_m$); heat generation parameter ($Q = Q_0 / (\rho c_p)_{nf}$); thermal radiation parameter ($R\ d = 16\sigma^* T_\infty^3 / 3k^* k_f$). Also,

$$
\begin{aligned}
\phi_1 &= (1-\phi)^{2.5}\left(1 - \phi + \phi\left(\frac{\rho_s}{\rho_f}\right)\right), \\
\phi_2 &= \frac{\sigma_{nf}}{\sigma_f} = 1 + \frac{3\phi\left(\left(\sigma_s/\sigma_f\right) - 1\right)}{\left(\left(\sigma_s/\sigma_f\right) + 2\right) - \phi\left(\left(\sigma_s/\sigma_f\right) - 1\right)}, \\
\phi_3 &= \frac{k_{nf}}{k_f} = \frac{k_s + 2k_f - 2\phi\left(k_f - k_s\right)}{k_s + 2k_f + 2\phi\left(k_f - k_s\right)}.
\end{aligned}
\tag{8}
$$

The mathematical form of Nusselt number is

$$
Nu_x = \frac{x q_w|_{y=0}}{k_f (T_w - T_0)},
\tag{9}
$$

where

$$
q_w = \left(-k_{nf} \partial_y T + q_r\right).
\tag{10}
$$

The dimensionless Nusselt number is addressed by

$$
Nu_x \mathrm{Re}_x^{-0.5} = -\frac{k_{nf}}{k_f} (1 + R\ d)\theta'(0),
\tag{11}
$$

in which $\mathrm{Re}_x (= U_w x / \nu_f)$ describes the local Reynolds number.

3. Numerical Method and Validation

In this segment, governing coupled ODEs (4–6) with suitable boundary conditions (7) have been solved numerically by utilizing the Runge–Kutta–Fehlberg method with the help of computational software MATHEMATICA. In the current work, the steady 2-D ethylene glycol-water-based nanoliquid transport with magnetohydrodynamic effect is considered. The results of the current analysis are accurate and more useful in engineering problems. The following procedure is used to reduce the higher-order equations:

$$
\begin{aligned}
f &= q_1, \\
f' &= q_2, \\
f'' &= q_3, \\
f''' &= q_3', \\
\theta &= q_4, \\
\theta' &= q_5, \\
\theta'' &= q_5', \\
g &= q_6, \\
g' &= q_7, \\
g'' &= q_7',
\end{aligned}
$$

Table 1: Comparative study of $-\theta'(0)$ for varying Pr when $M = Q = R\ d = \phi = 0$.

Pr	Ghalambaz et al. [49]	Khan and Pop [50]	Gorla and Sidawi [51]	Current results
0.7	0.4541	0.4539	0.4539	0.4540
2.0	0.9114	0.9113	0.9114	0.9115
7.0	1.8954	1.8954	1.8954	1.8954

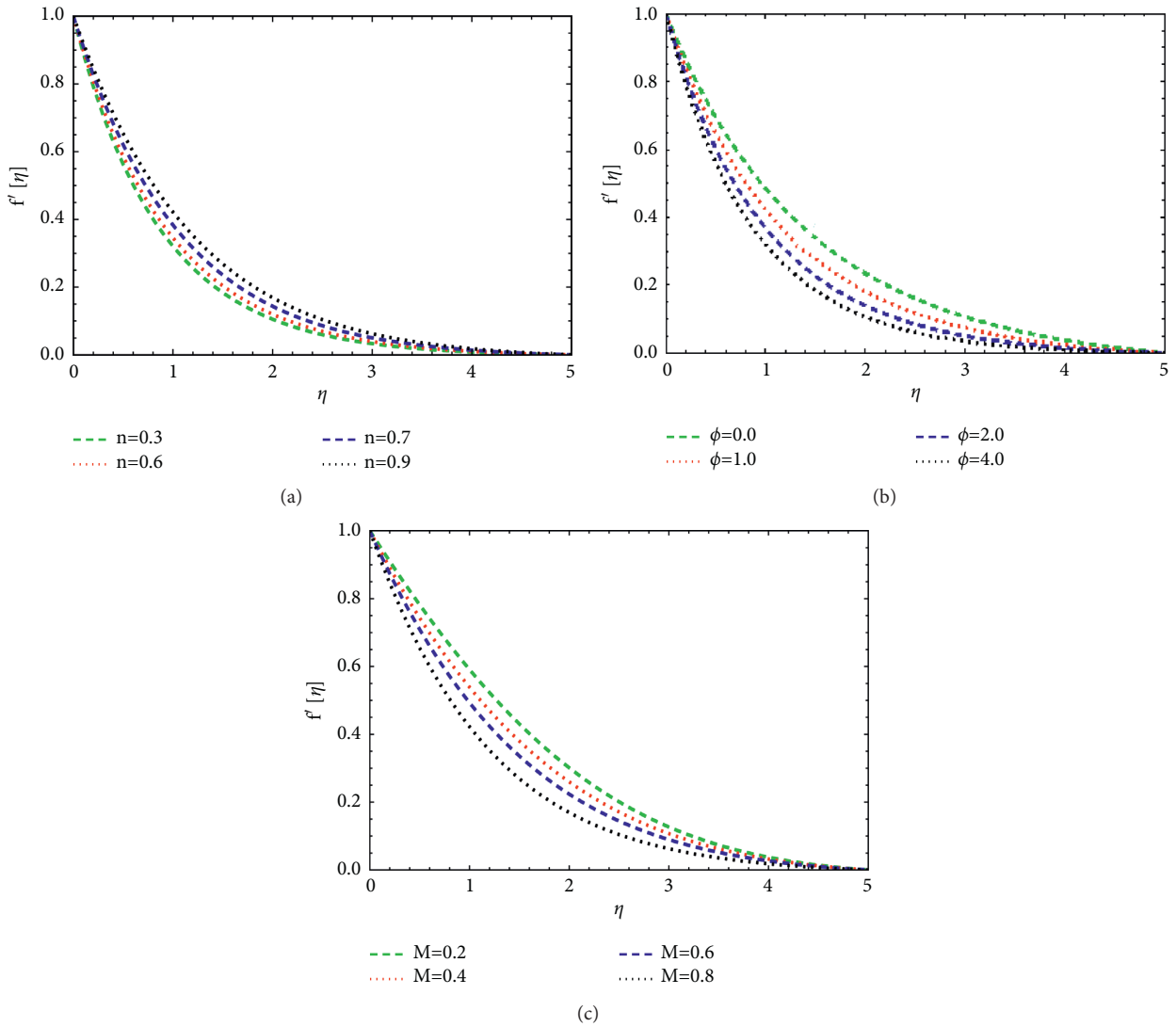

Figure 2: Fluctuations of the velocity field $f'[\eta]$ against the (a) exponential constant n, (b) nanoparticle volume fraction ϕ, and (c) magnetic parameter M.

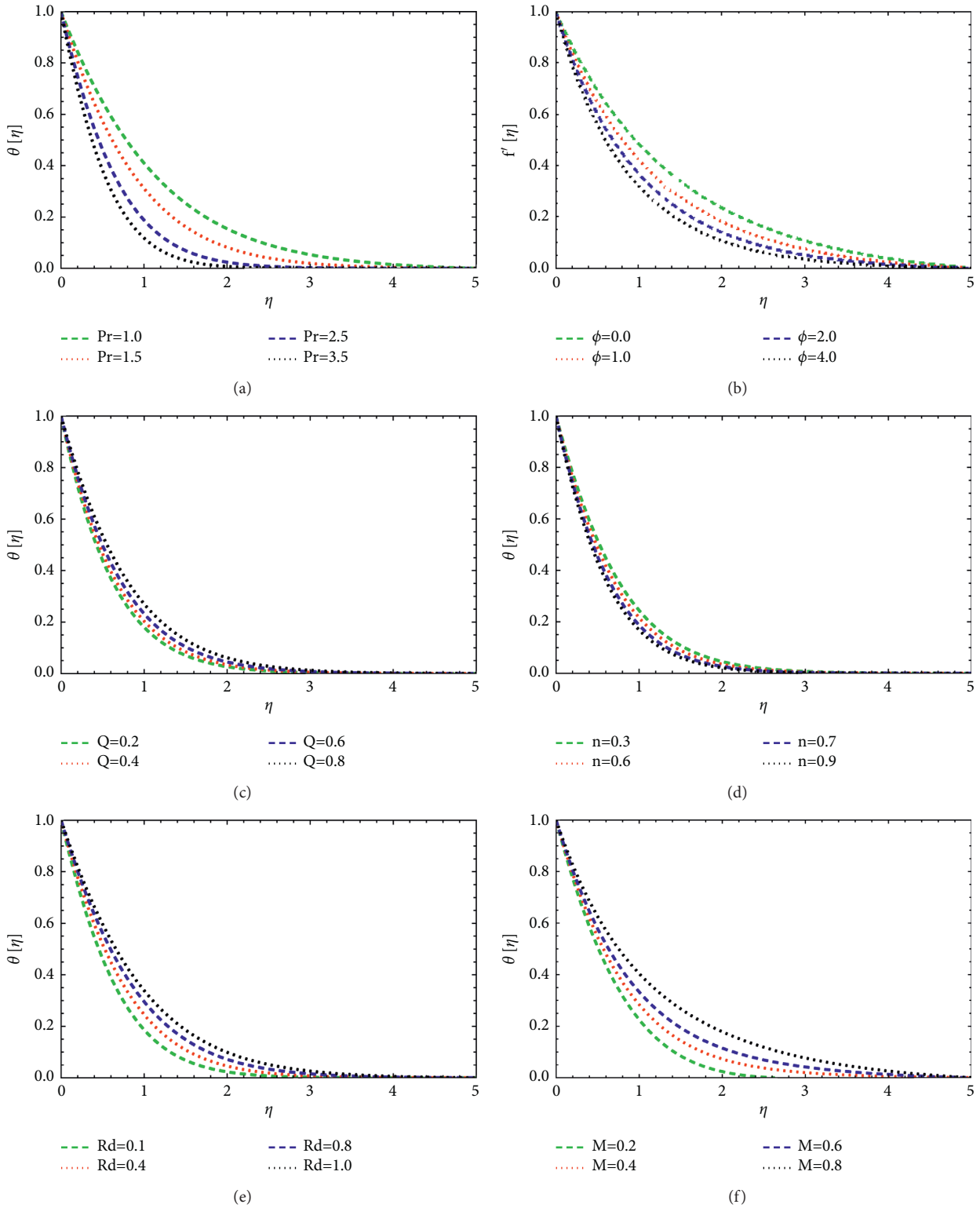

FIGURE 3: Fluctuations of the thermal field $\theta[\eta]$ against the (a) Prandtl number Pr, (b) nanoparticle volume fraction ϕ, (c) heat generation parameter Q, (d) exponential constant n, (e) thermal radiation parameter $R\,d$, and (f) magnetic parameter M.

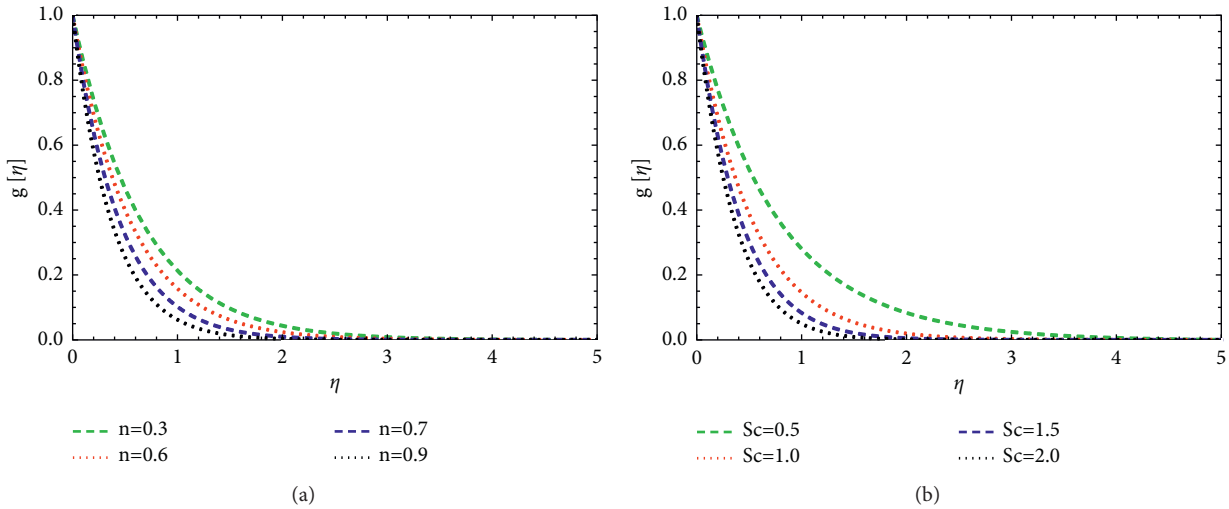

FIGURE 4: Fluctuations of the concentration field $g[\eta]$ against the (a) exponential constant n and (b) Schmidt number Sc.

$$
\begin{aligned}
q_3' &= \phi_1\left(-(2+n/3)q_1q_3 + (2n+1/3)q_2^2 + \phi_2 M q_2\right),\\
q_5' &= \frac{-(2+n/3)\mathrm{Pr}q_1q_5 + (1+n)\mathrm{Pr}q_1q_4 - Qq_4}{\phi_3\,(1+R\,d)},\\
q_7' &= -\frac{2+n}{3}Scq_1q_7 + (1+n)Scq_2q_6,\\
q_1(0) &= 0,\\
q_2(0) &= 1,\\
q_4(0) &= 1,\\
q_6(0) &= 1,\\
q_2(\infty) &\longrightarrow 0,\\
q_4(\infty) &\longrightarrow 0,\\
q_6(\infty) &\longrightarrow 0.
\end{aligned}
\tag{12}
$$

In Table 1, the comparative study of $-\theta'(0)$ for different values of Pr with already published works in a limiting situation is presented. Here, we have seen good agreement between the currents results and already published works in this limiting situation. We have set the relative tolerance to 10^{-5} and acquired high-precision results for this scrutinization.

4. Results and Discussion

Figure 2(a) discloses the nature of the velocity field $f'[\eta]$ against an exponential constant n for the Ag-ethylene glycol/water nanofluid. It is noted that flow is exaggerated by increasing the estimations of the exponential constant n. Figure 2(b) is drawn to depict the behavior of the nanoparticle volume fraction ϕ versus the velocity profile $f'[\eta]$. It is depicted that the velocity field $f'[\eta]$ is a decreasing function of the nanoparticle volume fraction ϕ. Figure 2(c) displays the effect of M on velocity $f'[\eta]$ for the Ag-ethylene glycol/water nanofluid. It is analyzed that $f'[\eta]$ declines with larger M. When the magnetic parameter rises, a significant resistance is created among the particles, causing heat to be developed in the fluid. A drag force termed "Lorentz force" was created by slapping the magnetic field. Figure 3(a) displays the estimations of the thermal field $\theta[\eta]$ via distinguished values of the Prandtl number Pr. It can be revealed that $\theta[\eta]$ declines with larger Pr. The Prandtl number has an inverse relationship with thermal diffusivity. As the Prandtl number rises, thermal diffusion weakens and the temperature distribution dissipates. The effects of nanoparticle volume fraction ϕ on the thermal field $\theta[\eta]$ are revealed through Figure 3(b). The increment in the thermal field $\theta[\eta]$ is observed by increasing values of the nanoparticle volume fraction ϕ. Figure 3(c) is designed to scrutinize the effect of the heat generation/absorption parameter Q on the thermal field $\theta[\eta]$. The thermal field $\theta[\eta]$ is boosted up with a larger heat generation/absorption parameter Q. Figure 3(d) is drawn to examine the variations of the thermal field $\theta[\eta]$ via the larger exponential constant n. From the variations of data, we observed that the thermal field $\theta[\eta]$ declines with greater magnitudes of exponential constant n. The consequence of $R\,d$ via the thermal field $\theta[\eta]$ is shown in Figure 3(e). Here, $\theta[\eta]$ is enhanced with increasing estimations of $R\,d$. For the higher thermal radiation parameter, the system's interior energy source grows physically. As a result, the thermal profile rises. Figure 3(f) is depicted to visualize the impact of M on the thermal field $\theta[\eta]$. Here, the thermal field $\theta[\eta]$ is upgraded with an increase in magnetic parameter M. Physically, the magnetic field increases the temperature, resulting in a thickening of the thermal layer. It is apparent that temperature distribution has been improved. Figure 4(a) signifies the effect of exponential constant n against concentration field $g[\eta]$. It is analyzed that concentration $g[\eta]$ is reduced for larger estimations of the exponential constant n. Figure 4(b) is captured to observe the effect of Schmidt number Sc against concentration distribution $g[\eta]$. It is interesting to notice that concentration $g[\eta]$ is reduced via a larger Schmidt number Sc. Tables 2 and 3 display thermophysical features of nanomaterials and base liquids.

Table 2: Thermophysical properties of nanomaterials [46].

Characteristics	Nanomaterials
Density	$\rho_{nf} = \rho_f(1-\phi+\phi\rho_s/\rho_f)$
Viscosity	$\mu_{nf} = \mu_f/(1-\phi)^{2.5}$
Thermal conductivity	$k_{nf}/k_f = k_s + 2k_f - 2\phi(k_f - k_s)/k_s + 2k_f + 2\phi(k_f - k_s)$
Heat capacity	$(\rho c_p)_{nf} = (\rho c_p)_f(1-\phi+\phi(\rho c_p)_s/(\rho c_p)_f)$
Electric conductivity	$\sigma_{nf}/\sigma_f = 1 + 3(\sigma-1)\phi/(\sigma+2) - (\sigma-1)\phi$

Table 3: Thermophysical properties of the base liquid and nanomaterials [46].

Properties	MoS_2	Ethylene glycol-water (50–50%)
ρ (kg/m^3)	5060	1063.8
k (W/mK)	904.4	400
c_p (J/kgK)	397.21	385
σ (Ω.m)	2.09×10^{-4}	9.75×10^{-4}

5. Conclusions

In this work, incompressible two-dimensional ethylene glycol- (50 – 50%) water-based nanoliquids containing molybdenum disulfide (MoS_2) particles over a stretching surface has been scrutinized. The analysis is executed during occurrences of thermal radiation and heat absorption/generation. Similarity transformations are used on the system of PDEs to get nondimensional ODEs. The obtained nondimensional ODEs are solved with the help of the Runge–Kutta–Fehlberg method via computational software MATHEMATICA. With increasing estimations of the exponential constant, the velocity field of the nanofluid enhances. The Prandtl number and nanoparticle volume fraction have opposite impacts on the thermal field [52–54]. The larger values of the thermal radiation parameter lead to a stronger thermal field. The concentration distribution is reduced with a higher exponential constant.

Nomenclature

u, v: Velocity components (ms^{-1})
C_0: Ambient concentration (mol.L^{-1})
x, y: Coordinates system (m)
T_w: Surface temperature (K)
B_0: Magnetic field strength (Nm^{-1}A^{-1})
C_w: Surface concentration (mol.L^{-1})
T: Temperature (K)
M: Magnetic parameter
q_r: Radiative heat flux
$R\,d$: Thermal radiation parameter
Q_0: Coefficient of heat generation/absorption
g: Dimensionless concentration
C: Concentration (mol.L^{-1})
Q: Heat generation/absorption parameter
T_0: Ambient temperature (K)
Sc: Schmidt number
n: Exponent constant
Pr: Prandtl number

Greek symbols and subscripts

μ_{nf}: Dynamic viscosity of the nanofluid (Pas)
w: Wall condition
σ_{nf}: Electric conductivity (Ω^{-1}m^{-1})
nf: Nanofluid
ρ_{nf}: Density of the nanofluid (kgm^{-3})
f: Base fluid
k_{nf}: Thermal conductivity of the nanofluid (Wm^{-1}K^{-1})
s: Solid particle
$(\rho c_p)_{nf}$: Specific heat (J.Kg^{-3}.K^{-1})
$(\rho c_p)_f$: Base fluid specific heat (J.Kg^{-1}.K^{-1})
ϕ: Volume fraction of the nanoparticle
θ: Dimensionless temperature.

Data Availability

The data used to support the findings of this study are included within the article.

Conflicts of Interest

The authors declare that they have no conflicts of interest.

Acknowledgments

The authors extend their appreciation to the Deanship of Scientific Research at King Khalid University, Abha, Saudi Arabia, for funding this work through the research groups program under grant number R.G.P-2/104/42.

References

[1] S. Suresh, K. P. Venkitaraj, P. Selvakumar, and M. Chandrasekar, "Synthesis of Al2O3-Cu/water hybrid nanofluids using two step method and its thermo physical properties," *Colloids and Surfaces A: Physicochemical and Engineering Aspects*, vol. 388, no. 1-3, pp. 41–48, 2011.

[2] G. G. Momin, "Experimental investigation of mixed convection with water-Al2O3 & hybrid nanofluid in inclined tube for laminar flow," *International Journal of Environmental Science and Technology*, vol. 2, no. 12, pp. 195–202, 2013.

[3] J. Sarkar, P. Ghosh, and A. Adil, "A review on hybrid nanofluids: recent research, development and applications," *Renewable and Sustainable Energy Reviews*, vol. 43, pp. 164–177, 2015.

[4] M.-W. Tian, S. Rostami, S. Aghakhani, A. S. Goldanlou, and C. Qi, "A techno-economic investigation of 2D and 3D configurations of fins and their effects on heat sink efficiency of MHD hybrid nanofluid with slip and non-slip flow,"

International Journal of Mechanical Sciences, vol. 189, Article ID 105975, 2021.

[5] A. F. Al-Hossainy and M. R. Eid, "Combined experimental thin films, tddft-dft theoretical method, and spin effect on [PEG-H2O/ZrO2+ MgO] h hybrid nanofluid flow with higher chemical rate," *Surfaces and Interfaces*, vol. 23, Article ID 100971, 2021.

[6] N. C. Roy, M. Hossain, and I. Pop, "Analysis of dual solutions of unsteady micropolar Hybrid nanofluid flow over a stretching/shrinking sheet," *Journal of Applied and Computational Mechanics*, vol. 7, no. 1, pp. 19–33, 2021.

[7] R. Alizadeh, J. M. N. Abad, A. Fattahi et al., "A machine learning approach to predicting the heat convection and thermodynamics of an external flow of hybrid nanofluid," *Journal of Energy Resources Technology*, vol. 143, no. 7, 2021.

[8] I. Fazeli, M. R. Sarmasti Emami, and A. Rashidi, "Investigation and optimization of the behavior of heat transfer and flow of MWCNT-CuO hybrid nanofluid in a brazed plate heat exchanger using response surface methodology," *International Communications in Heat and Mass Transfer*, vol. 122, Article ID 105175, 2021.

[9] K. G. Kumar, E. H. B. Hani, M. E. H. Assad, M. Rahimi-Gorji, and S. Nadeem, "A novel approach for investigation of heat transfer enhancement with ferromagnetic hybrid nanofluid by considering solar radiation," *Microsystem Technologies*, vol. 27, no. 1, pp. 97–104, 2021.

[10] A. Aziz, W. Jamshed, T. Aziz, H. M. S. Bahaidarah, and K. Ur Rehman, "Entropy analysis of Powell-Eyring hybrid nanofluid including effect of linear thermal radiation and viscous dissipation," *Journal of Thermal Analysis and Calorimetry*, vol. 143, no. 2, pp. 1331–1343, 2021.

[11] F. Haider, T. Hayat, and A. Alsaedi, "Flow of hybrid nanofluid through Darcy-Forchheimer porous space with variable characteristics," *Alexandria Engineering Journal*, vol. 60, no. 3, pp. 3047–3056, 2021.

[12] R. J. Punith Gowda, R. Naveen Kumar, A. Aldalbahi et al., "Thermophoretic particle deposition in time-dependent flow of hybrid nanofluid over rotating and vertically upward/downward moving disk," *Surfaces and Interfaces*, vol. 22, Article ID 100864, 2021.

[13] L. M. Jasim, H. Hamzah, C. Canpolat, and B. Sahin, "Mixed convection flow of hybrid nanofluid through a vented enclosure with an inner rotating cylinder," *International Communications in Heat and Mass Transfer*, vol. 121, Article ID 105086, 2021.

[14] P. Tiam Kapen, C. Gervais Njingang Ketchate, D. Fokwa, and G. Tchuen, "Linear stability analysis of (Cu-Al2O3)/water hybrid nanofluid flow in porous media in presence of hydromagnetic, small suction and injection effects," *Alexandria Engineering Journal*, vol. 60, no. 1, pp. 1525–1536, 2021.

[15] R. Ekiciler, "Effects of novel hybrid nanofluid (TiO2-Cu/EG) and geometrical parameters of triangular rib mounted in a duct on heat transfer and flow characteristics," *Journal of Thermal Analysis and Calorimetry*, vol. 143, no. 2, pp. 1371–1387, 2021.

[16] V. Kumar, J. Sarkar, and W.-M. Yan, "Thermal-hydraulic behavior of lotus like structured rGO-ZnO composite dispersed hybrid nanofluid in mini channel heat sink," *International Journal of Thermal Sciences*, vol. 164, Article ID 106886, 2021.

[17] S. S. M. Ajarostaghi, M. Zaboli, and M. Nourbakhsh, "Numerical evaluation of turbulence heat transfer and fluid flow of hybrid nanofluids in a pipe with innovative vortex generator," *Journal of Thermal Analysis and Calorimetry*, vol. 143, no. 2, pp. 1583–1597, 2021.

[18] F. Abbas, H. M. Ali, M. Shaban et al., "Towards convective heat transfer optimization in aluminum tube automotive radiators: potential assessment of novel Fe2O3-TiO2/water hybrid nanofluid," *Journal of the Taiwan Institute of Chemical Engineers*, 2021.

[19] H. Alfvén, "Existence of electromagnetic-hydrodynamic waves," *Nature*, vol. 150, no. 3805, pp. 405-406, 1942.

[20] E. K. Kholshchevnikova, "Influence of the Hall effect on the characteristics of a MHD generator with two pairs of electrodes," *Journal of Applied Mechanics and Technical Physics*, vol. 7, no. 4, pp. 48–54, 1966.

[21] N. A. Zainal, R. Nazar, K. Naganthran, and I. Pop, "Stability analysis of MHD hybrid nanofluid flow over a stretching/shrinking sheet with quadratic velocity," *Alexandria Engineering Journal*, vol. 60, no. 1, pp. 915–926, 2021.

[22] A. B. Patil, P. P. Humane, V. S. Patil, and G. R. Rajput, "MHD Prandtl Nanofluid flow due to convectively heated stretching sheet below the control of chemical reaction with thermal radiation," *International Journal of Ambient Energy*, pp. 1–13, 2021.

[23] M. Elayarani, M. Shanmugapriya, and P. Senthil Kumar, "Intensification of heat and mass transfer process in MHD carreau nanofluid flow containing gyrotactic microorganisms," *Chemical Engineering and Processing - Process Intensification*, vol. 160, Article ID 108299, 2021.

[24] A. S. Sabu, A. Mathew, T. S. Neethu, and K. Anil George, "Statistical analysis of MHD convective ferro-nanofluid flow through an inclined channel with hall current, heat source and soret effect," *Thermal Science and Engineering Progress*, vol. 22, Article ID 100816, 2021.

[25] M. Saqib, I. Khan, S. Shafie, and A. Q. Mohamad, "Shape effect on MHD flow of time fractional Ferro-Brinkman type nanofluid with ramped heating," *Scientific Reports*, vol. 11, no. 1, pp. 1–22, 2021.

[26] M. Almakki, H. Mondal, and P. Sibanda, "Onset of unsteady MHD Micropolar nanofluid flow with entropy generation," *International Journal of Ambient Energy*, pp. 1–14, 2021.

[27] A. Yasmin, K. Ali, and M. Ashraf, "MHD Casson nanofluid flow in a square enclosure with non-uniform heating using the Brinkman model," *The European Physical Journal Plus*, vol. 136, no. 2, pp. 1–14, 2021.

[28] W.-F. Xia, I. L. Animasaun, A. Wakif, N. A. Shah, and S.-J. Yook, "Gear-generalized differential quadrature analysis of oscillatory convective Taylor-Couette flows of second-grade fluids subject to Lorentz and Darcy-Forchheimer quadratic drag forces," *International Communications in Heat and Mass Transfer*, vol. 126, Article ID 105395, 2021.

[29] J. C. Umavathi and H. F. Oztop, "Investigation of MHD and applied electric field effects in a conduit cramed with nanofluids," *International Communications in Heat and Mass Transfer*, vol. 121, Article ID 105097, 2021.

[30] A. Wakif, I. L. Animasaun, and R. Sehaqui, "A brief technical note on the onset of convection in a horizontal nanofluid layer of finite depth via wakif-galerkin weighted residuals technique (WGWRT)," in *Defect and Diffusion Forum*, vol. 409, pp. 90–94, Trans Tech Publications Ltd, Freienbach, Switzerland, 2021.

[31] B. Ali, R. A. Naqvi, A. Mariam, L. Ali, and O. M. Aldossary, "Finite element study for magnetohydrodynamic (MHD) tangent hyperbolic nanofluid flow over a faster/slower stretching wedge with activation energy," *Mathematics*, vol. 9, no. 1, p. 25, 2021.

[32] A. Wakif and R. Sehaqui, "Generalized differential quadrature scrutinization of an advanced MHD stability problem concerned water-based nanofluids with metal/metal oxide nanomaterials: a proper application of the revised two-phase nanofluid model with convective heating and through-flow boundary conditions," *Numerical Methods for Partial Differential Equations*, 2020.

[33] M. Jawad, A. Saeed, and T. Gul, "Entropy generation for MHD maxwell nanofluid flow past a porous and stretching surface with dufour and soret effects," *Brazilian Journal of Physics*, pp. 1–12, 2021.

[34] A. Kardgar, "Numerical investigation of MHD oscillating power-law non-Newtonian nanofluid flow in an enclosure," *The European Physical Journal Plus*, vol. 136, no. 1, pp. 1–19, 2021.

[35] A. J. Hunt, *Small Particle Heat Exchangers, Report LBL-78421 for the US Department of Energy*, Lawrence Berkeley Laboratory, Berkeley, CA, USA, 1978.

[36] S. Siddiqa, N. Begum, M. A. Hossain, M. N. Abrar, R. S. R. Gorla, and Q. Al-Mdallal, "Effect of thermal radiation on conjugate natural convection flow of a micropolar fluid along a vertical surface," *Computers & Mathematics with Applications*, vol. 83, pp. 74–83, 2021.

[37] P. Sreedevi and P. Sudarsana Reddy, "Heat and mass transfer analysis of MWCNT-kerosene nanofluid flow over a wedge with thermal radiation," *Heat Transfer*, vol. 50, no. 1, pp. 10–33, 2021.

[38] M. Malek, N. Izem, M. S. Mohamed, M. Seaid, and M. Wakrim, "Numerical solution of Rosseland model for transient thermal radiation in non-grey optically thick media using enriched basis functions," *Mathematics and Computers in Simulation*, vol. 180, pp. 258–275, 2021.

[39] B. J. Gireesha, G. Sowmya, M. I. Khan, and H. F. Öztop, "Flow of hybrid nanofluid across a permeable longitudinal moving fin along with thermal radiation and natural convection," *Computer Methods and Programs in Biomedicine*, vol. 185, Article ID 105166, 2020.

[40] N. A. Zainal, R. Nazar, K. Naganthran, and I. Pop, "MHD flow and heat transfer of hybrid nanofluid over a permeable moving surface in the presence of thermal radiation," *International Journal of Numerical Methods for Heat and Fluid Flow*, 2020.

[41] T. Hayat, F. Haider, T. Muhammad, and A. Alsaedi, "Darcy-Forchheimer three-dimensional flow of carbon nanotubes with nonlinear thermal radiation," *Journal of Thermal Analysis and Calorimetry*, vol. 140, no. 6, pp. 2711–2720, 2020.

[42] M. R. Eid, A. Alsaedi, T. Muhammad, and T. Hayat, "Comprehensive analysis of heat transfer of gold-blood nanofluid (Sisko-model) with thermal radiation," *Results in physics*, vol. 7, pp. 4388–4393, 2017.

[43] P. Rana, N. Srikantha, T. Muhammad, and G. Gupta, "Computational study of three-dimensional flow and heat transfer of 25 nm Cu-H2O nanoliquid with convective thermal condition and radiative heat flux using modified Buongiorno model," *Case Studies in Thermal Engineering*, vol. 27, Article ID 101340, 2021.

[44] M. I. Khan, S. Qayyum, T. Hayat, M. I. Khan, and A. Alsaedi, "Entropy optimization in flow of Williamson nanofluid in the presence of chemical reaction and Joule heating," *International Journal of Heat and Mass Transfer*, vol. 133, pp. 959–967, 2019.

[45] M. I. Khan, A. Alsaedi, T. Hayat, and N. B. Khan, "Modeling and computational analysis of hybrid class nanomaterials subject to entropy generation," *Computer Methods and Programs in Biomedicine*, vol. 179, Article ID 104973, 2019.

[46] S. Qayyum, "Dynamics of Marangoni convection in hybrid nanofluid flow submerged in ethylene glycol and water base fluids," *International Communications in Heat and Mass Transfer*, vol. 119, Article ID 104962, 2020.

[47] W. Jamshed, S. Uma Devi S, M. Goodarzi et al., "Evaluating the unsteady casson nanofluid over a stretching sheet with solar thermal radiation: an optimal case study," *Case Studies in Thermal Engineering*, vol. 26, Article ID 101160, 2021.

[48] B. Venkateswarlu and P. V. Satya Narayana, "Cu-Al 2 O 3/H 2 O hybrid nanofluid flow past a porous stretching sheet due to temperatue-dependent viscosity and viscous dissipation," *Heat Transfer*, vol. 50, no. 1, pp. 432–449, 2021.

[49] M. Ghalambaz, E. Izadpanahi, A. Noghrehabadi, and A. Chamkha, "Study of the boundary layer heat transfer of nanofluids over a stretching sheet: passive control of nanoparticles at the surface," *Canadian Journal of Physics*, vol. 93, no. 7, pp. 725–733, 2015.

[50] W. A. Khan and I. Pop, "Boundary-layer flow of a nanofluid past a stretching sheet," *International Journal of Heat and Mass Transfer*, vol. 53, no. 11-12, pp. 2477–2483, 2010.

[51] R. S. Reddy Gorla and I. Sidawi, "Free convection on a vertical stretching surface with suction and blowing," *Applied Scientific Research*, vol. 52, no. 3, pp. 247–257, 1994.

[52] N. Boumaiza, M. Kezzar, M. R. Eid, and I. Tabet, "On numerical and analytical solutions for mixed convection falkner-skan flow of nanofluids with variable thermal conductivity," *Waves in Random and Complex Media*, 2019.

[53] R. Dadsetani, G. A. Sheikhzade, M. Goodarzi, A. Zeeshan, R. Ellahi, and M. R. Safaei, "Thermal and mechanical design of tangential hybrid microchannel and high-conductivity inserts for cooling of disk-shaped electronic components," *Journal of Thermal Analysis and Calorimetry*, vol. 143, no. 3, pp. 2125–2133, 2021.

[54] A. Riaz, A. Zeeshan, and M. M. Bhatti, "Entropy analysis on a three-dimensional wavy flow of eyring–powell nanofluid: a comparative study," *Mathematical Problems in Engineering*, 2021.